Direct Partial Oxidation of Natural Gas to Liquid Chemicals

Rasmussen, Christian Lund

Publication date:
2007

Direct Partial Oxidation of Natural Gas to Liquid Chemicals

Ph.D. Thesis

Christian Lund Rasmussen

July 15, 2007

Supervisor: Peter Glarborg

CHEC Research Centre
Department of Chemical Engineering
Technical University of Denmark

Abstract

Direct homogeneous partial oxidation of natural gas to liquid chemicals (GTL) is an attractive industrial process where natural gas is converted to a readily transportable state; preferably methanol (CH_3OH), in a simple one-step process under fuel rich, high pressure, and relatively low temperature conditions. The GTL process has a potential to improve the utilization of remote natural gas resources if an overall energy efficiency >50 % can be achieved. Past efforts to obtain competitive selectivities and yields of CH_3OH have been unsuccessful; partly due to a lack of understanding of the complex free radical mechanism that governs the hydrocarbon conversion and its interactions with a number of important process parameters. This project initially focuses on the fundamental understanding of the underlying chemistry through detailed kinetic modeling and well-defined experiments. A detailed chemical kinetic model (DCKM) has been developed to provide accurate descriptions of the oxidation chemistry of H_2/O_2, CO/CO_2, and C_{1-2} hydrocarbon fuels in the presence or absence of NO_x, and, to a limited extent, also SO_2, in the high pressure and intermediate temperature range. The DCKM has been developed from a critical review of data for individual elementary reactions with supplementary rate constants determined from reevaluation of literature data or *ab initio* CBS-QB3 calculations. The model performance has been validated with generally satisfactory results against experiments with $CO/H_2/NO_x$, CH_4, CH_4/C_2H_6, CH_4/NO_x, and CH_4/H_2S, at 598–898 K, 20–100 bar, and stoichiometric ratios $0.04 < \phi < 100$. This has justified a detailed outline and discussion of the governing reaction mechanisms based on model predictions. The experiments have been conducted in a novel laboratory scale high pressure flow reactor designed and constructed as a part of this project. The system enables well-defined investigations of homogeneous gas phase chemistry at pressures from 10 to 100 bar, and temperatures up to 925 K. The DCKM has subsequently been used to determine the optimal conditions for high yields of CH_3OH. For this purpose, a numerical global optimization routine has been developed that utilizes interval analysis to ensure location of the *global* optimum. The optimial conditions have been identified as 643 K, 97.4 bar, and a CH_4/O_2 ratio of 23.6 in the feed using a residence time $\geq$ 3 sec. These conditions yield a CH_3OH selectivity of 75 % and a CH_4 conversion of 5.6 % during a single pass of the reactor. This result is not sufficiently close to the defined commercial target range to guarantee industrial feasibility. Even so, the optimal conditions have constituted the basis for preliminary suggestions of potential commercial applications of the GTL process. This includes *first draft* proposals of process designs with supplementary flow sheet calculations. The preliminary results indicate a low overall energy efficiency in the range of ∼20 %, but industrial application may be feasible if further process optimization can improve the removal of unwanted side products from the reactant mixture; or if the purge gas can be capitalized.

Resumé (Summary in Danish)

Direkte delvis oxidation af naturgas til flydende kemikalier er en attraktiv industriel proces, hvor naturgas omdannes til stoffer; primært methanol (CH_3OH), som let kan transporteres over store afstande. Omdannelsen sker i en simpel ettrinsproces under højt tryk, lave forbrændingstemperaturer, samt brændselsrige betingelser. Processen har potentiale til at forbedre udnyttelsen af fjerne naturgas ressourcer, hvis det er muligt at opnå en samlet energieffektivitet på >50 %. Tidligere forsøg på at opnå et konkurrencedygtigt udbytte af CH_3OH har været forgæves, hvilket delvist skyldes en manglende forståelse for den komplicerede friradikalmekanisme som styrer kulbrinteomdannelsen, og dennes samspil med en række vigtige procesparametrer. Dette projekt fokuserer indledningsvist på at opnå en grundlæggende forståelse for den styrende kemi; dels gennem detaljeret kinetisk modellering, dels via eksperimenter udført under veldefinerede betingelser. Dette arbejde har ført til udviklingen af en ny, detaljeret kemisk kinetisk model, der beskriver forbrændingskemien for H_2/O_2, CO/CO_2 og C_{1-2}-kulbrinter med/uden tilsætning af NO_x samt, i et begrænset omfang, også SO_2, under højt tryk og middelhøje temperaturer. Den detaljerede kinetiske model er blevet udviklet på baggrund af en kritisk evaluering af individuelle målinger og karakteriseringer af elementarreaktioner fra litteraturen suppleret med nye hastighedskonstanter udledt fra en revurdering af litteraturdata samt *ab initio*-beregninger. Modellens nøjagtighed er blevet bekræftet ved sammenligninger med koncentrationsmålinger fra eksperimenter med $CO/H_2/NO_x$, CH_4, CH_4/C_2H_6, CH_4/NO_x og CH_4/H_2S, der er blevet udført ved 598–898 K, 20–100 bar, og reaktionsstøkiometriske forhold på $0.04 < \phi < 100$. Dette har yderligere givet anledning til en detaljeret gennemgang af de styrende reaktionsmekanismer baseret på modelforudsigelser. Forsøgene er blevet udført i en ny højtryks-flowreaktoropstilling bygget som en del af det nærværende projekt. Forsøgsopstillingen giver mulighed for at undersøge homogen gasfasekemi ved tryk mellem 10 og 100 bar, samt temperaturer op til 925 K. Den detaljerede kinetiske model har efterfølgende dannet grundlag for en bestemmelse af de optimale procesbetingelser mhp. at opnå et maksimalt udbytte af CH_3OH. En global optimeringsrutine er blevet udviklet til dette formål baseret på intervalanalyse, der sikrer bestemmelse af det *globale* optimum. De optimale procesbetingelser er 643 K, 97.4 bar, samt et CH_4/O_2 forhold på 23.6 i fødeblandingen ved brug af en opholdtid i reaktoren på ≥ 3 sek. Disse procesbetingelser giver anledning til en CH_3OH-selektivitet på 75 % og en omsætningsgrad af CH_4 på 5.6 % for ét reaktorgennemløb. Dette resultat er ikke tilstrækkeligt til umiddelbart at garantere en kommerciel udnyttelse af processen. Til trods herfor har de optimale betingelser dannet grundlag for flere forslag til mulig kommerciel udnyttelse, der hver især omfatter et skitseret procesdesign med tilhørende flowsheet-beregninger. De indledende beregninger har givet anledning til en lav energieffektivitet på omkring 20 %. En kommerciel udnyttelse kan dog blive aktuel, hvis forbedrede metoder til fjernelse af uønskede sideprodukter fra reaktantblandingen kan realiseres, eller såfremt det er muligt at kapitalisere afgangsgassen fra anlægget.

Preface

This thesis is written in partial fulfillment of the requirements to obtain the Doctor of Philosophy degree at the Technical University of Denmark (DTU). The work has been carried out at the CHEC (Combustion and Harmful Emission Control) Research Centre at the Department of Chemical Engineering, DTU, under the supervision of Asc. Prof. Peter Glarborg. The project was financially supported by the Technical University of Denmark and the Danish Technical Research Council.

I would like to express my sincere thanks to Peter Glarborg for giving me the opportunity to work with this project, and for always supporting my decisions and providing valuable inspiration and constructive criticism whenever needed. I am grateful for the confidence I have received and the continuous encouragements to take on new and challenging assignments; not only related to the project. It has brought me valuable skills and personal experiences that will be a great benefit in my future carreer.

A number of people have been involved in this project, and I gratefully acknowledge the contributions of (alphabetically): Kim Dam-Johansen, Jørn Hansen, Kees Hubregtse, Jon G. Jakobsen, Dani L. Johansson, Gorm Karstens, Georgios Kontogeorgis, Jorge Giménez López, Paul Marshall, Michael L. Michelsen, Hanne H. Nielsen, Kim H. Petersen, Anja E. Rasmussen, Niels Christian Schiødt, Martin S. Skjøth-Rasmussen, Jakob Sloth, Johannes Wesselingh, Thomas Wolfe, and people at the workshop.

Finally, I would like to thank Amra for all her love and support. Without her, this thesis would not have been completed within time and to my satisfaction.

Christian Lund Rasmussen
Kgs. Lyngby, Denmark
July 15, 2007

Contents

List of Figures

List of Tables

Chapter 1

Background

1.1 Introduction

A significant fraction of the World's natural gas resources are presently unavailable to the markets of utility due to extraction and transport limitations. Large quantities are allocated under the tundra and beneath the sea near the continental shelves. Even if only a fraction of these reserves could be recovered and converted to a readily transportable state, it would have a significant effect on the environmental impact of fuel and electrical power production as well as the production of chemical feedstock. In order to facilitate transportation and improved utilization, it is beneficial to convert the natural gas to a liquid chemical, known as the *gas-to-liquid* (GTL) process.

1.2 Natural Gas Resources

Natural gas is a fossil fuel, like coal and oil, formed in the Earth's crust from prehistoric organic remains exposed to millions of years of soil pressure and heat. Crude natural gas consists of a mixture of light saturated hydrocarbons with some inorganic species. The composition varies significantly depending on the geochemistry and physics of the individual reservoirs, but the major component is always methane (CH_4), which often constitutes >90 %. Ethane (C_2H_6) is the second largest hydrocarbon component, while propane (C_3H_8) and butane (C_4H_{10}) constitute minor fractions. Inorganic species include N_2, CO_2, H_2S, and perhaps some trace metals, e.g. mercury. If necessary, these can be removed using various gas pretreatment techniques, e.g. liquid extraction of H_2S and CO_2 with amine solutions followed by conversion of H_2S to elemental sulfur in a Claus plant and molesieve separation of CO_2. Nitrogen removal requires an air separation unit, while Hg can be removed

by fixed-bed adsorption [1]. Since methane is always the major component in natural gas, pure methane is often used as a replacement fuel for well-defined laboratory-scale investigations.

Methane has the highest hydrogen-to-carbon ratio among all hydrocarbon fuels. Combined with the absence of fuel-bound nitrogen and sulfur, combustion of natural gas represents reduced emissions of harmful components like CO_2 (greenhouse gas), and NO_x and SO_x (human health risk and acid rain) compared on an energy basis to other fossil fuels.

Natural gas is a major commodity used for electrical power production, heating energy for industrial and domestic appliances, as engine fuel, and chemical feedstock, e.g. for production of ammonia, urea, and various oxygenated hydrocarbons. The annual world consumption of natural gas was $\sim$2750 bill. m^3 in 2005 with an average annual growth rate of 2.2 % from 1995 to 2005 [2], and similar growth rates are predicted for the coming years [3,4]. Consumption rates rise much faster in areas undergoing rapid industrial development, like e.g. China, where the consumption of natural gas rose by more than 20 % during 2005 [2]. The current natural gas production relies solely on exploration of conventional gas reservoirs, where the gas is found in porous layers of sand- and limestone, or similar, deep under ground; often more than 3000 m below surface, and often in sparsely populated areas including off–shore locations far from markets of utility [5, 6]. Table 1.1 shows the top distributions and annual recovery of the available natural gas resources based on conventional reservoirs.

The ratio between the World's proved reserves and the current production rate predicts a depletion of the current resources within 65 years provided no future discoveries and improvements of existing recovery and transportation techniques. This is 25 years longer than predicted for the World's oil reserves [2]. Table 1.1 further ignores different unconventional natural gas resources that may become available in the future. These include gas deposits that are more difficult, and less economically sound to extract, usually because the technology to reach them has not been fully developed or is too expensive. Examples are very deep or dense deposits, coal- and oil-bedded deposits, and gas hydrates. The latter involves crystals of ice with light hydrocarbons encaged in the lattice structure in concentrations up to about 15 % on a molar basis [7,8]. This requires a combination of high pressure and low temperature, which is found e.g. in areas with permafrost, like the subterranean levels of the Siberian tundra, or beneath the ocean floor near the continental shelves, where large formations of sustainable ground ice can be formed [9, 10]. It is difficult to assess the magnitude of this natural gas resource, but coarse estimates predict about 20×10^6 bill. m^3 of pure natural gas [10–12], which is more than 100 times the proven conventional reserves in 2005, cf. Table 1.1.

Table 1.1: Top distributions and recovery of the World's natural gas resources in 2005 [2]. Proved reserves and share of total include quantities that with reasonable certainty can be recovered in the future from known reservoirs within existing economic and operating conditions. Annual production does not include gas recycling or flaring.

Rank	Country	Proved reserves 2005 [$10^9 m^3$]	Annual production 2005 [$10^9 m^3$]	Share of total [%]
1.	Russian Federation	47820	598.0	26.6
2.	Iran	26740	87.0	14.9
3.	Qatar	25780	43.5	14.3
4.	Saudi Arabia	6900	69.5	3.8
5.	United Arab Emirates	6040	46.6	3.4
6.	United States	5450	525.7	3.0
7.	Nigeria	5230	21.8	2.9
8.	Algeria	4580	87.8	2.5
9.	Venezuela	4320	28.9	2.4
10.	Iraq	3170	N/A	1.8
	Σ	136030	1508.8	75.6
	World	179830	2763.0	100.0

Due to high economic barriers, the World still awaits the first commercial exploration of these gas hydrate resources, so at present, a comparison with conventional resources is only hypothetical, but the potential is obviously very large.

1.3 Gas-to-Liquid (GTL)

Natural gas is very bulky and has a low energy content per unit volume of about 8000 $^{kcal}/_{STD\ m^3}$ compared to about 8×10^6 $^{kcal}/_{m^3}$ for oil based on lower heating values. Considering the volume-pressure behavior of natural gas, transportation costs per unit of energy to distant markets may be up to 10 times higher for natural gas than for oil [1, 13]. This is supported by earlier evaluations by Leibson *et al.* [14] and Parkyns *et al.* [15], who estimated transport costs of natural gas by pipeline from the Persian Gulf to Northern Europe to be about five times higher than an equivalent transport of liquid methanol by conventional tankers.

It imposes a significant challenge to bring the gas to the market, while ensuring the security of investment over a long period of time against market fluctuations, political changes, technological developments, trade embargoes,

terrorist activity, etc. If the gas can be pipelined, this normally is the most cost effective method of transportation. However, pipelines are only cost effective when the pipeline distance is reasonable and the terrain does not make construction costs prohibitive. Pipeline maintenance and security are also issues to be considered in this context, and furthermore, large quantities of gas must be available to sustain a steady operation [13, 16].

Transportation of natural gas over large distances is made easier by liquefying the gas. All important hydrocarbons in natural gas are brought to their liquid state when cooled below 111 K, which is the boiling point of methane. Liquid natural gas (LNG) has a volume about $^1/_{600}$ that of gas at room-temperature and can be transported overseas in specially designed refrigerated tankers [13]. LNG production facilities are expensive and complex installations with cooling and liquefaction units singly accounting for about half of the capital cost. Even though recent year's improvements of thermodynamic efficiencies have reduced construction and operating costs of LNG plants and enabled energy efficiencies up to 70 % to be achieved [17], the method is still only economically sound for large-scale production and sales to a few industrial customers. The latter issue arises from the expensive storage and regeneration facilities that must be employed by the consumers. Nevertheless, the market for LNG has quadrupled during the past 10 years and several LNG plants are currently operating or under construction around the World, e.g. in Nigeria, Angola, Qatar, Egypt, Trinidad, and Norway, at locations near large gas fields that can sustain a sufficient supply of raw material [1, 2, 13, 16–18].

An alternative to LNG production is the Fischer-Tropsch (FT) synthesis of larger hydrocarbons, like diesel, naphta, and other petrochemicals, with synthesis gas (CO/H_2) produced from natural gas as an intermediate step in the process [19, 20]. This technology has recently been commercialized in large-scale facilities, e.g. in Malaysia, South Africa, and Qatar [21–23], implying an economic enrichment of the natural gas and reduced transport costs for the resulting liquid fuels. However, with current technologies, construction of GTL-FT plants are limited to large production capacities in order to obtain satisfactory energy efficiencies; typically between 60 and 65 % [21]. This is mainly a consequence of the energy intensive production of synthesis gas via steam- or autothermal reforming.

The high transport costs are the main reason why only larger gas fields or clusters of fields can support extraction and distribution via gas pipelines, LNG production, or GTL-FT to petrochemicals. When minor sources appear, e.g. side-productions of gas in connection to crude oil recovery or coal deposits, the manufacturers can be forced to re-inject the gas into the ground, or worse, to burn the gas in massive flares resulting in extensive air pollution

and a waste of energy. The severity of the latter issue is illustrated in Figure 1.1 that shows how gas flares light up the night sky of the Persian Gulf; basically because it is economically unattractive to recover and transport the gas to central refineries for more efficient use.

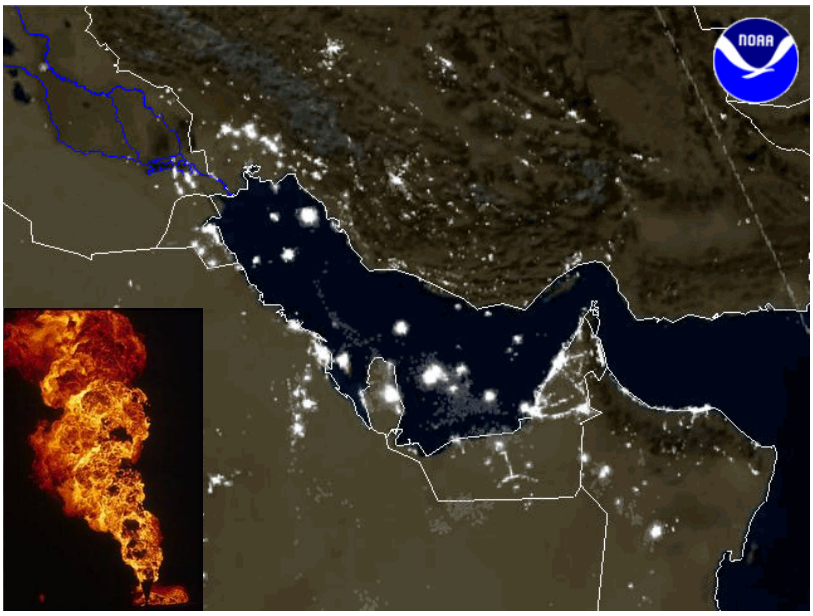

Figure 1.1: Satellite photo of the Persian Gulf by night. Giant gas flares (example in lower left corner) light up the night sky. Wasted energy and air pollution of this magnitude are beyond comparison. Source: National Oceanic & Atmospheric Administration (NOAA), 2001 [24].

There is a need for a simple and cheap process where natural gas is converted to a readily transportable state close to the gas deposit in order to reduce the transportation costs and improve the utilization of this valuable energy resource. Here, homogeneous direct partial oxidation of natural gas to methanol (CH_3OH), or mixtures of methanol and other oxygenated hydrocarbons is an attractive industrial GTL process. In this process, the natural gas is converted in a single reaction step without intermediate synthesis gas production or use of heterogeneous catalysis.

1.3.1 Methanol – Applications and Economy

Methanol is the oxygenate of primary interest, but other valuable products may as well be formed during the non-catalytic direct partial oxidation of natural gas, e.g. formaldehyde (CH_2O), ethanol (C_2H_5OH), and dimethylether

(CH_3OCH_3). These are all attractive fuels for combustion as well as chemical synthesis. The annual demand for methanol amounted to about 32×10^6 metric tons in 2006 [25] with the major application as feedstock in chemical industries; in particularly for production of formaldehyde, methyl *tert*-butylether (MTBE), and acetic acid, that currently account for more than $^2/_3$ of the total demand. Methanol has a high octane rating, which also makes it attractive as an automotive fuel or as antiknock additive either in its pure form or upgraded to MTBE. Light- and heavy-duty vehicles powered by internal combustion engines generally experience excellent acceleration and vehicle power when fueled with methanol, while emissions of toxic compounds, like unburned hydrocarbons, particulate matter, and nitrogen oxides, are low compared to gasoline or diesel-fueled counterparts. As a hydrogen carrier, methanol further has potential for fuel cell power. A future breakthrough in the gasoline markets of North America, Europe, and East Asia will undoubtedly trigger a significant increase of the current demands [26, 27]. Figure 1.2 shows the development in the average US market price for bulk methanol from 1990 to present day [28, 29]. The figure also compares city gate prices and wellhead prices of natural gas purchases from the US over the same period of time [30–32]. The *city gate price* includes costs, insurance, and freight of the gas to the junction with the given high-pressure delivery system, while the *wellhead price* represents all costs prior to shipment, i.e. charges for the recovery facility, gas pretreatment, gathering, compression costs, severance taxes, etc. It is calculated by dividing the total value of the gas at the wellhead by the total quantity as reported by appropriate agencies. Notice that prices in Figure 1.2 may deviate from those of the European and Asian markets [28].

The difference between the city gate price and the wellhead price of natural gas can be attributed to the transport costs. Despite market fluctuations, transport costs have remained fairly constant around 5–7 $^{\text{US\$}}/_{10^6\ \text{kcal}}$ equal to 45–75 $^{\text{US\$}}/_{10^3\ \text{STD m}^3}$ throughout the considered period of time. From 2003 to the present day, this has roughly corresponded to 15–30 % of the total city gate price of natural gas. Viewed in the light of an expected reduction in transport costs by a factor of 5–10; cf. estimated transport costs for natural gas versus oil/methanol reported in ref. [1, 13–15], this indicates the prospect of economic gain if natural gas can be transported by way of a liquid chemical.

The ratio between the price of natural gas and methanol indicates the maximum acceptable energy loss during a potential conversion of gas to methanol, i.e. the lower bound of the overall energy efficiency, in order for the investors to capitalize from the GTL process. Within recent years, this important process parameter has fluctuated around 50 %.

The price ranges presented in Figure 1.2 only cover natural gas resources

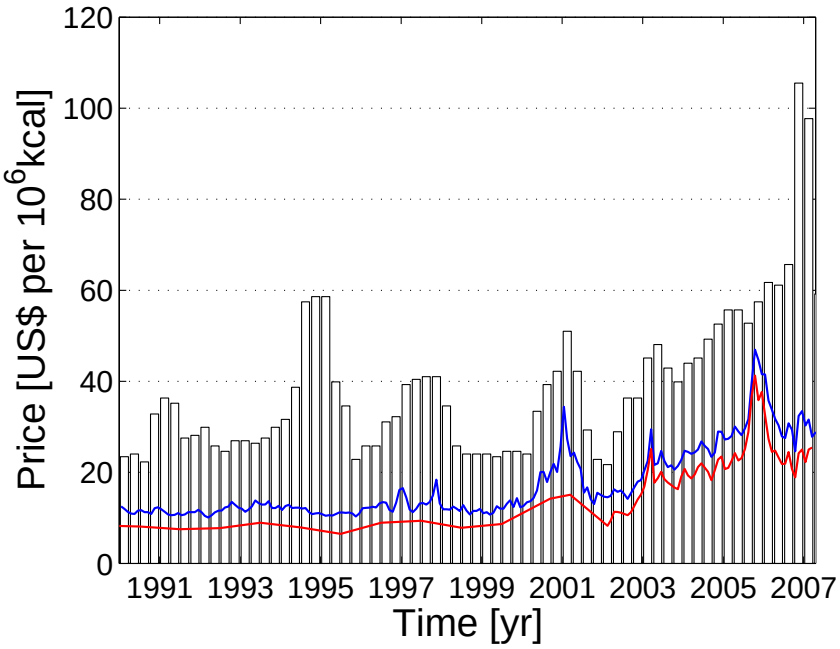

Figure 1.2: Development in average US market prices per energy content of bulk methanol (bars) and natural gas (top blue line: city gate prices; lower red line: wellhead prices) from 1990 to present day. City gate prices include cost, insurance, and freight. Wellhead prices include all costs prior to shipment (see text for more details). Sources of methanol prices: Methanex [28] and the Methanol Institute [29]. Sources of natural gas prices: US Energy Information Administration [30–32].

feasible for exploration with currently available technologies. Under conditions where natural gas production is unwanted, e.g. when minor yields appear in association with oil and coal recovery, the wellhead price will obviously become much lower than indicated by Figure 1.2 due to the fact that the gas recovery is too modest to be utilized, but partial recovery is still unavoidable in order to yield the fossil fuel of primary interest.

1.3.2 From Natural Gas to Methanol

Methanol is traditionally produced from natural gas or gasified coal in a complicated two-step process, where the hydrocarbon feed gas is initially converted to synthesis gas (CO/H_2) by steam- or autothermal reforming followed by catalytic reduction under high pressure to the desired product [33–35].

The primary global reactions involved are shown below:

$$\mathrm{CH_4 + H_2O \rightarrow CO + 3H_2} \qquad \Delta_r H_{298} = 49.2\,{}^{\mathrm{kcal}}/_{\mathrm{mol}} \tag{1.1}$$

$$\mathrm{CH_4 + CO_2 \rightarrow 2CO + 2H_2} \qquad \Delta_r H_{298} = 59.0\,{}^{\mathrm{kcal}}/_{\mathrm{mol}} \tag{1.2}$$

$$\mathrm{CH_4 + {}^1/_2O_2 \rightarrow CO + 2H_2} \qquad \Delta_r H_{298} = -8.6\,{}^{\mathrm{kcal}}/_{\mathrm{mol}} \tag{1.3}$$

$$\mathrm{CO + H_2O \rightarrow CO_2 + H_2} \qquad \Delta_r H_{298} = -9.8\,{}^{\mathrm{kcal}}/_{\mathrm{mol}} \tag{1.4}$$

$$\mathrm{CO + 2H_2 \rightarrow CH_3OH} \qquad \Delta_r H_{298} = -21.6\,{}^{\mathrm{kcal}}/_{\mathrm{mol}} \tag{1.5}$$

The strongly endothermic reforming reactions make it difficult to obtain high energy efficiencies unless large-scale installations are employed. Economic assessments [36,37] indicate that about 60–70 % of the cost of methanol is associated with the production of synthesis gas by reforming. The alternative direct conversion is shown in (1.6). This is an exothermic process, which makes it superior in terms of energy efficiency, and the single-step approach will further reduce the capital and operational costs related to methanol production.

$$\mathrm{CH_4 + {}^1/_2O_2 \rightarrow CH_3OH} \qquad \Delta_r H_{298} = -30.2\,{}^{\mathrm{kcal}}/_{\mathrm{mol}} \tag{1.6}$$

The selectivity of methanol, $S_{\mathrm{CH_3OH}}$, and the conversion of methane, $X_{\mathrm{CH_4}}$, in a *single pass* of the reactor are two key figures for the comparison of the direct and indirect process. Their definitions are shown in equation (1.7) and (1.8) where F denotes the molar flow rate in and out of the reactor. Multiplication further defines the yield, $Y_{\mathrm{CH_3OH}}$.

$$S_{\mathrm{CH_3OH}} = \frac{F_{\mathrm{CH_3OH},out}}{F_{\mathrm{CH_4},in} - F_{\mathrm{CH_4},out}} \tag{1.7}$$

$$X_{\mathrm{CH_4}} = \frac{F_{\mathrm{CH_4},in} - F_{\mathrm{CH_4},out}}{F_{\mathrm{CH_4},in}} \tag{1.8}$$

$$Y_{\mathrm{CH_3OH}} = S_{\mathrm{CH_3OH}} \times X_{\mathrm{CH_4}} = \frac{F_{\mathrm{CH_3OH},out}}{F_{\mathrm{CH_4},in}} \tag{1.9}$$

Technical economic evaluations of the direct homogeneous process by Kuo *et al.* [38] predicted that a selectivity of methanol of 90 % at 7.5 % conversion of methane will make the direct process competitive with conventional techniques. This evaluation assumed the process to run at 50 bar with a recycling ratio of 30 for unconverted hydrocarbons, and an estimated energy efficiency of 70 % compared to 65 % for the conventional syngas-based process. Kuo *et al.* further stated that higher product selectivities are more desirable than high fuel conversions based on a sensitivity analysis of their calculations. A

similar study by Lange and Tijm [39] estimated a methanol selectivity of 80 % to be competitive at 10 % methane conversion based on derived correlations between capital costs and energy efficiencies, energy loss, and momentum transfer duties (transfer of heat and matter) for different related chemical processes.

These economic evaluations date more than 10 years back and, consequently, do not reflect the latest technological developments of efficient process equipment and designs as well as changes in the markets of methanol and natural gas, cf. Figure 1.2. A limited confidence is therefore placed in these assessments. Moreover, both studies only consider large-capacity facilities where conventional syngas-based methanol plants are very competitive. It is expected that units of smaller scale are able to compete with conventional techniques at significantly lower methanol yields than indicated above, but updated technical economic calculations are needed for a quantitative assessment.

1.4 Project Objectives

The main objective of this project is to identify a combination of process conditions for the homogeneous direct partial oxidation of natural gas that results in a competitive yield of methanol or mixtures of methanol and other oxygenated hydrocarbons.

Due to the limited knowledge of the complex chemistry involved in the process, previous work has mainly been experimental. This project applies a different approach by focusing the attention on the fundamental understanding of the chemistry. Detailed chemical kinetic modeling (DCKM) is emphasized in contrast to previous work, where an experimental optimization was attempted or a simplified kinetic model was used. A comprehensive kinetic model will be developed based on available knowledge of hydrocarbon oxidation chemistry and its interaction with different gas phase initiators or sensitizers, e.g. nitrogen oxides (NO_x) and sulfur species (H_2S/SO_2). The model performance will be validated in close interaction between theory and experimental results obtained under well-defined conditions. The experiments will be conducted in a pressurized laboratory scale flow reactor designed to handle pressures up to 100 bar at 900 K. The construction and development of this setup comprise an important part of the current project.

1.4.1 From Fundamental Understanding to Process Optimization

The available studies in the field have demonstrated that low temperatures and high pressure, along with a high CH_4/O_2 ratio in the feed, are key parameters to obtain high selectivities of methanol. Experimental investigations at these conditions impose some difficulties as they require methane concentrations in the range of 90–95 % resulting in a significant heat release during the conversion. This makes it almost impossible to sustain a well-defined temperature profile during experiments. As a consequence, this project initially abandons the focus on the optimal conditions in favour of a search for the general mechanism that governs methane oxidation at an extended range of process conditions; including both lean and rich conditions. When a satisfactory disclosure of the kinetic scheme is completed, these results will eventually be utilized for a determination of the optimal process conditions using a numerical global optimization routine.

In the final stage of the project, first draft ideas and *back-of-the-envelope* flow sheet calculations will be presented for potential utilization of the present technology.

Chapter 2

Literature Review

Even though the technology required to utilize the direct homogeneous conversion of methane to methanol remains immature, the reaction itself is "old" with a long history of scientific investigations dating as far back as the early years of the 20^{th} century.

2.1 Historic Development

The process was first described as the *slow combustion* of methane at low temperatures by Bone and Wheeler [40, 41] in 1902–03 based on experiments in batch glass reactors at 573–773 K and atmospheric and slightly elevated pressures. In 1932, Newitt and Haffner [42] conducted the first consistent high-pressure experiments in a batch stainless steel reactor at 614 K and 108 bar. They obtained a peak methanol selectivity of 22.3 % at 7.9 % methane conversion. A few years later, in 1934, Wiezevich and Frölich [43] conducted the first continuous flow reactor experiments using both laboratory and pilot-scale setup. The latter was employed as the first semi-commercial plant and was equipped with both a reactant recirculation system and a continuous product purification system. After this, all subsequent experiments were conducted in continuous reactor systems.

It was also in the early thirties that the promoting effect of nitrogen oxides on hydrocarbon oxidation chemistry was first reported by Dixon and Higgins [44], who observed a significant reduction of the initiation temperature when small amounts of NO_2 were added to the reactant mixture. This was confirmed by Norrish and Wallace [45] in 1934, and Ashmore and Preston [46] in 1967.

In a series of papers from 1937, Boomer and co-workers [47–49] presented pioneering investigations into the corresponding catalytic process. They

passed a stream of methane and purified air through a fixed-bed reactor containing beads of either principal copper, silver, steel, or glass at varying temperatures and pressures from 698–748 K and 143–234 bar. Peak selectivities of about 74 % were measured at a single-pass carbon conversion of 2–2.5 % using copper and glass beads.

At the time, product analysis was limited to various wet-chemical methods that only allowed detection of the most stable species, e.g. methanol, formaldehyde, CO, and CO_2. As a result, the governing reaction mechanism and intermediate products were heavily debated in a significant number of publications from the late twenties and early thirties. Here, scientists expressed their personal conviction on the subject without being able to provide definite experimental proof, e.g. [49–56].

2.1.1 First Proposal of the Reaction Mechanism

For many years, the generally accepted mechanism for the slow combustion of methane was the "Hydroxylation Theory" proposed by Bone and coworkers [53] on the basis of their original slow methane oxidation experiments from the beginning of the century. The theory stated that a fast two-step hydroxylation mechanism was responsible for the initial conversion of methane, via methanol, to methanediol [$CH_2(OH)_2$] that was subsequently hydrolyzed to formaldehyde in a fast reaction. Continued hydroxylation of formaldehyde and dissociation led to the full oxidation products. The reaction sequence is shown below without stoichiometric amounts of O_2 as reactant:

$$\begin{array}{l} \mathrm{CH_4 \rightarrow CH_3OH \rightarrow CH_2\,(OH)_2 \overset{-H_2O}{\longrightarrow} CH_2O \rightarrow HC\,(OH)\,O \rightarrow C\,(OH)_2\,O} \\ \qquad\qquad\qquad\qquad\qquad\qquad\qquad\qquad\qquad\qquad\qquad\quad \downarrow \qquad\quad \downarrow \\ \qquad\qquad\qquad\qquad\qquad\qquad\qquad\qquad\qquad\qquad\qquad\quad \mathrm{CO + H_2O} \quad \mathrm{CO_2 + H_2O} \end{array} \tag{2.1}$$

2.1.2 Peroxides and Radical Chain Reactions

In 1927, Callendar [57] published his work on low to moderate temperature combustion of various C_{5-6} isomers in engines. Here, the author discarded the hydroxylation theory due to unsuccessful attempts to detect the presence of intermediate hydroxyl and dihydroxyl compounds. Instead, Callendar advocated the initial formation of a peroxide compound by the direct incorporation of an oxygen molecule in the carbon chain. This peroxide compound could then dissociate to aldehydes. The initial oxidation reaction is shown in (2.2) as proposed by Callendar [57]. "R" denotes an alkyl group.

$$\mathrm{RCH_2CH_2R + O_2 \rightarrow RCH\,(-OOH)\,CH_2R} \quad \text{or} \quad \mathrm{RCH_2 - OO - CH_2R} \tag{2.2}$$

Callendar's "Peroxide Theory" was ruled out by Bone and others loyal to the Hydroxylation Theory [42,53,58] based on missing experimental evidence of peroxide formation during the slow combustion process.

Around the same time the Russian scientist Semenov [59] developed the radical chain-reaction theory for combustion processes, while Hinshelwood [60] presented his work on the collision- and transition state theory based on studies of the H_2/O_2 system[1]. These new approaches to gas phase chemistry served as inspiration for the "Atom Chain Hypothesis" for the slow combustion of methane presented by Norrish [54, 61] in 1935. This was a chain-reaction theory that relied on the alternate formation of free oxygen atoms (O) and methylene radicals (CH_2) as demonstrated below:

$$O + CH_4 \rightarrow CH_2 + H_2O \tag{2.3}$$

$$CH_2 + O_2 \rightarrow CH_2O + O \tag{2.4}$$

$$\Sigma \quad CH_4 + O_2 \rightarrow CH_2O + H_2O \tag{2.5}$$

The chain was supposedly initiated at the reactor surface by a slow two-step mechanism, where formaldehyde is formed as the initial product followed by oxidation to performic acid [HC(=O)OOH] that decomposes to the normal acid and an O-atom:

$$CH_4 + O_2 \overset{\text{surface}}{\longrightarrow} CH_2O + H_2O \tag{2.6}$$

$$CH_2O + O_2 \rightarrow HC(=O)OOH \rightarrow HC(=O)OH + O \tag{2.7}$$

Formation of methanol was the result of a third-body collision (M) that terminated the chain. In addition, oxygen radicals were removed by recombination at the surface:

$$CH_4 + O + M \rightarrow CH_3OH + M \tag{2.8}$$

$$O + \text{surface} \rightarrow {}^1/_2\, O_2 \tag{2.9}$$

Based on this free-radical mechanism approach, Norrish was also able to explain why even small quantities of NO_2 in the reaction mixture were able to reduce the initiation period of the combustion process by acting as a source of chain-carrying O and CH_2 radicals:

$$NO + O_2 \rightarrow NO_2 + O \tag{2.10}$$

$$NO_2 \rightarrow NO + O \tag{2.11}$$

$$NO_2 + CH_4 \rightarrow CH_2 + NO + H_2O \tag{2.12}$$

[1] In 1956, Semenov and Hinshelwood shared the Nobel Prize in chemistry for their work with mechanisms of chemical reactions.

Following the chain propagation scheme in (2.13) and (2.14), Pease [62] instead proposed methoxy (CH_3O) and alkyl radicals (RCH_2) as the principal chain-carriers (R = –H, $–CH_3$, $–C_2H_5$, etc.), where the alkyl radicals originated from initial dissociation of the hydrocarbon fuel. Pease investigated the slow combustion of propane and therefore presented the mechanism with propyl radicals (C_3H_7) as the alkyl chain-carrier, but the analogy to slow combustion of methane with methyl radicals (CH_3) as chain-carrier is straightforward.

$$CH_3O + C_3H_8 \rightarrow CH_3OH + C_3H_7 \tag{2.13}$$

$$C_3H_7 + O_2 \rightarrow CH_3CHO + CH_3O \tag{2.14}$$

$$\Sigma \quad C_3H_8 + O_2 \rightarrow CH_3CHO + CH_3OH \tag{2.15}$$

The product CH_3CHO is acetaldehyde that could be further oxidized to formaldehyde, CO, and H_2O in subsequent reaction steps [62].

The mechanism suggested by Pease was generally accepted by the posterity with only few modifications. Ubbelohde [55] and Von Elbe and Lewis [63] advocated the formation of collisionally stabilized methylperoxyl radicals (CH_3OO) as a key intermediate during the slow combustion of methane at high pressure and fuel-rich conditions. Subsequent dissociation at the peroxidic bond; either unimolecularly or by reaction with a radical or a stable compound, yielded CH_3O as well as another radical or stable product. Von Elbe and Lewis [56] reconciled the suggestions of Pease [62], Ubbelohde [55] and Von Elbe and Lewis [63] in the following reaction scheme, which is similar to the scheme proposed nowadays.

$$CH_3 + O_2 + M \rightarrow CH_3OO + M \tag{2.16}$$

$$CH_3OO \rightarrow [\text{complex}] \rightarrow CH_2O + CH_3O \tag{2.17}$$

$$CH_3O + CH_4 \rightarrow CH_3OH + CH_3 \tag{2.18}$$

$$CH_3O + O_2 \rightarrow CO + H_2O + OH \tag{2.19}$$

2.2 Present-Day Investigations

The process of converting methane directly to liquid chemicals at high pressure and low temperatures has been studied intensively, but even so, no commercial applications are practiced to date. The majority of these studies are based on experimental investigations e.g. [42, 64–78]. A few modeling studies have also been published based on limited kinetic reaction mechanisms [76,79–84]. In addition, some reviews have appeared in the field [85–89]

as well as some patents [90–94]. Encouraged by the abundant natural gas reserves located beneath Russian soil (see the distribution of the World's natural gas resources in Table 1.1), Russian scientists have shown particular interest in this process and a number of related papers have been published by Arutyunov, Basevich, Vedeneev, and co-workers from Semenov Institute of Chemical Physics at the Russian Academy of Science in Moscow. Most of these papers are published in their native language and, hence, will not be included in this review due to linguistic barriers.

2.2.1 Overview of Experimental Achievements

Despite the extensive work in the field, measured yields of methanol are generally low, while a few promising results have proven difficult to reproduce. This is attributed to experimental and/or theoretical shortcomings arising from the limited knowledge of interactions between the complex chemistry involved in the process and a number of important process parameters.

The available studies have demonstrated that relatively low combustion temperatures in the range of 550–800 K and high pressures between 30–100 bar, along with a high CH_4/O_2 ratio in the feed, are key parameters to obtain high selectivities of methanol. However, influence may also arise from third-body effects from inert diluents, reactor residence time, reactor design, surface materials, and gas phase sensitizers including higher hydrocarbons and various inorganic compounds. In the present work, inorganic additives of particular interest are NO_x and H_2S, where the latter is typically found in trace amounts in crude natural gas. Under certain conditions, these compounds may interact with the hydrocarbon oxidation chain in a way that promotes the formation of the desired product. Some of these process parameters will be discussed in more details below. First, an overview of the most important experimental achievements from the literature is presented in Table 2.1. The author points to the large diversities in applied experimental conditions and hereof resulting methanol yields.

The subsequent Figure 2.1 presents a direct comparison of experimental selectivities of methanol as function of the methane conversion. These data are further compared with recent results obtained from the direct heterogeneous catalytic conversion of methane to methanol as well as the technical economic assessments previously discussed in Section 1.3.2. The reader is referred to this discussion for a critical view of the so-called "commercial target" in Figure 2.1. It is emphasized that the data shown in Figure 2.1 are not necessarily comparable in terms of applied experimental conditions. The figure merely provides an overview of the most promising achievements in the field as of today.

Table 2.1: Overview of the most important experimental achievements reported in the literature. Data include measurements of methanol selectivity (S_{CH_3OH}) and methane conversion (X_{CH_4}) as a function of the experimental conditions, i.e. temperature (T), pressure (P), reactor residence time (τ), CH_4/O_2 ratio, absolute concentrations of O_2 as well as N_2; if applied as diluent, reactor material (Wall), and reactor surface-to-volume ratio ($^S/_V$). The table does not include investigations involving gas phase sensitizers.

Reported by	T [K]	P [bar]	τ [sec]	CH_4/O_2	O_2 [%]	N_2 [%]	Wall	$^S/_V$ [$^1/_{cm}$]	S_{CH_3OH} [%]	X_{CH_4} [%]	Ref.
Newitt & Haffner, 1932	614	107.8	720	8.1	11.0	—	Steel	—	22.3	7.9	[42]
Lott & Sliepcevich, 1967	537	3450	420	11.6	7.9	—	Steel	2	40.1	6.3	[64]
Yarlagadda *et al.*, 1988	725	25.2	82	10.5	8.7	—	Pyrex	∼14	55.0	13.3	[65]
	684	36.0	284	11.5	8.0	—	Pyrex	∼14	55.1	10.6	
	724	50.7	211	13.9	6.7	—	Pyrex	∼14	76.0	9.5	
	729	66.2	236	18.6	5.1	—	Pyrex	∼14	83.0	8.0	
Burch *et al.*, 1989	723	50.0	200	39.0	2.5	—	Pyrex	10	36.0	∼5	[66]
	723	50.0	200	19.4	4.9	—	Pyrex	10	39.0	∼5	
	723	50.0	200	14.2	6.6	—	Pyrex	10	36.0	∼5	
Hunter *et al.*, 1990	628	30.4	174	19.8	4.8	—	Pyrex	3.8	89.5	8.0	[67]
	628	50.7	264	16.5	5.7	—	Pyrex	3.8	92.1	10.0	
Gesser *et al.*, 1991	637	60.8	42	32.3	3.0	—	Pyrex	3.7	74.7	2.7	[68]
	654	60.8	25	39.0	2.5	—	Pyrex	∼13.3	70.0	3.0	
Rytz & Baiker, 1991	723	50.7	9	19.0	5.0	—	Quartz	≫100	27.0	3.0	[69]
	748	50.7	9	19.0	5.0	—	Quartz	≫100	25.0	7.0	
Thomas *et al.*, 1992	713	20.0	24.6	16.0	5.0	—	Quartz	5	32.6	4.6	[70]
Foulds *et al.*, 1993	657	50.7	187	19.0	5.0	—	Quartz	6.7	33.7	4.6	[71]

Continues on next page

Continued from last page

Reported by	T [K]	P [bar]	τ [sec]	CH_4/O_2	O_2 [%]	N_2 [%]	Wall	S/V [1/cm]	S_{CH_3OH} [%]	X_{CH_4} [%]	Ref.
Chun & Anthony, 1993	704	50.7	5.9	22.0	4.4	—	Pyrex	10	39.7	4.0	[72]
Casey *et al.*, 1994	673	50.0	6.0	15.7	6.0	—	Quartz	∼17	22.0	∼4.2	[73]
Omata *et al.*, 1994	733	41.5	1	30.0	2.9	11.4	Quartz	∼25	23.0	2.2	[74]
Feng *et al.*, 1994	673	10.0	38	14.3	5.2	19.0	Sapphire	∼6	41.0	5.5	[75]
	633	30.0	126	14.3	5.2	19.0	Sapphire	∼6	71.0	10.4	
	603	50.0	220	14.3	5.2	19.0	Sapphire	∼6	83.0	12.3	
	603	70.0	308	14.3	5.2	19.0	Sapphire	∼6	75.0	11.0	
Lødeng *et al.*, 1995[a]	719–740	40.0	1.3	35.3	2.5	9.2	Al_2O_3	1.8	46.1	1.2	[76]
	727–809	40.0	1.2	22.0	3.8	13.8	Al_2O_3	1.8	30.8	2.6	
	696–744	60.0	1.3	35.3	2.5	9.2	Al_2O_3	1.8	45.6	1.3	
	710–786	59.9	1.3	35.1	2.5	9.5	Al_2O_3	1.8	39.2	2.3	
Chellappa *et al.*, 1997	703	34.0	60	16.0	4.5	16.5	Quartz	3.3	53.6	7.0	[77]
	703	50.0	60	16.0	4.5	16.5	Quartz	3.3	53.8	7.3	
Zhang *et al.*, 2002	723	50.0	33	10.0	8.0	8.0	Quartz	∼13	63.0	13.0	[78]

[a] The reaction does not yield 100 % O_2 conversion within the applied residence time.

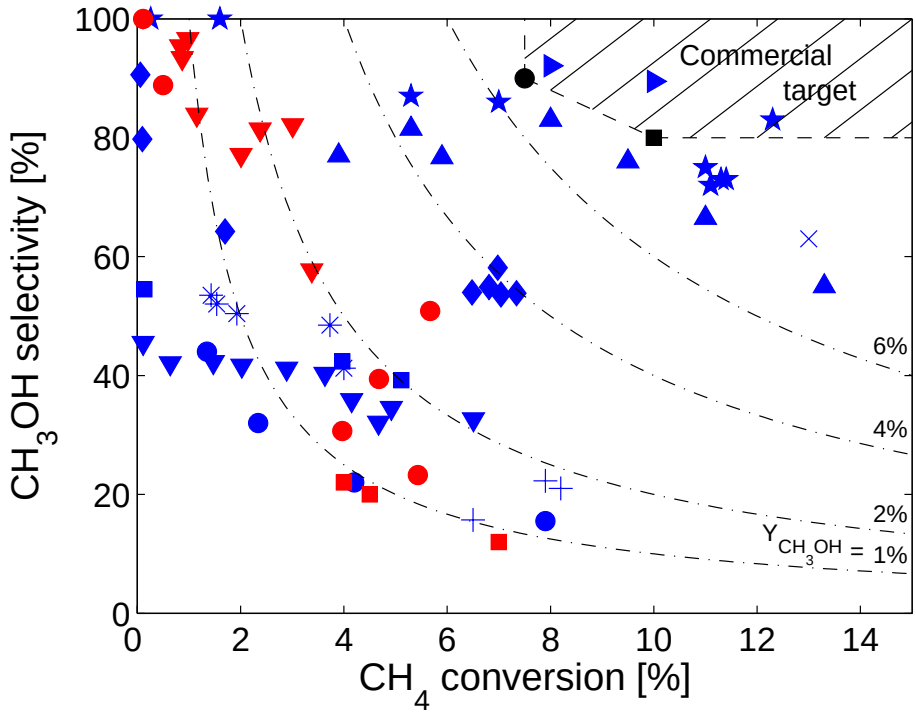

Figure 2.1: Comparison of experimental selectivities of methanol, S_{CH_3OH}, as a function of the methane conversion, X_{CH_4}, reported in the literature for the direct partial oxidation of methane to methanol. Homogeneous process (blue symbols): + Newitt & Haffner, 1932 [42]; ▲ Yarlagadda *et al.*, 1988 [65]; ■ Burch *et al.*, 1989 [66]; ▶ Hunter *et al.*, 1990 [67]; ▼ Thomas *et al.*, 1992 [70]; ✳ Chun & Anthony, 1993 [72]; ● Casey *et al.*, 1994 [73]; ★ Feng *et al.*, 1994 [75]; ♦ Chellappa *et al.*, 1997 [77]; × Zhang *et al.*, 2002 [78]. Heterogeneous process (red symbols): ● Chellappa & Viswanath, 1995 [95]; ▼ Wang *et al.*, 2003 [96]; ■ Hahm *et al.*, 2004 [97]. Technical economic evaluation (black symbols): ● Kuo *et al.*, 1989 [38]; ■ Lange & Tijm, 1996 [39]. Commercial target area (hatched) is estimated based on the values from Kuo *et al.* [38] and Lange & Tijm [39]. Dashed-dotted lines represent methanol yields of 1, 2, 4, and 6 %, in accordance with the definition of Y_{CH_3OH} in Equation (1.9).

As indicated in Table 2.1 and Figure 2.1, previous results from the literature are characterized by significant scatter in terms of measured peak selectivities and fuel conversions; even when seemingly identical reaction conditions have been applied. The work of Gesser and co-workers [65, 67, 68] displays very promising results in terms of high methanol yields as do the the results reported by Feng *et al.* [75] and Zhang *et al.* [78]. However, these data lie far from most other investigations conducted in the field, and this calls for suspicions. Burch *et al.* [66] dedicated their work to reproduce the

results of Yarlagadda *et al.* [65]. They investigated the homogeneous reaction at various temperatures and pressures from 648–723 K and 5–50 bar, as well as a broad range of O_2 concentrations in the feed, but despite all their efforts to recreate the conditions applied by Yarlagadda *et al.*, they remained unsuccessful in the sense that measured methanol selectivities and methane conversions were not even remotely close to those reported by Yarlagadda *et al.* [65]. Burch *et al.* finally attributed these continuous discrepancies to minor differences in the reactor design, but even so, their results question the integrity of the work of Yarlagadda *et al.* and, thus, also the other promising results reported by Gesser and co-workers. Nonetheless, it cannot be ruled out that deviations observed between various results have indeed been caused by secondary issues that have been overlooked by the respective authors, e.g. in relation to the reactor configuration. In any case, this lack of reproducibility emphasizes the need for a more fundamental process development strategy where a detailed understanding of the governing chemistry is in focus rather than a subjective experimental optimization.

2.2.2 Temperature and Pressure

The homogeneous oxidation of methane is governed by a free-radical mechanism, which is difficult to control. The very stable methane molecule must be converted to methanol without promoting further oxidation to undesired carbon oxides. The rate limiting step is the breaking of the very stable H–C bond in methane ($D^{298}_{\mathrm{H-CH_3}} = 104.9 \pm 0.1\,{}^{\mathrm{kcal}}/_{\mathrm{mol}}$ [98]). This typically requires high temperatures (>1000 K), which has an adverse effect on the selectivity of the desired products ($D^{298}_{\mathrm{H_3C-OH}} = 91.9 \pm 0.17\,{}^{\mathrm{kcal}}/_{\mathrm{mol}}$ and $D^{298}_{\mathrm{H-CH_2OH}} = 96.0 \pm 0.15\,{}^{\mathrm{kcal}}/_{\mathrm{mol}}$ [98]). The major intermediate and final products formed during high-temperature combustion of methane are shown in (2.20). The specific yields of higher hydrocarbons, represented by ethane (C_2H_6), as well as the full oxidation products, CO and CO_2, depend on the reaction stoichiometry.

$$\begin{array}{ccccccccc} \mathrm{CH_4} & \rightarrow & \mathrm{CH_3} & \rightarrow & \mathrm{CH_2O} & \rightarrow & \mathrm{HCO} & \rightarrow & \mathrm{CO} \rightarrow \mathrm{CO_2} \\ & & \downarrow & & & & & & \\ & & \mathrm{C_2H_6} & & & & & & \end{array} \tag{2.20}$$

The selectivity of oxygenated hydrocarbons is greatly improved by applying relatively low combustion temperatures combined with high pressure. An increase of pressure is equivalent with an increase of the collision frequency between molecules. Molecules can deliver, as well as absorb, certain amounts of momentum or internal energy upon collision without undergoing

chemical conversion itself. The former may help reactants pass an energy barrier and reach the product state, while absorption of excess energy from activated complexes (marked by '$*$') increases the probability of adduct stabilization instead of dissociation. The scheme in (2.21) illustrates the effect of collisional stabilization at high pressure.

$$\mathrm{CH_3 + OH \rightleftharpoons [H_3C \cdots OH]^*} \begin{cases} \nearrow & \mathrm{CH_2 + H_2O} \quad \text{(low pressure/ high temperature)} \\ \searrow & \mathrm{CH_3OH} \quad \text{(high pressure/ low temperature)} \end{cases} \tag{2.21}$$

Following Le Chatelier's Principle, high pressure also favors the overall conversion of methane and oxygen to oxygenated hydrocarbons, e.g. $\mathrm{CH_4 + {}^1\!/\!_2\, O_2 \rightarrow CH_3OH}$, in order to decrease the total number of molecules.

From a practical point of view, it is unfortunate if exceptionally high pressures must be applied in order to obtain competitive yields since gas compression is a very expensive unit operation. The wellhead pressure obtained at gas recovery sites varies significantly with the depth of the reservoir, but pressures in the range of 80–150 bar are typically available [99]. This range should not be exceeded in the GTL process in order to limit production costs. The issue was pursued by Lott and Sliepcevich [64], who conducted experiments at extremely high pressures from 3450 to 13800 bar using a fortified static steel reactor and a specially designed gas compression system consisting of air-driven hydraulic pumps and a pressure intensifier unit, among others. Lott and Sliepcevich obtained a peak methanol selectivity of 40.1 % at 6.3 % methane conversion when applying 537 K at the lowest investigated pressure. A further pressure increase proved to have no or, perhaps, a slight adverse effect on the methanol yield. Lott and Sliepcevich, however, recognized that catalytic activity at the steel surface could have influenced their results.

In a review from 1995, Arutyunov *et al.* [86] described how methanol formation reaches a maximum value at pressures between 100 and 150 bar with the largest gain occurring below 100 bar. This indicates that only a minor improvement of the methanol yield can be expected if the process is run above 100 bar; and this may be disproportionate to the production costs if it requires additional compression of the feed gas. In 2002, Arutyunov [100] published a thorough outline of the role of pressure in the partial oxidation process of methane. Here, the author reached a similar conclusion. The recommendation is also consistent with other reports from the literature, e.g. [69, 76, 87, 89].

Third-Body Effects

The major components in the reactant mixture are typically CH_4, O_2, and N_2, but larger molecules, like CO_2 and C_2H_6, are sometimes present in sufficient amounts to become frequent third-body collision partners. Larger molecules also exhibit a larger capacity to store energy absorbed upon impact with other molecules, and this may be beneficial in terms of promoting pressure dependent reactions that produce methanol or methanol precursors. This presumes that the given reaction does not operate at the *high-pressure limit* (defined later in Section 5.2.2.1), where the third-body collision partner has no influence on the reaction rate.

Feng *et al.* [75] increased the selectivity of methanol from 40 to 70 % when the total system pressure was increased from 10 to 50 bar through addition of CO_2. Feng *et al.* attributed this behavior to the enhanced third-body effect of CO_2, but their analysis did not exclude the possibility that the higher methanol selectivity may as well have been a result of the total pressure increase rather than the specific third-body effect of CO_2. Omata *et al.* [74] also studied the influence of CO_2 addition by comparing the methanol yield in the presence and absence of 10 % CO_2 as a substitute for CH_4. Experiments were conducted at 41.5 bar and 673–753 K using a constant CH_4/O_2 ratio of 30. The results indicated a minor decrease of the overall reaction initiation temperature of ∼20 K, while the peak methanol yield increased by about 20 %. Again, results were not directly comparable in terms of pure third-body effects due to the different absolute concentrations of fuel and oxidizer in the two experiments. Omate *et al.* [74] further suggested that addition of CO_2 may have a more direct chemical influence on the fuel conversion by acting as a source of chain-initiating OH radicals through reaction with H-atoms:

$$CO_2 + H \rightarrow CO + OH \tag{2.22}$$

$$CH_4 + OH \rightarrow CH_3 + H_2O \rightarrow ... \tag{2.23}$$

In this case, CO_2 acts as a chemical initiator instead of an inert third-body collision partner.

In kinetic modeling, third-body effects are considered in relation to pressure dependent reactions where the concentration of the inert collision partner "M" appears as a factor in the rate expression. This value can be multiplied by an enhancement factor $\neq 1$ when M represents colliding molecules that exhibit different potential for energy transfer compared to those encountered during the original measurements of the given rate constant. (See the later Section 5.2.2.1 for the mathematical treatment of third-body reactions

in modeling). Since rate constant data are typically derived from experiments conducted in inert atmospheres of He, Ar, or N_2, larger molecules, like e.g. CO_2 and C_2H_6, may exhibit third-body enhancement factors > 1.

The significance of the third-body effect relies on absolute concentrations of specific molecules, so in terms of the investigated GTL process, it is mainly relevant to consider a potential enhancement factor for CH_4. The third-body collision efficiencies of CO and CO_2 may also be of interest in relation to practical applications of the process that aim at converting the entire hydrocarbon load. This would require substantial recirculation of the reactants to compensate for the low fuel conversion obtained during a single pass of the reactor, which may facilitate build-up of CO and CO_2. However, from a practical point of view, it is considered unlikely that forced addition of CO, CO_2, or other inert third-body candidates to the reactant mixture will be economically sound considering the substantial amount necessary to yield a pronounced effect.

2.2.3 CH_4/O_2 Ratio

A high CH_4/O_2 ratio in the feed favors a high selectivity of methanol. The reason is found in the conversion of the intermediate methoxy radical (CH_3O), which is a precursor of methanol. Methoxy radicals are consumed through three major reaction pathways:

$$CH_3O + M \rightarrow CH_2O + H + M \tag{2.24}$$

$$CH_3O + O_2 \rightarrow CH_2O + HO_2 \tag{2.25}$$

$$CH_3O + CH_4 \rightarrow CH_3OH + CH_3 \tag{2.26}$$

Conversion of CH_3O to formaldehyde (CH_2O) is readily obtained by thermal dissociation (2.24) or reaction with molecular oxygen (2.25). Reaction (2.26) shows that CH_3O can also react with CH_4 and yield CH_3OH, but it requires that CH_4 is present in sufficient amounts to become the most frequent collision partner of CH_3O. As a consequence, high CH_4/O_2 ratios combined with a high absolute concentration of CH_4 will promote high selectivities of CH_3OH, while suppressing alternative reaction channels. The selectivity of CH_3OH approaches 100 % when $CH_4/O_2 \gg 100$, but too high ratios require very low absolute concentrations of O_2 and thereby limit the fuel conversion and the product yield. High absolute O_2 concentrations, consistent with low CH_4/O_2 ratios, will, on the other hand, result in a substantial adiabatic temperature rise caused by the exothermic fuel oxidation and hence, promote formation of the full oxidation products CO and CO_2. This trend of inverse proportionality between methanol selectivity and methane conversion

is recognized among the experimental series depicted in Figure 2.1 on page 18. Previous investigations listed in Table 2.1 cover CH_4/O_2 ratios from 8.1 to 39, but considering the large scatter in the present results, it is difficult to deduce a more narrow optimal range until more consistent investigations become available.

2.2.4 Gas Phase Sensitizers

Certain gaseous additives are able to catalyze the low-temperature conversion of methane to oxygenates. This can be achieved indirectly by promoting fuel conversion at lower temperatures, which favors oxygenated products with low thermal stability. The selectivity of desired products may also be directly promoted if these additives enable new and more attractive reaction pathways. Compounds with these abilities are called *initiators* and *promoters* respectively; or *gas phase sensitizers* in general, and they may prove to be an important parameter in the optimization of the partial oxidation process.

Gas phase sensitizers of particular interest in the current project include nitrogen oxides (NO_x, i.e. NO and NO_2) and sulfur compounds, like H_2S and SO_2, as well as higher hydrocarbons that are present in crude natural gas.

Nitrogen Oxides (NO_x)

The understanding of nitrogen chemistry during combustion of hydrocarbon fuels have evolved considerably throughout the past decades motivated by the increasing concern of harmful NO_x-emissions and the subsequent development of reburning and SNCR (Selective Non-Catalytic Reduction) technologies [101–106]. The sensitizing effects of NO_x on various hydrocarbon fuels have been the subject of numerous investigations and several recent papers are available including both experimental and modeling studies, e.g. [105–113]. Nitrogen oxides have the ability to reduce the initiation temperature of the hydrocarbon conversion, either through direct reactions with intermediate species from the hydrocarbon oxidation chain that exhibit lower energy barriers than their pure hydrocarbon counterparts, or indirectly through a number of radical reactions between NO/NO_2 and the H/O radical pool. Both mechanisms share the common feature that NO and NO_2 are continuously recirculated in so-called *auto-catalytic* cycles. As a consequence, even trace amounts of NO_x present in the reaction mixture may have a substantial impact on the oxidation chemistry of CH_4 and other hydrocarbon fuels. These auto-catalytic NO_x-cycles as well as the general reaction mechanism of NO_x will be discussed in more details in later sections of this

thesis. At the moment, NO_x is considered the most promising gas phase sensitizer.

Sulfur Compounds (H_2S/SO_2)

Gas phase sulfur chemistry at elevated temperatures relevant to combustion, and, in particular, the interactions between sulfur compounds and hydrocarbon fuels, are issues that are far less understood than the NO_x mechanism. There is reason to believe that SO_2 may act as a radical sink during hydrocarbon combustion [114] and, hence, exhibit an adverse effect on the fuel conversion, but publications in the field are limited and sometimes even contradictory [115, 116]. The high pressure relevant to the present work may, however, facilitate completely different reaction mechanisms. Some papers about sulfur/hydrocarbon kinetics have been published in Russia, e.g. by Arutyunov [117], but linguistic barriers make it difficult to approach this work. Nonetheless, it is interesting to disclose possible sensitizing (or inhibiting) effects of sulfur compounds in relation to low temperature and high pressure oxidation of light hydrocarbon fuels since small amounts of sulfur ($<1\,\%$) are typically found in crude natural gas. This is in the form of H_2S, which is readily oxidized to SO_2 upon contact with oxygen.

Higher Hydrocarbons (C_2H_6, etc.)

It has been demonstrated [85, 118] that natural gas is more susceptible to partial oxidation to oxygenated hydrocarbons than pure methane. This indicates a promoting effect of the higher hydrocarbons ($C_{>1}$) present in natural gas. These compounds typically represent 1 to 10 % of crude natural gas with C_2H_6 as the major constituent. Compared to CH_4, bond dissociation energies are lower in higher hydrocarbons, e.g. $D^{298}_{H_3C-CH_3} = 90.1 \pm 0.2\,\mathrm{kcal/mol}$ and $D^{298}_{H-CH_2CH_3} = 100.4 \pm 0.3\,\mathrm{kcal/mol}$ compared to $D^{298}_{H-CH_3} = 104.9 \pm 0.1\,\mathrm{kcal/mol}$ [98], and they are expected to react more easily and form radicals before methane, e.g. via reaction with molecular oxygen in (2.27) or thermal decomposition in (2.28):

$$C_2H_6 + O_2 \rightarrow C_2H_5 + HO_2 \tag{2.27}$$

$$C_2H_6 + M \rightarrow CH_3 + CH_3 + M \tag{2.28}$$

The released HO_2, C_2H_5, and CH_3 radicals may subsequently initiate the CH_4 oxidation chain.

2.2.5 Surface Reactions

Laboratory investigations of the homogeneous partial oxidation of natural gas typically involve low flow rates and large reactor surface-to-volume ratios ($^{S}/_{V}$). This gives rise to a substantial contact between the reaction mixture and the reactor surface, which makes it relevant to consider the issue of potential surface reactions. If the hydrocarbon conversion is influenced by catalytic activity at the surface of the reactor, adjacent fittings, tubings, etc., the resulting measurements do not reflect the pure homogeneous gas phase chemistry and hence, cannot be used to validate the process. The nature of these surface reactions can be very diverse. Chain-carrying radicals can be deactivated if they recombine at the surface and form stable compounds. This inhibits the chemistry and results in lower conversion rates and/or higher initiation temperatures. Opposite effects may also be obtained if surfaces promote initiation of the reaction sequence, e.g. by catalyzing radical formation at low temperatures. The desired products may also be oxidized at the surface. It is likely that certain materials are selective towards specific compounds and hence, promote different phenomena under different reaction conditions.

It is crucial to minimize, and preferably eliminate, catalytic activity at exposed surfaces to ensure the quality of the experimental results. This can be achieved either by applying an inert reactor material or by reducing the $^{S}/_{V}$ ratio. The latter is inherently obtained in large industrial scale reactors, so the issue of surface reactions is mainly a concern in relation to laboratory experiments.

Glasses, like quartz, pyrex, and sapphire, are generally regarded as inert materials with very little catalytic activity towards hydrocarbon oxidation chemistry, while various metals are known to catalyze hydrocarbon conversion. Burch *et al.* [66] conducted experiments in stainless steel, quartz, and pyrex reactors at pressures from 5 to 50 bar. They observed no significant differences in the performance of the two glass reactors, while the stainless steel reactor did not produce any methanol until $>$20 bar, and only at the highest pressure (50 bar) were they able to measure yields of methanol of comparable magnitude to those obtained in the glass reactors.

The problem with glass reactors is obviously the brittle nature of the material and low durability towards large pressure gradients. This issue has typically been solved by applying a steel reactor with a tightly fitted glass-lined interior. Even so, glasses generally exhibit very low thermal expansion coefficients compared to metals, which inevitably requires a certain spacing between the two materials in order to avoid crushing the glass-lining when the reactor is heated. In the process of designing such reactors, it is difficult

to avoid exposure of fittings, O-rings, locking-nuts, etc., which may be sufficient to establish a noticeable heterogeneous conversion of reactants and/or products [78].

As seen in Table 2.1, almost all experimental investigations conducted within the last two decades apply glass reactors. Rytz and Baiker [69] deliberately applied a very high $^{S}/_{V}$ ratio $\gg 100$ by inserting quartz wool into their tubular quartz reactor in order to investigate possible surface activities. They did not obtain high selectivities of methanol despite methane conversions up to 7 %, which can be interpreted in terms of catalytic oxidation of the product at the surface. This observation was supported by Ozturk *et al.* [119], who conducted a theoretical study of the partial oxidation of methane on a SiO_2 surface with multiple surface defects using the semiimperical MOPAC-PM3 method developed by Stewart [120]. They concluded that adsorbed O_2 is likely to react with methane at the silica surface and form adsorbed methanol followed by H-atom elimination and subsequent release of gaseous formaldehyde. The mechanism is sketched below. Bullets ($\bullet$) indicate that the compound is bound to a surface.

$$O_2 \rightarrow \bullet O_2 \tag{2.29}$$

$$\bullet O_2 + CH_4 \rightarrow \bullet CH_3OH + \bullet O \tag{2.30}$$

$$\bullet CH_3OH \rightarrow 2 \bullet H + CH_2O \tag{2.31}$$

The mechanism proposed by Ozturk *et al.* [119] can explain the low selectivity reported by Rytz and Baiker [69]. It is emphasized that Rytz and Baiker used an abnormally high surface area compared to typically applied reactor configurations; even for laboratory investigations. Even so, their observations still raise the question whether glass reactors can be regarded as completely inert in terms of surface reactions.

Unlike most others, Lødeng *et al.* [76] used a reactor made of *alsint* (Al_2O_3) for their studies of partial methane oxidation at high pressure. Alumina oxide is also regarded as a relatively inert material towards surface reactions, but only few experimental investigations exist to confirm this [100]. It is difficult to deduce any trends regarding surface activities of the reactor material based on the results reported by Lødeng *et al.* [76]. Their use of a very low $^{S}/_{V}$ ratio in the reactor (see Table 2.1), in any case limits the contact between the reaction mixture and the surface material. However, recent in-house experiments by Johansson [121] with CH_4 and CH_3OH oxidation at atmospheric pressure and flow reactors of different materials point towards increased surface activity of Al_2O_3 compared to quartz.

2.3 The Heterogeneous Process

The first investigations of the catalytic direct partial oxidation of natural gas to oxygenated hydrocarbons date back to the early years of the twentieth century where one of the first patents in the field was granted Lance and Elworthy [122] in 1906. They claimed that formaldehyde, formic acid, and methanol could be obtained by oxidizing methane with hydrogen peroxide at near-ambient conditions in the presence of iron sulfate ($FeSO_4$). Since then, a broad range of catalysts have been tested including principal metals and single- and multi-metal oxides of Mo, V, Ti, Fe, Ag, Cu, Sn, Zn, and others, as well as zeolites, e.g. [72, 95, 96, 118, 123–126]. These investigations have identified MoO_3/SiO_2 and V_2O_5/SiO_2 with O_2 or N_2O/NO_x as oxidizer, as the most promising catalytic systems. It is noticed that catalytic conversion of methane tends to yield mixtures of formaldehyde and methanol, where formaldehyde often appears as the major constituent in contrast to the homogeneous process that mainly produces methanol.

In 1971, Dowden and Walker [123] were granted a patent on a process that used multi-metal oxides of MoO_3 in combination with a wide range of other metal oxides. Dowden and Walker stated that in order to be a successful catalyst, the material had to possess a dual-functionality where at least one of the metal oxides is capable of catalyzing the oxidation of hydrocarbons by oxygen, while another metal oxide should catalyze the hydration of alkenes. They identified $Fe_2O_3(MoO_3)_3$ as the most active catalyst and obtained a 73 % peak selectivity of oxygenates at 2.1 % methane conversion from a 97/3 mixture of methane and oxygen at 712 K and 52 bar. The catalytic system proposed by Dowden and Walker was later re-investigated by Chellappa and Viswanath [95], who obtained a peak selectivity of 51 % oxygenated hydrocarbons at 5.7 % methane conversion at 743 K and 34 bar.

In 1997, Herman *et al.* [125] compared the catalytic performance of V_2O_5/SiO_2 and MoO_3/SiO_2 in a double-bed catalyst at 903 K and atmospheric pressure. The first bed contained 1 wt% sulphonated SrO/La_2O_3, which is a powerful methyl radical generator, while the second bed contained either 1 wt% of the vanadium catalyst or 2 wt% of the molybdenum catalyst. V_2O_5/SiO_2 proved to be far more active than the molybdenum based catalyst at these conditions, but it was difficult to control and the authors only managed to obtain about 36 % peak selectivity of oxygenated hydrocarbons at 4.4 % methane conversion. In a recent study from 2002, Barbero and coworkers [126] claim to have developed a 0.03 % V_2O_5/SiO_2 based catalyst with a specific surface area of only 1 m^2/g that produces up to 40 % selectivity of oxygenates at 40 % methane conversion from a slightly rich methane/oxygen mixture with addition of 1 % NO at temperatures from 803 to 1023 K

and atmospheric pressure.

Despite the very active interest in the heterogeneous route, no milestone achievements have yet been reported. The fact that homogeneous reactions may well take place in the void spaces of the catalyst bed makes it difficult to accurately characterize the performance of different heterogeneous systems and identify a set of optimal reaction conditions.

Experimental investigations of the heterogeneous process are scattered over a wide range of conditions including temperatures and pressures from 373 to 1173 K, and 1 to 70 bar [124]. However, the majority of the reported results share a striking likeness with the reported homogeneous experiments in terms of applied temperature, pressure, and CH_4/O_2 ratios, which indicates that both homogeneous and heterogeneous reactions may have played a pronounced role. Such multi-reacting systems exhibit interesting perspectives if the individual reaction mechanisms were sufficiently understood to enable proper utilization. Mackie [83] proposed a scenario where dissociation of CH_4 is facilitated at low temperatures by a heterogeneous reaction followed by diffusion of free radicals into the gas phase and subsequent initiation of the hydrocarbon oxidation chain. However, an important obstacle for designing this reacting system is the limited understanding of the homogeneous gas phase chemistry.

In 1993, Chun and Anthony [72] investigated the catalytic performance of a range of multi-metal oxides, including molybdenum and vanadium compounds, in a fixed-bed flow reactor at 640–750 K, 50.7 bar, and $CH_4/O_2 = 22$. They compared the results with data obtained in an empty reactor as well as a fixed-bed of pyrex beads under similar conditions, but they did not measure any improvements of the methanol selectivity as a result of changing the catalytic material. This observation led the authors to reject the catalytic system and instead suggest that a significant amount of the desired product was produced as a result of homogeneous reactions taking place in the void spaces of the packed bed.

2.4 Summary and Perspective

The homogeneous direct partial oxidation of natural gas to oxygenated hydrocarbons has received considerable attention throughout the past century with the earliest investigations dating back to 1902-03 [40, 41]. Most investigations have been concerned with an experimental optimization of the process, but despite the efforts applied, no commercial applications have yet been commissioned.

Reported results show significant scatter in terms of peak methanol se-

lectivities and corresponding methane conversions. The most promising results in terms of high methanol yields have been obtained by Gesser and co-workers [65, 67, 68], and Feng *et al.* [75], who measured combinations of methanol selectivities and methane conversions that extend into the commercially attractive range ($S_{CH_3OH} > 80$–$90\,\%$ and $X_{CH_4} > 7.5$–$10\,\%$). Here, the direct process is expected to become a direct competitor to conventional synthesis gas-based methanol plants, but attempts to reproduce these results have been unsuccessful for reasons currently unknown.

In light of the scattered results obtained at seemingly identical reaction conditions, only broad proposals of optimal reaction conditions can be justified at the present stage. These involve pressures from 30–100 bar, temperatures from 550–800 K, and $10 < CH_4/O_2 < 40$ in the feed. The use of gas phase sensitizers to promote the yield of the desired products has further been considered. Nitrogen oxides (NO_x) are currently the most promising gas phase sensitizers, but applications of sulfur compounds and higher hydrocarbons found in crude natural gas may also gain relevance. Experimental investigations in laboratory scale reactors typically involve high surface-to-volume ratios facilitating a substantial contact between the reaction mixtures and the reactor surface. This may give rise to undesired heterogeneous catalytic conversion of reactants and/or products. The issue can be limited by applying inert reactor materials; preferably quartz, or other glasses, but even so, experimental investigations indicate that glass materials may still exhibit a slight catalytic effect.

The presented review has demonstrated that a different approach is needed before a consistent process optimization is rendered possible. The new strategy; as advocated in the current project, should focus on the detailed chemical mechanisms that govern the hydrocarbon conversion. Not until this fundamental issue is clarified will it be possible to explain the significant diversities observed among results from the literature.

Chapter 3

Thermodynamic Properties

Thermodynamic properties of chemical compounds constitute the foundation for subsequent calculations of chemical kinetics, species transport, and energy relations relevant to the direct conversion of natural gas to liquid chemicals. General relations between temperature, T, pressure, P, and molar volume, V_m (or reciprocal density $1/\rho$), are predicted by *equations of state* (EoS) that are based on considerations of interactions between intermolecular forces and the energy and pressure in the fluid. The generic form of an EoS can be written as:

$$P = P(V_m, T) \tag{3.1}$$

This chapter presents a general outline of the approach to thermodynamic properties used in the present work. The content will be called upon on various occasions throughout the project.

3.1 Ideal Gas Properties

The *Ideal Gas Law*, written in Equation (3.2), is an example of a simple EoS. An ideal gas can be regarded as a gas of identical particles of zero volume with no intermolecular forces. Hence, in a mixture of ideal gases, each compound has the same physical properties as if it was alone in the same volume.

$$\frac{PV_m}{RT} = 1 \tag{3.2}$$

The main advantages of the Ideal Gas Law are its simplicity and the fact that no information are required about the specific compounds subjected to the analysis. In practice, real gases do not exhibit ideal gas properties, but the approximation often describes real gases fairly well. An important

exception is the combination of high pressure and low temperatures, where molecules and atoms are closer together on an average giving rise to a potential energy contribution and increased attractive forces. This is an issue in the present work, where high pressure is required to run the reaction. For that reason, more sophisticated thermodynamic relations should also be considered.

3.1.1 Reference State Thermodynamic Database

Before turning to the application of more complicated EoS, it is relevant to consider the thermodynamic functions: enthalpy, H^{ig}, and entropy, S^{ig}, at ideal gas conditions. These are calculated from Equation (3.3) and (3.4) respectively:

$$H^{ig}(T) = H_{ref}(T_{ref}) + \int_{T_{ref}}^{T} C_p^{ig}(T)\,\mathrm{d}T \tag{3.3}$$

$$\begin{aligned} S^{ig}(T,P) = S_{ref}(T_{ref},P_{ref}) &+ \int_{T_{ref}}^{T} \frac{C_p^{ig}(T)}{T}\,\mathrm{d}T \\ &- R\ln\left(\frac{P}{P_{ref}}\right) - R\sum_i y_i \ln y_i \end{aligned} \tag{3.4}$$

The last term in Equation (3.4) accounts for the *entropy change of mixing* for ideal solutions and is only relevant when mixtures are considered [127].

In many cases, calculations of thermodynamic state functions are only intended to reflect changes in the conditions of a system where the molar content in the fluid phase remains constant. Under these conditions, reference states can be chosen arbitrarily, but when state functions are calculated in relation to e.g. chemical reactions or chemical equilibrium, it is necessary to define consistent reference states for the involved species in order to predict the correct properties. When this situation occurs in the present work, a uniform reference state is defined at $T_{ref} = 298.15\,\mathrm{K}$ and $P_{ref} = 1\,\mathrm{bar}$ for all compounds. The molar enthalpies and entropies of an ideal gas at these reference conditions (H_{298} and S_{298}) are obtained from the literature, e.g. via the NIST Chemistry Webbook [128], or the Thermochemical Database of Burcat and Ruscic [129], where the latter includes some of the latest evaluations of enthalpies of formation from the Active Thermochemical Tables of Ruscic *et al.* [130, 131]. These are regarded as the most accurate sources available in the field.

Equation (3.3) and (3.4) assume that the molar heat capacity of the ideal gas, C_p^{ig}, is a known function of the temperature. Expressions of $C_p^{ig}(T)$

are often available in polynomial form; as in Equation (3.5), where C_p^{ig}/R is fitted to experimental data from the literature. Similar polynomial fits to H^{ig}/RT and S^{ig}/R have been developed by Gordon and McBride [132] for easy computation in connection to the NASA Chemical Equilibrium program. These are commonly referred to as "NASA polynomials" and are shown in Equation (3.6) and (3.7). Notice that the approximate expression of S^{ig}/R in (3.7) compares with the complete Equation (3.4), only when $P = P_{ref}$ and $y_i = 1$.

$$\frac{C_p^{ig}}{R} \cong a_1 + a_2 T + a_3 T^2 + a_4 T^3 + a_5 T^4 \tag{3.5}$$

$$\frac{H^{ig}}{RT} \cong a_1 + \frac{a_2}{2} T + \frac{a_3}{3} T^2 + \frac{a_4}{4} T^3 + \frac{a_5}{5} T^4 + \frac{a_6}{T} \tag{3.6}$$

$$\frac{S^{ig}}{R} \cong a_1 \ln(T) + a_2 T + \frac{a_3}{2} T^2 + \frac{a_4}{3} T^3 + \frac{a_5}{4} T^4 + a_7 \tag{3.7}$$

It is generally convenient to express the thermodynamic properties as dimensionless quantities, e.g. C_p^{ig}/R, in order to ease the use of any desired unit system through the choice of the universal gas constant.

The present work includes a reference state thermodynamic database in terms of H_{298}, S_{298}, and $C_p^{ig}(T)$ for all involved stable and unstable compounds found in the gas phase. The database is found in Table 3.1. For computational purposes, these data are also available in terms of 7-constant NASA polynomials (a_{1-7}).

Thermodynamic Properties of Peroxide Species

In the literature, thermodynamic properties of alkylperoxide species and their radical derivatives often vary considerably. In the present work, this involves CH_3OOH, CH_3OO, CH_2OOH, C_2H_5OOH, and C_2H_5OO that warrant a few supplementary comments regarding the origin of the data found in Table 3.1.

The preferred value of $H_{298}(CH_3OOH) = -30.1 \pm 1\,^{\text{kcal}}/_{\text{mol}}$ is obtained from the recent experimental work by Matthews *et al.* [133]. In their paper, Matthews *et al.* also presented supplementary *ab initio* calculations at a high-level of theory yielding a value of $-30.4\,^{\text{kcal}}/_{\text{mol}}$ in support of the experimental result. The preferred value is further substantiated by *ab initio* CBS-APNO calculations by Blanksby *et al.* [134], who reported a value of $-30.9 \pm 0.7\,^{\text{kcal}}/_{\text{mol}}$.

Table 3.1: Thermodynamic properties of chemical species in the gas phase considered in the present work. Units are $^{\text{kcal}}/_{\text{mol}}$ for H, and $^{\text{cal}}/_{\text{mol K}}$ for S and C_p. Temperature (T) range is in K.

Name	Formula	H_{298}	S_{298}	$C_{p,400}^{ig}$	$C_{p,600}^{ig}$	$C_{p,800}^{ig}$	$C_{p,1000}^{ig}$	$C_{p,1500}^{ig}$	T-range	Ref.
Atomic hydrogen	H	52.10	27.42	4.97	4.97	4.97	4.97	4.97	200–6000	[129]
Hydrogen	H_2	0.0	31.23	7.00	6.99	7.08	7.21	7.73	200–6000	[129]
Atomic oxygen	O	59.55	38.49	5.13	5.05	5.02	5.00	4.98	200–6000	[129]
Oxygen	O_2	0.0	49.03	7.20	7.67	8.07	8.34	8.72	200–6000	[129]
Hydroxyl radical	OH	8.92	43.91	7.07	7.06	7.15	7.34	7.88	200–6000	[129, 131]
Water	H_2O	–57.79	45.13	8.19	8.68	9.26	9.87	11.31	200–6000	[129]
Hydroperoxyl radical	HO_2	2.94	54.75	8.89	9.99	10.77	11.38	12.48	200–6000	[129, 131]
Hydroperoxide	H_2O_2	–32.43	56.05	11.09	12.79	13.99	14.95	16.59	200–6000	[129, 131]
Carbon monoxide	CO	–26.41	47.24	7.02	7.27	7.62	7.93	8.40	200–6000	[129]
Carbon dioxide	CO_2	–94.04	51.09	9.86	11.32	12.29	12.98	13.91	200–6000	[129]
Carboxyl radical	HOCO	–44.33	60.07	12.01	14.04	15.35	16.27	17.70	200–3000	[135][a]
Methyl radical	CH_3	35.01	46.36	9.98	11.50	12.86	14.09	16.25	200–6000	[129]
Methane	CH_4	–17.83	44.52	9.65	12.48	15.04	17.16	20.58	200–6000	[129]
Hydroxymethyl radical	CH_2OH	–4.11	58.35	12.79	15.36	17.08	18.44	20.59	200–6000	[129]
Methoxy radical	CH_3O	4.84	55.98	12.05	15.47	17.86	19.70	22.25	200–6000	[129]
Methanol	CH_3OH	–48.04	57.51	12.07	15.98	19.00	21.38	25.07	200–6000	[129]
Methylperoxyl radical	CH_3OO	3.00	64.44	15.05	19.17	22.05	24.20	27.31	200–6000	[129, 136]
Hydroperoxymethyl radical	CH_2OOH	15.79	65.89	17.16	21.28	24.16	26.31	29.42	200–2500	[137][b]
Methylperoxide	CH_3OOH	–30.10	65.94	18.83	23.02	25.52	27.50	30.65	200–6000	[129, 133]
Formaldehyde	CH_2O	–25.95	52.28	9.36	11.52	13.37	14.82	16.93	200–6000	[129]
Formyl radical	HCO	10.11	53.59	8.75	9.84	10.85	11.66	12.94	200–6000	[129]
Acetylene	C_2H_2	54.52	48.01	12.01	13.89	15.16	16.23	18.14	200–6000	[129]
Vinyl radical	C_2H_3	70.88	55.84	11.81	14.90	17.06	18.78	21.50	200–6000	[129]

Continues on next page

Continued from last page

Name	Formula	H_{298}	S_{298}	$C_{p,400}^{ig}$	$C_{p,600}^{ig}$	$C_{p,800}^{ig}$	$C_{p,1000}^{ig}$	$C_{p,1500}^{ig}$	T-range	Ref.
Ethylene	C_2H_4	12.54	52.41	12.58	16.95	20.05	22.49	26.19	200–6000	[129]
Ethyl radical	C_2H_5	28.36	59.05	14.59	19.35	22.93	25.78	30.16	200–6000	[129]
Ethane	C_2H_6	–20.04	54.77	15.57	21.36	25.80	29.32	34.71	200–6000	[129]
Ketene	CH_2CO	–11.40	57.80	14.20	16.89	18.79	20.25	22.48	200–6000	[129]
Acetyl radical	CH_3CO	–2.46	63.91	14.27	18.13	20.99	23.19	26.34	200–6000	[129]
Formylmethyl radical	CH_2CHO	6.00	64.02	15.15	18.60	21.30	23.34	26.35	300–5000	[129]
Acetaldehyde	CH_3CHO	–39.79	63.07	15.78	20.58	24.16	26.91	30.96	200–6000	[129]
Ethanol	C_2H_5OH	–56.15	67.05	19.31	25.96	30.59	34.15	39.53	200–6000	[129]
1-Hydroxyethyl radical	1-C_2H_4OH	–12.91	69.06	18.30	23.48	27.16	30.02	34.52	200–6000	[129]
2-Hydroxyethyl radical	2-C_2H_4OH	–5.70	69.70	19.38	24.40	27.94	30.70	35.00	200–6000	[129]
Hydroxyethylperoxyl radical	$HOC_2H_4O_2$	–38.60	84.71	24.77	30.25	34.42	37.74	41.73	300–2500	[138]
Ethoxy radical	C_2H_5O	–3.25	66.34	18.93	24.34	28.35	31.44	36.01	200–6000	[129]
Ethylperoxyl radical	C_2H_5OO	–6.80	71.69	21.52	28.48	33.41	37.06	42.30	200–6000	[129,134]
Ethylperoxide	C_2H_5OOH	–39.50	75.17	24.29	31.70	36.63	40.19	45.28	200–6000	[129,134]
1-Hydroperoxyethyl radical	CH_3CHOOH	6.43	74.84	23.60	30.57	35.50	39.15	44.39	200–2500	[137][c]
Vinyloxy radical	H_2CCHO	3.05	61.85	15.04	19.14	21.93	24.02	27.13	200–6000	[129]
Ethenol	H_2CCHOH	–29.80	69.30	17.72	22.86	26.31	28.91	32.82	200–6000	[129]
Nitric oxide	NO	21.76	50.36	7.16	7.46	7.83	8.12	8.54	200–6000	[129,131]
Nitrogen dioxide	NO_2	8.13	57.40	9.67	11.09	12.05	12.67	13.43	200–6000	[129,131]
Nitrate radical	NO_3	17.83	60.37	13.28	16.16	17.51	18.31	19.09	200–6000	[129]
Dinitrogen trioxyl radical	N_2O_3	20.56	75.22	18.57	20.36	21.72	22.58	23.64	200–6000	[129]
Dinitrogen tetroxide	N_2O_4	2.58	72.76	21.63	25.20	27.21	28.36	29.57	200–6000	[129]

Continues on next page

Continued from last page

Name	Formula	H_{298}	S_{298}	$C_{p,400}^{ig}$	$C_{p,600}^{ig}$	$C_{p,800}^{ig}$	$C_{p,1000}^{ig}$	$C_{p,1500}^{ig}$	T-range	Ref.
Nitrosyl hydride	HNO	25.52	52.80	8.48	9.54	10.56	11.40	13.28	200–6000	[129]
Nitrous acid	HONO	–18.74	60.72	12.41	14.43	15.69	16.58	17.88	200–6000	[129]
Nitrous acid isomer	HNO_2	–10.60	56.73	10.40	12.71	14.47	15.77	17.56	300–4000	[d]
Nitric acid	$HONO_2$	–32.03	63.76	15.32	18.73	20.72	21.96	23.34	200–6000	[129]
Nitrosomethane	CH_3NO	18.88	62.33	14.07	17.89	20.79	23.00	26.23	200–6000	[129]
Nitromethyl radical	CH_2NO_2	36.43	68.87	16.73	20.73	23.21	24.95	27.36	200–6000	[129]
Nitromethane	CH_3NO_2	–16.80	66.70	16.60	21.58	25.21	27.88	31.75	300–4000	[139]
Methylnitrite	CH_3ONO	–15.64	72.38	17.75	21.98	25.15	27.52	30.94	200–6000	[129]
Methylnitrate	CH_3ONO_2	–29.16	73.07	21.83	27.57	31.48	34.18	37.57	200–6000	[129]
Nitroethane	$C_2H_5NO_2$	–24.02	76.60	23.50	31.23	36.58	40.45	45.84	200–6000	[129]
Ethylnitrite	C_2H_5ONO	–24.18	80.30	23.50	31.23	36.58	40.45	45.84	200–6000	[140, 141][e]
Ethylnitrate	$C_2H_5ONO_2$	–37.04	78.59	28.17	37.04	42.96	47.12	52.56	200–6000	[129]

a: Data for HOCO adopted from *ab initio* calculations by Fabian and Janoschek [135] and fitted to 7-constant NASA polynomials.

b: $C_{p,298}^{ig} = 14.89\,{}^{\mathrm{cal}}/_{\mathrm{mol\,K}}$ obtained from Janoschek and Rossi [137]. $C_p^{ig}(T)$ is fitted to this value with the temperature dependence adopted from $C_p^{ig}(T)$ (CH_3OO) [129].

c: $C_{p,298}^{ig} = 19.70\,{}^{\mathrm{cal}}/_{\mathrm{mol\,K}}$ obtained from Janoschek and Rossi [137]. $C_p^{ig}(T)$ is fitted to this value with the temperature dependence adopted from $C_p^{ig}(T)$ (C_2H_5OO) [129].

d: Unpublished data [142] based on *ab initio* CBS-QB3 calculations.

e: H_{298} from Domalski and Hearing [140]. S_{298} estimate from Batt and Milne [141]. $C_p^{ig}(T) = C_p^{ig}(T)$ ($C_2H_5NO_2$).

The most recent experimental values of $H_{298}(CH_3OO)$ have been proposed by Knyazev and Slagle [143] ($2.1\pm1.2\,^{\text{kcal}}/_{\text{mol}}$), Blanksby *et al.* [134] ($4.8\pm1.2\,^{\text{kcal}}/_{\text{mol}}$), and latest by Meloni *et al.* [136] ($3.0\pm1.2\,^{\text{kcal}}/_{\text{mol}}$). The latter is in good agreement with the theoretical value of $3.4\,^{\text{kcal}}/_{\text{mol}}$ from Janoschek and Rossi [144] and is preferred in the present study. Supplementary values of S_{298} and $C_p^{ig}(T)$ for both CH_3OOH and CH_3OO are drawn from Burcat and Ruscic [129].

There are no experimental measurements of thermodynamic properties of CH_2OOH. Instead, recent *ab initio* calculations by Janoschek and Rossi [137] have provided the preferred values of H_{298} and S_{298}. It is noticed that their value of H_{298} is almost 45 % higher than the recommended value by Baulch *et al.* [145], who drew analogies to the thermodynamic properties of the parent molecule CH_3OOH with a correction for the missing H-atom that reflects the difference between properties of CH_3OH and CH_2OH. Janoschek and Rossi [137] only provided the heat of formation of CH_2OOH at 298 K, so the temperature dependence of the molar heat capacity has been adopted from the isomer CH_3OO with a constant displacement of the $C_p^{ig}(T)(CH_3OO)$-curve to fit $C_{p,298}(CH_2OOH)$.

Enthalpies of formation of C_2H_5OOH and C_2H_5OO are both drawn from the combined experimental and theoretical work of Blanksby *et al.* [134] yielding values of $H_{298} = -39.5\pm0.7$ and $-6.8\pm2.3\,^{\text{kcal}}/_{\text{mol}}$ respectively. Considering the experimental uncertainties, these values are in good agreement with the corresponding values -41.9 ± 3.1 and $-6.5\pm2.4\,^{\text{kcal}}/_{\text{mol}}$ from Knyazev and Slagle [143] that were also derived from combined experimental and theoretical studies. The preferred value of $H_{298}(C_2H_5OOH)$ is supported by several *ab initio* studies, e.g. Lay and Bozzelli [146] ($-39.9\,^{\text{kcal}}/_{\text{mol}}$), Jungkamp and Seinfeld [147] ($-39.71\,^{\text{kcal}}/_{\text{mol}}$), and Carstensen and Dean [148] ($-39.2\,^{\text{kcal}}/_{\text{mol}}$). Jungkamp and Seinfeld, and Carstensen and Dean also reported *ab initio* calculations of $H_{298}(C_2H_5OO)$ leading to $-5.78\,^{\text{kcal}}/_{\text{mol}}$ and $-5.3\,^{\text{kcal}}/_{\text{mol}}$ respectively. These values lie somewhat above the experimental values from Blanksby *et al.* [134] and Knyazev and Slagle [143], but still within the uncertainty limits. Again, supplementary values of S_{298} and $C_p^{ig}(T)$ for both C_2H_5OOH and C_2H_5OO have been adopted from Burcat and Ruscic [129].

3.2 Cubic Equations of State

The Ideal Gas Law does not account for the relations between molecular interactions and macroscopic properties of the fluid, but these effects are captured by the *cubic equations of state*. Cubic EoS are polynomial equations that are cubic in molar volume. Unlike, the Ideal Gas Law, this type of EoS

is able to predict both liquid- and vapor-phase volumetric behavior (VLE), while maintaining a reasonable compromise between generality and simplicity that makes them suitable for engineering calculations.

The concept of cubic EoS was formulated in 1873 by Van der Waals (VdW) [149] based on considerations of a fluid composed of particles of non-zero size and pairwise attractive interparticle forces. The VdW Equation in (3.8)–(3.9) employs the two characteristic macroscopic properties: critical pressure, P_c, and critical temperature, T_c, embedded in the constants a and b that represent attractive and repulsive forces respectively [150, 151]:

$$P = \frac{RT}{V_m - b} - \frac{a}{V_m^2} \tag{3.8}$$

$$a = \frac{RT_c}{8P_c}, \qquad b = \frac{27R^2T_c^2}{64P_c} \tag{3.9}$$

At given T,P equation (3.8) has three volume roots; as have all cubic EoS. Two of these roots may be complex, but in order to be physically meaningful, roots have to be real, positive, and larger than the constant b. There is always one real positive root when the temperature is above the critical temperature, $T > T_c$. Similarly, when the temperature is equal to the critical temperature, $T = T_c$; except when the pressure is equal to the critical pressure, $P = P_c$, in which case three real positive roots appear that are all equal to the critical molar volume, V_{mc}. When the temperature is below the critical temperature, $T < T_c$, there will be one real positive root at high pressure, while three real positive roots are obtained for a range of lower pressures. The middle root is here of no significance, but the smaller root represents a liquid volume, while the larger root is a vapor volume. This infers that saturated liquid and vapor molar volumes will be given by the smallest and the largest root when the pressure is equal to the saturated vapor pressure, $P = P^{sat}$, [127, 152].

A number of modified cubic EoS have emerged since the VdW Equation that enable more accurate predictions of experimental data [150, 151]. However, these modifications are essentially minor deviations from the original VdW Equation focusing on more accurate descriptions of the attractive and repulsive parameters a and b.

3.2.1 Soave-Redlich-Kwong Equation

The Soave-Redlich-Kwong Equation (SRK) [153] presented in (3.10)-(3.12) is a three-parameter modification from 1972 of the original Redlich-Kwong [154]

two-parameter cubic EoS development of the VdW Equation.

$$P = \frac{RT}{V_m - b} - \frac{a}{V_m^2 + bV_m} \tag{3.10}$$

$$a(T) = \frac{0.42747R^2T_c^2}{P_c}\left[1 + \xi\left(\omega\right)\left(1 - \sqrt{T_r}\right)\right]^2, \qquad b = \frac{0.08664RT_c}{P_c} \tag{3.11}$$

$$\xi\left(\omega\right) = 0.480 + 1.574\omega - 0.176\omega^2 \tag{3.12}$$

The SRK Equation presents two important modifications compared to the original VdW Equation. The first modification is the introduction of a temperature dependence of $a = a(T)$ by including the reduced temperature: $T_r = \frac{T}{T_c}$. Secondly, the SRK Equation introduces an additional characteristic parameter besides P_c and T_c, which is the *acentric factor*, ω, defined by:

$$\omega \equiv -1 - \log\left[P^{sat}_{r(T_r=0.7)}\right] \tag{3.13}$$

Here, $P^{sat}_{r(T_r=0.7)}$ is the reduced vapor pressure at $T_r = 0.7$ [155]. The acentric factor represents the acentricity, or non-sphericity, of a molecule, so by definition, ω is essentially zero for monatomic compounds. The acentric factor is influenced by the symmetry and polarity of a given molecule. Methane is close to spherical and non-polar and therefore exhibits a small value of $\omega_{\mathrm{CH_4}} = 0.012$, while the non-sphericity of ethane results in $\omega_{\mathrm{C_2H_6}} = 0.100$. For comparison, the strong polarity of methanol provides a value of $\omega_{\mathrm{CH_3OH}} = 0.564$.

3.2.2 Peng-Robinson Equation

The Peng-Robinson (PR) Equation [156] from 1976 is an alternative development of the VdW Equation. As seen in (3.14)-(3.16), it shares many similarities with the SRK Equation including a relatively high predictive ability of VLE data:

$$P = \frac{RT}{V_m - b} - \frac{a}{V_m^2 + 2bV_m - b^2} \tag{3.14}$$

$$a(T) = \frac{0.45724R^2T_c^2}{P_c}\left[1 + \xi\left(\omega\right)\left(1 - \sqrt{T_r}\right)\right]^2, \qquad b = \frac{0.07780RT_c}{P_c} \tag{3.15}$$

$$\xi\left(\omega\right) = 0.37464 + 1.54226\omega - 0.26992\omega^2 \tag{3.16}$$

Both the SRK and the PR equations are widely used in industry for chemical engineering calculations, but the PR Equation supposedly predicts

liquid densities with a slightly higher accuracy. Furthermore, regional interests have influenced the popularity of the two equations (the SRK and PR equations are developed in Europe and the US, respectively), which has made the PR Equation the preferred EoS in e.g. the oil industry [157, 158]. Thermodynamic calculations involved in the current project are dominated by gas phase calculations. However, in connection to practical applications of the current GTL technology; as will be considered in Chapter 8, liquid phases may occur e.g. during condensation of products (methanol, ethanol, water, etc.) or the use of water or other liquid fluids as cooling or heating agents in heat exchange units. These issues require accurate determination of liquid phase behavior, which is the reason why the PR Equation is the preferred cubic EoS for all subsequent calculations of *real* fluid properties. Values of the characteristic parameters: T_c, P_c, and ω for selected stable species are given in Table 3.2 together with intermolecular force parameters, which will be referred to in the proceeding chapter.

Table 3.2: Intermolecular force parameters [159], and critical constants and acentric factors [127] of selected stable species.

Species	Molecular weight	Lennard-Jones parameters		Critical properties		Acentric factor
	M [g/mol]	σ [Å]	ϵ/κ [K]	T_c [K]	P_c [bar]	ω
H_2	2.016	2.915	38.0	33.2	13.13	−0.216
O_2	31.999	3.433	113.	154.6	50.43	0.022
H_2O	18.015	—	—	647.1	220.55	0.345
N_2	28.014	3.681	91.5	126.2	34.00	0.038
CO	28.010	3.590	110.	132.9	34.99	0.048
CO_2	44.010	3.996	190.	304.2	73.83	0.224
CH_4	16.043	3.822	137.	190.6	45.99	0.012
C_2H_4	28.054	4.232	205.	282.3	50.40	0.087
C_2H_6	30.070	4.418	230.	305.3	48.72	0.100
CH_2O	30.026	—	—	408.0	65.90	0.282
CH_3OH	32.042	—	—	512.6	80.97	0.564
C_2H_5OH	46.069	—	—	513.9	61.48	0.645
CH_3CHO	44.053	—	—	466.0	55.50	0.291

It is sometimes convenient to express the EoS in terms of the *compressibility factor*, Z, which denotes the fluid's deviation from ideal behavior. Equation (3.14) is easily rewritten in (3.17) to express Z. The parameters $a(T)$ and b are unchanged from (3.15).

$$Z \equiv \frac{PV_m}{RT} = \frac{V_m}{V_m - b} - \frac{aV_m}{RT\left(V_m^2 + 2bV_m - b^2\right)} \tag{3.17}$$

Notice that the *right-hand-side* of Equation (3.17) approaches unity, when $a \to 0$ and $b \to 0$, corresponding to negligible intermolecular forces. In this case, the Ideal Gas Law is recovered ($Z = 1$). From Equation (3.17), the molar volume of the considered liquid or vapor is easily obtained from the definition of Z, which can be further converted to a volumetric flow rate by multiplication with the molar flow rate obtained from molar balances or given correlations.

3.2.3 Mixing Rules

The system at hand involves multicomponent mixtures of hydrocarbons, oxygenated hydrocarbons, and smaller inorganic species. Consequently, the thermodynamic relations for pure substances must be supplemented by appropriate mixing rules in order to ensure accurate predictions of the overall fluid properties. For cubic EoS, the customary mixing rules are based on a random mixing approximation [150]. The a_{mix} parameter is obtained from the quadratic mixing rule given in (3.18), and the combining rule in (3.19), while b can be obtained from a simple weighted average; as shown in (3.20).

$$a_{mix} = \sum_i \sum_j x_i x_j a_{ij} \tag{3.18}$$

$$\text{where} \quad a_{ij} = \sqrt{a_i a_j}\,(1 - k_{ij}) \tag{3.19}$$

$$b_{mix} = \sum_i x_i b_i \tag{3.20}$$

k_{ij} is a *binary interaction parameter*, which is an adjustable parameter that can be used to fit experimental data to the model; if such is available. Ideally, k_{ij} is small, and in the absence of experimental data, it is a fair approximation to set $k_{ij} = 0$. This is valid for many hydrocarbon mixtures, while binary mixtures of highly polar and asymmetric molecules deviate to some extent [157]. Light hydrocarbons constitute the predominant substance group in most mixtures occurring in relation to the present GTL process, so, as a starting point, it seems reasonable to set all binary interaction parameters equal to zero. The only multicomponent fluid where hydrocarbons are minor constituents is the liquid that may appear from a potential condensation unit designed to recover the desired products. This liquid phase is expected to contain methanol and water as the major components, and perhaps, a minor content of ethanol, dissolved CH_4, etc., which are considered negligible in the present context. In order to improve the accuracy of the vapor-liquid-equilibrium (VLE) in a potential condensation unit, an estimated value of $k_{ij} = -0.1$ for methanol/water is applied based

on a coarse overview of literature data [160, 161]. In future applications, where more accurate results may be required, it is recommended to apply EoS developed specifically to provide accurate predictions of the behavior of *associating* fluids; e.g. the CPA (Cubic-Plus-Association) EoS [162].

3.3 Deviations from Ideal Gas Behavior

The cubic EoS provide a mean to determine the fluid's deviation from ideal gas behavior during the experimental work of this project. This is done by calculating compressibility factors (Z) for representative gas mixtures under relevant conditions and evaluate the deviations from unity.

The experimental work enclosed in this project has been conducted at high pressures from 20 to 100 bar using medium combustion temperatures from 600 to 900 K. Table 3.3 shows values of Z calculated for representative multicomponent mixtures using the PR cubic EoS in the form of Equation (3.17) with appropriate mixing rules from (3.18)–(3.20) at representative pressures and temperatures.

Table 3.3 indicates that gas mixtures obtained during experiments, i.e. at temperatures >600 K, only deviate slightly from ideal behavior (within ∼4 %) and hence, with good approximation can be treated as an ideal gas.

At room-temperature, some deviations from ideal behavior are observed; in particular for gas mixtures containing methane as the major constituent, and the further presence of polar molecules, like H_2O and CH_3OH, clearly enhances this effect. Hence, $Z_{CH_4} = 0.830$ for pure CH_4 at 100 bar and 298 K meaning that the same number of molecules take up only 83 % of the volume occupied at ideal gas conditions. Nitrogen is far less compressible than methane ($Z_{N_2} = 0.987$ at 100 bar and 298 K), which is encouraging in relation to the use of N_2 as inert diluent in experiments. Even though compressibility factors at room temperature have little relevance to the present experimental and kinetic modeling work that focus on the conversion of the hydrocarbon fuel in a hot reaction zone, it may be import to certain practical applications of the GTL process where pressurized gas streams occur at low temperatures, e.g. during supply of feed gas or product condensation.

3.4 Residual Properties/Departure Functions

In order to extend the predictions of the *real* fluid properties to include enthalpies, entropies, fugacities, etc., the concept of *residual properties* is introduced. Residual properties define the difference between the real func-

Table 3.3: Deviations from ideal gas behavior ($Z = 1$) for representative gas mixtures that may be obtained during experiments. Compressibility factors are calculated using the Peng-Robinson EoS with appropriate mixing rules; see Section 3.2.2 and 3.2.3.

Pressure [bar]	CH_4	O_2	N_2	CO	H_2O	CH_3OH	Compressibility factor, Z [298 K]	[600 K]	[900 K]
100							0.830	1.013	1.024
50	100 %	0	0	0	0	0	0.899	1.005	1.012
20							0.957	1.001	1.005
100							0.836	1.013	1.024
50	95 %	5 %	0	0	0	0	0.903	1.005	1.012
20							0.959	1.002	1.005
100							0.749	1.005	1.023
50	90 %	0	0	3 %	3 %	4 %	0.860	1.000	1.011
20							0.942	1.000	1.004
100							0.987	1.036	1.030
50	0	0	100 %	0	0	0	0.986	1.018	1.015
20							0.992	1.007	1.006
100							0.982	1.035	1.030
50	5 %	0	95 %	0	0	0	0.983	1.017	1.015
20							0.991	1.007	1.006
100							0.985	1.035	1.030
50	0	5 %	95 %	0	0	0	0.985	1.017	1.015
20							0.992	1.007	1.006

tion/property and that of the ideal gas at either the same T,P or the same T,V_m. The residual property, which is also referred to as the "departure function" [150], can be expressed in the general form:

$$\Psi^{res} \equiv \Psi - \Psi^{ig} \tag{3.21}$$

where Ψ represents the thermodynamic state function of the *real* fluid. Ψ^{ig} is the same function/property if the fluid was behaving like an ideal gas, i.e. calculated from Equation (3.3) or (3.4) when Ψ represents H and S respectively.

From the definition of Ψ^{res} in Equation (3.21), it is seen that the real fluid property is calculated by adding contributions from the ideal gas and the residual function ($\Psi = \Psi^{res} + \Psi^{ig}$). The remaining task is therefore to develop a set of equations that expresses the residual functions in a way that is easy to comprehend from a computational point of view.

3.4.1 Residual Helmholtz Energy

The starting point is the residual *Helmholtz energy*, A^{res}, which is defined in (3.22) as the difference between the Helmholtz energy of the real fluid and that at the ideal gas conditions at the same T, V_m; in accordance with Equation (3.21).

$$A^{res}(T, V_m) = A(T, V_m) - A^{ig}(T, V_m) \tag{3.22}$$

Following the definition of A: $\left(\frac{\partial A}{\partial V_m}\right)_T = -P$ and $\left(\frac{\partial A}{\partial T}\right)_{V_m} = -S$, differentiation of A^{res} at constant T yields:

$$\left(\frac{\partial A^{res}}{\partial V_m}\right)_T = -P + \frac{RT}{V_m} \tag{3.23}$$

When the volume approaches infinity ($V_m \to \infty$) the fluid approaches ideal gas conditions and $A^{res} \to 0$. Consequently, A^{res} can be calculated by integrating Equation (3.23) from ∞ to V_m:

$$A^{res} = \int_{\infty}^{V_m} \left(-P + \frac{RT}{V_m}\right) \mathrm{d}V_m = \int_{V_m}^{\infty} \left(P - \frac{RT}{V_m}\right) \mathrm{d}V_m \tag{3.24}$$

3.4.2 Overview of Residual Functions

Expressions of desired residual state functions: H^{res}, S^{res}, and G^{res} are now derived by combining $A^{res}(T, V_m)$, defined in Equation (3.24), with the basic thermodynamic relations given in (3.25) and (3.26).

$$\left(\frac{\partial A}{\partial V_m}\right)_T = -P, \qquad \left(\frac{\partial A}{\partial T}\right)_{V_m} = -S \tag{3.25}$$

$$U = A + TS, \qquad G = A + PV_m, \qquad H = U + PV_m \tag{3.26}$$

Moreover, the integral I is defined from Equation (3.24):

$$\frac{A^{res}}{RT}(T, V_m) = \int_{V_m}^{\infty} \left(\frac{P}{RT} - \frac{1}{V_m}\right) \mathrm{d}V_m = I \tag{3.27}$$

The residual entropy, S^{res}, in Equation (3.28) follows directly from differentiation of (3.27) at constant V_m:

$$\begin{aligned}\frac{S^{res}}{R}(T,P) &= -\frac{1}{R}\left(\frac{\partial A^{res}}{\partial T}\right)_{V_m} + \ln\left(\frac{V_m}{V_m^{ig}}\right) \\ &= -I - T\left(\frac{\partial I}{\partial T}\right)_{V_m} + \ln Z \end{aligned} \tag{3.28}$$

For the present application, it is more convenient to apply T, P as reference instead of T, V_m. This implies a correction to the residual entropy that arises from the difference between $S^{ig}(T,P)$ and $S^{ig}(T,V_m)$ and is included in the last term of Equation (3.28). Here, $V_m^{ig} = RT/P \Rightarrow V_m/V_m^{ig} = PV_m/RT = Z$. Other residual state functions are given in Equation (3.29)–(3.31). Notice that the *fugacity*, f, and the *fugacity coefficient*, φ, are directly obtained from the expression of the residual Gibbs energy in Equation (3.31) [150].

$$\frac{U^{res}}{RT}(T,P) = -T\left(\frac{\partial I}{\partial T}\right)_{V_m} \tag{3.29}$$

$$\frac{H^{res}}{RT}(T,P) = -T\left(\frac{\partial I}{\partial T}\right)_{V_m} + Z - 1 \tag{3.30}$$

$$\frac{G^{res}}{RT}(T,P) = I + Z - 1 - \ln Z = \ln\left(\frac{f}{P}\right) = \ln\varphi \tag{3.31}$$

Example: Peng-Robinson EoS

Calculation of the residual properties via Equation (3.28)–(3.31) is straight forward once the integral I is evaluated. This work depends on the choice of EoS.

Using the PR cubic EoS from (3.14)–(3.16), the analytical expression of I becomes:

$$\begin{aligned} I &= \int_{V_m}^{\infty}\left(\frac{1}{V_m - b} - \frac{a}{RT\left(V_m^2 + 2bV_m - b^2\right)} - \frac{1}{V_m}\right)\mathrm{d}V_m \\ &= \ln\left(\frac{V_m}{V_m - b}\right) - \frac{a}{RT\left(V_m + b\right)} \end{aligned} \tag{3.32}$$

Differentiation by T at constant V_m further yields:

$$\left(\frac{\partial I}{\partial T}\right)_{V_m} = \frac{a}{RT^2\left(V_m + b\right)} - \frac{1}{RT\left(V_m + b\right)}\frac{\mathrm{d}a}{\mathrm{d}T} \tag{3.33}$$

The analytical expression of $\frac{\mathrm{d}a}{\mathrm{d}T}$ for pure substances is given by:

$$\frac{\mathrm{d}a}{\mathrm{d}T} = \frac{-0.45724 R^2 T_c^2}{P_c} \left[1 + \xi(\omega)\left(1 - \sqrt{T_r}\right)\right] \frac{\xi(\omega)}{T} \tag{3.34}$$

As a consequence of the quadratic mixing rule used for a_{mix}, Equation (3.19), the temperature dependence of $a_{mix}(T)$ becomes increasingly complex for multicomponent mixtures and a numeric solution method for $\frac{\mathrm{d}a_{mix}}{\mathrm{d}T}$ is therefore preferred.

The last quantity needed to calculate the residual properties is the compressibility factor Z, which was previously given in (3.17) for the PR EoS:

$$Z = \frac{V_m}{V_m - b} - \frac{a V_m}{RT\left(V_m^2 + 2bV_m - b^2\right)} \tag{3.17}$$

3.5 Vapor-Liquid Equilibrium (VLE)

Recovery of the desired product from the product gas is a key operation in any practical application of the current GTL technology. The efficiency and complexity of the method applied to extract oxygenated hydrocarbons from a gas phase containing mixtures of small density organic and inorganic species have a substantial impact on key figures used to evaluate the feasibility of the given design, like the energy efficiency. Reliable calculations must therefore be available.

The desired products, e.g. methanol, ethanol, formaldehyde, etc., share the common characteristic of having relatively high dew points compared to the unconverted reactants and side-products that may also be found in the product gas, e.g. CH_4, C_2H_6, CO, CO_2, N_2, and H_2. The only exception is water, which probably has the highest dew point among all the species found in significant amounts in the product gas. An obvious separation method is therefore to condense a maximum proportion of the oxygenated hydrocarbons together with the water contained in the gas phase followed by conventional distillation of the resulting liquid fraction. The condensation of gaseous products can be described as an *isothermal flash* operation for multicomponent mixtures.

Isothermal flash operations are characterized by a fixed temperature, T, and pressure, P, in all involved phases. Furthermore, the feed composition z and the total molar feed F are well-defined. The relevant equations are derived from overall and component balances.

First consider the vapor fraction leaving the vessel: $\beta = V/F = 1 - L/F$, where V/F and L/F denote the vapor- and liquid-to-feed ratios respectively.

Combining this overall balance with a component balance for compound i yields:

$$z_i = x_i\,(1-\beta) + y_i\beta \tag{3.35}$$

where x and y represent the species fraction in the resulting liquid and gas phase respectively.

The equilibrium relation $y_i = x_i K_i$ is now introduced in Equation (3.35) followed by rearrangement to yield the expressions of x_i and y_i shown in Equation (3.36) and (3.37) respectively.

$$x_i = \frac{z_i}{1+\beta\,(K_i-1)} \tag{3.36}$$

$$y_i = \frac{z_i K_i}{1+\beta\,(K_i-1)} \tag{3.37}$$

The K-value denotes the molar equilibrium ratio between the gas and liquid phase, which is dependent on the system's intensive variables, i.e. temperature, pressure, and composition. K_i may conveniently be calculated as the ratio between the fugacity coefficients of the two phases:

$$K_i(T,P,x,y) = \frac{\varphi_i^L(T,P,x)}{\varphi_i^G(T,P,y)} \tag{3.38}$$

where φ_i^L and φ_i^G are directly obtained from the calculation of the residual Gibbs energy via Equation (3.31).

Flash calculations face the characteristic problem to simultaneously satisfy the two constraints: $\sum_i x_i = 1$ and $\sum_i y_i = 1$. Typically, this issue is solved by combining the constraints in a single relation:

$$\left(\sum_i x_i - \sum_i y_i\right) = 0 \tag{3.39}$$

which yields Equation (3.40) when inserting the molar fractions from Equation (3.36) and (3.37).

$$f(\beta) = \sum_i \frac{z_i\,(1-K_i)}{1-\beta\,(K_i-1)} = 0 \tag{3.40}$$

Equation (3.40) can be solved iteratively [163] by guessing values of β between 0 and 1 until $f(\beta) = 0$. This is typically done using a numerical solution method, e.g. "Newtons method", which requires the first derivative $f'(\beta)$ given in (3.41):

$$f'(\beta) = \sum_i \frac{z_i \left(1 - K_i\right)^2}{\left[1 - \beta \left(K_i - 1\right)\right]^2} \tag{3.41}$$

Values of x, y, K, and β are unknown and determinations require an iterative solution strategy. The preferred algorithm is based on the *Rachford-Rice* solution method [164] developed by Rachford and Rice in 1952. The original algorithm assumes that K-values are (nearly) independent of the composition, i.e. $K = f(T, P)$, which may not be valid in the present application. Instead, the *modified* Rachford-Rice algorithm for VLE is preferred, see e.g. [163], which considers $K = f(T, P, x, y)$ in accordance with Equation (3.38) and uses separate nested iterations on β and (x, y). A brief outline of the algorithm is presented below:

1. Parameters T, P, z, and F are fixed.
2. Estimate values of (x, y).
3. Calculate $K = f(T, P, x, y)$ from Equation (3.38).
4. Iteratively calculate β using Equation (3.40) and (3.41).
5. Calculate new values (x^*, y^*) from Equation (3.36) and (3.37) and normalize.
6. Compare (x^*, y^*) with the previously estimated values (x, y). The loop is terminated if convergence is obtained. Otherwise return to Step 2 with $(x, y) = (x^*, y^*)$ as the new estimate and repeat.

In principle, it is not necessary to fix the total molar feed (F) in Step 1 in order to calculate final values of β and (x, y), but it is a necessary condition if the resulting relative values should be converted to absolute molar flows.

3.6 Summary

This chapter has presented methods to determine thermodynamic properties of chemical species involved in the current project; both under ideal and non-ideal conditions. For prediction of thermodynamic functions of *real* fluids, in particular for liquid phases, the Peng-Robinson cubic equation of state is

preferred using appropriate mixing rules when applied to multicomponent mixtures. The chapter includes a thermodynamic database with reference state enthalpies of formation and entropies, as well as molar heat capacities as function of the temperature for numerous stable compounds and unstable radicals. In order to extend these data to properties covering real fluids, methods have been developed based on residual functions and cubic EoS. The latter has enabled easy calculations of vapor-liquid-equilibrium (VLE), which may gain relevance in connection to practical applications involving condensation of oxygenated hydrocarbons.

In order to estimate deviations from ideal gas behavior during the experimental work of this project, compressibility factors have been calculated for relevant gas compositions at pressures up to 100 bar and temperatures from ambient to 900 K using the PR cubic EoS. These calculations have demonstrated that ideal gas behavior can readily be assumed in mathematical modeling where temperatures are >600 K, whereas gas mixtures rich in methane and/or water and methanol show considerable deviations from ideal behavior at room-temperature and high pressures.

Chapter 4

High Pressure Flow Reactor

4.1 Introduction

An important achievement of this project is the design, construction, and commissioning of a novel *high pressure flow reactor* setup. This facility enables investigations of homogeneous combustion chemistry involving gaseous reactants of the elements H, O, C, N, and S, at well-defined conditions including high pressures up to 100 bar.

The experimental setup was built during the spring and summer of 2004 in the pilot facility of the CHEC Research Centre at the Department of Chemical Engineering, DTU. The first consistent and reproducible experimental results were obtained in the late autumn of 2004. The author would like to acknowledge the contributing work of technician Jørn Hansen and Res. Ass. Anja E. Rasmussen from the CHEC Research Centre, during this phase of system design, commissioning, and characterization.

From the time of installation, several M. Sc. students have used the setup to complete their thesis work and further projects are underway. These have all contributed with valuable results and experiences enclosed in this Ph. D. work, and for that, the author wishes to thank the following persons: Anja E. Rasmussen, Jon G. Jakobsen, and Jorge G. López.

4.1.1 "Operations Manual"

All valuable experiences and guidelines relevant to the setup have been written in the system's *Operations Manual* [165], which is publicly available at the Department of Chemical Engineering, DTU. This manual contains detailed design descriptions, operational procedures for all equipment involved with the setup, detailed guidelines on how to efficiently plan, set up, and execute experiments; and interpret resulting data. The Operations Manual

also includes first-hand experiences and anecdotes that may become helpful in case of troubleshooting or future retrofitting of the equipment.

Parts of the Operations Manual are incorporated in this thesis, but for further details and practical aspects involved with the system, the reader is referred to this manual [165] for supplementary reading.

4.1.2 Prime Motivations

In order to validate the performance of the developed detailed chemical kinetic model, experimental results have to be available at relevant and, not least, well-defined conditions.

Within recent years, some of the most significant contributions concerning high-pressure combustion chemistry have emerged from flow reactor experiments by Dryer and co-workers, e.g. [109, 166–170], and jet-stirred reactors by Dagaut and co-workers, e.g. [171–173]. These systems were designed for operations within the range of moderately high pressures; up to 20 and 10 bar respectively. Flow reactor results at very high pressures (>50 bar) are still missing despite the relevance to a number of important industrial applications; not only the current GTL process, but also engines and gas turbines, among others.

The need for consistent high-pressure data was the prime motivation for the development and construction of the high pressure flow reactor setup. Moreover, a versatile application of the system was emphasized to enable future investigations of combustion systems not necessarily relevant to the direct partial oxidation of methane to methanol.

As previously discussed in the literature review, Section 2.2.5, laboratory scale reactors of the present kind are typically faced with the challenge to avoid undesired heterogeneous interference from surface materials. The problem can be minimized by applying inert reactor materials, like quartz or pyrex glass, but the nature of these materials imposes a problem when subjected to large pressure gradients or closely fitted to metal parts that expand differently during heating. Moreover, it is attractive to apply a simple reactor design that is easy to replace and maintain, and, not least, to reproduce in terms of mathematical modeling.

4.2 Description of the Setup

Figure 4.1 presents a general view of the high pressure flow reactor setup.

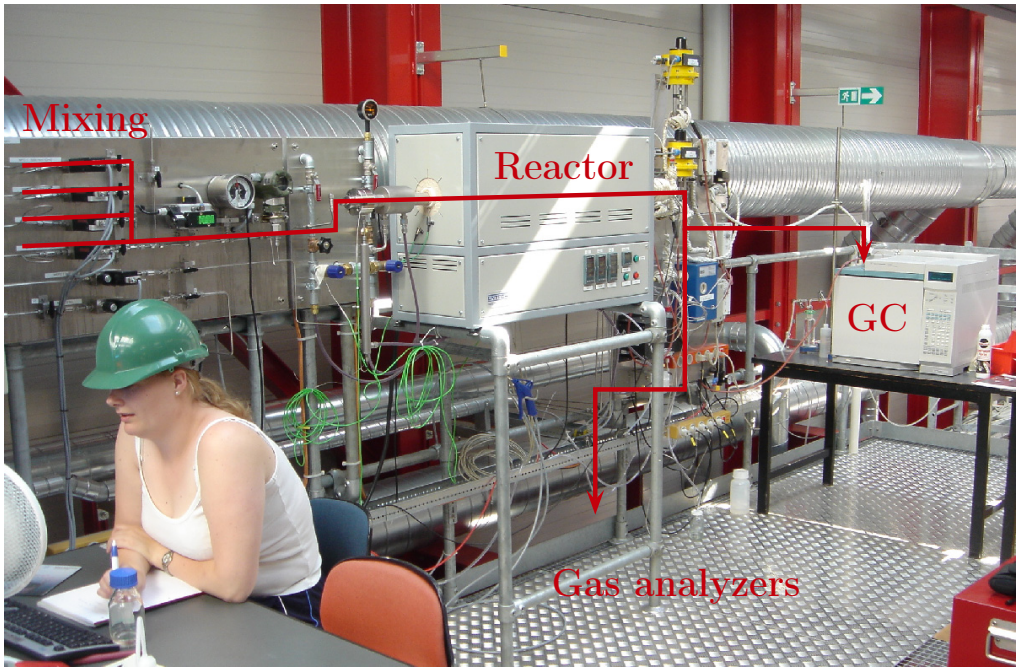

Figure 4.1: General view of the high pressure flow reactor setup. Photo was taken during operation by Res. Ass. Anja E. Rasmussen. The red lines indicate the main flow directions through the setup. Premixing of reactant gases takes place to the left about 1.5 m before the entrance to the reactor, which is positioned inside the oven (central grey box). After the reactor, product analysis is conducted by on-line GC-TCD/FID and IR-based gas analyzers. Photo by C. L. Rasmussen, 2005.

The system enables well-defined investigations of homogeneous gas phase chemistry at pressures from 10 to 100 bar and temperatures up to 925 K using volumetric flow rates of 1–5 $^{\mathrm{NL}}/_{\mathrm{min}}$[1]. The reaction takes place in a tubular reactor made of quartz to minimize surface reactions (i.d. 8 mm, o.d. 10 mm, lg. 1545 mm). The reactor is enclosed in a TP347 stainless steel tube (i.d. 22 mm, o.d. 38 mm) that acts as a pressure shell. A pressure control system consisting of two thermal mass flow pressure controllers (Model 5866 from Brooks Instruments) automatically delivers N_2 to the shell-side of the reactor to obtain a pressure similar to that inside the reactor, thus avoiding devastating pressure gradients across the fragile quartz glass. The steel tube

[1]"Normal" refers to the condition at 273.15 K and 1 bar.

is placed in an Entech tube oven with three individually controlled electrical heating elements that produce an isothermal reaction zone (±5 K) of approx. 50 cm. The reactor temperature is monitored by type K thermo-couples (±2.2 K or 0.75 %) positioned inside two steel thermo pockets placed in the void between the quartz reactor and the steel shell.

All tubings are 1/8" stainless steel with Swagelok fittings. A maximum of four different reactant gases are premixed before entering the reactor. The flow rates are regulated by high pressure digital mass flow controllers (Model 5850S from Brooks Instruments). The point of mixing is positioned about 1.5 m prior to the reactor inlet, which should yield sufficient time to ensure complete mixing regardless of the flow regime.

All gases used in the experiments are high purity gases or mixtures with certificated concentrations (±2 % uncertainty supplied by Linde Gas AGA). The system is pressurized from the feed gas cylinders. The reactor pressure is monitored before the reactor by a differential pressure transducer (DPharp EJX from Yokogawa) and controlled by a pneumatic pressure valve (Flowserve Kämmer) positioned after the reactor. The system employs two pressure valves designed for steady operation above and below 60 bar respectively. They are installed in parallel and can be manually selected through a three-way valve. A schematic overview of the system is provided in Figure 4.2, while a photo of the section surrounding the electrical oven and the pressure reduction valves is shown in Figure 4.3.

4.2.1 Mounting the Quartz Reactor

A unique feature of the design is the mounting of the quartz reactor inside the steel pressure shell. This system prevents the reactant gases from having any contact with surfaces other than the quartz wall throughout the entire reaction zone, while allowing the thermal expansion of the steel. This is facilitated by two AISI 316 stainless steel flanges positioned at each end of the stainless steel tube. The principle of the design is shown in Figure 4.4.

The quartz tube enters the flanges through holes of sufficient diameter to allow maximum expansion of the surrounding steel during heating. The holes turn into small compartments that enclose both ends of the reactor before the 1/4" Swagelok connectors that define the reactor in– and outlet. Inside each compartment, two small AISI 316 steel plates are mounted around the end of the reactor and tightly bolted to the flanges. These plates carry two Viton O-rings that press against the quartz tube and the steel surface of the flanges respectively, thereby sealing the reactor interior from the pressure shell compartment without damaging the glass during the thermal expansion of the metal. The N_2 inlet to the pressure shell compartment is incorporated

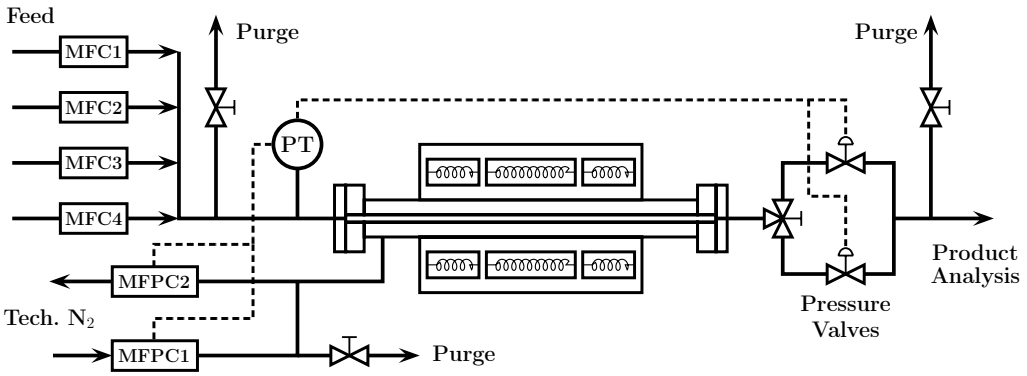

Figure 4.2: Simplified process diagram for the high pressure flow reactor system. Reactant gases are premixed from up to four different digital mass flow controllers (MFC) before the reactor inlet. Nitrogen is supplied to the pressure shell through two thermal mass flow pressure controllers (MFPC). The steel shell containing the tubular quartz reactor is positioned inside an electrically heated oven with three heating elements. Reduction of the pressure to atmospheric level is obtained in the downstream section through one of two pneumatic pressure valves. A pressure transducer (PT) provides the signal for the acting pressure control loops. The simplified control loops are indicated with dashed lines. Manually operated purge valves are used during startup and shutdown.

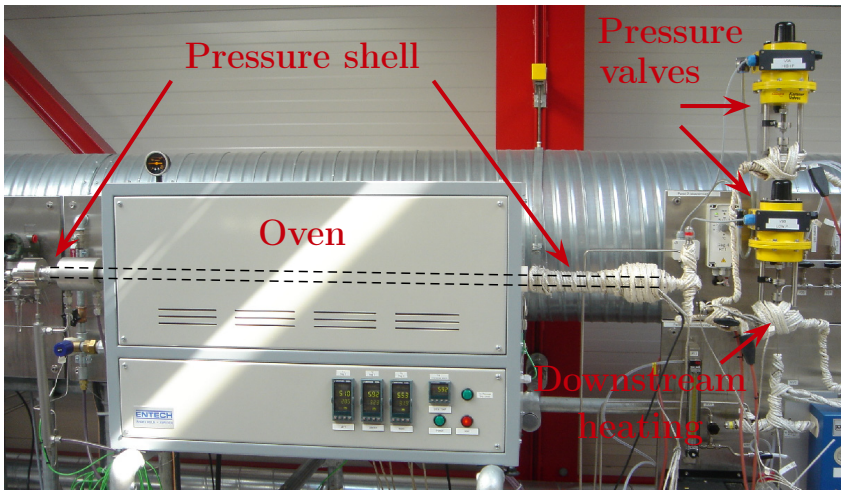

Figure 4.3: Photo of the electrical oven and steel pressure shell enclosing the reactor during operation. Dashed lines indicate the position of the enclosed quartz reactor. The yellow instruments (to the right) are the pressure reduction valves positioned in parallel after the reactor outlet. The downstream section is heated during operation using heating tapes to avoid condensation of condensible products. Photo by C. L. Rasmussen, 2005.

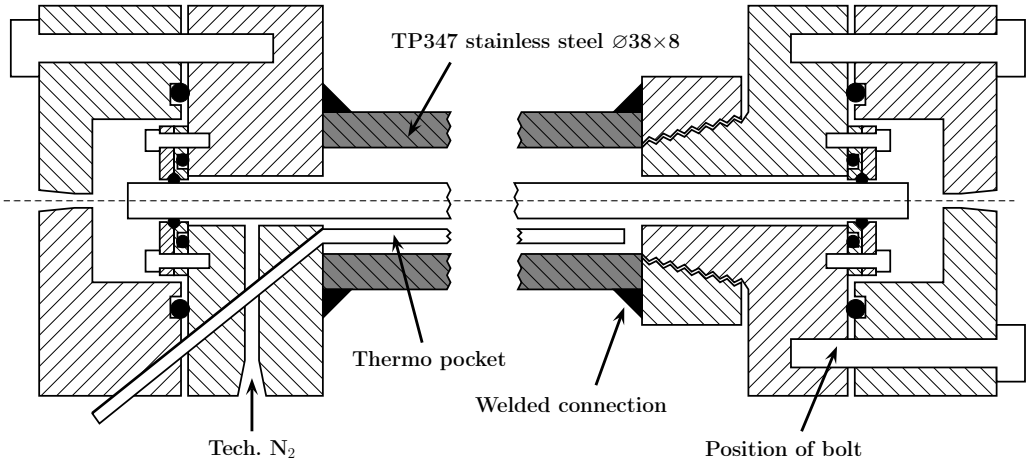

Figure 4.4: The principle of the design of the two AISI 316 stainless steel flanges (light hatched parts) with the two small AISI 316 steel plates and the tubular quartz reactor mounted inside. Positions of bolts are indicated by white silhouettes. Grey hatched parts illustrate the TP347 stainless steel pressure shell. Black circles are Viton O-rings, while black triangles indicate welded connections.

in one of the flanges and so is the access to the two steel pockets that contain the thermo-couples in the space between the reactor and the steel shell. The thermo pockets are sealed from any contact with the high pressure area by welding. The flanges are bolted together using a third Viton O-ring that seals the interior when flattened by the rising pressure from the inside. The bolts are easily removed to gain access to the reactor tube or the Viton O-rings in case they need maintenance.

The mounting system is, in principle, independent of the length or diameter of the quartz tube. These measures are defined by the length of the steel pressure shell and the size of the holes in the small steel plates mounted inside the flanges, where the latter easily can be varied should it be necessary to adjust the residence time. For easy model characterization, the residence time in the inlet section should be of sufficient magnitude to ensure a steady flow regime before the reactants enter the reaction zone (isothermal section).

4.2.2 Product Analysis

The pressure valves reduce the system pressure to atmospheric level prior to product analysis, which is conducted by on-line GC-TCD/FID (6890N Agilent Gas Chromatograph from Agilent Technologies) and a NO_x chemiluminescence gas analyzer (CLD 700 EL model from Eco Physics). The entire downstream section is gently heated during operation to avoid condensa-

tion of potential condensible components before product analysis, e.g. H_2O, CH_3OH, C_2H_5OH, etc. This is obtained by covering all tubings and exposed reactor parts with heating cables; as seen in the photo in Figure 4.3.

The GC has three operational columns (DB1, Porapak N, and Molesieve 13x). Using helium as carrier gas, this system generally allows detection of N_2, O_2, CO, CO_2, most saturated and unsaturated hydrocarbons ($<C_{5-6}$), several oxygenated hydrocarbons, a few nitrated hydrocarbons, SO_2, and H_2S. The overall relative uncertainty of the GC measurements is typically in the vicinity of ±2–5 % depending on the applied calibration gases, and the measuring range for most species spans from almost 100 % to the ppm-range [165]. A similar accuracy is obtained for measurements of NO and NO_2 using the NO_x chemiluminescence gas analyzer. However, it is noted that the zero-calibration of the current type of NO_x analyzer may gradually drift by up to ±10–20 ppm as a result of constant operation over ∼24 hr without recalibration. Since this is the approximate time span of a single experiment [165], this behavior may become apparent in the present experimental work.

Experimental data are obtained as mole fractions as a function of the reactor temperature measured at intervals of 25 K, and typically in duplicate, where average values are used as the resulting data points. Hence, each measurement represents the steady-state concentration at a constant temperature, pressure, and flow rate. This makes the residence time, τ, throughout an experimental series depend solely on the temperature in accordance with Equation (4.1):

$$\tau = \frac{V}{F[\mathrm{m^3/s}]} = \frac{\pi}{4} D^2 L_{iso} \left(F_\circ[\mathrm{Nm^3/s}] \, \frac{T}{273.15\,\mathrm{K}} \, \frac{1\,\mathrm{bar}}{P} \right)^{-1} \tag{4.1}$$

where V is the reactor volume calculated from the inner diameter of the reactor tube, D, and the isothermal length, L_{iso}. (See the following section for a determination of L_{iso}.) The volumetric flow rate, F, is typically given in units of *normal* cubic meters per second ($\mathrm{Nm^3/s}$), which refers to conditions at 273.15 K and 1 bar. Conversion to $\mathrm{m^3/s}$ is based on the application of the Ideal Gas Law, which has been verified in Section 3.3 for experimental conditions relevant to the current system.

4.2.3 Temperature Profiles

For correct interpretation of the experimental results, it is important to apply good control of the temperature profile during the course of the reaction. Maintaining a well-defined temperature profile may, however, prove to be difficult because of the substantial heat release from the exothermic conversion of the hydrocarbon fuels. As a consequence, experiments should be

designed in a way that limits the influence from the heat of reaction. Based on experience, a maximum adiabatic temperature rise of ∼25 K is accepted, which can only be achieved by applying inert diluents or very low absolute concentrations of the oxidizer. Notice that this issue of heat release during the reaction may well have been a contributing factor to the large scatter observed between literature data, as described in Chapter 2 (see e.g. Figure 2.1).

Figure 4.5 shows temperature profiles measured throughout the reactor. The measurements confirm that an isothermal reaction zone of 43 cm is obtained with an estimated absolute uncertainty of ±3 cm.

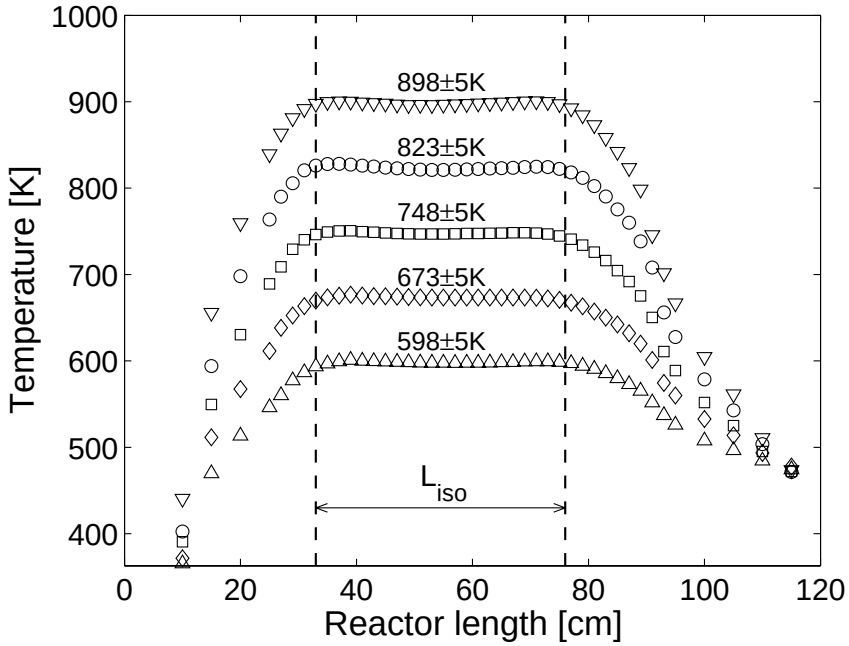

Figure 4.5: Temperature profiles measured across the reaction zone at isothermal values (±5 K) of 598, 673, 748, 823, and 898 K, using a pure N_2 flow of $3\,^{\mathrm{NL}}/_{\mathrm{min}}$ and 30 bar pressure. In practice, the positions of the temperature profiles are independent of the pressure [165]. The vertical dashed lines delimit the isothermal reaction zone: $L_{iso} = 43$ cm.

4.3 Characterization of the Flow Field

It is desirable to obtained flow characteristics in the reaction zone that are easily reproducible in terms of mathematical modeling.

The desired flow pattern is *plug flow*. This is a simple flow pattern that assumes each fluid element to pass orderly through the reactor as a "plug" or "piston" with no elements of fluid overtaking or mixing with any other element ahead or behind. There may be radial exchange of matter in plug flow, but the essential criterion for ideal plug flow is that each fluid element experience the same residence time in the reactor. In steady-state plug flow reactors, the fluid composition changes progressively through the reactor characterized by a flat velocity profile, which can be modeled as a simple one-dimensional system with integration of mass and energy equations in time [174].

Another flow pattern is *laminar flow*, which is characterized by fluid motion in parallel layers or streamlines with no mixing of the layers. Exchange of matter across laminar layers occurs solely by molecular diffusion. The flow pattern occurs when viscous forces gain importance relative to inertial forces expressed by the Reynolds' number in Equation (4.2). This facilitates radial velocity gradients with the maximum velocity at the fluid center resulting in a characteristic parabolic flow profile [159].

$$\mathrm{Re} = \frac{\text{inertial forces}}{\text{viscous forces}} = \frac{\rho u^2/D}{\mu u/D^2} = \frac{\rho u D}{\mu} \tag{4.2}$$

ρ [= $^{\mathrm{kg}}/_{\mathrm{m}^3}$] denotes the fluid density, D [= m] is the diameter of the flow cross section; or the hydraulic diameter for non-circular cross sections, u [= $^{\mathrm{m}}/_{\mathrm{s}}$] is the linear flow velocity, and μ [= $^{\mathrm{kg}}/_{\mathrm{m\,s}}$] is the dynamic fluid viscosity coefficient. Values of $\mathrm{Re} < 2100$ indicate that flow conditions lead to laminar flow, whereas higher Reynolds' numbers result in turbulent flow [159].

In order to account for the spatial distribution of reacting molecules in a fully developed laminar flow, two-dimensional mathematical models must be employed, which are more computational intensive than the simple plug flow model and hence, undesired for the present application.

4.3.1 Calculation of Transport Coefficients

This section presents a brief outline of the methodology behind calculations of characteristic transport coefficients necessary for subsequent determination of key figures used to evaluate the flow characteristics in the high pressure flow reactor. This involves the viscosity (μ) and binary diffusion coefficients ($\mathscr{D}_{AB}$) for low density gas mixtures as a function of the pressure (density) and/or temperature.

These quantities are determined from the *Chapman-Enskog* kinetic theory for multicomponent gases of low density [175] (also referred in [159]) that provides expressions of transport coefficients in terms of the potential energy of interactions $\varphi(r)$ between a pair of molecules in the gas phase. The force of interaction $\mathcal{F}$ is related to the potential energy by $\mathcal{F} = -\frac{\mathrm{d}\varphi}{\mathrm{d}r}$, where r denotes the distance between the molecules. A commonly used expression of $\varphi(r)$ is the empirical *Lennard-Jones* potential energy function:

$$\varphi(r) = 4\epsilon_{AB}\left[\left(\frac{\sigma_{AB}}{r}\right)^{12} - \left(\frac{\sigma_{AB}}{r}\right)^{6}\right] \tag{4.3}$$

in which ϵ_{AB} is the maximum energy of attraction between molecule A and B, and σ_{AB} [= Å] (10^{-10} m) is the collision diameter. ϵ is typically given as ϵ/κ [= K], where κ is Boltzmann's constant. These *Lennard-Jones parameters*, or *force constants*, are seldom available for gas mixtures, but for nonpolar molecules satisfactory estimates can be obtained from the properties of pure substances using the empirical combining rules in (4.4) and (4.5). Tabulated values of $(\epsilon/\kappa)_i$ and σ_i are available in Table 3.2 for selected compounds.

$$\epsilon_{AB} = \sqrt{\epsilon_A \epsilon_B} \tag{4.4}$$

$$\sigma_{AB} = \frac{\sigma_A + \sigma_B}{2} \tag{4.5}$$

Following Bird *et al.* [159], the viscosity coefficient μ for a pure monatomic gas of molecular weight M_w can be determined from Equation (4.6):

$$\mu = 8.4411 \times 10^{-5} \frac{\sqrt{M_w T}}{\sigma^2 \Omega_\mu} \tag{4.6}$$

where μ [= kg/m s]; M_w [= kg/mol]; and T [= K]. Ω_μ is a weak function of the dimensionless temperature $\kappa T/\epsilon$. Even though Equation (4.6) was originally derived for monatomic gases, it is recommended for polyatomic gases of low density as well.

For multicomponent mixtures of gases, the semiempirical mixing formula proposed by Wilke [176] is used. This relation, shown in Equation (4.7), as obtained from Bird *et al.* [159], has proven to be accurate within an average deviation of 1.9 % based on comparisons between experimental and calculated values of μ_{mix} for a wide range of gas mixtures.

$$\mu_{mix} = \sum_{i=1}^{n} \frac{y_i \mu_i}{\sum_{j=1}^{n} y_j \Phi_{ij}} \tag{4.7}$$

$$\text{where} \quad \Phi_{ij} = \frac{1}{\sqrt{8}}\left(1 + \frac{M_{w,i}}{M_{w,j}}\right)^{-1/2}\left[1 + \left(\frac{\mu_i}{\mu_j}\right)^{1/2}\left(\frac{M_{w,j}}{M_{w,i}}\right)^{1/4}\right]^2 \tag{4.8}$$

Here, n is the number of species in the mixture; y_i and y_j denote the molar fractions of component i and j with molecular weights $M_{w,i}$ and $M_{w,j}$ respectively. The pure component viscosities, μ_i and μ_j, can be evaluated from Equation (4.6). The coefficient Φ_{ij} is dimensionless and assumes the value of unity when $i = j$.

The formula for the binary diffusion coefficient $\mathscr{D}_{AB}$ is given in Equation (4.9):

$$\mathscr{D}_{AB} = 7.1613 \times 10^{-5} V_m \frac{\sqrt{T\left(\frac{1}{M_{w,A}} + \frac{1}{M_{w,B}}\right)}}{\sigma_{AB}^2 \Omega_{\mathscr{D}_{AB}}} \tag{4.9}$$

where $\mathscr{D}_{AB}$ [$= {}^{\mathrm{m}^2}/_{\mathrm{s}}$]. The molar volume V_m [$= {}^{\mathrm{m}^3}/_{\mathrm{mol}}$]. $\Omega_{\mathscr{D}_{AB}}$ is a function of the dimensionless temperature ${}^{\kappa\mathrm{T}}/_{\epsilon}$ similar to $\Omega_\mu({}^{\kappa\mathrm{T}}/_{\epsilon})$. It is noticed that $\mathscr{D}_{AB}$ is independent of the gas composition. Hirschfelder *et al.* [177] proposed a correction in terms of $\mathscr{D}_{AB} = \frac{\mathscr{D}_{AB,\mathrm{Eq.(4.9)}}}{1-\delta}$, where $\delta = f\left({}^{\kappa\mathrm{T}}/_{\epsilon_{\mathrm{AB}}}, \sigma_{AB}, P, T, M_{w,A}, M_{w,B}, y_A, y_B\right)$. The quantity δ usually exhibits values less than 0.03, cf. Ref. [177]. Moreover, values of $\mathscr{D}_{AB}$ obtained directly from Equation (4.9) are known to be accurate within an average deviation of 6 % from experimental values [159]. Considering the current application, it does not seem worth the effort to consider the extended approximation of $\mathscr{D}_{AB}$.

It has previously been shown in Section 3.3 that ideal gas behavior is a reasonable assumption for low density compounds under conditions relevant to the present experimental work. Substituting $V_m = RT/P$ thus yields:

$$\mathscr{D}_{AB} = 5.9543 \times 10^{-9} \frac{\sqrt{T^3\left(\frac{1}{M_{w,A}} + \frac{1}{M_{w,B}}\right)}}{P\sigma_{AB}^2 \Omega_{\mathscr{D}_{AB}}} \tag{4.10}$$

where P [= bar].

Bird *et al.* [159] have provided tabulated values of both $\Omega_\mu({}^{\kappa\mathrm{T}}/_{\epsilon})$ and $\Omega_{\mathscr{D}_{AB}}({}^{\kappa\mathrm{T}}/_{\epsilon})$ based on original data from Hirschfelder *et al.* [177]. From this, the six-constant polynomials in (4.11) and (4.12) have been approximated for $2 \leq {}^{\kappa\mathrm{T}}/_{\epsilon} \leq 20$.

$$\begin{aligned}\Omega_\mu\left({}^{\kappa\mathrm{T}}/_{\epsilon}\right) \cong\ & 1.5938 - 0.30458\left({}^{\kappa\mathrm{T}}/_{\epsilon}\right) + 0.052731\left({}^{\kappa\mathrm{T}}/_{\epsilon}\right)^2 \\ & - 4.6419 \times 10^{-3}\left({}^{\kappa\mathrm{T}}/_{\epsilon}\right)^3 + 1.9698 \times 10^{-4}\left({}^{\kappa\mathrm{T}}/_{\epsilon}\right)^4 \\ & - 3.1990 \times 10^{-6}\left({}^{\kappa\mathrm{T}}/_{\epsilon}\right)^5\end{aligned} \tag{4.11}$$

$$\begin{aligned}\Omega_{\mathscr{D}_{AB}}\left({}^{\kappa\mathrm{T}}/_{\epsilon}\right) \cong\ & 1.4593 - 0.27783\left({}^{\kappa\mathrm{T}}/_{\epsilon}\right) + 0.047334\left({}^{\kappa\mathrm{T}}/_{\epsilon}\right)^2 \\ & - 4.1253 \times 10^{-3}\left({}^{\kappa\mathrm{T}}/_{\epsilon}\right)^3 + 1.7388 \times 10^{-4}\left({}^{\kappa\mathrm{T}}/_{\epsilon}\right)^4 \\ & - 2.8109 \times 10^{-6}\left({}^{\kappa\mathrm{T}}/_{\epsilon}\right)^5\end{aligned} \tag{4.12}$$

4.3.2 Steady Laminar Flow

A first indication of the flow conditions in the high pressure flow reactor is obtained by calculating Reynolds' numbers, given in Equation (4.2), for gas streams containing representative mixtures of CH_4, N_2, and O_2. For this purpose, volumetric flow rates of 1–5 $^{NL}/_{min}$ are considered within the reaction zone delimited by the isothermal section in Figure 4.5. Moreover, relevant pressures of 10–100 bar and temperatures between 600 and 900 K are applied. The viscosity coefficient is calculated from Equation (4.6) and (4.7), while the mass density can be approximated by the Ideal Gas Law: $\rho^{ig} \cong P\overline{M}_w/RT$. Here, $\overline{M}_w$ denotes the weighted average molar weight of the given multicomponent gas mixture. The Ideal Gas Law is also used to convert the volumetric flow rate to the linear velocity. Notice that the P,T-dependence of ρ^{ig} cancels with the conversion of the volumetric flow rate from reference-state value to actual P,T-conditions: $F\,[^{L}/_{min}] = F[^{NL}/_{min}]\frac{1\,\text{bar}}{P}\frac{T}{273.15\,\text{K}}$ when applying the ideal gas assumption. This makes Re independent of the pressure and inversely proportional to $\sqrt{T}$ via μ.

Considering gas mixtures of pure N_2 and CH_4, as well as 95/5 mixtures of N_2/CH_4, N_2/O_2, and CH_4/O_2, calculated Reynolds' numbers span from Re = 564 (pure N_2, 5 $^{NL}/_{min}$, 600 K) to 75 (pure CH_4, 1 $^{NL}/_{min}$, 900 K). This clearly indicates that the reactor operates in the laminar flow regime.

It requires a certain *entrance length* L_e in the reactor, before the flow field is fully developed and reaches steady-state. From a mathematical point of view, this corresponds to flow in "long pipes" where end effects can be neglected, and it greatly reduces the computational efforts associated with a characterization of the flow pattern. Bird *et al.* [159] proposed the correlation in (4.13) to estimate L_e for laminar flows:

$$L_e = 0.035 D \mathrm{Re} \tag{4.13}$$

The correlation yields $2.1 < L_e < 15.8$ cm when inserting the Reynolds' numbers calculated above. In the high pressure flow reactor, the gas enters and leaves the reaction zone through undisturbed boundaries. In that respect, the entrance length can be regarded as the ∼30 cm initial heating section of the quartz tube; as indicated in Figure 4.5. This is more than sufficient to meet the requirement for a steady flow pattern. However, it is also not entirely accurate since the temperature is not constant in this section of the reactor. Even so, it is still reasonable to assume that steady laminar flow is obtained in the entire reaction zone under typical operation of the reactor.

4.3.3 Axial Dispersion and Plug Flow Approximation

It is reasonable to approximate the laminar flow field to plug flow if the gas is premixed and the radial velocity gradients are sufficiently small to allow each fluid element to exhibit similar residence times. Good mixing of reactant gases is readily obtained in the present experimental system, so the attention is focused on the magnitude of the radial velocity gradients.

A useful measure of the radial velocity gradients in laminar flow is the *longitudinal* or *axial dispersion* [174, 178]. It characterizes the spreading, or overtaking, of fluid elements as a result of different local flow velocities and molecular and turbulent diffusion, the magnitude of which is independent of position in the reactor cf. the assumption of steady-state conditions. This spreading process is represented by the *dispersion coefficient*, D_{disp} [$= \mathrm{m}^2/\mathrm{s}$]. Large values of D_{disp} indicate rapid spreading of fluid elements and hence, mixed flow, while lower values indicate slower spreading until $D_{disp} = 0$, which corresponds to ideal plug flow.

A key figure is the dimensionless group defined in Equation (4.14) as a measure of the *intensity of axial dispersion*:

$$\frac{D_{disp}}{uD} \quad \text{or} \quad \frac{D_{disp}}{uL} = \frac{\text{movement by axial dispersion}}{\text{movement by bulk flow}} \tag{4.14}$$

where D and L are the reactor diameter and length respectively. If L is used as the characteristic length, the dimensionless group in (4.14) is perhaps more accurately described as the *vessel dispersion number* [178].

The axial dispersion in a given system is best characterized by an experiment where a pulse of a tracer is introduced at the entrance of the system at $t = 0$ followed by concentration measurements at the outlet as a function of the time from the injection. This gives rise to a *residence time distribution* (RTD). From simple balance equations, a *dispersion model* can be formulated based on this imposed-pulse experiment; see e.g. the textbooks of Levenspiel [174, 178] that provide the analytical solution $E(\theta)$ to the RTD shown in Equation (4.15). Here θ represents the dimensionless mean residence time, i.e. $\theta = \frac{\tau}{\bar{\tau}} = \frac{\tau u}{V}$. Notice that (4.15) is only valid for "open vessels", i.e. systems with undisturbed boundaries.

$$E(\theta) = \frac{1}{\sqrt{4\pi \left(\frac{D_{disp}}{uL}\right) \theta}} \exp\left[- \frac{(1-\theta)^2}{4\theta \left(\frac{D_{disp}}{uL}\right)} \right] \tag{4.15}$$

When $\frac{D_{disp}}{uL}$ is low, the tracer curve is narrow, symmetrical, and gaussian, and the flow field thus only exhibits *small* deviations from plug flow. This

is roughly obtained when $\frac{D_{disp}}{uL} < 0.01$. At higher values, the tracer curve starts to tail off and deviations from plug flow can no longer be regarded as minor [174, 178].

The numeric value of the dispersion coefficient can be derived from Equation (4.15) when experimental data are available. Otherwise, it may be correlated with the diffusion coefficient in Equation (4.16) from Levenspiel [174,178] that was derived from the early work of Taylor [179] and Aris [180].

$$D_{disp} = \mathscr{D}_{AB} + \frac{u^2 D^2}{192 \mathscr{D}_{AB}} \tag{4.16}$$

Notice the strong dependence of molecular diffusion $\mathscr{D}_{AB}$ on the dispersion coefficient. At low flow rates, it promotes dispersion, while it has the opposite effect at high flow rates, where dispersion is instead facilitated by axial convection with radial diffusion. Consequently, there is an optimum relation between values of $\mathscr{D}_{AB}$, and u and D in terms of low axial dispersion. This ratio between mass transfer by convection and diffusion is expressed by the dimensionless *Bodenstein number* (Bo), which is defined in Equation (4.17) as the product of the Reynolds' number (Re) and the Schmidt number (Sc). The latter expresses the ratio between the kinetic and diffusive viscosity.

$$\mathrm{Bo} = \frac{\text{mass transfer by convection}}{\text{mass transfer by diffusion}} = \mathrm{Re\,Sc} = \frac{\rho u D}{\mu} \frac{\mu}{\rho \mathscr{D}_{AB}} = \frac{uD}{\mathscr{D}_{AB}} \tag{4.17}$$

Values of $\frac{D_{disp}}{uD}$ and Bo are now calculated for the same representative gas streams considered in the previous calculation of Reynolds' numbers; i.e. pure N_2 and CH_4, and 95/5 mixtures of N_2/CH_4, N_2/O_2, and CH_4/O_2, at 600–900 K, 10–100 bar, and flow rates from 1 to 5 $^{\mathrm{NL}}/_{\mathrm{min}}$. The resulting function value spans are depicted in Figure 4.6 that correlates $\frac{D_{disp}}{uD}$ with Bo. The original figure is a copy from Levenspiel, 1993 [178]. The bottom of the curve is found at Bo = 13 and $\frac{D_{disp}}{uD} = 0.14$, which defines the optimum conditions for low axial dispersion in laminar pipe flow, and hence, the conditions where the plug flow assumption is most accurate.

The colored intervals of $\frac{D_{disp}}{uD}$ and Bo in Figure 4.6 reveal that optimum conditions in terms of low axial dispersion are nearly obtained at the lowest possible flow rate ($1\,^{\mathrm{NL}}/_{\mathrm{min}}$) suggesting an excellent plug flow assumption. Plug flow may, on the other hand, be a questionable assumption when the system is operated at the highest volumetric flow rate ($5\,^{\mathrm{NL}}/_{\mathrm{min}}$). Moreover, the relatively high values of Bo indicate that dispersion is generally caused by axial convection rather than molecular diffusion.

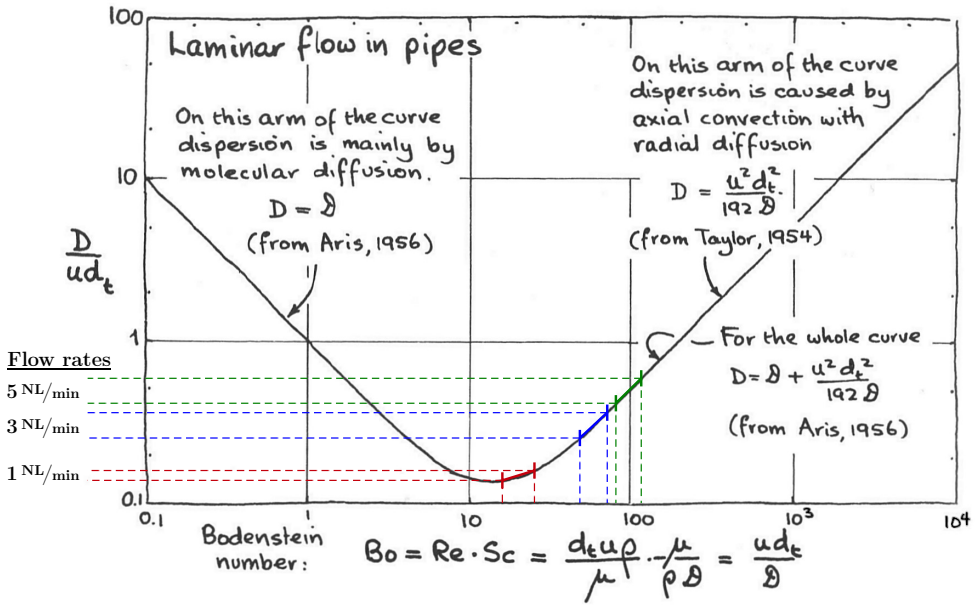

Figure 4.6: Intensity of axial dispersion $\left(\frac{D_{disp}}{uD}\right)$ correlated with the Bodenstein number (Bo). The bottom of the curve defines the optimum conditions for low axial dispersion in laminar pipe flow, and hence, the desired conditions where the plug flow assumption is most accurate. Colored line segments denote ranges of $\frac{D_{disp}}{uD}$ and Bo obtained for representative gas mixtures of N_2, O_2, and CH_4 (see text) at 600–900 K and 10–100 bar. Results for volumetric flow rates of 1, 3, and 5 $^{NL}/_{min}$ are indicated by red, blue, and green lines, respectively. Original figure is taken from Levenspiel, 1993 [178]. Here, "D" denotes the dispersion coefficient (D_{disp}), while "d_t" is the diameter of the flow cross section (D in the present work).

In the present work, all experiments have been conducted with a volumetric flow rate of 3 $^{NL}/_{min}$ under which conditions, it is still reasonable to assume plug flow.

As a final measure of the axial dispersion, values of the vessel dispersion number ($\frac{D_{disp}}{uL}$) are now calculated. For the volumetric flow rate of practical application, 3 $^{NL}/_{min}$, this yields a function value span of $0.0047 < \frac{D_{disp}}{uL} < 0.0066$, which is well below the critical limit of 0.01 that delimits "small" deviations from plug flow. Residence time distributions have further been computed from Equation (4.15) using different values of $\frac{D_{disp}}{uL}$ including those representative of the experimental conditions at 3 $^{NL}/_{min}$. The results are shown in Figure 4.7, which confirm a narrow and symmetrical RTD for practical applications of the system at hand and hence, a reliable plug flow approximation.

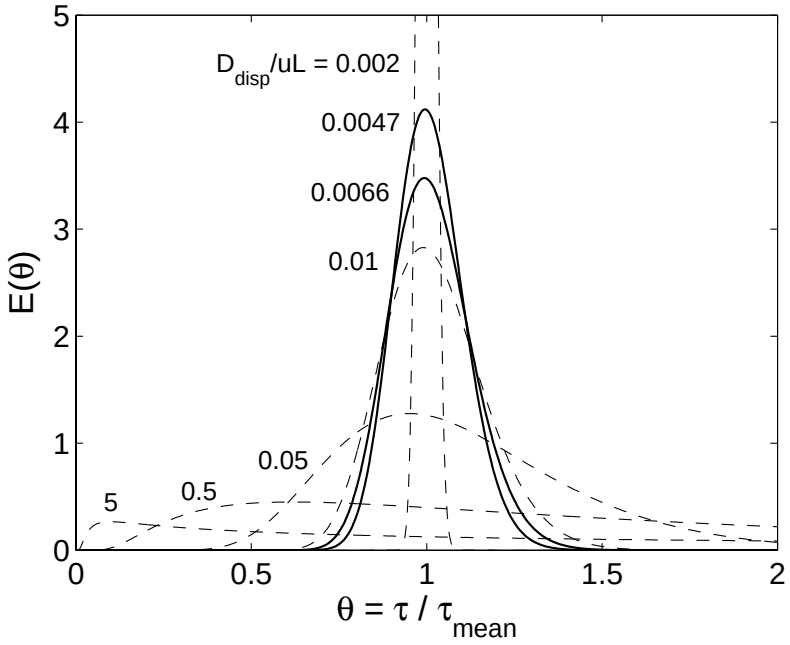

Figure 4.7: Computed residence time distributions from Equation (4.15) at varying $\frac{D_{disp}}{uL}$. The trace curves at $\frac{D_{disp}}{uL} = 0.0047$ and 0.0066 denote the range obtained at conditions relevant to the present experimental work. The limiting tracer curve is $\frac{D_{disp}}{uL} = 0.01$ beyond which, asymmetry becomes significant and the laminar flow pattern begins to deviate considerably from plug flow.

For the limiting volumetric flow rates of 1 and 5 $^{\mathrm{NL}}/_{\mathrm{min}}$, values of $\frac{D_{disp}}{uL}$ span the ranges 0.0025–0.0029 and 0.0074–0.011 respectively. The fact that the latter range is close to the limit of 0.01 confirms the previous observations from Figure 4.6 that also indicated a questionable plug flow assumption when the gas flow rate is set to its maximum value of 5 $^{\mathrm{NL}}/_{\mathrm{min}}$.

4.4 Summary

A novel laboratory scale high pressure flow reactor setup has been designed and constructed with the purpose to enable well-defined investigations of most homogeneous combustion systems involving gaseous reactants of the elements H, O, C, N, and S at pressures from 10 to 100 bar and temperatures up to 925 K. These data are intended for validation of the performance of a detailed chemical kinetic model.

The reaction takes place in a quartz tube (i.d. 8 mm, o.d. 10 mm, lg. 1545 mm), which is enclosed in a stainless steel tube (i.d. 22 mm, o.d. 38 mm) that acts as a pressure shell. A pressure control system automatically delivers N_2 to the shell-side of the reactor to avoid devastating pressure gradients across the fragile quartz glass. The quartz reactor is mounted via two specially designed steel flanges that maintain a tight sealing of the quartz reactor without subjecting the glass to any stress during thermal expansion of the metal. The steel pressure shell is positioned inside an electrically heated oven that produces an isothermal reaction zone of 43 cm. A maximum of four different reactant gases or gas mixtures are premixed before entering the reactor using an overall volumetric flow of 1–5 $^{NL}/_{min}$. Product analysis is comprised of on-line GC-TCD/FID and a NO_x chemiluminescence analyzer that enable measurements of N_2, O_2, CO, CO_2, a range of saturated, unsaturated, and oxygenated hydrocarbons, a few nitrated hydrocarbons, SO_2, H_2S, NO, and NO_2; typically within an overall measuring uncertainty of ±2–5 %.

Experimental results are obtained as mole fractions as a function of the reactor temperature at constant pressure and flow rate. This makes the residence time depend solely on the temperature.

The high pressure flow reactor operates in the laminar flow regime ($75 < Re < 564$), but with good premixing and low radial velocity gradients, considered in terms of axial dispersion, it has been shown that the laminar flow field can be approximated to plug flow. This enables fast computation in terms of mathematical modeling of the reaction zone where conservation equations can be treated as a simple one-dimensional model with integration in time.

Chapter 5

Detailed Kinetic Modeling

5.1 Introduction

Detailed kinetic models; commonly referred to as *detailed chemical kinetic models* or *DCKM*, are complex mechanistic models built from an inherent understanding of the real chemical processes. They represent the unsimplified conversion of reactants and formation of products as it actually takes place through a chain of elementary reaction steps. This is in contrast to empirical models. Ideally, the nature of a DCKM allows extrapolation to reaction conditions outside the range of experimental verification, including different reactor designs, with an expected accurate response. This makes DCKM a powerful tool in the development and analysis of chemical systems. Throughout decades, a continuous development and refinement of detailed kinetic models have been undertaken in order to unravel the complexities of chemical reactions across a wide range of conditions and ultimately, to close in on a final solution.

5.1.1 Hierarchical Structure of Reaction Mechanisms

DCKM are based on elementary reaction steps and do not include empirical constants. The construction and development of these models are greatly simplified by considering individual chemical subsystems in turns. This approach is possible because chemical reaction mechanisms are connected in a strict hierarchy where mechanisms of complex molecules are comprised of submechanisms that involve more simple molecules [181]. Hence, the reaction mechanism of the H_2/O_2 system controls the radical pool of H, O, OH, and HO_2, which is fundamental in all combustion systems involving hydrocarbons and oxygen. The H_2/O_2 mechanism is relevant to the oxidation of CO in moist air. The resulting H_2/O_2/CO-mechanism is further a submech-

anism in the combustion of natural gas and various transport fuels, and so forth. The general principle is illustrated in Figure 5.1.

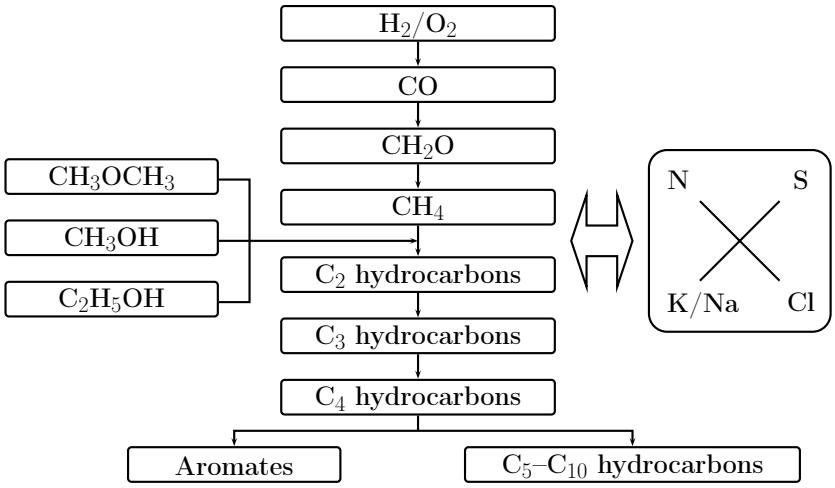

Figure 5.1: Hierarchical structure and interrelationship of chemical reaction mechanisms involved in hydrocarbon combustion. The H_2/O_2 submechanism constitutes the basis of the hierarchy. The individual submechanisms may exhibit interactions with mechanisms of various inorganic elements relevant to combustion, e.g. N, S, K, Na, and Cl. The figure is freely adopted from Westbrook and Dryer [181].

5.2 Computational Approach

Mathematical modeling of detailed chemistry in combustion systems involves simultaneous treatment of the chemical kinetic behavior of large reaction systems combined with convective and diffusive transport of mass, momentum, and energy. Such models require the evaluation of chemical rate expressions, transport properties, and equations of state, including availability of reference state thermochemical properties, i.e. H_{ref}, S_{ref}, and C_p^{ig}.

The mathematical treatment of the reacting system in the high pressure flow reactor is greatly simplified by employing the Ideal Gas Law as the preferred equation of state, cf. the validation of the ideal gas assumption in Chapter 3. Moreover, by approximating the laminar flow pattern to plug flow, as proposed in Chapter 4, it is possible to neglect spatial convective and diffusive transport of matter, which means that the system can be described solely by mass and energy conservation equations integrated over time.

5.2.1 Mass and Energy Conservation

From a modeling point of view, the reaction is considered to take place in a closed system with no exchange of mass across boundaries. This is consistent with a premixed volume or "plug" of reactants that enters the hot reaction zone at time $t = 0$ and is allowed to react under isolated conditions until $t = \tau$. Consequently, the total mass of the system is given by $m = \sum_{i=1}^{N_{sp}} m_i$ with $\frac{\mathrm{d}m}{\mathrm{d}t} = 0$. Here, m_i is the mass of the ith species and N_{sp} is the total number of species in the mixture. The individual species are produced or destroyed according to Equation (5.1):

$$\frac{\mathrm{d}m_i}{\mathrm{d}t} = \hat{r}_i V M_{w,i} \qquad i = 1, \ldots, N_{sp} \tag{5.1}$$

$\hat{r}_i$ represents the *molar net production rate* of the ith species by elementary reactions. This quantity will be defined later in Section 5.2.2. $M_{w,i}$ is the molecular weight of species i. V is the volume of the system. The present experimental work is conducted at isobaric conditions, which means that V may vary in time, i.e. $V = V(t)$, unless the temperature is also constant. By assuming constant total mass, Equation (5.1) can be rewritten in (5.2) in terms of the mass fraction $Y_i = \frac{m_i}{m}$. The specific volume on a mass basis $\dot{V} = \frac{V}{m}$ is further introduced:

$$\frac{\mathrm{d}Y_i}{\mathrm{d}t} = \hat{r}_i \dot{V} M_{w,i} \qquad i = 1, \ldots, N_{sp} \tag{5.2}$$

If the system is simulated at isothermal conditions, the energy equation is unnecessary and the problem is completely defined by Equation (5.2). For an adiabatic and isobaric system, the energy conservation equation can be written as

$$\overline{C}_p \frac{\mathrm{d}T}{\mathrm{d}t} + \dot{V} \sum_{i=1}^{N_{sp}} \hat{r}_i H_i \; M_{w,i} = 0 \tag{5.3}$$

Here, $\overline{C}_p$ is the mean specific heat capacity of the mixture given on mass basis; i.e. $\overline{C}_p = \sum_{i=1}^{N_{sp}} Y_i C_{p,i} M_{w,i}$ when $C_{p,i}$ is the molar heat capacity of the ith compound, as obtained from the thermochemical database in Table 3.1. H_i denotes the molar enthalpy of species i, which is computed from Equation (3.3) when ideal gas behavior is assumed.

The system of equations needed to be solved for the adiabatic and isobaric closed system at hand contains N_{sp} equations (5.2) for the mass fractions of individual species and one energy equation (5.3).

5.2.2 Chemical Reaction Rates

A comprehensive description of the oxidation and pyrolysis chemistry of hydrocarbon fuels involves numerous stable and unstable chemical species participating in hundreds, or maybe thousands of elementary reactions. First, consider a complex system of N_{re} reversible elementary reactions involving N_{sp} species represented in the general form:

$$\sum_{i=1}^{N_{sp}} \nu'_{ij} \Lambda_i \rightleftharpoons \sum_{i=1}^{N_{sp}} \nu''_{ij} \Lambda_i \qquad j = 1, \ldots, N_{re} \tag{5.4}$$

where Λ_i represents the ith chemical compound. The stoichiometric coefficients ν_{ij} exhibit integral numbers that satisfy linear relations associated with the conservation of all individual atomic elements describing the reacting system:

$$\sum_{i=1}^{N_{sp}} \left(\nu'_{ij} - \nu''_{ij}\right) e_{ik} = 0 \qquad \begin{matrix} j = 1, \ldots, N_{re} \\ k = 1, \ldots, N_{el} \end{matrix} \tag{5.5}$$

Here, e_{ik} is the kth atomic element of the ith species.

Using the stoichiometric coefficients, the molar net production rate $\hat{r}_i$ of the ith species is now defined in Equation (5.6):

$$\hat{r}_i = \sum_{j=1}^{N_{re}} \left(\nu'_{ij} - \nu''_{ij}\right) \hat{q}_j \qquad i = 1, \ldots, N_{sp} \tag{5.6}$$

where $\hat{q}_j$ denotes the *progress rate* for the jth reaction defined by the difference between the forward and the reverse reaction rates (calculated with signs):

$$\hat{q}_j = k_{f_j} \prod_{i=1}^{N_{sp}} [\Lambda_i]^{\nu'_{ij}} - k_{r_j} \prod_{i=1}^{N_{sp}} [\Lambda_i]^{\nu''_{ij}} \qquad j = 1, \ldots, N_{re} \tag{5.7}$$

$[\Lambda_i]$ represents the molar concentration of the ith species, and k_{f_j} and k_{r_j} are the forward and reverse rate constants of the jth reaction. The forward rate constants are generally assumed to follow the temperature dependence expressed by the *modified* Arrhenius equation:

$$k_{f_j} = A_j T^{\beta_j} \exp\left(\frac{-E_j}{RT}\right) \tag{5.8}$$

where the pre-exponential factor A_j, the temperature exponent β_j, and the activation energy E_j [$= {}^{\text{cal}}/_{\text{mol}}$] are constant model parameters that need specification. k_{f_j} has the units of ${}^{1}/_{\text{s}}$, ${}^{\text{cm}^3}/_{\text{mol s}}$, or ${}^{\text{cm}^6}/_{\text{mol}^2\,\text{s}}$ for uni-, bi-, and ternary reactions respectively.

The forward and reverse rate constants are related through the thermodynamic equilibrium constant K_j:

$$K_j = \frac{k_{f_j}}{k_{r_j}} \tag{5.9}$$

K_j is expressed in Equation (5.10) based on the thermodynamic relation with Gibb's free energy ($\Delta G = -RT \ln K = \Delta H - T\Delta S$), and includes a pressure correction for reactions that involve different total numbers of reactants and products:

$$K_j = \exp\left[\frac{\Delta S_j^{ig}}{R} - \frac{\Delta H_j^{ig}}{RT}\right]\left(\frac{P_{atm}}{RT}\right)^{\sum_{i=1}^{N_{sp}}\left(\nu'_{ij}-\nu''_{ij}\right)} \tag{5.10}$$

P_{atm} denotes atmospheric pressure. ΔH_j^{ig} and ΔS_j^{ig} correspond to the changes in the *ideal gas* enthalpy and entropy that occur when reactants are completely converted to products in the jth reaction. Appropriate values of H_i^{ig} and S_i^{ig} are obtained from Equation (3.3) and (3.4) using reference state data from the thermochemical database in Table 3.1.

5.2.2.1 Pressure Dependent Reactions

Association or dissociation reactions are typical examples of pressure dependent reactions. Consider the elementary association (or self-recombination) of CH_3 radicals to C_2H_6: At low pressures, this reaction displays third-order kinetics behavior, but as the pressure increases, the kinetic dependence changes and the reaction eventually becomes second-order at sufficiently high pressures [182]. This behavior is most appropriately described by the reaction schemes in (5.11) and (5.12), which are called the *low-* and the *high-pressure limit* respectively. "M" in (5.11) represents a *third-body* collision partner (See Section 2.2.2 for an outline of this terminology):

$$\mathrm{CH_3 + CH_3 + M \rightleftharpoons C_2H_6 + M} \tag{5.11}$$

$$\mathrm{CH_3 + CH_3 \rightleftharpoons C_2H_6} \tag{5.12}$$

During the transition from the low- to the high-pressure limit, the reaction exhibits neither third- or second-order kinetics. This region is called the *fall-off* region. To denote that a reaction is in the fall-off region, the third-body

collision partner M is typically written in parenthesis, as shown in (5.13):

$$CH_3 + CH_3(+M) \rightleftharpoons C_2H_6(+M) \tag{5.13}$$

When reactions are at their high-pressure limit, rate expressions are readily described by the equations presented above. The equations become a little more complex when treating reactions in the fall-off region or at the low-pressure limit. The latter involves mathematical treatment of third-body collision partners in elementary reactions.

Third-Body Reactions

As previously discussed in Section 2.2.2, certain atoms or molecules may act more efficiently as collision partners than others. This effect is incorporated in the equation for the molar progress rate from (5.7) by multiplying the original expression by the concentration of colliding molecules times a third-body *enhancement factor* α_{ij}, which is defined for specific molecules.

$$\hat{q}_j = \left(\sum_{i=1}^{N_{sp}} \alpha_{ij} \left[\Lambda_i\right]\right) \left(k_{f_j} \prod_{i=1}^{N_{sp}} \left[\Lambda_i\right]^{\nu'_{ij}} - k_{r_j} \prod_{i=1}^{N_{sp}} \left[\Lambda_i\right]^{\nu''_{ij}}\right) \qquad j = 1, \ldots, N_{re} \tag{5.14}$$

Notice that if all species in the reacting mixture contribute equally as third-bodies, all enhancement factors $\alpha_{ij} = 1$. The first factor in Equation (5.14) thus corresponds to the total concentration in the mixture, i.e. $[M] = \sum_{i=1}^{N_{sp}} [\Lambda_i] = P/(RT)$.

Reaction Rates in the Fall-Off Region

The description of reaction rates in the fall-off region is based on the Lindemann theory [183] (also referred in e.g. [182]). This theory was originally developed for unimolecular dissociation reactions based on the general reaction scheme in (5.15) for the conversion of reactant "A" to product "P":

$$\begin{aligned} A + M &\rightleftharpoons A^* + M \\ A^* &\rightarrow P \end{aligned} \tag{5.15}$$

The reacting molecule A becomes excited through collision with M and yields the energized state A^*. This intermediate adduct may either be collisionally de-activated (through the reverse reaction) or react to form product P.

The Lindemann approach combines the high-pressure limit (k_∞) and the low-pressure limit (k_0) to yield the overall expression of the rate constant:

$$k = k_\infty \left(\frac{P_r}{1 + P_r} \right) F \tag{5.16}$$

where P_r is a *reduced pressure* defined by:

$$P_r = \frac{k_0[\mathrm{M}]}{k_\infty} \tag{5.17}$$

[M] is the concentration of the reacting mixture including inert species and potentially enhanced third-body effects. Using the Arrhenius form, the expressions of k_∞ and k_0 are given in Equation (5.18) and (5.19) respectively.

$$k_\infty = A_\infty T^{\beta_\infty} \exp\left(\frac{-E_\infty}{RT} \right) \tag{5.18}$$

$$k_0 = A_0 T^{\beta_0} \exp\left(\frac{-E_0}{RT} \right) \tag{5.19}$$

The parameter F in Equation (5.16) is a *broadening factor*, which assumes the value of unity for the original Lindemann expression. In practice, the fall-off behavior of most reactions appears to be more complex than captured by the simple Lindemann expression. A more satisfactory treatment of the broadening factor has been developed by Troe and co-workers [184, 185] that incorporates effects of both strong and weak collisions between molecules. For fast computation, they developed an approximative formalism, where F is given by:

$$\log F = \left[1 + \left[\frac{\log P_r + c}{n - d\,(\log P_r + c)} \right]^2 \right]^{-1} \log F_{cent} \tag{5.20}$$

in which, the constants c, n, and d are:

$$c = -0.4 - 0.67 \log F_{cent} \tag{5.21}$$

$$n = 0.75 - 1.27 \log F_{cent} \tag{5.22}$$

$$d = 0.14 \tag{5.23}$$

The *center broadening factor*, F_{cent}, is approximated by the expression in (5.24) as a function of the temperature:

$$F_{cent} = (1 - a) \exp\left(\frac{-T}{T^{***}} \right) + a \exp\left(\frac{-T}{T^{*}} \right) + \exp\left(\frac{-T^{**}}{T} \right) \tag{5.24}$$

where a, T^{***}, T^{*}, and T^{**} are the *Troe parameters* that can be fitted from experiments.

5.2.3 Chemkin Software Package

The computer software used to evaluate the kinetic model is the Chemkin–II Software Package [186]. It is a Fortran based program designed to facilitate numerical simulations of elementary chemical reactions in flowing systems. The basic components of the Chemkin package include an *interpreter* module for the chemical reactions and the thermochemical database, a *linking file*, and a *gas phase subroutine library* containing more than 100 subroutines.

The input files to the Chemkin interpreter need specifications of involved elements, chemical species, and reactions, where the latter are represented by the three Arrhenius parameters and, possibly, Troe parameters for reactions in the fall-off regime and/or third-body enhancement factors if these deviate from unity. The thermochemical database must be given in terms of the 7-constant NASA polynomials from Equation (3.5)–(3.7). The output from the Chemkin interpreter is the linking file, which is passed to the gas phase subroutine library that provides the evaluation of information about e.g. elements, species, reaction, mole/mass conversion, equations of state, thermodynamic properties, equilibrium constants, net production rates, progress rates, sensitivity parameters, and appropriate derivatives of the above.

The computational solution is performed by the Senkin code [187], which is a part of the Chemkin–II Software Package. It performs an integration in time based on the governing equations presented in Section 5.2.1 and utilizes the Chemkin subroutine library as a preprocessor. The Senkin code further demands a *keyword input file* defining the state of the gas, i.e. pressure or density, temperature, and composition.

The Senkin code uses the numerical solver Dasac [188], which is a modification and extension of the implicit integrator Dassl [189]. Dasac is designed to solve nonlinear stiff differential equations based on the backwards difference method with efficient simultaneous computation of first-order sensitivity coefficients, ω_{lj}, defined by:

$$\omega_{lj} = \frac{\partial Z_l}{\partial A_i} \qquad \begin{matrix} j = 1, \ldots, N_{re} \\ l = 1, \ldots, N_{sp} + 1 \end{matrix} \tag{5.25}$$

where Z is the vector containing the independent variables, i.e. temperature and mass fractions: $Z = [T, Y_i, \ldots, Y_{N_{sp}}]$, while A_j represents the pre-exponential factor of the jth elementary reaction.

First-order sensitivity coefficients provide a powerful tool to identify bottlenecks in the reaction network. As an approximate interpretation of the numeric values of ω_{lj}, the impact on Z_l is roughly said to be a factor of ω_{lj}

(with sign) when A_j is multiplied by a factor of 2. However, the first-order nature of the method implies that only smaller numeric values of ω_{lj} should be trusted, and care should be taken when interpreting larger numeric values.

The SENKIN code used in the present work further includes an in-house modification [190] that allows the program to interpolate between measured temperature profiles in order to derive one profile that fits a specified temperature in the isothermal reaction zone and includes the preheating and subsequent cooling sections in the reactor tube as well. As a consequence, the experimental temperature profiles from the high pressure flow reactor, previously shown in Figure 4.5, can be used as a direct input to the simulations. This approach to isothermal temperatures in modeling is not preferred in the present work; mainly because this feature is more computationally demanding than the original constant-temperature approach. It may, however, be relevant in situations where certain components in the reactant or product mixtures tend to undergo conversion at low combustion temperatures.

5.3 Novel Detailed Chemical Kinetic Model

When increasing the temperature from low-temperature conditions, relevant to atmospheric chemistry research, towards the high temperatures typically obtained in combustion systems, the governing kinetic mechanisms roughly fall in two regimes that are diverse in nature. At low temperatures, the kinetic scheme is operated by seemingly slow chain-propagating reactions controlled by HO_2 radicals and intermediate H_2O_2 formation, whereas high temperatures facilitate a fast chain-branching regime operated by a radical pool dominated by the very reactive O, H, and OH radicals. The primary operational range of the present kinetic model is roughly temperatures from 500–1000 K and pressures from atmospheric to 100 bar. This region encompasses the transition between these two kinetic mechanisms. Consequently, it is relevant to revisit the involved reaction subsets with special attention to pressure dependent reactions and intermediate temperature evaluations of rate constants, and to draw upon previous experiences from both low- and high-temperature investigations.

The novel DCKM proposed in the present work consists of detailed reaction mechanisms for the chemical systems: H_2/O_2, CO/CO_2, C_1 and C_2 hydrocarbons, NO_x, and SO_2. The NO_x reaction mechanism moreover includes direct reactions between NO_x and C_{1-2} hydrocarbon species. No previously reported DCKM underlie the present model. Instead, the individual submechanisms have been developed from critical reviews and discussions of available rate constant determinations reported in the literature.

5.3.1 H_2/O_2 Reaction Mechanism

The H_2/O_2 reaction mechanism is important in a number of fields related to energy conversion and propulsion. It plays a key role in fundamental chemical kinetic research where the elementary reactions of H, O, OH, HO_2, and H_2O_2 govern the composition of the radical pool in hydrocarbon reaction systems. Comprehensive modeling studies have been conducted in this field; and recent examples [168, 191, 192] are based on numerous individual reaction rate measurements and theoretical estimates. Nevertheless, some details remain unsettled. The proposed H_2/O_2 reaction subset is shown in Table 5.1 and will be discussed in the following.

Table 5.1: Reactions from the H_2/O_2 reaction mechanism. Units are mol, cm, s, cal.

	Reactions	A	β	E	Note/Ref.
1.	$H + H + M \rightleftharpoons H_2 + M^a$	7.00×10^{17}	–1.0	0	[193, 194]
	$H + H + H_2 \rightleftharpoons H_2 + H_2$	1.00×10^{17}	–0.6	0	[193, 194]
	$H + H + N_2 \rightleftharpoons H_2 + N_2$	5.40×10^{18}	–1.3	0	[193, 194]
2.	$H + O + M \rightleftharpoons OH + M^b$	6.20×10^{16}	–0.6	0	[101]
3.	$H + O_2 \rightleftharpoons O + OH$	3.55×10^{15}	–0.41	16600	[192, 195]
4.	$H + O_2(+M) \rightleftharpoons HO_2(+M^c)$	1.48×10^{12}	0.6	0	[196]
	Low-pressure limit:	3.50×10^{16}	–0.41	–1116	[192]
	Troe parameters: 0.5 10^{-30} 10^{30} 10^{30}				
	$H + O_2(+Ar) \rightleftharpoons HO_2(+Ar)$	1.48×10^{12}	0.6	0	[196]
	Low-pressure limit:	9.04×10^{19}	–1.5	490	[192, 197]
	Troe parameters: 0.5 10^{-30} 10^{30} 10^{30}				
	$H + O_2(+N_2) \rightleftharpoons HO_2(+N_2)$	1.48×10^{12}	0.6	0	[196]
	Low-pressure limit:	6.37×10^{20}	–1.72	520	[192, 197]
	Troe parameters: 0.8 10^{-30} 10^{30} 10^{30}				
5.	$O + O + M \rightleftharpoons O_2 + M^d$	1.89×10^{13}	0.0	–1788	[194]
[e]6.	$O + H_2 \rightleftharpoons OH + H$	3.82×10^{12}	0.0	7950	[145]
		8.79×10^{14}	0.0	19170	
7.	$O + H_2O \rightleftharpoons OH + OH$	4.50×10^{4}	2.7	14550	[198]
8.	$OH + H + M \rightleftharpoons H_2O + M^f$	4.50×10^{22}	–2.0	0	[191, 194]
9.	$OH + H_2 \rightleftharpoons H + H_2O$	2.14×10^{8}	1.52	3450	[198]
10.	$H_2 + O_2 \rightleftharpoons HO_2 + H$	7.40×10^{5}	2.433	53500	[199]
11.	$HO_2 + H \rightleftharpoons OH + OH$	8.40×10^{13}	0.0	400	see text
12.	$HO_2 + H \rightleftharpoons H_2O + O$	1.40×10^{12}	0.0	0	[145]
13.	$HO_2 + O \rightleftharpoons OH + O_2$	1.63×10^{13}	0.0	–445	[145]
[e]14.	$HO_2 + OH \rightleftharpoons H_2O + O_2$	3.60×10^{21}	–2.1	9000	see text
		2.00×10^{15}	–0.6	0	
		-2.20×10^{96}	–24.0	49000	
[e]15.	$HO_2 + HO_2 \rightleftharpoons H_2O_2 + O_2$	1.94×10^{11}	0.0	–1408	[200]
		1.03×10^{14}	0.0	11034	

Continues on next page

Continued from last page

	Reactions	A	β	E	Note/Ref.
16.	$H_2O_2(+M) \rightleftharpoons OH + OH(+M^g)$	4.00×10^{11}	0.0	37137	[200]
	Low-pressure limit:	2.29×10^{16}	0.0	43640	
	Troe parameters: 0.5 10^{-30} 10^{30} 10^{30}				
17.	$H_2O_2 + H \rightleftharpoons HO_2 + H_2$	1.69×10^{12}	0.0	3760	[145]
18.	$H_2O_2 + H \rightleftharpoons H_2O + OH$	1.02×10^{13}	0.0	3580	[145]
19.	$H_2O_2 + O \rightleftharpoons HO_2 + OH$	9.55×10^{6}	2.0	3970	[194]
[e]20.	$H_2O_2 + OH \rightleftharpoons H_2O + HO_2$	1.00×10^{12}	0.0	0	[201]
		5.80×10^{14}	0.0	9560	

a: Enhanced third-body efficiencies: $N_2 = 0, H_2 = 0, H_2O = 14.3$
b: Enhanced third-body efficiencies: $H_2O = 5$
c: Enhanced third-body efficiencies: $N_2 = 0, Ar = 0, H_2 = 2, O_2 = 0.78, H_2O = 11$
d: Enhanced third-body efficiencies: $N_2 = 1.5, O_2 = 1.5, H_2O = 10$
e: Expressed as the sum of the rate constants
f: Enhanced third-body efficiencies: $Ar = 0.38, H_2 = 0.73, H_2O = 12$
g: Enhanced third-body efficiencies: $Ar = 0.64, H_2 = 2.5, H_2O = 12$

Interaction with O_2 and the radical pool is largely governed by H atom consumption via the branching reaction (R3) to form O+OH or the competing reaction (R4) that yields collisionally stabilized HO_2 radicals. HO_2 is far less reactive than H causing an inhibition of the overall reaction rate when (R4) dominates. The ratio $^{R3}/_{R4}$ thus becomes a decisive parameter when determining if the overall governing reaction mechanism is mainly chain-branching (fast) or chain-propagating (slow) in nature. The reactions (R3) and (R4) have recently been subjected to thorough revision by Li *et al.* [192]. Following their recommendations, reaction (R3) is drawn from the work of Hessler [195]. Reaction (R4) is represented by the high-pressure limit from Cobos *et al.* [196] and newly fitted low-pressure limits [192], with corresponding Troe parameters to describe the fall-off region, based on experimental data with different bath gases from Michael *et al.* [197]. A high value of $^{R3}/_{R4}$ gives rise to a significant O radical pool, which further promotes the chain branching reaction O+H_2 $\rightleftharpoons$ OH+H (R6). This reaction is well-characterized by numerous experimental measurements and literature evaluations at temperatures from 300–2500 K. The preferred rate constant from Baulch *et al.* [145] matches these data across the entire temperature range.

H_2 is converted directly to H_2O in reaction (R9) by oxidation with OH radicals. This is an important H_2O formation reaction and the rate expres-

sion is well-established from multiple experimental measurements [145, 198]. Other H_2O formation channels are the radical termination reactions OH+OH (–R7) and OH+H+M (R8). The rate constant for (R7) originates from the transition state calculations by Michael [198] at temperatures from 700–2500 K, which are in excellent agreement with the high-temperature flash photolysis-shock tube measurements by Lifshitz and Michael [202] (1500–2400 K), and Sutherland *et al.* [203] (1053–2023 K). k_{R8} is adopted from the H_2 oxidation modeling study of Conaire *et al.* [191] where the recommended value of Tsang and Hampson [194] was increased by a factor of two to improve the prediction of experimental data from a wide range of conditions and experimental facilities. This revision is within the uncertainty limits of existing evaluations of (R8) [191] including the latest high-temperature measurements of k_{-R8} by Srinivasan and Michael [204].

The radical association reactions of H_2 (R1) and O_2 (R5) are drawn from the review of Tsang and Hampson [194] with specific values implemented for H_2, N_2, and H_2O as third-body collision partners. Reaction (R1) originates from the early recommendation of Cohen and Westberg [193], which is primarily based on shock tube measurements at high temperatures by Sutton [205]. Reaction (R1) and (R5) are only expected to play a secondary role at low temperatures. The recombination reaction of H and O radicals (R2) is taken from Miller and Bowman [101], which is about five times slower than recommended by Tsang and Hampson [194].

The mechanism includes three competitive product channels from the reaction between HO_2 and H yielding the stable products H_2+O_2 (–R10), two OH radicals (R11), and H_2O+O (R12) respectively. In the forward direction, (R10) further constitutes the primary initiation reaction of H_2/O_2 mixtures. Consistent rate data for HO_2+H are limited to a few room-temperature measurements [206, 207]; an experimental/modeling study of the second pressure limit of explosion of H_2/O_2 in boric acid-coated vessels at 773 K [208]; and recent shock tube measurements of H_2+O_2 by Michael *et al.* [199] at high temperatures (1662–2097 K). Michael *et al.* combined their measurements with *ab initio* calculations and the low-temperature data from Sridharan *et al.* [206] and Keyser [207] to derive k_{R10} applied in Table 5.1, which covers the temperature range 400–2300 K. Baldwin *et al.* [208] expressed rate constant data as optimized values for $k_{-R10}/\left(k_{R3}k_{R15}^{1/2}\right)$ and $k_{R11}/\left(k_{R3}k_{R15}^{1/2}\right)$ at 773 K. Following the approach of Mueller *et al.* [168], the value of the latter parameter has been updated in the present work by incorporating k_{R3} and k_{R15} from Table 5.1 to yield k_{R11} at 773 K. The resulting value has further been combined with the room-temperature measurements from Sridharan *et al.* [206] and Keyser [207] to match an updated expression of k_{R11} =

$8.4 \times 10^{13} \exp\left(\frac{-400}{RT}\right) {}^{\mathrm{cm}^3}/_{\mathrm{mol\,s}}$. The resulting rate coefficients are almost identical to the recommendation by Mueller *et al.* [168] at room temperature, whereas slightly higher values are obtained at elevated temperatures; hence, by a factor of 1.11 and 1.16 at 773 and 2000 K respectively. The branching ratio $k_{\mathrm{R11}}/(k_{-\mathrm{R10}} + k_{\mathrm{R11}} + k_{\mathrm{R12}}) = 89\,\%$ at room temperature, which is in excellent agreement with recommendations from both Sridharan *et al.* and Keyser. The ratio decreases to 87 % and 65 % at 773 and 2000 K respectively. The third product channel to H_2O+O (R12) is included in the model despite experimental indications of a low contribution [206, 207]. k_{R12} is taken from the recent review by Baulch *et al.* [145] and yields $k_{\mathrm{R12}}/(k_{-\mathrm{R10}} + k_{\mathrm{R11}} + k_{\mathrm{R12}})$ = 2.9, 1.9, and 1.2 % at 298, 773, and 2000 K respectively, which is consistent with Sridharan *et al.* [206] and Keyser [207].

The reaction of HO_2 with O (R13) has only one possible product channel leading to OH+O_2. The reaction plays an important role in the degeneration of HO_2 radicals in the upper atmosphere, which has encouraged a number of experimental rate measurements at low temperatures (229–391 K), e.g. [206, 209, 210]. These indicate a slightly negative temperature dependence. High-temperature measurements are sparse and subjected to significant uncertainties and hence, provide no conclusive indications of the temperature dependence in this range. The present mechanism applies the recent recommendation by Baulch *et al.* [145], which includes a negative temperature dependence that matches the available low-temperature measurements.

The conversion of HO_2 with H and O competes against the important OH radical termination reaction HO_2+OH $\rightleftharpoons$ H_2O+O_2 (R14). This reaction needs special attention due to a highly non-Arrhenius temperature dependence at conditions relevant to this study. Figure 5.2 shows experimental measurements [200, 211–223] and comparisons with recently recommended rate expressions [145, 224] including an updated fit by the author (full line). Reaction (R14) plays an important role in the conversion of HO_2 and OH in the upper atmosphere and, as a consequence, numerous studies have been conducted at low temperatures from 231 to 420 K [213–219]. These findings fall into two low-temperature groups with rate constants between 2–5$\times 10^{13}$ and 6–8$\times 10^{13}$ ${}^{\mathrm{cm}^3}/_{\mathrm{mol\,s}}$ respectively; all indicating a negative temperature dependence (see Figure 5.2). Keyser [219] suggested that the systematic discrepancy between the measurements of these two groups is a result of secondary reactions with H and O causing a lower rate constant determination by Sridharan *et al.* [218] and others. Keyser avoided this interference by addition of NO_2 to remove H and O radicals. Keyser also noticed that the reaction shows little or no pressure dependence below 1.3 bar across the investigated temperature range. Subsequent literature evaluations [145, 225, 226] have adopted the rate expression proposed by Keyser [219] in the low-temperature

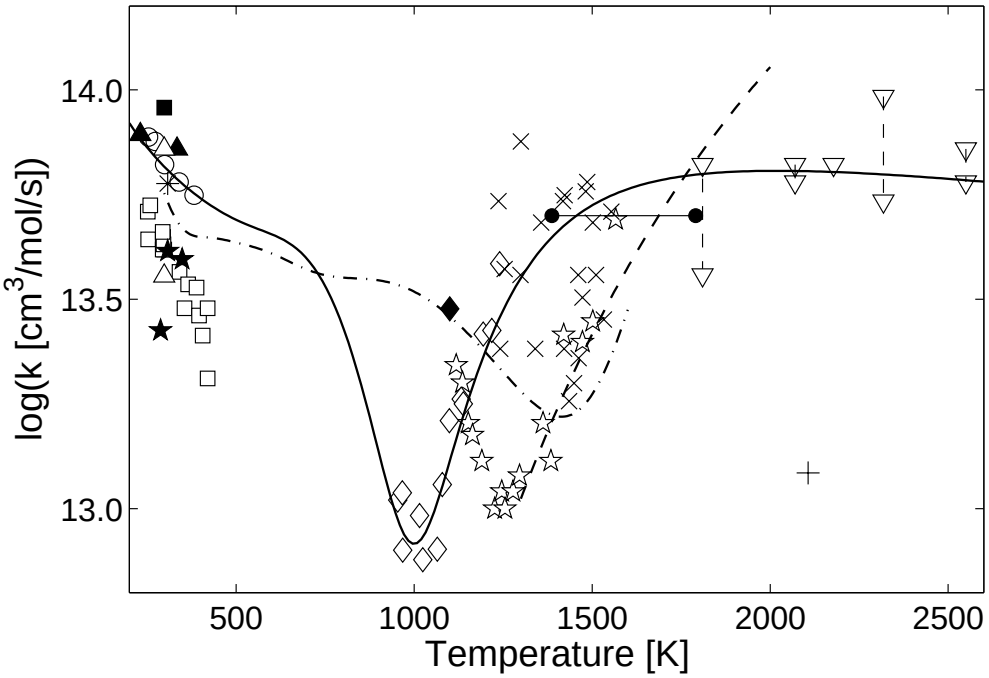

Figure 5.2: Rate constant of reaction (R14) as a function of temperature. + Friswell & Sutton, 1972 [211]; •–• Peeters & Mahnen, 1973 [212]; ▲ DeMore, 1979 [213]; ★ Burrows *et al.*, 1981 [214]; ∗ Cox *et al.*, 1981 [215]; ■ Kurylo *et al.*, 1981 [216]; △ DeMore, 1982 [217]; □ Sridharan *et al.*, 1984 [218]; ○ Keyser, 1988 [219]; ▽–▽ Gooding & Hayhurst, 1988 [220]; ♦ Hippler *et al.*, 1990 [221]; ☆ Hippler *et al.*, 1995 [222]; ◊ Kappel *et al.*, 2002 [200]; × Srinivasan *et al.*, 2006 [223]; - - Baulch *et al.*, 2005 [145]; -·- Sivaramakrishnan *et al.*, 2007 [224]; — This work: $k_{\mathrm{R14}} = \left[3.6 \times 10^{21} T^{-2.1} \exp\left(\frac{-9000}{RT}\right) + 2.0 \times 10^{15} T^{-0.6} - 2.2 \times 10^{96} T^{-24.0} \exp\left(\frac{-49000}{RT}\right)\right]$ $^{\mathrm{cm}^3}/_{\mathrm{mol\,s}}$.

region. However, this rate constant does not reproduce the available high-temperature data [200,211,212,220–223]. Hippler *et al.* [222] conducted shock tube measurements of the thermal decomposition of H_2O_2 and located the deep and unusally narrow rate constant minimum at 1250 K. In a more recent study from the same group, Kappel *et al.* [200] confirmed this behavior but located the rate constant minimum at ∼1000 K. Kappel *et al.* were able to measure reactant concentrations more accurately than Hippler *et al.*, which reduced the uncertainty of their rate constant measurements considerably. As a consequence, more confidence is placed in the later results from Kappel *et al.* [200]. At high temperatures from 1300–2300 K, temperature-independent rate constants of about 4–6×10^{13} $^{\mathrm{cm}^3}/_{\mathrm{mol\,s}}$ have been determined by Peeters and Mahnen [212], Gooding and Hayhurst [220] and, most recently, by Srinivasan *et al.* [223], even though the latter results show considerable scatter.

The proposed fit by the author (full line in Figure 5.2) reproduces the low-temperature data of Keyser [219] as well as the high-temperature data of Peeters and Mahnen [212], Gooding and Hayhurst [220], and Srinivasan *et al.* [223]. The intermediate temperature region, that includes the characteristic rate constant minimum, is consistent with the measurements reported by Kappel *et al.* [200]. The author notes that the proposed rate expression needs validation in the range 400–950 K, but this is currently impossible due to the lack of experimental data at these conditions.

Self-association of HO_2 to H_2O_2+O_2 (R15) and subsequent decomposition of H_2O_2 to OH via (R16) is the main conversion path of H_2O_2. The reaction rates are adopted from Kappel *et al.* [200] including fall-off curves for the decomposition reaction. Kappel *et al.* did not observe any pressure dependence of (R15) in the investigated temperature range 950–1250 K. Other possible H_2O_2 consumption channels are the radical reactions with H (R17,R18), O (R19), and OH (R20). The reaction with H is analogous to HO_2+H and has two product channels yielding HO_2+H_2 (R17) and H_2O+OH (R18). The present mechanism includes the rate coefficients recommended by Baulch *et al.* [145] that provide an almost constant branching ratio $k_{R17}/(k_{R17} + k_{R18})$ close to 90 %. These recommendations are based on available experimental data [227–229] obtained at 300–1000 K. Baulch *et al.* advocated a significantly lower positiv temperature dependence than Tsang and Hampson [194]. However, both studies assigned large uncertainty margins to the recommended rate coefficients; mainly due to possible interference from secondary reactions during the underlying experimental work. The reaction between H_2O_2 and O has two principal product channels that are chain branching and terminating in nature yielding HO_2+OH (R19) and H_2O+O_2 respectively. Experimental investigations of the product branching ratio $k_{R19}/k_{H_2O_2+O\rightarrow prod.}$ are very uncertain and indicate values from >0.2 [230] to unity [231]. In the present study, k_{R19} is set equal to the overall rate constant of H_2O_2+O → prod., as recommended by Tsang and Hampson [194].

5.3.2 CO/CO_2 Reaction Mechanism

The oxidation of CO to CO_2 is a highly exothermic reaction that accounts for a substantial fraction of the heat release during hydrocarbon combustion. Accurate model description is therefore a requirement in order to give reliable predictions of hydrocarbon oxidation chemistry. The CO/CO_2 reaction mechanism is provided in Table 5.2. The author notes that CO may also be converted to oxygenated hydrocarbon species, e.g. formyl radicals (HCO) and formaldehyde (CH_2O), under reducing conditions. This part of

the mechanism will be presented later in this chapter in connection to the C_1 hydrocarbon reaction mechanism.

Table 5.2: Reactions from the CO/CO_2 reaction mechanism. Units are mol, cm, s, cal.

	Reactions	A	β	E	Note/Ref.
21.	$CO + O(+M) \rightleftharpoons CO_2(+M^a)$	1.80×10^{10}	0.0	2384	[232, 233]
	Low-pressure limit:	1.35×10^{24}	–2.79	4191	[233, 234]
	Troe parameters: 1.0 10^{-30} 10^{30} 10^{30}				
22.	$CO + HO_2 \rightleftharpoons CO_2 + OH$	1.57×10^{5}	2.18	17940	[235]
[b]23.	$CO + OH \rightleftharpoons CO_2 + H$	8.00×10^{10}	0.0	0	see text, 1 bar
		8.80×10^{5}	1.77	954	1 bar
	$CO + OH \rightleftharpoons CO_2 + H$	3.70×10^{12}	0.0	12518	10 bar
		9.30×10^{7}	1.1	0	10 bar
	$CO + OH \rightleftharpoons CO_2 + H$	2.90×10^{12}	0.0	11922	20 bar
		4.50×10^{7}	1.2	0	20 bar
	$CO + OH \rightleftharpoons CO_2 + H$	1.50×10^{12}	0.0	13909	50 bar
		5.80×10^{6}	1.5	0	50 bar
	$CO + OH \rightleftharpoons CO_2 + H$	1.50×10^{11}	0.0	1987	100 bar
		1.87×10^{5}	1.94	0	100 bar
[b]24.	$CO + OH \rightleftharpoons HOCO$	2.00×10^{26}	–5.6	2881	see text, 1 bar
	$CO + OH \rightleftharpoons HOCO$	1.50×10^{25}	–5.0	1987	10 bar
		1.30×10^{37}	–8.4	7948	10 bar
	$CO + OH \rightleftharpoons HOCO$	4.20×10^{26}	–5.7	1927	20 bar
		7.50×10^{28}	–6.0	3775	20 bar
		4.00×10^{39}	–9.0	9935	20 bar
	$CO + OH \rightleftharpoons HOCO$	4.90×10^{25}	–5.2	1987	50 bar
		4.00×10^{38}	–9.0	6955	50 bar
		5.00×10^{43}	–10.0	13015	50 bar
	$CO + OH \rightleftharpoons HOCO$	1.10×10^{28}	–6.0	2384	100 bar
		1.84×10^{36}	–8.0	7153	100 bar
		2.00×10^{54}	–13.0	19671	100 bar
[c]25.	$HOCO \rightleftharpoons CO_2 + H$	$P[\text{bar}]^{0.95}\times3.50\times10^{56}$	–15.0	46500	see text
		$P[\text{bar}]^{0.95}\times2.50\times10^{69}$	–18.0	60000	
[c]26.	$HOCO + OH \rightleftharpoons CO_2 + H_2O$	4.56×10^{12}	0.0	–89	[236]
	$HOCO + OH \rightleftharpoons CO_2 + H_2O$	9.54×10^{6}	2.0	–89	
27.	$HOCO + O_2 \rightleftharpoons CO_2 + HO_2$	9.91×10^{11}	0.0	0	[237]

a: Enhanced third-body efficiencies: $H_2 = 2.5, H_2O = 12, CO = 1.9, CO_2 = 3.8$
b: Expressed as the sum of the rate constants at a given pressure
c: Expressed as the sum of the rate constants

Conversion of CO with OH is the most important reaction in the subset. Besides being responsible for a substantial part of the heat release during hydrocarbon combustion, the reaction also regulates the OH radical concentration, which plays a decisive role in HO_x and NO_x cycles that are important

in both combustion and atmospheric chemistry research. The reaction of CO+OH exhibits complex pressure and temperature dependencies with two regimes of markedly different activation energies. At low temperatures, the reaction shows a weakly decreasing temperature dependence, whereas a significant positive temperature dependence is observed at high temperatures. A rate minimum marks the transition, whose characteristics depend on the pressure.

The non-Arrhenius behavior of CO+OH has encouraged numerous experimental and theoretical studies of the reaction across a wide range of conditions, e.g. [238–250]. The accepted mechanism was first proposed by Smith and Zellner [238] and Smith [239]. It involves initial association of the reactants to form the activated *trans*-HOCO* complex followed by *cis*/*trans* isomerization before decomposition to CO_2+H; reaction (R23). The thermal decomposition competes with stabilization of HOCO (R24) and redissociation (–R24). The abnormal change in activation energy can be explained by two important transition states of comparable magnitudes located along the reaction coordinate. At low temperatures, energy is insufficient to overcome the second *cis*-HOCO decomposition barrier, allowing the first association transition state to control the overall reaction rate. This favors either stabilization (R24) or redissociation to CO+OH (–R24) depending on the gas density. Once formed, collisionally stabilized HOCO may also decompose to CO_2+H (R25), or it may be converted by other available reactants, like OH (R26) and O_2 (R27). At high temperatures and/or low pressures, the second transition state controls the overall reaction rate and the dissociation channel (R23) predominates. The pressure dependence is related to the overall conversion of CO+OH given by $k_{\mathrm{CO+OH}} = k_{\mathrm{R23}} + k_{\mathrm{R24}}$. At the high-pressure limit, stabilized HOCO is the sole product as $k_{\mathrm{CO+OH}} \to k_{\mathrm{R24}}$ when $P \to \infty$, while CO_2+H are the dominating products as the low-pressure limit is approached; i.e. $k_{\mathrm{CO+OH}} \to k_{\mathrm{R23}}$ when $P \to 0$. Fulle *et al.* [243] and Troe [244] developed a complex expression to describe the fall-off behavior within these limits. Following this work, $k_{\mathrm{R23}} = k_0 \left[1 - [x/(1+x)]\, F(x)\right]$ and $k_{\mathrm{R24}} = k_{\mathrm{R24,0}} \left[(1+y)/(1+x)\right] F(x)$, where $x = k_{\mathrm{R24,0}}/(k_\infty - k_0)$, $y = k_0/(k_\infty - k_0)$, and k_∞ and k_0 refer to $k_{\mathrm{CO+OH},\infty}$ and $k_{\mathrm{CO+OH,0}}$ respectively. The pressure dependence is included in $k_{\mathrm{R24,0}} = k_0 A_0^* \exp\left(\frac{-T}{T^*}\right) P$, where $A_0^* = 5.9\,\mathrm{bar}^{-1}$ for N_2 as bath gas, and $T^* = 161\,\mathrm{K}$. The broadening factor $F(x) = F_{cent}^{\left(1/\left[1+(\log x)^2\right]\right)}$ with $F_{cent} = 0.49 + 0.51 \exp\left(\frac{-T}{300\,\mathrm{K}}\right)$. Troe [244] proposed values of $k_\infty = \left[1.23 \times 10^{15} \exp\left(\frac{-7520\,\mathrm{K}}{T}\right) + 1.1 \times 10^{13} \exp\left(\frac{-1850\,\mathrm{K}}{T}\right) + 8.0 \times 10^{11} \exp\left(\frac{-120\,\mathrm{K}}{T}\right)\right]\,{}^{\mathrm{cm}^3}/_{\mathrm{mol\,s}}$ and $k_0 = \left[1.0 \times 10^{13} \exp\left(\frac{-8050\,\mathrm{K}}{T}\right) + 9.0 \times 10^{11} \exp\left(\frac{-2300\,\mathrm{K}}{T}\right) + 1.01 \times 10^{11} \exp\left(\frac{-30\,\mathrm{K}}{T}\right)\right]\,{}^{\mathrm{cm}^3}/_{\mathrm{mol\,s}}$ to accurately fit experimental data of $k_{\mathrm{CO+OH}}$ from [240–243] and others within an extensive temper-

ature range of 80–2370 K and pressures from 0.001–1000 bar. The proposed expression has later been recommended in its complete form by Baulch *et al.* [145].

Fulle *et al.* [243] and Troe [244] estimated a value of $H_{298}(\mathrm{HOCO}) = -48.34\ {}^{\mathrm{kcal}}/_{\mathrm{mol}}$. However, in a recent experimental investigation, Ruscic and Litorja [246] determined a lower limit of $H_{298}(\mathrm{HOCO}) > -46.5\,{}^{\mathrm{kcal}}/_{\mathrm{mol}}$, which has later been confirmed by *ab initio* calculations of the *trans*-HOCO well-depth in the CO+OH potential energy surface [135, 137, 247, 248]. The most recent recommendation by Fabian and Janoschek [135] yields a value of $H_{298}(\mathrm{HOCO}) = -44.33\,{}^{\mathrm{kcal}}/_{\mathrm{mol}}$, which is applied in the present study.

The potential energy surface calculations of Yu *et al.* [248] provided the foundation of another extensive investigation of the pressure and temperature dependence of the CO+OH kinetics by Senosiain *et al.* [249,250] using a master equation and RRKM theory. Senosiain *et al.* proposed new analytical rate expressions of k_{R24} and k_{R23}, which enabled them to accurately simulate the available experimental data of $k_{\mathrm{CO+OH}}$ across the same temperature and pressure range as Troe [244]. However, a practical problem arises when applying the proposed rates of either Troe [244] or Senosiain *et al.* [249, 250] since neither of them are suited for direct implementation in Chemkin (cf. the outline of chemical reaction rates in modeling in Section 5.2.2); or in the case of [250], insufficiently covers the pressure range relevant to this study. As a consequence, the author has refitted the expression of Troe [244] for $k_{\mathrm{CO+OH}}$ using suitable rate expressions in the modified Arrhenius form given in Equation (5.8). A comparison with the original expression is shown in Figure 5.3 at temperatures from 300–2000 K and selected pressures. The fitted Arrhenius parameters of k_{R24} and k_{R23} are provided in Table 5.2. It is of little concern that the original work is based on a too low value of $H_{298}(\mathrm{HOCO})$, since the proposed rates by [244] are forward rates derived directly from experimental data.

Fulle *et al.* [243] and Troe [244] have also provided a rate constant for the dissociation of stabilized HOCO to CO_2+H (R25) based on the equilibrium constant $K_{\mathrm{R24}} = k_{\mathrm{R24}}/k_{-\mathrm{R24}}$ and the valid relation $k_{-\mathrm{R24}}/k_{\mathrm{R25}} = k_{\mathrm{CO+OH},\infty}/k_{\mathrm{CO+OH},0} - 1$. Fulle *et al.* proposed a value of $K_{\mathrm{R24}}(T) = 18.6T^{0.2} \exp\left(\frac{-15680\,\mathrm{K}}{T}\right)\ {}^{\mathrm{mol}}/_{\mathrm{cm}^3}$ based on their estimated value of $H_{298}(\mathrm{HOCO})$. This value is corrected (K'_{R24}) in the present study to reflect updated thermochemical properties of the involved species using the correlation $K'_{\mathrm{R24}}(T) = K_{\mathrm{R24}}(T) \exp\left(\frac{\Delta H_{\mathrm{R24}}(T) - \Delta H'_{\mathrm{R24}}(T)}{RT} - \frac{\Delta S_{\mathrm{R24}}(T) - \Delta S'_{\mathrm{R24}}(T)}{R}\right)$ that has been derived from Equation (5.10). Based on the updated value of K'_{R24}, as well as k_{R24}, $k_{\mathrm{CO+OH},\infty}$, and $k_{\mathrm{CO+OH},0}$ from [244], the rate constant of k_{R25} has been refitted across a temperature and pressure range of 300–2000 K and 1–100 bar. The

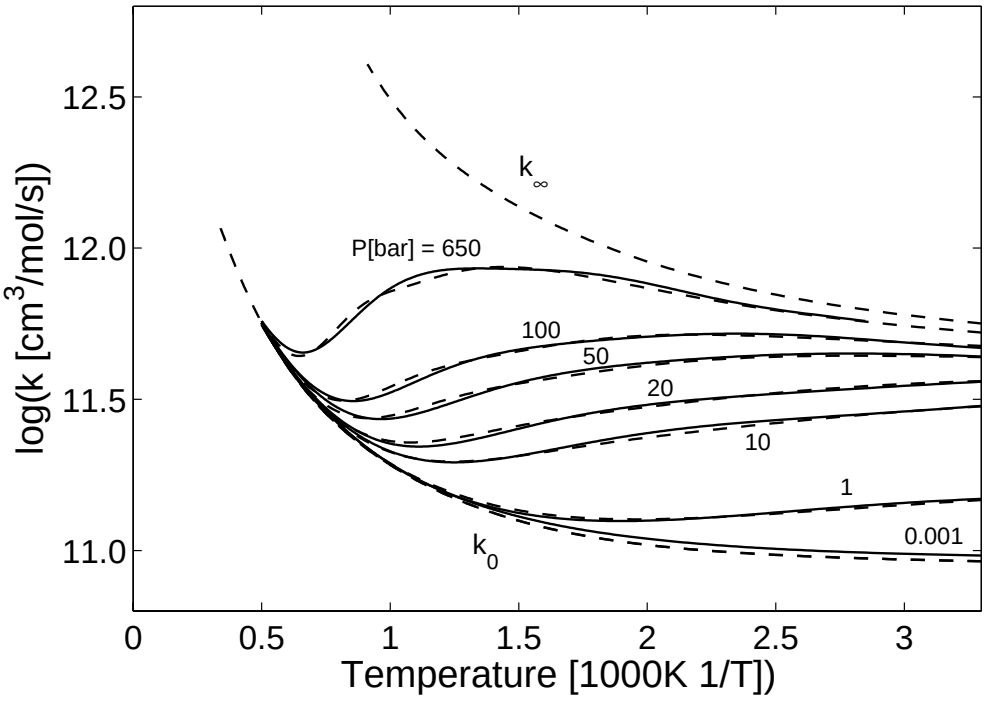

Figure 5.3: Values of $k_{\mathrm{CO+OH}} = k_{\mathrm{R23}} + k_{\mathrm{R24}}$ using N_2 as bath gas. Dashed lines represent the original rate constant from Troe [244]. Full lines denote the refitted rate expression in modified Arrhenius form as provided in Table 5.2.

resulting pressure dependent expression is $k_{\mathrm{R25}} = [3.5 \times 10^{56} T^{-15} \exp\left(\frac{-46500}{RT}\right) + 2.5 \times 10^{69} T^{-18} \exp\left(\frac{-60000}{RT}\right)] P^{0.95}$ s^{-1}.

Even though OH is considered to be the most important reactant to CO, the mechanism also includes radical reactions with O (R21), HO_2 (R22), and H (–R112), where (R21) and (–R112) are pressure dependent association reactions. The latter is considered in the opposite direction (R112) in Section 5.3.3.10. The rate constant k_{R22} is several orders of magnitude lower than $k_{\mathrm{CO+OH}}$, but it is still of interest in the present study due to the importance of HO_2 radicals at high pressure. The reaction has received considerable attention within recent years, e.g. [169, 224, 235, 251–253], but even so, considerable scatter is still observed among experimental as well as theoretical determinations. The preferred rate constant is obtained from the recent theoretical work by You *et al.* [235] based on *ab initio* transition state theory with master equation modeling. Their calculations of the potential energy surface of CO+HO_2 revealed barrier heights of 17.9 and 18.9 $^{\mathrm{kcal}}/_{\mathrm{mol}}$ for initial *trans*- and *cis*-HOOCO* formation respectively. The subsequent conversion of the energized HOOCO* adduct was thoroughly examined in

terms of hindered internal rotations and relevant transition states, which demonstrated that stabilization of HOOCO is negligible and the reaction can be considered independent of pressure up to 500 bar at 300–2500 K using $k_{\mathrm{R22}} = 1.57 \times 10^5 T^{2.18} \exp\left(\frac{-9030}{T}\right)$ $^{\mathrm{cm}^3}/_{\mathrm{mol\,s}}$. You *et al.* [235] emphasized a substantial uncertainty factor for the low-temperature range of this rate expression yielding a value of 8 at 300 K. At high temperatures, the uncertainty factor decreases to a value of 2 and 1.7 at 1000 and 2000 K respectively. Despite these error limits, almost all previous rate constant determinations fall outside the prediction of You *et al.* The only exception are data from recent autoignition experiments by Mittal *et al.* [251] at 950–1100 K that are predicted within 10 % accuracy. Limited support is also found in the *ab initio* study by Sun *et al.* [252] from which, the calculated rate constant is larger than the preferred value by a factor of 2.5–1.7 at temperatures ranging from 300 to 2000 K. Prior experimentally based proposals of the rate constant, e.g. by Tsang and Hampson [194] and Mueller *et al.* [169], lie significantly higher.

5.3.3 C_1 Hydrocarbon Reaction Mechanism

The proposed C_1 hydrocarbon reaction mechanism is presented in Table 5.3. The mechanism only includes subsets of elementary reactions for compounds relevant to the investigated reaction conditions. Reaction pathways leading to e.g. methylene (CH_2) and methylidyne (CH) from saturated hydrocarbon fuels are typically very endothermic, which makes them unimportant at the intermediate temperature range of interest. Subsets involving CH_2 (singlet and triplet) and CH are therefore neglected in the present work. In order to extend the application of the present mechanism to combustion systems operated at higher temperatures, relevant subsets of these species can be included from a number of recent modeling studies, e.g. [105, 138, 233, 254–257].

The mechanism further excludes the stable oxygenated hydrocarbon formic acid (HC(O)OH) and its radical derivatives. In combustion systems, HC(O)OH would typically be produced from oxidation of formaldehyde (CH_2O) followed by dissociation to CO+H_2O or CO_2+H_2. Consequently, HC(O)OH formation does not facilitate important alterations in the carbon oxidation chain compared to the typical pathway to CO/CO_2 via intermediate formation of formyl radicals (HCO). However, it is noted that HC(O)OH reaction subsets have been proposed in recent kinetic modeling studies by e.g. Held and Dryer [167] and Marinov [138], and can be added to the present model in order to extend its application. Preliminary modeling investigations using these subsets have shown that HC(O)OH only plays a minor role at the experimental conditions used in the present work.

Table 5.3: Reactions from the C_1 hydrocarbon reaction mechanism. Units are mol, cm, s, cal.

	Reactions	A	β	E	Note/Ref.
		CH_4 (methane)			
28.	$CH_4 + H \rightleftharpoons CH_3 + H_2$	4.10×10^{3}	3.156	8755	[258]
29.	$CH_4 + O \rightleftharpoons CH_3 + OH$	4.40×10^{5}	2.5	6580	[145]
30.	$CH_4 + OH \rightleftharpoons CH_3 + H_2O$	1.00×10^{6}	2.182	2506	[259]
31.	$CH_4 + HO_2 \rightleftharpoons CH_3 + H_2O_2$	4.70×10^{4}	2.5	21000	[145]
—	$CH_4 + O_2 \rightleftharpoons CH_3 + HO_2$	*see reverse*			
		CH_3 (methyl radical)			
32.	$CH_3 + H(+M) \rightleftharpoons CH_4(+M^a)$	2.11×10^{14}	0.0	0	[260]
	Low-pressure limit:	6.47×10^{23}	–1.8	0	
	Troe parameters: 0.638 10^{-30} 3230 10^{30}				
33.	$CH_3 + O \rightleftharpoons CH_2O + H$	6.91×10^{13}	0.0	0	[145, 261]
34.	$CH_3 + O \rightleftharpoons H_2 + CO + H$	1.52×10^{13}	0.0	0	[145, 261]
35.	$CH_3 + OH(+M) \rightleftharpoons CH_3OH(+M)$	4.34×10^{15}	–0.79	0	[262]
	Low-pressure limit:	3.84×10^{37}	–6.21	1333	
	Troe parameters: 0.25 210 1434 10^{30}				[b]
[c]36.	$CH_3 + O_2 \rightleftharpoons CH_3OO$	5.00×10^{22}	–3.85	2000	1 bar, [263][d]
	$CH_3 + O_2 \rightleftharpoons CH_3OO$	3.35×10^{21}	–3.2	2300	10 bar
	$CH_3 + O_2 \rightleftharpoons CH_3OO$	4.10×10^{20}	–2.94	1900	20 bar
		3.25×10^{29}	–5.6	6850	20 bar
	$CH_3 + O_2 \rightleftharpoons CH_3OO$	2.83×10^{18}	–2.2	1400	50 bar
		5.60×10^{28}	–5.25	6850	50 bar
	$CH_3 + O_2 \rightleftharpoons CH_3OO$	1.05×10^{19}	–2.3	1800	100 bar
		4.10×10^{30}	–5.7	8750	100 bar

Continues on next page

Continued from last page

	Reactions	A	β	E	Note/Ref.
37.	$CH_3 + O_2 \rightleftharpoons CH_3O + O$	7.55×10^{12}	0.0	28297	[264]
38.	$CH_3 + O_2 \rightleftharpoons CH_2O + OH$	1.87×10^{11}	0.0	9842	[264]
39.	$CH_3 + HO_2 \rightleftharpoons CH_3O + OH$	2.00×10^{13}	0.0	1075	[265]
40.	$CH_3 + HO_2 \rightleftharpoons CH_4 + O_2$	2.55×10^{8}	1.25	–1645	[266], 300–800 K
		1.82×10^{3}	2.83	–3730	800–3000 K
41.	$CH_3 + CH_3(+M) \rightleftharpoons C_2H_6(+M)$	3.60×10^{13}	0.0	0	[145]
	Low-pressure limit:	1.27×10^{41}	–7.0	2760	
	Troe parameters: 0.62 73 1180 10^{30}				
42.	$CH_3 + CH_3 \rightleftharpoons C_2H_5 + H$	5.42×10^{13}	0.0	16055	[145]
	CH_3OO (methylperoxyl radical)				
43.	$CH_3OO + H \rightleftharpoons CH_3O + OH$	9.64×10^{13}	0.0	0	[194]
44.	$CH_3OO + O \rightleftharpoons CH_3O + O_2$	1.63×10^{13}	0.0	–445	($= k_{R13}$)
45.	$CH_3OO + OH \rightleftharpoons CH_3OH + O_2$	2.00×10^{15}	–0.60	0	see text
46.	$CH_3OO + OH \rightleftharpoons CH_3O + HO_2$	4.00×10^{11}	0.60	0	see text
47.	$CH_3OO + HO_2 \rightleftharpoons CH_3OOH + O_2$	2.50×10^{11}	0.0	–1490	[267]
48.	$CH_3OO + CO \rightleftharpoons CH_3O + CO_2$	1.57×10^{5}	2.18	17940	($=k_{R22}$)
49.	$CH_3OO + CH_3 \rightleftharpoons CH_3O + CH_3O$	5.06×10^{12}	0.0	–1410	[268]
50.	$CH_3OO + CH_4 \rightleftharpoons CH_3OOH + CH_3$	4.70×10^{4}	2.50	21000	($= k_{R31}$)
51.	$CH_3OO + CH_3O \rightleftharpoons CH_3OOH + CH_2O$	3.00×10^{11}	0.0	0	[194]
52.	$CH_3OO + CH_3OH \rightleftharpoons CH_3OOH + CH_2OH$	3.98×10^{13}	0.0	19400	($= k_{R88}$)
53.	$CH_3OO + CH_2O \rightleftharpoons CH_3OOH + HCO$	4.11×10^{4}	2.5	10206	($= k_{R109}$)
54.	$CH_3OO + HCO \rightleftharpoons CH_3O + H + CO_2$	3.00×10^{13}	0.0	0	($= k_{R117}$)

Continues on next page

Continued from last page

	Reactions	A	β	E	Note/Ref.
[e]55.	$CH_3OO + CH_3OO \rightleftharpoons CH_3O + CH_3O + O_2$	1.10×10^{18}	–2.40	1800	see text, [267]
		7.00×10^{10}	0.0	800	
56.	$CH_3OO + CH_3OO \rightleftharpoons CH_3OH + CH_2O + O_2$	2.00×10^{11}	–0.55	–1600	see text, [267]
57.	$CH_3OO + C_2H_5 \rightleftharpoons CH_3O + C_2H_5O$	5.06×10^{12}	0.0	–1410	($= k_{R49}$)
58.	$CH_3OO + C_2H_6 \rightleftharpoons CH_3OOH + C_2H_5$	1.94×10^{1}	3.64	17100	[148]
	CH_3OOH (methylperoxide)				
[f]59.	$CH_3OOH \rightleftharpoons CH_3O + OH$	1.95×10^{35}	–6.7	47450	[266], 1 bar
	$CH_3OOH \rightleftharpoons CH_3O + OH$	1.12×10^{28}	–4.15	46190	10 bar
	$CH_3OOH \rightleftharpoons CH_3O + OH$	2.80×10^{26}	–3.5	46340	50 bar
	$CH_3OOH \rightleftharpoons CH_3O + OH$	2.22×10^{17}	–0.42	44622	k_∞
60.	$CH_3OOH + H \rightleftharpoons CH_2OOH + H_2$	5.40×10^{10}	0.0	1860	see text, [269]
61.	$CH_3OOH + H \rightleftharpoons CH_3OO + H_2$	5.40×10^{10}	0.0	1860	see text, [269]
62.	$CH_3OOH + H \rightleftharpoons CH_3O + H_2O$	1.20×10^{10}	0.0	1860	see text, [269]
63.	$CH_3OOH + O \rightleftharpoons CH_2OOH + OH$	1.61×10^{13}	0.0	4750	see text, [145]
64.	$CH_3OOH + O \rightleftharpoons CH_3OO + OH$	8.65×10^{12}	0.0	4750	see text, [145]
65.	$CH_3OOH + OH \rightleftharpoons CH_2OOH + H_2O$	7.23×10^{11}	0.0	–258	[145,270]
66.	$CH_3OOH + OH \rightleftharpoons CH_3OO + H_2O$	1.08×10^{12}	0.0	–437	[145,270]
67.	$CH_3OOH + HO_2 \rightleftharpoons CH_3OO + H_2O_2$	4.11×10^{4}	2.5	10206	($= k_{R109}$)
	CH_2OOH (hydroperoxymethyl radical)				
68.	$CH_2OOH \rightarrow CH_2O + OH$	2.44×10^{12}	–0.925	1567	[271], 1 bar
	$CH_2OOH \rightarrow CH_2O + OH$	2.49×10^{13}	–0.927	1579	10 bar

Continues on next page

Continued from last page

	Reactions	A	β	E	Note/Ref.
	$CH_2OOH \rightarrow CH_2O + OH$	6.95×10^{14}	–1.064	1744	100 bar
		CH_3O (methoxy radical)			
69.	$CH_3O(+M) \rightleftharpoons CH_2O + H(+M)$	6.80×10^{13}	0.0	26154	[272]
	Low-pressure limit:	1.87×10^{25}	–3.0	24290	
	Troe parameters: 0.5 1000 2000 10^{30}				g
70.	$CH_3O + H \rightleftharpoons CH_2O + H_2$	5.31×10^{13}	0.0	745	[273]
71.	$CH_3O + H \rightleftharpoons CH_3 + OH$	4.59×10^{12}	0.0	745	[273]
72.	$CH_3O + H(+M) \rightleftharpoons CH_3OH(+M^h)$	2.43×10^{12}	0.515	50	[256]
	Low-pressure limit:	4.66×10^{41}	–7.44	14080	
	Troe parameters: 0.7 100 9×10^5 10^5				
73.	$CH_3O + O \rightleftharpoons CH_2O + OH$	3.76×10^{12}	0.0	0	[145, 274]
74.	$CH_3O + OH \rightleftharpoons CH_2O + H_2O$	1.80×10^{13}	0.0	0	[194]
75.	$CH_3O + HO_2 \rightleftharpoons CH_2O + H_2O_2$	3.00×10^{11}	0.0	0	[194]
76.	$CH_3O + O_2 \rightleftharpoons CH_2O + HO_2$	2.17×10^{10}	0.0	1750	see text, [275]
77.	$CH_3O + CO \rightleftharpoons CH_3 + CO_2$	9.54×10^{25}	–4.93	9080	see text, [276]
78.	$CH_3O + CH_4 \rightleftharpoons CH_3OH + CH_3$	1.32×10^{14}	0.0	15070	[277]
79.	$CH_3O + CH_3 \rightleftharpoons CH_2O + CH_4$	2.40×10^{13}	0.0	0	[194]
80.	$CH_3O + CH_2O \rightleftharpoons CH_3OH + HCO$	1.02×10^{11}	0.0	2980	[194]
81.	$CH_3O + CH_3O \rightleftharpoons CH_3OH + CH_2O$	6.03×10^{13}	0.0	0	[194]
		CH_3OH (methanol)			
82.	$CH_3OH + H \rightleftharpoons CH_2OH + H_2$	2.92×10^9	1.24	4490	see text, [145]

Continues on next page

Continued from last page

	Reactions	A	β	E	Note/Ref.
83.	$CH_3OH + H \rightleftharpoons CH_3O + H_2$	5.15×10^{8}	1.24	4490	see text, [145]
84.	$CH_3OH + O \rightleftharpoons CH_2OH + OH$	2.10×10^{13}	0.0	5305	see text, [145]
85.	$CH_3OH + O \rightleftharpoons CH_3O + OH$	3.70×10^{12}	0.0	5305	see text, [145]
86.	$CH_3OH + OH \rightleftharpoons CH_2OH + H_2O$	5.27×10^{6}	1.92	–286	[145]
87.	$CH_3OH + OH \rightleftharpoons CH_3O + H_2O$	9.30×10^{5}	1.92	–286	[145]
88.	$CH_3OH + HO_2 \rightleftharpoons CH_2OH + H_2O_2$	3.98×10^{13}	0.0	19400	[278]
89.	$CH_3OH + O_2 \rightleftharpoons CH_2OH + HO_2$	2.10×10^{13}	0.0	44900	[279]
	CH_2OH (hydroxymethyl radical)				
90.	$CH_2OH(+M) \rightleftharpoons CH_2O + H(+M^{i})$	2.80×10^{14}	–0.73	32820	[167]
	Low-pressure limit:	6.01×10^{33}	–5.39	36200	
	Troe parameters: 0.96 67.6 1855 7543				
91.	$CH_2OH + H(+M) \rightleftharpoons CH_3OH(+M)$	4.34×10^{15}	–0.79	0	($=k_{R35}$)
	Low-pressure limit:	3.84×10^{37}	–6.21	1333	
	Troe parameters: 0.25 210 1434 10^{30}				
92.	$CH_2OH + H \rightleftharpoons CH_2O + H_2$	1.40×10^{13}	0.0	0	see text
93.	$CH_2OH + H \rightleftharpoons CH_3 + OH$	6.00×10^{12}	0.0	0	see text
94.	$CH_2OH + O \rightleftharpoons CH_2O + OH$	6.56×10^{13}	0.0	–693	[280]
95.	$CH_2OH + OH \rightleftharpoons CH_2O + H_2O$	2.40×10^{13}	0.0	0	[279]
96.	$CH_2OH + HO_2 \rightleftharpoons CH_2O + H_2O_2$	1.20×10^{13}	0.0	0	[279]
[f]97.	$CH_2OH + O_2 \rightleftharpoons CH_2O + HO_2$	7.23×10^{13}	0.0	3736	[145]
		2.89×10^{16}	–1.5	0	
98.	$CH_2OH + CH_4 \rightleftharpoons CH_3OH + CH_3$	2.16×10^{1}	3.1	16227	[279]

Continues on next page

Continued from last page

	Reactions	A	β	E	Note/Ref.
99.	$CH_2OH + HCO \rightleftharpoons CH_3OH + CO$	1.00×10^{13}	0.0	0	see text
100.	$CH_2OH + HCO \rightleftharpoons CH_2O + CH_2O$	1.50×10^{13}	0.0	0	[281]
101.	$CH_2OH + CH_2O \rightleftharpoons CH_3OH + HCO$	5.48×10^{3}	2.81	5862	[279]
102.	$CH_2OH + CH_2OH \rightleftharpoons CH_3OH + CH_2O$	4.82×10^{12}	0.0	0	[279]
103.	$CH_2OH + CH_3O \rightleftharpoons CH_3OH + CH_2O$	2.41×10^{12}	0.0	0	[279]
	CH_2O (formaldehyde)				
104.	$CH_2O(+M) \rightleftharpoons HCO + H(+M)$	8.00×10^{15}	0.0	87730	[282]
	Low-pressure limit:	3.73×10^{15}	0.0	73480	
105.	$CH_2O(+M) \rightleftharpoons CO + H_2(+M)$	3.70×10^{13}	0.0	71970	[282]
	Low-pressure limit:	5.66×10^{15}	0.0	65850	
106.	$CH_2O + H \rightleftharpoons HCO + H_2$	4.10×10^{8}	1.47	2444	[145]
107.	$CH_2O + O \rightleftharpoons HCO + OH$	4.16×10^{11}	0.57	2760	[145]
108.	$CH_2O + OH \rightleftharpoons HCO + H_2O$	7.82×10^{7}	1.63	–1055	[283]
109.	$CH_2O + HO_2 \rightleftharpoons HCO + H_2O_2$	4.11×10^{4}	2.5	10206	[284]
110.	$CH_2O + O_2 \rightleftharpoons HCO + HO_2$	2.44×10^{5}	2.5	36460	[145]
111.	$CH_2O + CH_3 \rightleftharpoons HCO + CH_4$	3.19×10^{1}	3.36	4310	[145]
	HCO (formyl radical)				
112.	$HCO \rightleftharpoons H + CO$	$P[\text{bar}]^{0.865}\times9.83\times10^{11}$	–0.865	16755	[285]
113.	$HCO + H \rightleftharpoons CO + H_2$	1.10×10^{14}	0.0	0	[286]
114.	$HCO + O \rightleftharpoons CO + OH$	3.00×10^{13}	0.0	0	[145]
115.	$HCO + O \rightleftharpoons CO_2 + H$	3.00×10^{13}	0.0	0	[145]

Continues on next page

Continued from last page

	Reactions	A	β	E	Note/Ref.
116.	$HCO + OH \rightleftharpoons CO + H_2O$	1.08×10^{14}	0.0	0	[145]
117.	$HCO + HO_2 \rightleftharpoons CO_2 + OH + H$	3.00×10^{13}	0.0	0	[194]
118.	$HCO + O_2 \rightleftharpoons CO + HO_2$	2.71×10^{10}	0.68	–469	[145]
119.	$HCO + CH_3 \rightleftharpoons CO + CH_4$	2.80×10^{13}	0.0	0	[287]
120.	$HCO + HCO \rightleftharpoons CO + CH_2O$	2.70×10^{13}	0.0	0	[286]

a: Enhanced third-body efficiencies: $CH_4 = 1.9, C_2H_6 = 4.8$
b: Fitted to $F_{cent,\mathrm{R35}} = -0.756\exp\left(\frac{-70.7}{T}\right) + \exp\left(\frac{-T}{5646}\right)$ [262] in Ref. [145]
c: Expressed as the sum of the rate constants at a given pressure
d: Fitted to original expression from [263]
e: Expressed as the sum of the rate constants
f: Arrhenius parameters fitted to discrete data points from [266]
g: Fitted to $F_{cent,\mathrm{R69}} = 0.97 - \frac{T}{1950}$ [272]
h: Enhanced third-body efficiencies: $Ar = 0.7, H_2 = 2, H_2O = 6, CH_4 = 3, CO = 1.5, CO_2 = 2, C_2H_6 = 3$
i: Enhanced third-body efficiencies: $H_2 = 2, H_2O = 5, CO = 2, CO_2 = 3$

5.3.3.1 CH_4 Reactions

Methane is converted through a number of H-abstraction reactions. Most importantly, the radical reactions with H (R28), O (R29), and OH (R30), as well as the initiation reaction with molecular oxygen (–R40). Reactions with hydrocarbon radicals; e.g. CH_3O (R78) and HCO (–R111), gain importance under reducing conditions, whereas reactions involving peroxy radicals, e.g. HO_2 (R31) and CH_3OO (R50) become typical conversion channels at high pressure and/or low temperatures.

Reaction with OH (R30) is the most important source of CH_4 conversion in atmospheric chemistry as well as combustion. Naturally, this has encouraged a large number of experimental studies. The applied rate constant is drawn from the recent work by Srinivasan *et al.* [259], who combined own shock tube measurements at 840–2025 K with prior results; most importantly [288–291], to yield a validated rate expression over the temperature range 195–2025 K. At temperatures <400 K, the rate constant proposed by Srinivasan *et al.* is in excellent agreement with the literature evaluation by Baulch *et al.* [145], while it is more than 20 % below Baulch *et al.* at temperatures >750 K.

Reported measurements of the reaction CH_4+H (R28) are in good agreement at high temperatures >900 K, e.g. [258, 292–294], whereas some scatter is observed in the available low temperature measurements [295]. k_{R28} is taken from the most recent experimental study by Sutherland *et al.* [258], who combined own shock tube measurements of the forward and the reverse rate with previous results to yield a validated expression at 348–1950 K.

The available high and intermediate temperature measurements of CH_4+ O (R29), e.g. [296–300], are generally in good agreement, while low temperature studies by Cadle and Allen [301], and Westenberg and De Haas [302] deviate by more than one order of magnitude. Cohen [303] analyzed selected low to intermediate temperature measurements (<600 K) and discovered a significant sensitivity to secondary reactions with O atoms, which had not been accounted for by [301, 302], and others. According to Cohen, this issue would lead to an overprediction of k_{R29} by a factor of 2–3 from the involved measurements. The present mechanism uses k_{R29} from the recent review by Baulch *et al.* [145] (400–2500 K), which is based on the referred experimental studies with a correction to the low temperature data in accordance with [303]. This rate expression is 30–40 % higher than the recent theoretical value from Corchado *et al.* [304] based on variational transition state theory calculations with multidimensional tunneling correction.

Experimental characterization of the abstraction reaction by HO_2 (R31) is limited to a single relative rate measurement of $k_{R31}/k_{R15}^{1/2}$ at 716 K reported

by Baldwin *et al.* [305]. Scott and Walker [306] drew analogies between HO_2 abstraction reactions from alkanes, alkenes, and aromatics, and proposed the modified Arrhenius expression (Equation (5.8)), with $\beta = 2.5$ to describe the general HO_2 abstraction reaction HO_2+RH $\rightleftharpoons$ H_2O_2+R. The value of β was adopted from the combined literature review and high-temperature shock tube study of HO_2+CH_2O (R109) at 541–1600 K by Eiteneer *et al.* [284]. Eiteneer *et al.* confirmed that β lies between 1.8 and 3.4 for alkane-reactions based on *ab initio* calculations using the methods developed by Bozzelli and co-workers [307]. Scott and Walker estimated values of the pre-exponential factor and the activation energy for CH_4+HO_2 (R31) based on the analogue reaction C_2H_6+HO_2, where experimental measurements are available at 673–793 K [308]. In their recent review, Baulch *et al.* [145] recommend k_{R31} from Scott and Walker with a four times increase of the pre-exponential factor in order to coincide with the relative rate measurement by Baldwin *et al.* [305]. The present mechanism follows this recommendation.

Until recently [309], there were no direct measurements of the initiation reaction CH_4+O_2 $\rightleftharpoons$ CH_3+HO_2 (–R40). Baulch *et al.* [145] proposed a rate constant for the forward reaction based on analogies with the reaction CH_2O+O_2 (R110), where reliable measurements at intermediate [310] and high temperatures [264, 311] are available. Baulch *et al.* corrected the pre-exponential factor of $k_{\mathrm{CH_2O+O_2}}$ to account for the extra availability of H atoms and further adjusted the activation energy to reflect differences in $\Delta_r H$ of the title reaction compared to CH_2O+O_2. Values of the reverse rate constant (k_{R40}) have been determined from *ab initio* calculations by Zhu and Lin [266] and indirectly from flow reactor experiments at 1000 K by Scire *et al.* [312]. These results are in excellent agreement. Conversion of k_{R40} from Zhu and Lin to $k_{-\mathrm{R40}}$ at 500–1500 K, using thermodynamic data from Table 3.1, yields values that are a factor of 1.5–2.5 higher than $k_{-\mathrm{R40}}$ from Baulch *et al.* Moreover, the experimentally based value of k_{R40} from Scire *et al.* yields $2.6 \times k_{-\mathrm{R40,Baulch\ et\ al.,2005}}$ at 1000 K. However, these deviations are covered by an estimated uncertainty factor of 3 at 500–1000 K proposed by Baulch *et al.*, and likewise, was an uncertainty factor of 2.89 calculated by Scire *et al.* [312] for their value of k_{R40} at 1000 K. In a recent combined experimental and theoretical study, Srinivasan *et al.* [309] presented the first direct measurements of CH_4+O_2. They used a reflected shock tube apparatus and derived values of $k_{-\mathrm{R40}}$ at high temperatures between 1655 and 1822 K from measurements of OH radicals using multipass absorption spectrometry. At these conditions, HO_2 rapidly dissociates to H atoms followed by almost instantaneous conversion to OH via H+O_2 $\rightarrow$ O+OH (R3). The OH radical formation, thus, becomes a direct measure of the reaction rate of CH_4+O_2. An experimental uncertainty of $\sim$50 % was attributed to these

rate constant measurements; mainly due to uncertainties in the primary side reaction between CH_4+O (R29). The results show some scatter and hence, confirm both rate constants from Baulch *et al.* [145] and Zhu and Lin [266] when considering all appropriate uncertainties. Srinivasan *et al.* also conducted supplementary *ab initio* calculations and obtained a rate expression for (–R40) that confirms the experiments, but falls only slightly below the *ab initio* results from Zhu and Lin, which led Srinivasan *et al.* to recommend k_{R40} from Zhu and Lin for use in further combustion modeling. All these observations point in the direction of a higher rate constant than proposed by Baulch *et al.* [145], even though the uncertainties involved render a definite conclusion impossible. The present work follows the recommendation of Srinivasan *et al.* [309] and applies the rate constant for the reverse reaction CH_3+HO_2 (R40) from Zhu and Lin [266], but it is clear that further experimental investigations remain of relevance. At this point, the reader is reminded of the related pathway CH_3+HO_2 $\rightleftharpoons$ CH_3O+OH (R39). Reaction (R39) will be discussed in a later paragraph that extends the characterization of the reaction path of CH_4+O_2.

5.3.3.2 CH_3 Reactions

Thermal decomposition of CH_4 (–R32) is unimportant at the intermediate temperatures relevant to the present study. However, at reducing conditions and high pressure, the reverse H-addition reaction with CH_3 may become an important source of radical termination. Cobos and Troe [260] reevaluated the early shock tube experiments by Hartig *et al.* [313] to yield important information about the fall-off region and high-pressure limit. They combined these data with theoretical rate coefficients derived from the methods of Troe and co-workers [184, 185] to yield an expression of k_{R32} that shows remarkable consistency with available experimental data [292,314–320] obtained at a wide range of conditions including temperatures from 300–3000 K, pressures covering the entire fall-off region, and different bath gases (He, Ar, CH_4, C_2H_6). It is noted that k_{R32} in Table 5.3 assumes He as collision partner in the absence of experimental investigations with bath gases of more practical importance, like N_2. Nitrogen is often a slightly more efficient collision partner than He, so when N_2 is used as bath gas, as in the current experimental study, there is a potential of a minor underprediction of k_{R32} when using the rate constant in its present form. Experimental evidence is, however, needed for verification.

The reaction between CH_3 and O-atoms is expected to proceed through a highly energized CH_3O^* radical adduct with an internal energy of $\sim$90 $^{kcal}/_{mol}$. The adduct either undergoes C–H bond cleavage to CH_2O+H (R33) or elim-

inates H_2 and HCO. In the latter case, HCO rapidly decomposes at the relatively weak C–H bond ($\sim$16 $^{\text{kcal}}/_{\text{mol}}$) under the influence of the large excess energy from the adduct resulting in the final products H_2+CO+H (R34) [321, 322]. The reaction has other potential product channels involving e.g. stabilized HCO, CH_2, and CH; but none of these products have been detected experimentally. The available experimental measurements of the overall reaction, e.g. [261, 321–325], are consistent and indicate little or no dependence of temperature from 298 to 2300 K. A mean value from [145] yields $k_{\text{CH}_3+\text{O}\rightarrow\text{prod.}} = 8.43\times10^{13}\ ^{\text{cm}^3}/_{\text{mol s}}$. This is used together with the latest measurement of the branching ratio $k_{\text{R34}}/\left(k_{\text{R33}}+k_{\text{R34}}\right) = 0.18 \pm 0.04$, from Preses *et al.* [261] to obtain the preferred values of k_{R33} and k_{R34}. The experimental branching ratio was determined at room temperature and agrees well with the theoretical prediction of 0.15 by Marcy *et al.* [322]. It is noted that Marcy *et al.* predicted a weak temperature dependence of the branching ratio yielding 0.13 at 1000 K, which is disregarded in the present work.

The reaction of CH_3 with OH proceeds through an excited CH_3OH^* adduct that may be collisionally stabilized to CH_3OH (R35), or decompose to a number of products, e.g. $^1CH_2$+H_2O, $^3CH_2$+H_2O, CH_2O+H_2, HCOH+H_2, CH_2OH+H, etc., [262, 326]. A large number of experimental results have been reported at room-temperature, e.g. [262, 327–331], while only a few experimental studies extend the temperature range to higher values. These are Oser *et al.* [332] at 480 K, De Avillez Pereira *et al.* [262] and Humpfer *et al.* [333] at 700 K, and Bott and Cohen [334] at 1200 K. The experiments near room-temperature indicate that the reaction is almost independent of pressure above $\sim$0.1 bar, and it is close to the high-pressure limit at 1 bar where stabilized CH_3OH is the sole product. The overall rate constant is fairly well established, but in the low-pressure and fall-off region, branching ratios are unclear and proposals from the literature deviate significantly depending on the considered temperature range; e.g. see [262, 331, 333, 335]. Bott and Cohen [334] did not measure the product distribution from their high-temperature experiment at 1200 K and atmospheric pressure, but they estimated a selectivity of CH_3OH of only $\sim$75 % from theoretical considerations. This is in good agreement with the early QRRK calculations by Dean and Westmoreland [335] at 1 bar N_2 that predicted a decreasing CH_3OH selectivity from near-unity at room-temperature to 0.9 at 1000 K and 0.5 at 1550 K. According to Dean and Westmoreland, (R35) is mainly competing against the bimolcular channel producing CH_2OH+H. The experimental study by Humpfer *et al.* [333] at 700 K and 0.65–3.25 mbar showed no signs of CH_2OH formation, but, instead, suggested contributions from the product channels leading to CH_2O and its isomer HCOH. The recent combined experimental and theoretical study by De Avillez Pereira *et al.* [262] indicated that

the bimolecular channel to $^1CH_2$+H_2O may become more important than the stabilization channel at low pressure and/or high temperatures. The latter is supported by the room-temperature measurements from Deters *et al.* [331] at low pressures from 45 to 467 mbar. However, according to De Avillez Pereira *et al.*, the channel to $^1CH_2$+H_2O has a strong negative dependence of pressure, which makes it very unlikely to gain importance at the conditions relevant to the present study. A similar negative pressure dependence was predicted for the channel producing isomeric formaldehyde (HCOH+H_2). The preferred value of k_{R35} is taken from the study by De Avillez Pereira *et al.* [262] with He as bath gas. It is largely consistent with the available measurements in the field, as well as a previous literature evaluation [336]. It is impossible to make a definite recommendation of branching ratio based on the available results for CH_3+OH. Besides (R35), the mechanism also includes the bimolecular channel to CH_2OH+H via the reverse reaction (–R93). It may be a coarse approximation to exclude the other bimolecular channels, but since the pressure and temperature ranges of interest in this study support (R35) as the dominating product channel, the author finds it reasonable in the given situation. A discussion of (–R93) will be provided in connection to the outline of the CH_2OH reaction subset.

The reaction of CH_3 with molecular oxygen (R36,R37,R38) plays an important role in both atmospheric and combustion chemistry, which has encouraged numerous experimental and theoretical investigations; most importantly [196, 263, 264, 311, 337–341]. The association/stabilization channel to CH_3OO (R36) is dependent of pressure and is expected to proceed without an energy barrier, whereas the two bimolecular channels, CH_2O+OH (R38) and CH_3O+O (R37), both have to overcome energy barriers lying above the potential energy of the reactants [340]. Consequently, (R36) predominates at high pressure and/or low and intermediate temperatures (<1000 K), whereas (R37) and (R38) are only competitive at high temperatures.

Due to the importance of (R36) in both atmospheric and combustion chemistry, most investigations of the pressure dependency are concerned with conditions below 1 bar. Only in the recent work by Fernandes *et al.* [263] have very high pressures (1–1000 bar) been combined with intermediate temperatures (300–700 K). Fernandes *et al.* used a high-pressure flow cell, laser flash photolysis of azomethane or acetone to generate CH_3, and UV absorption for direct measurement of the CH_3OO concentration. The results included direct measurements of the low-pressure rate limit yielding $k_{R36,0} = 6.9 \times 10^{24} T^{-3}$ $^{cm^6}/_{mol^2\,s}$ for both Ar and N_2 as bath gas. The high-pressure limit was approached within the experimental matrix yielding $k_{R36,\infty} = 7.8 \times 10^{9} T^{0.9}$ $^{cm^3}/_{mol\,s}$. The fall-off range was represented by the simplified

expression $k_{\mathrm{R36}}/k_{\mathrm{R36},\infty} \approx [x/(1+x)]\, F_{cent}^{1/\{1+[(\log x)/N]^2\}}$ with $x = k_{\mathrm{R36},0}/k_{\mathrm{R36},\infty}$, $F_{cent} \approx 0.33$, and $N \approx 1.47$. This representation of the Troe formalism is not directly compatible with the CHEMKIN software [186] used for the numerical aspects of the present work. Consequently, the author has refitted resulting rate constants from Fernandes *et al.* [263] at specific pressures to modified Arrhenius expressions given in Table 5.3.

The high-temperature channels from CH_3+O_2 (R37,R38) are adopted from the recent shock-tube study by Srinivasan *et al.* [264], who proposed optimum values of k_{R37} and k_{R38} based on own measurements as well as other comparable studies, e.g. [338, 339, 341], across the temperature range 1237–2430 K. At temperatures above 2000 K, the experimentally based values from Srinivasan *et al.* agree well with calculated values from Zhu *et al.* [340], while extrapolations to temperatures <1000 K lie more than one order of magnitude above the theoretical predictions by Zhu *et al.*

The reaction of CH_3 with HO_2 offers a direct oxidation path to CH_3O (R39), or regeneration of CH_4 (R40), which are both indirectly promoted by high pressure through enhanced formation of HO_2 via H+O_2(+M) $\rightleftharpoons$ HO_2(+M) (R4). Reaction (–R40) is also the principal initiation reaction in CH_4 combustion and has previously been discussed in Section 5.3.3.1. The increased availability of HO_2 at high pressure brings the path to CH_3O+OH (R39) in direct competition with the intermediate formation of CH_3OO via (R36) and subsequent conversion channels; see the later discussions of the CH_3OO and CH_3OOH reaction subsets in Section 5.3.3.3 and 5.3.3.4. Measurements of the rate constant for CH_3+HO_2 impose significant challenges due to the simultaneous presence of various radical species that give rise to a number of possible side reactions. Consequently, only a few experimental values of k_{R39} [265, 312, 342] have been proposed and they all rely on indirect determinations. Colket *et al.* [342] conducted well-defined N_2-diluted experiments with CH_3CHO oxidation in a turbulent flow reactor at 1 bar and 1030–1115 K. Under these conditions, (R39) was believed to control CH_3 oxidation, which enabled a fit of $k_{\mathrm{R39}} = 2 \times 10^{13}$ $^{\mathrm{cm}^3}/_{\mathrm{mol\,s}}$ using a detailed kinetic model with 25 elementary reaction steps. In their recent review, Baulch *et al.* [145] advocated this constant rate coefficient from Colket *et al.*, but they assigned a large uncertainty factor of 10 across the temperature range 600–1200 K; mainly due to uncertainties in side reactions. The experimental rate coefficients from Scire *et al.* [312] and Reid *et al.* [265] are based on a similar approach as Colket *et al.* [342]. Scire *et al.* [312] conducted pressurized flow reactor experiments (∼10 bar, ∼1000 K) on CH_4-perturbed moist CO oxidation and fitted $k_{\mathrm{R39}} = 1.48 \times 10^{13}$ $^{\mathrm{cm}^3}/_{\mathrm{mol\,s}}$ from kinetic modeling with an uncertainty factor of 2.24; determined mainly from uncertainties

in side reactions. Reid *et al.* [265] investigated the spontaneous ignition of CH_4/air at temperatures around 900 K and atmospheric pressure, and estimated the temperature dependent rate expression $k_{R39} = 2 \times 10^{13} \exp\left(\frac{-1075}{RT}\right)$ $^{cm^3}/_{mol\,s}$ using a detailed kinetic model. This rate expression yields a value of 1.2×10^{13} $^{cm^3}/_{mol\,s}$ at 1000 K in good agreement with the constant rate coefficients from Colket *et al.* [342] and Scire *et al.* [312]. Zhu and Lin [266] proposed a theoretical value based on *ab initio* calculations. This work has previously been referred in connection to the discussion of CH_4+O_2 (–R40). However, this rate expression lies significantly higher than the experimentally based values referred above. Instead, the present work advocates the temperature dependent rate expression from Reid *et al.* [265].

The recombination of CH_3 radicals to stabilized C_2H_6 (R41) is well established over a large temperature and pressure range except for some controversy about the temperature dependence of the high-pressure limit [145]. Shock wave experiments reported by Hwang and co-workers [343, 344] and Hessler and co-workers [345] at high temperatures; 1200–1700 K and 1175–1750 K respectively, indicate a slightly negative temperature dependence. This behavior is supported by recent theoretical studies [346, 347], but it contradicts the earlier experiments by Glänzer *et al.* [348, 349]. In a subsequent publication, Hessler *et al.* [350] proposed a global fit to the experimental data from Refs. [343, 345, 348, 349, 351–353] that covers the temperature and pressure ranges 296–1750 K and 0.2–213 bar. The analysis gave a negative temperature dependence of $k_{R41,\infty}$, but more importantly, it led to an unrealistic temperature dependence of $k_{R41,0}$ that did not conform with the available data for the reverse dissociation reaction. Instead, the pressure dependent rate expression from Baulch *et al.* [145] is preferred in the present study. It is based on the data of Glänzer *et al.* [348,349], Hippler *et al.* [351], Macpherson *et al.* [354], and Slagle *et al.* [352], and uses a constant high-pressure limit. The rate expression is given for Ar as bath gas, but Baulch *et al.* assumed it to be valid for N_2 as well. It is noted that Baulch *et al.* assigned an uncertainty factor of 2 to both $k_{R41,\infty}$ and $k_{R41,0}$. At high temperatures, (R41) competes against the dissociation pathways C_2H_5+H (R42) and C_2H_4+H_2. More recent experiments [355–358] indicate that the latter path is only important at very high temperatures; probably >2500 K, for which reason it is neglected in the present study. The present mechanism applies the recommended expression of k_{R42} from Baulch *et al.* [145], which is based on experimental data from Frank and Braun-Unkhoff [356], Lim and Michael [357], and Davidson *et al.* [358], and covers the temperature range 1200–2500 K. Other experiments [355, 359] deviate considerably from this value, but this issue is of less concern in the present study where (R42) is expected to play a secondary role compared to (R41).

5.3.3.3 CH_3OO Reactions

Methylperoxyl radicals (CH_3OO) are typically converted through an addition/elimination mechanism involving cleavage of the weak O–O bond, or through H-abstraction from a stable molecule, e.g. CH_4, C_2H_6, CH_2O, and H_2O_2, to form stable CH_3OOH and a new radical species. The former mechanism can be fast radical-radical exchange, to form CH_3O and another oxygenated radical, or radical termination yielding two or more stable products via H atom shift within the peroxide adduct before O–O bond cleavage. Details about CH_3OOH reactions are provided in the proceeding section, but at this point, it is noteworthy that further conversion of CH_3OOH typically happens through unimolecular decomposition at the O–O bond to CH_3O and OH radicals, thereby resulting in a net gain of reactive compounds and overall reactivity of the chemical system at hand.

Alkyl peroxide species are characteristic intermediates in the hydrocarbon oxidation chain at high pressure and/or low to intermediate temperatures due to the promotion of the addition/stabilization reactions between alkyl radicals (CH_3, C_2H_5, etc.) and molecular oxygen. However, since most combustion research has been conducted at high temperatures (>1000 K) and/or low to atmospheric pressure, alkyl peroxide species, like CH_3OO and C_2H_5OO, have traditionally gained less attention in the combustion literature, and only a few elementary reactions have been subjected to experimental investigations. As a consequence, available recommendations are often based either on extrapolations from atmospheric chemistry research, where peroxide species also play important roles, or from simple analogies with e.g. hydroperoxide chemistry [145, 194]. The latter issue warrant some attention: The bond strength of HOO–H ($D_{298} = 87.49 \pm 0.07$ kcal/mol [131]) and CH_3OO–H (87.8 ± 1.0 kcal/mol [134]) are very similar. This indicates that analogue H-abstraction reactions from the peroxy-group of H_2O_2 and CH_3OOH exhibit comparable rates. A similar comparison of the strength of the O–O bond in HO–OH ($D_{298} = 51.3$ kcal/mol [360]) and CH_3O–OH ($\sim 42.6 \pm 1$ kcal/mol [133]) reveals a somewhat weaker O–O bond in CH_3OOH. These considerations are expected to apply to the corresponding radical species HO_2 and CH_3OO as well. They suggest that reactions from the alkylperoxide subsets involving O–O bond cleavage could be somewhat faster than analogue reactions with hydroperoxides, but more investigations are needed for verification. In the present study, rate constant estimates of alkyl peroxide reactions are occasionally drawn directly from analogue hydroperoxide reactions without any corrections to compensate for the different O–O bond strength.

The radical reactions between CH_3OO and H (R43), and O (R44) are expected to proceed at rates close to collisional involving rapid incision of

the O–O bond. A few room-temperature measurements of (R44) are available [361–363], which confirm this behavior. They propose rate constants of $2.6 < k_{R44} < 6.0 \times 10^{13}\,\mathrm{cm^3/mol\,s}$ in excellent agreement with the constant rate coefficient proposed earlier by Tsang and Hampson [194]. The analogue hydroperoxyl reaction $HO_2{+}O \rightleftharpoons OH{+}O_2$ (R13) from Baulch *et al.* [145] displays a minor negative temperature dependence, which is expected to provide the most accurate representation of the temperature dependence of $CH_3OO{+}O$ (R44) over the intermediate temperature range of interest. k_{R13} further yields a value of $3.5 \times 10^{13}\,\mathrm{cm^3/mol\,s}$ at 298 K consistent with the measurements of k_{R44}. This encourages the author to recommend $k_{R44} = k_{R13}$ with an estimated uncertainty factor of 3.

There are no available measurements of (R43). Tsang and Hampson [194] proposed a constant value of $k_{R43} = 9.6 \times 10^{13}\,\mathrm{cm^3/mol\,s}$, which is about two times higher than the current value of $k_{HO_2+H} = k_{R11} + k_{R12}$. The author prefers the former recommendation from Tsang and Hampson because the higher value potentially compensates for the weaker O–O bond in CH_3OO compared to HO_2.

In the absence of reported studies of the reaction between CH_3OO and OH (R45,R46), the author again resolves to a comparison with an analogue reaction. The hydroperoxyl reaction $HO_2{+}OH \rightleftharpoons H_2O{+}O_2$ (R14) shows a highly non-Arrhenius temperature dependence with a characteristic rate minimum around 1000 K (see Figure 5.2). The reaction is expected to proceed through an initial adduct involving a three-membered O atom chain (CH_3O–O–OH*) with a terminal H atom that can be transfered to the primary O atom during incision of the CH_3O–OOH* bond to yield the stable products $CH_3OH{+}O_2$ (R45). At increasing temperatures, this O–O bond cleavage becomes more efficient and may take place without the H atom transfer. As a result, formation of the radical species $CH_3O{+}HO_2$ (R46) is expected to gain more importance at increasing temperatures. This second product channel is not considered in the analogue system ($HO_2{+}OH$) where the same mechanism simply conserves the reactants. The author is not familiar with any experimental or theoretical evidence of the second product channel (R46) that yields two new radicals, and thereby preserves the reactivity of the system, but the different nature of the two channels obviously calls for a certain interest in the branching ratio k_{R45}/k_{R46}. The proposed rate constants for (R45) and (R46) are based on the assumption that the termination channel can be described by a similar rate expression as $HO_2{+}OH$ (R14) in the lower temperature range. This yields $k_{R45} = 2 \times 10^{15} T^{-0.6}\,\mathrm{cm^3/mol\,s}$, which roughly applies to k_{R14} at temperatures < 700 K. From 700 to 1300 K, k_{R14} experiences a sudden drop to a minimum value about five times lower. This behavior is not considered in the present analysis of $CH_3OO{+}OH$. The ter-

mination channel (R45) is expected to dominate at low temperatures, but the rate decreases with temperature as (R46) gains more influence. This behavior is represented by the branching ratio $k_{R45}/k_{R46} = 5000T^{-1.2}\,\mathrm{K}^{1.2}$, which yields a value of $k_{R45} + k_{R46}$ that ranges from 7.8 to $5.7 \times 10^{13}\,{}^{\mathrm{cm}^3}/_{\mathrm{mol\,s}}$ at 298–1500 K. This is consistent with the constant estimated value of $k_{R45} = 6 \times 10^{13}\,{}^{\mathrm{cm}^3}/_{\mathrm{mol\,s}}$ by Tsang and Hampson [194], who did not consider the alternative path (R46). The author estimates an overall uncertainty factor of 7.3, which is composed of a factor of 5 for potential unaccounted rate constant deviations with temperature; as observed with HO_2+OH; a factor of 5 for the branching ratio estimate, and a factor of 2 to cover the potential impact from differences in the O–O bond strength in HO_2 and CH_3OO.

The overall reaction of CH_3OO with HO_2 is fairly well established from a number of experiments, e.g. [364–369]. These were all based on flash photolysis/UV absorption methods and cover a temperature and pressure range of 228–719 K and 0.02–1 bar. There are no reports of signs of a pressure dependency within this range. The most extensive studies originate from the work of Lightfoot and co-workers [368, 369] and Kurylo and co-workers [364, 365]. These data indicate a similar negative temperature dependence, while the data from Kurylo and co-workers systematically fall 1.5–2 times below the reported measurements from Lightfoot *et al.* suggesting the influence from systematic errors. In a recent critical review, Tyndall *et al.* [267] reanalyzed these data based on updated recommendations for the UV absorption cross section for key species involved in the reaction and derived the preferred overall rate expression, which lies close to the experimental values from Lightfoot *et al.* Studies of the branching ratio by Wallington and Japar [370], Wallington [371], and, recently, Elrod *et al.* [372], indicate that CH_3OO+$HO_2 \rightleftharpoons CH_3OOH$+$O_2$ (R47) is the dominating product channel with a minor contribution from the alternative route to CH_2O+H_2O+O_2. The most direct measurements are those reported by Wallington and co-workers suggesting a branching ratio $k_{R47}/k_{CH_3OO+HO_2\rightarrow prod.} = 0.92 \pm 0.08$ at 295 K. Elrod *et al.* measured a value of 0.89 ± 0.02 at 298 K an further calculated an increasing temperature dependence of the ratio represented by $k_{R47}/k_{CH_3OO+HO_2\rightarrow CH_2O+H_2O+O_2} = 498\exp\left(\frac{-1160}{T}\right)$ at 218–298 K. Extrapolation of the temperature to e.g. 500 K yields a value of $k_{R47}/k_{CH_3OO+HO_2\rightarrow prod.} = 0.98$. Lightfoot *et al.* [369] also observed strong indications that (R47), by far, is the predominant product channel at temperatures above ambient, which convinced Tyndall *et al.* [267] to recommend a branching ratio of unity at 295–700 K. This recommendation is followed in the present study.

The reaction between CH_3OO and CO (R48) involves addition/elimination around the terminal O atom to form CH_3O+CO_2. Sander and Wat-

son [373] reported an upper limit of $k_{R48} \leq 4.2 \times 10^6\,{}^{cm^3}/_{mol\,s}$ at 298 K based on a flash photolysis study of CH_3OO+CH_3OO with addition of CO. This value is probably much too high, because it assumes zero competition from the comparatively fast reaction between CH_3O and CO (R77). Due to the lack of direct measurements, the preferred value of k_{R48} is the rate constant of the analogue reaction of CO+HO_2 (R22) that was recently estimated from *ab initio* calculations by You *et al.* [235]. It is noted that k_{R22} is mainly reliable in the high-temperature range (>1000 K), where You *et al.* assigned an uncertainty factor < 2. At room-temperature, the uncertainty of k_{R22} has increased to a factor of 8.

The similar O-abstraction reaction from CH_3OO by CH_3 radicals (R49) has been experimentally characterized at room-temperature [374,375], while temperature dependent measurements up to 530 K have been reported by Keiffer *et al.* [376]. Keiffer and co-workers reevaluated their own data in Ref. [268] using a global analysis technique to relate data from multiple CH_3 decay profiles obtained from flash photolysis of acetone in O_2/Ar at varying temperatures and pressures (0.03–0.8 bar). The resulting rate expression is preferred in this study. It shows a significant negative temperature dependence and falls a factor of 1.5 above the earlier rate constant estimate by Park [374] at 298 K and a factor of 2.6 or less above k_{R39} from the analogue reaction between CH_3+HO_2 at temperatures >500 K.

The mechanism contains a number of other reactions between CH_3OO and carbon species for which there are no direct measurements, e.g. CH_4 (R50), CH_3OH (R52), CH_2O (R53), HCO (R54), and C_2H_5 (R57). As a consequence, rate constants from analogue reaction with HO_2, or CH_3, in case of (R57), have been adopted in the mechanism. The author expects these estimates to be valid within a factor of 3 at the intermediate temperatures of interest, but experimental verifications are needed. Two relative rate determinations of an earlier date are available for CH_3OO+CH_3O (R51) [377,378]. The preferred rate expression is drawn from Tsang and Hampson [194], who re-evaluated these data from Dever and Calvert [377], and Heicklen and Johnston [378], using more accurate rate estimates for the involved side reactions. Even so, Tsang and Hampson assigned a large uncertainty factor of 10 to the resulting estimates. There are no available measurements of CH_3OO+C_2H_6 (R58) either, but Carstensen and Dean [148] recently proposed rate constants for CH_3OO+C_2H_6 (R58) and C_2H_5OO+C_2H_6 (R168) based on *ab initio* CBS-QB3 calculations. Carstensen and Dean also used identical methods to obtain a theoretical value of the rate constant for the analogue reaction HO_2+C_2H_6 (R124), which is in fair agreement with the preferred experimentally based recommendation of k_{R124} from Baulch *et al.* [145]; see the later Section 5.3.4.1. This is considered an indirect validation of the values of k_{R58}

and k_{R168} from Carstensen and Dean [148].

The self-reaction of CH_3OO (R55,R56) is the most studied peroxyl reaction in the mechanism. This is due to its importance in both low-temperature combustion and atmospheric chemistry, where conditions facilitate a strong competition between the radical termination channel to CH_3OH+CH_2O+O_2 (R56) and the non-terminal channel to CH_3O+CH_3O+O_2 (R55). The third product channel to CH_3OOCH_3+O_2 is neglected in the present study due to the lack of compelling evidence of its existence [267]. Most experimental studies have used flash photolysis of Cl_2/CH_4 or azomethane in the presence of O_2 to generate CH_3OO radicals and then monitor the second-order decay ($\mathrm{d}\left[CH_3OO\right]/\mathrm{d}t = -2k_{obs}\left[CH_3OO\right]^2$) using UV absorption [369, 374, 379–385], or, in a few cases, FTIR [386–389] or other techniques [390,391]. These measurements cover the temperature range 223–719 K and pressures $\leq$1 bar. Variations in k_{obs} from the UV absorption-based results can, to some extent, be attributed to deviations in the applied UV absorption spectrum of CH_3OO (range from roughly 200 to 300 nm). Critical evaluations [267,392,393] have later established that the optimal UV absorption cross section of CH_3OO lies at 240 nm or above. Furthermore, the system is affected by a number of unavoidable side reactions, so the *observed* removal rate constant k_{obs} needs a correction to yield the *true* overall rate constant for the self-reaction ($k_{true} = k_{\mathrm{R55}} + k_{\mathrm{R56}}$). The most important secondary conversion of CH_3OO is governed by the rapid oxidation of CH_3O with molecular oxygen to CH_2O+HO_2 (R76) followed by CH_3OO scavenging by HO_2 via (R47). Sander and Watson [382] showed that the observed and the true rate constants can be related by the simple correlation $k_{obs} = (1+\alpha)\left[k_{\mathrm{R55}} + k_{\mathrm{R56}}\right]$, where α is the branching ratio of the non-terminal channel, i.e. $\alpha = k_{\mathrm{R55}}/(k_{\mathrm{R55}} + k_{\mathrm{R56}})$. This is valid since the reaction CH_3OO+HO_2 (R47) is significantly faster than the self-reaction of CH_3OO ($k_{\mathrm{R47}}/(k_{\mathrm{R55}} + k_{\mathrm{R56}}) \approx 15$ at 298 K) and thereby prevents build-up of HO_2 radicals that would otherwise complicate the system of secondary reactions; in particular via the self-reaction of HO_2, i.e. HO_2+$HO_2 \rightarrow H_2O_2$+O_2 (R15). This would imply that $(1+\alpha)\left[(k_{\mathrm{R55}} + k_{\mathrm{R56}})\right] \geq k_{obs} \geq k_{\mathrm{R55}} + k_{\mathrm{R56}}$ and hence, call for a more complex correlation between k_{obs} and $k_{\mathrm{R55}} + k_{\mathrm{R56}}$ [393], in which case supplementary measurements of the branching ratio would be needed to obtain accurate values of the rate of the self-reaction. Wallington *et al.* [392], Lightfoot *et al.* [393], and Tyndall *et al.* [267] revisited several earlier measurements to yield independent values of k_{obs} and α, which are all in fair agreement. The present study follows the most recent work by Tyndall *et al.* [267], who combined measurements of the temperature dependence of α from Horie *et al.* [388], Alcock and Mile [391], and Lightfoot *et al.* [385], covering temperatures from 223 to 573 K, with an adjustment to match the direct measurement of $\alpha_{298} =$

0.37 ± 0.06 at room temperature by Tyndall *et al.* [389]. The resulting ratio $k_{R55}/k_{R56} = \alpha/(1-\alpha) = (26.2 \pm 6.6) \exp\left[\frac{-(1130\pm240)}{T}\right]$ was used together with the UV absorption measurements from Sander and Watson [382], Kurylo and Wallington [383], and Lightfoot *et al.* [385] to yield the final recommendation of $k_{R55} + k_{R56} = 5.7 \times 10^{10} \exp\left(\frac{390\pm100}{T}\right)$ $^{cm^3}/_{mol\,s}$. The individual values of k_{R55} and k_{R56} in Table 5.3 are fitted expressions based on these values of $\alpha(T)$ and $k_{R55} + k_{R56}$.

5.3.3.4 CH_3OOH Reactions

There are a number of potential CH_3OOH conversion channels included in the mechanism, but at the temperature and pressure ranges of interest, the most important path is the thermal decomposition to the radical products CH_3O+OH (R59). This reaction has a second product channel to CH_2O+H_2O, which is neglected in the present study due to indications of a very low contribution [266]. Earlier measurements have been reported by Kirk [394], who used a flow reaction system operated at 565–651 K and 33 mbar. Lightfoot *et al.* [369] later based their measurements on flash photolysis of $CH_4/CH_3OH/O_2$ mixtures at 600–719 K and 1 bar. Both studies used N_2 as bath gas. Kaiser *et al.* [395] obtained a value of k_{R59} at 533 K based on GC/MS measurements of CH_3OOH concentrations during oxidation of acetaldehyde in a static reactor and a subsequent fit by a complex mechanism. However, as noted by Kaiser *et al.*, these specific results were possibly influenced by heterogeneous conversion of CH_3OOH at the reactor wall, which questions their reliability. In a recent theoretical work, Zhu and Lin [266] studied the potential energy surface of CH_3+HO_2, including the decomposition channels of CH_3OOH, and derived values of k_{R59} at different N_2 pressures based on variational RRKM theory. These theoretical estimates are in excellent agreement with the experimental results from Kirk [394] and Lightfoot *et al.* [369], as well as the proposed high-pressure limit by Baulch *et al.* [225] that was derived from thermochemical considerations and analogies to low-temperature measurements of unimolecular decomposition rates of $C_7H_{15}OOH$ isomers [396]. The pressure dependent rate constants provided in Table 5.3 are fitted expressions to discrete values of $k_{CH_3OOH\rightarrow prod.}$ given by Zhu and Lin [266]. It is expected that the reaction is close to the high-pressure limit at 100 bar.

The reaction between CH_3OOH and OH is expected to proceed through a H-abstraction mechanism with two possible product channels: CH_2OOH+H_2O (R65) and CH_3OO+H_2O (R66). There is no compelling evidence of a contribution from a third product channel involving O–O bond cleav-

age. Hydroperoxymethyl (CH_2OOH) is unstable and rapidly decomposes to CH_2O+OH (R68); see Section 5.3.3.5. This makes the branching ratio between (R65) and (R66) of particular importance because the former reaction gives back the very reactive OH radical via (R68). Vaghjiani and Ravishankara [270] measured both product channels, including their temperature dependence from 203 to 423 K, using pulsed photolytic generation of OH radicals that were detected by laser-induced fluorescence. Since (R66) is the only contributor to the OH radical removal, observations of the OH decay in excess CH_3OOH provided a direct measure of k_{R66}. The product channel through CH_2OOH was subsequently isolated by substituting OH radicals with ^{18}OH and OD and then monitoring the OH formation profiles. The rate measurements by Vaghjiani and Ravishankara are consistent with earlier indirect determinations of $k_{R65} + k_{R66}$ and the branching ratio at 298 K by Niki *et al.* [397] based on a relative rate method. k_{R65} and k_{R66} in Table 5.3 are fitted values from Baulch *et al.* [225] to the branching ratio and overall rate measurements from Vaghjiani and Ravishankara [270].

Only a few rate measurements are available for H-abstraction from CH_3OOH by O atoms (R63,R64). There are other potential product channels resulting from attack on the second O atom (CH_3O–O–H), but these are neglected in the present mechanism with reference to the analogue reaction H_2O_2+O (R19), where H-abstraction is expected to predominate despite some deviations in experimental reports [230, 231]; see Section 5.3.1. Vaghjiani and Ravishankara [398] have reported the only direct measurement of $k_{CH_3OOH+O\rightarrow prod.} = (6.38 \pm 1.6) \times 10^9$ $^{cm^3}/_{mol\,s}$ at 297 K by monitoring the O atom decay generated from O_3 photolysis in excess CH_3OOH. They confirmed this value using relative rate methods in a similar study [363] that was published the same year. The preferred value is taken from the recent evaluation by Baulch *et al.* [145], who drew analogies to equivalent reactions with CH_3OH and CH_2O to yield $k_{CH_3OOH+O\rightarrow prod} = 2.47\times10^{13} \exp\left(\frac{-2390}{T}\right)$ $^{cm^3}/_{mol\,s}$, which is valid in the temperature range 300–1000 K and in excellent agreement with Vaghjiani and Ravishankara [398] at the lowest temperature. Baulch *et al.* did not provide a branching ratio between the two product channels, CH_3O+OH (R64) and CH_2OOH+OH (R63), but they advocated the dominance of the latter with reference to the analogue reaction H_2O_2+O (R19), where H-abstraction from H–OOH is comparatively slow. In the present study, a constant branching ratio $k_{R63}/(k_{R63} + k_{R64}) = 0.65$ is assumed in agreement with the branching ratio for the H-abstraction reaction CH_3OOH+OH; $k_{R65}/(k_{R65} + k_{R66})$ that ranges between 0.6 and 0.7 at temperatures from 298 to 1000 K.

Considering the reaction between CH_3OOH and H (R60,R61,R62), the current mechanism includes the product channel resulting from attack on

the second O atom and subsequent O–O bond cleavage that was otherwise, neglected for CH_3OOH+O. See the discussion in the previous paragraph. This product channel to CH_3O+H_2O (R62) has been included because the analogue product channel from H_2O_2+H (R18) contributes about 10 % [145]. Slemr and Warneck [269] used a flow reactor system with photoionization mass spectrometry to measure concentrations of stable key species based on the reactions CH_3OOH+H and CH_3OOD+H at 249–358 K. They determined a value of the overall rate constant $k_{CH_3OOH+H\rightarrow prod.} = (1.2 \pm 0.5) \times 10^{11} \exp\left[\frac{-(1860\pm190)}{RT}\right]$ $^{cm^3}/_{mol\,s}$, which is significantly lower than the estimated upper limit at 298 K proposed by Vaghjiani and Ravishankara [363]. Slemr and Warneck also report branching ratios for the three product channels, but they disregarded some important side reactions in their analysis, which puts their recommendations in some doubt. The present mechanism applies the overall rate constant from Slemr and Warneck [269] with branching ratios $k_{R60}/k = k_{R61}/k = 0.45$ and $k_{R62}/k = 0.10$; where $k = k_{R60} + k_{R61} + k_{R62}$. These ratios have been estimated in the present study based on analogies with the reaction between H_2O_2+H and the assumption of an even distribution between the two products CH_3OO and CH_2OOH. However, these are merely coarse estimates and experimental verification is needed. Consequently, the author assigns a large uncertainty factor of 5 to the resulting rate coefficients.

As previously discussed, the OO–H bond strengths in H_2O_2 and CH_3OOH are very similar, which means that the H-abstraction reaction between CH_3OOH and HO_2 (R67) exhibits a very low thermodynamic driving force. Hence, $\Delta_r G_{298} \approx -0.1$ $^{kcal}/_{mol}$ meaning that the equilibrium constant is close to unity. There are no direct measurements of this reaction in either direction, and the only available rate expression originates from Tsang and Hampson [194], who proposed $k_{-R67} = 2.4 \times 10^{12} \exp\left(\frac{-5000}{T}\right)$ $^{cm^3}/_{mol\,s}$ with a large uncertainty factor of 10. In the present model, analogies are drawn to the reaction CH_2O+HO_2 (R109), because of the similar bond strength of H–CHO ($D_{298} = 88.0 \pm 0.2$ $^{kcal}/_{mol}$ [399]). Hence, the model adopts k_{R109} from Eiteneer *et al.* [284] to govern (R67). The resulting room-temperature value of k_{-R67} is substantially lower than proposed by Tsang and Hampson; by a factor of 27, whereas the two rate expressions lie within a factor of 10 of each other at temperatures >450 K.

5.3.3.5 CH_2OOH Reactions

There are no direct measurements of the fast unimolecular decomposition of CH_2OOH to CH_2O+OH (R68), which is expected to be irreversible in practice. Vaghjiani and Ravishankara [270] determined a lower limit of $k_{R68} \geq$

5×10^4 1/s at 205 K and 0.07 bar in connection to a study of CH_3OOH+OH, but the reaction is expected to be significantly faster at elevated temperatures. The current mechanism applies pressure-dependent values of k_{R68} from a recent *ab initio* study by Bozzelli and co-workers [271]. No uncertainty limits are reported for these calculations, but k_{R68} exhibits values on the order of 10^9 to 10^{11} 1/s at temperatures and pressures ranging from 298–1500 K and 1–100 bar, which, in any case, is sufficiently fast to ensure a very short lifetime of CH_2OOH and a minimum sensitivity in model predictions.

5.3.3.6 CH_3O Reactions

Methoxy radicals act as precursors for several stable oxygenated hydrocarbons, e.g. methanol, dimethylether, and formaldehyde, that all exhibit a commercial potential as products from the GTL process. This makes CH_3O a key species in the hydrocarbon oxidation chain and emphasizes the need for detailed knowledge about the conversion pathways at different reaction conditions.

The thermal decomposition of CH_3O to CH_2O+H (R69) was recently studied by Hippler *et al.* [272] in a combined experimental and theoretical work involving laser-photolysis/laser-induced fluorescence measurements and high-level *ab initio* calculations. The experiments covered temperatures and pressures from 680–810 K and 1–90 bar with He as bath gas, which provided a good representation of the fall-off curve. The results from Hippler *et al.* are in good agreement with the low-pressure measurements from Oguschi *et al.* [400] at 0.13–0.6 bar and 610–740 K using a similar experimental technique and He, as well as N_2, as bath gas. Here, the experimentally derived low-pressure limit in He atmosphere lies within a factor of 1.5 of the measured low-pressure limit from Hippler *et al.* across the temperature interval 600–800 K. Hippler *et al.* re-analyzed the results obtain by Oguschi *et al.* in N_2 atmosphere and combined them with their own measurements and *ab initio* calculations to yield the preferred fall-off parameters with N_2 as collision partner. The preferred rate expression is also consistent with the experimental low-pressure limit from Wantuck *et al.* [277] in N_2 atmosphere at 673–973 K, but it lies more than one order of magnitude above the value from Zaslonko *et al.* [401] at 900–1600 K. Choudhury and co-workers [402,403] used a static reactor setup and shock tube measurements to cover the temperature range 550–1620 K, while extrapolation to lower temperatures was based on supplementary *ab initio* calculations. These calculations predicted a significant contribution from H-atom tunneling resulting in rate constants that are several orders of magnitude above the preferred rate expression. Hippler *et al.* [272] conducted a theoretical investigation of this issue of tun-

neling effects but observed no significant dependence at the intermediate temperatures used in their experimental study (680–810 K). Even so, they did not rule out possible tunneling effects at lower temperatures. If this indeed is the case, the preferred rate expression may underpredict (R69) at low temperatures.

The reaction between CH_3O and H proceeds via direct H-abstraction to CH_2O+ H_2 (R70) or by addition/elimination to CH_3+OH (R71). High pressure may facilitate a significant contribution from stabilization of the intermediate CH_3OH* adduct (R72). Dóbé *et al.* [273] observed small amounts of CH_3OH, which was attributed to the stabilization channel (R72), while other experimental studies [404–406] and literature evaluations [145,194,407] have neglected this channel. The measurements of Dóbé *et al.* [273] at 298–490 K constitute the only available data for the temperature dependence of CH_3O+H. They were obtained using a discharge flow reactor system with laser-induced fluorescence detection of the CH_3O decay under conditions with excess H atoms. Dóbé *et al.* proposed the overall rate constant $k_{CH_3O+H\rightarrow prod.} = 6.55\times10^{13} \exp\left(\frac{-745}{RT}\right)$ $^{cm^3}/_{mol\,s}$, and the branching ratios $k_{R70}/k = 0.81\pm0.12$ and $k_{R71}/k = 0.07 \pm 0.03$; where $k = k_{R70} + k_{R71} + k_{R72}$. The overall rate constant is in excellent agreement with the room-temperature measurement by Hoyermann *et al.* [405], while the proposed branching ratios from Dóbé *et al.* deviate somewhat from other experimental results. Hence, Moortgat *et al.* [404] advocated $k_{R70}/k = 0.31 \pm 0.30$ and $k_{R71}/k = 0.69 \pm 0.30$, while Heinemann-Fiedler and Hoyermann [406] determined $k_{R71}/k \approx 0.3$. Even so, the preferred values of k_{R70} and k_{R71} are based on the work of Dóbé *et al.* [273] including their proposed branching ratios. The author estimates an uncertainty factor of 3 due to the uncertainties related to the product distribution. The pressure dependent addition/stabilization reaction to CH_3OH (R72) has been adopted from the GRI-Mech 3.0 release [256] and is based on RRKM calculations on the CH_3OH system.

Two product channels are considered from the reaction of CH_3O with atomic oxygen: CH_2O+OH (R73) and CH_3+O_2 (–R37). Stabilization of the CH_3OO* adduct is not expected to play a significant role. The channel to CH_3+O_2 is well established in the reverse direction from both experimental and theoretical evaluations; see the previous discussion of CH_3+O_2 in Section 5.3.3.2. The former, however, is only based on the single room-temperature measurement by Ewig *et al.* [274], $k_{CH_3O+O\rightarrow prod.} = 1.5 \times 10^{13}$ $^{cm^3}/_{mol\,s}$, obtained from laser photolysis of CH_3ONO/O_3 mixtures in N_2 and laser-induced fluorescence detection of CH_3O and OH. A branching ratio of $k_{R73}/(k_{R73} + k_{-R37}) = 0.12$ was also proposed. This ratio is in reasonable agreement with the estimated value of $k_{-R37}/(k_{R73} + k_{-R37}) = 0.65$ at 298 K by Heinermann-Fiedler and Hoyermann [406], which was derived from direct measurements

of the CH_3 yield during loss of CH_3O in excess O in a discharge flow reactor. In their recent evaluation, Baulch *et al.* [145] advocated the constant overall rate coefficient from Ewig *et al.* [274] and a mean value of $k_{R73}/(k_{R73} + k_{-R37}) = 0.25$, which is also preferred in the present study.

There are no direct measurements of the exothermic reactions of CH_3O with OH (R74) and HO_2 (R75). The preferred rate expressions are constant value estimates from the evaluation by Tsang and Hampson [194]. They estimated the former to be fast, while k_{R75} is comparatively slow with an adopted rate constant from the analogue reaction between CH_3OO and CH_3O (R51).

Oxidation of CH_3O to CH_2O by molecular oxygen (R76) has been subjected to many experimental investigations at low and intermediate temperatures (298–1000 K), e.g. [275, 401, 408–410]. Recent high-level *ab initio* calculations by Bofill *et al.* [411] suggest that the reaction takes place through direct H-atom transfer instead of following an addition/elimination mechanism that involves formation of a CH_3OOO^* adduct and subsequent 1,4-H-atom shift before elimination of HO_2. The experimental results are generally in good agreement at lower temperatures, but the results from Zaslonko *et al.* [401] and Wantuck *et al.* [275] indicate a non-linear Arrhenius behavior above ∼600 K where the reaction rate starts to increase dramatically. Wantuck *et al.* used methanol photolysis to generate CH_3O radicals in a low-pressure O_2/Ar atmosphere at 437–973 K and subsequently measured the CH_3O decay using laser-induced fluorescence. Hence, the resulting rate constant had to be a measure of the sum of all active removal reactions, and it is likely that the thermal decomposition of CH_3O (R69), in particular, may have had a significant influence on the high-temperature results and facilitated the *observed* non-Arrhenius behavior. As a consequence, the present mechanism only applies the low-temperature term of the bi-exponential rate expression proposed by Wantuck *et al.* [275], which is also the approach advocated by Baulch *et al.* [145]. It is noted that the resulting rate expression is still in good agreement with the direct measurements from Batt and Robinson [408] (383–433 K), Gutman *et al.* [409] (413–628 K), and Lorenz *et al.* [410] (298–450 K).

The available experimental measurements of $CH_3O+CO \rightleftharpoons CH_3+CO_2$ (R77) show very little consistency. Wantuck *et al.* [412] used the same experimental setup as for the CH_3O+O_2 measurements referred above. They simply changed the O_2/Ar atmosphere to CO/Ar and measured the sum of all active CH_3O removal reactions at 437–973 K; see the above discussion of (R76) for the implications of this method. Their resulting rate expression lies more than one order of magnitude above the low-temperature measurements by Lissi *et al.* [413] (396–426 K), who measured the CO_2 formation rate dur-

ing thermal decomposition of dimethylperoxide in the presence of CO. Lissi *et al.* reported little or no detection of CH_2O and CH_3OH, which are potential products from side reactions, thereby suggesting that the only removal reaction of importance in their system indeed had to be (R77). Wiebe and Heicklen [414] conducted photolysis experiments with CH_3ONO in the presence of NO and CO. The photolysis products are CH_3O+NO, which were believed to react either via (R77) or the sequence CH_3O+NO $\rightleftharpoons$ CH_2O+HNO (R264) and HNO+HNO $\rightleftharpoons$ H_2O+N_2O. However, product measurements of CO_2 and N_2O revealed significantly lower CO_2 formation than predicted from simple balance equations. This indicated that the principal products from CH_3O+CO were not CO_2 at the investigated conditions, but probably some stabilized adduct. The proposal would imply that the rate constant derived by Lissi *et al.* from their experiments is too low. Recently, *ab initio* calculations performed by Wang *et al.* [276] have thrown some light on this issue by confirming that stabilization of the initially formed radical adduct CH_3OCO^* is the dominant product channel at temperatures <1000 K and 1 bar. At higher temperatures, addition/elimination to CH_3+CO_2 and direct H atom abstraction to CH_2O+HCO predominate. Wang *et al.* calculated an overall rate constant at atmospheric pressure and 200–1000 K that lies above the results of Lissi *et al.* [413] at low temperatures and below those of Wantuck *et al.* [412] at high temperatures, and it further complies with the room-temperature upper limit proposed by Sander *et al.* [415]. The CH_3OCO radical is analogue to HOCO, which can be collisionally stabilized from the reaction between CO and OH at high pressure. The role of HOCO was discussed in details in Section 5.3.2. Here, model predictions indicated that conversion of HOCO mainly takes place through thermal decomposition to CO_2+H or by H-abstraction with molecular oxygen, which could serve as a basis for an analogue reaction subset for CH_3OCO. However, due to the general lack of knowledge about CH_3OCO chemistry, the present mechanism neglects this species and instead assumes that CH_3+CO_2 remains the sole product channel from CH_3O+CO. Hence, the expression of $k_{\mathrm{CH3O+CO\rightarrow prod.}}$ from Wang *et al.* [276] has been assigned to k_{R77}. Based on the above considerations, it is expected that this rate constant overpredicts the conversion of CH_3O+CO to CH_3+CO_2; especially at the high pressures relevant to the present study where stabilization of the adduct will probably be even more pronounced than assumed with the current atmospheric-pressure value of k_{R77}.

The H-abstraction reaction from CH_4 by CH_3O (R78) is the most important source of CH_3OH formation in fuel-rich combustion of natural gas. If the predominant collision partner is CH_4, formation of CH_3OH via (R78) may even outcompete the alternative decomposition of CH_3O via (R69)

at medium temperatures. Despite the importance in fuel-rich combustion systems, only few experimental studies of (R78) are available. The preferred rate constant is the combined experimental and theoretical determination by Wantuck *et al.* [277], who used laser photolysis/laser-induced fluorescence technique to measure the overall removal rate of CH_3O at 673–973 K in atmospheres containing either CH_4 or one of the non-reactive collision partners: Ar, N_2, Xe, and CF_4. The measured removal rate constant in the CH_4 atmosphere included contributions from both reaction (R78) and dissociation (R69), while CH_3O removal in the inert atmospheres could be attributed solely to (R69). The results obtained with the inert bath gases were scaled using supplementary RRKM calculations before a comparison of results enabled Wantuck *et al.* to extract the value of $k_{\mathrm{R78}} = (1.3 \pm 1.2) \times 10^{14} \exp\left[\frac{-(7585\pm466)}{T}\right]$ $^{\mathrm{cm}^3}/_{\mathrm{mol\,s}}$. Notice the substantial uncertainty limits reported by Wantuck *et al.* [277]. The earlier recommendation of k_{R78} from Tsang and Hampson [194] is based on the experimental work of Shaw and Thynne [416] at 403–523 K with corrections for updated thermochemical data. This rate constant falls about one order of magnitude below the preferred expression from Wantuck *et al.* at 673–973 K, but it is within a factor of two at 403–523 K. Even so, the deviation is covered by the uncertainty limits reported by Wantuck *et al.* [277]. The fact that k_{R78} has only been determined with limiting accuracy is of some concern in the present work, since this reaction is expected to govern CH_3OH formation in the GTL process.

Rate expressions for reactions between CH_3O and other hydrocarbon species: CH_3 (R79), CH_2O (R80), and self-reaction with CH_3O to CH_3OH+CH_2O (R81), all follow the recommendations by Tsang and Hampson [194], which are based on limited available data in the low-temperature range 298–455 K [377, 378, 417–421]. Eremin *et al.* [422] reported the only experiments with (R81) at temperatures from 800 to 1000 K. These results were obtained from decomposition of CH_3ONO in a shock tube and involve large uncertainties. Even so, they suggest a negative temperature dependence and yield values that are ∼6 times below the constant rate coefficient proposed by Tsang and Hampson. The expectation of a negative temperature dependence is further encouraged by a comparison with the analogue reaction CH_3O+CH_3O ⇌ CH_3OO+CH_3 (−R49) that exhibits a well-established negative temperature dependence; see the previous discussion of (R49) in Section 5.3.3.3. However, more experiments are needed for verification, and until then, the constant value of k_{R81} from Tsang and Hampson [194] is preferred. Reaction (R79) and (R81) compete against the addition/stabilization channels to dimethylether (CH_3OCH_3) and dimethylperoxide (CH_3OOCH_3), which are

expected to contribute to the product matrix at low-temperature and/or high-pressure conditions. Tsang and Hampson [194] suggested branching ratios of $k_{R79}/k_{CH_3OCH_3} = 1.9 \pm 0.3$ and $k_{R81}/k_{CH_3OOCH_3} = 40 \pm 30$ based on the experimental work by Quee *et al.* [418, 419], Dever and Calvert [377], and Heicklen and Johnston [378], but in the present mechanism both stabilization channels are neglected. Considering the relatively low value of $k_{R79}/k_{CH_3OCH_3}$, it may seem like a poor assumption to neglect CH_3O+CH_3 $\rightleftharpoons$ CH_3OCH_3, but model predictions indicate that this reaction does not play a pronounced role at the N_2-diluted conditions applied in the present experimental work.

5.3.3.7 CH_3OH Reactions

Methanol is an important transport fuel as well as a chemical feedstock in industrial processes. This has spawned a considerable interest in the governing combustion mechanisms; latest by Dryer and co-workers [423]. At medium temperatures, conversion of CH_3OH almost exclusively takes place through H-abstraction. The overall rates of the most important elementary reactions are generally well established from numerous experimental and theoretical investigations, see e.g. the literature evaluations [145, 167, 279, 424, 425]; but there are disputes concerning the product distributions. The carbon flux initially divides between the two radical isomers CH_2OH and CH_3O, where the former is favored by the thermochemistry and the availability of H atoms in CH_3OH. These two radical products may potentially undergo unimolecular isomerization. Again, $CH_3O \rightarrow CH_2OH$ is favored by the thermochemistry, which makes the isomerization reaction a direct competitor to the unimolecular decomposition of $CH_3O \rightarrow CH_2O$+H (R69) and, hence, a source of H atom loss. However, theoretical and thermochemically based estimates [271, 272, 400, 426, 427] indicate that the rate of isomerization is significantly lower than the rate of unimolecular conversion of CH_3O, and it is therefore neglected in the present study. CH_2OH may either decompose to CH_2O+H (R90) or react with molecular oxygen to form CH_2O+HO_2 (R97). The former path yields a net result identical to the CH_3O decomposition channel, while the reaction with O_2 effectively substitutes the released H atom with the far less reactive HO_2 radical. The latter issue is a decisive factor for the ignition delay of CH_3OH in combustion and the main reason why a precise determination of the CH_3O/CH_2OH product branching ratio is so important in combustion research.

Abstraction of H atoms by OH (R86,R87) is the most important source of CH_3OH oxidation in the mechanism. The preferred overall rate constant from Baulch *et al.* [145], $k_{CH_3OH+OH\rightarrow prod.} = 6.2 \times 10^6 T^{1.92} \exp\left(\frac{286}{RT}\right)$ $^{cm^3}/_{mol\,s}$,

reflects the room-temperature measurements from [428–435], as well as available intermediate to high temperature measurements [436–441]. These results show good consistency throughout a temperature interval from 292 to ∼2000 K. Reports of the branching ratio $k_{\mathrm{R86}}/\left(k_{\mathrm{R86}}+k_{\mathrm{R87}}\right)$ vary between 0.75 and 0.89 at room-temperature; and even more at higher temperatures. Baulch *et al.* recommended a room-temperature value of 0.85. Hess and Tully [440] proposed a negative temperature dependence of the branching ratio based on experiments at 294–864 K with isotopically substituted CH_3OH, and predicted a value close to 0.5 at ∼880 K. A similar behavior was proposed by Hägele *et al.* [437], who predicted that (R87) will be dominant at temperatures roughly above 1000 K. However, a substantial uncertainty is attributed to the proposal by Hägele *et al.*, which is based on linear extrapolation of branching ratio measurements at 298 and 393 K. In a recent *ab initio* study, Xu and Lin [442] determined an overall rate constant $k_{\mathrm{CH_3OH+OH\rightarrow prod.}} = 2.80\times10^4 T^{2.68}\exp\left(\frac{823}{RT}\right)\ {}^{\mathrm{cm^3}}/_{\mathrm{mol\,s}}$, which is in very good agreement with the value from Baulch *et al.* at low- and elevated temperatures, while it predicts somewhat higher values at high temperatures. Xu and Lin also considered the product branching ratio and predicted an almost temperature-independent value of $k_{\mathrm{R86}}/\left(k_{\mathrm{R86}}+k_{\mathrm{R87}}\right)$ ranging from 0.96 to 0.89 throughout the temperature range 200–3000 K. These calculated values support the experimentally based recommendation of $k_{\mathrm{CH_3OH+OH\rightarrow prod.}}$ from Baulch *et al.* [145] as well as the application of the room-temperature branching ratio of 0.85 throughout a larger temperature interval. This approach has been adopted in the present mechanism.

A large body of experimental [424, 436, 443–447] and theoretical investigations [448–450] have described the H-abstraction reaction from CH_3OH by H atoms (R82,R83). The latest experimental study by Li and Williams [447] was concerned with a fuel-rich two-stage counterflowing CH_3OH/air flame. Modeling predictions indicated that (R82) and (R83) accounted for the majority of the fuel conversion (>85 %) at the applied conditions, thereby revealing a large sensitivity to these reactions that allowed Li and Williams to fit the rate constant and the branching ratio with reasonable accuracy. The latter proved to exhibit a negative temperature dependence expressed by $k_{\mathrm{R82}}/k_{\mathrm{R83}} = 0.43\exp\left(\frac{674}{T}\right)$. This ratio ranges from a value of 4 at room-temperature to unity at 800 K, and it enabled Li and Williams to predict their flame data with a high accuracy at temperatures ranging from 300–2100 K. The overall rate expression for CH_3OH+H by Li and Williams is generally in good agreement with other high- [424, 436, 445, 446] and low-temperature measurements [443, 444], but the proposed branching ratio does not concur well with others. Recent theoretical calculations by Kerkeni and Clary [450] indicate a value of $k_{\mathrm{R82}}/k_{\mathrm{R83}}$ as high as 50 at 500 K. In con-

trast, Tsang and Hampson [194] recommended $k_{R82}/k_{R83} \approx 4$. Furthermore, Kerkeni and Clary predicted an overall rate constant that is about 4 times lower than Li and Williams. Baulch *et al.* [145] reviewed the available data and proposed an overall rate expression, which is in good agreement with Li and Williams [447] and others, but they were not able to provide a definite recommendation for the branching ratio. In the present mechanism, the overall rate constant from Baulch *et al.* is applied together with the temperature independent branching ratio from the analogue reaction with OH discussed above; i.e. $k_{R82}/(k_{R82} + k_{R83}) = 0.85$ corresponding to $k_{R82}/k_{R83} = 5.7$.

A similar lack of consistency between branching ratio measurements is observed for the analogue H-abstraction reaction from CH_3OH with O atoms (R84,R85). Measurements of the overall rate constant, e.g. [451–455], are in reasonable agreement except near room-temperature, where the results deviate by more than a factor of 10. The present mechanism again relies on the experimentally based overall rate constant from Baulch *et al.* [145] combined with a temperature dependent branching ratio $k_{R84}/(k_{R84} + k_{R85}) = 0.85$ identical to the applied branching ratios for CH_3OH+OH and CH_3OH+H.

The reaction between CH_3OH and HO_2 is endothermic with the product channel to CH_3O+H_2O_2 being $\sim 9\,^{\text{kcal}}/_{\text{mol}}$ more endothermic than CH_2OH + H_2O_2 (R88). Consequently, the mechanism only considers the latter channel. There are no direct measurements of (R88) and previous estimates [279, 424] have been based on analogies with HO_2+alkane reactions. The preferred rate constant has been obtained from Cathonnet *et al.* [278], who multiplied k_{R88} by a factor of 6.6 from the original kinetic model by Westbrook and Dryer [424] in order to predict ignition-times from self-ignition experiments with CH_3OH/air mixtures in a static silica reactor at 773–873 K. Westbrook and Dryer [424] originally adopted the rate constant from Aronowitz *et al.* [456], who drew analogies to HO_2+C_2H_6. Hence, it is expected that the modification imposed to k_{R88} by Cathonnet *et al.* is within the uncertainty limits of this early estimate.

There are no available measurements of the abstraction reaction by molecular oxygen (R89). The forward reaction is an important initiation reaction, when CH_3OH is used as fuel, but it is unlikely to prevail over the fast radical abstraction reactions when CH_3OH only appears as an intermediate product, e.g. in combustion of natural gas. The applied rate constant has been adopted from the review by Tsang [279], who based the present recommendation on analogies with O_2+alkane reactions and assigned a large uncertainty factor of 10.

5.3.3.8 CH_2OH Reactions

At typical combustion conditions, it is expected that the CH_2OH radical mainly decays to CH_2O via unimolecular decomposition (R90) or H-abstraction by molecular oxygen (R97); as outlined in the introduction to CH_3OH reactions in the previous section. The pressure range relevant to the current study may also promote CH_2OH as an important source of CH_3OH or C_2H_5OH via addition of H (R91) or CH_3 (–R189) respectively. The latter reaction will be considered later in connection to the ethanol subset. There is generally a lack of experimental characterization of elementary reactions with CH_2OH as reactant [145, 279], and applied rate constants for radical-radical reactions between CH_2OH and OH (R95), HO_2 (R96), CH_2OH (R102), CH_3O (R103), as well as reactions with some stable hydrocarbons: CH_4 (R98) and CH_2O (R101), are all estimated values from the review by Tsang [279] based on analogies to related reactions, thermochemical considerations, or extrapolations from limited room-temperature measurements. Tsang assigned uncertainty factors of 2–3 to all these rate constant estimates. The author notes that model predictions enclosed in the present work generally indicate low sensitivities to these reactions.

Some determinations of the rate constant for the unimolecular decomposition of CH_2OH (R90) are available at high temperatures [446, 457–459], covering the range 1372–2740 K, while a single value has been determined at 323 K [460]. These were all obtained from fitting a complex mechanism to experimental results and they all show considerable scatter; mainly due to uncertainties in important side reaction. The pressure effects are poorly characterized, but theoretical investigations by Greenhill *et al.* [461] indicate that fall-off effects are important. Some literature evaluations of (R90) are also available; e.g. by Westbrook and Dryer [424], Warnatz [407], Tsang [279], and Held and Dryer [167], but they too show little consistency. It is evident that a more careful characterization of the reaction is required, but in the absence of such, the preferred rate coefficient is adopted from the latest evaluation by Held and Dryer [167], who fitted the calculated fall-off data in N_2 atmosphere from Tsang [279] to the Troe formalism (see Section 5.2.2.1) across the temperature range 300–2500 K.

The reaction between CH_2OH and H atoms initially yields a highly energized CH_3OH^* adduct that can undergo stabilization to CH_3OH (R91) or elimination to CH_2O+H_2 (R92) or CH_3+OH (R93). Experimental results from Hoyermann and co-workers [405, 406] and Dóbé *et al.* [462] at room-temperature and very low pressures (1–3 mbar) are in good agreement and indicate a ratio between the bimolecular channels of $k_{R92}/(k_{R92}+k_{R93}) \approx 0.7$. The energized CH_3OH^* adduct is similar to the adduct formed from

the addition of CH_3 and OH (R35) with only a minor difference in the level of energization. Reaction (R35) was previously discussed in Section 5.3.3.2. Here, experimental results at room-temperature indicated that collisionally stabilized CH_3OH is the dominant pathway at atmospheric pressure or above and low to intermediate temperatures. It was further argued that (–R93) can be considered as a the sole competitive product channel at higher temperatures even though this proposal implied large uncertainties. Since it is expected that (R91) behaves similar to (R35), k_{R35} is taken as the preferred value of k_{R91} including the fall-off parameters. An alternative RRKM-based value of k_{R91} has been proposed in the GRI-Mech 3.0 release [256], but the fall-off treatment of this rate expression was develop to reconcile with the low-pressure results from Dóbé *et al.* [462] that advocated the bimolecular channels over the stabilization reaction. Consequently, the rate expression from GRI-Mech 3.0 yields a room-temperature value of k_{R35} that is about two orders of magnitude below the preferred expression. Baulch *et al.* [145] recommended a value of $k_{CH_2OH+H\rightarrow prod.} = 3.5 \times 10^{13}\,{}^{cm^3}/_{mol\,s}$ at 298 K based on the available experiments [405, 406, 462]. In the present study, a constant value of $k_{R92} + k_{R93} = 2 \times 10^{13}\,{}^{cm^3}/_{mol\,s}$ has been estimated together with the proposed ratio $k_{R92}/\left(k_{R92} + k_{R93}\right) = 0.7$ at all relevant temperatures. Considering the pressure dependent expression of k_{R91} ($= k_{R35}$), this yields an overall value of $k_{CH_2OH+H\rightarrow prod.} \approx 6.5 \times 10^{13}\,{}^{cm^3}/_{mol\,s}$ at 298 K and 1 bar, which may be too high compared to the experimentally based value from Baulch *et al.*, but k_{R91} decreases reasonably fast with increasing temperatures and the ratio between the uni- and bimolecular pathways, k_{uni}/k_{bi}, becomes unity at ∼530 K and further approaches zero above 1000 K. The current estimate further yields a value of $k_{-R93}/\left(k_{-R93} + k_{R35}\right) \approx 0.04$ at 1000 K and 1 bar, which is considered too low if (–R93) should account for all bimolecular product channels from CH_3+OH, as argued in the previous discussion in Section 5.3.3.2. Obviously, more investigations in the field are required to resolve this issue.

Only two experimental studies [280, 463] are available for the reaction of CH_2OH with atomic oxygen (R94). The preferred rate constant is adopted from the work by Seetula *et al.* [280], who photolyzed He-diluted mixtures of SO_2 and acetol and monitored the CH_2OH decay as a function of the O atom concentration at pressures and temperatures from 1.5–6.5 mbar and 300–508 K using a photoionization mass spectrometer. Seetula *et al.* also detected a significant formation of CH_2O and formic acid (HC(O)OH), but the detection sensitivity of the setup in combination with the highly diluted conditions prevented a quantitative determination of the product branching fractions. However, the formation of both CH_2O and HC(O)OH indicate initial formation of an energized adduct OCH_2OH^* that can undergo both

C–OH and C–H bond cleavage. Potential energy surface calculations are needed to confirm this. In the present work, only the path to CH_2O (R94) is considered using a rate constant equivalent to the overall rate constant $k_{CH_2OH+O\rightarrow prod.}$ proposed by Seetula *et al.* [280]. This value is 2.4 times larger than the room-temperature measurement of $k_{CH_2OH+O\rightarrow prod.}$ from Grotheer *et al.* [463], who used a discharge flow reactor setup with a mass spectrometer for species detection. The rate constant from Grotheer *et al.* was derived from a 12-step mechanism that, among others, included regeneration of CH_2OH through oxidation of CH_3OH, and it is possible that an overprediction of this reaction step has resulted in the lower value of $k_{CH_2OH+O\rightarrow prod}$.

Oxidation of CH_2OH by O_2 (R97) has been characterized by experiments over a wide temperature range. The discharge flow reactor study by Grotheer *et al.* [464] covered the intermediate temperatures 298–684 K. Within this range, the results revealed a distinct non-Arrhenius behavior represented by a declining rate constant from 300 to ∼450 K, where a local rate-minimum was observed; then followed by a strong increase with further increasing temperatures. Despite this unusual behavior, the results of Grotheer *et al.* are well in line with the high-temperature CH_3OH/O_2 flame results reported by Vandooren and Van Tiggelen [436] at 1123–1928 K, and they further reconcile with the latest room-temperature measurements [465–470]. Experiments have also been conducted at very low temperatures by Nesbitt *et al.* [471] (215–300 K) in a discharge flow reactor system. The results revealed a strongly declining rate constant as the temperature decreases from room-temperature and hence, suggests the existence of a second local rate-extrema around 300 K. It has been speculated [464, 471] that the reaction occurs via formation of an initial adduct $OOCH_2OH^*$, which can either dissociate back to the reactants or isomerize to $HOOCH_2O^*$ that, in turn, dissociates to the observed products HO_2+CH_2O. Nesbitt *et al.* [471] suggested that the isomerization reaction is subjected to a significant energy barrier, which causes the declining rate at temperatures below ambient. Above room-temperature, the dissociation of $OOCH_2OH^*$ back to reactants starts to compete favorably with the isomerization reaction thereby facilitating a declining rate constant until about 450 K where the addition/isomerization mechanism is finally outcompeted by direct abstraction. Grotheer *et al.* [465] showed that CH_2O accounts for 95±5 % of the reacted carbon at room-temperature and ∼1 mbar, which suggests little or no contribution from collisional stabilization of the involved adducts. It is unclear whether this is accurate for higher pressures. The preferred rate constant is the non-Arrhenius expression proposed by Baulch *et al.* [145] that provides the best fit to the referred experimental results across the temperature range 298–1200 K. It is noted that the current expression of k_{R97} is not compatible with the low-temperature results from

Nesbitt *et al.* [471].

Until recently, no measurements of the reaction between CH_2OH and HCO (R99,R100) were available and previous combustion modeling typically relied on the very fast reaction rate estimated by Tsang [279] ($k_{CH_2OH+HCO\rightarrow prod.} = 3 \times 10^{14}\,{}^{cm^3}/_{mol\,s}$). However, in a recent shock-tube study of the thermal decomposition of CH_2O at 1675–2080 K, Friedrichs *et al.* [281] were able to isolate the self-reaction of CH_2O (–R100) to a sufficient degree to extract values of k_{-R100}. Combining these results with a thermochemical prediction of the equilibrium constant and assuming k_{R100} independent of temperature allowed Friedrichs *et al.* to yield a value of $k_{R100} = 1.5 \times 10^{13}\,{}^{cm^3}/_{mol\,s}$. This value is used for (R100), whereas k_{R99} is derived from the branching fraction $k_{R99}/k_{R100} = 2/3$ proposed by Tsang [279]. This approach yields a value of $k_{R99}+k_{R100}$, which is about one order of magnitude below the value originally proposed by Tsang.

5.3.3.9 CH_2O Reactions

Formaldehyde is an important intermediate in the hydrocarbon oxidation chain; both at high and low temperatures. This has encouraged many experimental and theoretical investigations across a wide range of temperatures and pressures that have provided rate constants for a number of important elementary reactions in the CH_2O subset with considerable accuracy. These are e.g. CH_2O reactions with H (R106), O (R107), HO_2 (R109), and CH_3 (R111) for which, experimentally based rate constants are drawn from the recent evaluation by Baulch *et al.* [145] and, in case of (R109), from the combined experimental study and review of CH_2O+HO_2 by Eiteneer *et al.* [284]. Other reactions from the CH_2O subset still warrant some attention with respect to their origin.

Experimental investigations have demonstrated that the thermal decomposition of CH_2O to HCO+H (R104) or CO+H_2 (R105) displays second order kinetics under typical combustion conditions, i.e. high temperatures and near-ambient pressure, with an effective rate constant close to the low-pressure limit. The reaction has been studied intensively at high temperatures (1160–3200 K) and low to near-atmospheric pressures. The more recent shock-tubes results [281,284,472–476] all seem to be in good agreement, while elder results typically appear to be somewhat higher; see Ref. [145]. Most experimental work has been carried out using equipment and reaction conditions that favor detection of the radical forming channel (R104). Consequently, knowledge of the branching ratio is limited. Recently, Friedrichs *et al.* [281] conducted a combined experimental and theoretical study, where (R104) was determined directly from measurements of concentration profiles

of CH_2O and HCO behind reflected shock waves using vacuum-UV absorption and frequency modulation spectroscopy respectively, while a two-channel RRKM/master equation analysis was employed to characterize the branching fraction. This work showed that the branching ratio is strongly pressure dependent across the range 1–100 bar with CO+H_2 (R105) as the dominant channel at low pressures switching to HCO+H (R104) within the pressure range 1–50 bar depending on the applied temperature. The proposed bimolecular rate expressions by Friedrichs *et al.* are consistent with previous experiments, and they are in excellent agreement with the comprehensive theoretical analysis of Troe [282], from which the preferred rate expressions are obtained. Troe used RRKM/master equation analysis to determine low-pressure rate coefficients, while the branching ratio was determined from knowledge of the quantum yields from CH_2O photolysis and classical trajectory calculations following the recent work of Zhang *et al.* [477]. The high-pressure rate coefficients were calculated from simple transition state theory, which yields more coarse approximations, but the current lack of experimental data for verification in the high-pressure range evidently appoints large uncertainties to the calculated values regardless of the applied level of theory. For the same reason, Troe opposed any further attempt to inspect the fall-off curves until more detailed information about branching ratios and individual rate constants in the fall-off region become available.

There are many reports of measurements of CH_2O+OH (R108), but they show considerable scatter throughout the characterized temperature interval; especially at high temperatures where elder measurements lie significantly higher than more recent results; see Ref. [145]. This could indicate a non-Arrhenius behavior, as predicted by several theoretical studies [283, 478, 479]. The reaction has two potential product channels involving direct H-abstraction to HCO+H_2O (R108) and addition/elimination to HC(O)OH+H. However, experimental investigations of the branching ratio at room-temperature [480–482] suggest that the reaction proceeds almost exclusively through the abstraction channel. This is supported by potential energy surface calculations by D'Anna *et al.* [483] that revealed a high energy barrier for the OH-addition mechanism compared to H-abstraction. The preferred rate expression is taken from the most recent work in the field by Vasudevan *et al.* [283], who combined own shock-tube measurements at 934–1670 K with recent low-temperature measurements from Sivakumaran *et al.* [482] at 202–399 K to fit a modified Arrhenius expression that was supported by TST calculations at a high-level of theory. The preferred value is further in very good agreement with other low-temperature experiments by Atkinson and Pitts [484], Stief *et al.* [485], Temps and Wagner [486], Niki *et al.* [480], and Yetter *et al.* [481] covering the temperature range 228–426 K, as

well as the high-temperature measurements by Bott and Cohen [441], Vandooren *et al.* [487], and Peeters and Mahnen [212] at 1200–1550 K. Support is also found in the slightly higher values obtained from laser photolysis/laser-induced fluorescence experiments at 296–576 K by Zabarnick *et al.* [478].

Direct measurements of CH_2O+O_2 (R110) have been reported by Baldwin *et al.* [310] at intermediate temperatures from 713–813 K, and at high temperatures by Michael and co-workers [264, 311] (1608–2109 K), and Vasudevan *et al.* [476] (1480–2367 K). The preferred value of k_{R110} has been obtained from Baulch *et al.* [145] as an average between the studies of Baldwin *et al.* and Michael and co-workers. It is further in excellent agreement with the most recent high-temperature expression proposed by Vasudevan *et al.* at temperatures >1500 K. Baulch *et al.* [145] assigned an uncertainty factor of 3 to k_{R110} at 500–1000 K and a factor of 5 at temperatures above 2000 K, but with the latest high-temperature confirmation by Vasudevan *et al.* this increased uncertainty at high temperatures is probably exaggerated. Another high-temperature shock-tube study was conducted at 1160–1890 K by Hidaka *et al.* [474]. They used a detailed kinetic model to predict the induction period and time-dependent conversion of CH_2O from which, they derived an indirect value of k_{R110} that differs substantially from the preferred value.

5.3.3.10 HCO Reactions

The thermal dissociation of HCO (R112) is the predominant HCO radical sink in most combustion systems due to the relatively weak H–C bond in HCO ($D_{298} = 15.69 \pm 0.19\,{}^{\mathrm{kcal}}/_{\mathrm{mol}}$ [399]). As a consequence, comparatively low concentrations of HCO radicals are typically present, which makes most bimolecular channels less important except when the reaction stoichiometry facilitates particularly high concentrations of reactive collision partners such as molecular oxygen in fuel-lean combustion. In this particular case, H-abstraction by O_2 (R118) may become an equally important reaction channel.

Previous experimental investigations of the unimolecular dissociation of HCO (R112) have been conducted at low or near-ambient pressures, e.g. [286, 488, 489] and involve direct measurements of k_{R112} over a wide range of temperatures. In this pressure range, the reaction is assumed to be at the low-pressure limit (HCO+M $\rightleftharpoons$ H+CO+M) and as a consequence, most studies have only proposed second-order rate expressions. Recent measurements at atmospheric pressure by Krasnoperov and co-workers [489, 490] (498–769 K), and Friedrichs *et al.* [286] (835–1230 K) are in excellent agreement, but they consistently lie a factor of 2 below the earlier low-pressure measurements (<10 mbar) by Timonen el al. [488] at 673–832 K. In order to

explain the systematic discrepancy, Krasnoperov and co-workers [490] proposed the influence from surface activities in the experimental system used by Timonen *et al.*, but this has never been confirmed. In a more recent study, Krasnoperov and co-workers [490] also included measurements at high pressure up to 100 bar obtained from high pressure flow reactor experiments. These results convinced Krasnoperov and co-workers that the reaction is at the low-pressure limit at atmospheric pressure, while fall-off behavior could be observed at elevated pressures >10 bar. Early theoretical investigations of (R112) by Wagner and Bowman [491] showed some unusual fall-off behavior caused by the low density of vibrational states in HCO that are mostly isolated and nonoverlapping; even at energies above the threshold energy. This is a result of the weak H–CO bond and the few degrees of freedom in the HCO molecule, and it causes large fluctuations among rate constants resulting from specific occupied states. These state-specific rate constants have been subjected to both experimental [492, 493] and theoretical investigations [491,494–496], but their actual influence on the thermal rate constant is somewhat uncertain. Wagner and Bowman showed that this fluctuating behavior of the rate constants at specific internal energies complicates the theoretical description of the fall-off curves. As a consequence, "normal" statistical-based methods like e.g. the Lindemann model, or the more recently developed master equation formalism are expected to be inadequate. Instead, Wagner and Bowman advocated models focusing on isolated resonances to provide accurate descriptions of the fall-off behavior. This approach was implemented in the recent combined experimental and theoretical work by Hippler *et al.* [285], who extended the experimentally investigated pressure range to cover 1–140 bar of He at 590–800 K using a high-pressure flow cell. These results were supplemented by additional measurements at 1–14 bar of N_2 and 700 K, as well as the previously referred low-pressure results from Timonen *et al.* [488], and measurements of the reverse recombination reaction by Ahumada *et al.* [497] at room-temperature and 0.1–0.8 bar. These data all showed very good agreement with predicted fall-off curves when an isolated resonance RRKM model was employed using the calculated resonances of HCO in the electronic ground state from Keller *et al.* [495]. The isolated resonance model further indicated that the fall-off curves were much broader than predicted by normal RRKM-calculations at the experimental conditions applied by Hippler *et al.* extending down to the sub-μbar pressure range before the rate constant complied with the low-pressure limit. Based on this finding, Hippler *et al.* [285, 498] concluded that Krasnoperov and coworkers [489,490,499], and others, were wrong to assume that the reaction is still at the low-pressure limit at 1 bar, as advocated by Krasnoperov and coworkers [489,490,499]. The successful theoretical treatment of (R112) allowed

Hippler *et al.* to derive the simple temperature- and pressure-dependent rate expression applied in the present study. The estimated accuracy is ±30 % at 500–1000 K and 0.01–100 bar of N_2.

The reaction between HCO and O_2 (R118) has been studied intensively at room-temperature, e.g. [470, 500–503], and most results are in good agreement yielding an average value $k_{R118}^{298} \approx 3 \times 10^{12}\,\mathrm{cm^3/mol\,s}$. The intermediate temperature region is covered by three experimental studies by Veyret and Lesclaux [504] at 298–503 K, Timonen *et al.* [505] at 298–703 K, and, most recently, by DeSain *et al.* [506] at 298–673 K. The latter results showed little or no dependence of the temperature within the considered range, while the former work by Veyret and Lesclaux indicated a slightly negative temperature dependence, which is opposite of Timonen *et al.*, who reported a minor positive dependence. It is further noted that the data from Veyret and Lesclaux provide an excellent extrapolation of the low-temperature discharge flow reactor results from Nesbitt *et al.* [503] (200–398 K). However, values of k_{R118} from overlapping temperature intervals are generally in good agreement when the experimental uncertainties are taken into account. The available high-temperature results [212, 487, 507–509] show significant scatter and hence, offer no indications of the temperature dependence of (R118). Based on *ab initio* calculations, Hsu *et al.* [510] suggested that the reaction follows an addition/elimination mechanism involving initial formation of an energized adduct HC(O)OO* that rapidly dissociates to HO_2+CO with no other competitive product channels of practical importance. The direct abstraction channel becomes important at very high temperature >2000 K, but this will not change the resulting product distribution. Hsu *et al.* [510] calculated a rate expression that exhibits a slightly negative temperature dependence at temperatures <450 K followed by a gradual increase at higher temperatures. The preferred rate constant has been adopted from the recent evaluation by Baulch *et al.* [145], who advocated an optimized rate constant involving the theoretically based temperature dependency from Hsu *et al.* and a fit to the room-temperature mean value given above. The resulting rate expression is in good agreement with the low-temperature data from Nesbitt *et al.* [503] and the results from Veyret and Lesclaux [504], and DeSain *et al.* [506] at intermediate temperatures. Moreover, reasonable agreement is found with the high-temperature results of Cherian *et al.* [509] and Tsuboi [507], while the experimental data from Timonen *et al.* [505] fall a factor of 1.3–1.7 above k_{R118} at 298–703 K.

Other pathways in the HCO subset involve fast radical-radical reactions that are expected to proceed close to collisional with little or no dependence of temperature and pressure. These include abstraction reactions with O (R114,R115) and OH (R116) drawn from the the experimentally based eval-

uations of Baulch *et al.* [145], and the addition/elimination reaction with HO_2 (R117) from Tsang and Hampson [194]. The abstraction reactions with H (R113) and the self-reaction of HCO (R120) are taken from the experimental study by Friedrichs *et al.* [286], while the addition/elimination channel HCO+CH_3 $\rightleftharpoons$ CH_4+CO (R119) has been adopted from Callear and Cooper [287], who measured the reaction rate in an annulus quartz vessel at 423 K. In the latter study, the radical reactants were prepared through preliminary reactions of CH_3Br and CO with atomic hydrogen. The competitive addition/stabilization channel to acetaldehyde (CH_3CHO) (–R217) will be discussed in connection to the CH_3CHO subset in Section 5.3.4.8.

5.3.4 C_2 Hydrocarbon Reaction Mechanism

Table 5.4 shows the proposed C_2 hydrocarbon reaction mechanism. Considering the diluted conditions applied in the experimental work, this part of the detailed kinetic model is only expected to gain significance when C_2H_6 is used directly as fuel, and, to a minor extent, when CH_4 is combusted under fuel-rich conditions. Even so, the individual elementary reactions given in Table 5.4 have been reviewed with similar thoroughness as the reactions from the C_1 hydrocarbon mechanism.

It is noticed that the mechanism does not include the stable oxygenated hydrocarbon dimethylether (CH_3OCH_3) and its radical derivatives. Dimethylether is primarily formed from addition/stabilization of CH_3O+CH_3, and it decomposes through an oxidation chain involving several intermediate ether radical species. Dryer and co-workers [170, 511] have provided a thorough outline and validation of this mechanism including a subset of elementary reactions, which is recommended in order to extend the present mechanism. However, CH_3OCH_3 is not used as fuel in the present study, and preliminary modeling investigations, using the reaction subset from [170,511], have further indicated that CH_3OCH_3 only plays a minor role at the relevant experimental conditions. These are the main reasons why the subset is not included in the model.

There are some C_2 hydrocarbon species included in the proposed mechanism that are not shown in Table 5.4 in terms of their complete reaction subsets. These are species that typically appear during hydrocarbon combustion at high temperatures and include acetylene (C_2H_2) and its derivatives ethynyl (C_2H), ketyl (HCCO), and ethynol (HCCOH); as well as some oxygenated derivatives of the vinyl radical (C_2H_3), e.g. vinoxy (H_2CCHO), hydroxyvinyl (HCCHOH), and ethenol (H_2CCHOH). These species have been included in the mechanism mainly because of their importance in high-temperature combustion modeling, see e.g. Refs. [105,138,233,254–257], but at conditions

relevant to the present work, they hardly contribute to the hydrocarbon conversion. For the same reason, minimum efforts have been made to review or update this part of the reaction mechanism.

5.3.4.1 C_2H_6 Reactions

Ethane (C_2H_6) is the second most important hydrocarbon in crude natural gas, and if not directly present in the fuel, the CH_3 radical association reaction to C_2H_6 (R41) ensures rapid establishment of a considerable C_2H_6 pool in most combustion systems operated at near-stoichiometric to fuel-rich conditions. This relates C_2H_6 chemistry to the combustion mechanisms of almost any common hydrocarbon fuel and justifies a thorough revisit of the most important elementary reactions related to the main conversion pathways.

The reaction between C_2H_6 and H atoms (R121) is well-defined from experiments at both low and high temperatures and the applied rate expression from the latest evaluation of Baulch *et al.* [145] provides a good representation at 280–1900 K. The corresponding abstraction reaction with O atoms (R122) is also fairly well established from experiments conducted over a wide temperature range. Different rate constant proposals typically agree within a factor of 2 except at lower temperatures (<500 K) where results deviate by up to a factor of ∼6 [512, 513]. The most reliable experimental data are considered to be those of Caymax and Peeters [514], Mahmud *et al.* [515], and Miyoshi *et al.* [300], that all involve direct measurements of k_{R122} covering the temperature range 297–1267 K. The rate expression from Mahmud *et al.* is preferred in the present study due to the more extensive experimental temperature validation and the excellent agreement with transition state theory calculations conducted by Mahmud *et al.* for verification. The rate expression lies within a factor of 2 of the experimental data from Caymax and Peeters [514] and Miyoshi *et al.* [300]. In the low-temperature range, Mahmud *et al.* [515] obtained relatively high values of k_{R122}. It was suggested that tunneling provided a large contribution to the rate constant in this temperature range, but more consistent evaluations are needed for verification, and until then, the applied rate expression is expected to be most reliable at temperatures >500 K.

The most important radical reaction with C_2H_6 at the intermediate temperatures relevant to the present study is the H-abstraction reaction with OH (R123). This reaction is also a very important player in the degradation of C_2H_6 in the atmosphere and consequently, a large body of experimental results are available extending from sub-ambient temperatures to high temperatures >1000 K; see Ref. [145] for an overview. Measurements of the rate

Table 5.4: Reactions from the C_2 hydrocarbon reaction mechanism. Units are mol, cm, s, cal.

	Reactions	A	β	E	Note/Ref.
		C_2H_6 (ethane)			
121.	$C_2H_6 + H \rightleftharpoons C_2H_5 + H_2$	9.82×10^{13}	0.0	9220	[145]
122.	$C_2H_6 + O \rightleftharpoons C_2H_5 + OH$	1.14×10^{-7}	6.5	274	[515]
123.	$C_2H_6 + OH \rightleftharpoons C_2H_5 + H_2O$	9.15×10^{6}	2.0	990	[516]
124.	$C_2H_6 + HO_2 \rightleftharpoons C_2H_5 + H_2O_2$	1.10×10^{5}	2.5	16850	[145]
125.	$C_2H_6 + O_2 \rightleftharpoons C_2H_5 + HO_2$	7.29×10^{5}	2.5	49160	[145]
[a]126.	$C_2H_6 + CH_3 \rightleftharpoons C_2H_5 + CH_4$	5.60×10^{10}	0.0	9418	[145]
		8.43×10^{14}	0.0	22250	
		C_2H_5 (ethyl radical)			
127.	$C_2H_5 + H(+M) \rightleftharpoons C_2H_6(+M^b)$	5.21×10^{17}	–0.99	1580	[256, 517]
	Low-pressure limit:	1.99×10^{41}	–7.08	6685	
	Troe parameters: 0.8422 125 2219 6882				
128.	$C_2H_5 + O \rightleftharpoons CH_3 + CH_2O$	4.24×10^{13}	0.0	0	[518]
129.	$C_2H_5 + O \rightleftharpoons CH_3CHO + H$	5.32×10^{13}	0.0	0	[518]
130.	$C_2H_5 + O \rightleftharpoons C_2H_4 + OH$	3.06×10^{13}	0.0	0	[518]
131.	$C_2H_5 + OH \rightleftharpoons C_2H_4 + H_2O$	2.40×10^{13}	0.0	0	[194]
132.	$C_2H_5 + HO_2 \rightleftharpoons C_2H_5O + OH$	3.10×10^{13}	0.0	0	[519]
133.	$C_2H_5 + O_2(+M) \rightleftharpoons C_2H_5OO(+M)$	2.02×10^{10}	0.98	–64	[520]
	Low-pressure limit:	8.49×10^{29}	–4.29	220	
	Troe parameters: 0.897 10^{-30} 601 10^{30}				
134.	$C_2H_5 + O_2 \rightleftharpoons C_2H_4 + HO_2$	1.41×10^{7}	1.09	–1975	(= k_0 [520])
135.	$C_2H_5 + CH_3 \rightleftharpoons C_2H_4 + CH_4$	9.03×10^{11}	0.0	0	[145]
136.	$C_2H_5 + HCO \rightleftharpoons C_2H_6 + CO$	4.34×10^{13}	0.0	0	[521]

Continues on next page

Continued from last page

	Reaction	A	β	E	Note/Ref.
		C_2H_4 (ethylene)			
137.	$C_2H_4(+M) \rightleftharpoons C_2H_2 + H_2(+M^b)$	8.00×10^{12}	0.44	88770	[256]
	Low-pressure limit:	1.58×10^{51}	–9.3	97800	
	Troe parameters: 0.735 180 1035 5417				
138.	$C_2H_4 + H \rightleftharpoons C_2H_3 + H_2$	2.35×10^{2}	3.62	11266	[145]
139.	$C_2H_4 + H(+M) \rightleftharpoons C_2H_5(+M)$	3.97×10^{9}	1.28	1292	[145]
	Low-pressure limit:	4.71×10^{18}	0.0	755	
	Troe parameters: 0.76 40 1025 10^{30}				
[a]140.	$C_2H_4 + O \rightleftharpoons CH_3 + HCO$	3.86×10^{12}	0.0	1494	[522]
		6.23×10^{13}	0.0	6855	
[a]141.	$C_2H_4 + O \rightleftharpoons H_2CCHO + H$	1.74×10^{12}	0.0	1494	[522]
		2.80×10^{13}	0.0	6855	
142.	$C_2H_4 + OH(+M) \rightleftharpoons$ 2-$C_2H_4OH(+M)$	2.26×10^{5}	2.28	–2466	[523]
	Low-pressure limit:	5.02×10^{19}	-8.87	2470	[c]
143.	$C_2H_4 + OH \rightleftharpoons H_2CCHOH + H$	6.08×10^{7}	1.38	1615	[523]
144.	$C_2H_4 + OH \rightleftharpoons C_2H_3 + H_2O$	7.17×10^{0}	3.71	435	[523]
145.	$C_2H_4 + O_2 \rightleftharpoons H_2CCHO + OH$	3.50×10^{7}	1.8	39000	see text, [524]
146.	$C_2H_4 + O_2 \rightleftharpoons CH_2O + CH_2O$	3.50×10^{7}	1.8	39000	see text, [524]
147.	$C_2H_4 + CH_3 \rightleftharpoons C_2H_3 + CH_4$	6.00×10^{7}	1.56	16630	[145]
		C_2H_3 (vinyl radical)			
148.	$C_2H_3 + H(+M) \rightleftharpoons C_2H_4(+M)$	3.88×10^{13}	0.20	0	[525]

Continues on next page

Continued from last page

	Reaction	A	β	E	Note/Ref.
	Low-pressure limit:	2.10×10^{24}	–1.3	0	[526]
	Troe parameters: 0.5 10^{-30} 10^{30} 10^{30}				
149.	$C_2H_3 + H \rightleftharpoons C_2H_2 + H_2$	4.50×10^{13}	0.0	0	[526]
150.	$C_2H_3 + O \rightleftharpoons CH_2CO + H$	3.00×10^{13}	0.0	0	[145]
151.	$C_2H_3 + OH \rightleftharpoons C_2H_2 + H_2O$	2.00×10^{13}	0.0	0	[254]
152.	$C_2H_3 + HO_2 \rightleftharpoons H_2CCHO + OH$	3.00×10^{13}	0.0	0	[194]
153.	$C_2H_3 + O_2 \rightleftharpoons CH_2O + HCO$	3.85×10^{12}	0.0	–238	[145]
154.	$C_2H_3 + CH_3 \rightleftharpoons C_2H_2 + CH_4$	2.10×10^{13}	0.0	0	[527]
155.	$C_2H_3 + HCO \rightleftharpoons C_2H_4 + CO$	9.00×10^{13}	0.0	0	[194]
	C_2H_5OO (ethylperoxyl radical)				
156.	$C_2H_5OO(+M) \rightleftharpoons C_2H_4 + HO_2(+M)$	7.14×10^{4}	2.32	27955	[520]
	Low-pressure limit:	8.31×10^{21}	–0.651	22890	
	Troe parameters: 1.0 10^{-30} 106 10^{30}				
157.	$C_2H_5OO + H \rightleftharpoons C_2H_5O + OH$	9.64×10^{13}	0.0	0	($= k_{R43}$)
158.	$C_2H_5OO + O \rightleftharpoons C_2H_5O + O_2$	1.63×10^{13}	0.0	–445	($= k_{R44}$)
159.	$C_2H_5OO + OH \rightleftharpoons C_2H_5OH + O_2$	2.00×10^{15}	–0.6	0	($= k_{R45}$)
160.	$C_2H_5OO + OH \rightleftharpoons C_2H_5O + HO_2$	4.00×10^{11}	0.6	0	($= k_{R46}$)
161.	$C_2H_5OO + HO_2 \rightleftharpoons C_2H_5OOH + O_2$	4.50×10^{11}	0.0	–1391	[267]
162.	$C_2H_5OO + CO \rightleftharpoons C_2H_5O + CO_2$	6.92×10^{6}	1.61	17500	($= k_{R162}$)
163.	$C_2H_5OO + CH_3 \rightleftharpoons C_2H_5O + CH_3O$	5.06×10^{12}	0.0	–1411	($= k_{R49}$)
164.	$C_2H_5OO + CH_4 \rightleftharpoons C_2H_5OOH + CH_3$	4.70×10^{4}	2.5	21000	($= k_{R31}$)

Continues on next page

Continued from last page

	Reaction	A	β	E	Note/Ref.
165.	$C_2H_5OO + CH_3OH \rightleftharpoons C_2H_5OOH + CH_2OH$	3.98×10^{13}	0.0	19400	$(= k_{R52})$
166.	$C_2H_5OO + CH_2O \rightleftharpoons C_2H_5OOH + HCO$	4.11×10^{4}	2.5	10206	$(= k_{R53})$
167.	$C_2H_5OO + C_2H_5 \rightleftharpoons C_2H_5O + C_2H_5O$	5.06×10^{12}	0.0	–1411	$(= k_{R49})$
168.	$C_2H_5OO + C_2H_6 \rightleftharpoons C_2H_5OOH + C_2H_5$	8.60×10^{0}	3.76	17200	[148]
169.	$C_2H_5OO + CH_3CHO \rightleftharpoons C_2H_5OOH + CH_3CO$	2.40×10^{19}	–2.2	14030	$(= k_{R225})$
170.	$C_2H_5OO + CH_3CHO \rightleftharpoons C_2H_5OOH + CH_2CHO$	2.32×10^{11}	0.4	14864	$(= k_{R226})$
171.	$C_2H_5OO + C_2H_5OO \rightleftharpoons C_2H_5O + C_2H_5O + O_2$	2.85×10^{11}	–0.27	408	see text, [528]
172.	$C_2H_5OO + C_2H_5OO \rightleftharpoons CH_3CHO + C_2H_5OH + O_2$	4.27×10^{9}	0.0	–850	see text, [528]
	C_2H_5OOH (ethylperoxide)				
173.	$C_2H_5OOH \rightleftharpoons C_2H_5O + OH$	1.95×10^{35}	–6.7	47450	$(= k_{R59})$, 1 bar
	$C_2H_5OOH \rightleftharpoons C_2H_5O + OH$	1.12×10^{28}	–4.15	46190	10 bar
	$C_2H_5OOH \rightleftharpoons C_2H_5O + OH$	2.80×10^{26}	–3.5	46340	50 bar
	$C_2H_5OOH \rightleftharpoons C_2H_5O + OH$	2.22×10^{17}	–0.42	44622	k_∞
174.	$C_2H_5OOH + H \rightleftharpoons CH_3CHOOH + H_2$	6.48×10^{10}	0.0	1860	$(= k_{R60})$
175.	$C_2H_5OOH + H \rightleftharpoons C_2H_5OO + H_2$	4.32×10^{10}	0.0	1860	$(= k_{R61})$
176.	$C_2H_5OOH + H \rightleftharpoons C_2H_5O + H_2O$	1.20×10^{10}	0.0	1860	$(= k_{R62})$
177.	$C_2H_5OOH + O \rightleftharpoons CH_3CHOOH + OH$	1.61×10^{13}	0.0	4750	$(= k_{R63})$
178.	$C_2H_5OOH + O \rightleftharpoons C_2H_5OO + OH$	8.65×10^{12}	0.0	4750	$(= k_{R64})$
179.	$C_2H_5OOH + OH \rightleftharpoons CH_3CHOOH + H_2O$	7.23×10^{11}	0.0	–258	$(= k_{R65})$
180.	$C_2H_5OOH + OH \rightleftharpoons C_2H_5OO + H_2O$	1.08×10^{12}	0.0	–437	$(= k_{R66})$
181.	$C_2H_5OOH + HO_2 \rightleftharpoons C_2H_5OO + H_2O_2$	4.11×10^{4}	2.5	10206	$(= k_{R109})$

Continues on next page

Continued from last page

	Reaction	A	β	E	Note/Ref.
		CH_3CHOOH (1-hydroperoxyethyl radical)			
182.	$CH_3CHOOH \rightarrow CH_3CHO + OH$	3.50×10^{12}	–0.947	979	[271], 1 bar
	$CH_3CHOOH \rightarrow CH_3CHO + OH$	3.50×10^{13}	–0.947	980	10 bar
	$CH_3CHOOH \rightarrow CH_3CHO + OH$	5.75×10^{14}	–1.012	1068	100 bar
		C_2H_5O (ethoxy radical)			
183.	$C_2H_5O(+M) \rightleftharpoons CH_3 + CH_2O(+M)$	1.10×10^{13}	0.0	16790	[529]
	Low-pressure limit:	2.00×10^{16}	0.0	13970	
	Troe parameters: 0.78 10^{-30} 1235 10^{30}				
184.	$C_2H_5O \rightleftharpoons CH_3CHO + H$	1.30×10^{13}	0.0	20060	($= k_\infty$ [529])
185.	$C_2H_5O + H \rightleftharpoons CH_3CHO + H_2$	3.00×10^{13}	0.0	0	est
186.	$C_2H_5O + OH \rightleftharpoons CH_3CHO + H_2O$	3.00×10^{13}	0.0	0	est
187.	$C_2H_5O + O_2 \rightleftharpoons CH_3CHO + HO_2$	1.45×10^{10}	0.0	645	[530]
188.	$C_2H_5O + CO \rightleftharpoons C_2H_5 + CO_2$	9.54×10^{25}	–4.93	9080	($= k_{R77}$)
		C_2H_5OH (ethanol)			
189.	$C_2H_5OH(+M) \rightleftharpoons CH_2OH + CH_3(+M^d)$	5.94×10^{23}	–1.68	91163	[138]
	Low-pressure limit:	2.88×10^{85}	–18.9	109914	
	Troe parameters: 0.5 200 890 4600				
190.	$C_2H_5OH(+M) \rightleftharpoons C_2H_5 + OH(+M^d)$	1.25×10^{23}	–1.54	96005	[138]
	Low-pressure limit:	3.25×10^{85}	–18.81	114930	
	Troe parameters: 0.5 300 900 5000				

Continues on next page

Continued from last page

	Reaction	A	β	E	Note/Ref.
191.	$C_2H_5OH(+M) \rightleftharpoons C_2H_4 + H_2O(+M^e)$	2.79×10^{13}	0.090	66136	[138]
	Low-pressure limit:	2.57×10^{83}	–18.85	86452	
	Troe parameters: 0.7 350 800 3800				
192.	$C_2H_5OH(+M) \rightleftharpoons CH_3CHO + H_2(+M^e)$	7.24×10^{11}	0.095	91007	[138]
	Low-pressure limit:	4.46×10^{87}	–19.42	115586	
	Troe parameters: 0.9 900 1100 3500				
193.	$C_2H_5OH + H \rightleftharpoons 1\text{-}C_2H_4OH + H_2$	2.58×10^{7}	1.65	2827	[138]
194.	$C_2H_5OH + H \rightleftharpoons 2\text{-}C_2H_4OH + H_2$	1.23×10^{7}	1.8	5098	[138]
195.	$C_2H_5OH + H \rightleftharpoons C_2H_5O + H_2$	1.50×10^{7}	1.65	3038	[138]
196.	$C_2H_5OH + O \rightleftharpoons 1\text{-}C_2H_4OH + OH$	1.88×10^{7}	1.85	1824	[138]
197.	$C_2H_5OH + O \rightleftharpoons 2\text{-}C_2H_4OH + OH$	9.41×10^{7}	1.7	5459	[138]
198.	$C_2H_5OH + O \rightleftharpoons C_2H_5O + OH$	1.58×10^{7}	2.0	4448	[138]
199.	$C_2H_5OH + OH \rightleftharpoons 1\text{-}C_2H_4OH + H_2O$	4.64×10^{11}	0.15	0	[138]
200.	$C_2H_5OH + OH \rightleftharpoons 2\text{-}C_2H_4OH + H_2O$	1.74×10^{11}	0.27	600	[138]
201.	$C_2H_5OH + OH \rightleftharpoons C_2H_5O + H_2O$	7.46×10^{11}	0.3	1634	[138]
202.	$C_2H_5OH + HO_2 \rightleftharpoons 1\text{-}C_2H_4OH + H_2O_2$	8.20×10^{3}	2.55	10750	[138]
203.	$C_2H_5OH + HO_2 \rightleftharpoons 2\text{-}C_2H_4OH + H_2O_2$	1.23×10^{4}	2.55	15750	[138]
204.	$C_2H_5OH + HO_2 \rightleftharpoons C_2H_5O + H_2O_2$	2.50×10^{12}	0.0	24000	[138]
205.	$C_2H_5OH + CH_3 \rightleftharpoons 1\text{-}C_2H_4OH + CH_4$	7.28×10^{2}	2.99	7948	[138]
206.	$C_2H_5OH + CH_3 \rightleftharpoons 2\text{-}C_2H_4OH + CH_4$	2.19×10^{2}	3.18	9622	[138]
207.	$C_2H_5OH + CH_3 \rightleftharpoons C_2H_5O + CH_4$	1.45×10^{2}	2.99	7649	[138]

1-C_2H_4OH (1-hydroxyethyl radical)

Continues on next page

Continued from last page

	Reaction	A	β	E	Note/Ref.
208.	1-$C_2H_4OH + M \rightleftharpoons CH_3CHO + H + M$	1.00×10^{14}	0.0	25000	[138]
209.	1-$C_2H_4OH + O \rightleftharpoons CH_3CHO + OH$	1.00×10^{14}	0.0	0	[138]
210.	1-$C_2H_4OH + H \rightleftharpoons CH_2OH + CH_3$	3.00×10^{13}	0.0	0	[138]
211.	1-$C_2H_4OH + H \rightleftharpoons C_2H_4 + H_2O$	3.00×10^{13}	0.0	0	[138]
212.	1-$C_2H_4OH + OH \rightleftharpoons CH_3CHO + H_2O$	5.00×10^{12}	0.0	0	[138]
213.	1-$C_2H_4OH + HO_2 \rightleftharpoons CH_3CHO + OH + OH$	4.00×10^{13}	0.0	0	[138]
[a]214.	1-$C_2H_4OH + O_2 \rightleftharpoons CH_3CHO + HO_2$	8.43×10^{15}	–1.2	0	[138]
		4.82×10^{14}	0.0	5017	
	2-C_2H_4OH (2-hydroxyethyl radical)				
215.	2-$C_2H_4OH + O_2 \rightleftharpoons HOC_2H_4O_2$	1.00×10^{12}	0.0	–1100	[138]
	$HOC_2H_4O_2$ (hydroxyethylperoxyl radical)				
216.	$HOC_2H_4O_2 \rightleftharpoons CH_2O + CH_2O + OH$	6.00×10^{10}	0.0	24500	[138]
	CH_3CHO (acetaldehyde)				
217.	$CH_3CHO(+M) \rightleftharpoons CH_3 + HCO(+M)$	4.29×10^{22}	–1.88	85480	[531]
	Low-pressure limit:	2.22×10^{76}	–11.81	95040	
	Troe parameters: 0.23 80 7000 10^{30}				[f]
218.	$CH_3CHO + H \rightleftharpoons CH_3CO + H_2$	4.66×10^{13}	–0.35	3000	[138, 225]
219.	$CH_3CHO + H \rightleftharpoons CH_2CHO + H_2$	1.85×10^{12}	0.4	5359	[138, 225]
220.	$CH_3CHO + O \rightleftharpoons CH_3CO + OH$	1.77×10^{18}	–1.9	2975	[138, 225]

Continues on next page

Continued from last page

	Reaction	A	β	E	Note/Ref.
221.	$CH_3CHO + O \rightleftharpoons CH_2CHO + OH$	3.72×10^{13}	–0.2	3556	[138, 225]
222.	$CH_3CHO + OH \rightleftharpoons CH_3CO + H_2O$	2.35×10^{11}	0.3	–1000	[532, 533][g]
223.	$CH_3CHO + OH \rightleftharpoons CH_2CHO + H_2O$	3.00×10^{13}	–0.6	800	[532, 533][g]
224.	$CH_3CHO + O_2 \rightleftharpoons CH_3CO + HO_2$	1.20×10^{5}	2.5	37550	[145]
225.	$CH_3CHO + HO_2 \rightleftharpoons CH_3CO + H_2O_2$	2.40×10^{19}	–2.2	14030	[138, 225]
226.	$CH_3CHO + HO_2 \rightleftharpoons CH_2CHO + H_2O_2$	2.32×10^{11}	0.4	14864	[138, 225]
227.	$CH_3CHO + CH_3 \rightleftharpoons CH_3CO + CH_4$	3.90×10^{-7}	5.8	2200	[138, 225]
228.	$CH_3CHO + CH_3 \rightleftharpoons CH_2CHO + CH_4$	2.45×10^{1}	3.15	5727	[138, 225]
	CH_3CO (acetyl radical)				
229.	$CH_3CO \rightleftharpoons CH_3 + CO$	6.45×10^{18}	–2.52	16436	[534], 1 bar
	$CH_3CO \rightleftharpoons CH_3 + CO$	8.18×10^{19}	–2.55	17263	10 bar
	$CH_3CO \rightleftharpoons CH_3 + CO$	1.26×10^{20}	–2.32	18012	100 bar
	$CH_3CO \rightleftharpoons CH_3 + CO$	1.07×10^{12}	0.63	16895	k_∞
230.	$CH_3CO + H \rightleftharpoons CH_3 + HCO$	2.10×10^{13}	0.0	0	[535, 536]
231.	$CH_3CO + H \rightleftharpoons CH_2CO + H_2$	1.20×10^{13}	0.0	0	[535, 536]
232.	$CH_3CO + O \rightleftharpoons CH_3 + CO_2$	1.60×10^{14}	0.0	0	[145]
233.	$CH_3CO + O \rightleftharpoons CH_2CO + OH$	5.30×10^{13}	0.0	0	[145]
234.	$CH_3CO + OH \rightleftharpoons CH_2CO + H_2O$	1.20×10^{13}	0.0	0	[194]
235.	$CH_3CO + CH_3OO \rightleftharpoons CH_3 + CO_2 + CH_3O$	2.40×10^{13}	0.0	0	[194]
236.	$CH_3CO + CH_3 \rightleftharpoons C_2H_6 + CO$	3.26×10^{13}	0.0	0	[537]
237.	$CH_3CO + CH_3 \rightleftharpoons CH_2CO + CH_4$	5.33×10^{13}	0.0	0	[537]

Continues on next page

Continued from last page

	Reaction	A	β	E	Note/Ref.
238.	$CH_3CO + O_2 \rightleftharpoons CH_2O + CO + OH$	1.93×10^{12}	0.0	0	[538]
	CH_2CHO (formylmethyl radical)				
239.	$CH_2CHO \rightleftharpoons CH_3 + CO$	1.17×10^{43}	–9.83	43756	[138], 1 bar
240.	$CH_2CHO \rightleftharpoons CH_2CO + H$	1.81×10^{43}	–9.61	45868	[138], 1 bar
241.	$CH_2CHO \rightleftharpoons CH_3CO$	2.80×10^{37}	–7.393	57015	[271], 1 bar
	$CH_2CHO \rightleftharpoons CH_3CO$	6.40×10^{32}	–5.877	55941	10 bar
	$CH_2CHO \rightleftharpoons CH_3CO$	1.02×10^{16}	–0.654	50433	100 bar
242.	$CH_2CHO + H \rightleftharpoons CH_3 + HCO$	5.00×10^{13}	0.0	0	[138]
243.	$CH_2CHO + H \rightleftharpoons CH_2CO + H_2$	2.00×10^{13}	0.0	0	[138]
244.	$CH_2CHO + O \rightleftharpoons CH_2O + HCO$	1.00×10^{14}	0.0	0	[539]
245.	$CH_2CHO + OH \rightleftharpoons CH_2CO + H_2O$	3.00×10^{13}	0.0	0	[539]
246.	$CH_2CHO + O_2 \rightleftharpoons CH_2O + CO + OH$	5.66×10^{17}	–1.757	11067	[271], 1 bar
	$CH_2CHO + O_2 \rightleftharpoons CH_2O + CO + OH$	1.05×10^{14}	–0.610	11422	10 bar
	$CH_2CHO + O_2 \rightleftharpoons CH_2O + CO + OH$	1.50×10^{-10}	6.690	4868	100 bar
247.	$CH_2CHO + CH_3 \rightleftharpoons C_2H_5 + CO + H$	4.90×10^{14}	–0.50	0	[539]
248.	$CH_2CHO + HO_2 \rightleftharpoons CH_2O + HCO + OH$	7.00×10^{12}	–0.50	0	[138]
249.	$CH_2CHO + HO_2 \rightleftharpoons CH_3CHO + O_2$	3.00×10^{12}	–0.50	0	[138]
	CH_2CO (ketene)				
250.	$CH_2CO + H \rightleftharpoons H_2CCHO$	1.99×10^{9}	1.43	6050	[534], k_∞
251.	$CH_2CO + H \rightleftharpoons CH_3CO$	2.30×10^{8}	1.61	2627	[534], k_∞

Continues on next page

Continued from last page

	Reaction	A	β	E	Note/Ref.
252.	$CH_2CO + H \rightleftharpoons CH_3 + CO$	3.30×10^{10}	0.851	2840	[540]
253.	$CH_2CO + H \rightleftharpoons HCCO + H_2$	3.00×10^{7}	2.0	10000	[105]
254.	$CH_2CO + O \rightleftharpoons HCCO + OH$	2.00×10^{7}	2.0	10000	[105]
255.	$CH_2CO + OH \rightleftharpoons CH_2OH + CO$	1.01×10^{12}	0.0	–1013	[145, 541]
256.	$CH_2CO + OH \rightleftharpoons CH_3 + CO_2$	6.74×10^{11}	0.0	–1013	[145, 541]

a: Expressed as the sum of the rate constants
b: Enhanced third-body efficiencies: $Ar = 0.7, H_2 = 2, H_2O = 6, CH_4 = 3, CO = 1.5, CO_2 = 2, C_2H_6 = 3$
c: The expression of $k_{R142,0}$ is valid for 600–3000 K. Zhu *et al.* [523] have also provided an expression for 200–500 K
d: Enhanced third-body efficiencies: $H_2 = 2, H_2O = 5, CO = 2, CO_2 = 3$
e: Enhanced third-body efficiencies: $H_2O = 5$
f: Troe parameters fitted to $F_{cent,R217} = 0.601T^{-0.162}\exp\left(\frac{-1.07}{RT}\right)$ [531]
g: Estimate based on $k_{CH_3CHO+OH\rightarrow prod.}$ [532] and branching ratios [533]

constant indicate a non-Arrhenius behavior over the entire temperature range that calls for a three-parameter fit of the rate coefficient using the modified Arrhenius expression (Equation (5.8)). The results are in particular good agreement in the low and intermediate temperature range where the experimental work of Tully and co-workers [542, 543] and Talukdar *et al.* [544] together provide representative values from 231–800 K. At higher temperature, the results become more scattered. The present mechanism follows the recommendation of Baulch *et al.* [145] and apply the rate expression originally proposed in the literature evaluation by Atkinson [516], which is in excellent agreement with most experimental studies including those referred in the present study. At temperatures above 800 K, the proposed rate constant mainly relies on the shock-tube studies of Bott and Cohen [334], and Koffend and Cohen [545] at 1225 and 970 K respectively.

Experimental measurements of C_2H_6+HO_2 (R124) are few and generally of an earlier date. The most recent study has been conducted by Baldwin *et al.* [308] using thermal decomposition of tetramethylbutane in the presence of O_2 as a source of HO_2 mixed with C_2H_6/N_2 in KCl- and boric acid coated pyrex vessels at 673–773 K. The relative yields of *i*-butene and C_2H_4 were subsequently monitored from which, values of $k_{R124}/k_{R15}^{1/2}$ were deduced. These relative rate measurements were reevaluated by Baulch *et al.* [145] using an updated value of k_{R15} to derive a reliable expression of k_{R124}. This is also the recommended expression in the present study. The rate constant is in good agreement with an earlier relative rate measurement of $k_{R124}/k_{R15}^{1/2}$ from Baldwin and Walker [546] at 713 K, and it extrapolates convincingly well to the rate expression proposed by Sampson [547] that was deduced from flow reactor experiments with C_2H_6/air at 873–903 K. Baulch *et al.* [145] assigned a relatively low uncertainty factor of 1.4 to k_{R124} within 500–800 K rising to a factor of 2 at 1000 K.

The only experimental determinations of the initiation reaction between C_2H_6 and O_2 (R125) include some relative rate measurements at intermediate temperatures reported by Trotman-Dickenson and co-workers [548,549] in the late fifties and early sixties. These are considered unreliable due to large uncertainties in reference- and potential side reactions. Baulch *et al.* [145] proposed a rate expression based on analogies with the experimentally derived rate expression of CH_2O+O_2 (R110) with a correction to the pre-exponential factor of $k_{CH_2O+O_2}$ in accordance with the increased availability of H atoms and an adjustment of the activation energy to reflect differences in $\Delta_r H$ of C_2H_6+O_2 compared to CH_2O+O_2. Baulch *et al.* used a similar approach for their recommendation of CH_4+O_2 (–R40), which was previously found to underpredict the few available experiments with CH_4+O_2; see Section 5.3.3.1. However, no experimental and/or theoretical determinations of C_2H_6+O_2

are currently available for comparison. The present mechanism has adopted k_{R125} from Baulch *et al.* [145], but emphasizes the uncertainty factor of 3 assigned by Baulch *et al.* at 500–1000 K rising to a factor of 10 at 2000 K.

Experimental data of the abstraction reaction with CH_3 (R126) are available over a wide temperature range revealing a distinct non-Arrhenius behavior. Most of the results are of an earlier date, but nevertheless, show very good agreement except for some scatter observed at temperatures >1000 K. Baulch *et al.* [145] recommended a rate expression comprised of the sum of two simple Arrhenius expressions in order to fit the most reliable experiments at low to intermediate [550–552] and high temperatures [553–556]. The resulting rate constant is valid over the temperature range 350–1500 K with a corresponding uncertainty factor ranging from 1.3 to 1.6.

5.3.4.2 C_2H_5 Reactions

The fast radical-radical reaction between C_2H_5 and H is an important secondary step to the reactions of H+C_2H_4 and H+C_2H_6, and all experimental studies of C_2H_5+H are consequently limited to indirect measurements extracted from experimental work on these systems. The reaction can proceed via radical association and subsequent stabilization or dissociation of the adduct to C_2H_6 (R127) or CH_3+CH_3 (–R42) respectively; or through a direct abstraction mechanism yielding C_2H_4+H_2. The addition/elimination reaction (–R42) has previously been discussed in connection to the self-reaction of CH_3 in Section 5.3.3.2 and will therefore not be considered in details here. Experimental investigations of C_2H_5+H are concentrated around room-temperature measurements [557–562] and show significant scatter with deviations up to one order of magnitude. It is noteworthy that the most recent experiments by Sillesen *et al.* [562] have provided the highest value of $k_{R127} + k_{-R42} = 2 \times 10^{14}\,{}^{\mathrm{cm}^3}/_{\mathrm{mol\,s}}$ based on pulsed-radiolysis of H_2/C_2H_4 mixtures at 298 K and 10–100 mbar. This value lies significantly above the value of $4 \times 10^{13}\,{}^{\mathrm{cm}^3}/_{\mathrm{mol\,s}}$ recommended by Baulch *et al.* [145] as an average between earlier experiments [558–561]. Experimental determinations of the temperature dependence are inconsistent suggesting both small positive [555, 557, 560, 561] and negative dependences [563]; or no dependence at all [559]. Recent *ab initio* calculations by Harding and Klippenstein [564] predicted a slight positive temperature dependence and rate constants for the association channel k_{R127}+k_{-R42} ranging from 1.6 to $2.2\times10^{14}\,{}^{\mathrm{cm}^3}/_{\mathrm{mol\,s}}$ at 200–1900 K. This is consistent with the room-temperature measurement reported by Sillesen *et al.* [562]. It also agrees reasonably well with the experimental value of $9 \times 10^{13}\,{}^{\mathrm{cm}^3}/_{\mathrm{mol\,s}}$ at 963 K obtained from a relative rate measurement by Pacey and Wimalasena [555]. Harding and Klippenstein [564] calculated

stationary points on the potential energy surface of C_2H_5+H that provided evidence of the dominance of the association channel (R127)+(–R42) over the direct abstraction channel (C_2H_5+H $\rightleftharpoons$ C_2H_4+H_2). This has been confirmed by experiments from Camilleri *et al.* [559], but opposed by Hidaka *et al.* [565], who needed a comparatively high rate constant of $4.5 \times 10^{13}\,{}^{\mathrm{cm}^3}/_{\mathrm{mol\,s}}$ for the abstraction channel to fit a complex mechanism to shock-tube measurements of C_2H_6 pyrolysis. Nevertheless, the abstraction channel is neglected in the present study in accordance with the recommendation of Harding and Klippenstein [564]. Conversion of the forward rate expression of (R42) to $k_{-\mathrm{R42}}$ using thermochemical data from Table 3.1 yields a value of $\sim 2\times10^{14}\,{}^{\mathrm{cm}^3}/_{\mathrm{mol\,s}}$; almost independent of the temperature. The pressure dependent rate expression for (R127) is drawn from the GRI-Mech 3.0 Release [256], where it was originally derived from RRKM-calculations on the reverse reaction by Stewart *et al.* [517]. At ambient pressure, k_{R127} yields a room-temperature value of $7 \times 10^{13}\,{}^{\mathrm{cm}^3}/_{\mathrm{mol\,s}}$ increasing to $1 \times 10^{14}\,{}^{\mathrm{cm}^3}/_{\mathrm{mol\,s}}$ at 460 K followed by a gradual decrease to $3 \times 10^{13}\,{}^{\mathrm{cm}^3}/_{\mathrm{mol\,s}}$ at ∼1000 K. Combined with the almost constant value of $k_{-\mathrm{R42}}$, this is considered to be in reasonable agreement with the theoretical work of Harding and Klippenstein [564].

The reaction between C_2H_5 and O atoms has a number of potential product channels, e.g. CH_3+CH_2O (R128), CH_3CHO+H (R129), C_2H_4+OH (R130), CO+CH_4+H, and CO+CH_3+H_2. Slagle *et al.* [518] investigated the C_2H_5+O reaction in a tubular reactor with photoionization mass-spectroscopic detection and reactant generation via simultaneous photodissociation of SO_2 and diethyl ketone at 193 nm. The overall rate constant was determined from time-resolved measurements of C_2H_5 decay profiles obtained at excess O atom concentrations at 295–600 K and 1–10 mbar, under which conditions, no dependence of temperature or pressure was observed. Slagle *et al.* also determined the branching fractions $k_{\mathrm{R128}}/k = 0.32\pm0.06$, $k_{\mathrm{R129}}/k = 0.40\pm0.04$, and $k_{\mathrm{R130}}/k = 0.23\pm0.07$ from experiments conducted at 298–450 K. Here, k denotes $k_{\mathrm{C_2H_5+O\rightarrow prod.}}$. These values also appeared to be independent of the temperature and pressure. Slagle *et al.* confirmed the branching fractions of (R128) and (R129) via RRKM-calculations, but the theoretical prediction only yielded $k_{\mathrm{R130}}/k = 0.02$, which led Slagle *et al.* to believe that most of the observed C_2H_4+OH had to be indirect products from an unaccounted conversion path. Direct measurements of product yields from C_2H_5+O by Hoyermann *et al.* [566] confirmed all three experimental branching fractions reported by Slagle *et al.* The experiments by Hoyermann *et al.* were undertaken in a flow reactor at room-temperature and 1–3 mbar using a molecular beam mass-spectrometer. Hoyermann *et al.* also conducted supplementary *ab initio* calculations for verification, but, like Slagle *et al.*, they too were not able to predict the experimental value of k_{R130}/k. Lindner *et al.* [567]

measured the vibrational levels in OH radicals released from the reaction of C_2H_5+O in order to determine details about the reaction mechanism. Their results pointed towards a direct abstraction mechanism for (R130) instead of an addition/elimination mechanism as assumed by both Slagle *et al.* and Hoyermann *et al.* Thus, if the *ab initio* calculations by Slagle *et al.* and Hoyermann *et al.* were based on an erroneous mechanism, this could explain the very large deviations between experimental and calculated values of k_{R130}/k. The alternative product channels to CO+CH_4+H and CO+CH_3+H_2 constitute recent proposals by Reid *et al.* [568], who introduced them in order to explain formations of vibrationally excited CO detected with a FTIR emission spectrometer in a laser-photolysis study of C_2H_5+O. However, more investigations are needed to confirm this finding, and at present, only the three product channels listed in Table 5.4 are considered with rate constants and branching fractions equivalent to the experimental findings of Slagle *et al.* [518].

The only measurement of C_2H_5+OH (R131,–R190) has been reported by Fagerström *et al.* [569] at room-temperature and pressures from 0.25–1 bar using pulse radiolysis of $C_2H_6/H_2O/SF_6$ mixtures and monitoring of C_2H_5 and CH_3 concentrations by transient UV absorption spectrometry. The experimental rate constant yielded a value of $(7.1 \pm 1.0) \times 10^{13}\,{}^{\mathrm{cm}^3}/_{\mathrm{mol\,s}}$ independent of the pressure. Supplementary *ab initio* calculations of the high-pressure limit of the addition/stabilization channel to ethanol (C_2H_5OH) at 200–400 K yielded $k_{-R190,\infty} = (7.7 \pm 1.0) \times 10^{13}\,{}^{\mathrm{cm}^3}/_{\mathrm{mol\,s}}$. These results suggest dominance of the addition/stabilization channel at ambient conditions where the reaction is close to the high-pressure limit, but experimental verification is needed; especially at an extended temperature range. The pressure dependent rate expression of k_{-R190} is drawn from recent *ab initio* calculations of the reverse reaction by Marinov [138]; see the later outline of the C_2H_5OH subset in Section 5.3.4.7, while k_{R131} is an estimated constant value from Tsang and Hampson [194], who assigned an uncertainty factor of 4 at temperatures and pressures above 800 K and 1 bar.

The reaction mechanism of C_2H_5+HO_2 involves initial formation of a highly energized C_2H_5OOH* adduct that either decomposes to C_2H_5O+OH (R132) through immediate O–O bond fission (equivalent to the reaction CH_3+HO_2) or proceeds via H-atom transfer prior to dissociation that yields C_2H_4+H_2O_2 or C_2H_6+O_2 (–R125). The channel to C_2H_6+O_2 is already included in the mechanism via the reverse reaction (–R125); see the discussion of C_2H_6+$O_2 \rightleftharpoons C_2H_5$+$HO_2$ (R125) in the previous section. Calculations of k_{-R125} at different temperatures using thermochemical data from Table 3.1 yield values between 2×10^{11} and $3 \times 10^{11}\,{}^{\mathrm{cm}^3}/_{\mathrm{mol\,s}}$ at 300–1500 K, which is in agreement with the estimated value of k_{-R125} from Tsang and Hampson [194].

In a recent study, Ludwig *et al.* [519] reported a room-temperature value of $k_{C_2H_5+HO_2\rightarrow prod.} = (3.1 \pm 1.0) \times 10^{13}\,{}^{cm^3}/_{mol\,s}$ based on experiments undertaken at 1.2 mbar in a laser-photolysis/flow reactor system with a mass spectrometer. Well-defined concentrations of the reactants were produced from laser-photolysis of $H_2O_2/C_2H_6/(COCl)_2$ mixtures, and the rate constant was deduced from time-resolved decay profiles of HO_2 and C_2H_5. Ludwig *et al.* were also able to obtained clear mass-signals corresponding to the time-resolved formation of C_2H_5O. These measurements could be accurately predicted by a scaled numerical simulation using a simple mechanism where the determined rate constant of $C_2H_5+HO_2 \rightarrow$ prod. was assigned exclusively to (R132). Additionally, the measured rate constant of Ludwig *et al.* is in excellent agreement with the estimated value of k_{R132} from Tsang and Hampson [194] as well as the theoretical expression from Bozzelli and Dean [570] based on *ab initio* calculations. It is noted that the primary objective in the referred study by Bozzelli and Dean was to characterize the reaction $C_2H_5+O_2$, and the calculated rate constant for $C_2H_5+HO_2$ was only briefly presented in connection to a simple reaction mechanism without details about the underlying parameters used in the the calculations. Thus, it is unclear whether Bozzelli and Dean even considered alternative reaction pathways for $C_2H_5+HO_2$. Dobis and Benson [571] measured the rate constant of the competitive product channel to $C_2H_4+H_2O_2$ at 243–368 K and extremely low pressures ($\sim$1 μbar) using a low-pressure flow reactor system with a mass-spectrometer. Surprisingly, they were not able to detect any products related to the formation of C_2H_5O and OH. Even so, their measured rate constant $k_{C_2H_5+HO_2\rightarrow C_2H_4+H_2O_2} = (1.79 \pm 0.07) \times 10^{12}\,{}^{cm^3}/_{mol\,s}$ is still more than one order of magnitude below $k_{C_2H_5+HO_2\rightarrow prod.}$ from Ludwig *et al.* inevitably indicating a very low contribution from this alternative channel to $C_2H_4+H_2O_2$. In the present mechanism, $k_{C_2H_5+HO_2\rightarrow prod.}$ has been adopted from Ludwig *et al.* as the preferred expression of k_{R132}, while a potential contribution from $C_2H_4+H_2O_2$ is neglected. Potential energy calculations are needed to verify this product distribution and so are experimental investigations of the temperature dependence of the reaction, which are currently unavailable.

The experimental database on the reaction between C_2H_5 and molecular oxygen is substantial at low and intermediate temperatures up to $\sim$1000 K, e.g. [572–581]. The investigated pressure range extends from low to near-atmospheric pressure with the exception of the experiments by Dilger *et al.* [580], who characterized the reaction at 1.5–60 bar and 295–425 K using a muon spin relaxation (μSR) technique in longitudinal magnetic fields. Here, spin-polarized muonium, which is chemically an isotope of hydrogen with a positive muon nucleus, is added to the double bond of C_2H_4 to create muon-substituted ethyl radicals. The isotope is detectable through resonances in

magnetic fields caused by a spin-flip upon reaction with the paramagnetic O_2 molecule. At the conditions applied by Dilger *et al.*, the reaction is at the high-pressure limit. At temperatures roughly below ∼750 K, the available experiments indicate an increasing overall rate constant with increasing pressure and/or declining temperatures. The rate constant shows little or no dependence of both pressure and temperature at higher temperatures. Wagner *et al.* [575] proposed a model for this behavior according to which, the reaction proceeds by initial formation of the adduct $C_2H_5OO^*$ that can either be collisionally stabilized to C_2H_5OO (R133), dissociate back to the reactants, or yield the products C_2H_4+HO_2 (R134). The theoretical work of Wagner *et al.* has recently been extended in a comprehensive theoretical study by Miller and co-workers [520, 582] based on master equation analysis with stationary points on the potential energy surface of C_2H_5+O_2 calculated with a Gaussian-2 like method developed by Curtiss *et al.* [583]. The potential energy surface calculations clearly showed that direct elimination of HO_2 (R134) from the adduct $C_2H_5OO^*$ is the energetically favorable route among potential bimolecular product channels. This is consistent with previous density functional theory calculations (DFT) performed by Ignatyev *et al.* [584]. Miller and co-workers predicted a competitive formation of oxirane (C_2H_4O+OH) via 1,4-H-atom shift with a yield of ∼1 % at 800 K and independent of pressure, which is in excellent agreement with relative yield measurements by Baldwin *et al.* [585] at 673–813 K. There is also a potential bimolecular path to acetaldehyde (CH_3CHO+OH), which has no practical interest due to an enhanced energy barrier. The model of Miller and coworkers predicted that below 575 K, the reaction between C_2H_5 and O_2 will be dependent of pressure and temperature in a way that is typical for adduct formation, i.e. high pressure and/or low temperatures favoring stabilization of the adduct, while concentrations of the bimolecular products increases when the conditions shift towards low pressure and/or high temperatures. The model forecasted the product distribution $k_{R134}/\left(k_{R133}+k_{R134}\right) < 1\,\%$ at room-temperature and atmospheric pressure, which has been confirmed by experiments [576–581]. Between 575 and 750 K, the reaction enters a transition region where the rate constant exhibits a bi-exponential decay to become equivalent with the low-pressure limit at 750 K regardless of the system pressure. The ratio $k_{R134}/\left(k_{R133}+k_{R134}\right)$ increases towards unity within this temperature span, and at temperatures above 750 K, the reaction has effectively become bimolecular with no appriciable formation of C_2H_5OO. In addition, the rate constant has become independent of pressure and only weakly dependent of temperature. Clifford *et al.* [581] recently measured the HO_2 yield from C_2H_5+O_2 across this transition regime covering the temperatures 294–698 K and pressures from 13 to 138 mbar by means of time-resolved

infrared frequency modulation spectroscopy. The reactant C_2H_5 was generated from attack on C_2H_6 by Cl-atoms produced via laser-photolysis of Cl_2. The model developed by Miller and co-workers [520,582] provides an excellent fit to these data. Other experimental results obtained in this temperature range are also predicted reasonably well by Miller and co-workers, e.g. Slagle *et al.* [572] (294–1002 K, 0.6–21 mbar) and Wagner *et al.* [575] (298–850 K, 0.7–20 mbar). In Ref. [520], Miller and Klippenstein fitted the theoretical model to Arrhenius-based rate expressions for the three elementary reactions: $C_2H_5+O_2 \rightleftharpoons C_2H_5OO$ (R133), $C_2H_5+O_2 \rightleftharpoons C_2H_4+HO_2$ (R134), and $C_2H_5OO \rightleftharpoons C_2H_4+HO_2$ (R156). Miller and Klippenstein [520] noted that the fitted expression for k_{R156} overpredicts the rate constant throughout the middle-section of the fall-off region by up to 50–75 % because is was not possible to incorporate the drain of C_2H_5OO via (–R133) in the Arrhenius expression. It is noted that reaction (R156) is still in the fall-off region at 100 bar and temperatures >700 K, which are conditions relevant to the present study. Miller and Klippenstein fitted k_{R133} and k_{R134} within 25 % of their original model. The present mechanism includes the pressure dependent rate expressions of (R133) and (R156), while (R134) is exclusively described by $k_{R134,0}$ at all relevant temperatures and pressures. This simplification is reasonable considering the behavior of the stabilization reaction (R133): At low temperatures (before the narrow transition region) and pressures relevant to the present study, k_{R133} falls close to the high-pressure limit, which is effectively about two orders of magnitude above $k_{R134,0}$ and consistent with the complete dominance of (R133). At high temperatures (after the transition region), the reaction is nearly independent of pressure and runs almost exclusively through (R134) at the low-pressure limit. This is consistent with $k_{R134} \cong k_{R134,0}$.

The rate constant for the reaction between C_2H_5 and HCO (R136) is drawn from the experimental work of Baggott *et al.* [521]. This value of k_{R136} is ∼3 times lower than the estimated rate expression proposed by Tsang and Hampson [279] based on analogies with the similar reaction with CH_3 instead of C_2H_5. However, this difference corresponds to the assigned uncertainty factor by Tsang and Hampson.

The C_2H_5 reaction mechanism may include other reactions with hydrocarbon species, e.g. CH_2O, CH_3OH, C_2H_x, etc., but these are not expected to gain significant importance under most combustion conditions including those relevant to the present work. There are no experimental and/or theoretical characterizations available for reactions with CH_2O and CH_3OH. Tsang and Hampson [194] and Tsang [279] advocated the use of rate constants similar to those for analogue reactions with CH_3, but these are considered to be upper limits due to the lower reactivity of C_2H_5.

5.3.4.3 C_2H_4 Reactions

Unimolecular decomposition of C_2H_4 can yield C_2H_3+H (–R148) and C_2H_2+H_2 (R137), but both channels are highly endothermic ($\Delta_r H_{298}$ = 110 and 42 $^{\text{kcal}}/_{\text{mol}}$ respectively), which makes them unlikely to occur in considerable scale at the temperature range relevant to the present study. The experimental conditions used in this work hardly favor a noticeable formation of C_2H_2, while small amounts of C_2H_3 could appear from H-abstraction of C_2H_4. The reverse association reaction of C_2H_3+H (R148) is potentially an important drain of C_2H_3, and so, it may gain importance in the present work unlike the association of C_2H_2+H_2 (–R137). The rate constant k_{R137} is taken from GRI-Mech 3.0 [256] without further notice. The association reaction of C_2H_3+H (R148) will be discussed in connection to the C_2H_3 reaction subset in Section 5.3.4.4.

The reaction mechanism of C_2H_4+H can either be abstraction/elimination yielding C_2H_3+H_2 (R138) or addition/stabilization to form C_2H_5 (R139). The latter is favored by high pressure and/or low to intermediate temperatures, while (R138) does not provide a significant contribution unless the temperature is above ∼1500 K. Hence, it is unlikely that (R138) will play an important role at conditions relevant to the present study. The two product channels have been subjected to numerous investigations, and temperature and pressure dependencies are fairly well established over a wide range of conditions. Preferred rate expressions for (R138) and (R139) have been obtained from Baulch *et al.* [145]. This value of k_{R138} largely rely on the the combined experimental and theoretical work of Knyazev *et al.* [586], who measured values of $k_{-\text{R138}}$ at 499–947 K based on laser-photolysis of C_2H_3Br at 193 nm as a source of C_2H_3 with photoionization mass spectroscopic detection of the radical decay profiles at varying H_2 concentrations. Knyazev *et al.* combined the experimental results with *ab initio* calculations to determine the temperature dependence of the reverse reaction. At higher temperatures, Baulch *et al.* further aligned k_{R138} with the flame-results from Bhargava and Westmoreland [587] at 1850–2150 K, and the earlier shock-tube measurements by Just *et al.* [588] at 1700–2200 K. Tranter *et al.* [589] recently advocated a 25 % increase of the rate expression proposed by Tsang and Hampson [194] in order to fit their shock-tube measurements of ethane oxidation at 5–1000 bar and 1100–1500 K. The original rate expression from Tsang and Hampson was based on the high-temperature data from Just *et al.* [588] combined with bond energy-bond order calculations (BEBO). The adjusted rate constant from Tranter *et al.* [589] is slightly higher than k_{R138} used in the present study, but still within the uncertainty factor of 2.5 assigned by Baulch *et al.* [145]. The pressure dependent expression of k_{R139} for the addition/sta-

bilization channel (R139) is the result of a theoretical treatment of experimental results by Baulch *et al.* [145] following the Troe formalism for strong collision rate constants of thermal unimolecular reactions [184]. Baulch *et al.* fitted the fall-off curves to the laser-photolysis/resonance fluorescence experiments of Kurylo *et al.* [558], Lightfoot and Pilling [590], and Hanning-Lee *et al.* [591], at temperatures and pressures from 285–800 K and 7–800 mbar; using the experimental reaction threshold energy of 36.97 $^{\text{kcal}}/_{\text{mol}}$ reported by Feng *et al.* [592]. It is noted that the reaction is near the high-pressure limit at room-temperature and ambient pressure, while it is well within the fall-off region at 800 K. The referred experimental studies all used He as bath gas, but comparisons with N_2-diluted experiments in the fall-off region by Braun and Lenzi [593], and Clarke *et al.* [594] indicate no appreciable differences between He and N_2 as collision partner. Experiments at the high-pressure limit by Lee *et al.* [595], Sugawara *et al.* [596], and Lightfoot and Pilling [590] are in excellent agreement and have provided the temperature dependence of $k_{\text{R139},\infty}$, while the low-pressure limit was determined from the experimental results of Lightfoot and Pilling [590], and Braun and Lenzi [593].

There are a number of experimental studies of the reaction between C_2H_4 and O atoms that have provided a solid characterization of the overall rate constant over a wide range of conditions. The most reliable results are believed to be those obtained from the flash-photolysis/resonance fluorescence studies of Klemm and co-workers [522, 597] and Mahmud *et al.* [598]. The results from the early work of Klemm and co-workers [597] cover the temperature range 244–1052 K and are in very good agreement with the independent measurements from the same year by Mahmud *et al.* [598] at 290–1510 K. The later study by Klemm *et al.* [522] extended this temperature range up to 2284 K. The preferred overall rate constant is the bi-exponential expression from Klemm *et al.* [522] derived as a best-fit to the referred measurements including some earlier work in the field [599–603]. Potential energy surface calculations by Melius (referred in e.g. [598, 604]) and observations of experimental product yields led Schmoltner *et al.* [604] to propose an addition/elimination mechanism for C_2H_4+O involving initial formation of a triplet bi-radical adduct $^3CH_2CH_2O^*$ that can easily undergo intersystem crossing to the singlet state (barrier is only $\sim$0.6 $^{\text{kcal}}/_{\text{mol}}$ [605]) followed by 1,2-H-atom shift and C–C bond cleavage to CH_3+HCO (R140). The energetically favored product on the triple surface is direct elimination of a H atom to vinyloxy ($^3H_2CCHO$) (R141), whereas dissociation to $^3CH_2$+CH_2O, or 1,2-H-atom shift/elimination to CH_2CO+H_2 both exhibit prohibitively large energy barriers to compete at the investigated conditions of the present study. This is also the case for the direct abstraction channel of C_2H_4+O to C_2H_3+OH that is unlikely to play a role unless very high temperatures are

applied. Schmoltner *et al.* [604] employed single collision conditions by means of a crossed molecular beam method and were able to detected both HCO and H_2CCHO from C_2H_4+O reactions at room-temperature. They subsequently proposed the branching ratio $k_{R140}/k_{R141} = 2.5 \pm 0.9$. Other experimental studies [606–610] have proposed ratios of $0.27 \leq k_{R141}/k_{C_2H_4+O\rightarrow prod.} \leq 0.35$. These were all obtained at room-temperature except for Smalley *et al.* [607], who determined experimental values of $k_{R141}/k_{C_2H_4+O\rightarrow prod.}$ ranging from 0.28 to 0.35 at 515–769 K thereby indicating a slight positive temperature dependence, but the experimental uncertainties were too large to make a definite conclusion. The present mechanism only considers (R140) and (R141) with a constant branching ratio $k_{R141}/(k_{R140} + k_{R141}) = 0.31$ as a mean value of the range shown above. This is equivalent to $k_{R140}/k_{R141} = 2.2$ in good agreement with k_{R140}/k_{R141} from Schmoltner *et al.* [604].

Experimental data of the overall reaction between C_2H_4+OH are available over the temperature range 299–1400 K, e.g. [441, 611–618]. These data indicate a clear non-Arrhenius behavior caused by marked changes in the fractional contribution of different product channels and the different nature of these pathways. There have been several theoretical investigations of the reaction, e.g. [523, 619, 620]. Potential energy surface and rate constant calculations from the most recent *ab initio* study in the field by Zhu *et al.* [523] have identified three important product channels yielding collisionally stabilized 2-C_2H_4OH (hydroxyethyl) (R142), H_2CCHOH+H (ethenol) (R143), and C_2H_3+H_2O (R144). An alternative pathway to CH_3+CH_2O involves H-atom-shift from the HO-group to the secondary C-atom and subsequent dissociation of the resulting C_2H_5O* adduct, but this path is constrained by a high energy barrier for the H-migration step and therefore, does not provide a significant contribution. The calculated rate constants from Zhu *et al.* indicate that at atmospheric pressure and temperatures <500 K, the reaction almost exclusively proceeds via (R142) to form 2-C_2H_4OH with a slight negative temperature dependence. This is in good agreement with experiments [613, 615, 617]. At temperatures roughly between 800 and 1000 K, both bimolecular channels, (R143) and (R144), become competitive. The rate constant governing the path to C_2H_3+H_2O shows a strong positive temperature dependence, which makes (R144) the predominant reaction channel >1000 K. Zhu *et al.* [523] provided the high- and low-pressure limits for (R142) in their paper, but resigned from further analysis of the fall-off regime. However, experiments concerning (R142) at room-temperature and low to near-atmospheric pressures [612, 614, 616]; as well as measurements of the high-pressure limit [618], all compare reasonably well with calculated values of k_{R142} confirming that the reaction is close to the high-pressure limit at ambient conditions. Zhu *et al.* also compared calculated values of

$k_{R142} + k_{R143} + k_{R144}$ with experimental data of $k_{C_2H_4+OH\rightarrow prod.}$ with an encouraging response. Based on these considerations, the present mechanism has adopted the calculated rate expressions from Zhu *et al.* [523] including the Lindemann expression for the pressure dependent reaction (R142).

Experimental characterization of reaction $C_2H_4+HO_2$ is limited to a number of relative rate measurements by Baldwin *et al.* [621–623] at intermediate temperatures from 673 to 773 K. These are all based on measured yields of oxirane (C_2H_4O), which is a potential product from the reaction. In the most recent of their studies, Baldwin *et al.* [623] combined new results with previous measurements to yield the rate constant $3.79 \times 10^{12} \exp\left(\frac{-17850}{RT}\right)$ $^{cm^3}/_{mol\,s}$ for $C_2H_4+HO_2 \rightleftharpoons C_2H_4O+OH$. It was argued that the reaction proceeds through intermediate formation of stable CH_2CH_2OOH before ring-closure. However, calculations of the potential energy surface of $C_2H_5+O_2$ [582, 584, 624]; that has $C_2H_4+HO_2$ as a potential product channel, have indicated an energetically more favorable path to CH_3CH_2OO (hereinafter denoted as C_2H_5OO in accordance with Table 5.4). Using high-level *ab initio* calculations, Rienstra-Kiracofe *et al.* [624] determined that the threshold energy for C_2H_5OO formation from association of $C_2H_4+HO_2$ is 12.1 $^{kcal}/_{mol}$ higher than the potential energy of the reactants. For comparison, Miller *et al.* [582] calculated a barrier height of 9.7 $^{kcal}/_{mol}$ using a Gaussian-2 like method [583], while Ignatyev *et al.* [584] obtained 11.2 $^{kcal}/_{mol}$ from density functional theory calculations. These values are all somewhat above the experimentally based value of 8.4 $^{kcal}/_{mol}$ deduced by Miller *et al.* [582] from rate coefficient measurements of $C_2H_5+O_2$ by Slagle *et al.* [572] and Wagner *et al.* [575]. Following Rienstra-Kiracofe *et al.* [624] and Miller *et al.* [582], the internal energy of the transition state governing the competitive channel to CH_2CH_2OOH lies at 14.4–14.6 $^{kcal}/_{mol}$ relative to the reactants. This yields a barrier difference of 2.3–4.9 $^{kcal}/_{mol}$ in favor of C_2H_5OO formation. The isomerization reaction $C_2H_5OO \rightarrow CH_2CH_2OOH$ is limited by a large barrier of 38 $^{kcal}/_{mol}$ relative to the C_2H_5OO ground state (average of [582, 624]). This is ∼3 $^{kcal}/_{mol}$ above the dissociation barrier to $C_2H_5+O_2$, but ∼5 $^{kcal}/_{mol}$ below the barrier governing dissociation to acetaldehyde (CH_3CHO+H), which has been assumed the main product channel in previous combustion modeling [105]. The reaction of $C_2H_4+HO_2$ to C_2H_5OO is already included in the mechanism via the reverse reaction (–R156) that originates from the theoretical work of Miller and Klippenstein [520] and is based on the referred potential energy surface calculations from Miller *et al.* [582]. However, this rate expression provides an almost temperature independent value of k_{-R156}, which does not reconcile with the expected energy barrier of $C_2H_4+HO_2 \rightarrow C_2H_5OO$. In contrast, the experimentally based activation energy for $C_2H_4+HO_2 \rightleftharpoons C_2H_4O+OH$ from Balwin *et al.* [623] is substantially higher than the calculated energy

barrier for the initial rate determining association step of C_2H_4+HO_2. It is noted that Baldwin *et al.* [621–623] used high absolute concentrations of O_2 for HO_2 radical generation via reaction with tetramethylbutane. This could have affected the interpretation of their results through inaccurately determined secondary reactions and, perhaps, explain the inconsistency between experimental and theoretical predictions. In the present mechanism, the reaction between C_2H_4 and HO_2 is represented by the reverse reactions (–R134) and (–R156) from the C_2H_5 and C_2H_5OO subsets despite the fact that $k_{-\mathrm{R156}}$ does not accurately reflect the expected activation energy barrier. Instead, the author emphasizes the need for improved experimental investigations of this complex reaction mechanism. The alternative H-abstraction channel C_2H_4+$HO_2 \rightleftharpoons C_2H_3$+$H_2O_2$ is endothermic with $\Delta_r H_{298} = 23\,^{\mathrm{kcal}}/_{\mathrm{mol}}$, which makes it an unlikely contributor to the removal of C_2H_4+HO_2 at the conditions relevant to the present study. This particular pathway was not considered in the referred potential energy surface calculations, since these were originally concerned with C_2H_5+O_2. Moreover, no experimental characterization has yet been undertaken.

There are no measurements of the initiation reaction of C_2H_4 with molecular oxygen (R145,R146). Benson [524] proposed a reaction mechanism involving initial association to the bi-radical adduct CH_2CH_2OO* that can dissociate through two possible pathways. One path involves H-atom migration to the peroxy-group with consequent reestablishment of the carbon double bond and finally dissociation of O–O to yield vinoxy radicals (H_2CCHO+OH (R145)). Benson [524] originally proposed formation of formylmethyl (CH_2CHO+OH) instead of vinoxy, but updated thermochemistry has shown that vinoxy formation is about $3\,^{\mathrm{kcal}}/_{\mathrm{mol}}$ more exothermic than formylmethyl. Alternatively, the fate of the bi-radical adduct involves ring-closure via association of the two unpaired electrons followed by cleavage of the O–O and C–C bonds to yield formaldehyde (CH_2O+CH_2O (R146)). From thermochemical considerations, Benson estimated that the initial adduct formation step will be rate-determining with an activation energy of about $39\,^{\mathrm{kcal}}/_{\mathrm{mol}}$ and that both pathways will contribute actively to the product formation. This proposed activation energy is substantially lower than the activation energy of the alternative direct abstraction reaction to C_2H_3+HO_2 that was estimated to $58\,^{\mathrm{kcal}}/_{\mathrm{mol}}$ by Tsang and Hampson [194] based on thermochemistry and analogies to the reaction C_2H_6+O_2. In the present work, analogies are preferably drawn to the reaction between C_2H_2 and O_2. This reaction was also considered by Benson [524], who outlined a very similar mechanism except that the ring-closure pathway is most likely the dominant route of C_2H_2+O_2 because the alternative path via H-migration and C≡C bond formation involves significant strain energy. Benson [524] proposed the up-

dated expression for $k_{C_2H_2+O_2\rightarrow prod.} = 7\times10^7 T^{1.8} \exp\left(\frac{-30600}{RT}\right)$ $^{cm^3}/_{mol\,s}$ instead of the earlier estimate by Miller *et al.* [625]. This temperature-dependent pre-exponential factor is adopted in the overall rate expression of C_2H_4+O_2 with Benson's estimated activation energy of 39 $^{kcal}/_{mol}$. Finally, a branching fraction of $k_{R145}/k_{R146} = 1$ has been estimated in the present study. The resulting rate expressions are expected to include substantial uncertainties and thus, call for experimental verification.

The reaction between C_2H_4 and CH_3 is only represented in the mechanism by the abstraction channel to C_2H_3+CH_4 (R147) despite indications from experiments [554, 563, 626–630] that the competitive association/stabilization reaction to *n*-propyl radicals (*n*-C_3H_7) is likely to predominate at temperatures roughly up to 1000 K. The preferred rate constant of (R147) is taken from the evaluation by Baulch *et al.* [145], which is based on the referred experimental work.

5.3.4.4 C_2H_3 Reactions

Vinyl radicals (C_2H_3) are important intermediates in combustion processes operated at high temperatures. The experimental database is fairly well established for most important elementary reactions [145], but there is still need for further characterization including potential energy surface calculations to accurately deduce governing reaction mechanisms and product branching ratios. When simple alkanes are combusted at intermediate temperatures, like in the present study, the formation of C_2H_3 is mainly expected to rise from thermal dissociation of intermediate C_2H_4 or H-abstraction from C_2H_4 by radical reactants. These are energy intensive pathways due to the large bond dissociation energy of CH_2CH–H ($D_{298} = 110.6 \pm 0.6$ $^{kcal}/_{mol}$ [631]), and as a consequence, C_2H_3 is not expected to play a significant role in the present study. Hence, only a few comments are provided in connection to the C_2H_3 reaction mechanism, which is mostly collected from the literature evaluations of Tsang and Hampson [194] and Baulch *et al.* [145].

The reaction of C_2H_3+H (R148,R149) is important in the C_2H_3 mechanism; especially the reverse dissociation of C_2H_4 (–R148), which is expected to be the main source of C_2H_3 radical formation at the investigated conditions. The available experimental data are limited to measurements at low pressure and temperatures below or near ambient; most recently by Fahr and co-workers [527, 632] and Monks *et al.* [526], who obtained values of the overall rate constant $k^{298}_{C_2H_3+H\rightarrow prod.}$ that range from $0.6 - 1.2\times10^{14}$ $^{cm^3}/_{mol\,s}$. The experimental work of Monks *et al.* [526] was undertaken in a discharge-flow system at 1.3 mbar of He using a mass spectrometer for product detection. Monks *et al.* measured the rate constant at both 213 and 298 K, which indi-

cated a slight positive temperature dependence. Fall-off extrapolations using the Troe formalism [184, 185] further provided high- and low-pressure limits of the addition/stabilization channel: $k_{\mathrm{R148},\infty} = 1.0 \times 10^{14}\,{}^{\mathrm{cm}^3}/_{\mathrm{mol\,s}}$, $k_{\mathrm{R148,0}} = 2.1 \times 10^{24} T^{-1.3}\,{}^{\mathrm{cm}^6}/_{\mathrm{mol}^2\,\mathrm{s}}$, with $F_{cent,\mathrm{R148}} = 0.49$. The high-pressure limit and the center broadening factor were determined specifically at 298 K. The high-pressure limit agrees well with the temperature dependent expression $k_{\mathrm{R148},\infty} = 3.88 \times 10^{13} T^{0.20}\,{}^{\mathrm{cm}^3}/_{\mathrm{mol\,s}}$ from recent *ab initio* calculations by Klippenstein and Harding [525, 633]. Monks *et al.* also conducted experiments with fully deuteriated vinyl radicals (C_2D_3) and comparison of C_2D_3H and HD yields as a measure of the branching ratio. This resulted in the values $k_{\mathrm{R148}}/k_{\mathrm{C_2H_3+H\rightarrow prod.}} = 0.24 \pm 0.09$ and 0.33 ± 0.13 at 213 and 298 K respectively, which is significantly higher than the corresponding calculated values of $k_{\mathrm{R148}}/k_{\mathrm{C_2H_3+H\rightarrow prod.}} = 0.047$ and 0.024 by Klippenstein and Harding [633] based on identical conditions as Monks *et al.* The preferred values of k_{R148} and k_{R149} are largely based on the work of Monks *et al.* [526], employing $k_{\mathrm{R148,0}}$ and $F_{cent,\mathrm{R148}}$ directly together with the temperature dependent expression of $k_{\mathrm{R148},\infty}$ from Harding *et al.* [525] that coincides with $k^{298}_{\mathrm{R148},\infty}$ from Monks *et al.* [526]. In addition, a constant value of $4.5 \times 10^{13}\,{}^{\mathrm{cm}^3}/_{\mathrm{mol\,s}}$ is used for k_{R149} consistent with the measurements by Monks *et al.* The author emphasizes the need for experimental verification of these rate constants at higher temperatures, but the uncertainty is accepted in the present study where C_2H_3 presumably plays a minor role.

The reaction between C_2H_3 and OH offers a potential pathway to ethenol (H_2CCHOH) via collisional stabilization of the adduct. This reaction could potentially gain influence at high pressure, but there are no experimental or theoretical determinations available. The only available rate constant for C_2H_3+OH is the estimated constant value of $k_{\mathrm{R151}} = 2 \times 10^{13}\,{}^{\mathrm{cm}^3}/_{\mathrm{mol\,s}}$ for the abstraction channel to C_2H_2+H_2O (R151), as originally proposed by Miller and Melius [254]. For want of more elaborate information about the association reaction, the author has considered assigning the pressure dependent rate constant of the analogue association reaction between C_2H_5 and OH (–R190) to the addition/stabilization channel. This analogue reaction originates from *ab initio* calculations by Marinov [138] and is included in the mechanism in the reverse direction. Calculations of $k_{-\mathrm{R190}}$ based on thermochemical data from Table 3.1 yield values on the order of $\sim 5 \times 10^{9}\,{}^{\mathrm{cm}^3}/_{\mathrm{mol\ s}}$ at atmospheric pressure. Moreover, it is noticed that $k_{-\mathrm{R190}}$ approaches $k_{-\mathrm{R190},\infty}$ at pressures above ambient and temperatures roughly below 800 K. Even though the analysis is based on the decomposition reaction of C_2H_5OH instead of H_2CCHOH, the difference of about four orders of magnitude between $k_{-\mathrm{R190}}$ and k_{R151} inevitably suggests the dominance of the abstraction channel from C_2H_3+OH to C_2H_2+H_2O (R151) over the association/stabi-

lization reaction. Consequently, no further efforts are made to revive the path from C_2H_3+OH to H_2CCHOH.

5.3.4.5 C_2H_5OO/C_2H_5OOH Reactions

Ethylperoxides (C_2H_5OO/C_2H_5OOH) are important species in the C_2 hydrocarbon oxidation chain at the high pressure and elevated temperature conditions relevant to the present study; similar to the vital role of methylperoxides (CH_3OO/CH_3OOH) in the conversion of C_1 hydrocarbons. The main route to C_2H_5OO is the addition/stabilization reaction between C_2H_5 and molecular oxygen (R133), which is promoted by high pressure and/or low temperatures. This reaction, as well as the related C_2H_5OO dissociation reaction to C_2H_4+HO_2 (R156), have already been discussed in connection to the C_2H_5 reaction mechanism in Section 5.3.4.2. Further conversion of the C_2H_5OO radical pool is expected to resemble the conversion of CH_3OO with ethoxy radicals (C_2H_5O), instead of methoxy (CH_3O), as the major product; either produced directly through addition/elimination reactions involving O–O bond dissociation, or indirectly via H-abstraction reactions and intermediate formation of stable C_2H_5OOH before dissociation to C_2H_5O+OH.

Unfortunately, there is a severe lack of experimental and theoretical data on elementary reactions involving C_2H_5OO and C_2H_5OOH. Consequently, rate coefficients for several reactions rely on estimates based on analogies between C_1 and C_2-peroxy chemistry. In most cases, this is expected to be a reasonable assumption considering the similarities of bond dissociation energies. Hence, $D_{298}(C_2H_5OO\text{–}H) = 84.8 \pm 2.2\,{}^{\text{kcal}}/_{\text{mol}}$ [134] is within range of $D_{298}(CH_3OO\text{–}H) = 87.8 \pm 1.0\,{}^{\text{kcal}}/_{\text{mol}}$ [134], and $D_{298}(C_2H_5O\text{–}OH) = 45.2\,{}^{\text{kcal}}/_{\text{mol}}$[1] compares reasonably well with $D_{298}(CH_3O\text{–}OH) = 42.6 \pm 1\,{}^{\text{kcal}}/_{\text{mol}}$ [133]. Despite the resemblance of bond dissociation energies, significant uncertainties are still attributed to the estimated rate constants; especially to the reactions from the CH_3OO/CH_3OOH subsets that have already been estimated from similar comparisons with analogue reactions involving HO_2. This is clearly not satisfactory considering the importance of hydrocarbonperoxy chemistry under the investigated conditions, and experimental and theoretical clarifications are most wanted.

The reaction of C_2H_5OO+HO_2 (R161) is one of the few elementary reactions from the C_2H_5OO subset that has been investigated experimentally. The interest in this reaction is mainly related to atmospheric chemistry research, where peroxyl radicals play important roles. Consequently, all measurements [528, 634–637] have been conducted at low temperatures cov-

[1] Calculated from $D_{298}(\text{R–X}) = H_{298}(\text{R}) + H_{298}(\text{X}) - H_{298}(\text{RX})$

ering the range 210–480 K. At room-temperature, measurements are scattered and k^{298}_{R161} ranges from $3.2 - 6.6 \times 10^{12}\,{}^{\mathrm{cm}^3}/_{\mathrm{mol\,s}}$ with an average value of $(4.7 \pm 2.4) \times 10^{12}\,{}^{\mathrm{cm}^3}/_{\mathrm{mol\,s}}$ based on all the referred studies. Dagaut *et al.* [635] measured the rate constant at 248–380 K and deduced the overall temperature dependent rate expression: $k_{\mathrm{C_2H_5OO+HO_2\rightarrow prod.}} = (3.4{\pm}1.4){\times}10^{11}$ $\exp\left[\frac{-(650{\pm}125)}{T}\right]\,{}^{\mathrm{cm}^3}/_{\mathrm{mol\,s}}$, which is in very good agreement with the expression $\left(4.2^{+1.3}_{-1.0}\right)\times10^{11}\exp\left[\frac{-(702{\pm}69)}{T}\right]\,{}^{\mathrm{cm}^3}/_{\mathrm{mol\,s}}$ proposed by Maricq and Szente [636] from a flash-photolysis study at 210–363 K. Fenter *et al.* [528] determined an activation energy that is nearly twice as high based on experiments at 248–480 K. All experiments applied UV absorption spectrometry to monitor radical decay profiles, and the results therefore depend on the accuracy of corresponding absorption cross sections; in particular the absorption cross section of C_2H_5OO, which has only been determined with a limited accuracy; see e.g. Lightfoot *et al.* [393] or Nielsen *et al.* [638]. On this background, Tyndall *et al.* [267] recently recommended an increase of the measurements of Dagaut *et al.* [635] by ∼5 %, while those of Fenter *et al.* [528] should be lowered by 10 %. Wallington and Japar [639] obtained a product yield of C_2H_5OOH of 102±6 % at 295 K using FTIR spectroscopy in excellent agreement with more recent measurements by Spittler *et al.* [640] yielding 104±5 % C_2H_5OOH and 2±4 % CH_3CHO; and Hasson *et al.* [641], who measured >93±10 % of C_2H_5OOH relative to other products. Both of the latter studies were conducted at near-ambient conditions. These observations indicate complete dominance of the direct abstraction channel to $C_2H_5OOH{+}O_2$ (R161) at room-temperature, which is supported by recent *ab initio* calculations from Hou *et al.* [642]. According to these calculations, the reaction to $C_2H_5OOH{+}O_2$ proceeds on the triplet surface. It is the exclusive product channel at ambient conditions due to a transition state positioned ∼2.3 ${}^{\mathrm{kcal}}/_{\mathrm{mol}}$ below the internal energy of the reactants. However, at elevated temperatures; roughly above 450 K, alternative reaction pathways on the singlet surface of $C_2H_5OO{+}HO_2$ start to compete. These mechanisms involve intermediate formation of a tetraoxide adduct $C_2H_5OOOOH^*$ that dissociates to products through ring-like transition states involving variations of H-atom transfer and O–O bond scission. The main alternative path yields $CH_3CHO{+}OH{+}HO_2$ with an energy barrier lying 6.5 ${}^{\mathrm{kcal}}/_{\mathrm{mol}}$ above the level of the reactants. According to Hou *et al.*, this pathway exhibits a positive temperature dependences. It becomes dominant above 600 K and yields values that are more than 10 times higher than k_{R161} at temperatures >900 K. Hou *et al.* calculated an overall rate constant that is in reasonable agreement with the previously referred experimental studies, but since these experiments exclusively fall in the temperature range where

$C_2H_5OOH+O_2$ formation dominates, it is currently impossible to verify the importance of alternative routes. Hence, the present mechanism only considers the pathway to $C_2H_5OOH+O_2$ (R161). This rate constant is taken from the evaluation by Tyndall *et al.* [267] and is based on the measured temperature dependence of Maricq and Szente [636] and the experimental average value of k^{298}_{R161} listed above. The resulting expression of k_{R161} consistently lies 50–60 % above the rate constant of the analogue reaction between CH_3OO and HO_2 at 298–500 K, which agrees qualitatively with the experimental findings of Boyd *et al.* [637], who noticed a slight, but general increase in the rate constants of RO_2+HO_2 with increasing size of R.

There are a significant number of measurements of the self-reaction of C_2H_5OO to $C_2H_5O+C_2H_5O+O_2$ (R171) and $CH_3CHO+C_2H_5OH+O_2$ (R172) [528, 576, 634, 643–649]. These all fall in the low-temperature range from 218 to 490 K. The room-temperature measurements of the overall rate constant are generally in good agreement, but there are some controversy regarding the temperature dependence where both slight positive [645,646,648] and negative [528] dependences have been reported, as well as zero temperature dependence [634]. The commonly applied experimental technique relies on photolysis of azoethane or Cl_2/C_2H_6 mixtures in excess O_2 as the radical source with UV absorption spectroscopy to monitor the second-order decay according to $\mathrm{d}\left[C_2H_5OO\right]/\mathrm{d}t = -2k_{obs}\left[C_2H_5OO\right]^2$. This is the same approach used in experimental investigations of the analogue self-reaction of CH_3OO that was previously discussed in Section 5.3.3.3, and the reader is referred to this section for a more elaborate discussion of implications related to this measuring technique. However, it is important to notice that a secondary removal of C_2H_5OO inevitably takes place in the chemical system via $C_2H_5OO+C_2H_5O \rightarrow$ prod., $C_2H_5O+O_2 \rightarrow CH_3CHO+HO_2$, and $C_2H_5OO+HO_2 \rightarrow$ prod. So essentially, the measured rate constant k_{obs} represents the overall removal rate of C_2H_5OO and needs a correction to yield the *true* overall rate constant of $C_2H_5OO+C_2H_5OO$ ($k_{true} = k_{\mathrm{R171}}+k_{\mathrm{R172}}$). Since the reaction between C_2H_5OO and HO_2 (R161) is significantly faster than the self-reaction of C_2H_5OO ($k_{\mathrm{R161}}/(k_{\mathrm{R171}}+k_{\mathrm{R172}}) = 95$ at 298 K), the observed and the true rate constants can be correlated by $k_{obs} = (1+\alpha)[k_{\mathrm{R171}}+k_{\mathrm{R172}}]$, with $\alpha = k_{\mathrm{R171}}/\left(k_{\mathrm{R171}}+k_{\mathrm{R172}}\right)$; similar to the self-reaction of CH_3OO [393]. The preferred temperature dependent expression of $\alpha = \beta/(1+\beta)$, where $\beta = 10.2\exp\left(\frac{-533}{T}\right)$, has been obtained from the literature evaluation of Lightfoot *et al.* [393] and is based on the temperature dependent branching ratio measurements by Anastasi *et al.* [645] (302–373 K) with an adjustment to match the average room-temperature value of $\alpha_{298} = 0.63 \pm 0.06$ determined from results of Niki *et al.* [644], Anastasi *et al.* [645], and Wallington *et al.* [647]. The most recent experimental study of the temperature de-

pendence of C_2H_5OO+C_2H_5OO → prod. by Fenter *et al.* [528] covers the most extensive temperature range from 248 to 490 K. The highest temperatures considered by Fenter *et al.* gave rise to some additional challenges, because these approach the temperature range where the thermal unimolecular decomposition of ethoxy radicals ($C_2H_5O(+M) \rightarrow CH_3+CH_2O(+M)$ (R183)) starts to compete against the reaction with O_2. It can be expected that the CH_3 radicals produced via (R183) will react with O_2 via (R36) to form CH_3OO that will react further; initially with C_2H_5OO, and later with itself, to produce a variety of oxygenated hydrocarbon species; eventually resulting in a very complicated chemical system. Fenter *et al.* [528] observed a change in the experimental decay profiles at the highest temperature of their study (490 K), which could not be matched purely by a second-order kinetic expression. This was attributed to the rising interference from thermal decomposition of C_2H_5O. In order to substantiate this postulate, they developed a simple kinetic model, including a scheme for C_2H_5O decomposition, which provided an excellent prediction of the affected decay profiles and further indicated a minor appearance of CH_3OO. Fenter *et al.* consequently limited their rate constant derivation of the self-reaction to the results obtained from 248 to 460 K where second-order kinetics provided a good correlation. Based on this, they derived the following expressions of k_{obs} and $k_{R171} + k_{R172}$, where the latter was obtained by division of k_{obs} with the temperature dependent expression of $(1 + \alpha)$ from Lightfoot *et al.* [393]. Hence, $k_{obs} = (8.43 \pm 0.7) \times 10^{10} \exp\left[\frac{-(20\pm40)}{T}\right]$ $^{cm^3}/_{mol\,s}$ and $k_{R171} + k_{R172} = (4.0 \pm 0.4) \times 10^{10} \exp\left(\frac{60\pm40}{T}\right)$ $^{cm^3}/_{mol\,s}$. As previously mentioned, other studies have opposed the slight negative temperature dependence reported by Fenter *et al.*, but this discussion is mainly relevant for the temperature range below ambient, which has little interest in the present study. The lack of experimental verification at temperatures relevant to combustion (>500 K) is of more concern, but clearly, it will be a difficult task to achieve this due to the interference from thermal decomposition reactions. The individual values of k_{R171} and k_{R172} in Table 5.4 are fitted expressions based on $k_{R171} + k_{R172}$ from Fenter *et al.* [528] and $\alpha(T)$ from Lightfoot *et al.* [393].

At the elevated temperatures used in the present study, thermal unimolecular dissociation of C_2H_5OOH (R173) is expected to provide the primary drain of C_2H_5OOH, similar to CH_3OOH; see Section 5.3.3.4. The early work of Kirk and Knox [650] has provided the only experimental characterization using temperatures and pressures from 553–653 K and 13–26 mbar. The experiments were conducted in a flow reactor system under pyrolytic conditions with benzene as bath gas and resulted in the Arrhenius expression $k_{R173} = 10^{(13.4\pm0.3)} \exp\left[\frac{-(37700\pm700)}{RT}\right]$ $^1/_s$. It is reasonable to expect the reaction to be

in the fall-off range at the conditions applied by Kirk and Knox. In the present situation, the author assigns the pressure dependent rate expression of the analogue decomposition reaction of CH_3OOH (R59) obtained from *ab initio* calculations by Zhu and Lin [266]. Within the investigated temperature interval of Kirk and Knox, the experimental rate expression lies a factor of ∼2 above the calculated rate expression for atmospheric pressure, which is an acceptable deviation considering the lack of other experimental and/or theoretical data for verification.

Hydrogen-atom abstraction from the alkyl group is expected to be more pronounced for C_2H_5OOH compared to CH_3OOH considering the presence of secondary H atoms. However, due to the lack of experimental data, rate constants for the H-abstraction reactions (R174), (R177), and (R179) have all been adopted directly from corresponding reactions with CH_3OOH assuming CH_3CHOOH (1-hydroperoxyethyl) to be the dominant radical product analogues to CH_2OOH. This approach probably implies an underestimation of the involved rate constants, because the effect of secondary H atoms is not included. However, like CH_2OOH, the author expects CH_3CHOOH to undergo rapid dissociation at the O–O bond and subsequent irreversible formation of CH_3CHO+OH (R182) with little influence on model predictions. Pressure dependent rate expressions have been obtained from a recent *ab initio* study by Bozzelli and co-workers [271] and carry great resemblance to the corresponding rate constants for CH_2OOH dissociation (R68) predicting a very short lifetime of CH_3CHOOH regardless of the applied conditions.

5.3.4.6 C_2H_5O Reactions

The thermal unimolecular dissociation of C_2H_5O proceeds either through scission of the C–C bond to yield CH_3+CH_2O (R183), or by elimination of one of the secondary H atoms to form CH_3CHO+H (R184). Batt [651] used novel static reactor experiments as well as previous, e.g. [141, 652], to derive limiting rate constants at high pressure: $k_{\mathrm{R183},\infty} = 1.0 \times 10^{15} \exp\left(\frac{-21600}{RT}\right)$ 1/s and $k_{\mathrm{R184},\infty} = 2.51 \times 10^{14} \exp\left(\frac{-23400}{RT}\right)$ 1/s. The underlying experimental conditions ranged from 393 to 491 K and near-atmospheric pressure. Choo and Benson [653] later reconsidered the former expression using more accurate thermochemistry to determine an updated value of $k_{\mathrm{R183},\infty} = 4.0 \times 10^{13} \exp\left(\frac{-20000}{RT}\right)$ 1/s. Within recent years, a number of studies of the thermal decomposition of C_2H_5O have been published [272, 529, 654, 654–657] as well as some reviews [516, 658, 659]. Among these, Caralp *et al.* [529] conducted the only experimental investigation by measuring complete fall-off curves at total pressures between 0.001 and 60 bar and temperatures from 391 to 471 K. In order to cover this wide pressure range, two different experimental techniques were

employed involving laser-flash photolysis and a fast-flow reactor, where the latter technique enabled measurements at the lowest pressures (<0.01 bar). Both setup used laser-induced fluorescence to monitor the C_2H_5O decay profiles. Under the investigated conditions, dissociation to CH_3+CH_2O predominated and low- and high-pressure limiting rate coefficients could be directly determined from the experiments by an analysis of the measured fall-off curves yielding $k_{\mathrm{R183},0} = [\mathrm{He}]\, 2.0 \times 10^{16} \exp\left(\frac{-13970}{RT}\right)$ $^{\mathrm{cm}^3}/_{\mathrm{mol\,s}}$, $k_{\mathrm{R183},\infty} = 1.1 \times 10^{13} \exp\left(\frac{-16790}{RT}\right)$ $^1/_{\mathrm{s}}$, and $F_{cent,\mathrm{R183}} = 0.76 - \frac{T}{2060}$. Caralp *et al.* also conducted supplementary *ab initio* and density functional theory (DFT) calculations that showed excellent agreement with the experimental measurements and provided a reliable view of the potential energy surface of the reaction. The latter indicated that the energy barrier governing the C–C bond dissociation channel lies about 3 $^{\mathrm{kcal}}/_{\mathrm{mol}}$ below the barrier for the competitive C–H bond dissociation, and hence, explains the dominance of (R183) at low temperatures. The theoretical work further enabled Caralp *et al.* to calculate the high-pressure limit of the competitive pathway to CH_3CHO+H: $k_{\mathrm{R184},\infty} = 1.3 \times 10^{13} \exp\left(\frac{-20060}{RT}\right)$ $^1/_{\mathrm{s}}$. The experimental values of $k_{\mathrm{R183},\infty}$ from Caralp *et al.* [529] lie significantly higher than the values reported by Choo and Benson [653] based on the "corrected" experimental data from Batt and co-workers referred above. This discrepancy can, to some extent, be attributed to the applied pressure range in the early experiments where the reaction is still slightly within the fall-off region. More recent *ab initio* calculations by Somnitz and Zellner [655, 656] at 220–300 K yielded $k_{\mathrm{R183},0} = 1.0 \times 10^{18} \exp\left(\frac{-17180}{RT}\right)$ $^{\mathrm{cm}^3}/_{\mathrm{mol\,s}}$ and $k_{\mathrm{R183},\infty} = 2.95 \times 10^{13} \exp\left(\frac{-17940}{RT}\right)$ $^1/_{\mathrm{s}}$ in reasonable agreement with the results from Caralp *et al.* [529] when extrapolating the calculated rate expressions to the experimental temperature range 391–471 K. Hence, $k_{\mathrm{R183},\infty}$ from Somnitz and Zellner [656] is 40–20 % below the experimental rate coefficient, while $k_{\mathrm{R183},0}$ spans from 20 % above to 60 % below the experimentally based expression. Somnitz and Zellner assumed N_2 as collision partner for the calculations, while Caralp *et al.* used He in their experiments, but it is impossible to deduce any reliable indications of the impact of different bath gases from a first-hand comparison, considering the large deviations in the individual Arrhenius parameters. The latter is to be expected when the fitted data points all lie within short temperature intervals. In another recent theoretical study, Rauk *et al.* [657] obtained $k_{\mathrm{R183},\infty} = 4.0 \times 10^{13} \exp\left(\frac{-16810}{RT}\right)$ $^1/_{\mathrm{s}}$, which consistently lies a factor of 3.6 above the experimental rate expression from Caralp *et al.* [529]. However, Rauk *et al.* pointed out themselves that their calculations predicted a surprisingly low activation energy of 6.0 $^{\mathrm{kcal}}/_{\mathrm{mol}}$ for the reverse association reaction CH_3+$CH_2O \rightarrow C_2H_5O$ (–R183) compared to the experimentally determined value of 7.4 $^{\mathrm{kcal}}/_{\mathrm{mol}}$ [653], which could have led to the observed systematic de-

sprecancy concerning $k_{\mathrm{R183},\infty}$. In the present work, the experimentally based expression of k_{R183} from Caralp *et al.* [529] is preferred including the broadening factor $F_{cent,\mathrm{R183}} = 0.78 \exp\left(\frac{-T}{1235}\right)$ in Troe-format; see Section 5.2.2.1, which is fitted to discrete values of $F_{cent,\mathrm{R183}}$ from [529] across the experimental temperature range 391–471 K. It is noted that the application of the preferred rate expression in the present study involves extrapolations to temperatures outside experimental verification, which implies an increased uncertainty; especially considering the narrow temperature interval underlying the rate constant derivation. Owing to the dominance of the C–C bond dissociation channel at low temperatures, recent studies of the alternative channel to CH_3CHO+H (R184) have all been theoretical and concerned with the limiting rate constant at high pressure. Hippler *et al.* [272] compared high level *ab initio* calculations for several larger alkoxy radicals from their previous work [529, 660, 661] with "cheap" small-basis set DFT calculations and obtained a very good agreement between transition structures and energies. Confident that the DFT calculations provided a sufficiently accurate predictive tool, they further calculated activation barriers and Arrhenius parameters for the high-pressure limits for several alkoxy radical decomposition reactions including $k_{\mathrm{R184},\infty} = 2.0 \times 10^{13} \exp\left(\frac{-23450}{RT}\right)$ 1/s. For comparison, Zhang *et al.* [654] calculated the expression $k_{\mathrm{R184},\infty} = 1.30 \times 10^{9} T^{1.42} \exp\left(\frac{-20470}{RT}\right)$ 1/s using the QCISD(T) method developed by Pople *et al.* [662], while Rauk *et al.* [657] proposed a value of $k_{\mathrm{R184},\infty} = 2.45 \times 10^{13} \exp\left(\frac{-20920}{RT}\right)$ 1/s from *ab intio* CBS-RAD calculations. The proposed expressions of $k_{\mathrm{R184},\infty}$ by Batt [651], Caralp *et al.* [529], Hippler *et al.* [272], Rauk *et al.* [657], and Zhang *et al.* [654] show significant scatter when extrapolated towards high temperatures. This may again be attributed to the relatively narrow temperature ranges considered in all the referred studies. Again, the preferred rate expression is taken from Caralp *et al.* [529], which lies within 50 % range of the average extrapolated value of $k_{\mathrm{R184},\infty}$ at 500–1000 K. None of these studies provide rate coefficients for the low-pressure limit of (R184) suitable for implementation in kinetic modeling. As a consequence, (R184) is only represented by the high-pressure limit in the present mechanism. This undoubtedly results in an overprediction of the contribution from the C–H dissociation channel unless very high pressures are applied. Hence, at atmospheric pressure, (R184) becomes dominant at temperatures above 690 K, while it happens >1130 K at 50 bar. This may be within reason, but experimental and/or theoretical verification is needed.

Direct measurements of C_2H_5O+O_2 (R187) are available from Gutman *et al.* [409], Hartmann *et al.* [663], and Fittschen *et al.* [530], who all used laser-photolysis/laser-induced fluorescence with C_2H_5ONO/O_2 mixtures in the low-temperature range. These experiments cover temperatures from 295–

411 K, and the obtained values of k_{R187} are in very good agreement within the common range 296–353 K. Relative rate measurements reported by Zabarnick and Heicklen [664] at 225–393 K, and recent *ab initio* results from Setokuchi and Sato [665] at 200–400 K confirm the direct measurements. The preferred rate expression is drawn from the most recent work by Fittschen *et al.* [530] yielding $k_{R187} = (1.45 \pm 0.5) \times 10^{10} \exp\left[\frac{-(645\pm240)}{RT}\right]$ $^{cm^3}/_{mol\,s}$, but experimental verification remains of relevance at the elevated temperature range considered in the present study.

The abstraction reactions between C_2H_5O and H (R185), and OH (R186), are expected to be fast and proceed with little or no energy barrier. The activation energies are probably less than 1 $^{kcal}/_{mol}$; similar to the analogue reactions between CH_3O+H (R70,R71) and CH_3O+OH (R74). There are no available measurements of the rate coefficients of (R185) and (R186), so in the present mechanism, estimated constant rate coefficients of 3×10^{13} $^{cm^3}/_{mol\,s}$ have been assigned to both reactions. The reaction between C_2H_5O+H may have other potential product channels, e.g. C_2H_5+OH, C_2H_4+H_2O, and CH_3+CH_2OH. However, according to *ab initio* calculations by Marinov [138], these dissociation channels all exhibit energy barriers that lie significantly higher than the internal energy of the reactants. As a consequence, they are not expected to contribute significantly at the temperatures of interest in the present study compared to the direct abstraction reaction.

5.3.4.7 C_2H_5OH and 1-/2-C_2H_4OH Reactions

Complete reaction subsets for ethanol (C_2H_5OH) and the two alkyl radical derivatives 1- and 2-hydroxyethyl (1-C_2H_4OH and 2-C_2H_4OH) have been adopted from the detailed kinetic model of Marinov [138] that describes high-temperature combustion of C_2H_5OH. The C_2H_5OH subset includes rate coefficients for multichannel decomposition of C_2H_5OH and H-abstraction reactions according to the general scheme: C_2H_5OH+X → products, where X = H, O, OH, HO_2, and CH_3. The multichannel decomposition reaction includes pathways to CH_2OH+CH_3 (R189), C_2H_5+OH (R190), C_2H_4+H_2O (R191), and CH_3CHO+H_2 (R192) that were all analyzed via RRKM/master equation calculations. An empirical branching ratio estimation procedure was applied to determine the temperature dependent branching ratios of the H-abstraction from the three distinct reaction sites in C_2H_5OH yielding C_2H_5O, 1-C_2H_4OH, and 2-C_2H_4OH respectively. This procedure utilized available kinetic and thermochemical data from analogue reactions with the two model compounds: methanol (CH_3OH) and propane (C_3H_8), including corrections to account for the different availability of H atoms. These two compounds

were selected for the comparison because they exhibit similar bond strengths and structural properties as C_2H_5OH. The resulting rate constants were eventually subjected to thorough discussions and comparisons with available data from the literature, even though the latter was limited to comparisons with some single-temperature measurements of C_2H_5OH+X and some scattered experimental and theoretical data concerning the decomposition reaction. The reader is referred to Ref. [138] for an elaborate discussion. Radical-radical reactions with 1- and 2-C_2H_4OH are expected to be fast and fairly independent of temperature. Marinov [138] estimated constant rate coefficients for these reactions. Experimental data are generally not available except for 1-C_2H_4OH+O (R209) and 1-C_2H_4OH+H (R210+R211), where a few low-temperature studies have been reported [666–668] proposing rate coefficients in good agreement with the estimated values by Marinov. Eventually, Marinov [138] validated the complete detailed kinetic model against experimental data sets obtained from several very different experimental systems including laminar flames, shock tubes, and jet-stirred and turbulent flow reactors; all with a satisfactory response. The considered reaction subset was validated across a temperature and pressure range of 1000–1700 K and 1–4.5 bar respectively, as well as stoichiometric ratios from slightly lean to rich (0.5–2).

5.3.4.8 CH_3CHO/CH_3CO Reactions

Acetaldehyde (CH_3CHO) is either converted via thermal unimolecular dissociation to CH_3+HCO ($D_{298} = 84.9\,{}^{\text{kcal}}/_{\text{mol}}$[2]), or by H-abstraction to formylmethyl (CH_2CHO) or acetyl radicals (CH_3CO) facilitated by radical reactants. The latter path involves H–C scission of the primary H atom ($D_{298} = 89.66\,{}^{\text{kcal}}/_{\text{mol}}$ [137]), which is thermodynamically favored by a significantly lower bond strength compared to the secondary H–C bond scission ($D_{298} = 97.9\,{}^{\text{kcal}}/_{\text{mol}}$[2]) leading to CH_2CHO. This suggests that the unimolecular dissociation reaction to CH_3+HCO will predominate at the high pressure and intermediate temperature conditions applied in the present work, with a minor contribution from the H-abstraction pathway to CH_3CO. At the temperature range of interest, the only favorable argument of CH_2CHO formation is the higher availability of secondary H atoms in CH_3CHO. A similar comparison of bond dissociation energies of CH_3CO; $D_{298}(CH_3\text{–}CO) = 11.1\,{}^{\text{kcal}}/_{\text{mol}}$[2] and $D_{298}(H\text{–}CH_2CO) = 43.2\,{}^{\text{kcal}}/_{\text{mol}}$[2], provides strong indications that C–C scission prevails over further radical abstraction of H atoms and subsequent C=C bond formation to ketene (CH_2CO). The mechanism presented in Ta-

[2]Calculated from $D_{298}(\text{R–X}) = H_{298}(\text{R}) + H_{298}(\text{X}) - H_{298}(\text{RX})$

ble 5.4 includes complete reaction subsets of CH_3CHO, CH_3CO, CH_2CHO, and CH_2CO with rate coefficient drawn from literature evaluations, well-established combustion modeling, and individual studies of elementary reaction rates. Here, the discussion will be limited to the important unimolecular dissociation reactions of CH_3CHO (R217) and CH_3CO (R229).

Several earlier studies of the dissociation of CH_3CHO to CH_3+HCO (R217) are available, e.g. [669–673]. Colket *et al.* [671] studied the pyrolysis of 1 % CH_3CHO diluted in N_2 in a turbulent flow reactor at temperatures from roughly 1000 to 1200 K and ambient pressure. These measurements were combined with earlier static pyrolysis data of pure CH_3CHO from Laidler and Liu [669, 670] at temperatures around 800 K from which, they derived a high-pressure limiting rate constant. The assumption that the reaction would be at the high-pressure limit at 1 bar was contradicted by the work of Ernst and co-workers [672, 673], who conducted high-temperature (1350–1650 K) pyrolysis experiments behind reflected shock waves in CH_3CHO/Ar mixtures at a wide pressure range from 0.2–73 bar and observed fall-off behavior even at the highest pressure. In a recent combined experimental and theoretical study, Gupte *et al.* [531] used shock wave heating of CH_3CHO/Kr mixtures with laser schlieren density gradient measurements at 1550–2400 K and 53–667 mbar, as well as modern RRKM calculations employing high-level *a priori* varational transition state theory and two-dimensional master equation simulations to fit the experiments in the fall-off region. Their low-pressure experiments were well-predicted by the *ab initio* calculations. Moreover, excellent agreement was obtained with the high-pressure measurements of $k_{\mathrm{R217},\infty}$ and fall-off curves at 1400, 1500, and 1600 K from Ernst and co-workers [672, 673]. The present mechanism therefore applies the pressure dependent rate expression proposed by Gupte *et al.* [531] including low- and high-pressure limiting rate coefficient and fall-off parameters in Troe-format.

Measurements of the unimolecular decomposition of CH_3CO to CH_3+CO (R229) are limited to a few low-temperature photolysis studies in the fall-off range, e.g. Watkins and Word [674], Anastasi and Maw [675], and Baldwin *et al.* [676], that cover temperatures and pressures from 260–500 K and 0.004–2.8 bar. Baulch *et al.* [145] used these data to determine $k_{\mathrm{R229},\infty} = 2.0 \times 10^{13} \exp\left(\frac{-8630}{T}\right)$ $1/\mathrm{s}$ including a minor correction in order to reconcile with experimental data from the reverse association reaction [675]. The low-pressure limit $k_{\mathrm{R229},0} = 6.0 \times 10^{15} \exp\left(\frac{-7080}{T}\right)$ $\mathrm{cm^3/mol\,s}$ was fitted to the fall-off data from Bencsura *et al.* [677] with He as collision partner and a center broadening factor of $F_{cent,\mathrm{R229}} = 0.5$. This experimentally based rate expression is generally in good agreement with calculated rate coefficients at specific pressures (0.01, 0.025, 0.1, 1, 10, and 100 bar of Ar; and k_∞) reported by Senosiain *et al.* [534]. These expressions were obtained from a

RRKM/master equation model and they all fall less than a factor of 2 above the recommended expression by Baulch *et al.* [145] at 400–1000 K; which is covered by the estimated uncertainty limit reported by Baulch *et al.* for Ar as bath gas. It is expected that Ar resembles N_2 more accurately than He in terms of collision efficiency, and since N_2 is applied as diluent in the present experimental work, the preferred rate coefficients are those obtained from the theoretical work of Senosiain *et al.* [534].

5.3.5 NO_x Reaction Mechanism

It is well established that NO and NO_2 radicals can significantly enhance hydrocarbon oxidation at low and intermediate temperatures [44, 45, 105, 107, 108,110,139,678,679]. This sensitizing behavior is a result of interactions with the radical pool as well as direct reactions between NO_x and stable species, e.g. H_2, O_2, CH_4, CH_2O, and C_2H_6. A number of reactions take place that recycle NO and NO_2 directly or through intermediate formation and subsequent decomposition of nitrous acid (HONO); both within the $H/O/OH/HO_2$ and the hydrocarbon radical pool. These NO/NO_2 recycling mechanisms promote the hydrocarbon oxidation scheme; either indirectly via formation of important chain-carrying radicals, like OH and CH_3; e.g. $NO_2+H \rightleftharpoons NO+OH$ (R270), $NO+HO_2 \rightleftharpoons NO_2+OH$ (R260), $NO_2+HO_2 \rightleftharpoons HONO/HNO_2+O_2$ (R276,R277), $NO_2+CH_4 \rightleftharpoons HONO/HNO_2+CH_3$ (R284,R285), and $HONO (+M) \rightleftharpoons NO+OH(+M)$ (–R259); or by direct acceleration of the hydrocarbon oxidation chain; most importantly $NO+CH_3OO \rightleftharpoons NO_2+CH_3O$ (R266), $NO_2+CH_3 \rightleftharpoons NO+CH_3O$ (R283), and $NO_2+CH_2O \rightleftharpoons HONO/HNO_2+HCO$ (R289,R290).

The NO_x reaction mechanism is provided in Table 5.5 including direct reactions between NO_x and hydrocarbon species. Some of these are association reactions to form nitrated hydrocarbons, e.g. CH_3NO, CH_3NO_2, and $C_2H_5NO_2$, that may gain importance at the current high pressure conditions. Some reactions only play secondary roles under the conditions of interest, and hence, will not be discussed in detail. Compounds like N_2O and N_xH_y are not included in the mechanism, since these are only formed from NO_x at temperatures beyond those relevant to this study. Relevant subsets for these species can, however, be obtained from previous combustion models, e.g. [233, 680–682], in order to extend the operational temperature range of the present mechanism.

Table 5.5: Reactions from the NO_x reaction mechanism. Units are mol, cm, s, cal.

	Reactions	A	β	E	Note/Ref.
	NO (nitric oxide)				
257.	$NO + H(+M) \rightleftharpoons HNO(+M^a)$	1.52×10^{15}	–0.41	0	[683]
	Low-pressure limit:	2.36×10^{14}	0.206	–1550	[684]
	Troe parameters: 0.82 10^{-30} 10^{30} 10^{30}				
[b]258.	$NO + O(+M) \rightleftharpoons NO_2(+M)$	1.30×10^{15}	–0.75	0	[683]
	Low-pressure limit:	4.72×10^{24}	–2.87	1550	
	Troe parameters: 0.88 10^{-30} 10^{4} 10^{30}				1 bar
	Troe parameters: 0.87 10^{-30} 10^{30} 10^{30}				10 bar
	Troe parameters: 0.85 10^{-30} 10^{30} 10^{30}				20 bar
	Troe parameters: 0.82 10^{-30} 10^{30} 10^{30}				50 bar
	Troe parameters: 0.78 10^{-30} 10^{30} 10^{30}				100 bar
259.	$NO + OH(+M) \rightleftharpoons HONO(+M)$	1.10×10^{14}	–0.3	0	[685]
	Low-pressure limit:	3.39×10^{23}	–2.5	0	
	Troe parameters: 0.75 10^{-30} 10^{30} 10^{30}				
260.	$NO + HO_2 \rightleftharpoons NO_2 + OH$	2.05×10^{12}	0.0	–497	[145]
261.	$NO + CH_3(+M) \rightleftharpoons CH_3NO(+M)$	9.00×10^{12}	0.0	192	[686]
	Low-pressure limit:	2.50×10^{16}	0.0	–2841	
	Troe parameters: 5.0 10^{-30} 120 10^{30}				see text
262.	$NO + HCO \rightleftharpoons HNO + CO$	6.90×10^{12}	0.0	0	[687]
263.	$NO + CH_2OH \rightleftharpoons HNO + CH_2O$	1.30×10^{12}	0.0	0	[688]
[c]264.	$NO + CH_3O \rightleftharpoons HNO + CH_2O$	7.53×10^{12}	0.0	2017	[689]
		2.49×10^{18}	–2.56	0	
265.	$NO + CH_3O(+M) \rightleftharpoons CH_3ONO(+M)$	5.99×10^{14}	–0.6	0	[689]
	Low-pressure limit:	8.14×10^{25}	–2.8	0	
	Troe parameters: 1.0 10^{-30} 900 10^{30}				

Continues on next page

Continued from last page

	Reactions	A	β	E	Note/Ref.
266.	$NO + CH_3OO \rightleftharpoons NO_2 + CH_3O$	1.40×10^{12}	0.0	–715	[690]
267.	$NO + C_2H_5OO \rightleftharpoons NO_2 + C_2H_5O$	1.60×10^{12}	0.0	–755	[690]
268.	$NO + C_2H_5O \rightleftharpoons HNO + CH_3CHO$	6.60×10^{12}	0.0	0	[691]
269.	$NO + C_2H_5O(+M) \rightleftharpoons C_2H_5ONO(+M)$	1.20×10^{13}	0.0	–143	[530]
	Low-pressure limit:	9.43×10^{19}	0.0	0	[691]
	Troe parameters: 0.6 10^{-30} 10^{30} 10^{30}				[690]
	NO_2 (nitrogen dioxide)				
270.	$NO_2 + H \rightleftharpoons NO + OH$	1.32×10^{14}	0.0	362	[692]
271.	$NO_2 + H_2 \rightleftharpoons HONO + H$	1.30×10^{4}	2.76	29770	[693]
272.	$NO_2 + H_2 \rightleftharpoons HNO_2 + H$	2.43×10^{0}	3.73	32400	[142]
273.	$NO_2 + O \rightleftharpoons NO + O_2$	1.05×10^{14}	–0.52	0	[694]
274.	$NO_2 + O(+M) \rightleftharpoons NO_3(+M)$	3.52×10^{12}	0.24	0	[695]
	Low-pressure limit:	2.45×10^{20}	–1.5	0	
	Troe parameters: 0.71 10^{-30} 1700 10^{30}				
275.	$NO_2 + OH(+M) \rightleftharpoons HONO_2(+M)$	3.00×10^{13}	0.0	0	[696]
	Low-pressure limit:	2.94×10^{25}	–3.0	0	
	Troe parameters: 0.4 10^{-30} 10^{30} 10^{30}				
276.	$NO_2 + HO_2 \rightleftharpoons HONO + O_2$	1.91×10^{0}	3.32	3044	[142]
277.	$NO_2 + HO_2 \rightleftharpoons HNO_2 + O_2$	1.85×10^{1}	3.26	4983	[142]
278.	$NO_2 + NO_2 \rightleftharpoons NO + NO + O_2$	4.51×10^{12}	0.0	27600	[693]
279.	$NO_2 + NO_2 \rightleftharpoons NO_3 + NO$	9.64×10^{9}	0.73	20900	[683]
280.	$NO_2 + NO(+M) \rightleftharpoons N_2O_3(+M)$	1.62×10^{9}	1.4	0	[697]

Continues on next page

Continued from last page

	Reactions	A	β	E	Note/Ref.
	Low-pressure limit:	1.33×10^{33}	–7.7	0	
	Troe parameters: 0.6 10^{-30} 10^{30} 10^{30}				
281.	$NO_2 + NO_2(+M) \rightleftharpoons N_2O_4(+M)$	6.00×10^{12}	0.0	0	[697]
	Low-pressure limit:	1.31×10^{24}	–3.8	0	
	Troe parameters: 0.4 10^{-30} 10^{30} 10^{30}				
282.	$NO_2 + CO \rightleftharpoons NO + CO_2$	9.03×10^{13}	0.0	33800	[698]
283.	$NO_2 + CH_3 \rightleftharpoons NO + CH_3O$	4.00×10^{13}	–0.2	0	[139]
284.	$NO_2 + CH_4 \rightleftharpoons HONO + CH_3$	6.50×10^{14}	0.0	45800	[699]
285.	$NO_2 + CH_4 \rightleftharpoons HNO_2 + CH_3$	6.00×10^{14}	0.0	37600	[699]
286.	$NO_2 + HCO \rightleftharpoons NO + CO_2 + H$	2.30×10^{13}	0.0	0	[687]
287.	$NO_2 + HCO \rightleftharpoons HONO + CO$	4.95×10^{12}	0.0	0	[687]
288.	$NO_2 + HCO \rightleftharpoons NO + CO + OH$	4.95×10^{12}	0.0	0	[687]
289.	$NO_2 + CH_2O \rightleftharpoons HONO + HCO$	1.42×10^{-7}	5.64	9220	[700]
290.	$NO_2 + CH_2O \rightleftharpoons HNO_2 + HCO$	1.07×10^{-1}	4.22	19850	[700]
291.	$NO_2 + CH_2OH \rightleftharpoons HONO + CH_2O$	5.00×10^{12}	0.0	0	[688]
292.	$NO_2 + CH_3O \rightleftharpoons HONO + CH_2O$	6.00×10^{12}	0.0	2285	[701]
293.	$NO_2 + CH_3O(+M) \rightleftharpoons CH_3ONO_2(+M)$	2.19×10^{15}	–0.88	0	[702]
	Low-pressure limit:	2.91×10^{23}	–1.74	0	
	Troe parameters: 0.6 10^{-30} 10^{30} 10^{30}				
294.	$NO_2 + CH_3OH \rightleftharpoons HONO + CH_2OH$	1.45×10^{2}	3.32	20035	[703]
295.	$NO_2 + CH_3OH \rightleftharpoons HNO_2 + CH_2OH$	2.41×10^{3}	2.90	27470	[703]
296.	$NO_2 + C_2H_5 \rightleftharpoons NO + C_2H_5O$	4.00×10^{13}	–0.2	0	($= k_{R283}$)

Continues on next page

Continued from last page

	Reactions	A	β	E	Note/Ref.
297.	$NO_2 + C_2H_5O \rightleftharpoons HONO + CH_3CHO$	1.70×10^{12}	0.0	0	[704, 705]
298.	$NO_2 + C_2H_5O(+M) \rightleftharpoons C_2H_5ONO_2(+M)$	5.06×10^{15}	–1.0	0	[706]
	Low-pressure limit:	5.88×10^{30}	–4.0	0	
	Troe parameters: 0.6 10^{-30} 10^{30} 10^{30}				
299.	$NO_2 + C_2H_6 \rightleftharpoons HONO + C_2H_5$	6.50×10^{14}	0.0	41400	est[d]
300.	$NO_2 + C_2H_6 \rightleftharpoons HNO_2 + C_2H_5$	6.00×10^{14}	0.0	33200	est[e]
	NO_3 (nitrate radical)				
301.	$NO_3 + H \rightleftharpoons NO_2 + OH$	6.00×10^{13}	0.0	0	[707]
302.	$NO_3 + O \rightleftharpoons NO_2 + O_2$	1.00×10^{13}	0.0	0	[226]
303.	$NO_3 + OH \rightleftharpoons NO_2 + HO_2$	1.40×10^{13}	0.0	0	[226]
304.	$NO_3 + HO_2 \rightleftharpoons NO_2 + O_2 + OH$	1.50×10^{12}	0.0	0	[707]
305.	$NO_3 + NO_2 \rightleftharpoons NO_2 + NO + O_2$	5.00×10^{10}	0.0	2940	[708]
	HNO (nitrosyl hydride)				
306.	$HNO + H \rightleftharpoons NO + H_2$	4.40×10^{11}	0.72	650	[709]
307.	$HNO + O \rightleftharpoons NO + OH$	2.30×10^{13}	0.0	0	[710]
308.	$HNO + OH \rightleftharpoons NO + H_2O$	1.30×10^{7}	1.88	–956	[711]
309.	$HNO + O_2 \rightleftharpoons HO_2 + NO$	2.20×10^{10}	0.0	9140	[712]
[c]310.	$HNO + NO_2 \rightleftharpoons HONO + NO$	4.42×10^{4}	2.64	4040	[713]
311.	$HNO + CH_3 \rightleftharpoons NO + CH_4$	2.30×10^{14}	0.0	8400	see text
312.	$HNO + HCO \rightleftharpoons NO + CH_2O$	5.83×10^{-1}	3.84	115	[714]
313.	$HNO + CH_3O \rightleftharpoons NO + CH_3OH$	3.20×10^{13}	0.0	0	[715]

Continues on next page

Continued from last page

	Reactions	A	β	E	Note/Ref.
314.	$HNO + CH_2OH \rightleftharpoons NO + CH_3OH$	3.00×10^{13}	0.0	0	[716]
	HONO (nitrous acid)				
315.	$HONO + O \rightleftharpoons NO_2 + OH$	1.20×10^{13}	0.0	5960	[683]
316.	$HONO + OH \rightleftharpoons NO_2 + H_2O$	1.70×10^{12}	0.0	–520	[717]
317.	$HONO + NO_2 \rightleftharpoons HONO_2 + NO$	2.00×10^{11}	0.0	32700	[693]
318.	$HONO + HONO \rightleftharpoons NO + NO_2 + H_2O$	3.49×10^{-1}	3.64	12140	[718]
	HNO_2 (nitrous acid isomer)				
319.	$HNO_2(+M) \rightleftharpoons HONO(+M)$	2.50×10^{14}	0.0	32300	[142]
	Low-pressure limit:	3.10×10^{18}	0.0	31500	
	Troe parameters: 1.149 10^{-30} 3125 10^{30}				
320.	$HNO_2 + O \rightleftharpoons NO_2 + OH$	1.70×10^{8}	–1.5	2000	[719]
321.	$HNO_2 + OH \rightleftharpoons NO_2 + H_2O$	4.00×10^{13}	0.0	0	[142]
	$HONO_2$ (nitric acid)				
322.	$HONO_2 + H \rightleftharpoons H_2 + NO_3$	5.56×10^{8}	1.5	16400	[720]
323.	$HONO_2 + H \rightleftharpoons H_2O + NO_2$	6.08×10^{1}	3.3	6285	[720]
324.	$HONO_2 + H \rightleftharpoons OH + HONO$	3.82×10^{5}	2.3	6976	[720]
325.	$HONO_2 + OH \rightleftharpoons H_2O + NO_3$	1.03×10^{10}	0.0	–1240	[721]
	CH_3NO_2 (nitromethane)				
326.	$CH_3NO_2(+M) \rightleftharpoons NO_2 + CH_3(+M)$	1.78×10^{16}	0.0	58500	[139, 722]
	Low-pressure limit:	1.26×10^{17}	0.0	42000	

Continues on next page

Continued from last page

	Reactions	A	β	E	Note/Ref.
	Troe parameters: 0.183 10^{-30} 10^{30} 10^{30}				
327.	$CH_3NO_2 + H \rightleftharpoons HONO + CH_3$	3.27×10^{12}	0.0	0	[139]
328.	$CH_3NO_2 + H \rightleftharpoons CH_3NO + OH$	1.40×10^{12}	0.0	3730	[139]
329.	$CH_3NO_2 + H \rightleftharpoons CH_2NO_2 + H_2$	5.40×10^{2}	3.5	5200	[139]
330.	$CH_3NO_2 + O \rightleftharpoons CH_2NO_2 + OH$	1.50×10^{13}	0.0	5350	[139]
331.	$CH_3NO_2 + O_2 \rightleftharpoons CH_2NO_2 + HO_2$	2.00×10^{13}	0.0	57000	[110]
332.	$CH_3NO_2 + OH \rightleftharpoons CH_3OH + NO_2$	2.00×10^{10}	0.0	–1000	[139]
333.	$CH_3NO_2 + OH \rightleftharpoons CH_2NO_2 + H_2O$	5.00×10^{5}	2.0	1000	[139]
334.	$CH_3NO_2 + HO_2 \rightleftharpoons CH_2NO_2 + H_2O_2$	3.00×10^{12}	0.0	23000	[110]
335.	$CH_3NO_2 + CH_3 \rightleftharpoons CH_2NO_2 + CH_4$	5.50×10^{-1}	4.0	8300	[139]
336.	$CH_3NO_2 + CH_3O \rightleftharpoons CH_2NO_2 + CH_3OH$	3.00×10^{11}	0.0	7000	[110]
337.	$CH_3NO_2 + NO_2 \rightleftharpoons CH_2NO_2 + HONO$	3.00×10^{11}	0.0	32000	[139]
	CH_2NO_2 (nitromethyl radical)				
338.	$CH_2NO_2 \rightleftharpoons NO + CH_2O$	1.00×10^{13}	0.0	36000	[139]
339.	$CH_2NO_2 + H \rightleftharpoons NO_2 + CH_3$	5.00×10^{13}	0.0	0	[110]
340.	$CH_2NO_2 + O \rightleftharpoons NO_2 + CH_2O$	5.00×10^{13}	0.0	0	[110]
341.	$CH_2NO_2 + OH \rightleftharpoons NO_2 + CH_2OH$	1.00×10^{13}	0.0	0	[110]
342.	$CH_2NO_2 + OH \rightleftharpoons HONO + CH_2O$	1.00×10^{13}	0.0	0	[110]
	$C_2H_5NO_2$ (nitroethane)				
343.	$C_2H_5NO_2(+M) \rightleftharpoons NO_2 + C_2H_5(+M)$	2.00×10^{15}	0.0	54000	see text
	Low-pressure limit:	1.00×10^{18}	0.0	36000	[723]

Continues on next page

Continued from last page

	Reactions	A	β	E	Note/Ref.
344.	$C_2H_5NO_2 + OH \rightleftharpoons NO_2 + C_2H_5OH$	2.00×10^{10}	0.0	–1000	($= k_{R332}$)
	CH_3ONO/C_2H_5ONO (methyl- and ethylnitrite)				
345.	$CH_3ONO + OH \rightleftharpoons NO_2 + CH_3OH$	6.00×10^{13}	0.0	3505	[724]
346.	$C_2H_5ONO + OH \rightleftharpoons NO_2 + C_2H_5OH$	1.57×10^{14}	0.0	3505	see text, [724]
	$CH_3ONO_2/C_2H_5ONO_2$ (methyl- and ethylnitrate)				
347.	$CH_3ONO_2 + OH \rightleftharpoons HONO_2 + CH_3O$	4.94×10^{11}	0.0	2027	[725]
[c]348.	$C_2H_5ONO_2 + OH \rightleftharpoons HONO_2 + C_2H_5O$	2.22×10^{12}	0.0	2140	[725]
		3.20×10^{10}	0.0	–250	

a: Enhanced third-body efficiency: $N_2 = 1.6$
b: Troe parameters fitted to $F_{cent,R258} = 0.95 - 1 \times 10^{-4}T$ [683]
c: Expressed as the sum of the rate constants
d: Pre-exponential factor: (R284). Activation energy: (R284) subtracted difference in $\Delta_r H_{298}$
e: Pre-exponential factor: (R285). Activation energy: (R285) subtracted difference in $\Delta_r H_{298}$

5.3.5.1 NO Reactions

The reaction between NO and H has two important product channels leading to collisionally stabilized HNO (R257) and N+OH. At high temperatures, (–R257) also becomes an important HNO decomposition channel. Formation of N+OH is strongly endothermic with $\Delta_r H_{298} = 48\,^{\mathrm{kcal}}/_{\mathrm{mol}}$, which makes it unimportant at the temperature range of interest. The third pathway to NH+O is even more endothermic than the N+OH channel by about $23\,^{\mathrm{kcal}}/_{\mathrm{mol}}$ and is therefore also neglected. The association channel (R257) has mainly been studied at room temperature; and only in the forward direction [145]. Clyde and Thursh [726] conducted experiments at 700 K, and the recommendation by Tsang and Herron [683] strongly relies on this work. Hydrogen is the preferred bath gas in most studies, whereas investigations of collision partners of more practical importance, like N_2 and H_2O, are limited to indirect determinations. Campbell and Handy [727] estimated the rate constant at 395 K based on discharge flow-stirred reactor experiments with $H_2/O_2/NO$, while Allen *et al.* [728] and Glarborg *et al.* [729] used a complex mechanism and N_2-diluted flow reactor results from the N_2O/H_2 system at 995 K and $CO/O_2/H_2O/NO$ system at 1000–1170 K respectively to fit the rate constant. The flow reactor results are in good agreement with the recent direct measurements of the low-pressure limit at 295–905 K by Riley *et al.* [684], who used a high-temperature photochemistry reactor with Ar as bath gas. The low-temperature estimate by Campbell and Handy agrees well with Tsang and Herron [683], whereas the two flow reactor studies [728, 729] and the direct measurements [684] around 1000 K consistently fall about a factor of three below the recommended value by Tsang and Herron. This may be the result of uncertainties in the estimated third-body efficiency of N_2 by Tsang and Herron or the characterization of the pressure dependency in general. The present mechanism has adopted the low-pressure limit from Riley *et al.* [684], including their recommended enhanced third-body efficiency factor of 1.6 for N_2, together with the high-pressure limit from Tsang and Herron [683] and recommended fall-off parameters. The author is aware that this description of the fall-off region is questionable due to the uncertain characterization of the pressure dependency.

Two possible product channels are available for the reaction between NO and O leading to collisionally stabilized NO_2 (R258) and $N+O_2$. Again, the bimolecular pathway only becomes important at high temperatures outside the range of interest in the current study and it is therefore neglected. The recombination reaction is well characterized across wide temperature and pressure intervals, e.g. [730–733]; and old [683] and recent [145] literature based evaluations are generally in good agreement. The present mechanism

has adopted the high- and low-pressure limits from Tsang and Herron [683]. The Troe parameters are given at specific pressures based on a fit to the original center broadening factor from Tsang and Herron, $F_{cent,\mathrm{R258}} = 0.95 - 1 \times 10^{-4} T$, that does not comply with the required format of the Chemkin input file [186]. The pressure dependent rate expression in Table 5.5 is valid for N_2 as collision partner, but a separate expression for M = Ar is also available from Tsang and Herron [683].

The association reaction of NO+OH to HONO (R259) plays an important role in the HO_x cycle by either consuming or liberating (through the reverse reaction) OH radicals depending on the reaction conditions. In the present study, (–R259) is expected to gain particular importance as a major OH formation channel due to the establishment of a significant HONO pool from NO_2+H_2 ⇌ HONO+H (R271), NO_2+HO_2 ⇌ HONO+O_2 (R276), and isomerization of HNO_2 (R319). The addition reaction NO+OH(+M) ⇌ HONO(+M) has only been studied at lower temperatures in the range of 100–500 K, see e.g. [683, 697] for an overview. Tsang and Herron [683] based their recommendation on available low-temperature data combined with transition state and RRKM calculations to extend the temperature and pressure range and yield high- and low-pressure limits at temperatures up to 2500 K with N_2 as bath gas. They accompanied their final rate expression with an uncertainty factor ranging from 1.4 at room temperature to a value of 3 at the highest temperature. Recent experimental investigations of the pressure dependence of (R259) by Forster *et al.* [734] (1–150 bar) and Fulle *et al.* [685] (1–1400 bar) both used He as bath gas and maximum temperatures of 298 and 400 K respectively. The pressure dependent rate constant proposed by Fulle *et al.* matches the recommendation by Tsang and Herron at low pressures and/or high temperatures, but exceeds it by more than a factor of 4 at 100 bar and elevated temperatures relevant to this study. The more recent experimentally based rate expression from Fulle *et al.* [685] is preferred in the present study despite the uncertainties related to the temperature extrapolation and change of collision partner compared to the rate constant from Tsang and Herron.

The reaction NO+HO_2 ⇌ NO_2+OH (R260) is one of the most important reactions in the NO_x sensitized conversion of hydrocarbon fuels, because it effectively substitutes less reactive HO_2 radicals with highly reactive OH radicals. *Ab initio* calculations [735] indicate that NO_2+OH is the predominant product channel following an addition/stabilization mechanism with HOONO* as the intermediate adduct and subsequent 1,2-migration of the HO-group prior to bond cleavage. Only at very high temperatures may the reaction give rise to a competitive yield of HNO+O_2, but this is of no importance at the temperature range of interest in the present study. The rate con-

stant for (R260) is well-established from more recent experiments [736–741] that cover the overall temperature range 206–1760 K. The preferred rate constant from Baulch *et al.* [145] is based on these data; in particular, the discharge flow reactor results from Howard [738,739] (232–1271 K) and Seeley *et al.* [741] (206–295 K) that are in excellent agreement and allowed Baulch *et al.* to assign a small uncertainty factor of 1.4 to the rate constant estimate. The experiments by Seeley *et al.* were conducted at varying pressures from 93–253 mbar, but showed no signs of a pressure effect. This observation was confirmed by room-temperature measurements by Bohn and Zetzsch [742] at 0.1–1 bar. Support of the preferred rate constant is also found in the more scattered results from Leu [737] at 270–425 K, and the room-temperature measurement by Hack *et al.* [740]. High-temperature data for the reverse reaction, i.e. $k_{-\mathrm{R260}}$, from Glänzer and Troe [736] (1340–1760 K) are also consistent with the preferred rate constant even though these data involve a number of uncertainties related to important side reaction.

5.3.5.2 NO_2 Reactions

The reaction NO_2+H $\rightleftharpoons$ NO+OH (R270) is an important source of OH radicals. A large body of experimental data are available in the low to intermediate temperature range [145], but a comparison of the measurements reveals significant scatter; especially at temperatures above 400 K. Earlier data [743, 744] indicate a rate constant that may be up to two times faster than more recent measurements [692]. Baulch *et al.* [145] recommended a least square fit to all available data within 230–800 K yielding an activation energy of 676 $^{\mathrm{cal}}/_{\mathrm{mol}}$. However, the low to medium-temperature photochemistry experiments (260–760 K) by Ko and Fontijn [692] indicate a smaller activation energy of 362 $^{\mathrm{cal}}/_{\mathrm{mol}}$ for the reaction. Their recommended rate constant matches the evaluation of Baulch *et al.* [145] at room temperature, but yields values that are lower by a factor of 1.4–1.7 across the temperature range 500–1300 K. The recent shock-tube study by Su *et al.* [745] covered temperatures in the range 1100–2000 K. They interpreted the results in terms of a temperature independent rate constant, supported by earlier low-temperature data from Michael *et al.* [746], but the resulting rate constant falls significantly below the recommendation by Baulch *et al.* at high temperatures. However, the scatter in their data prevents an accurate determination of the activation energy. The present mechanism applies the rate constant of k_{R270} from Ko and Fontijn [692] that exhibits a low reported uncertainty limit of ±21 %. *Ab initio* calculations by Nguyen *et al.* [747] indicate that (R270) completely predominates over the stabilization of the unimolecular products, i.e. NO_2+H(+M) $\rightleftharpoons$ HNO_2/HONO(+M), except

at high-pressure/low-temperature conditions beyond those relevant to this study (>100 bar and <298 K). As a consequence, (R270) is the only product channel from NO_2+H included in the mechanism.

The reaction between NO_2 and O has two competing product channels. Most experimental data on the bimolecular channel to NO+O_2 (R273) fall in the low-temperature region, see e.g. [683,697]. Bemand *et al.* [694] measured k_{R273} at temperatures from 298–1055 K with an overall uncertainty factor of 1.37 using two independent discharge flow systems. Tsang and Herron [683] recommended the slightly higher low-temperature estimate (230–350 K) from Atkinson *et al.* [748], but extended the valid temperature range to 200–2500 K, while keeping the original uncertainty factor of 1.2 from Atkinson *et al.* At temperatures below 350 K, the discrepancy between measurements of Bemand *et al.* and literature recommendations of Tsang and Herron is less than 10 %, but the deviation increases at higher temperatures to yield values outside the uncertainty limits above 1200 K. This study prefers the measured rate constant from Bemand *et al.* [694] due to the extended temperature validation. Experimental characterization of the competing addition reaction to NO_3 (R274) is restricted to the low-temperature region. Tsang and Herron [683] recommended the high-pressure limit from Atkinson *et al.* [748] (200–400 K) with an uncertainty factor of 2 together with an extrapolated low-pressure limit to cover the temperature range of 200–2500 K and N_2 as collision partner. The rate constant used in the present mechanism has been adopted from Hahn *et al.* [695], who conducted a combined experimental and theoretical study of the temperature and pressure dependence of (R274) using laser flash-photolysis and trajectory calculations on standardized valence potentials of the involved species at conditions ranging from 300–400 K and 1–900 bar N_2 atmosphere. The proposed rate constant agrees well with values from Tsang and Herron at temperatures and pressures below 500 K and 100 bar. However, further extrapolation to 800 and 1100 K yields values that are about 1.5–2 times higher than predicted by k_{R274} from Tsang and Herron [683].

The reactions of NO_2+H_2 to HONO+H (R271) and HNO_2+H (R272) constitute the principal initiation mechanism in the H_2/NO_x system. Tsang and Herron [683] recommended the use of k_{R271} from Slack and Grillo [749], which is based on shock tube measurements of the ignition delay of H_2/air mixtures perturbated with NO_2 at 760–1000 K and 1–4 bar. It is noted that Tsang and Herron assigned a high uncertainty factor of 5 to this rate expression. More recent investigations [169,693,750] indicate that k_{R271} should be somewhat lower. Expressions of k_{R271} and k_{-R271} were derived by Park *et al.* [693] based on *ab initio* calculations with transition state parameters from Hsu *et al.* [751]. These rate constants are in good agreement

with the single flow reactor measurement at 833 K reported by Mueller *et al.* [750]. No previous reports have mentioned the alternative product channel to HNO_2+H (R272), which is a thermodynamically less stable species of HONO. Even so, the competitive formation of HNO_2 may be important because HNO_2 cannot dissociate to OH radicals like HONO. Instead, it may act to remove OH through HNO_2+OH $\rightleftharpoons$ NO_2+H_2O (R321). However, recent *ab initio* CBS-QB3 calculations by Marshall [142] (see more details in Section 5.3.5.12) indicate that (R272) is unimportant at temperatures roughly <1600 K, while the path to HNO_2 can be associated with ∼10 % of the product yield from NO_2+H_2 at temperatures >1600 K. Marshall calculated the rate constant $k_{R272} = 2.43T^{3.73} \exp\left(\frac{-16306}{T}\right)$ $^{cm^3}/_{mol\,s}$ across the temperature range 700–2000 K including an Eckart tunneling correction [752] that contributed less than a factor of 1.45 within the investigated temperature range. Similarly, H-atom tunneling only affected the calculated expression of $k_{R271} = 12.4T^{3.70} \exp\left(\frac{-14733}{T}\right)$ $^{cm^3}/_{mol\,s}$ by a factor of 1.2. The rate constant of k_{R271} from Marshall confirms the previous value of k_{R271} from Park *et al.* [693], which is therefore still recommended for combustion modeling. It is noted that the referred experimental studies of NO_2+H_2 by Slagle and Grillo [749], and Mueller *et al.* [750] were both conducted at temperatures <1000 K, where formation of HNO_2 is negligible, so it is unlikely that the previous experimental rate determinations of k_{R271} have been subjected to secondary interference from (R272). The present mechanism includes the calculated expressions of k_{R271} and k_{R272} from Park *et al.* [693] and Marshall [142] respectively, even though it is evident that (R271) will be the dominant product channel at conditions relevant to the present work.

Experimental data on the NO_2+OH association reaction to $HONO_2$ (R275) are available at low temperatures (<480 K) [697, 753–755], while a few dissociation experiments (–R275) have been reported at 800–1200 K [756, 757]. At high pressures, the reaction is complicated by competitive formation of the HOONO isomer [755, 758, 759]. Troe [696] conducted a theoretical analysis of the temperature and pressure dependence of (R275) over the range 50–1400 K and pressures up to 1000 bar. Troe also considered the impact from potential formation of HOONO based on an estimated rate expression, and found it to be negligible at pressures below 1 bar, whereas yields up to 20 % may occur at 100 bar and 200–400 K. HOONO is also the intermediate adduct in the important OH formation reaction NO+HO_2 $\rightleftharpoons$ NO_2+OH (R260), which is energetically favored in the forward direction [735]. Consequently, it is expected that HOONO will mainly redissociation back to NO_2+OH with no net impact on concentrations of species involved in (R275). The preferred expression of k_{R275} has been adopted from the work of Troe [696] and is consistent with the available experimental data

despite a limited accuracy of the estimated values of F_{cent}, $k_{\mathrm{R275},0}$, and $k_{\mathrm{R275},\infty}$ due to uncertainties in a number of important molecular parameters.

A recent flow reactor and detailed kinetic modeling study of NO_x/hydrocarbon interactions by Glarborg *et al.* [113] has identified NO_2+HO_2 $\rightleftharpoons$ HONO+O_2 (R276) as an important HO_2 removal channel in competition with HO_2+ HO_2 $\rightleftharpoons$ H_2O_2+O_2 (R15) and NO+HO_2 $\rightleftharpoons$ NO_2+OH (R260). Glarborg *et al.* used $k_{\mathrm{R276}} = 6.3 \times 10^7 T^{1.25} \exp\left(\frac{-5000}{RT}\right)$ $^{\mathrm{cm}^3}/_{\mathrm{mol\,s}}$ from Hori *et al.* [760], whose estimate complies with the room temperature upper limit [761] and rate constant data derived from high-temperature shock tube measurements by Glänzer and Troe [736]. The accuracy of the latter results are, however, in question due to uncertainties in important side reactions. Hori *et al.* [760] disregarded the competitive formation of HNO_2+O_2 (R277) and used (R276) as the sole product channel from NO_2+HO_2 in a detailed kinetic model with 126 species and >600 reactions from the NO_x/C_{1-3} system without any further discussion or reasoning. The uncertainty of this estimated rate constant is expected to be in the range of one to two orders of magnitude. Chan and Pritchard [762] recently published an *ab initio* study of important reactions from the HNO_2 subset including recommendations for both k_{R276} and k_{R277}. These calculations favored the HNO_2+O_2 product channel (R277) over HONO+O_2 (R276) by more than a factor of two at temperatures above 500 K, and suggested that the overall rate constant for NO_2+HO_2 should be one to five orders of magnitude lower than estimate by Hori *et al.* at temperatures ranging from ∼2000 K towards ambient. The reaction mechanism has recently been scrutinized by Marshall [142] based on as yet unpublished *ab initio* CBS-QB3 calculations; see Section 5.3.5.12 for more details. It seems that at sub-ambient temperatures, NO_2 and HO_2 predominantly add to form stabilized $HOONO_2$, as described by Gierzcak *et al.* [763], but this pathway is suppressed at elevated temperatures relevant to combustion; including the intermediate temperature range considered in the present study. Here, the reactants instead form a hydrogen-bonded adduct at the entrance of the reaction coordinate favoring the orientation leading to HONO+O_2 (H$\cdots$N association is weaker than H$\cdots$O for NO_2). However, while hydrogen-bonding stabilizes the transition state to HONO+O_2, it also makes the entropy unfavorable, and consequently, the reaction to HONO+O_2 (R276) becomes slower relative to HNO_2+O_2 (R277) when the temperature increases. The predicted rate expressions for k_{R276} and k_{R277} by Marshall [142] are included in the model in Table 5.5. It is seen that $k_{\mathrm{R277}}/k_{\mathrm{R276}} > 1$ at temperatures roughly >500 K, and the ratio yields values of 2.4 and 3.3 at 1000 and 1500 K respectively. The overall rate constant $k_{\mathrm{R276}} + k_{\mathrm{R277}}$ is more than 10 times lower than the expression from Hori *et al.* [760], but substantially higher than the corresponding overall rate con-

stant calculated by Chan and Pritchard [762].

Reactions are available to account for the direct conversion between NO, NO_2 (R278), NO_3 (R279, R305), and the dimers N_2O_3 (R280) and N_2O_4 (R281). This conversion is driven by increasing pressure and the availability of molecular oxygen, e.g. through $NO+NO+O_2 \rightleftharpoons NO_2+NO_2 \rightleftharpoons N_2O_4$, whereas increasing temperatures promote the reverse decomposition reactions. A shock tube study of the thermal decay of NO_2 by Röhrig *et al.* [732] has recently provided experimental data for (R278) and (R279) at high temperatures (1350–2100 K). Park *et al.* [693] combined these data for (R278) with results from pyrolysis experiments with NO_x at intermediate temperatures (602–954 K) to yield an expression of k_{R278} across the temperature range 600–1450 K. Data for (–R278) are also available from Olbregts [764], who conducted static reactor experiments with NO/O_2 mixtures at intermediate temperatures from 226–758 K. They obtained an expression of k_{-R278} that agrees within 15 % of the expression advocated by Park *et al.* at temperatures from 600–1450 K. The rate constant for the bimolecular channel $NO_2+NO_2 \rightleftharpoons NO_3+NO$ (R279) has been adopted from Tsang and Herron [683], who based their recommendation on the low-temperature evaluation by Atkinson *et al.* [748] as well as high-temperature shock tube data from Freund and Palmer [698]. The data from Freund and Palmer showed considerable scatter, which led Tsang and Herron to estimate an uncertainty factor of 5 at temperatures above 600 K. Nevertheless, a comparison of k_{R279} from Tsang and Herron with the high-temperature measurements from Röhrig *et al.* [732] reveals excellent agreement within a factor of 1.2 at 1350–2100 K.

Rate constants governing the formation of the dimers N_2O_3 (R280) and N_2O_4 (R281) have been drawn from the evaluation by Atkinson *et al.* [697] including fall-off parameters and corrections for N_2 as collision partner. These rate constants are largely based on the low-temperature studies by Markwalder *et al.* [765] and Borrel *et al.* [766]. Formation of N_2O_5 from NO_2+NO_3 is not included in the mechanism due to an expected low availability of NO_3.

The direct oxidation of CO by NO_2 (R282) has been characterized in a number of experimental studies. The early high-temperature shock tube measurements from Milks *et al.* [767], and Freund and Palmer [698, 768] are all in excellent agreement. They are also consistent with earlier studies at moderate to high temperatures (500–1500 K), e.g. [769–772]. On this background, Tsang and Herron [683] recommended the direct use of the rate constant from Freund and Palmer [698] including the original experimental uncertainty factor of 2.5. The present work follows this recommendation.

5.3.5.3 NO_x/Alkane Reactions

NO_x radicals exhibit a certain affinity for H-atom abstraction from CH_4, which has significant potential in relation to low-temperature initiation of CH_4. Yamaguchi and co-workers [699, 773] conducted a theoretical study of the selective oxidation of CH_4 with NO_x at 800 K and 1 bar with particular emphasis on the NO_x induced H-abstraction from CH_4 based on *ab initio* molecular orbital theory. These calculations confirmed that NO_2+CH_4 has two important product channels forming CH_3 and either of the two isomers HONO (R284) and HNO_2 (R285), where the latter is favored by a slightly lower energy barrier. A comparison with the corresponding initiation reaction CH_4+O_2 $\rightleftharpoons$ CH_3+HO_2 (–R40) indicates that the energy barrier is lowered by about 20–25 $^{kcal}/_{mol}$ when NO_2 is the reactant rather than O_2. In the earlier of their two papers, Yamaguchi *et al.* [699] also considered the initiation reaction NO+CH_4 $\rightleftharpoons$ HNO+CH_3 (–R311), but the potential energy surface calculations revealed a barrier height of similar magnitude as CH_4+O_2. Consequently, NO_2+CH_4 is expected to prevail as the dominant initiation reaction in the $CH_4/O_2/NO_x$ system. It is noticed that the reverse reaction of NO+CH_4 (i.e. HNO+CH_3 $\rightleftharpoons$ NO+CH_4 [R311]) faces a lower energy barrier of +8.4 $^{kcal}/_{mol}$ relative to HNO+CH_3, and hence, may become important for CH_3 radical termination at elevated temperatures. This reaction will be discussed in Section 5.3.5.11. A theoretical study by Chan *et al.* [774] have presented *ab initio* calculations of the NO_2 induced initiation of different aliphatic hydrocarbon fuels at 600–1100 K, including CH_4 and C_2H_6, based on a similar level of theory as Yamaguchi and co-workers. Contrary to Yamaguchi and co-workers, who only considered the typical *trans*-isomer of HONO, Chan *et al.* distinguished between the *cis*- and the *trans*-isomer and found that the reaction path to *cis*-HONO has the lowest activation energy, while the channel to *trans*-HONO has the largest activation energy with formation of the third isomer HNO_2 lying in between. Chan *et al.* explained the lower energy path through the *cis*-configuration by the involvement of a transition state composed of a five-membered ring-like structure with its attendant stabilization. This phenomenon has previously been reported by Bofill *et al.* [411] in connection to the reaction between CH_3O+O_2. The transition state leading to *cis*-HONO is, however, much tighter than the transition state for HNO_2 formation due to the constrained nature of the involved ring-structure, so Chan *et al.* still predicted a slightly higher rate coefficient for HNO_2 formation. A comparison between the proposed rate coefficients from Yamaguchi and co-workers [699, 773] and Chan *et al.* [774] shows excellent agreement above 700 K for the reaction path leading to HNO_2, whereas the rate coefficient from Chan *et al.* for the for-

mation of *trans*–HONO is higher than the rate constant from Yamaguchi and co-workers by a factor of 23 at 600 K falling to a factor 3 at 1100 K. *trans*-HONO is only slightly more energetically favorable than *cis*-HONO; by about 0.3 $^{\mathrm{kcal}}/_{\mathrm{mol}}$ [775], and there is a relatively high *cis/trans* interconversion barrier of 11.7 $^{\mathrm{kcal}}/_{\mathrm{mol}}$. This means that once *cis*-HONO is formed, e.g. via NO_2+CH_4, it is likely to remain in the reaction mixture. Unfortunately, there are no experimental results available to substantiate the theoretical predictions regarding the product distribution from NO_2+CH_4. Early shock tube experiments were conducted at 1300–1900 K by Slack and Grillo [776], who proposed an activation energy of 30.0 $^{\mathrm{kcal}}/_{\mathrm{mol}}$ for the reaction between NO_2 and CH_4; originally with a pre-exponential factor of 7.0×10^{11} that was later revised to 1.2×10^{13} $^{\mathrm{cm}^3}/_{\mathrm{mol\,s}}$ [777]. Slack and Grillo only considered one reaction channel to HONO+CH_3, so their proposed rate coefficient may be considered as an overall rate constant. The theoretically predicted overall rate coefficients from Yamaguchi and co-workers [699, 773] and Chan *et al.* [774]; obtained by summation of individual reaction channels, both lie considerably higher than the experimental value at 1300–1900 K. The theoretical prediction from Chan *et al.* reveals the largest deviation by a factor of 4 at 1300 K increasing to a factor of 11 at 1900 K. However, all experimental and theoretical values are consistent within a factor of 2.5 in the intermediate temperature range 800–1100 K. The present mechanism has adopted the theoretical rate coefficients from Yamaguchi and co-workers [699,773], which means that no distinction is made between the *cis*- and the *trans*-isomer of HONO. This has also been the common approach in previous modeling work. It is expected that HONO is primarily removed through dissociation, i.e. HONO(+M) $\rightleftharpoons$ NO+OH(+M) (–R259). Considering the almost identical energy content of the *cis*- and *trans*-isomers, it is expected that their dissociation rate constants will also be similar, in which case, the potential error invoked by neglecting the different isomeric structures will be minimal. It is noted, though, that bimolecular reactions with *cis*- and *trans*-HONO may exhibit very different rate constants, as specified by Chan and Pritchard [762] in their proceeding publication about the subject. An alternative choice of k_{R284} is the combined value of $k_{\mathrm{NO_2+CH_4 \rightarrow \textit{trans}\text{-HONO+CH_3}}}$ + $k_{\mathrm{NO_2+CH_4 \rightarrow \textit{cis}\text{-HONO+CH_3}}}$ from Chan *et al.* [774]. This would have resulted in a significantly higher value of k_{R284} than currently applied in the mechanism, but experimental investigations are needed to clarify this discrepancy.

There are no experimental studies of the corresponding initiation reaction between NO_2+C_2H_6 (R299,R300), but the reaction is expected to proceed similar to NO_2+CH_4. In the absence of prior investigations, rate coefficients are therefore estimated based on k_{R284} and k_{R285} for NO_2+CH_4 with a correction of the activation energies of -4.4 $^{\mathrm{kcal}}/_{\mathrm{mol}}$ to reflect the difference in

$\Delta_r H_{298}$. These estimates need experimental and/or theoretical verification; especially considering the uncertainties related to NO_2+CH_4; as discussed above.

5.3.5.4 NO_x/Alkyl Reactions

A key reaction in NO_x sensitized oxidation of hydrocarbon fuels is the disproportionation reaction of NO_2+CH_3 to NO+CH_3O (R283). The reaction takes place via adduct formation with a side production of collisionally stabilized CH_3NO_2 (nitromethane) (–R326), which may become substantial at the high pressure conditions used in the present work. *Ab initio* calculations [778–780] have indicated that competitive formation of CH_3ONO (methylnitrite) is energetically unfavorable, and even if CH_3ONO is formed, it will mainly dissociate to NO+CH_3O, even at intermediate temperatures, making it indistinguishable from the bimolecular channel (R283). For this reason, most previous modeling work have neglected the formation of CH_3ONO from NO_2+CH_3 and the present study is no exception. Nitromethane and similar energetic materials are of interest as propellant fuels, e.g. for race car engines and rockets, and the thermal decomposition mechanism further serves as model reaction for more complex nitrogenated hydrocarbons used in e.g. high explosives, like trinitrotoluene (TNT) [781]. Consequently, most experimental studies of the association channel from NO_2+CH_3 to CH_3NO_2 focus on the reverse decomposition reaction. Glänzer and Troe [722, 782] conducted shock tube experiments with highly diluted mixtures of CH_3NO_2 in Ar at 900–1400 K and 1.1–41 bar to determine the rate coefficients for both the disproportionation reaction (R283) and the thermal dissociation of CH_3NO_2 (R326). The results were interpreted in terms of a simplified mechanism involving only (R283) and (R326), where the latter was described by a simple Lindemann expression ($F_{cent,\mathrm{R326}} = 1$) with $k_{\mathrm{R326},\infty} = 1.78\times10^{16}\exp\left[\frac{-(58500\pm500)}{RT}\right]\ ^1/_\mathrm{s}$ and $k_{\mathrm{R326},0} = 1.26\times10^{17}\exp\left(\frac{-42000}{RT}\right)\ ^{\mathrm{cm}^3}/_{\mathrm{mol\,s}}$. The bimolecular channel was assigned $k_{\mathrm{R283}} = 1.3\times10^{13}\ ^{\mathrm{cm}^3}/_{\mathrm{mol\,s}}$. These rate expressions have found support in several other studies in the field at both low [783,784], intermediate [785–787], and high temperatures [788–791]. Despite this consistency between literature data, there have been indications [791] of a more complex pyrolysis chemistry of CH_3NO_2 than proposed by Glänzer and Troe. In order to clarify this issue, Glarborg *et al.* [139] recently challenged the rate coefficients from Glänzer and Troe. They reanalyzed experimental data from Glänzer and Troe [722], Hsu and Lin [789], and Zhang and Bauer [791], covering temperatures and pressures from 1000–1400 K and 0.5–6.0 bar, and used a detailed reaction mechanism for the ther-

mal decomposition of CH_3NO_2 to characterize the fall-off behavior of (R326). Glarborg *et al.* concluded that the high- and low-pressure limiting rate coefficients proposed by Glänzer and Troe are consistent with recent measurements provided a center broadening factor of $F_{cent,\mathrm{R326}} = 0.183$ is introduced to describe the fall-off behavior. Glarborg *et al.* [139] additionally proposed a slight negative temperature dependence of $k_{\mathrm{R283}} = 4.0 \times 10^{13} T^{-0.2} \mathrm{cm^3/mol\,s}$ to reconcile the high-temperature value from Glänzer and Troe with the room-temperature measurements of $1.4 \times 10^{13}\ \mathrm{cm^3/mol\,s}$ by Yamada *et al.* [783] and Biggs *et al.* [784]. The more recent shock tube measurements by Srinivasan *et al.* [259] confirm this value in the high-temperature range 1360–1695 K, whereas Wollenhaupt and Crowley [792] report a low-temperature value (233–356 K) of $k_{\mathrm{R283}} = 1.1 \times 10^{13}\ \mathrm{cm^3/mol\,s}$, which is slightly below the recommendation of Glarborg *et al.* Nevertheless, the present mechanism has adopted rate expressions of k_{R283} and k_{R326} from Glarborg *et al.* [139].

A few experimental studies of the thermal decomposition of $C_2H_5NO_2$ (nitroethane) (R343) have also been published yielding the reverse rate constant for the analogue association channel of NO_2+C_2H_5. Glänzer and Troe [723] conducted shock tube measurements at 900–1350 K and 0.33–33 bar in Ar atmosphere, where the reaction is near the high-pressure limit. This study was similar to the previously referred work by Glänzer and Troe concerning CH_3NO_2 decomposition, and again, a simple Lindemann expression was proposed ($F_{cent,\mathrm{R343}} = 1$) with $k_{\mathrm{R343},\infty} = 7.94 \times 10^{15} \exp\left(\frac{-57000}{RT}\right)\ \mathrm{1/s}$ and $k_{\mathrm{R343,0}} = 1.0 \times 10^{18} \exp\left(\frac{-36000}{RT}\right)\ \mathrm{cm^3/mol\,s}$. This rate expression lies somewhat below available measurements from Cottrell *et al.* [793], Wilde [794, 795], and Dubikhin *et al.* [796] in the intermediate temperature range 593–715 K and total pressures from 0.1 to 1 bar. In order to reconcile these data with the high-temperature results from Glänzer and Troe, the present mechanism uses the high-pressure limiting rate coefficient $k_{\mathrm{R343},\infty} = 2.0 \times 10^{15} \exp\left(\frac{-54000}{RT}\right)$ $\mathrm{1/s}$, modified in the present work, together with $k_{\mathrm{R343,0}}$ and $F_{cent,\mathrm{R343}} = 1$ taken directly from Glänzer and Troe [723]. The resulting rate expression is not expected to be fairly accurate outside the temperature range of experimental validation. The competitive disproportionation channel NO_2+C_2H_5 $\rightleftharpoons$ NO+C_2H_5O (R296) is represented in the mechanism by the rate coefficient of the analogue reaction between NO_2 and CH_3 (R283). This is in poor agreement with the relative rate measurement of $k_{\mathrm{R296}}/k_{-\mathrm{R343}} = 0.84$ at room-temperature and 0.02 bar reported by Canosa *et al.* [797]. It predicts a value of k_{R296} about two orders of magnitude below the preferred rate coefficient when applying the current expression of k_{R343} with thermodynamic data enclosed in this work to calculate the equilibrium constant. However, this discrepancy may just as well be an indication of the uncertainty that can be attributed to the proposed expression of k_{R343} in the sub-ambient

temperature range.

The reaction between NO and CH_3 is only represented by the addition/stabilization channel to CH_3NO (nitrosomethane) (R261). Formation of bimolecular products, like CH_2N+OH, HCN+H_2O, and HNO+CH_2, is limited by substantial energy barriers making these pathways negligible at the intermediate temperature range of interest. The preferred pressure dependent expression of k_{R261} has been adopted from the work of Davies *et al.* [686], who measured the rate constant at 296, 407, and 509 K, and varying pressures from 0.03 to 0.8 bar in an Ar atmosphere using laser flash photolysis and time-resolved IR absorption spectroscopy to follow the CH_3 radical decay. The results were analyzed using a master equation approach from which, the limiting rate coefficients were derived: $k_{\mathrm{R261},\infty} = 9.0 \times 10^{12} \exp\left(\frac{-60}{T}\right)$ $^{\mathrm{cm}^3}/_{\mathrm{mol\,s}}$ and $k_{\mathrm{R261},0} = 2.5 \times 10^{16} \exp\left(\frac{1430}{T}\right)$ $^{\mathrm{cm}^6}/_{\mathrm{mol}^2\,\mathrm{s}}$. The room-temperature photolysis experiments by Pilling *et al.* [798], Van den Bergh and Callear [799], Wallington *et al.* [800], and Kaiser [337] confirm these rate measurements. The latest results from Kaiser [337] cover a wide pressure range from 0.04 to 10 bar constituting an excellent high-pressure continuation of the results from Davies *et al.* [686]. Room-temperature measurements of the title reaction were also presented by Jodkowski *et al.* [801], who used pulse radiolysis of acetone/NO mixtures with absorption spectrometric detection of the CH_3 conversion. They combined own measurements with previous results on which basis, they derived limiting rate coefficients in good agreement with those from Davies *et al.* All reported rate measurements are in the fall-off regime showing a strong pressure dependence. The preferred rate expression is based on the limiting rate constants from Davies *et al.* [686] with a fitted center broadening factor of $F_{cent,\mathrm{R261}} = 5.0 \times \exp\left(\frac{-T}{120}\right)$ to describe the fall-off behavior. It has been necessary to fit $F_{cent,\mathrm{R261}}$ to obtain the conventional Troe expression, cf. Equation (5.24), suitable for kinetic modeling with the Chemkin software [186]. The fitted rate expression describes the fall-off behavior of (R261) reasonably well at elevated temperatures, cf. comparisons with the data sets from Davies *et al.* at 407 and 509 K, whereas the available room-temperature data are generally underpredicted. This discrepancy is accepted in the present study considering the elevated temperature range of interest.

5.3.5.5 NO_x/Alkoxy Reactions

The reaction of NO with CH_3O either follows a disproportionation pathway to HNO+CH_2O (R264) or an association path to CH_3ONO (R265). The alternative path to NO_2+CH_3 was previously considered in the reverse direction. This channel is endothermic when it proceeds from NO+CH_3O

making it an unlikely competitor to the HNO+CH_2O formation pathway. The preferred rate expressions originate from the recent combined experimental and theoretical study by Caralp *et al.* [689]. They measured the overall rate of NO+CH_3O in a He atmosphere using a discharge flow system for low-pressure investigations (0.7–7 mbar, 248–473 K) and a pulsed laser photolysis system for higher pressures (0.04–0.667 bar, 284–364 K). Both experimental systems utilized laser-induced fluorescence detection of CH_3O decay profiles. The results were combined with previous experimental data from the literature [802–805] on which basis, a multichannel RRKM analysis was developed, fitted to the experimental database, and used to characterize the reaction mechanism and predict limiting rate constants, fall-off behavior, and branching fractions. The potential energy surface calculations indicated that the disproportionation reaction (R264) occurs simultaneously by direct H-abstraction at the nitrogen atom of NO, and by formation of the adduct CH_3ONO^* followed by rearrangement and bond cleavage to HNO+CH_2O. The latter path further competes against stabilization of the adduct (R265). This gives rise to a non-Arrhenius behavior of (R264) represented by $k_{\mathrm{R264}} = 7.53 \times 10^{12} \exp\left(\frac{-1015}{T}\right) + 2.49 \times 10^{18} T^{-2.56}$ $^{\mathrm{cm}^3}/_{\mathrm{mol\,s}}$ that exhibits a characteristic rate minimum around 400 K. The pressure dependent rate expression for the competitive stabilization channel was fitted to the conventional Troe expression using $k_{\mathrm{R265},\infty} = 5.99 \times 10^{14} T^{-0.6}$ $^{\mathrm{cm}^3}/_{\mathrm{mol\,s}}$, $k_{\mathrm{R265},0} = 8.14 \times 10^{25} T^{-2.8}$ $^{\mathrm{cm}^6}/_{\mathrm{mol}^2\,\mathrm{s}}$, and $F_{cent,\mathrm{R265}} = \exp\left(\frac{-T}{900}\right)$. These expressions of k_{R264} and k_{R265} from Caralp *et al.* [689] are in good agreement with proposed values from a previous combined experimental and theoretical study by He *et al.* [715] covering temperatures and pressures from 450–520 K and 0.067–1 bar, as well as the early static reactor experiments from Batt *et al.* [806] at 440–473 K and 0.9 bar. Zaslonko *et al.* [401] proposed a high-temperature value of k_{R264} based on shock tube experiments with thermal decomposition of CH_3ONO and CH_3ONO_2 at 850–1200 K, which is 4–5 times below the preferred rate constant. Hsu *et al.* [807] also measured the thermal decomposition of CH_3ONO behind reflected shock waves; this time at 680–955 K and 0.8–2 bar, where the reaction is in the fall-off region. From these experiments, Hsu *et al.* fitted a second-order Arrhenius expression, which is in good agreement with the value of $k_{-\mathrm{R265}}$ calculated from the pressure dependent formulation from Caralp *et al.* [689] using thermodynamic data from Table 3.1 to determine the equilibrium constant.

The mechanism of the reaction between NO_2 and CH_3O (R292,R293) is expected to resemble that of NO+CH_3O discussed above. McCaulley *et al.* [701] used a discharge flow reactor with laser-excited fluorescence spectroscopy to conduct measurements at low pressures (0.8–5.4 mbar) across the temperature range 220–473 K from which, they derived temperature depen-

dent expressions of k_{R292} and the low-pressure limit $k_{\mathrm{R293,0}}$. The former was accepted in later studies by Biggs *et al.* [784] and Frost and Smith [704], who subtracted k^{298}_{R292} from low-pressure/room-temperature measurements of $k_{\mathrm{NO_2+CH_3O\rightarrow prod.}}$ in order to determine the contribution from the association pathway to CH_3ONO_2 (R293). These results demonstrated that CH_3ONO_2 is the dominant product at total pressures above ∼1.3 mbar and ambient temperature. More recent measurements were reported by Martínez *et al.* [702], who used laser photolysis of CH_3ONO to generate CH_3O radicals in NO_2/He mixtures and laser-induced fluorescence to monitor the conversion of CH_3O. The experiments were conducted at 250–390 K and 0.067–0.8 bar, and the measurements were corrected for loss of CH_3O radicals by diffusion away from the observation zone in the experimental setup as well as side reactions between CH_3O and the radical precursor CH_3ONO. Martínez *et al.* further subtracted values of k_{R292} (from McCaulley *et al.* [701]) to obtain absolute rate constant measurements for the association channel. These data were combined with the previous data from McCaulley *et al.* [701] and Biggs *et al.* [784] and fitted to the conventional Troe expression using a center broadening factor of $F_{cent,\mathrm{R293}} = 0.6$ to yield limiting high- and low-pressure rate constants for (R293). The present mechanism has adopted this rate expression together with k_{R292} from McCaulley *et al.* [701]. Wollenhaupt and Crowley [792] conducted a similar photolysis study of the association reaction (R293) across the temperature and pressure ranges 233–365 K and 0.013–0.267 bar. Their limiting high- and low-pressure rate constants are in reasonable agreement with those from Martínez *et al.* within this temperature range.

The mechanism also includes reactions between NO/NO_2 and C_2H_5O that are expected to behave similar to the analogue reactions between NO/NO_2 and CH_3O. The limiting high-pressure rate coefficient for $NO+C_2H_5O$, forming stabilized C_2H_5ONO (R269), is based on recent photolysis experiments by Fittchen *et al.* [530] at 286–388 K and 0.04–0.67 bar. The reaction appears to be independent of pressure at these conditions. The preferred value of $k_{\mathrm{R269,\infty}}$ is in good agreement with the earlier room-temperature measurements by Frost and Smith [802] and relative rate measurements reported by Batt *et al.* [652]. Following the recent recommendation by Atkinson *et al.* [690], the fall-off behavior is best described using the low-pressure limit $k_{\mathrm{R269,0}}$ from the discharge flow reactor study by Däele *et al.* [691] at 295 K with an estimated center broadening factor of $F_{cent,\mathrm{R269}} = 0.6$. Däele *et al.* [691] also considered the bimolecular channel $NO+C_2H_5O \rightleftharpoons HNO+CH_3CHO$ (R268) and determined the constant rate coefficient $k_{\mathrm{R268}} = (6.6 \pm 3.0) \times 10^{12}\ {}^{\mathrm{cm^3}}/_{\mathrm{mol\ s}}$ in good agreement with the measured branching ratio $k_{\mathrm{R268}}/k_{\mathrm{R269,\infty}} = 0.3$ from Baker and Shaw [808] and the value $6 \times 10^{12}\ {}^{\mathrm{cm^3}}/_{\mathrm{mol\ s}}$ from the indirect

study of Batt and Milne [141].

The high-pressure limiting rate constant for NO_2+$C_2H_5O \rightleftharpoons C_2H_5ONO_2$ (R298) was characterized experimentally by Frost and Smith [704] at 295 K and 2–130 mbar of He yielding $k_{R298,\infty} = (1.7 \pm 0.2) \times 10^{13}\,{}^{cm^3}/_{mol\,s}$. This is in reasonable agreement with the recommended value of $2.5 \times 10^{13}\,{}^{cm^3}/_{mol\,s}$ from the review of Batt [705] based on unpublished data. Batt further advocated the branching ratio $k_{R297}/k_{R298,\infty} = 0.1$ for the bimolecular channel. In the recent evaluation by DeMore *et al.* [706], a limiting high-pressure rate constant was recommended based on the value from Frost and Smith [704]. DeMore *et al.* further estimated a low-pressure limit based on analogies to related reactions. Their recommendation is followed in the present work including an estimated center broadening factor of $F_{cent,R298} = 0.6$ identical to the analogue reaction between NO_2 and CH_3O discussed above. The rate coefficient for the bimolecular channel to HONO+CH_3CHO (R297) has been obtained from the branching ratio proposed by Batt [705] using the constant value of $k_{R298,\infty}$ from Frost and Smith [704]. The resulting value of k_{R297} is consistent with the rate constant for the corresponding bimolecular channel from NO_2+CH_3O.

5.3.5.6 NO_x/Alkylperoxyl Reactions

The reactions between NO and hydrocarbon peroxyl radicals, CH_3OO (R266) and C_2H_5OO (R267), are expected to gain particular importance at the high pressure and intermediate temperature conditions of the present work where peroxide species are readily available. No rate measurements have been reported above ∼400 K, whereas numerous investigations are available at low temperatures relevant to atmospheric chemistry research. Recent *ab initio* calculations of the potential energy surface of NO+CH_3OO by Zhao *et al.* [809] and Lesar *et al.* [810] have confirmed that the reaction follows an addition/elimination mechanism through the intermediate adduct CH_3OONO* followed either by direct cleavage of the peroxy bond or rearrangement to CH_3ONO_2* before breakage to NO_2+CH_3O. The reaction involving C_2H_5OO is expected to follow an analogue mechanism. Lesar *et al.* noted that the second adduct, CH_3ONO_2*, could be stabilized under suitable temperature and pressure conditions. However, the available experimental data indicate that this stabilization channel should be neglected unless very low temperatures are applied. Hence, Simonaitis and Heicklen [811], and Scholtens *et al.* [812] observed deviations from the Arrhenius behavior of k_{R266} at temperatures <220 K and pressures of 133–267 mbar, which could be interpreted in terms of formation of stable CH_3ONO_2, but no direct experimental evidence could be obtained and these results were further contradicted by data

from Villalta *et al.* [813] and Bacak *et al.* [814]. In case of $C_2H_5ONO_2$; obtained from NO+C_2H_5OO, more compelling evidence of the occurrence of the stabilization channel has been presented by the experimental studies of Atkinson *et al.* [815] and Ranschaert *et al.* [816], even though the measured contributions to the product distribution were only in the range of $\sim$1 % at ambient conditions. This is still considered negligible in context with the present study. Several experimental techniques have been used to conduct room-temperature measurements of k_{R266} [811–814, 817–821] and k_{R267} [691, 816, 820, 822–824]. The resulting rate constants are generally in good agreement and average values of $k^{298}_{\mathrm{R266}} = (4.6 \pm 1.1) \times 10^{12}\,{}^{\mathrm{cm}^3}/_{\mathrm{mol\,s}}$ and $k^{298}_{\mathrm{R267}} = (5.5 \pm 1.3) \times 10^{12}\,{}^{\mathrm{cm}^3}/_{\mathrm{mol\,s}}$ were recommended in the recent evaluation by Atkinson *et al.* [690]. Atkinson *et al.* also proposed temperature dependent rate expressions based on data from Villalta *et al.* [813], Bacak *et al.* [814], Eberhard and Howard [823], Maricq and Szente [824], and Ranschaert *et al.* [816] with corrections to match the average values at 298 K. The resulting rate coefficients, $k_{\mathrm{R266}} = 1.4 \times 10^{12} \exp\left(\frac{360\pm100}{T}\right)\,{}^{\mathrm{cm}^3}/_{\mathrm{mol\,s}}$ and $k_{\mathrm{R267}} = 1.6 \times 10^{12} \exp\left(\frac{380\pm50}{T}\right)\,{}^{\mathrm{cm}^3}/_{\mathrm{mol\,s}}$, have been validated at temperatures from 200 to $\sim$400 K. The present mechanism includes these rate expressions even though the author is concerned with the substantial uncertainties associated with the temperature dependencies and the limited temperature range of experimental validation.

5.3.5.7 NO_x/CH_3OH Reactions

The H-abstraction reaction of NO_2+CH_3OH (R294,R295) is the primary initiation reaction in the $CH_3OH/O_2/NO_x$ system. Recent *ab initio* calculations by Xiao *et al.* [703] indicate that CH_2OH+*cis*-HONO are the major products formed via two possible transition state configurations depending on the attacking orientation of NO_2. Xiao *et al.* calculated energy barriers of 21.2 and 20.5 ${}^{\mathrm{kcal}}/_{\mathrm{mol}}$ for these channels in good agreement with experimental results from Anastasi and Hancock [825], and Koda and Tanaka [826], who obtained activation energies of 21.4 and 22.6 ${}^{\mathrm{kcal}}/_{\mathrm{mol}}$ respectively for the overall reaction. Xiao *et al.* also investigated competitive channels leading to CH_2OH+HNO_2, CH_2OH+*trans*-HONO, CH_3O+*cis*-HONO, and others, that all displayed higher energy barriers. In the three specific cases, values of 24.1, 27.0, and 32.7 ${}^{\mathrm{kcal}}/_{\mathrm{mol}}$ were predicted yielding negligible contributions to the overall product distribution. Other theoretical calculations have been presented by Teng *et al.* [827], but they only considered the formation of the HNO_2 isomer. Their calculated energy barriers are in agreement with those obtained for HNO_2+CH_2OH/CH_3O by Xiao *et al.*, but the overall rate coefficient is much lower than predicted by Xiao *et al.* due to the absence of the

different HONO formation channels. The experimental values from Anastasi and Hancock [825], which are based on laser-induced fluorescence measurements in a static reactor at 639–713 K, are in line with the faster reaction rate proposed by Xiao *et al.* [703], whereas the experimental results from Koda and Tanaka [826] support the lower rate constant from Teng *et al.* [827]. In the present mechanism, the more extensive theoretical treatment by Xiao *et al.* is preferred yielding rate expressions for both HONO (R294) and HNO_2 formation (R295), but further experimental work is needed for verification. Notice that the former rate expression ($k_{R294} = 145\,T^{3.32} \exp\left(\frac{-20035}{RT}\right)$ $^{cm^3}/_{mol\,s}$) represents a summation of the *cis*- and *trans*-HONO formation channels from Xiao *et al.* [703].

There are no direct studies of the corresponding reaction between NO and CH_3OH. A single measurement of the reverse reaction of HNO+CH_3O to NO+CH_3OH (R313) was reported by McGraw and Johnston [828] based on room-temperature photolysis experiments with molecular-modulation spectrometry. The obtained rate coefficient $k_{R313} = (3.0 \pm 0.6) \times 10^{13}$ $^{cm^3}/_{mol\,s}$ is consistent with the rate expression $k_{R313} = 3.2^{+4.8}_{-1.9} \times 10^{13} \exp\left(\frac{0\pm400}{RT}\right)$ $^{cm^3}/_{mol\,s}$ proposed by He *et al.* [715]. The latter was obtained by fitting a detailed mechanism to CH_3OH and N_2O concentration profiles measured during static reactor experiments with thermal decomposition of CH_3ONO at 450–520 K. Measurements of the competitive channel NO+CH_3OH $\rightleftharpoons$ HNO+CH_2OH (–R314) are unavailable in either direction. Glarborg *et al.* [716] have previously proposed a constant rate coefficient of 3.0×10^{13} $^{cm^3}/_{mol\,s}$ for the reverse reaction (R314), which is similar to k_{R313}. This recommendation is followed in the present work together with k_{R313} from He *et al.* [715].

5.3.5.8 NO_x/CH_2OH Reactions

Radical reactions between NO_x and CH_2OH (R263,R291) are expected to be fast, which is also indicated by the few experimental investigations [468, 688] available in the field. Nesbitt *et al.* [688] used a low-pressure (0.7–2 mbar) discharge flow system with a mass spectrometer to investigate NO_2+CH_2OH (R291) at room-temperature as well as the reaction between NO and isotopically substituted CD_2OH at 230–473 K. From these data, constant rate coefficients were derived: $k_{R263} = (1.3 \pm 0.2) \times 10^{12}$ $^{cm^3}/_{mol\,s}$ and $k_{R291} = (5.0 \pm 2.5) \times 10^{12}$ $^{cm^3}/_{mol\,s}$. It is noted that Nesbitt *et al.* obtained an activation energy of 1.2 $^{kcal}/_{mol}$ for (R263) at 230–298 K, whereas the reaction appeared to be independent of temperature at higher values corresponding to the constant rate coefficient listed above. Another experimental study was conducted by Pagsberg *et al.* [468]. They investigated the title reactions at ambient conditions using a pulsed radiolysis technique with UV

absorption detection of the CH_2OH radical decay and proposed $k_{R263} = (1.5 \pm 0.01) \times 10^{13}\,{}^{cm^3}/_{mol\,s}$ and $k_{R291} = (1.4 \pm 0.2) \times 10^{13}\,{}^{cm^3}/_{mol\,s}$, which are somewhat higher than the rate constants obtained by Nesbitt *et al.* There are no current explanation of this discrepancy and more experimental investigations are needed for clarification. At present, the rate coefficients from Nesbitt *et al.* [688] are used in the model. It is noticed that the reaction between NO_2 and CH_2OH is only represented by the product channel to HONO+CH_2O (R291). In light of the previous discussion of the formation of isomeric structures of HONO (*cis*-/*trans*-HONO and HNO_2), e.g. in connection to NO_2+CH_4, this issue should be addressed; mainly to clarify the relative importance of HONO and HNO_2 formation, since no distinction is made between the *cis*- and *trans*-isomers of HONO in the present mechanism. Zhang *et al.* [829] recently conducted a detailed theoretical study of the potential energy surface of NO_2+CH_2OH to illuminate the reaction mechanism and aid the identification of important product channels. They predicted an initial barrierless association at the C$\cdots$N site forming the adduct $HOCH_2NO_2$* that can dissociate through simultaneous H-shift and C–N bond rupture to CH_2O+*trans*-HONO. This channel passes through a transition state that lies 36.0 ${}^{kcal}/_{mol}$ below the potential energy level of the initial reactants and hence, gives rise to a fast overall reaction, as observed in experiments. Alternative pathways involve adduct rearrangement to $HOCH_2ONO$* through a second transition state lying 0.6 ${}^{kcal}/_{mol}$ above the potential energy of NO_2+CH_2OH. The second adduct dissociates through concerted internal rotations, H-shift, and bond rupture to yield CH_2O+*cis*-HONO, CH_2O+HNO_2, and HOCHO+HNO as the final products. These pathways involve transition states at -32.1, -30.2, and -30.2 ${}^{kcal}/_{mol}$ respectively, relative to NO_2+CH_2OH, and are therefore expected to form in comparable yields. However, due to the substantial difference between the energy barriers for the conversion of the first adduct, Zhang *et al.* concluded that the pathway to CH_2O+*trans*-HONO is the dominant product channel from NO_2+CH_2OH with only minor contributions from competitive channels. These results support the current disregard of product channels other than HONO+CH_2O (R291).

5.3.5.9 NO_x/CH_2O/HCO Reactions

Two product channels are considered from NO_2+CH_2O yielding HCO+HONO (R289) and the isomer HNO_2 (R290). The preferred rate constants are taken from the recent *ab initio* study by Xu and Lin [700] covering the temperature range 200–3000 K. The theoretical analysis indicates that HONO (R289) is the dominant isomer at temperatures below 1500 K, whereas

both product channels contribute evenly above 1500 K. The calculated rate coefficients compare favorably with experimental data from He *et al.* [830] (393–476 K) and Lin *et al.* [831] (1140–1650 K), which encourages the present recommendation of k_{R289} and k_{R290}.

Formyl radicals (HCO) are converted rapidly and without energy barrier to CO or CO_2 in the presence of NO_x (R262,R286–R288). The rate constants are drawn from a recent shock tube study by Friedrichs *et al.* [687], who measured the title reactions at near-atmospheric pressure and intermediate to high temperatures (770–1305 K and 805–1190 K for NO+HCO and NO_2+HCO respectively) using glyoxal laser-photolysis and frequency modulation spectroscopy to generate and detect the very short-lived HCO radical. The value of k_{R262} ranges within 21 % of the recent *ab initio* calculations by Xu *et al.* [832] at 500–1500 K, and the flash-photolysis experiments of Veyret and Lesclaux [504] at 298–503 K. The present mechanism only includes the H-abstraction channel from NO+HCO (R262). The competing association/stabilization channel to HC(O)NO is strongly pressure dependent, but it also has a strong negative temperature dependence that makes it insignificant except at high-pressure/low-temperature conditions (>10 bar and <298 K) [832]. Friedrichs *et al.* [687] measured the overall rate constant of NO_2+HCO ($k_{R286} + k_{R287} + k_{R288}$) and reviewed existing experimental data to estimate the individual branching ratios used in the mechanism. The value of $k_{R286} + k_{R287} + k_{R288}$ exceeds the recommendation from Tsang and Herron [683] by 25–60 % at temperatures between 298 and 1400 K, but this is within the uncertainty limits of the rate constant from Tsang and Herron.

5.3.5.10 NO_3 Reactions

The NO_3 subset (R301)–(R305) has been adopted from the previous combustion model of Glarborg *et al.* [680]. It is noticed that all references from this subset are concerned with atmospheric chemistry and hence, lack evaluation at high temperatures. However, model predictions at conditions relevant to the present study have indicated that NO_3 formation has little influence on the overall kinetic scheme. Consequently, no efforts have been made to reevaluate this part of the mechanism.

5.3.5.11 HNO Reactions

Many reactions from the HNO subset are included in the mechanism in the reverse direction with HNO as product. These reactions have already been discussed in previous sections and will therefore not be commented in this section.

Experimental data of HNO+OH (R308) are limited to some early post-flame studies at high temperatures >1600 K, see Ref. [683]. The preferred rate constant has been obtained from the more recent transition state calculations by Soto *et al.* [711]. This rate constant is 3–4 times lower than the recommended expression from Tsang and Herron [683] at temperatures from 500–1100 K, and 3–9 times below the constant estimated rate coefficient $k_{\mathrm{R308}} = 3.6 \times 10^{13}\,{}^{\mathrm{cm}^3}/_{\mathrm{mol\,s}}$ from Miller and Bowman [101].

No experimental characterization has been attempted for the reaction $\mathrm{HNO}+\mathrm{NO_2} \rightleftharpoons \mathrm{HONO}+\mathrm{NO}$ (R310). Tsang and Herron [683] proposed an estimated rate constant of $k_{\mathrm{R310}} = 6 \times 10^{11} \exp\left(\frac{-1990}{RT}\right)\,{}^{\mathrm{cm}^3}/_{\mathrm{mol\,s}}$ with an uncertainty factor of 5. This expression is in poor agreement with recent *ab initio* calculations by Mebel *et al.* [713] based on potential energy surfaces calculations for various $\mathrm{HNO}+\mathrm{NO_2}$ product channels at temperatures from 300–5000 K. Hence, deviations in the forward rate constant yield more than one order of magnitude at $500 \geq T \geq 1500\,\mathrm{K}$ with k_{R310} from Mebel *et al.* being significantly larger at high temperatures, while being the smaller at low temperatures. The mechanism includes the calculated Arrhenius coefficients from Mebel *et al.* due to an expected higher accuracy.

The reaction between HNO and $\mathrm{CH_3}$ (R311) was addressed superficially in relation to the initiation of $\mathrm{CH_4}$ by NO (–R311), where *ab initio* calculations by Yamaguchi *et al.* [699] predicted an activation energy barrier of $8.4\,{}^{\mathrm{kcal}}/_{\mathrm{mol}}$ for $\mathrm{HNO}+\mathrm{CH_3} \rightarrow \mathrm{NO}+\mathrm{CH_4}$. There are no available measurements for (R311). The only previous characterization is the estimated constant value of $2.0 \times 10^{12}\,{}^{\mathrm{cm}^3}/_{\mathrm{mol\,s}}$ at 833–913 K proposed by Laidler *et al.* [833] in an experimental study of the thermal decomposition of propane. The applied rate constant is based on the calculated activation energy barrier of $8.4\,{}^{\mathrm{kcal}}/_{\mathrm{mol}}$ from Yamaguchi *et al.* [699] with a pre-exponential factor scaled to match the estimated rate constant from Laidler *et al.* [833].

Xu and Lin [714] recently published a theoretical study of the H-abstraction reaction between HNO and HCO. This work showed that both reactants can act as H-donor yielding $\mathrm{NO}+\mathrm{CH_2O}$ and $\mathrm{H_2NO}+\mathrm{CO}$ respectively. The former is slightly favored by an energy barrier of 3.7 compared to $3.9\,{}^{\mathrm{kcal}}/_{\mathrm{mol}}$. No experimental measurements are available to verify these calculations. Tsang and Herron [683] estimated a rate coefficient for the $\mathrm{NO}+\mathrm{CH_2O}$ product channel, which is of comparable magnitude as the rate constant from Xu and Lin at temperatures around 1000 K, but it deviates by more than one order of magnitude above and below the calculated expression at temperatures <400 K and >1100 K respectively. The theoretical characterization by Xu and Lin [714] is preferred in the present work. It is noted that the current mechanism only includes the product channel to $\mathrm{NO}+\mathrm{CH_2O}$ (R312) in order to avoid considering a reaction subset for $\mathrm{H_2NO}$. In light of the calculations

presented by Xu and Lin, this is probably a poor assumption, but the error is accepted because HNO+HCO is only expected to play a minor role at the conditions relevant to the present study.

5.3.5.12 $HONO/HNO_2/HONO_2$ Reactions

Elementary reactions involving HONO, HNO_2, and $HONO_2$ have been collected from literature mechanisms [169,233,693,719] with updates from single theoretical and/or experimental reaction rate studies [710, 713, 714, 717] as well as unpublished *ab initio* calculations by Marshall [142] regarding the role of HNO_2 in combustion systems. The method applied by Marshall involved *ab initio* CBS-QB3 calculations [834] using geometries and frequencies derived with density functional theory, followed by an approximate extrapolation of coupled-cluster theory to the complete basis set. HNO_2 is a thermodynamically less stable isomer of HONO. Its existence has been verified experimentally by Koch and Sodeau [835] from photochemistry experiments with $HONO_2$ in a cryogenic environment (4.2 K), but even so, the compound is rarely considered in combustion modeling. The compound is important because it does not decompose to OH radicals like HONO. Instead, it may act as a OH radical sink through HNO_2+OH $\rightleftharpoons$ NO_2+H_2O (R321), and consequently, inhibit the overall fuel conversion rate. This effect will, however, be diminished if isomerization to HONO (R319) is sufficiently fast. The *ab initio* calculations by Marshall indicated that the transition state for HNO_2+OH lies well below the level of the reactants, which means that the reaction is essentially barrierless with a high rate constant. Hence, Marshall predicted $k_{\mathrm{R321}} \approx 4 \times 10^{13}\,{}^{\mathrm{cm}^3}/_{\mathrm{mol\,s}}$ at 600–1200 K. The calculated CBS-QB3 barriers to isomerization (R319) were 47.3 and 55.3 ${}^{\mathrm{kcal}}/_{\mathrm{mol}}$ relative to HNO_2 and HONO respectively, which is consistent with previous *ab initio* results from Chan *et al.* [774] that indicated an isomerization barrier between HNO_2 and HONO in excess of 50 ${}^{\mathrm{kcal}}/_{\mathrm{mol}}$. A QRRK analysis further provided the pressure dependent rate expression for $HNO_2(+\mathrm{M}) \rightleftharpoons \mathrm{HONO}(+\mathrm{M})$ at 700–1300 K: $k_{\mathrm{R319},\infty} = 2.5 \times 10^{14} \exp\left(\frac{-49700}{RT}\right)\ {}^{1}/_{\mathrm{s}}$ and $k_{\mathrm{R319,0}} = 3.1 \times 10^{18} \exp\left(\frac{-48900}{RT}\right)\ {}^{\mathrm{cm}^3}/_{\mathrm{mol\,s}}$ with a fitted $F_{cent,\mathrm{R319}} = 1.149 \exp\left(\frac{-T}{3125}\right)$. However, calculations of Eckart barriers [752] for H-atom tunneling facilitated a substantial reduction of the activation energies by 17.4 ${}^{\mathrm{kcal}}/_{\mathrm{mol}}$ leading to the final expression of k_{R319} found in Table 5.5. Notice that the latter correction corresponds to an acceleration of the reaction rate by about 3–4 orders of magnitude within the considered temperature range.

The reaction between HONO+OH to NO_2+H_2O (R316) is another potential OH scavenger that essentially removes two OH radicals by also preventing subsequent decomposition of HONO via (–R259). The reaction is well-docu-

mented at low-temperature conditions. The experimental investigation by Burkholder *et al.* [717] indicated a slightly negative temperature dependence at increasing temperatures from 298 to 373 K. The proposed rate constant is in reasonable agreement with the only available high-temperature determination by Fifer [836], who conducted shock tube measurements at 1000–1400 K to yield the constant rate coefficient $k_{\mathrm{R316}} = 1.6 \times 10^{12}\,{}^{\mathrm{cm}^3}/_{\mathrm{mol\,s}}$. This is 1.4–1.9 times below corresponding values from Burkholder *et al.* when their rate expression is extrapolated to 500–1100 K. However, the high-temperature results from Fifer may have been influenced by an inaccurate description of the important side reaction HONO(+M) $\rightleftharpoons$ NO+OH(+M) (–R259), which increases the uncertainty of the final results. Other low-temperature data have been presented by Jenkin and Cox [837] based on photolysis experiments at 278–343 K. These results are of the same magnitude as those from Burkholder *et al.* [717], but they oppose the results of Burkholder *et al.* by indicating a positive temperature dependence. Tsang and Herron [683] based their recommendation on the results of Jenkin and Cox, but the author finds the low-temperature determination by Burkholder *et al.* more reliable due to the consistency with the results of Fifer [836].

The self-reaction of HONO (R318) has been obtained from the recent theoretical evaluation by Mebel *et al.* [718]. The reaction yields H_2O and N_2O_3 that further decomposes to NO+NO_2 according to (R280). The fact that Mebel *et al.* have embedded this subsequent decomposition of N_2O_3 in their calculated rate constant is not an issue of concern since (R280) is fast and rapidly equilibrates the N_2O_3 concentration. A number of experimental values of k_{R318} are available at room temperature, e.g. [838–841], but they all consistently lie orders of magnitude above the calculated rate of Mebel *et al.* Experimental studies have later established that reaction (R318) is readily catalyzed at room temperature by various surface materials, e.g. pyrex [839,842,843] and borosilicate glass [844]. This catalytic effect can be somewhat diminished by the presence of water vapor, which suggests a competition between H_2O and HONO for active surface sites. The rapid loss of HONO at glass surfaces can explain the very high experimental values of k_{R318} compared to the theoretical determination of the pure gas phase reaction by Mebel *et al.* [718]. Nevertheless, the author is concerned with the fact that HONO can deactivate at glass surfaces in laboratory-scale reactors at room temperature, because it suggests that a certain loss of HONO; and effectively OH radicals, may also take place at higher temperatures and perhaps facilitate an inhibition of the fuel conversion in the present work.

5.3.5.13 Nitrated Hydrocarbon Reactions

The proposed kinetic model includes several radical association reactions that yield nitrated hydrocarbons; both from the C_1 and C_2 subset. These are promoted by the high pressures considered in the present work. A number of secondary reactions may conceivably compete with thermal dissociation for the consumption of these nitrated hydrocarbons. Many of these have been studied experimentally, but only at low temperatures.

In the presented experimental work, NO_x reactions have only been considered in relation to diluted experiments with $CH_4/O_2/NO_x$, where C_2 compounds only tend to form in relatively low concentrations; mainly via self-recombination of CH_3 radicals to C_2H_6 and subsequent oxidation to C_2H_5, etc. As a consequence, most nitrogenated hydrocarbons are only represented in the mechanism by limited reaction subsets. For future modeling of $C_2H_y/O_2/NO_x$ systems at high pressure and/or low to intermediate temperatures; or systems involving nitrogenates directly in the fuel, it is recommended to consider an extension of the present mechanism.

Nitromethane (CH_3NO_2) is expected to be the predominant nitrated hydrocarbon formed during fuel-rich combustion of CH_4 with NO_x at high pressure. A detailed reaction mechanism for for high-temperature conversion of CH_3NO_2 (>1000 K) has been proposed by Glarborg *et al.* [139] including secondary reactions with the $H/O/OH/CH_3$ radical pool. The current model has adopted this subset together with supplementary rate constant estimates from a subsequent modeling work by Glarborg and co-workers [110]. Rate coefficients enclosed herein are based on literature data and largely follow the recommendations of Bromly *et al.* [108]. Glarborg and co-workers also used low-temperature rate measurements from Nielsen and co-workers [845–848], and others, combined with own estimated temperature extrapolations.

It is reasonable to expect $C_2H_5NO_2$ to behave similar to CH_3NO_2 and rate coefficients should be of equivalent magnitude. Liu *et al.* [848] measured the overall rate constant for $C_2H_5NO_2$+OH yielding $k_{C_2H_5NO_2+OH\rightarrow prod.} = 1.1 \times 10^{12} \exp\left(\frac{-960}{T}\right)$ $^{cm^3}/_{mol\,s}$ that compares favorably to the corresponding value of $k_{CH_3NO_2+OH\rightarrow prod.} = k_{R332} + k_{R333}$ from Glarborg *et al.* [139]. The present model only considers the path involving adduct formation and subsequent C–N bond rupture to NO_2+C_2H_5OH (R344) using the rate coefficient for the analogue reaction between CH_3NO_2+OH (R332).

Rate expressions for the reactions between OH and CH_3ONO_2 (R347), and $C_2H_5ONO_2$ (R348), have been obtained from the pulsed laser photolysis/laser-induced fluorescence study of the overall reactions by Talukdar *et al.* [725] at 220–410 K. The reaction with $C_2H_5ONO_2$ showed non-Arrhenius behavior at the lowest temperatures and was fitted to the sum of two expo-

nentials. Both k_{R347} and k_{R348} are consistent with the discharge flow reactor experiments conducted by Shallcross *et al.* [849] at 298–373 K and the literature evaluation by Demore *et al.* [706], whereas experimental results from Nielsen and co-workers [850] at 298–393 K lie somewhat higher and indicate a negative temperature dependence opposite the results obtained by Talukdar *et al.* There are some uncertainties related to the product distributions from both alkylnitrates. Reaction (R347) and (R348) both involve attack on the N-atom followed by O–N bond cleavage to form $HONO_2$ and alkoxy radicals. However, direct H-abstraction or attack on the terminal C-atom would both have given rise to different products. Talukdar *et al.* [725] advocated a simple H-abstraction mechanism based on circumstantial evidence of the absence of adduct formation that would have resolved from attack on the N- or the C-atom. Adduct formation is often accompanied by a negative temperature dependence. The experiments by Nielsen *et al.* [850] were conducted at atmospheric pressure, whereas Talukdar *et al.* used lower pressures around 0.1 bar. The fact that the results obtained at higher pressure indicate a negative temperature dependence could be interpreted in terms of a pressure dependent reaction mechanism involving both direct H-abstraction and adduct formation, but theoretical verification is needed. The uncertainty related to this issue is currently accepted, because the reaction is not expected to play a significant role under relevant conditions of this study.

Rate coefficients for the overall reactions between OH and the two alkylnitrites: CH_3ONO (R345) and C_2H_5ONO (R346) have been obtained from another experimental study by Nielsen *et al.* [724] concerning OH radical reactions with various *n*-alkylnitrites at 1 bar and 298–393 K. Nielsen *et al.* derived a temperature dependent rate expression for CH_3ONO+OH with a positive temperature dependence. This rate expression is consistent with the average measured room-temperature value of $1.3 \times 10^{11}\,{}^{\mathrm{cm}^3}/_{\mathrm{mol\,s}}$ obtained from reports of Nielsen and co-workers [724, 846] and Tuazon *et al.* [432]. Nielsen *et al.* [724] further measured a room-temperature value of $4.2 \times 10^{11}\,{}^{\mathrm{cm}^3}/_{\mathrm{mol\,s}}$ for the corresponding reaction with C_2H_5ONO (R346). The applied rate expression for (R346) is based on the temperature dependence of CH_3ONO+OH (R345) with a scaled pre-exponential factor to comply with this room-temperature value from Nielsen *et al.*

5.3.6 SO_2 Reaction Mechanism

The behavior of gaseous sulfur species during fuel-rich and high-pressure combustion of light hydrocarbons is poorly characterized. Interactions with the hydrocarbon oxidation chain is, nonetheless, of considerable interest in relation to the practical utilization of the GTL process because sulfur is

typically present in trace amounts in crude natural gas. This is in the form of H_2S that readily oxidizes to SO_2 upon contact with oxygen. Experiments at low to atmospheric pressure [116, 851–858] have demonstrated that SO_2 can act to catalyze H atom removal in combustion processes operated at stoichiometric or fuel-rich conditions and intermediate to high temperatures. This behavior will inhibit the fuel oxidation chemistry with an expected adverse effect on the yield of oxygenated hydrocarbons.

The mechanism of radical removal by SO_2 has been investigated by the author in collaboration with Prof. Paul Marshall from Department of Chemistry at the University of North Texas, and Asc. Prof. Peter Glarborg from Department of Chemical Engineering, DTU. The results of this work have recently been presented at the *31st International Symposium on Combustion* in Heidelberg, Germany, and subsequently published [114] in the conference proceedings. A transcript of the paper is enclosed in Appendix A of this thesis. Based on *ab initio* calculations for key reactions, this paper presents an updated detailed kinetic model for the chemistry of the S/H/O system. The model was successfully validated against experimental results from different types of reacting systems covering a wide range of temperatures from 784 to 2115 K, which permitted a reliable investigation of the underlying sulfur chemistry. The updated reaction mechanism for SO_2 interactions with the H/O radical pool is presented in Table 1 in the paper (see Appendix A). It is noticed that this kinetic scheme is incomplete in the sense that underlying reactions relevant to e.g. the conversion of H_2S are not shown. However, these reactions are implicitly included from previous modeling work of Alzueta *et al.* [115] and Sendt *et al.* [859], as also stated in the paper. This involves elaborate reaction subsets for e.g. H_2S, S_2H_x, SH, S, and S_2. These subsets have also been adopted in the present work, including relevant thermochemical reference state data, so that the resulting sulfur mechanism essentially becomes identical to the mechanism used in the paper by Rasmussen *et al.* [114].

Sulfur shares many similarities with oxygen. This means that *sulfurnated* species analogue to oxygenated compounds involved in the hydrocarbon oxidation chain, in principle, can be expected to form during the fuel conversion, e.g. CH_3S, CH_3SH, CH_2S, HCS, CS, and CS_2. The issue may gain particular relevance under the reducing and high-pressure/low-temperature conditions used in the present work. Investigations of elementary reactions with these compounds are very limited. Some work has been conducted by Russian scientists; e.g. Arutyunov and co-workers [860–862], who proposed rate constants for the reactions: $SO_3+CH_3 \rightleftharpoons CH_3O+SO_2$ and $SO_2+CH_3OO \rightleftharpoons SO_3+CH_3O$ that are analogue to important reactions from the NO_x/hydrocarbon mechanism; see Section 5.3.5.4 and 5.3.5.6. Unfortunately, this work is difficult to approach due to linguistic barriers. Limited

reaction subsets for sulfurnated hydrocarbons have also been considered in connection to atmospheric chemistry research; see e.g. the literature evaluations of DeMore *et al.* [706] and Atkinson *et al.* [697], but these generally involve coarse and uncertain rate constant estimates.

Due to time limitations of the present Ph.D. study, sulfur chemistry relevant to the investigated GTL process has only received limited attention. Hence, a few high-pressure experiments have been conducted using the high pressure flow reactor presented in Chapter 4, and kinetic model development has been addressed to the extent that is presented in the enclosed paper in Appendix A. The experimental results will be presented in the proceeding chapter including model predictions based on the sulfur mechanism from Rasmussen *et al.* [114] without elementary reactions to account for direct hydrocarbon interactions. This is expected to yield insufficient modeling results, and probably, more than anything, demonstrate the need for future work in the field.

5.4 Summary

Conversion of hydrocarbon fuels in combustion processes is the result of a complex chain of hundreds of fast radical reactions that propagate towards the final combustion products through subsequent formation and consumption of reactive compounds. Detailed chemical kinetic models are comprehensive mechanistic models that approach these chemical mechanisms on an elementary reaction level. The elementary reactions are defined by temperature and pressure dependent rate constants determined either experimentally or predicted from theory using data from quantum mechanical computations.

In the present work, a detailed kinetic model has been developed to provide accurate descriptions of the oxidation chemistry of C_{1-2} hydrocarbon fuels under high pressure and intermediate temperature conditions, and in the presence of NO_x, and, to a limited extent, also SO_2. The model includes fundamental reaction mechanisms for the conversion of the H_2/O_2 radical pool and CO/CO_2. Moreover, detailed mechanisms have been developed for C_{1-2} hydrocarbons species as well as a submechanism including NO_x/hydrocarbon reactions. Finally, the model includes a mechanism describing SO_2 interactions with the H_2/O_2 radical pool. The latter has recently been published [114], and a transcript of the paper can be found in Appendix A. Rate constant parameters have been adapted to the modified Arrhenius expression, and the model has been structured for applications with the Chemkin software [186], which is a numerical simulation tool designed for computations with elementary chemical reactions in flowing systems.

In general, no previous detailed kinetic models underly the present model. Instead, rate constants have been obtained from an extensive and critical review of data for individual elementary reactions with particular emphasis on the conditions relevant to the present work. In a few cases, updated rate constants have been proposed for key reactions based on a reevaluation of literature experiments or *ab initio* CBS-QB3 calculations. These involve $OH+HO_2 \leftrightharpoons H_2O+O_2$, $CO+OH \leftrightharpoons [HOCO] \leftrightharpoons CO_2+H$, $NO_2+H_2 \leftrightharpoons HNO_2+H$, $NO_2+HO_2 \leftrightharpoons HONO/HNO_2+O_2$, $HNO_2(+M) \leftrightharpoons HONO(+M)$, and others. Hence, the chapter has presented detailed discussions of 348 elementary reactions relevant to hydrocarbon combustion. This elaborate approach has ensured that the resulting detailed chemical kinetic model is probably as reliable as can be with the current status of combustion kinetic research. Even so, this chapter has clearly demonstrated that improved characterization is needed for a substantial number of elementary reactions relevant to hydrocarbon oxidation chemistry; in particular reactions involving alkylperoxy species, e.g. CH_3OO, CH_3OOH, C_2H_5OO, end C_2H_5OOH.

Chapter 6

Experiments and Modeling

6.1 Introduction

A number of experimental campaigns have been conducted during the present Ph.D. work involving the chemical systems: $CO/H_2/NO_x/O_2$, CH_4/O_2, $CH_4/C_2H_6/O_2$, $CH_4/NO_x/O_2$, and $CH_4/H_2S/O_2$. All the experiments have been conducted in the high pressure flow reactor setup presented in Chapter 4. The main objective of this work has been to produce experimental results at well-defined conditions that can serve to verify the performance of the detailed chemical kinetic model.

In order to ensure a thorough model validation, the experimental work has been structured in accordance with two overall strategies: First, the chemical systems have been selected for investigation because they represent distinct sections of the hydrocarbon oxidation mechanism with an increasing order of complexity. This is in accordance with the hierarchal structure of the reaction network, as outlined in Section 5.1.1. Hence, results from the $CO/H_2/NO_x$ system serve to validate fundamental mechanisms from the H_2/O_2, CO/CO_2, and NO_x reaction subsets that underlie e.g. the conversion of CH_4/NO_x, etc. This strategy ensures a more reliable interpretation of modeling results and identification of potential issues in the kinetic model.

The second overall strategy deals with the application of varying reaction conditions; in particular conditions that prompt different chemical reaction mechanisms in order to challenge the mechanistic capabilities of the model. Consequently, the experimental database covers pressures from moderately high (20 bar) to high (100 bar) and different stoichiometric ratios ranging from extremely rich to very lean conditions, even though it probably has little practical relevance to the GTL process to consider e.g. pressures of only 20 bar and fuel conversion under oxidizing condition. Nevertheless, it ensures

a broad applicability of the model and justifies a general characterization of the detailed reaction mechanisms.

An implication of the experimental work is the heat release from the exothermic hydrocarbon oxidation reactions that hinders a good control of the reactor temperature unless it is minimized by dilution of the reactant mixture with an inert bath gas; in the present case N_2. Even so, a few experiments have been conducted with high absolute fuel concentrations that promote high CH_3OH yields and hence, resemble conditions relevant to the investigated GTL process.

6.1.1 Overview of Experiments

Table 6.1 provides an overview of the experimental database. The individual experimental results will be presented throughout this chapter together with corresponding modeling predictions obtained from plug flow simulations with Chemkin. Moreover, discussions of governing reaction mechanisms will be included based on *net rate* analyses and *sensitivity* analyses; see Section 5.2.2 and 5.2.3 for underlying calculation methods. Results of the net rate analyses are processed by the numerical software tool XSenkPlot [863] that provides a graphical overview.

The experiments with CH_4/NO_x were conducted in collaboration with Res. Ass. Anja E. Rasmussen, during the Autumn 2005, while the results from the CH_4/C_2H_6 system are selected data from the thesis work of M.Sc. Jon G. Jakobsen [864], that was completed during the Spring of 2006 under the supervision of the author and Assoc. Prof. Peter Glarborg from Department of Chemical Engineering, DTU. The author wishes to acknowledge these people for their contributions.

Overall measuring uncertainties are provided for each experimental series in terms of the percentage uncertainty calculated as the square root of the sum of the squares of the percentage uncertainties associated with individual measurements, e.g. uncertainties from calibration gases, accuracy of the measuring equipment, and raw data analysis. Some oxygen measurements have been corrected for a "background" contribution arising from a cross-sensitivity of argon in the applied gas chromatograph. Argon may have entered the system via the N_2 dilution. The increased uncertainties of the involved O_2 measurements have been incorporated in the listed overall uncertainties.

Table 6.1: Overview of the experimental database. All experiments have been conducted in the high pressure flow reactor setup presented in Chapter 4. The experiments are listed in the order of appearance throughout this chapter. Calculation of stoichiometric ratios are based on the complete conversion of reactants to full oxidation products, i.e. H_2O, CO_2, and SO_2. Detailed reaction conditions will be given in connection with the presentation of the individual experiments.

Exp.	Reaction mixture								Pres.	Temp.	Stoich.
id.	N_2	O_2	H_2	CO	CH_4	C_2H_6	NO_x	H_2S	[bar]	[K]	ratio (ϕ)
A	×	×	×	×			×		100	598–898	0.064
B	×	×	×	×			×		50	598–898	0.063
C	×	×	×	×			×		20	598–898	0.063
D	×	×			×				100	598–898	98.8
E	×	×			×				100	598–898	45.6
F	×	×			×				90	598–898	25.2
G	×	×			×				50	598–898	95.5
H	×	×			×				100	673–898	1.09
I	×	×			×				90	598–898	1.03
J	×	×			×				100	648–898	0.042
K	×	×			×				90	598–898	0.040
L	×	×			×				50	648–898	0.042
M	×	×			×	×			100	598–848	44.1
N	×	×			×	×			50	598–898	41.4
O	×	×			×	×			100	598–898	0.936
P	×	×			×	×			100	598–898	0.036
Q	×	×			×	×			50	673–898	0.039
R	×	×			×		×		100	598–898	116.
S	×	×			×		×		50	598–898	102.
T	×	×			×		×		20	598–898	99.0
U	×	×			×		×		100	598–848	1.14
V	×	×			×		×		50	598–898	1.15
W	×	×			×		×		20	598–898	1.05
X	×	×			×		×		100	598–898	0.042
Y	×	×			×		×		50	598–898	0.044
Z	×	×			×		×		20	598–898	0.045
$\mathcal{A}$	×	×			×			×	50	598–898	22.6
$\mathcal{B}$	×	×			×			×	50	598–898	1.09
$\mathcal{C}$		×			×				100	598–763	114.
$\mathcal{D}$		×			×				100	598–763	40.9

6.2 $CO/H_2/NO_x$ Experiments

Nitrogen diluted mixtures of CO, H_2, O_2, and NO_x have reacted at three different pressures: 100, 50, and 20 bar under oxidizing conditions ($\phi = 0.06$). The oxidation of CO to CO_2 in the presence of H_2 constitutes a fundamental reaction system in hydrocarbon oxidation chemistry. Model validation is therefore important before simulations of more complicated chemical systems are undertaken. The further addition of NO_x had a dual purpose. First of all, the reaction kinetics of NO_x is also a fundamental mechanism in many combustion systems, and experiments with only $CO/H_2/O_2$ provided an opportunity to validate the proposed NO_x mechanism at conditions that did not involve direct NO_x/hydrocarbon interactions. The second purpose rose from the fact that the experimental system is limited to operations <925 K. However, NO_x has a promoting effect on the fuel initiation that enabled measurements of reactant conversion at lower temperatures than otherwise obtained with pure CO/H_2 oxidation.

6.2.1 Experimental Conditions

The experimental conditions are summarized in Table 6.2. Measured concentrations of CO, CO_2, O_2, NO, and NO_2 are presented in Figure 6.2 including corresponding modeling predictions.

Table 6.2: Reaction conditions applied during experiments with $CO/H_2/NO_x$. The reactant concentrations are balanced by N_2. The volumetric flow rate was $\sim 3\,^{NL}/_{min}$ in all experiments. The exact flow rates are incorporated in the expressions of the temperature dependent residence times $\tau(T)$ obtained from Equation 4.1. See the text about NO_x concentrations and residence times.

	Reactant concentrations							
Exp. id.	CO [ppm]	H_2 [ppm]	O_2 [%]	NO_x(NO) [ppm]	Pres. [bar]	Temp. [K]	ϕ [a]	τ [s K]
A	502	440	1.48	151(6)	100	598–898	0.064	$^{11990}/_{T}$
B	518	446	1.54	151(26)	50	598–898	0.063	$^{6030}/_{T}$
C	518	453	1.53	149(113)	20	598–898	0.063	$^{2350}/_{T}$

[a] Stoichiometric ratio (ϕ) is based on $CO + H_2 + O_2 \rightarrow CO_2 + H_2O$

τ denotes the temperature dependent residence time in the isothermal section of the reactor. The diluted conditions ensured a low heat development during the reaction, and calculations of the adiabatic temperature rise indicate values <8 K for all conducted experiments. The carbon balance is satisfied within 1 % in all three experiments.

NO_x was supplied to the system as pure NO diluted in N_2. However, the high pressure and excess O_2 promoted a substantial conversion of NO to NO_2 via $NO + NO + O_2 \rightleftharpoons NO_2 + NO_2$ (–R278). Simulations indicate that under the given pressures and stoichiometries, conversion takes place even at room temperature and before the reactor inlet. The resulting inlet distribution of NO_x species is reflected in the reactant concentrations listed in Table 6.2. These correspond to the average concentrations measured at low reactor temperatures before fuel conversion is initiated. A similar conversion of NO_x is expected to take place in the downstream section of the setup, until the pressure is reduced to atmospheric level by the pressure reduction valves; see the description of the setup in Section 4.2. This post-conversion of NO_x will not be reproduced by kinetic modeling if isothermal conditions are applied together with the temperature dependent residence times listed in Table 6.2. Thus, in order to accurately predict the NO_x concentration profiles under oxidizing conditions, it may be necessary to include the complete experimental temperature profiles in the calculations together with sufficient residence times to cover the full reactor length as well as the downstream section of the setup until the pressure reduction valves. Estimated average residence times from the reactor inlet to the pressure reduction valves are ∼110, ∼55, and ∼22 s for the 100, 50, and 20 bar experiments respectively. This should cover the path through the heating, isothermal, and cooling section of the reactor as well as about 1 m of 1/8" steel tubings that lead from the reactor outlet to the reduction valves. These are uncertain estimates, but modeling results are not sensitive to the values. The impact on the model performance is illustrated by showing NO and NO_2 profiles calculated both under the assumption of an isolated isothermal section of the reactor and by use of interpolation between experimental temperature profiles based on the modified SENKIN code previously described in Section 5.2.3.

6.2.2 Discussion of Experimental and Modeling Results

The numerical predictions of the measured concentration profiles in Figure 6.1 are satisfactory for all the experiments. The results reveal a decreasing CO initiation temperature from about 800 to 700 K when the pressure increases from 20 to 100 bar. The most significant decrease takes place between 20 and 50 bar, which suggests a declining pressure dependency with increasing pressure. Simulations with varying residence times have confirmed that this behavior is indeed a result of increasing pressure and not an effect of increasing residence times.

It is noteworthy that the concentration profiles from all three experiments display similar trends; even though they appear at different temperatures.

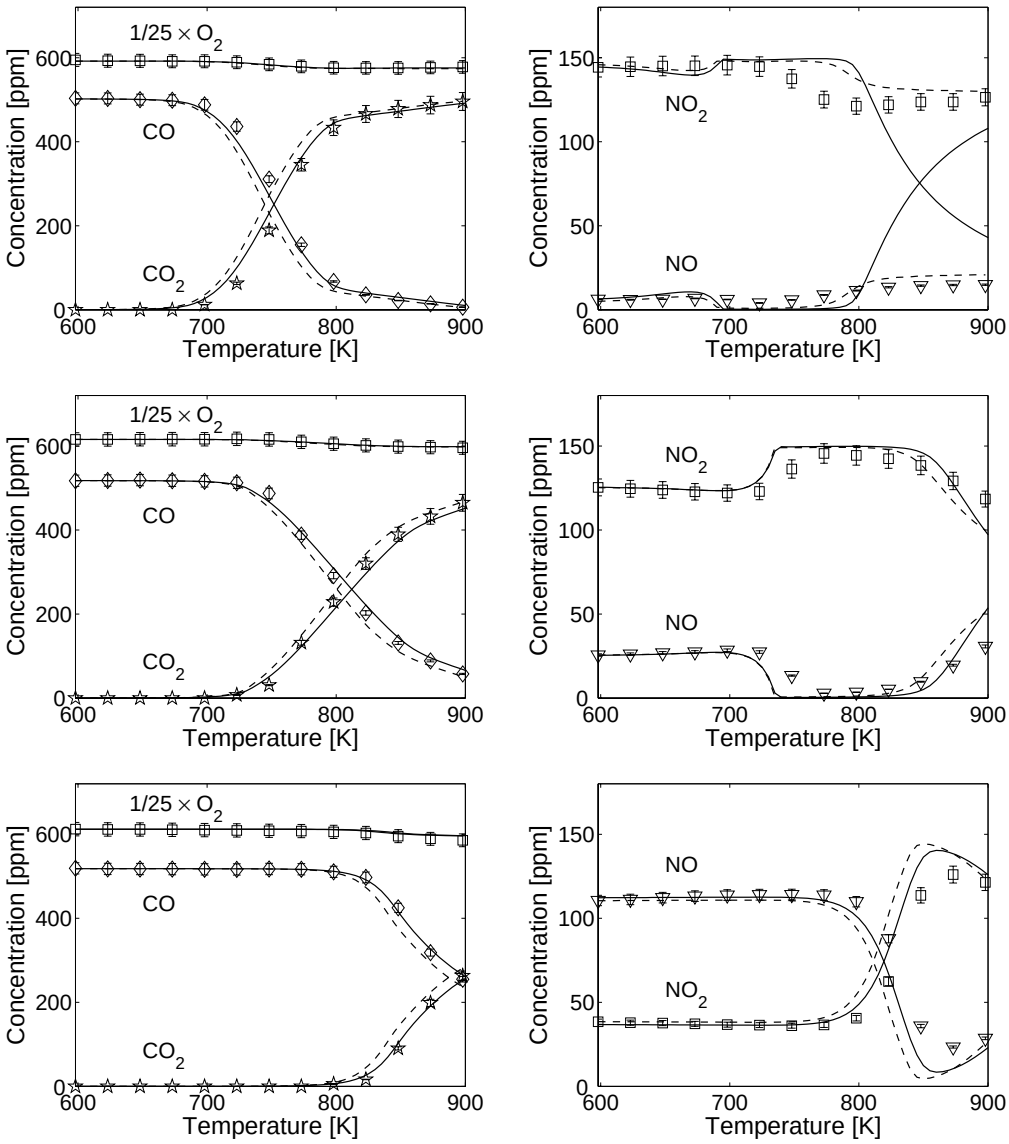

Figure 6.1: Results of experiments with $CO/H_2/NO_x/O_2$. Concentration profiles are shown as a function of the reactor temperature at 100 (top), 50 (middle) and 20 bar (bottom) cf. experiments A–C. Reaction conditions are provided in Table 6.2. Symbols mark experimental results, while full lines denote model predictions obtained at isothermal conditions using the temperature dependent residence times from Table 6.2. Dashed lines represent simulations with the experimental temperature profiles; see text. Measuring uncertainties are ±2.6 % for O_2/CO, ±4.3 % or ±3 ppm for CO_2, and ±2.8 and 4.0 % for NO and NO_2 respectively.

This suggests a similar governing chemistry in all the experiments.

Deviations between modeling results obtained at isothermal conditions (full lines in Figure 6.1) and with the complete experimental temperature profiles (dashed lines) are minor except at the highest pressure and temperatures >800 K, where the behavior of the NO_x profiles are only accurately captured by the model when applying the experimental temperature profiles. This is in line with the previous discussion of the potential conversion of NO_x outside the isothermal section of the reactor.

6.2.3 Governing Reaction Mechanisms

The satisfactory prediction of the experimental results justifies a characterization of the important reaction pathways based on the kinetic model.

The fuels CO and H_2 are oxidized to the stable products CO_2 and H_2O by reaction with OH radicals; either directly or, in the case of CO, through intermediate formation of HOCO. Hydroxyl is generated through subsequent conversion of the radical by-products HO_2 and H in a number of possible reaction pathways that involve recycling of NO/NO_2. The most important mechanisms are shown in Figure 6.2 and 6.3.

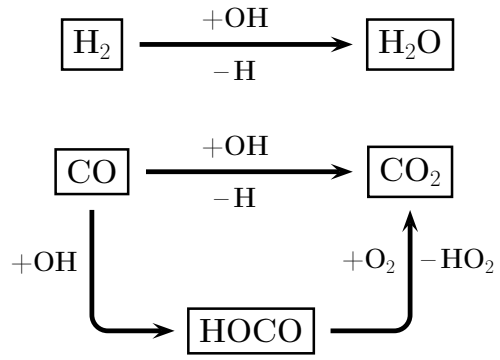

Figure 6.2: Main reaction pathways for CO/H_2 conversion at the investigated conditions of experiment A–C.

The conversion of CO to CO_2 is governed by two competitive pathways that lead to CO_2+H, either directly (R23), or through intermediate formation of HOCO (R24) and subsequent oxidation by molecular oxygen via (R27). Both channels consume OH radicals. The model indicates that (R27) completely dominates over the unimolecular decomposition of HOCO (R25) independently of ϕ and pressure. The ratio $^{R27}/_{(R23+R27)}$ increases with increasing pressure and/or low temperatures. Hence, at 750 K, about 75 and 60 % of the CO conversion during the 100 and 50 bar experiments involve intermediate

HOCO formation. At 900 K, these contributions have decreased to about 50 and 35 % respectively. In the 20 bar experiment, the importance of (R27) is reduced to <30 %.

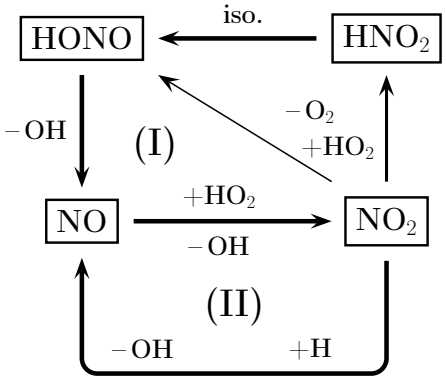

Figure 6.3: NO_x interactions with the H/O radical pool are the main source of OH radicals at the investigated conditions of experiment A–C. The sums of the two sequences yield (I): $HO_2+HO_2 \rightleftharpoons OH+OH+O_2$, (II): $HO_2+H \rightleftharpoons OH+OH$.

The two NO/NO_2 recycling sequences (I) and (II) in Figure 6.3 are the major sources of the important chain-carrying OH radicals at the investigated conditions. Hydroperoxyl is the sole radical reactant in (I). First, NO is oxidized to NO_2 followed by reduction to HONO; either directly via (R276), or through intermediate formation and isomerization of HNO_2 (R277)+(R319). Nitrous acid readily decomposes to NO+OH (–R259) and completes the cycle, while yielding a net formation of two OH radicals. About $^2/_3$ of the nitrogen flux in (I) pass through HNO_2, but the HNO_2 pool remains very low due to rapid isomerization to HONO. In mechanism (II), NO is directly regenerated from NO_2 through reaction with H atoms (R270). This also yields a net formation of two OH radicals per cycle at the expense of HO_2+H.

The ratio between the two NO/NO_2 cycles is controlled by the availability of H and HO_2 radicals. Hydrogen atoms are produced from the direct conversion of H_2 to H_2O (R9), and CO to CO_2 (R23), but at high pressure and/or low temperatures a considerable fraction of the H atom pool is converted to HO_2 through $H+O_2(+M) \rightleftharpoons HO_2(+M)$ (R4), thereby promoting (I) over (II). The calculations indicate that the ratio $^{(I)}/_{(II)} \approx {}^{R4}/_{R270}$ that yields values > 5 at 100 bar and 750 K. The ratio decreases with the temperature to ∼3.5 at 900 K. At 50 bar, the ratio is below unity, and at 20 bar or below, reaction (R270), i.e. sequence (II), dominates completely. It is noticed that the introduction of (R4) as a source of HO_2 radicals in mechanism (I) makes the net gain from the two pathways identical, as illustrated below:

$$\begin{aligned} H + O_2(+M) &\rightleftharpoons HO_2(+M) && \text{(R4)} \\ NO_2 + HO_2 &\rightleftharpoons HONO + O_2 && \text{(R276 or R277 + R319)} \\ HONO(+M) &\rightleftharpoons NO + OH(+M) && \text{(−R259)} \\ \hline \Sigma \quad NO_2 + H &\rightleftharpoons NO + OH && \text{(R270)} \end{aligned}$$

This means that the general reactivity of the system is conserved at all investigated pressures even though the underlying mechanism changes. This is consistent with the almost identical shapes of the CO conversion profiles observed in Figure 6.1.

At the investigated conditions, OH radicals are produced from the two NO/NO_2 cycles shown in Figure 6.3. Calculations reveal that in the *absence* of NO_x, OH would either be produced from HO_2+H ⇌ OH+OH (R11) or from HO_2 self-recombination to H_2O_2 (R15) and subsequent decomposition to OH+OH via (R16). The latter path is favored by high pressure and/or low temperatures.

6.3 Measurements of k_{NO_2+H} at 850–875 K

It is a complicated task to measure rate constants of key elementary reactions relevant to combustion in the medium to high-temperature range (600–1300 K), because of the increasing interference from radical side reactions. However, through careful design of experiments, accurate data can be obtained in high-temperature reactors, e.g. flow reactors, which are normally unsuited for obtaining reaction-specific informations. A common approach is to perform perturbation experiments on the well-understood H_2 and/or CO oxidation systems, which has successfully been applied to study the chemistry of reactive nitrogen [103, 104, 116, 169, 678, 729, 865–867], sulfur [115, 116, 868, 869], and potassium [870]. More specifically, investigations of the oxidation of CO and/or H_2 doped with nitrogen oxides have yielded high-temperature rate data for several elementary reactions including H+O_2(+M) (R4) [871, 872], NO+H(+M) (R257) [728, 729], NO_2+H_2 (R271) [750], and N_2O+OH [865].

In the present work, model predictions of the experiment with $CO/H_2/NO_x$ at 20 bar indicate an augmented sensitivity to the elementary reaction NO_2+H ⇌ NO+OH (R270) in the temperature range 825–900 K, where no previous measurements have been reported. This has been utilized to derive values of k_{R270}.

The sensitivity of k_{R270} is illustrated in Figure 6.4, where the measured concentration profiles of $CO/CO_2/O_2$ and NO/NO_2 are compared to model predictions carried out with different values of k_{R270}. Here, calculations are shown for an optimized value of k_{R270} (solid lines), ±50 % perturbations of this value (dotted lines), and the previously accepted value from Ko and Fontijn [692] (dashed lines), which is about 15 % lower than the optimized rate constant.

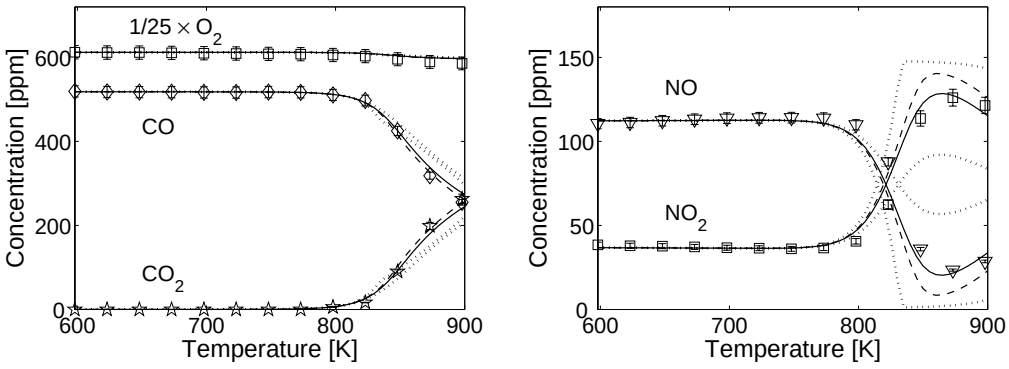

Figure 6.4: Comparison of measured (symbols) and calculated $CO/CO_2/O_2$ and NO/NO_2 concentration profiles from the 20 bar experiment with $CO/H_2/NO_x$ using different rate constants for $NO_2+H \rightleftharpoons NO+OH$ (R270). Full lines denote modeling results based on the optimized rate expression $k_{R270} = 1.64 \times 10^{14} \exp(-500/[RT])$ $^{cm^3}/_{mol\,s}$. The dotted lines are simulations obtained from ±50 % perturbations of the optimized rate constant. Dashed lines represent modeling predictions with k_{R270} from Ko and Fontijn [692], cf. Table 5.5. Other specifications are identical to Figure 6.1.

Figure 6.4 reveals that variations of k_{R270} have little impact on the model predictions of the CO and CO_2 profiles within the investigated temperature range. However, curiously both increasing and decreasing values lead to a slight inhibition of CO oxidation above 850 K. For NO and NO_2, small variations in k_{R270} have a significant impact on the model predictions. A 50 % decrease causes all the NO_x to be in the form of NO_2 above 825 K, while a similar increase leads to a significant underprediction of the NO_2 concentration. For the temperatures 850 and 875 K, the rate constant k_{R270} has been adjusted to obtain the best fit between the observed NO/NO_2 partitioning and the model predictions. At temperatures below 850 K and above 875 K, the relative sensitivity of the model predictions to side reactions was significantly higher, so these data points have not been used for deriving a value of k_{R270}.

Figure 6.5 shows the first order sensitivity coefficients for the predicted

NO formation at 850 and 875 K. The sensitivity analysis confirms that reaction (R270) acts as the predominant bottleneck at the specific conditions, and it supports the indications from Figure 6.4 that even minor changes in k_{R270} facilitate a significant difference in the predicted NO and NO_2 concentrations.

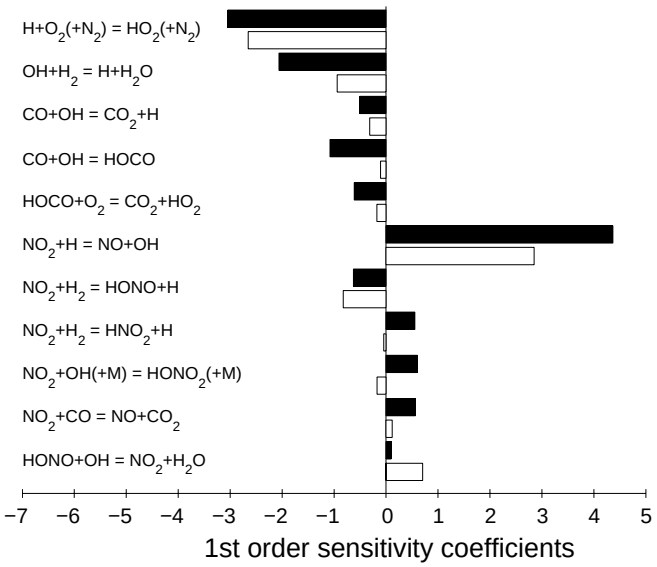

Figure 6.5: Normalized first-order sensitivity coefficients calculated for NO formation during the 20 bar experiment with $CO/H_2/NO_x$. The open bars denote sensitivity coefficients calculated at 850 K; the closed bars denote values at 875 K. The figure shows the most sensitive reactions, i.e. those exhibiting a sensitivity coefficient >10 % of the value for NO_2+H (R270).

The most important side reaction is the recombination reaction between atomic hydrogen and O_2; $H+O_2(+M) \rightleftharpoons HO_2(+M)$ (R4). The accuracy of the rate constant for this reaction has a large impact on the estimated uncertainty limits for k_{R270}. The $H+O_2(+M)$ reaction has mainly been characterized using Ar as collision partner. The scatter in the data for $H+O_2+Ar$ is significant above 750 K [145]. However, recent experimental results [197, 872–875], probably all at the low-pressure limit [876], are in quite good agreement and indicate that in the 800–900 K range, $k_{R4,Ar}$ is known within ±30 %. For N_2 as collision partner, fewer data have been reported. However, the available results [145, 197] are in essential agreement and indicate an accuracy of k_{R4,N_2} similar to that reported for Ar. Dryer and co-workers [192,872,877] have thoroughly discussed the uncertainty for k_{R4,N_2} in the 800–900 K range. Even though their work on the $H_2/O_2/NO_x$ system

yields a rate constant $k_{\mathrm{R4,N_2}}$ in close agreement with other studies, this value is dependent on their choice of k_{R270} (drawn from Ko and Fontijn [692]) and cannot be considered independent in relation to the present work. However, as discussed by Li *et al.* [192], experimental data for the explosion limit of the H_2/O_2 system at 800–900 K also place severe constraints on the ratio $k_{\mathrm{H+O_2\rightarrow O+OH\,(R3)}}/k_{\mathrm{R4,N_2}}$ supporting a high accuracy of $k_{\mathrm{R4,N_2}}$ in this temperature range.

According to the sensitivity analysis in Figure 6.5, other side reactions also gain some impact on the model predictions of NO. The sensitivity coefficients for the reaction of OH+H_2 (R9) are comparatively high, but the rate constant for this reaction is known quite accurately. Other side reactions are less well characterized but exhibit smaller sensitivity coefficients.

The impact from uncertainties in side reactions, $U_{sr,\mathrm{R270}}$, can be determined by scaling the individual uncertainties with the sensitivity coefficients according to Equation (6.1):

$$U_{sr,j} = \sqrt{\sum_i \left(S_{\mathrm{NO},i} \frac{\Delta k_i}{k_i} \right)^2} \Bigg/ \left(S_{\mathrm{NO},j} \right), \qquad i \neq j \tag{6.1}$$

Here, $S_{\mathrm{NO},i}$ represents the sensitivity coefficient for the ith reaction included in the sensitivity analysis for NO formation except for the investigated reaction j. Thus, i = (R4), (R9), (R23), etc., while j = (R270) in the present case. The factor $\Delta k_i/k_i$ represents the uncertainty associated with the ith reaction. The overall uncertainty limit $U_{tot,\mathrm{R270}}$ is subsequently determined by:

$$U_{tot,j} = \sqrt{(U_{sr,j})^2 + (U_{exp})^2 + (U_\tau)^2} \tag{6.2}$$

where U_{exp} is the experimental uncertainty, which is modest in the present case (±2.8 % for NO) compared to $U_{sr,\mathrm{R270}}$. U_τ represents the uncertainty associated with the applied residence time in the modeling. Calculations indicate an approximate impact of ±5 % from deviations in τ. Table 6.3 provides a list of estimated uncertainties ($\Delta k_i/k_i$) for the reactions included in the sensitivity analysis in Figure 6.5.

By fitting the rate constant k_{R270} to match the measured concentrations of NO at 850 and 875 K, respectively, and considering the combined uncertainties in accordance with the methodology outlined above, values of $k_{\mathrm{R270}}(850\,\mathrm{K}) = 1.31 \times 10^{14}$ (±36 %) $^{\mathrm{cm^3}}/_{\mathrm{mol\,s}}$ and $k_{\mathrm{R270}}(875\,\mathrm{K}) = 1.23 \times 10^{14}$ (±42 %) $^{\mathrm{cm^3}}/_{\mathrm{mol\,s}}$ have been obtained. Figure 6.6 summarizes the data for the NO_2+H rate constant.

Table 6.3: Estimated uncertainties for reactions included in the sensitivity analysis for NO at 850 and 875 K (Figure 6.5) during the 20 bar experiment with $CO/H_2/NO_x$.

i	Reaction	$\Delta k_i/k_i$
(R4)	$H + O_2(+N_2) \rightleftharpoons HO_2(+N_2)$	0.3
(R9)	$OH + H_2 \rightleftharpoons H + H_2O$	0.2
(R23)	$CO + OH \rightleftharpoons CO_2 + H$	0.2
(R24)	$CO + OH \rightleftharpoons HOCO$	1.0
(R27)	$HOCO + O_2 \rightleftharpoons CO_2 + HO_2$	1.0
(R271)	$NO_2 + H_2 \rightleftharpoons HONO + H$	0.5
(R272)	$NO_2 + H_2 \rightleftharpoons HNO_2 + H$	1.0
(R275)	$NO_2 + OH(+M) \rightleftharpoons HONO_2(+M)$	1.0
(R282)	$NO_2 + CO \rightleftharpoons NO + CO_2$	0.2
(R316)	$HONO + OH \rightleftharpoons NO_2 + H_2O$	0.5

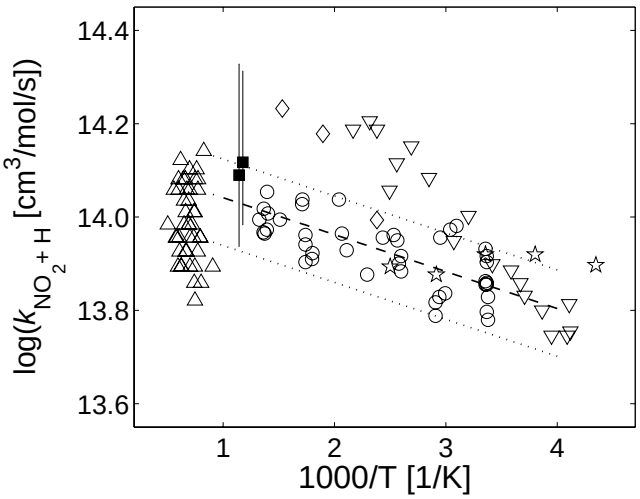

Figure 6.6: Arrhenius plot of the fitted rate constant of k_{R270} (■ with errorbars) and comparison with previous measurements. ○ Ko & Fontijn [692]; ◊ Clyne & Monkhouse [744]; ▽ Wagner *et al.* [743]; ☆ Michael *et al.* [746]; △ Su *et al.* [745]; - - Ko & Fontijn [692] with ±21 % overall uncertainty limits represented by dotted lines.

The results obtained in the present work indicate a value of k_{R270} that is slightly higher than that obtained by Ko and Fontijn [692], but within their reported uncertainty limit of ±21 %. Compared to the results of Su *et al.* [745], the present rate constant measurements are about a factor of 1.5 higher and outside their reported accuracy of 18 %. However, the data are in

agreement within the combined uncertainty limits. The fitted rate constants lie a factor of 1.4 below the least square estimate to available literature data at 230–800 K proposed by Baulch et al. [145], but this rate expression was assigned an uncertainty factor of 2 and is therefore consistent with the proposed data.

Based on the present data, as well as those from the literature, it appears that the rate for the NO_2+H reaction does increase slightly with temperature, and it is recommended that the rate coefficient of $k_{\mathrm{R270,\,Ko\ \&\ Fontijn,\ 1991}} = 1.3 \times 10^{14} \exp\left(\frac{-362}{RT}\right)\ {}^{\mathrm{cm}^3}/_{\mathrm{mol\,s}}$ is used for combustion modeling.

6.4 CH_4 Experiments

The experiments with pure CH_4 (D–L) constitute a key segment of the experimental database. Satisfactory predictions of these data are a fundamental requirement for the later utilization of the kinetic model during the optimization of the GTL process.

6.4.1 Experimental Conditions

Experiments are available at three different pressures: 100, 90, and 50 bar and different stoichiometric ratios representing reducing ($25 < \phi < 99$), stoichiometric ($\phi \approx 1$), and oxidizing conditions ($\phi \approx 0.04$). No recognizable conversion was observed at 20 bar without a chemical promoter, like e.g. NO_x. This was also the case at 50 bar and stoichiometric conditions. The experimental conditions are summarized in Table 6.4. It is noted that calculations of the adiabatic temperature rise gave values <26 K for all experiments and the carbon balances were satisfied within 6 %.

Measurements include concentration profiles of CH_4, O_2, CO, and CO_2 for all experiments. In addition, measurements of C_2H_6, C_2H_4, and CH_3OH are presented for the reducing experiments D–G. These species were also observed during the stoichiometric experiments, but in too low concentrations to facilitate a reliable model validation. Likewise, was C_2H_5OH only observed in trace amounts. At the oxidizing conditions, only CO and CO_2 were observed as products.

6.4.2 Fuel Initiation and Surface Reactions

Before presenting the complete set of experimental results, simulations of three experiments representative of reducing, stoichiometric, and oxidizing

Table 6.4: Reaction conditions applied during experiments with CH_4/O_2. Concentrations are in ppm if otherwise not stated. See caption of Table 6.2 for other specifications.

	Reactant concentrations					
Exp. id.	CH_4 [ppm]	O_2 [ppm]	Pres. [bar]	Temp. [K]	ϕ [a]	τ [s K]
D	4.63 %	936	100	598–898	98.8	$^{12070}/_{T}$
E	4.42 %	1940	100	598–898	45.6	$^{11690}/_{T}$
F	1.12 %	889	90	598–898	25.2	$^{10450}/_{T}$
G	4.66 %	976	50	598–898	95.5	$^{5870}/_{T}$
H	1587	2903	100	673–898	1.09	$^{11870}/_{T}$
I	1491	2888	90	598–898	1.03	$^{10430}/_{T}$
J	964	4.57 %	100	648–898	0.042	$^{12020}/_{T}$
K	993	5.00 %	90	598–898	0.040	$^{10740}/_{T}$
L	968	4.60 %	50	648–898	0.042	$^{6030}/_{T}$

[a] Stoichiometric ratio (ϕ) is based on $CH_4 + 2O_2 \rightarrow CO_2 + 2H_2O$

conditions are initially considered in Figure 6.7. The reason is that the numerical results display a premature fuel ignition under all the experimental conditions compared to the measured concentration profiles. This issue needs to be addressed before a reliable outline of the underlying reaction mechanisms can be justified.

The premature fuel ignition is most severe in the reducing experiment in Figure 6.7 (left) where the model predicts an initiation temperature that is ∼50 K lower than indicated by the experiments. For comparison, the results obtained at stoichiometric and oxidizing conditions in Figure 6.7 (right) both display an onset of the chemistry at ∼25 K below the initiation temperature in the experiments. The fact that the feed concentrations of CH_4 were almost the same in the stoichiometric and oxidizing experiments indicates that the phenomenon is related to the absolute concentration of CH_4 rather than the stoichiometric ratio. Without showing the results, the author confirms that this behavior is consistent throughout the remaining experiments with CH_4/O_2 listed in Table 6.4.

The principal initiation reaction in the chemical system at hand is $CH_4 + O_2 \rightleftharpoons CH_3 + HO_2$ (–R40), but the observed initiation temperature shows negligible sensitivity to perturbations in the corresponding rate constant. Moreover, calculations indicate that no other elementary reactions included in the kinetic model can be tweaked sufficiently to close the gap between experiments and simulations, while maintaining the specific rate constants within reasonable limits of their original determinations. This suggests that a

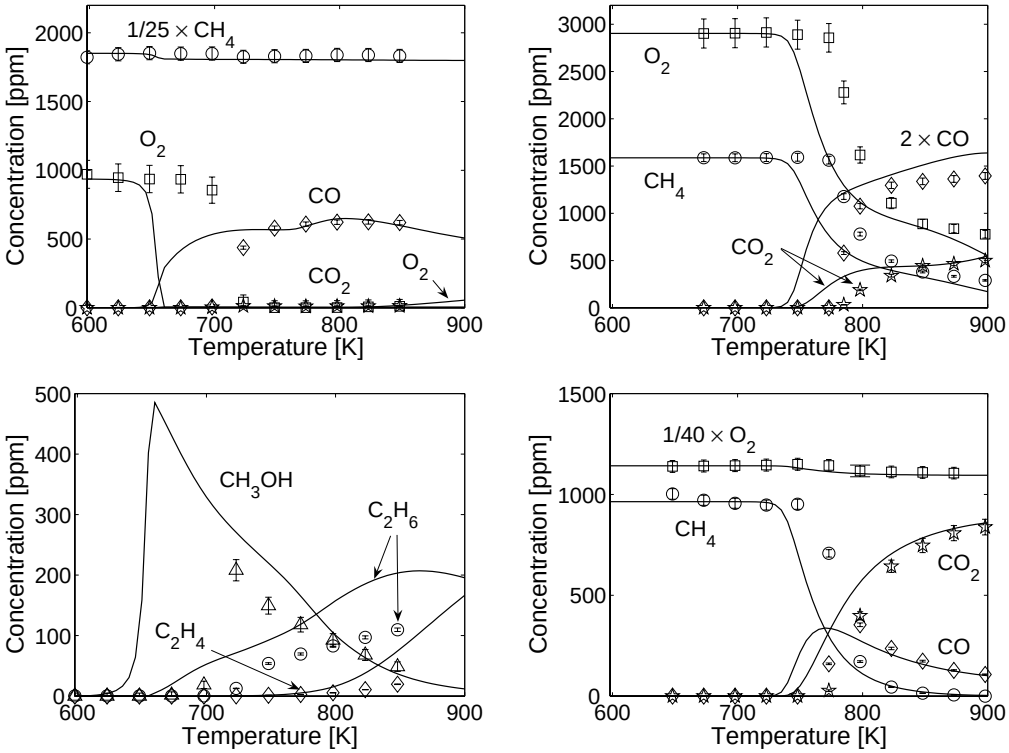

Figure 6.7: Results of selected experiments with CH_4/O_2 at 100 bar. Left: Reducing exp. D ($\phi = 98.8$). Top right: Stoichiometric exp. H ($\phi = 1.09$). Bottom right: Oxidizing exp. J ($\phi = 0.042$). Reaction conditions are provided in Table 6.4. Symbols mark experimental results. Lines denote model predictions obtained at isothermal conditions. Measuring uncertainties are ±2.6 % for $CO/CH_4/C_2H_4/C_2H_6$, ±4.3 % or ±3 ppm for CO_2, and ±6.0 % or ±3 ppm for CH_3OH. Uncertainties of O_2 measurements are ±5.3 % (top left and right), and ±2.6 % (bottom right).

vital part of the kinetic scheme is either missing in the model or the premature fuel ignition should instead be attributed to issues related to the experimental conditions. The latter may either be associated with uncertainties in the residence time or a potential loss of radical species at the reactor wall.

The residence time in the isothermal reaction zone is a function of the volumetric flow rate, temperature, pressure, and reactor dimensions; as shown in Equation 4.1. These parameters have been determined with high accuracy (estimated to be within ±1 % or less) except for the isothermal reactor length that was determined from the measured temperature profiles previously shown in Figure 4.5 with an estimated absolute uncertainty of ±3 cm. However, in order to compensate for the premature fuel ignition predicted

by the model in Figure 6.7 the isothermal reactor length needs to be reduced to ∼13 cm. Compared to the present reactor length of 43 cm, this is clearly unreasonable and rules out the possibility that the observed discrepancies between experiments and numerical results are caused (mainly) by residence time effects.

Instead, the attention is drawn to the potential deactivation of radical species at the reactor wall, which is equivalent to a loss of reactivity in the chemical system. As previously discussed in the literature review in Section 2.2.5, this phenomenon is of particular concern in laboratory reactors that typically exhibit large surface-to-volume ratios ($^S/_V$). The applied reactor material is quartz, which is traditionally considered to be inert towards surface reactions. Experiments [69] and theoretical investigations [119] have, nonetheless, indicated that even quartz may exhibit a minor reactivity towards hydrocarbon oxidation. It is difficult to quantify the extent of surface activity in the present work based on the available measurements. As mentioned above, radical deactivation seems to increase with increasing CH_4 concentrations. The previous experiments with $CO/H_2/NO_x$ did not show a noticeable difference between the predicted and observed fuel ignition, and hence, also point in the direction of hydrocarbon radical removal.

Modeling results presented in Figure 6.8 confirm that the fuel ignition observed in the experiments can be accurately predicted when an irreversible deactivation reaction of CH_3OO radicals to $CH_3OO^\bullet$ (R349) is added to the kinetic model:

$$CH_3OO \rightarrow CH_3OO^\bullet \qquad \text{(R349)}$$

Here, '•' indicates that CH_3OO is attached to a surface and hence, cut off from further gas phase conversion. The rate constant has been fitted to the reducing experiments D–G yielding $k_{R349} = 45\,{}^1/_s$, while a value of $9.5\,{}^1/_s$ was fitted to the stoichiometric and oxidizing experiments H–L.

The CH_3OO radical has been selected for deactivation for different reasons. First of all, calculations indicate that CH_3OO formation constitutes an important bottleneck in the low-temperature ignition of CH_4 at high pressures. Calculations also show that the conversion of reactants *after* initiation exhibits minimal sensitivity to the proposed removal of CH_3OO via (R349). This is in contrast to other important hydrocarbon radicals, like CH_3 and CH_3O, where similar deactivation reactions gave rise to markedly different behaviors in the fuel conversion than observed in the experiments. Moreover, the removal of CH_3OO has previously been considered in combustion modeling of rich CH_4/O_2 mixtures at >50 bar and 600–800 K by Vedeneev *et al.* [80].

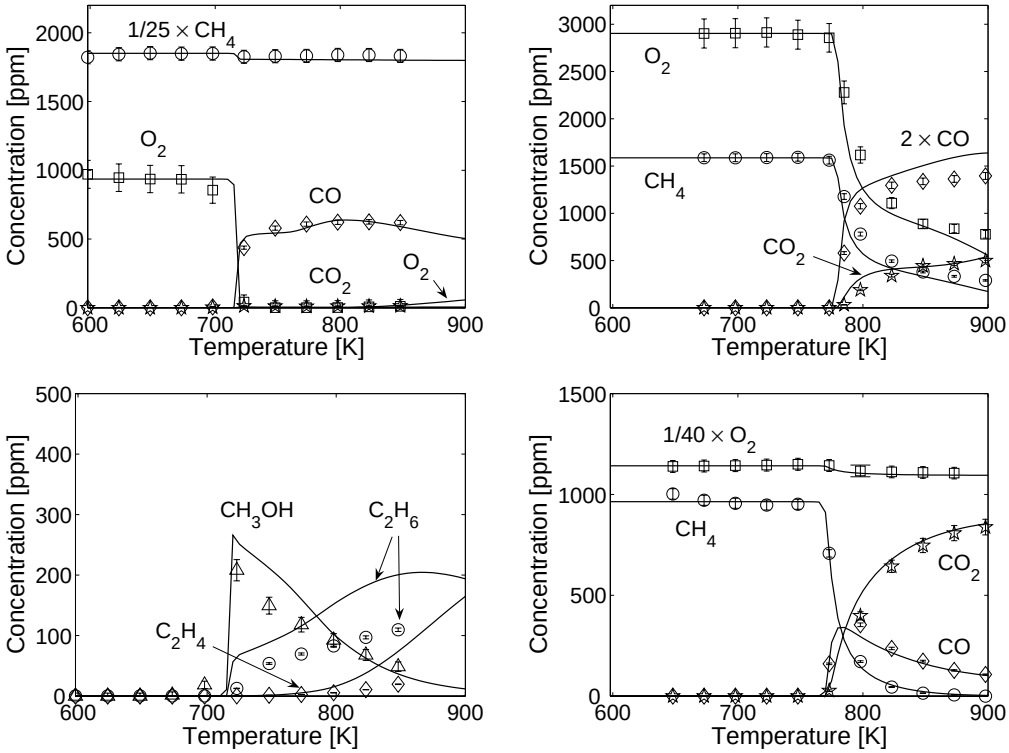

Figure 6.8: Model predictions of CH_4/O_2 experiments at 100 bar when the surface reaction $CH_3OO \rightarrow CH_3OO^{\bullet}$ (R349) is included. Left: Reducing exp. D ($\phi = 98.8$). Top right: Stoichiometric exp. H ($\phi = 1.09$). Bottom right: Oxidizing exp. J ($\phi = 0.042$). Rate constant $k_{R349} = 45\,{}^{1}/_{s}$ (left) and $9.5\,{}^{1}/_{s}$ (right). Other specifications are given in the caption of Figure 6.7.

The fate of $CH_3OO^{\bullet}$ is uncertain, but it seems reasonable to expect heterogeneous conversion to mixtures of partial and full oxidation products. In order to avoid build-up of $CH_3OO^{\bullet}$ during modeling, fast irreversible reactions like $CH_3OO^{\bullet}+CH_3OO^{\bullet} \rightarrow CH_2O+CO+2H_2O$ or $CH_3OO^{\bullet}+CH_3OO^{\bullet}+O_2 \rightarrow CO+CO_2+3H_2O$ can be included in the kinetic model. However, the simulations indicate a modest removal of hydrocarbon matter via (R349) with no significant impact on the magnitudes of the predicted concentration profiles, so it has not been necessary to force the conversion of $CH_3OO^{\bullet}$ to gaseous products.

It is emphasized that deactivation of CH_3OO radicals via (R349) is limited to modeling of the present experimental results and should not be inherited in future applications of the kinetic model including the later optimization of the GTL process. The high pressure flow reactor applies a ${}^{S}/_{V}$ ratio of

5.0 $^1/_{cm}$, but this value is expected to decrease significantly in a potential industrial scale reactor, which will reduce the contact between the reacting mixture and surfaces and probably make surface effects negligible.

6.4.3 Discussion of Experimental and Modeling Results

The following Figures 6.9–6.11 present experimental results obtained from oxidation of pure CH_4 at various stoichiometries and pressures including corresponding model predictions. Together with the results already presented in Figure 6.8, these data constitute the complete set of experimental and modeling results with CH_4/O_2 (Exp. D–L). All simulations include the surface reaction $CH_3OO \rightarrow CH_3OO^\bullet$ (R349) discussed in the previous section.

Simulations of the major species CH_4, O_2, CO, and CO_2 are everywhere in very good agreement with the experimental concentration profiles. The stoichiometric experiments shown in Figure 6.8 (top right) and Figure 6.10, as well as the reducing experiment F and G at 90 and 50 bar (Figure 6.9, middle and bottom) reveal a marked change in the conversion rate of fuel and oxidizer at temperatures just above the initiation temperature. In the stoichiometric experiments, the net conversion of CH_4 (and O_2) tends to slow down between ∼800 and 900 K, whereas the two reducing experiments display a decreasing net conversion of O_2 that culminates at 900 K. (The current scaling of the graphs does not permit a similar view of the CH_4 concentration profile). Net rate analyses indicate that this phenomenon can be attributed to a significant build-up of CH_3 and HO_2 radicals that drives the reaction CH_3+$HO_2 \rightleftharpoons CH_4$+$O_2$ (R40) towards the original fuel and oxidizer. It is noticed that the phenomenon is not observed in all the reducing experiments. Considering the differences in the experimental conditions in Table 6.4, it is seen that almost identical reactant concentrations were used in the reducing exp. D at 100 bar (Figure 6.8, left) and exp. G at 50 bar (Figure 6.9, bottom), but only the 50 bar experiment displays the characteristic increase of the O_2 concentration at the higher temperatures. This suggests a pressure or a residence time effect. Calculations indicate that *both* effects play a role in combination with the stoichiometric ratio. The latter is causing the phenomenon to appear in the reducing experiment at 90 bar (Figure 6.9, middle left), where a lower stoichiometric ratio ($\phi = 25.2$) was used compared to the other reducing experiments.

Considering the simulations of CH_3OH at reducing conditions in Figure 6.8 (bottom left) and Figure 6.9 (right), the results are generally satisfactory. A substantially higher concentration of CH_3OH is observed at 100 bar than at 50 bar, which suggests that optimal conditions for high CH_3OH yields lie closer to 100 bar. It is difficult to make the same direct comparison of the

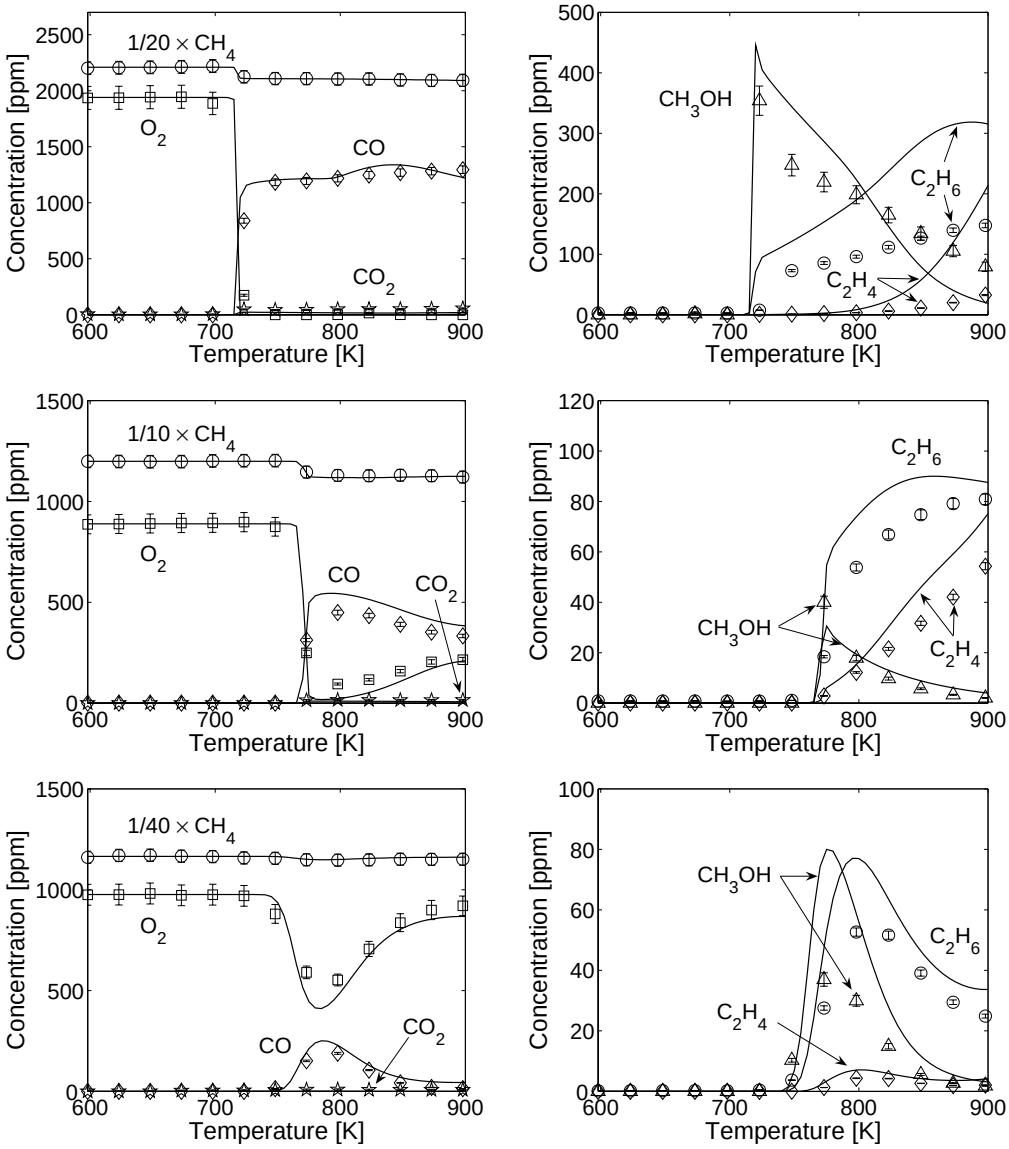

Figure 6.9: Results of reducing experiments with CH_4/O_2. Top: Exp. E (100 bar, $\phi = 45.6$). Middle: Exp. F (90 bar, $\phi = 25.2$). Bottom: Exp. G (50 bar, $\phi = 95.5$). Reaction conditions are provided in Table 6.4. Symbols mark experimental results. Lines denote model predictions obtained at isothermal conditions. Measuring uncertainties are ±2.6 % for $CO/CH_4/C_2H_4/C_2H_6$, ±5.3 % for O_2, ±4.3 % or ±3 ppm for CO_2, and ±6.0 % or ±3 ppm for CH_3OH.

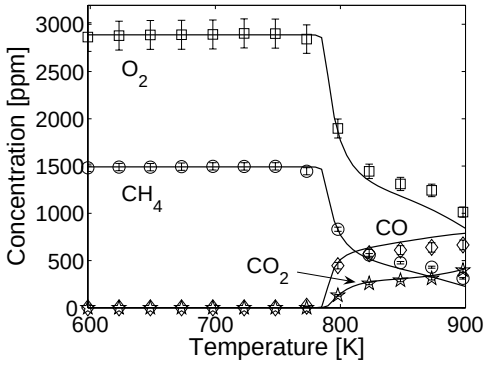

Figure 6.10: Results of stoichiometric CH_4/O_2 experiment I (90 bar, $\phi = 1.03$). Symbols mark experimental results. Lines denote model predictions obtained at isothermal conditions. Measuring uncertainties are $\pm 2.6\,\%$ for CO/CH_4, $\pm 5.3\,\%$ for O_2, and $\pm 4.3\,\%$ or ± 3 ppm for CO_2.

results at 100 and 90 bar because of the somewhat lower stoichiometric ratio used in the 90 bar experiment. The only significant deviation between experiments and modeling results is observed at 50 bar (Figure 6.9, bottom right), where the measured peak concentration of CH_3OH is overpredicted by roughly a factor of 2. However, the present calculations of the CH_3OH concentration are very sensitive to the magnitude of fuel conversion and even minor discrepancies between measured and calculated concentrations of CH_4 (and O_2) may have a substantial impact on the formation of CH_3OH. Considering the different magnitudes of the CH_3OH and the CH_4/O_2 concentrations in Figure 6.9 (bottom) it is therefore likely that the overprediction of the peak CH_3OH concentration is simply caused by a minor overprediction of the O_2 conversion instead of an erroneous description of the CH_3OH formation mechanism. A similar effect may account for the minor deviations observed between simulated and experimental CH_3OH profiles during the other reducing experiments.

Simulations of C_2H_6 and C_2H_4 are satisfactory to the point that the main trends are reproduced by the model. However, the model overpredicts the measured concentration profiles by up to a factor of 2 during the reducing 100 bar experiment in Figure 6.8 (bottom left) and Figure 6.9 (top right), whereas the discrepancies are less pronounced during the corresponding experiments at 90 and 50 bar in Figure 6.9 (middle and bottom right). The formation of C_2H_6 and C_2H_4 are closely dependent, so even though the formation of C_2H_6 is overpredicted, the model may still accurately capture the conversion of C_2H_6 to C_2H_4. The later experiments with CH_4/C_2H_6 may

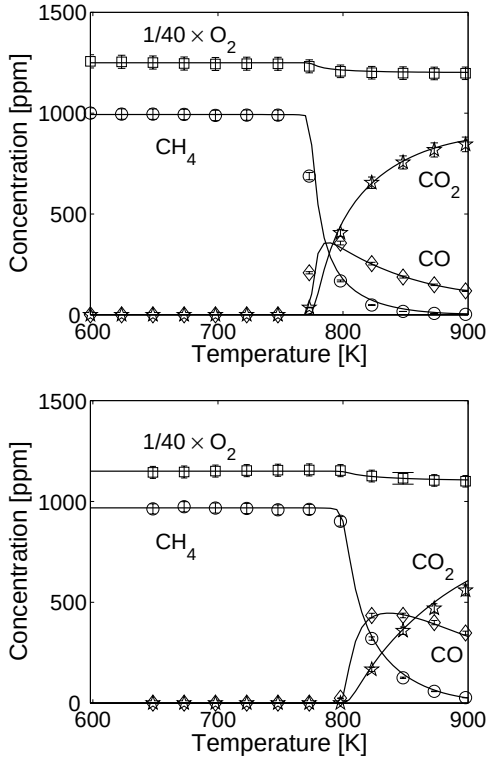

Figure 6.11: Results of oxidizing experiments with CH_4/O_2. Top: Exp. K (90 bar, $\phi = 0.040$). Bottom: Exp. L (50 bar, $\phi = 0.042$). Reaction conditions are provided in Table 6.4. Symbols mark experimental results. Lines denote model predictions obtained at isothermal conditions. Measuring uncertainties are ±2.6 % for $O_2/CO/CH_4$, and ±4.3 % or ±3 ppm for CO_2.

clarify this issue. Net rate analyses indicate that the self-association reaction of CH_3 radicals (R41) is the main route to C_2H_6 under the investigated conditions and the numerical results show a considerable sensitivity to perturbations of the corresponding rate constant. The pressure dependent rate expression of (R41) was taken from the literature evaluation by Baulch *et al.* [145], who assigned uncertainty factors of 2 to both the high- and low-pressure limits at 300–2000 K. At 100 bar and 800–900 K, the rate constant is within 10 % of the high-pressure limit, which have been subjected to some dispute concerning the temperature dependence, see Section 5.3.3.2. However, there are other reactions that indirectly act as a bottleneck for the C_2H_6 formation, e.g. $CH_4+HO_2 \rightleftharpoons CH_3+H_2O_2$ (R31), where uncertainties may partly facilitate the observed discrepancies. At present, the observed overpredictions of the C_2H_6 and C_2H_4 concentrations are mainly attributed

to an inaccurate model description of the conversion of C_1 to C_2, which essentially concerns the self-association reaction of CH_3 (R41). Future work should involve a thorough reevaluation of this part of the reaction mechanism.

6.4.4 Main Reaction Pathways of CH_4 Oxidation

Figure 6.12 provides an overview of the most important pathways involved in the oxidation of CH_4 at high pressure. The figure indicates several competing pathways whose fractional contributions are dependent on the reaction conditions. This section will outline the major dependencies.

The CH_4 oxidation chain is initiated by H-atom abstraction facilitated by OH radicals via (R30). This is the predominant fuel initiation reaction at all stoichiometries except when CH_4 is available in sufficient concentrations to make it a frequent collision partner. Then, CH_4 may react with other radical species with a noticeable contribution to the overall consumption of CH_4. This is e.g. the case for the prime CH_3OH formation reaction $CH_3O+CH_4 \rightleftharpoons CH_3OH+CH_3$ (R78). However, CH_4+OH (R30) remains the dominant reaction for fuel consumption at the diluted conditions used in the experimental work.

The OH radicals are mainly produced from thermal dissociation of H_2O_2 (R16) that originates from self-association of HO_2 radicals, i.e. $HO_2+HO_2 \rightleftharpoons H_2O_2+O_2$ (R15). The HO_2 radicals are typical products of the high pressure conditions formed mainly from the pressure dependent association of $H+O_2$ (R4). At oxidizing conditions, a significant contribution may also arise from H-abstraction from hydrocarbon species by molecular oxygen, e.g. $HCO+O_2 \rightleftharpoons CO+HO_2$ (R118) and $HOCO+O_2 \rightleftharpoons CO_2+HO_2$ (R27).

As indicated in Figure 6.12, there are a number of important consumption channels from the CH_3 radical pool. High pressure and low temperatures facilitate reaction with molecular oxygen to stabilized CH_3OO (R36). This oxidation path is important roughly below 800 K, and it is further enhanced at oxidizing conditions where O_2 is readily available. However, as the temperature increases to 900 K, the branching ratio shifts towards the competing product channel $CH_3+O_2 \rightleftharpoons CH_2O+OH$ (R38) as a result of the comparatively low thermal stability of CH_3OO. Reaction (R36) is the only active pathway to CH_3OO, which means that the potential consumption of CH_3 through the subsequent reaction between CH_3OO+CH_3 (R49) is restrained by the carbon flux through (R36).

The reaction between CH_3+HO_2 is important at all stoichiometries and pressures considered in the experimental work; even though it is to a lesser extent at oxidizing conditions where reaction with O_2 dominates, as described above. The branching ratio between the two competing pathways

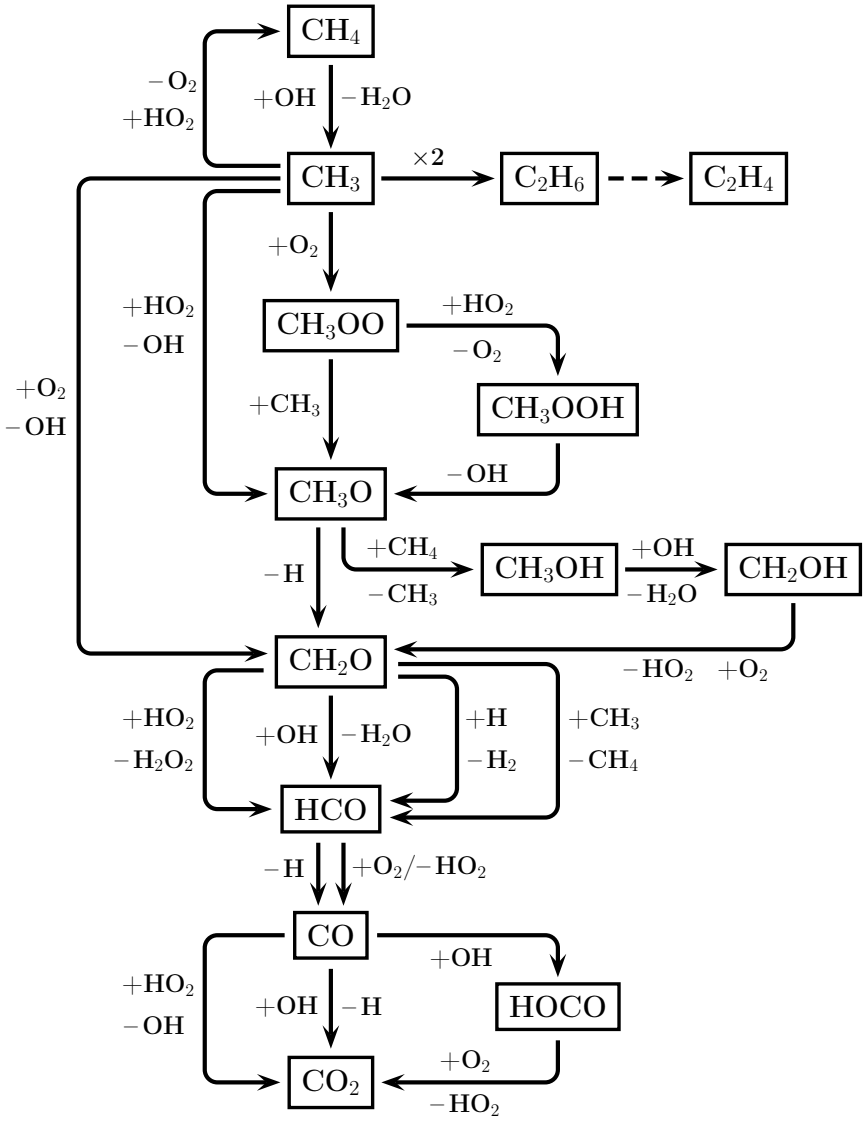

Figure 6.12: Main reaction pathways for CH_4 conversion at the investigated conditions of experiment D–L. The fractional contributions of competing pathways are dependent on the reaction conditions (see text). The dashed line denotes a more complex underlying mechanism that will be considered in details in Section 6.5.3.

to CH_3O+OH (R39) and CH_4+O_2 (R40) is ∼3 at 800–900 K in favor of (R39), but under conditions with high CH_3 and HO_2 concentrations ($\phi \geq 1$) this is still sufficient to facilitate a substantial regeneration of CH_4+O_2 via (R40), as observed in the experiments. At these conditions, CH_3 is also consumed by reactions with hydrocarbon species, most importantly the self-

recombination reaction CH_3+CH_3(+M) $\rightleftharpoons$ C_2H_6(+M) (R41) and reaction with formaldehyde, CH_2O+CH_3 $\rightleftharpoons$ HCO+CH_4 (R111).

The CH_3OO radicals are converted to CH_3O, either directly through reaction with CH_3 (R49), or indirectly via formation of CH_3OOH (R47) and subsequent dissociation to CH_3O+OH (R59), which is favored at $\phi < 1$. It is noticed that the latter path effectively yields a net result identical to CH_3+HO_2 $\rightleftharpoons$ CH_3O+OH (R39).

Thermal dissociation of CH_3O radicals (R69) is the main source of CH_3O removal at the diluted conditions applied in the experimental work. Even so, the observed formation of CH_3OH in the experiments can be attributed to the competitive reaction with CH_4 (R78). The absolute concentrations of CH_4 in the reducing experiments are not nearly sufficient to facilitate a significant contribution from (R78) compared to (R69). However, as previously mentioned, when high concentrations of CH_4 are applied, the branching ratio shifts towards CH_3OH as the dominant product. Oxidation of CH_3OH involves intermediate formation of CH_2OH; mainly via reaction with OH radicals (R86). The CH_2OH radicals are further oxidized to CH_2O by molecular oxygen (R97). At higher temperatures, the latter conversion may also be facilitated by thermal dissociation of CH_2OH (R90), but this reaction is not important at the investigated temperatures. In general, the intermediate formation of CH_2OH is only important when CH_3OH is available in sufficient concentrations, which means that this branch of the reaction network only plays a secondary role at the diluted conditions used in the present experimental work. However, it will gain significant importance at conditions with high CH_4 loads relevant to the investigated GTL process. It is noted that association of CH_2OH with CH_3 (–R189) is the main route to C_2H_5OH during conversion of C_1 fuels. This means that formation of C_2H_5OH is largely restrained by the availability of CH_3OH, which is generally low at the present diluted conditions, and hence, explains why only trace amounts of C_2H_5OH were observed during the experiments with pure CH_4.

As indicated in Figure 6.12, CH_2O can be oxidized through several channels, but most important are the reactions with OH (R108) and HO_2 (R109). The reaction with CH_3 (R111) and H atoms (R106) only provide significant contributions at reducing conditions. The subsequent conversion of HCO to CO is mainly governed by thermal dissociation (R112) except at oxidizing conditions where H-abstraction by molecular oxygen (R118) becomes more important due to the high availability of O_2.

The mechanism that governs the oxidation of CO to CO_2 is more or less unchanged from the previous outline in Section 6.2.3. As shown in Figure 6.12, a contribution from CO+HO_2 (R22) can also be observed, but this is only significant at reducing conditions where OH radicals are sparse. More-

over, as indicated by the low CO_2 concentrations obtained during the reducing experiments in Figure 6.8 (top left) and Figure 6.9 (left), these conditions do not favor CO oxidation in the first place, and (R22) is therefore only of minor practical importance in the present work.

6.5 CH_4/C_2H_6 Experiments

This section presents experiments with mixtures of CH_4 and C_2H_6, where C_2H_6 constitutes 10 % of the hydrocarbon feed on a molar basis. This is a realistic composition compared to raw natural gas. In the literature study in Section 2.2.4, it was implied that the presence of C_2H_6 may have a promoting effect on the initiation of the CH_4 oxidation chain. Moreover, the previous experiments with pure CH_4 indicated certain disagreements between measurements of C_2H_6 and C_2H_4 and corresponding model predictions. It is the objective of this section to elucidate these issues through analyses of the present experiments and the underlying chemical reaction mechanisms.

The present experiments have been selected from the M.Sc. work of Jakobsen [864] that includes a more detailed experimental database with CH_4/C_2H_6 than currently presented. In this work, Jakobsen considered the potential formation of higher hydrocarbons, i.e. $C_{\geq 3}$, but simulations predicted low selectivities (<4 %) even at the most reducing conditions applied. Moreover, Jakobsen reported that visual inspection of the reactor interior after the experiments revealed no indications of soot formation that may have resulted from a substantial yield of larger hydrocarbons. Based on these observations, it is expected that the current kinetic model adequately represents the chemical system at hand even though the model only considers C_{1-2} hydrocarbon species.

6.5.1 Experimental Conditions

The presented experiments include pressures at 100 and 50 bar, and three different stoichiometric ratios comparable to those applied in the previous study of pure CH_4 oxidation. The experimental conditions are summarized in Table 6.5. Calculations of the adiabatic temperature rise gave values <24 K for all experiments. Moreover, the carbon balances were satisfied within 5 %.

Measurements include concentration profiles of CH_4, C_2H_6, C_2H_4, O_2, CO, and CO_2 for all experiments. Moreover, measurements of CH_3OH and C_2H_5OH are presented for the reducing experiments. At the stoichiometric and oxidizing conditions, measurements of the alcohols were either absent or too close to the detection limit to facilitate a reliable model validation.

Table 6.5: Reaction conditions applied during experiments with CH_4/C_2H_6. Concentrations are in ppm if otherwise not stated. See caption of Table 6.2 for other specifications.

	Reactant concentrations						
Exp. id.	CH_4 [ppm]	C_2H_6 [ppm]	O_2 [ppm]	Pres. [bar]	Temp. [K]	ϕ [a]	τ [s K]
M	3.56 %	3987	1929	100	598–848	44.1	$^{11680}/_{T}$
N	3.53 %	3963	2040	50	598–898	41.4	$^{5920}/_{T}$
O	916	99	2328	100	598–898	0.936	$^{11880}/_{T}$
P	773	99	5.28 %	100	598–898	0.036	$^{11320}/_{T}$
Q	900	99	5.50 %	50	673–898	0.039	$^{5940}/_{T}$

[a] Stoichiometric ratio (ϕ) is based on $\alpha CH_4 + \beta C_2H_6 + (2\alpha + 7/2\beta)\, O_2 \rightarrow (\alpha + 2\beta)\, CO_2 + (2\alpha + 3\beta)\, H_2O$

6.5.2 Discussion of Experimental and Modeling Results

The experimental and modeling results from the mixed CH_4/C_2H_6 experiments M–Q are presented in the following Figures 6.13–6.15. Simulations are conducted with the fitted surface reaction $CH_3OO \rightarrow CH_3OO^{\bullet}$ (R349) from Section 6.4.2, i.e. $k_{R349} = 45\,^1/_s$ and $9.5\,^1/_s$ for the reducing and stoichiometric/oxidizing experiments respectively. No surface deactivation of the analogue C_2H_5OO radical is included due to the significantly higher concentration of CH_4 than C_2H_6 in the feed. Moreover, simulations have confirmed that k_{R349} is indeed sufficient to counteract the otherwise premature fuel ignition predicted by the model compared to the experiments.

There is generally a good agreement between experimental and calculated concentration profiles. In particular at reducing conditions, where the simulations of all the measured compounds are satisfactory. In relation to the later optimization of the GTL process, it is noteworthy that predictions of both CH_3OH and C_2H_5OH in Figure 6.13 (bottom) are in reasonable agreement with the experiments.

The reducing experiment M at 100 bar (Figure 6.13, left) is directly comparable with the pure CH_4 experiment E that was previously presented in Figure 6.9 (top). These results show negligible differences in terms of the initiation temperature, but a slightly higher yield of alcohols is obtained when C_2H_6 is present in the feed including a small contribution from C_2H_5OH that was not observed during the pure CH_4 experiment. However, significant uncertainties are attributed to the observations of higher alcohol yields, which makes it impossible to conclude if C_2H_6 has a minor promoting effect or not.

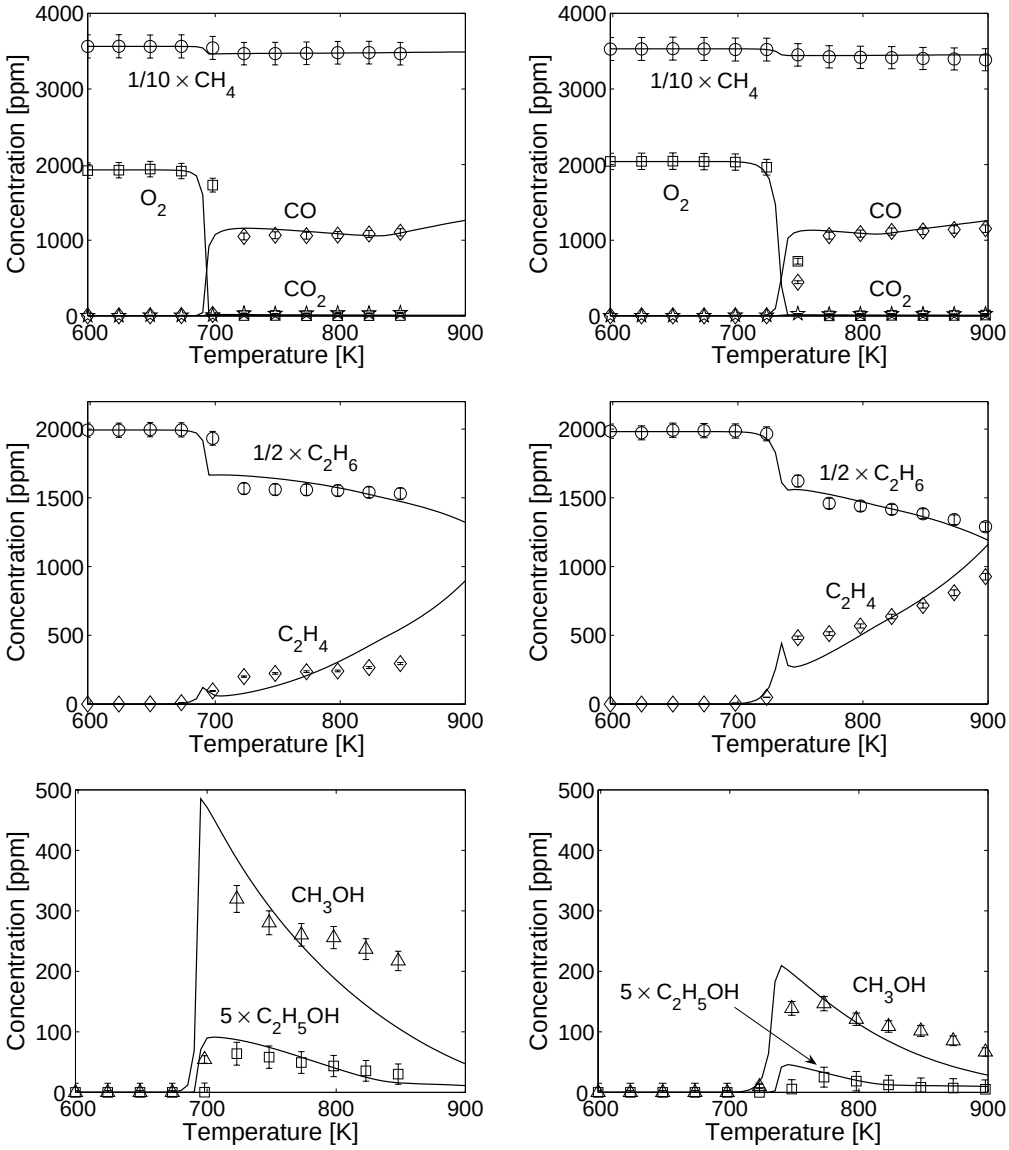

Figure 6.13: Results of reducing experiments with CH_4/C_2H_6. Left: Exp. M (100 bar, $\phi = 44.1$). Right: Exp. N (50 bar, $\phi = 41.4$). Reaction conditions are provided in Table 6.5. Symbols mark experimental results. Lines denote model predictions obtained at isothermal conditions. Measuring uncertainties are $\pm 4.3\,\%$ for CO/CH_4, $\pm 2.6\,\%$ for C_2H_4/C_2H_6, $\pm 5.3\,\%$ for O_2, $\pm 4.3\,\%$ or ± 3 ppm for CO_2, and $\pm 6.0\,\%$ or ± 3 ppm for CH_3OH/C_2H_5OH.

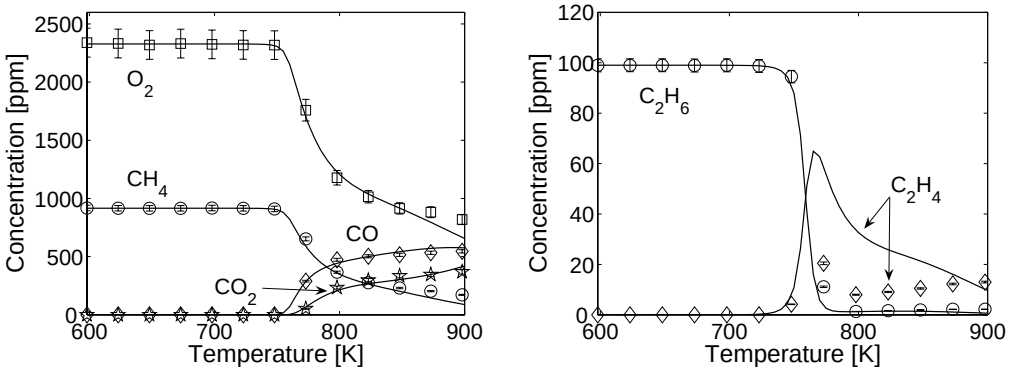

Figure 6.14: Results of stoichiometric CH_4/C_2H_6 experiment O (100 bar, $\phi = 0.936$). Reaction conditions are provided in Table 6.5. Symbols mark experimental results. Lines denote model predictions obtained at isothermal conditions. Measuring uncertainties are $\pm 2.6\,\%$ for $CO/CH_4/C_2H_4/C_2H_6$, $\pm 5.3\,\%$ for O_2, and $\pm 4.3\,\%$ or ± 3 ppm for CO_2.

In the stoichiometric and oxidizing experiments in Figure 6.14 and 6.15, the model overpredicts the concentration of C_2H_4 that arises shortly after the fuel initiation temperature. From the previous outline of the major reaction pathways of CH_4 in Section 6.4.4, it is known that hardly any CH_4 can be expected to convert to C_2H_6 at these conditions. The observed C_2H_4 can therefore exclusively be associated with the initial concentration of C_2H_6. The fact that the C_2H_6 concentrations in Figure 6.14 and 6.15 are well-predicted by the model therefore suggests that the description of the C_2H_4 consumption is incomplete at $\phi \leq 1$. At the reducing conditions in Figure 6.13 (middle), the predicted C_2H_4 concentrations follow the experimental measurements reasonably well. In order to be consistent with the above considerations, the conversion of C_2H_4 has to be operated by a different mechanism at $\phi \gg 1$. This issue will be investigated in the later analysis of the underlying reaction mechanisms in Section 6.5.3.

At reducing conditions (Figure 6.13, middle) and temperatures just above the fuel initiation temperature, the model tends to overpredict the C_2H_6 concentrations, which results in a proportional underprediction of the C_2H_4 concentrations. At higher temperatures, this trend seems to be opposite, but even so, the model is still in reasonable agreement with the experiments. This is somewhat different from the reducing experiments with pure CH_4 in Figure 6.8 (left) and Figure 6.9, that revealed a general overprediction of the C_2H_6 and C_2H_4 profiles throughout the entire temperature interval after initiation. The main difference between the two sets of experiments is the

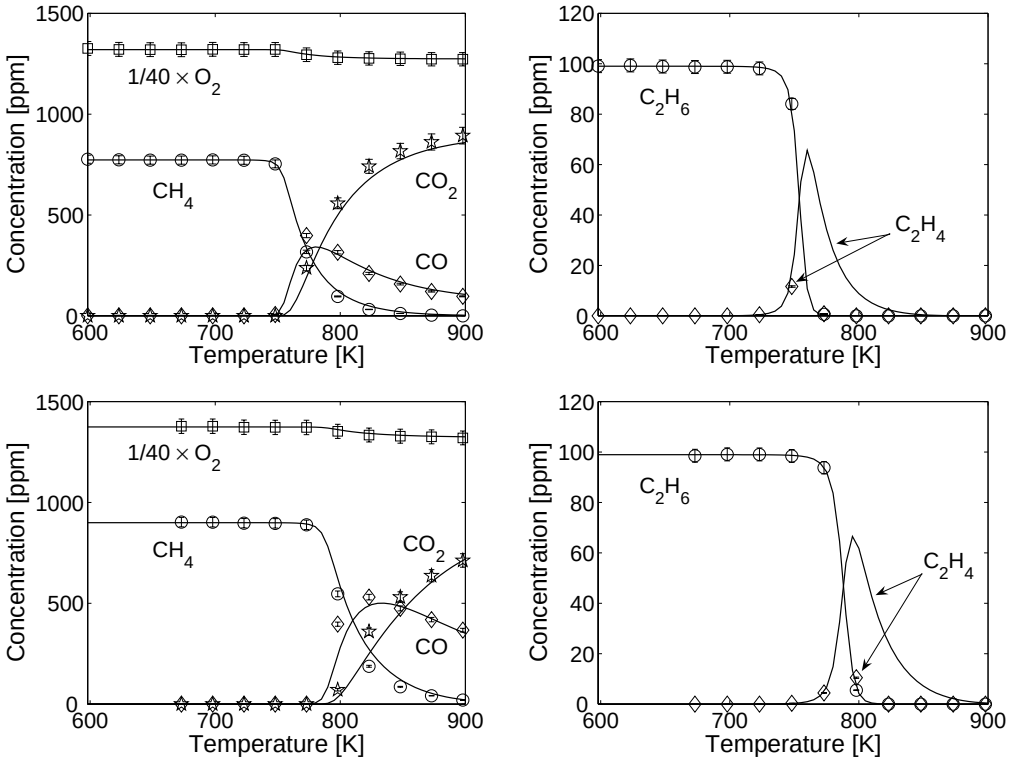

Figure 6.15: Results of oxidizing experiments with CH_4/C_2H_6. Top: Exp. P (100 bar, $\phi = 0.036$). Bottom: Exp. Q (50 bar, $\phi = 0.039$). Reaction conditions are provided in Table 6.5. Symbols mark experimental results. Lines denote model predictions obtained at isothermal conditions. Measuring uncertainties are ±2.6 % for $O_2/CO/CH_4/C_2H_4/C_2H_6$, and ±4.3 % or ±3 ppm for CO_2.

presence of C_2H_6 in the fuel. In the experiments with pure CH_4, less than 1 % of the fuel was converted to C_2H_6 and C_2H_4. In the experiments with CH_4/C_2H_6, this amount is insignificant compared to the amount of C_2H_6 already present in the fuel, and a potential overprediction of the conversion of $CH_4 \rightarrow C_2H_6$ would therefore have a negligible impact on the observed concentration profiles. These observations point in the direction of an incomplete model description of the conversion from $CH_4 \rightarrow C_2H_6$ rather than an erroneous prediction of the further conversion of C_2H_6 that would have yielded a similar overprediction of the C_2H_6 and C_2H_4 concentrations during the CH_4/C_2H_6 experiments.

6.5.3 Main Reaction Pathways of C_2H_6 Oxidation

The oxidation of C_2H_6 is governed by a reaction mechanism that involves C_2 hydrocarbon species and an underlying mechanism for C_1 hydrocarbons. The latter was previously outlined in Section 6.4.4 (see e.g. Figure 6.12). The presence of 10 % C_2H_6 in the hydrocarbon feed is not expected to impose significant changes in the C_1 reaction mechanism and it will therefore not be subjected to discussions in the following. Figure 6.16 provides an overview of the C_2 reaction network. There are a number of competing pathways whose individual contributions are very dependent on the reaction conditions.

Similar to CH_4, the C_2H_6 oxidation chain is mainly initiated by H-abstraction facilitated by OH radicals (R123). Even though they are not shown in Figure 6.16, the competing reactions between C_2H_6+CH_3 (R126) and C_2H_6+H (R121) may account for up to 20 % of the initial C_2H_6 conversion at $\phi \gg 1$. There is no contribution from thermal dissociation of C_2H_6 to CH_3 radicals (–R41). Instead, association of CH_3 radicals provides a minor contribution to the C_2H_6 concentration at $\phi > 1$.

The C_2H_5 radical also shares similarities with the analogue CH_3 radical in terms of preferred reaction channels. At $\phi \leq 1$, the main reactant is molecular oxygen that either yields stabilized C_2H_5OO (R133) or C_2H_4+HO_2 (R134). The branching ratio $^{R133}/_{R134}$ changes markedly across the investigated temperature range. Thus, formation of C_2H_5OO is favored by high pressure and low temperatures (<750 K), whereas (R134) dominates at higher temperatures regardless of the pressure. This is consistent with the characteristic temperature and pressure dependence of C_2H_5+O_2 that displays a "transition region" between 575 and 750 K [520, 582]. Here, the reaction changes from a typical association/stabilization mechanism operating close to the high-pressure limit at the investigated pressures, to assume the low-pressure limit and almost complete dominance of the bimolecular channel. (See Section 5.3.4.2 for a more detailed discussion of C_2H_5+O_2.) In the stoichiometric and oxidizing experiments, the fuel initiation temperature is close to 750 K, which means that C_2H_5 is almost completely converted to C_2H_4 via (R134). However, in the reducing experiments, the intermediate formation of C_2H_5OO gains substantial importance during the low-temperature conversion of the fuels.

The peroxyl radical C_2H_5OO is further converted to C_2H_5O; either directly via addition/elimination with CH_3 (R163) or C_2H_5 (R167), or indirectly through intermediate formation of C_2H_5OOH by H-abstraction from HO_2 (R161) and subsequent dissociation to C_2H_5O+OH (R173). This mechanism is equivalent to the conversion of CH_3OO, as previously illustrated in Figure 6.12. A small yield of C_2H_4+HO_2 may arise from dissociation of

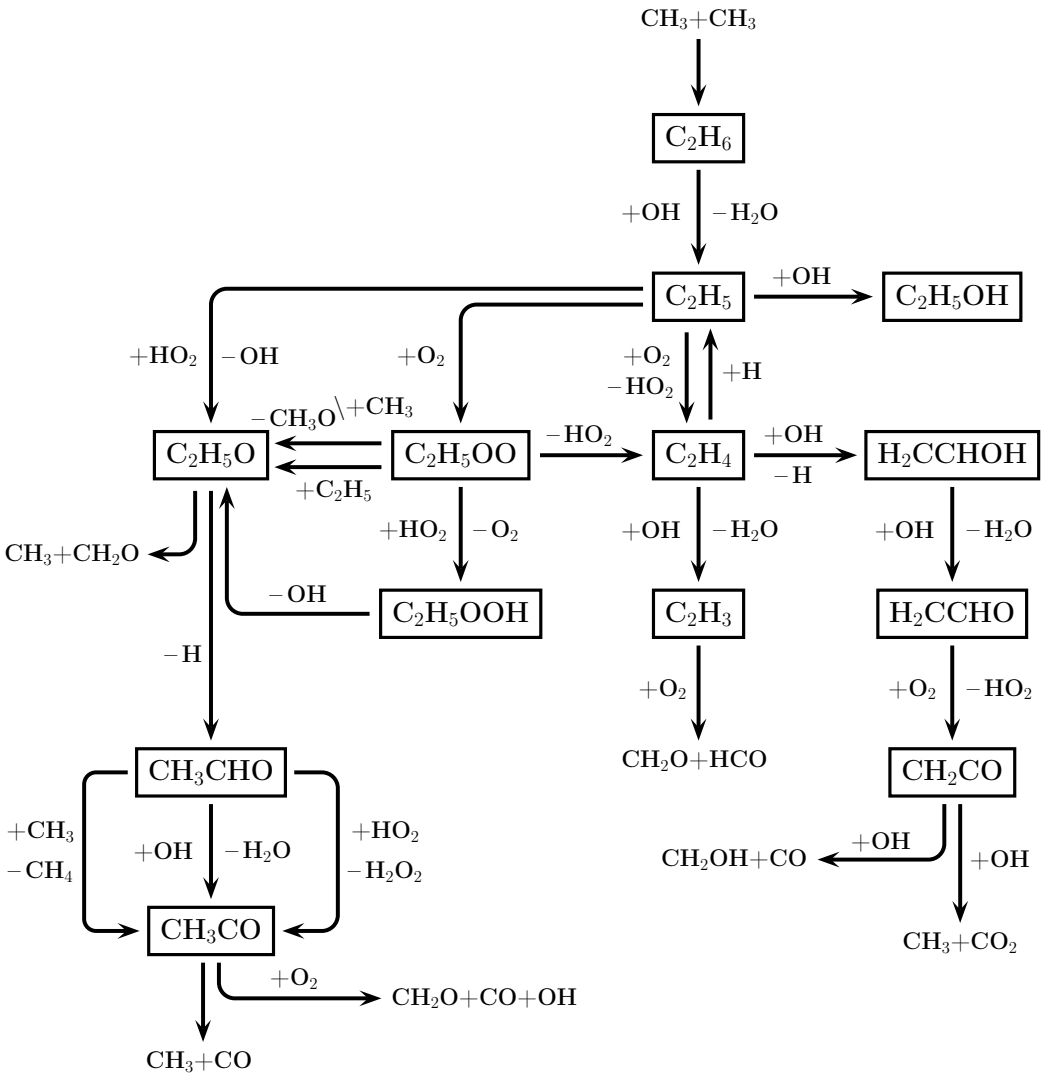

Figure 6.16: Main reaction pathways for C_2H_6 conversion at the investigated conditions of experiment M–Q. The fractional contributions of competing pathways are dependent on the reaction conditions (see text). The mechanism of CH_4 conversion from Figure 6.12 underlies the current reaction network. The reader may notice a number of similarities between these mechanisms.

C_2H_5OO (R156). This channel becomes more important at higher temperatures, but here, the concentrations of C_2H_5OO are typically low because of the shift in the branching ratio of $C_2H_5+O_2$, which means that (R156), in practice, gains little importance during the conducted experiments.

The reaction $C_2H_5+O_2 \rightleftharpoons C_2H_4+HO_2$ (R134) accounts for >90 % of the

formation of C_2H_4 at all investigated conditions. A substantial fraction may be converted back to C_2H_5 through association with H atoms (R139), whereas reactions with OH lead to C_2H_3 (R144) and H_2CCHOH (R143) in comparable yields. At high pressures >50 bar, the numerical value of the branching ratio $^{R139}/_{(R144+R143)}$ more or less follows the value of ϕ. Hence, $^{R139}/_{(R144+R143)} \gg 1$ at the reducing conditions applied in experiments M and N, whereas values ≈ 0.5 and $\ll 1$ are obtained during the stoichiometric and oxidizing experiments respectively. As a result, two different mechanisms seems to govern the conversion of C_2H_4: At reducing conditions, the formation of C_2H_4 is controlled by the interconversion between C_2H_5 and C_2H_4, whereas a direct oxidation mechanism operates at $\phi \leq 1$ corresponding to $C_2H_6 \rightarrow C_2H_5 \rightarrow C_2H_4 \rightarrow C_2H_3 \rightarrow$ etc. The reader is here reminded of the fact that the model overpredicted the measured concentrations of C_2H_4 at $\phi \leq 1$, whereas a reasonable correlation was obtained between experimental and numerical results at $\phi \gg 1$. This led to the previous suggestion of different operating mechanisms, which has now been substantiated by the kinetic model. All observations point in the direction of an incomplete model description of the direct oxidation of C_2H_4, while confidence is placed in the indirect oxidation path through $C_2H_5/C_2H_5OO/C_2H_5O$/etc.; see Figure 6.16. The current model description of the oxidation of C_2H_4 by OH was taken from the theoretical work of Lin and co-workers [523]. The reaction displays a complicated temperature and pressure dependence that was not treated in details by Lin and co-workers, so it is possible that more thorough investigations may yield higher rate coefficients consistent with an increased consumption of C_2H_4, as indicated by the experiments. The issue has not been pursued in the present work since this part of the mechanism is not expected to gain significant importance at the reducing conditions used in the GTL process.

The reaction between C_2H_5 and HO_2 is mainly important at reducing conditions, where it competes with C_2H_5+O_2. Regeneration of C_2H_6+O_2 is negligible, so the only significant products are C_2H_5O+OH (R132). This is different from the CH_4 mechanism where a considerable fraction of the CH_4 and O_2 is regenerated through the analogue reaction CH_3+$HO_2 \rightleftharpoons CH_4$+$O_2$ (R40); see Section 6.4.4. A minor fraction of the C_2H_5 radical pool may be converted directly to stabilized C_2H_5OH by addition of OH radicals (–R190). At the applied experimental conditions, this is the main route to C_2H_5OH at temperatures >850 K, whereas the association of CH_2OH+CH_3 (–R189) predominates at lower temperatures.

The conversion of C_2H_5O takes place through thermal dissociation to CH_3+CH_2O (R183) and CH_3CHO+H (R184) where the former channel accounts for >75 % of the overall consumption of C_2H_5O at all the investigated conditions. The minor fraction that yields CH_3CHO may undergo further

oxidation to CH_3CO through different reaction channels. The main reactants are OH (R222) and HO_2 (R225), while reaction with CH_3 (R227) only becomes important at reducing conditions. The CH_3CO radical is rapidly converted to C_1 products through C–C bond cleavage either facilitated by reaction with molecular oxygen (R238) or by thermal dissociation (R229).

As indicated in Figure 6.16, there are several channels that convert C_2 to C_1 species. At oxidizing and stoichiometric conditions, this happens through addition/elimination reactions of C_2H_3+O_2 (R153) and/or CH_2CO+OH (R255,R256). At reducing conditions, decomposition of C_2H_5O (R183) and CH_3CO (R229,R238) constitute the main pathways to the C_1 network. The resulting C_1 products include mixtures of CH_3, CH_2OH, CH_2O, HCO, CO, and CO_2. Considering the position of these species in the C_1 reaction network in Figure 6.12, it is observed that only the carbon atom enclosed in CH_3 is capable of yielding the desired product CH_3OH. Since CH_3 never constitutes more than one of the products from the $C_2 \rightarrow C_1$ conversion, this means that maximum 50 % of the carbon matter enclosed in the original feed of C_2H_6 can be converted to CH_3OH. However, it is noted that these considerations do not include the potential yield of C_2H_5OH, which may form directly from C_2H_5+OH (–R190) as an attractive secondary product from the GTL process.

6.6 CH_4/NO_x Experiments

This section presents diluted experiments with CH_4/NO_x. It is well established that NO_x has a promoting effect on the hydrocarbon oxidation chemistry; even when it is only present in very small quantities. Nevertheless, well-defined experiments at very high pressures have never been reported in the literature.

From a kinetic modeling point of view, the present CH_4/NO_x experiments represent the reaction mechanisms of C_1 hydrocarbons and NO_x including an extended reaction subset to govern their mutual interactions. The performance of the individual reaction mechanisms of NO_x and C_1 were previously validated in relation to the experiments with $CO/H_2/NO_x$ (Section 6.2) and pure CH_4 (Section 6.4), so the natural focus of this section will be on the direct interactions between NO_x and hydrocarbon species. The experiments with CH_4/NO_x were conducted at conditions that resemble those applied during the pure CH_4 experiments except for the additional presence of ∼200 ppm of NO_x. This should allow a direct comparison with the previous results from Section 6.4.3 and a good display of the sensitizing effects of NO_x.

6.6.1 Experimental Conditions

The promoting effect of NO_x on the hydrocarbon oxidation chemistry allowed experiments to be conducted at pressures from 100 bar and down to 20 bar, while still obtaining complete conversion of the fuel and/or oxidizer within the residence time and temperature limitations of the high pressure flow reactor setup. Moreover, three different stoichiometric ratios were applied comparable to those used in the previous study of pure CH_4 oxidation chemistry. Table 6.6 summarizes the experimental conditions. It is noted that the specified concentrations of NO and NO_2 reflect the concentrations at the reactor inlet *after* the initial feed concentration of NO has been partially converted to NO_2 via $NO+NO+O_2 \rightleftharpoons NO_2+NO_2$ (–R278) upon mixing with O_2. The reader is referred to the previous discussion of this phenomenon in Section 6.2.1 and the treatment hereof during modeling.

Calculations of the adiabatic temperature rise gave values <33 K for the stoichiometric experiments, while considerably less was obtained for the reducing and oxidizing experiments. The carbon balance everywhere closed within 6 %.

Table 6.6: Reaction conditions applied during experiments with CH_4/NO_x. Concentrations are in ppm if otherwise not stated. See caption of Table 6.2 for other specifications.

	Reactant concentrations						
Exp. id.	CH_4 [ppm]	O_2 [ppm]	NO_x(NO) [ppm]	Pres. [bar]	Temp. [K]	ϕ [a]	τ [s K]
R	4.66 %	803	193(25)	100	598–898	116.	$^{12050}/_{T}$
S	4.62 %	908	212(106)	50	598–898	102.	$^{5860}/_{T}$
T	4.58 %	925	214(200)	20	598–898	99.0	$^{2440}/_{T}$
U	1605	2804	179(10)	100	598–848	1.14	$^{12000}/_{T}$
V	1610	2798	188(43)	50	598–898	1.15	$^{6100}/_{T}$
W	1548	2935	182(150)	20	598–898	1.05	$^{2370}/_{T}$
X	956	4.55 %	201(0)	100	598–898	0.042	$^{11920}/_{T}$
Y	995	4.50 %	200(8)	50	598–898	0.044	$^{5950}/_{T}$
Z	1023	4.53 %	200(76)	20	598–898	0.045	$^{2410}/_{T}$

[a] Stoichiometric ratio (ϕ) is based on $CH_4 + 2O_2 \rightarrow CO_2 + 2H_2O$

6.6.2 Discussion of Experimental and Modeling Results

The results of the CH_4/NO_x experiments are presented in Figure 6.17, 6.18, and 6.19, representing reducing, stoichiometric, and oxidizing conditions respectively. The figures also show corresponding model predictions of the

major species: CH_4, O_2, CO, CO_2, NO, NO_2, and CH_3NO_2. A considerable formation of CH_3OH was observed during the reducing experiments, whereas concentrations of C_2H_6 and C_2H_4 were below the detection limit (<1 ppm) at all investigated conditions.

In the pure hydrocarbon experiments, it was necessary to fit the surface reaction $CH_3OO \rightarrow CH_3OO^{\bullet}$ (R349) in order to reconcile the predicted initiation temperatures with those observed in the experiments. However, the hydrocarbon experiments also showed that this surface deactivation had no pronounced effect on the fuel conversion once the oxidation chain had started. The initiation of the chemical system at hand can be attributed to the presence of NO_x that did not show indications of surface activities in the previous experiments with $CO/H_2/NO_x$ (see Figure 6.1). Thus, it is not expected that potential surface reactions will gain significant influence in the present experiments with CH_4/NO_x either, and all simulations have therefore been conducted without (R349).

The reducing experiments in Figure 6.17 do not include measurements of CH_3NO_2 because of experimental shortcomings at the time of their completion. Simulated concentrations of CH_3NO_2 are therefore shown in Figure 6.17 (dotted lines) without experimental support.

The results presented in Figure 6.17–6.19 demonstrate that the kinetic model adequately captures the behavior of the chemical system at all investigated conditions. The results indicate a significant intermediate formation of CH_3NO_2 at the expense of NO and NO_2 shortly after the reaction has initiated. This formation of CH_3NO_2 exhibits a strong pressure dependency as the peak concentration ranges from almost 100 % conversion of NO_x at 100 bar and $\phi \geq 1$ (Figure 6.17 and 6.18, top) to ∼25 % during the corresponding experiments at 20 bar (Figure 6.17 and 6.18, bottom). The oxidizing experiments in Figure 6.19 follow the same trend even though the peak concentration of CH_3NO_2 at 100 bar only represents about 75 % of the available NO_x. The concentration of CH_3NO_2 rapidly drops towards zero as the fuel and/or oxidizer approach depletion. In this process, NO and/or NO_2 are regenerated.

In the experiments at 100 bar, the model seems to predict a slightly lower initiation temperature than obtained in the experiments. This discrepancy can be observed at all investigated stoichiometries and is most profound in the calculated NO_2 and CH_3NO_2 concentrations that are displaced by about 25 K towards lower temperatures compared to the experiments. The phenomenon may be related to an inaccurate description of the initiation reaction between NO_2 and CH_4 (R285,R284). However, this would probably have facilitated a premature fuel ignition in all the CH_4/NO_x experiments, but the results in Figure 6.17–6.19 indicate that the discrepancy becomes insignificant when

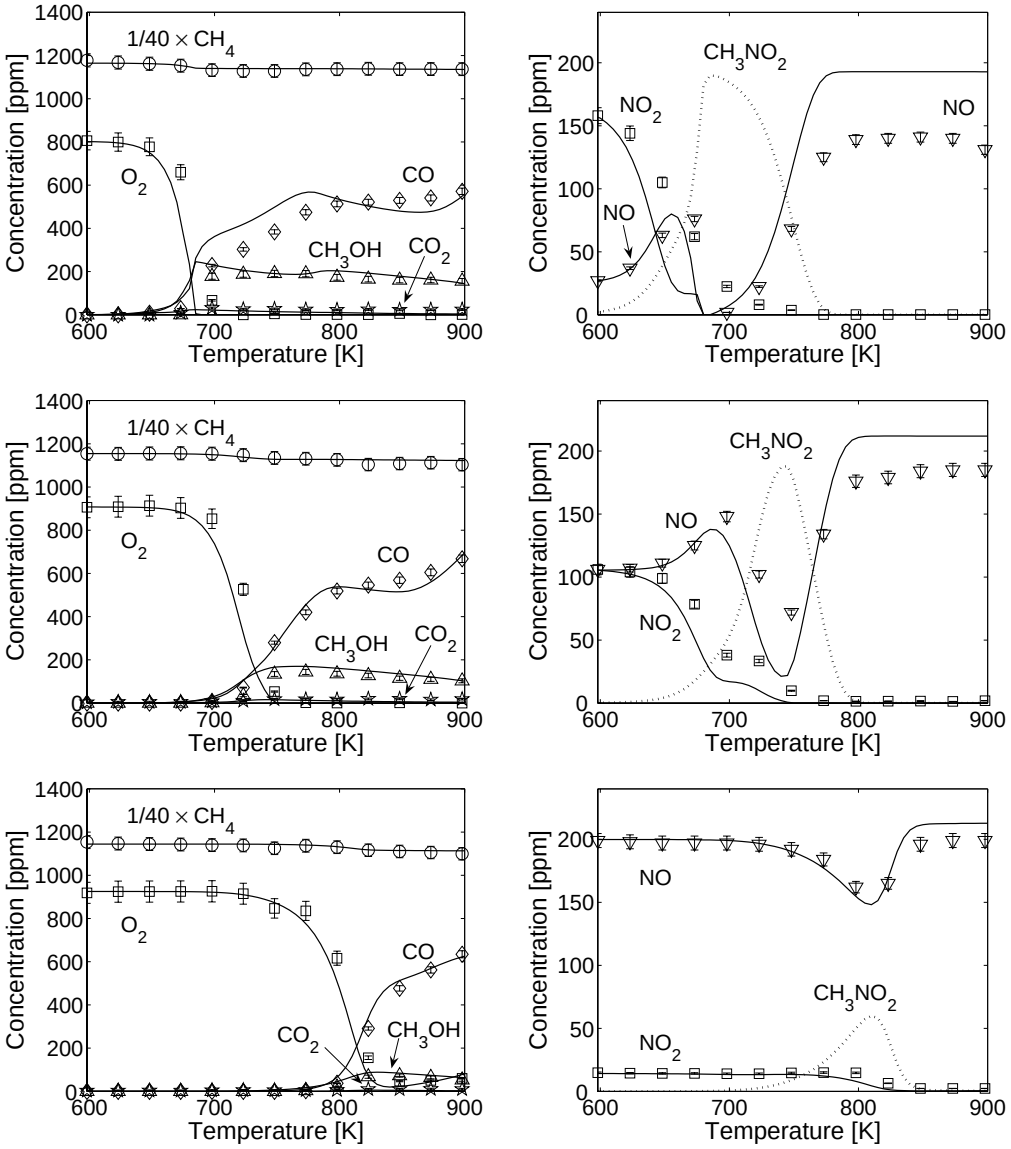

Figure 6.17: Results of reducing experiments with CH_4/NO_x. Top: Exp. R (100 bar, $\phi = 116$). Middle: Exp. S (50 bar, $\phi = 102$). Bottom: Exp. T (20 bar, $\phi = 105$). Reaction conditions are provided in Table 6.6. Symbols mark experimental results. Lines denote model predictions obtained at isothermal conditions. Dotted lines indicate predicted CH_3NO_2 concentrations where measurements are not available. Measuring uncertainties are ±2.6 % for CO/CH_4, ±5.3 % for O_2, ±4.3 % or ±3 ppm for CO_2, ±6.0 % or ±3 ppm for CH_3OH, ±2.8 % for NO, and ±4.0 % for NO_2.

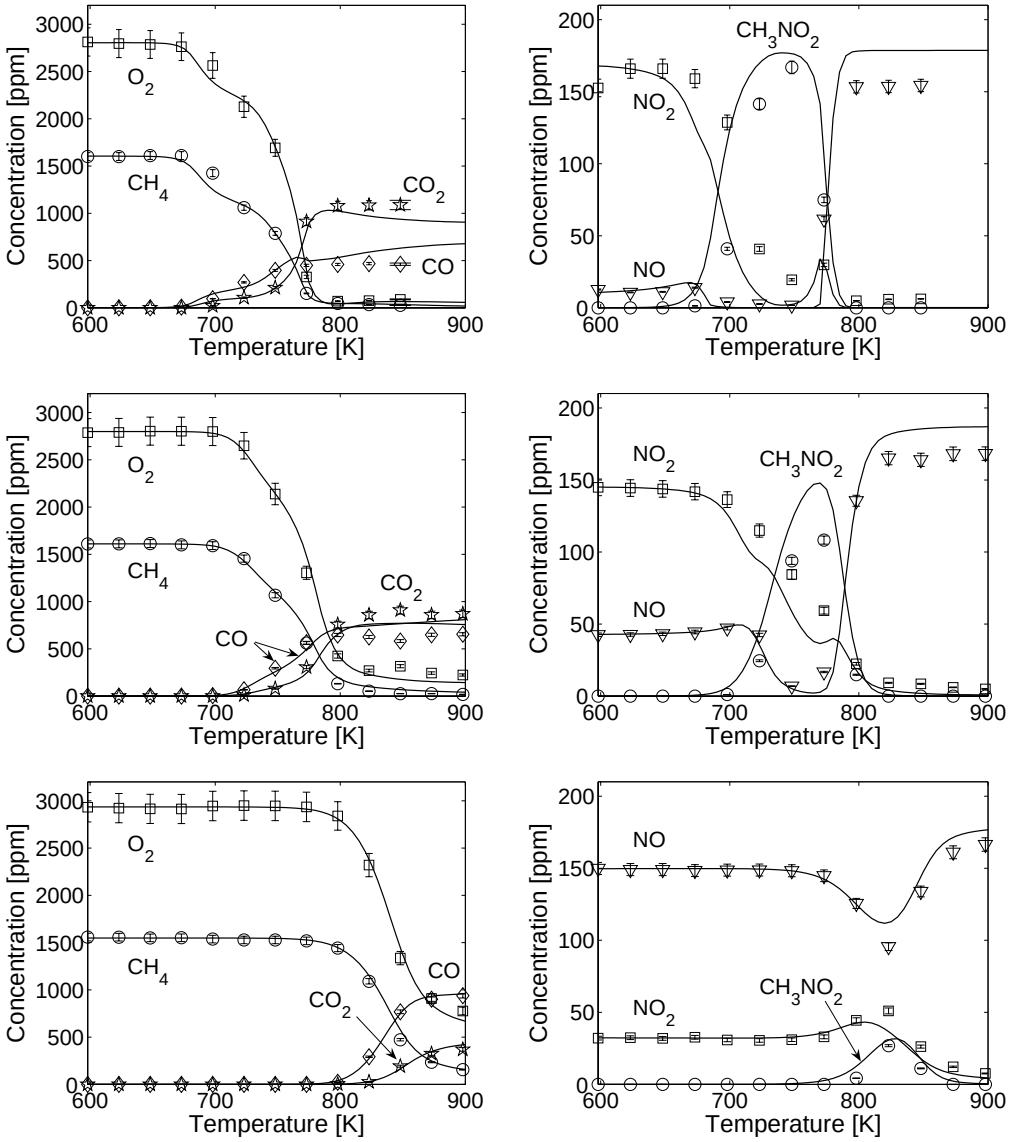

Figure 6.18: Results of stoichiometric experiments with CH_4/NO_x. Top: Exp. U (100 bar, $\phi = 1.14$). Middle: Exp. V (50 bar, $\phi = 1.15$). Bottom: Exp. W (20 bar, $\phi = 1.05$). Reaction conditions are provided in Table 6.6. Symbols mark experimental results. Lines denote model predictions obtained at isothermal conditions. Measuring uncertainties are ±2.6 % for $CO/CH_4/CH_3NO_2$, ±5.3 % for O_2, ±4.3 % or ±3 ppm for CO_2, ±2.8 % for NO, and ±4.0 % for NO_2.

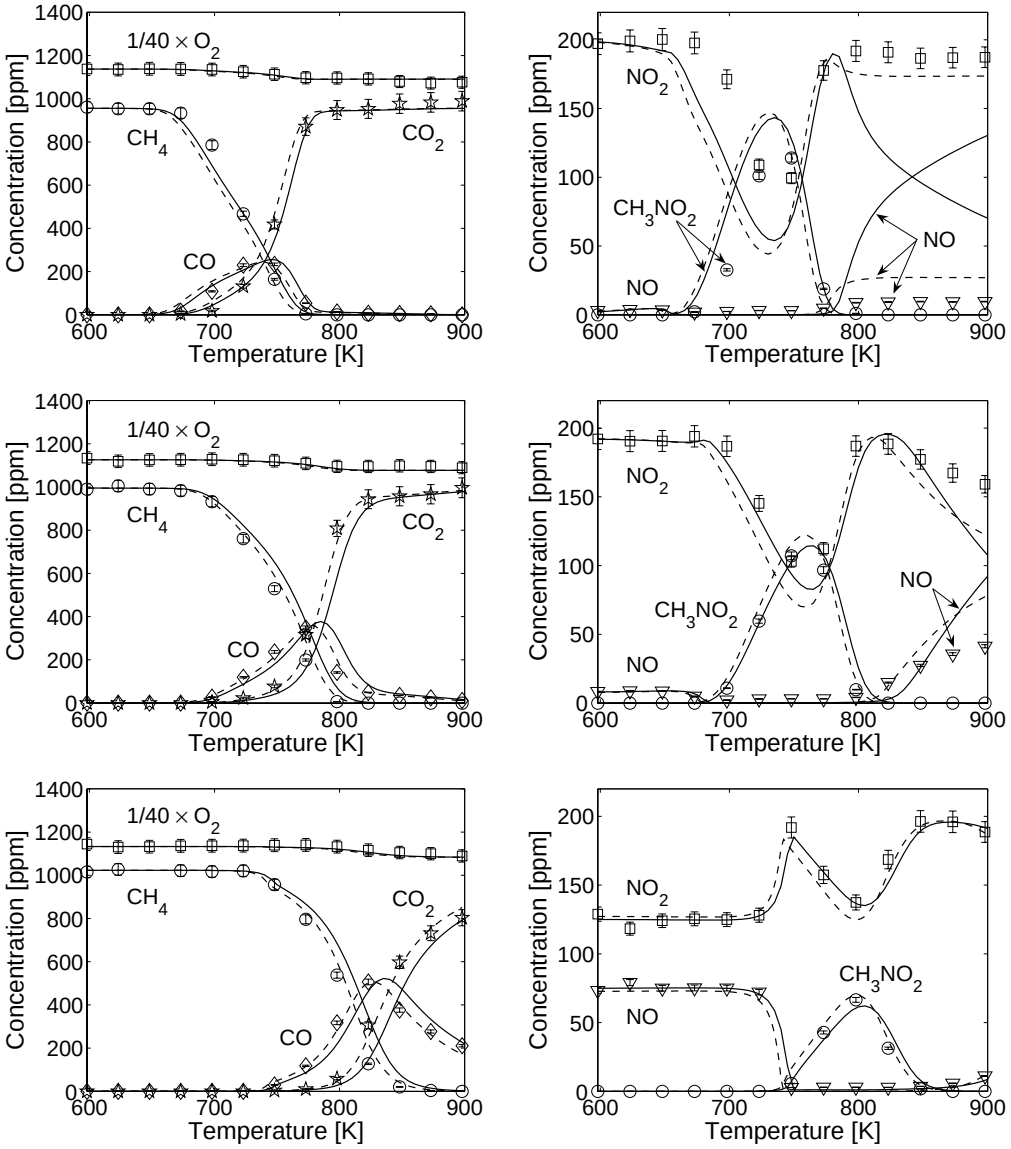

Figure 6.19: Results of oxidizing experiments with CH_4/NO_x. Top: Exp. X (100 bar, $\phi = 0.042$). Middle: Exp. Y (50 bar, $\phi = 0.044$). Bottom: Exp. Z (20 bar, $\phi = 0.045$). Reaction conditions are provided in Table 6.6. Symbols mark experimental results. Full lines denote model predictions obtained at isothermal conditions. Dashed lines represent simulations with the experimental temperature profiles. Measuring uncertainties are ±2.6 % for $O_2/CO/CH_4/CH_3NO_2$, ±4.3 % or ±3 ppm for CO_2, ±2.8 % for NO, and ±4.0 % for NO_2.

lower pressures are applied. This points in the direction of an incomplete description of the pressure dependency of the CH_3NO_2 formation mechanism at very high pressures.

Selected results from the CH_4/NO_x experiments are directly comparable with results from the experiments with pure CH_4. At reducing conditions, experiment R (CH_4/NO_x, 100 bar, $\phi = 116$) and S (CH_4/NO_x, 50 bar, $\phi = 102$) in Figure 6.17 (top and middle) are comparable to experiment D (CH_4, 100 bar, $\phi = 98.8$) and G (CH_4, 50 bar, $\phi = 95.5$) in Figure 6.8 (left) and Figure 6.9 (bottom) respectively. The most profound difference is the fuel initiation temperature, which is decreased by roughly 50 K upon addition of NO_x. Moreover, the CH_3OH formation is significantly higher at 50 bar when NO_x is present, and this concentration is sustained at a comparatively high level throughout the remaining investigated temperature range opposite the corresponding experiment with pure CH_4. A similar, almost constant level of CH_3OH is obtained during the 100 bar experiment with NO_x, but here, the measured peak concentration is of comparable magnitude with the peak concentration in the pure CH_4 experiment. Moreover, no C_2 compounds of measurable quantities are observed when NO_x is present, which is different from the experiments with pure CH_4.

The NO_x promoted decrease of the initiation temperature is even more pronounced at stoichiometric and oxidizing conditions. Thus, a comparison of the stoichiometric experiments U (CH_4/NO_x, 100 bar, $\phi = 1.14$) in Figure 6.18 (top) and H (CH_4, 100 bar, $\phi = 1.09$) in Figure 6.8 (top right) reveals a reduction of the initiation temperature of almost 100 K. A similar observation is made when comparing the oxidizing experiments X (CH_4/NO_x, 100 bar, $\phi = 0.042$) and Y (CH_4/NO_x, 50 bar, $\phi = 0.044$) in Figure 6.19 (top and middle) with the pure CH_4 oxidation experiments J (CH_4, 100 bar, $\phi = 0.042$) and L (CH_4, 50 bar, $\phi = 0.042$) in Figure 6.8 (top right) and Figure 6.11 (bottom) respectively.

6.6.3 Sensitizing Effects of NO_x

The sensitizing effects of NO_x can be attributed to the cyclic conversion between NO and NO_2 through interactions with the H/O and hydrocarbon radical pools. The former is a source of chain carrying OH radicals, which is an important contributing factor to the observed reduction of the fuel initiation temperature in the CH_4/NO_x experiments. The NO_x interactions with the H/O radical pool were previously considered in Section 6.2.3 in connection to the $CO/H_2/NO_x$ experiments, and the reader is referred to this section for an elaborate outline. Instead, the following discussion will focus on the direct interactions between NO_x and hydrocarbon species.

NO and NO_2 may interact with hydrocarbon species through a number of reactions, but most important is the direct conversion of the radical species CH_3OO and CH_3 to CH_3O that takes place in accordance with the mechanism illustrated in Figure 6.20.

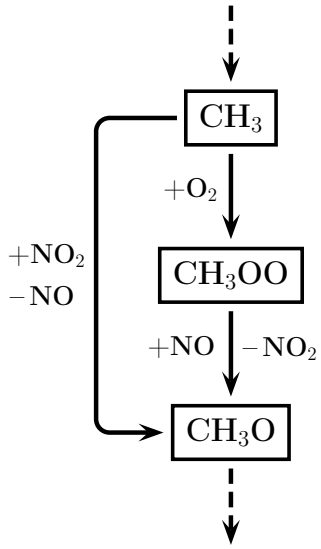

Figure 6.20: Direct NO_x interaction with the hydrocarbon oxidation chain. Cyclic conversion of NO and NO_2 carries the chain forward. This mechanism substitutes the ordinary conversion of CH_3 to CH_3O from the previous Figure 6.12 at all investigated conditions with CH_4/NO_x. The dashed lines denote more complex underlying mechanisms.

The two pathways from CH_3 to CH_3O shown in Figure 6.20 completely substitute the pure hydrocarbon conversion channels of CH_3 and CH_3OO, cf. Figure 6.12, at all investigated conditions and thus, become the main sources of CH_3O radicals when NO_x is added to the reacting mixture. It is noticed that the sum of NO+CH_3OO $\rightleftharpoons$ NO_2+CH_3O (R266) and NO_2+CH_3 $\rightleftharpoons$ NO+CH_3O (R283) is equivalent to the reaction CH_3OO+CH_3 $\rightleftharpoons$ CH_3O+CH_3O (R49), but the two NO_x induced reactions outcompete the pure hydrocarbon reaction. Another consequence of the dominance of the mechanism in Figure 6.20 is the suppression of the association reaction between CH_3 radicals to C_2H_6 (R41); even at highly reducing conditions, which explains the absence of C_2 compounds during the present experimental work.

Hydrogen abstraction from hydrocarbon species by NO_2 also plays an important role during the investigated conditions. In particular the reactions:

NO_2+CH_4 ⇌ HNO_2+CH_3 (R285), NO_2+CH_3O ⇌ HONO+CH_2O (R292), and NO_2+CH_2O ⇌ HONO+HCO (R289). Here, NO is regenerated through subsequent decomposition of HONO to NO+OH (–R259), which includes prior isomerization of HNO_2 to HONO (R319) in case of (R285). The former reaction between CH_4 and NO_2 is the principal initiation reaction and the assigned rate constant therefore has a substantial impact on the calculated initiation temperature. As previously discussed in Section 5.3.5.3, the reaction has been subjected to some dispute concerning the temperature dependence and branching ratios between different theoretical [699, 774] and experimental sources [777]. However, with the applied rate expression from Yamaguchi and co-workers [699, 773], a reasonable agreement between experimental and modeling results seems to be obtained in the present work. The reactions between NO_2 and CH_3O (R292) and CH_2O (R289) are also mainly associated with the initial conversion of the hydrocarbon fuel, where they facilitate a net production of OH radicals. However, the reactions are quickly overtaken by the ordinary consumption channels of CH_3O and CH_2O shown in the previous Figure 6.12.

The substantial formation of CH_3NO_2 observed during the experiments is a characteristic high-pressure phenomenon facilitated by the direct association of CH_3 and NO_2 via (–R326). Net rate analyses reveal that the reverse reaction (R326) is also the predominant consumption channel. This means that CH_3NO_2 is accumulated until an equilibrium concentration is reached, which may be of considerable magnitude as indicated by the experiments. The concentration of CH_3NO_2 remains stable until the fuel and/or oxidizer start to approach depletion, which drives the equilibrium backwards in order to release the embedded radicals. As a consequence, formation of CH_3NO_2 facilitates a temporary inactivation of NO and NO_2 shortly after initiation of the hydrocarbon oxidation chain. The model shows no indications that the propagation of the pure hydrocarbon oxidation chain is self-sustaining under this condition unless the temperature is high enough for the pure hydrocarbon oxidation chain to operate without the promoting effect of NO_x. As a result, the overall conversion rate may temporarily slow down. This phenomenon can be vaguely observed in e.g. the stoichiometric experiment U at 100 bar (Figure 6.18, top), where the declining concentrations of CH_4 and O_2 display a short intermediate delay between 700 and 735 K corresponding to the temperature interval where the concentration of CH_3NO_2 accounts for almost 100 % of the available NO_x.

There are no contributions from reactions between nitrogen containing species and hydrocarbons that lead directly to CH_3OH. Instead, the main route to CH_3OH is facilitated by H-abstraction from CH_4 by CH_3O (R78) in accordance with the pure hydrocarbon mechanism in Figure 6.12. It was

expected that the lower conversion temperature would have reduced the thermal dissociation of CH_3O to CH_2O+H (R69) and thereby indirectly enhanced the fractional contribution from CH_3O+CH_4 (R78). However, as previously mentioned, there is negligible difference between the observed peak concentrations of CH_3OH at 100 bar with or without the addition of NO_x. A net rate analysis at the conditions of the reducing experiment R (100 bar, $\phi = 116$) indicates that the branching fraction between (R69) and (R78) indeed has shifted towards the attractive CH_3OH forming channel at low temperatures, but the net gain is counteracted by new CH_3O consumption channels like NO_2+$CH_3O \rightleftharpoons$ HONO+CH_2O (R292) and NO+$CH_3O \rightleftharpoons$ HNO+CH_2O (R292).

From a process design point of view, introducing NO_x as a gas phase sensitizer complicates the GTL process. This means that a proportional increase of the resulting yield of the desired product should be achieved in order to counteract the additional expenses associated with the more complex design. The current observations of peak concentrations of CH_3OH obtained both with and without addition of NO_x do not indicate such an effect, which lowers the expectations to the use of NO_x as a chemical promoter in the GTL process. On the other hand, experiments indicate that resulting CH_3OH concentrations may be stabilized across a wider temperature and pressure range, which are attractive characteristics in terms of an industrial implementation of the process.

6.7 CH_4/H_2S Experiments

Raw natural gas typically contains trace amounts of sulfur in the form of H_2S. It is therefore relevant to investigate the influence of H_2S (or SO_2) on the hydrocarbon oxidation chemistry under high-pressure conditions. Prior investigations of the interactions between SO_2 and the H/O radical pool, e.g. [114], have pointed out that SO_2 can act as an efficient radical sink, but only limited knowledge is available concerning the direct interactions with hydrocarbon species at high pressures.

As previously discussed in Section 5.3.6, the applied kinetic model only includes a limited sulfur reaction mechanism without direct interactions between hydrocarbon and sulfur compounds. As a consequence, expectations to the model performance are limited, but even so, the present investigation may help elucidating important issues that can inspire future work in the field.

6.7.1 Experimental Conditions

Two experiments have been conducted with CH_4/H_2S; both at 50 bar, but with different stoichiometries. The reaction conditions are summarized in Table 6.7. Calculations of the adiabatic temperature rise gave values <21 K. The carbon and sulfur balances closed within 3 and 7 % respectively in both experiments. Measured concentration profiles of CH_4, O_2, CO, CH_3OH, H_2S, and SO_2 are shown in Figure 6.21 including corresponding model predictions that were obtained without including any surface reactions. C_2H_6 and C_2H_4 were only detected during the reducing experiment $\mathcal{A}$, while CO_2 was below the detection limit in this experiment. Measurements of CO_2 are therefore only presented for the stoichiometric experiment $\mathcal{B}$.

Table 6.7: Reaction conditions applied during experiments with CH_4/H_2S. Concentrations are in ppm if otherwise not stated. See caption of Table 6.2 for other specifications.

	Reactant concentrations						
Exp. id.	CH_4 [ppm]	O_2 [ppm]	H_2S [ppm]	Pres. [bar]	Temp. [K]	ϕ [a]	τ [s K]
$\mathcal{A}$	1.25 %	1119	202	50	598–898	22.6	$^{5990}/_{T}$
$\mathcal{B}$	1494	3012	202	50	598–898	1.09	$^{5920}/_{T}$

[a] Stoichiometric ratio (ϕ) is based on $\alpha CH_4 + \beta H_2S + (2\alpha + {}^3/_2\beta)\,O_2 \rightarrow \alpha CO_2 + \beta SO_2 + (2\alpha + \beta)\,H_2O$

6.7.2 Discussion of Experimental and Modeling Results

Figure 6.21 shows a poor agreement between the experimental and numerical results. The most profound discrepancy is observed between the measured and calculated initiation temperatures, where the model predicts values that are about 150 K higher than observed in both experiments. Considering a corresponding temperature-displacement of the calculated concentration profiles, the model may seem to capture the conversion profiles of O_2 and H_2S/SO_2 during the reducing experiment (Figure 6.21, left), whereas a substantial overprediction of the fuel conversion is obtained during the stoichiometric experiment (Figure 6.21, right).

The consumption of H_2S seems to be closely correlated with the rising concentration of SO_2. This is confirmed by the sulfur balances that closed within 7 % throughout both experiments when only considering the measured concentrations of H_2S and SO_2. It indicates a modest intermediate yield of stable mixed carbon-sulfur species analogue to e.g. CH_3NO_2, that was observed as a major compound during the CH_4/NO_x experiments in Section

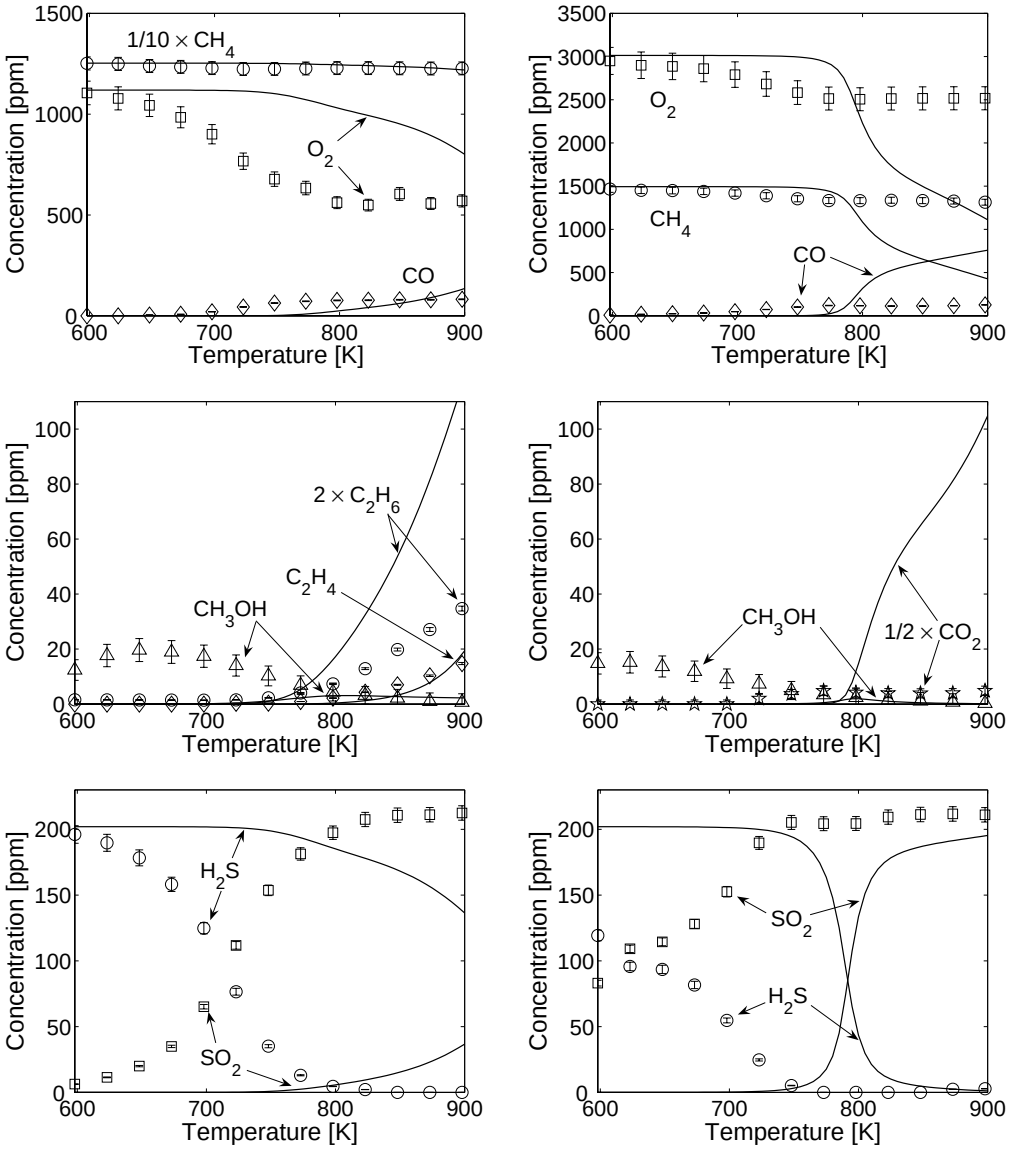

Figure 6.21: Results of experiments with CH_4/H_2S at 50 bar. Left: Exp. $\mathcal{A}$ ($\phi = 22.6$). Right: Exp. $\mathcal{B}$ ($\phi = 1.09$). Reaction conditions are provided in Table 6.7. Symbols mark experimental results. Full lines denote model predictions obtained at isothermal conditions. Measuring uncertainties are ±2.6 % for $CO/CH_4/C_2H_4/C_2H_6/SO_2$, ±5.3 % for O_2, ±4.3 % or ±3 ppm for CO_2, ±6.0 % or ±3 ppm for CH_3OH, and ±3.4 % for H_2S.

6.6, but it does not mean that direct reactions between hydrocarbon and sulfur species are absent during the experiments. Net rate analyses indicate that the principal initiation reaction is the thermal decomposition of H_2S to $S+H_2$. The S atom is further reacted through a complex network involving SH, HSSH, HSS, S_2, SO, HSO, HOSO, and SO_2. However, a detailed outline of this mechanisms cannot be justified considering the poor agreement between the kinetic model and the experiments.

At present, it can only be speculated what causes the observed discrepancies between measured and calculated concentration profiles. It is noted that the thermal dissociation of H_2S is only represented in the model by the low-pressure limit, i.e. $H_2S+M \rightleftharpoons S+H_2+M$ using the rate expression $k_{H_2S+M} = 1.6 \times 10^{24} T^{-2.613} \exp\left(\frac{-89100}{RT}\right)$ $^{cm^3}/_{mol\,s}$ from the experimental study of Shiina *et al.* [878] and including an enhanced third-body efficiency of 1.5 for N_2. It is uncertain if this provides an adequate description of the reaction at the high pressure and low temperature conditions used in the present work, but at present, there are no reports of the fall-off behavior or the high-pressure limit. It is also possible that a completely different mechanism is in play; e.g. involving the initiation reaction between H_2S and O_2, or the further conversion of the S atom released from the thermal dissociation of H_2S. Moreover, sulfur species are known to be active on surfaces [879], which may also be a contributing factor to the observed fuel initiation at low temperatures.

The experimental results indicate a minor yield of CH_3OH at the lowest temperatures. It is expected that this yield is associated with the release of H atoms during the gradual conversion of H_2S to SO_2, but it cannot be ruled out that H_2S exhibits e.g. some distinct catalytic effect similar to that observed for NO_x (see Section 6.2.3 and 6.6.3).

In order to properly characterize the influence of sulfur on hydrocarbon oxidation chemistry, it is necessary to compare the current results with similar measurements obtained without sulfur. The reducing experiment with CH_4/H_2S can roughly be compared to the 90 and 50 bar experiments with pure CH_4: exp. F (90 bar, $\phi = 25.2$) and exp. G (50 bar, $\phi = 95.5$) in Figure 6.9 (middle and bottom). The pure CH_4 experiments both revealed a substantial conversion of the fuel and oxidizer shortly after fuel initiation, which took place around 750–775 K. However, no changes of similar magnitudes are observed in the concentration profiles during the reducing experiment with CH_4/H_2S; especially not at temperatures above 800 K, where the O_2 concentration is almost constant. This suggests that sulfur indeed has an inhibiting effect on the hydrocarbon conversion even though the results are not conclusive. As previously stated, there are no experimental results available with pure CH_4 at 50 bar because no considerable fuel conversion could be observed within the investigated temperature range. This is consistent

with the limited conversion of CH_4 observed throughout measurements at the stoichiometric conditions with CH_4/H_2S in Figure 6.21 (top right). The experimental conversion of CH_4 yields about 200 ppm, which is comparable to the conversion of 200 ppm of H_2S to SO_2 and the proportional release of H atoms, but it provides no confirmation of an inhibiting effect of sulfur.

It is not possible to draw any definite conclusions regarding the influence of sulfur on the hydrocarbon oxidation chemistry at high pressure; mainly due to the limited number of experiments and the incomplete model description that render a detailed characterization of the underlying reaction mechanisms impossible. Even so, the available experiments show indications of an inhibiting effect consistent with the removal of radical species. This is not an attractive feature in relation to the investigated GTL process and suggests that sulfur should be removed from the feed gas before the partial oxidation process.

6.8 Undiluted CH_4 Experiments

The previous experiments have all been conducted at N_2 diluted conditions in order to minimize the heat release from the exothermic hydrocarbon oxidation reaction. This has ensured a well-defined temperature profile and allowed a reliable interpretation of the measurements and corresponding modeling results based on isothermal plug flow simulations. However, as previously discussed, this condition is not optimal for high yields of CH_3OH, because CH_4 needs to be the most frequent collision partner of CH_3O in order to promote the reaction $CH_3O+CH_4 \rightleftharpoons CH_3OH+CH_3$ (R78) over the thermal dissociation of CH_3O to CH_2O+H (R69) that inevitably leads to the undesired full oxidation products (see Figure 6.12). Even so, the reducing (and N_2 diluted) experiments with pure CH_4, CH_4/C_2H_6, and CH_4/NO_x have all resulted in minor yields of CH_3OH that have facilitated a satisfactory validation of the model performance in terms of CH_3OH formation.

The final experiments with CH_4/O_2 have also been conducted at highly reducing conditions, but without an inert diluent. These are conditions that promote high yields of CH_3OH and hence, resemble those of practical use in the investigated GTL process even though it is very unlikely that the present experiments correspond to the optimal conditions. The drawback of this approach is obviously the substantial heat release from the reaction, which means that the measurements have little value in terms of kinetic model validation. Instead, the experimental data may provide some indications of what to expect from the authentic GTL process.

6.8.1 Experimental Conditions

Two undiluted experiments with CH_4/O_2 are presented below. They have both been conducted at 100 bar and reducing conditions, but with varying O_2 loads corresponding to CH_4/O_2 ratios of 57.0 and 20.5, i.e. $\phi = 114$ and 40.9 respectively. As previously discussed in the literature review in Section 2.2.1, a reverse proportionality exists between high selectivities of CH_3OH and the conversion of CH_4. This issue will be elucidated by the experiments. The experimental conditions are summarized in Table 6.8, and the experimental results are shown in Figure 6.22 including corresponding model predictions that use the fitted rate constant $k_{R349} = 131\,{}^1/_s$ for the surface reaction $CH_3OO \rightarrow CH_3OO^\bullet$ (R349) (see e.g. the discussion of (R349) in Section 6.4.2).

Table 6.8: Reaction conditions applied during undiluted experiments with CH_4/O_2. See caption of Table 6.2 for other specifications.

	Reactant concentrations					
Exp. id.	CH_4 [%]	O_2 [%]	Pres. [bar]	Temp. [K]	ϕ [a]	τ [s K]
$\mathcal{C}$	98.3	1.73	100	598–763	114.	${}^{12020}/_T$
$\mathcal{D}$	95.3	4.66	100	598–763	40.9	${}^{11900}/_T$

[a] Stoichiometric ratio (ϕ) is based on $CH_4 + 2O_2 \rightarrow CO_2 + 2H_2O$

Calculations of the adiabatic temperature rise gave values >100 K for experiment $\mathcal{C}$, while the higher O_2 feed concentration in experiment $\mathcal{D}$ facilitated an adiabatic temperature rise >200 K. Obviously, it is no longer valid to assume isothermal conditions in the reactor and kinetic modeling has therefore been conducted as adiabatic plug flow simulations, even though this may not be very accurate either. The temperature rise also facilitates a decreasing residence time, which is difficult to account for during the simulations. The presented numerical results are based on the initial reactor temperatures and the temperature dependent residence times listed in Table 6.8 even though this is only valid for isothermal conditions and corresponds to an upper limit of τ. A lower limit of the residence time can be obtained by including the calculated adiabatic temperature rise in the expression of $\tau(T)$ from Table 6.8. In case of experiment $\mathcal{D}$, this yields a potential deviation in the residence time of up to 4 sec. However, calculations indicate that the main fuel conversion takes place within the first second of the residence in the reactor after which, the calculated concentration profiles show limited sensitivity to changes in the residence time.

In practice, it turned out to be difficult to operate the high pressure flow reactor at the conditions listed in Table 6.8, and instabilities in the temperature and pressure control were occasionally observed during the experiments; especially during experiment $\mathcal{D}$ that applied the highest O_2 load. In order to counteract this phenomenon, product sampling was conducted three times at every investigated temperature level instead of the usual duplicate measurements. Even so, some of the resulting average concentrations shown in Figure 6.22 still reveal considerable scatter. The carbon balance was satisfied within 0.5 % throughout experiment $\mathcal{C}$, while occasional deviations in the carbon balance of experiment $\mathcal{D}$ were up to 2.8 %. Considering a total carbon feed of 95.3 % in experiment $\mathcal{D}$, the latter results in a substantial quantity of 2.7 % of carbon matter that cannot be accounted for by the measurements. This is mainly expected to be associated with the observed fluctuations in the CH_3OH concentrations in Figure 6.22 (top right).

6.8.2 Discussion of Experimental and Modeling Results

Figure 6.22 reveals some deviations between experimental and numerical results, but this does not come unexpected considering the uncertainties associated with the actual temperatures and residence times obtained during the experiments. Care should therefore be taken to validate the model performance based on the observed discrepancies.

As expected, CH_3OH is the major product in both experiments even though the CO measurements yield almost similar magnitudes in experiment $\mathcal{D}$ with the high O_2 load (Figure 6.22, right). Figure 6.23 shows an example of calculated concentration profiles of selected species as functions of the residence time during the time period of the main fuel conversion. The figure is based on an adiabatic plug flow simulation of experiment $\mathcal{D}$ (100 bar, $\phi = 40.9$) using an initial reactor temperature of 683 K. A peak concentration of CH_3OH is obtained by the time of O_2 depletion followed by a minor conversion until an almost constant level is obtained shortly after. A net rate analysis confirms that the light consumption of CH_3OH is mainly facilitated by OH radicals to yield CH_2OH (R86) in accordance with the reaction mechanism outlined in Figure 6.12. The peak concentration of CH_3OH is indicated by the small arrow in Figure 6.23. It is very sharp making it practically impossible to balance an industrial process at the corresponding conditions. However, as also shown in Figure 6.23, the removal of CH_3OH is modest even though the temperature is high and the example indicates less than 11 % loss of CH_3OH after 1 sec from full conversion of the O_2 feed. Similar observations can be made for the undiluted experiment $\mathcal{C}$ ($\phi = 114$), even though the post-conversion of CH_3OH is much less pronounced under

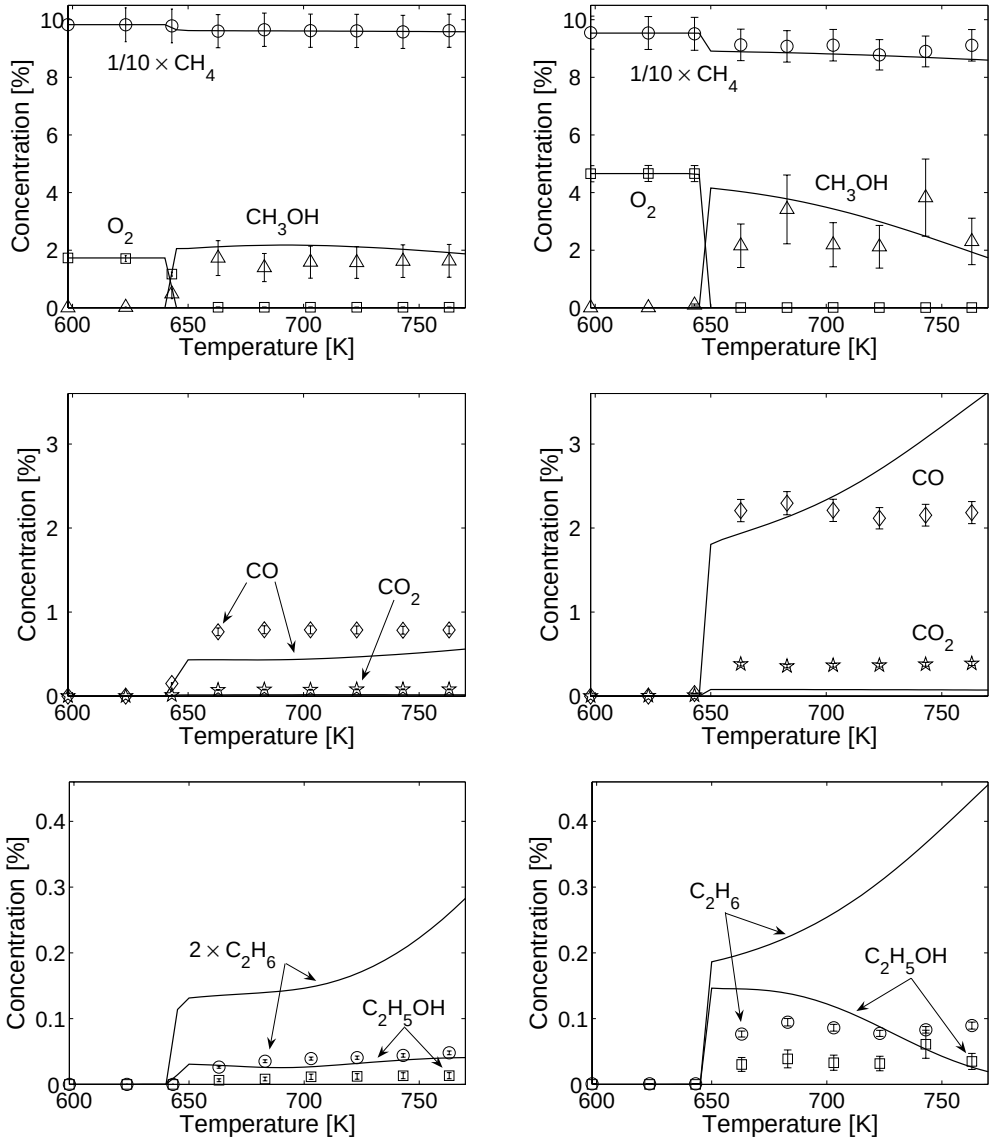

Figure 6.22: Results of experiments with undiluted CH_4/O_2 at 100 bar. Left: Exp. $\mathcal{C}$ ($\phi = 114$). Right: Exp. $\mathcal{D}$ ($\phi = 40.9$). Reaction conditions are provided in Table 6.8. Symbols mark experimental results. Full lines denote adiabatic plug flow simulations. Estimated experimental uncertainties are $\pm 6.0\,\%$ for $O_2/CO/CO_2/CH_4/C_2H_6$, and $\pm 35\,\%$ for CH_3OH/C_2H_5OH based on observations of scattering between consequtive measurements at the same reactor temperature.

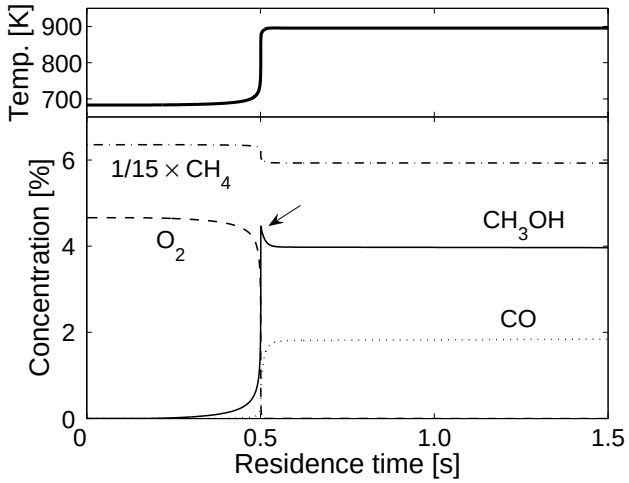

Figure 6.23: Temperature and concentration profiles as a function of the residence time based on adiabatic plug flow simulations of the undiluted experiment $\mathcal{D}$ (100 bar, $\phi = 40.9$). Experimental conditions are found in Table 6.8. The initial reactor temperature is 683 K. The figure only shows the initial section of the reactor where the main fuel conversion takes place. The arrow indicates the peak concentration of CH_3OH.

these conditions due to the lower heat release.

A calculation of the average CH_3OH selectivity during the experiment with the lowest feed concentration of O_2 (Figure 6.22, left) yields $\overline{S}_{CH_3OH} = 74.6\,\%$ based on the measurements obtained from 675–763 K. The corresponding average conversion of CH_4 yields $\overline{X}_{CH_4} = 2.2\,\%$ throughout the same temperature interval. As can be seen in Figure 6.22 (left), the remaining carbon matter is almost exclusively found as CO. It is noted that the highest measured selectivity of CH_3OH during experiment $\mathcal{C}$ yields 79 % at 1.8 % CH_4 conversion at 683 K.

The lower CH_4/O_2 ratio in experiment $\mathcal{D}$ results in a somewhat higher CH_4 conversion ($\overline{X}_{CH_4} = 5.3\,\%$), while the average selectivity of CH_3OH has decreased to $\overline{S}_{CH_3OH} = 53.7\,\%$. Even so, this implies a significant increase of the absolute concentration of CH_3OH. Again, these values are based on the measurements conducted at 675–763 K with CO as the major secondary carbon product. The peak selectivity of CH_3OH during this experiment is also measured at 683 K yielding 74 % at 4.8 % CH_4 conversion, but the general scatter in the CH_3OH concentrations makes the value of $S_{CH_3OH,max}$ quite uncertain.

The two experiments can be compared in terms of the *yield* of CH_3OH,

which is calculated as the product of S_{CH_3OH} and X_{CH_4}, as previously defined in Equation (1.9). This results in average CH_3OH yields of 1.6 and 2.8 % for experiment $\mathcal{C}$ and $\mathcal{D}$ respectively, which suggests that lower CH_4/O_2 ratios may be preferable despite the increased heat release during the reaction. This is consistent with the previous literature evaluation in Section 2.4 where optimal CH_4/O_2 ratios between 10 and 40 were proposed.

6.9 Summary

This chapter has presented experimental results and detailed model investigations of the chemical systems: $CO/H_2/NO_x/O_2$, CH_4/O_2, $CH_4/C_2H_6/O_2$, $CH_4/NO_x/O_2$, and $CH_4/H_2S/O_2$. The experiments have been conducted at temperatures from 598–898 K, pressures from 20–100 bar, and stoichiometric ratios ranging from highly reducing ($\phi < 100$) to oxidizing conditions ($\phi > 0.04$) by use of the high pressure flow reactor setup described in Chapter 4. With few exceptions, reactant mixtures have been diluted with N_2 in order to minimize the heat release from the exothermic oxidation reactions and ensure a well-defined temperature profile. The experimental database has facilitated a thorough validation of the novel detailed chemical kinetic model with a generally satisfactory response.

The C_{1-2} hydrocarbon oxidation mechanism has been characterized through oxidation experiments with pure CH_4 and fuel mixtures with 10 % C_2H_6 on a molar basis. Satisfactory correlations between experiments and numerical results have been obtained, which encourage the use of the present kinetic model during the optimization of the GTL process. There have been indications of an incomplete model description of the conversion of C_1 to C_2 hydrocarbons; more specifically, the conversion of CH_3 to C_2H_6 (R41), which may be too fast under the investigated conditions. Moreover, the current description of the direct oxidation path of C_2H_4 is incomplete, but both issues have little influence at the conditions relevant to the investigated GTL process. The formation of CH_3OH is promoted by high absolute concentrations of CH_4 through the reaction $CH_3O+CH_4 \rightleftharpoons CH_3OH+CH_3$ (R78). Model validation of this mechanism has been satisfactory. A few experiments with CH_4/O_2 have been conducted at undiluted conditions resembling those applied during the GTL process. These experiments provided substantial yields of CH_3OH with average selectivities of 74.6 and 53.7 % at CH_4/O_2 ratios of 57 and 20 respectively. The corresponding average CH_4 conversions yielded 2.2 and 5.3 %. However, the undiluted experiments were subjected to substantial uncertainties regarding the reactor temperature and the residence time, which have made the results unsuited for kinetic model validation.

The oxidizing experiment with $CO/H_2/NO_x$ at 20 bar revealed an augmented sensitivity to the rate constant of the elementary reaction NO_2+H $\rightleftharpoons$ NO+OH (R270) that has been utilized to derive a value of $k_{R270}(850–875\,K) = 1.3 \times 10^{14}$ ($\pm 40\,\%$) $^{cm^3}/_{mol\,s}$. Based on this result, as well as data from the literature, it has been recommended to use the rate coefficient of $k_{R270,\,Ko\ \&\ Fontijn,\ 1991} = 1.3 \times 10^{14} \exp\left(\frac{-362}{RT}\right)$ $^{cm^3}/_{mol\,s}$ for combustion modeling.

The sensitizing effects of NO_x have been characterized through experiments with $CO/H_2/NO_x$ and CH_4/NO_x. It has been demonstrated that the presence of NO_x has a promoting effect on the hydrocarbon oxidation chain and facilitates significantly lower initiation temperatures. This is a result of the cyclic conversion of NO/NO_2 through interactions with the H_2/O_2 radical pool and hydrocarbon species. The former leads to a net gain of chain carrying OH radicals, while direct interactions with hydrocarbon radicals carries the oxidation chain forward; most important is the reaction sequence $NO+CH_3OO \rightleftharpoons NO_2+CH_3O$ (R266) and $NO_2+CH_3 \rightleftharpoons NO+CH_3O$ (R283). The experiments with CH_4/NO_x revealed a substantial intermediate formation of CH_3NO_2 through association/stabilization of CH_3 and NO_2 (–R326). The formation of CH_3NO_2 is a characteristic high-pressure phenomenon that facilitates an intermediate inactivation of important chain carrying components and hence, slows down the overall fuel conversion rate. There are indications that the current model description of the pressure dependency of (–R326) is inaccurate at very high pressures. Despite the generally promoting effect of NO_x on the hydrocarbon oxidation chain, the results indicated a negligible net gain of CH_3OH, which is unlikely to compensate for the expected additional expenses associated with a more complex process design necessary to utilize NO_x as a chemical promoter in the GTL process. This has led to a preliminary rejection of the use of NO_x during the GTL process.

The present work only includes a limited investigation of the influence of sulfur on hydrocarbon oxidation chemistry at high pressure. The kinetic model provides a poor description of the experimental results; particularly in relation to the initiation of the chemistry. There are indications that sulfur has an inhibiting effect on the hydrocarbon oxidation process, but the results are inclusive, and further investigations are needed before a reliable characterization can be made.

Chapter 7

Process Optimization

7.1 Introduction

The main work of this project has so far been concerned with the development and validation of the novel detailed chemical kinetic model. Through comparison with numerous experimental results, it has been demonstrated that the model possesses satisfactory predictive capabilities when it comes to oxidation of light hydrocarbons under a wide range of conditions including those relevant to the GTL process.

Having a reliable understanding of the fundamental chemical mechanisms in place; now represented by the kinetic model, it is time to return to the overall objective of the project, which is to identify the optimal conditions for high yields of CH_3OH (Y_{CH_3OH}). The task will be limited to the search for the optimal combination of the three independent process parameters: *temperature*, *pressure*, and *feed composition*. Since all kinetic model calculations are conducted as adiabatic plug flow simulations, it is implicitly assumed that the reaction takes place in a flow reactor. Moreover, it is assumed that the reactor surface-to-volume ratio is sufficiently low to justify a negation of potential surface effects, and that a *critical* residence time is exceeded, long enough to allow full conversion of the O_2 load. As previously discussed in Section 6.8.2, only a limited conversion of the desired product happens after depletion of O_2, which means that Y_{CH_3OH}, in practice, can be considered independent of the residence time when $\tau > \tau_{[O_2]\rightarrow 0}$. The use of NO_x and/or H_2S/SO_2 as potential gas phase sensitizers has been discouraged in the previous chapter based on experimental observations and model predictions are therefore not considered during the present analysis. For simplicity, it is further assumed that the hydrocarbon feed is solely composed of CH_4, which means that the feed composition is defined by only one parameter; namely

the CH_4/O_2 ratio $(\hat{\phi})$ [1]. The optimal reaction conditions may be restrained by limitations of secondary process equipment used in a full scale application of the technology as well as the economic feasibility of the process, but these issues are not considered either.

Based on the above assumptions, the optimization of the GTL process is now limited to the task of maximizing the function $Y_{CH_3OH}(T, P, \hat{\phi})$, i.e.

$$\arg\max_{T,P,\hat{\phi}} \left\{ Y_{CH_3OH}(T, P, \hat{\phi}) \right\} \tag{7.1}$$

Unfortunately, the problem cannot be considered as an ordinary non-linear least square problem, because the function $Y_{CH_3OH}(T, P, \hat{\phi})$ probably has several local maxima from which only the highest is of interest. In other words, it is only the *global* maximum $Y_{CH_3OH}(T_{opt}, P_{opt}, \hat{\phi}_{opt})$ that is desired.

In order to meet this requirement, a global optimization routine has been developed that utilizes the features of *interval analysis* to narrow down the global minimizer of a given objective function within a finite region of the independent variables. The algorithm behind this software tool will be presented in this chapter as well as some basic computational aspects of interval analysis that underlie the programme code. Moreover, a test example will be presented based on a simple 1D objective function with an analytical solution. This enables a illustrative graphical representation of the iteration procedure. Finally, the objective function $Y_{CH_3OH}(T, P, \hat{\phi})$; based on the detailed kinetic model, will be subjected to the global optimization routine in order to identify the optimal conditions of the GTL process.

A substantial part of this work has been conducted in collaboration with Ph.D. Kim H. Petersen, from the Department of Chemical Engineering, DTU, during mutual participation of the course "02611 Optimization and Datafitting" in the Autumn 2004 at Department of Informatics and Mathematical Modelling, DTU. The author wishes to acknowledge the contributing work of KHP.

7.2 Interval Computations

Interval analysis, introduced by Moore [880] in 1959, is a tool for automatic control and quantification of the general sources of error in numerical computations, which are rounding errors, truncation errors, and input errors. Notice that the latter may be viewed in terms of uncertainty limits associated with

[1] The CH_4/O_2 ratio $\hat{\phi}$ should not be confused with the *stoichiometric ratio* ϕ that was used extensively in Chapter 6. Notice that $\hat{\phi} = \frac{1}{2}\phi$ in the pure CH_4/O_2 system.

a given measurable quantity obtained in the laboratory, e.g. temperature, concentration, dimension, time, etc.

An important feature of interval analysis is the ability to enclose ranges of functions. This can be utilized to e.g. solve equations with interval coefficients, prove existence of certain solutions, and to solve global optimization problems, which has found wide use within rigorous mathematics and computer sciences [880–882]. As an example of the ability to enclose ranges of functions, consider the simple objective function $f : \mathbb{R} \mapsto \mathbb{R}$:

$$f(x) = x(x^2 - 1) \tag{7.2}$$

defined within the interval $X_0 \in [-1, 2]$. Interval computations yield

$$\begin{aligned} f([-1,2]) &= [-1,2]\,([-1,2]\,[-1,2] - 1) \\ &= [-1,2]\,([-2,4] - 1) \\ &= [-1,2]\,[-3,3] \\ &= [-6,6] \end{aligned}$$

which encloses the exact range of the function value $\left[-\frac{2\sqrt{3}}{9}, 6\right]$. The interval analysis severely overestimates the lower bound of the exact function value span. A method to reduce the overestimation is to divide the initial interval into smaller extensions, as illustrated in Figure 7.1.

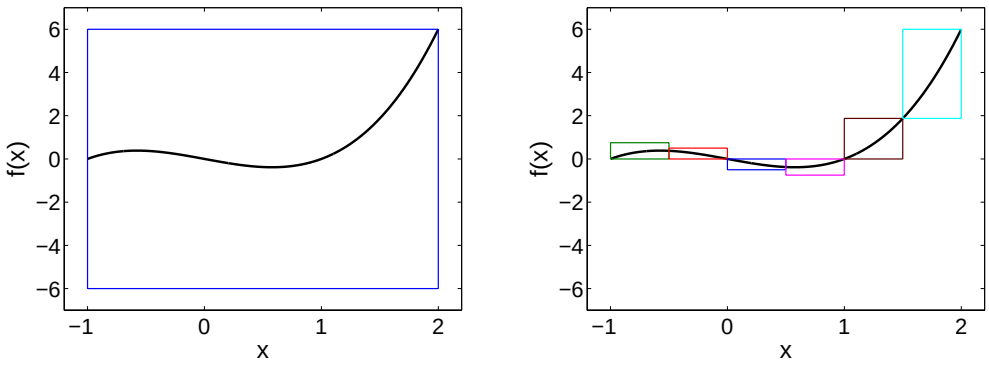

Figure 7.1: Example of interval computations based on $f(x) = x(x^2-1)$ for $X_0 \in [-1, 2]$. The widths and heights of the colored squares represent interval extensions of x and $f(x)$ respectively. Subdivision of X_0 reduces the overprediction of the function value ranges that enclose the exact function values.

Before more complicated use of interval analysis is undertaken, it is necessary at this point to introduce some basic concepts related to interval arithmetic.

7.2.1 Basic Interval Arithmetic

A *real* interval A is a delimited, closed subset of real numbers defined by

$$A = [\underline{a}, \overline{a}] = \{x \in \mathbb{R} \,|\, \underline{a} \leq x \leq \overline{a}\} \tag{7.3}$$

where $\underline{a}, \overline{a} \in \mathbb{R}$ and $\underline{a} \leq \overline{a}$. The lower and upper bounds of an interval are commonly referred to as the *infimum* and the *supremum* respectively. The *midpoint* $m(A)$, the *radius* $r(A)$, and the *width* $w(A)$ are defined in Equation (7.4)–(7.6) respectively:

$$m(A) = 1/2\,(\underline{a} + \overline{a}) \tag{7.4}$$

$$r(A) = 1/2\,(\overline{a} + \underline{a}) \tag{7.5}$$

$$w(A) = (\overline{a} - \underline{a}) = 2r(A) \tag{7.6}$$

Notice that an interval is equally well defined by its midpoint and radius, i.e. $<m(A), r(A)>$, as by the infimum and supremum values cf. Equation (7.3). *Interval vectors* and *interval matrices* are vectors and matrices in the usual sense with components given as intervals [880]. Additionally, $w(\mathbf{A}) = \max_{\mathrm{i}} \{\mathrm{w(A_i)}\}$, while $m(\mathbf{A})$ and $r(\mathbf{A})$ follow straightforward from the definitions above yielding vectors or matrices with scalar values.

Interval arithmetic is an arithmetic defined on sets of intervals instead of real numbers, but even so, there are many similarities. The four elementary operations commonly obey

$$A \diamond B = \{a \diamond b \,|\, a \in A \wedge b \in B\}\,, \qquad \diamond = +, -, \cdot, / \tag{7.7}$$

where A/B is undefined if $0 \in B$. A and B are defined in accordance with (7.3), which means that $A \diamond B$ is also an interval. The operational versions of (7.7) are given in Equation (7.8)–(7.11):

$$A + B = \left[\underline{a} + \underline{b}, \overline{a} + \overline{b}\right] \tag{7.8}$$

$$A - B = \left[\underline{a} - \overline{b}, \overline{a} + \underline{b}\right] \tag{7.9}$$

$$\begin{aligned} A \cdot B = \big[&\min\left(\underline{a}\cdot\underline{b}, \underline{a}\cdot\overline{b}, \overline{a}\cdot\underline{b}, \overline{a}\cdot\overline{b}\right), \\ &\max\left(\underline{a}\cdot\underline{b}, \underline{a}\cdot\overline{b}, \overline{a}\cdot\underline{b}, \overline{a}\cdot\overline{b}\right)\big] \end{aligned} \tag{7.10}$$

$$A/B = A \cdot \left[1/\overline{b}, 1/\underline{b}\right] \tag{7.11}$$

The arithmetic operations are both *cummutative* and *associative*, i.e. $A+B = B+A$ and $A \cdot B = B \cdot A$, but the *distributive* rule is not valid in general. Instead, $A \cdot (B+C) \subseteq A \cdot B + A \cdot C$, which is referred to as *sub-distributive* [880].

Only in special cases will the two latter forms be equal; e.g. when $w(A) = 0$ corresponding to $\underline{a} = \overline{a}$ or when A is a scalar value (a degenerate interval).

The basic interval arithmetic implies an almost "normal" use of rational functions except when applying different formulations of the same function, which may lead to different interval extensions because of the non-validity of the distributive rule.

7.2.2 Implementation in Scientific Computing

In order to allow rigorous applications of interval analysis, fast algorithms need to be available for computation of interval arithmetic. Moreover, it is necessary to control the procedure of rounding-off. Interval arithmetic operations on computers are conducted with floating point values[(2)]. Even so, only a finite numerical range is available in computers as well as a limited number of digits. This means that certain decimal numbers like e.g. π and $1/3$ cannot be expressed with infinite accuracy and will eventually be rounded off. In terms of interval arithmetic, a given result must always be rounded *outwards* to the machine number nearest to the mathematically correct result in order to ensure that the resulting interval represented in the computer always contains the mathematically correct result. Implementation of codes that enable control of the rounding procedure is possible on most modern computer systems that support IEEE (Institute of Electrical and Electronics Engineers) standard arithmetic [883].

In the present work, all computational aspects of interval analysis are carried out in MATLAB using the INTLAB (INTerval LABoratory) toolbox [884, 885]. This software package is based on the *Basic Linear Algebra Subroutines* (BLAS) [886–888] developed for fast computations of linear algebra arithmetic. INTLAB also includes rounding procedures according to the above discussion. The toolbox supports interval arithmetic with real and complex intervals, vectors, and matrices. With the application of BLAS, tests have shown that the algorithms are almost as fast as the fastest pure floating point algorithms available [884].

7.3 Global Optimization Routine

This section presents the algorithm behind the global optimization routine based on the work of Madsen and co-workers, e.g. [882,889,890]. The present routine has not been developed for the sole purpose of finding the global

[2] An example of a 3 digit floating point is 1.54×10^{-4} that would yield .000154 in a fixed point system.

maximum of $Y_{\mathrm{CH_3OH}}(T, P, \hat{\phi})$, but for a general application with continuous nonlinear functions of the kind $f : \mathbb{D} \mapsto \mathbb{R}$, where $\mathbb{D} \subseteq \mathbb{R}^n$. Using interval analysis, the current method aims to determine the global minimum of f, i.e. $f^* = \inf\{f(x) \,|\, x \in \mathbb{D}\}$, and the points where it is attained: $X^* = \{x \in \mathbb{D} \,|\, f(x) = f^*\}$. Notice that in mathematical terms, an optimization problem should always be formulated as a search for the *minimizer* of a given function. This is consistent with the inverse maximizer.

7.3.1 Basic Algorithm

The basic algorithm works with a *candidate set* C, which is a finite set of subregions $C_{(j)} \subseteq \mathbb{D}$ where $\bigcup_j C_{(j)}$ contains the set of minimizers X^* of f. The interval extension of f is denoted by F, and the upper and lower bounds of $F(C_{(j)})$ are given by $U(C_{(j)})$ and $L(C_{(j)})$ respectively. Notice that

$$\min_j \left\{L(C_{(j)})\right\} \leq f^* \leq \min_j \left\{U(C_{(j)})\right\} \equiv \xi \tag{7.12}$$

which means that if $L(C_{(j)}) > \xi$ then $C_{(j)}$ does not contain a global minimizer, and it can safely be discarded from C. As previously illustrated in Figure 7.1, narrow function value bounds can be obtained by splitting $C_{(j)}$ into smaller subregions. In the global optimization algorithm, this is done by simple bisection. When $j > 1$, the interval extension containing $\min_j \left\{L(C_{(j)})\right\}$ is selected for the split, since this is the most likely extension to contain X^* even though it is not guaranteed. Moreover, when considering multiple dimensions, the bisection is conducted in the direction of the largest radius of $C_{(j)}$.

In the basic algorithm, the candidate set C is divided into a work set S and a result set R, where $X^* \in S \cup R$. If

$$w(F(S_{(j)})) \leq \delta \tag{7.13}$$

then $S_{(j)}$ is moved from S to R. The algorithm is now based on continuous bisection of $S_{(j)}$ followed by updates of ξ, in accordance with Equation (7.12), and subsequent evaluation of the solution criterion in Equation (7.13) until $S = \varnothing$.

7.3.2 Modified Algorithm

The basic algorithm works well, but converges slowly [891]. This is improved in the modified version of the algorithm that utilizes informations from the interval extension F' of the gradient $f' = \left(\frac{\partial f}{\partial x_1}, \cdots, \frac{\partial f}{\partial x_n}\right)$ (the *Jacobian*).

If the elements of the Jacobian are all positive ($F'(S_{(j)}) > 0$) or all negative ($F'(S_{(j)}) < 0$) then there are no stationary points ($f'(x) \neq 0$) and the function is *monotonically* increasing or decreasing respectively. When this happens, the interval extension can safely be reduced to its lower (respectively upper) bound. If $S_{(j)}$ is moreover an interior to the original domain, it can be discarded completely from S, since an interior minimum must be a stationary point, i.e. $f'(x) = 0$.

The Jacobian is also used to determine whether stationary points exist within an interval subdomain. This is done by the interval version of *Newton's method* [880], which introduces the *Newton operator* $N(x, X)$ as an outer range of an interval that contains a root x^* to the equation $f'(x) = 0$:

$$x^* \in N(x, X) \equiv x - \frac{f(x)}{F'(X)} \tag{7.14}$$

Since $x^* \in X \Rightarrow x^* \in N(x, X)$, the root must lie in the intersect between X and $N(x, X)$, i.e. $x^* \in X \cap N(x, X)$. The Newton iteration now involves a continuous update of the Newton operator in accordance with Equation (7.14) based on a nested sequence of intervals that satisfies $X_{(k+1)} = X_{(k)} \cap N(x_{(k)}, X_{(k)})$ for $x_{(k)} \in X_{(k)}$ and $k = 0, 1, 2, \ldots$. This implies that $X_{(0)} \supseteq X_{(1)} \supseteq \ldots \supseteq X_{(k)}$ corresponding to intervals of decreasing widths: $w(X_{(0)}) > w(X_{(1)}) > \ldots > w(X_{(k)})$, which means that there exists a limit X^* that contains x^*. In order to locate a stationary point, i.e. a root to the gradient, the reformulation of Equation (7.14) in (7.15) is used for the present calculations. Recall that $m(X)$ denotes the midpoint of X:

$$N(m(X), X) = m(X) - \frac{f'(m(X))}{F''(X)} \tag{7.15}$$

This formulation of Newton's method does not allow the second derivative (the *Hessian*) to become zero within X. This happens if X contains an inflection point. Newton's method is expected to yield quadratic convergence, so the minimizer is typically located within a few iteration steps.

The modified algorithm is shown below using pseudo code and in accordance with Caprani *et al.* [882]. The sign ":=" is programming notation for a *dynamic* equation mark, which means that the variable is assigned the value of the argument. This is opposite to the *static* equation mark "=" that facilitates no changes of the variable. Notice that the basic algorithm is readily obtained by excluding the **if**-statement that evaluates "Monotone(X)" and "Newton(X)".

$S_{(1)} := \mathbb{D};\ S := \{S_{(1)}\};\ \xi := U(S_{(1)});\ R := \varnothing$
while $S \neq \varnothing$
  $i := \arg\min_j \{L(S_{(j)})\}$
  $X := S_{(j)}$; remove $S_{(j)}$ from S
  if Monotone(X) **then**
    X is reduced to RX
  elseif Newton(X) works **then**
    X is reduced to RX
  else Split(X) to $RX := \{X_{(1)}, X_{(2)}\}$ with $X = X_{(1)} \cup X_{(2)}$
  end
  use RX to determine $\hat{\xi}$ cf. Eq. (7.12)
  if $\hat{\xi} < \xi$ **then**
    $\xi := \hat{\xi}$
    use Eq (7.13) to reduce S
  end
  for $k = 1$: elements in RX
    if $L(X_{(k)}) \leq \xi$ **then**
      if $w(F(X_{(k)})) \leq \delta$ **then** $R := R \cup X_{(k)}$
                else $S := S \cup X_{(k)}$
      end
    end
  end
end

The modified algorithm requires implementation of the first and second derivatives of f given by the Jacobian and Hessian matrices. Considering the function $f : \mathbb{R}^n \mapsto \mathbb{R}$, their general forms are presented in Equation (7.16) and (7.17) respectively.

$$\frac{\partial f}{\partial \mathbf{x}} = \left(\frac{\partial f}{\partial x_1}, \cdots, \frac{\partial f}{\partial x_n} \right) \tag{7.16}$$

$$\frac{\partial^2 f}{\partial \mathbf{x}^2} = \begin{pmatrix} \frac{\partial^2 f}{\partial x_1^2} & \frac{\partial^2 f}{\partial x_2 \partial x_1} & \cdots & \frac{\partial^2 f}{\partial x_n \partial x_1} \\ \frac{\partial^2 f}{\partial x_1 \partial x_2} & \frac{\partial^2 f}{\partial x_2^2} & \cdots & \frac{\partial^2 f}{\partial x_n \partial x_2} \\ \vdots & \vdots & & \vdots \\ \frac{\partial^2 f}{\partial x_1 \partial x_n} & \frac{\partial^2 f}{\partial x_2 \partial x_n} & \cdots & \frac{\partial^2 f}{\partial x_n^2} \end{pmatrix} \tag{7.17}$$

The Jacobian and Hessian matrices are easily obtained as long as f is continuous and represented by an analytical expression of relative simplicity. However, some functions may be too complex to yield an analytical expression of $f'(x)$ and $f''(x)$. This is e.g. the case with $Y_{\mathrm{CH_3OH}}(T, P, \hat{\phi})$, which is based on the detailed kinetic model from Chapter 5. In this case, numerical solution methods based on real numbers and ordinary arithmetic calculus would have resigned to an approximation of the partial derivatives in Equation (7.16) and (7.17). This method of differential calculus is based upon limits of approximation; e.g. consider the *central* differences approach:

$$\frac{\partial F}{\partial x} = \lim_{h \to 0} \frac{F(x+h) - F(x-h)}{2h} \tag{7.18}$$

In practice, the step length h is made sufficiently small to make truncation errors negligible. Unfortunately, the approach is invalid in connection to interval analysis. This is due to the fact that small values of h will almost always yield interval extensions of $F(x+h)$ and $F(x-h)$ that overlap each other, i.e. $F(x+h) \cap F(x-h) \neq \varnothing$. Following the interval arithmetic rule of subtraction from Equation (7.9), this implies that the resulting approximation to $\frac{\partial F}{\partial x}$ will include 0 corresponding to positive and negative supremum and infimum values respectively.

In general, no numerical approximation methods for partial derivatives are available for use with interval analysis [892]. As a consequence, only the basic algorithm of the global optimization routine is available for applications with complex objective functions, like e.g. $Y_{\mathrm{CH_3OH}}(T, P, \hat{\phi})$, that do not support analytical expressions of the derivatives.

7.3.3 Example: Graphical Illustration of 1D Test Case

In order to test and illustrate the procedure of the global optimization routine, a simple 1D test case is selected that allows a graphical view of the progress of the iteration. The aim is to minimize the objective function $f : \mathbb{R} \mapsto \mathbb{R}$:

$$f(x) = \exp(x) - \sin(x) \tag{7.19}$$

in the interval $X_0 \in [-2, 1]$. The first and second derivatives are given in Equation (7.20) and (7.21) respectively:

$$f'(x) = \exp(x) - \cos(x) \tag{7.20}$$

$$f''(x) = \exp(x) + \sin(x) \tag{7.21}$$

The progress of the iteration procedure is shown in Figure 7.2 based on the modified algorithm where the candidate set is refined in accordance with the three procedures: "Split", "Monotone", and "Newton" that refer to the interval operations described in Section 7.3.1 and 7.3.2.

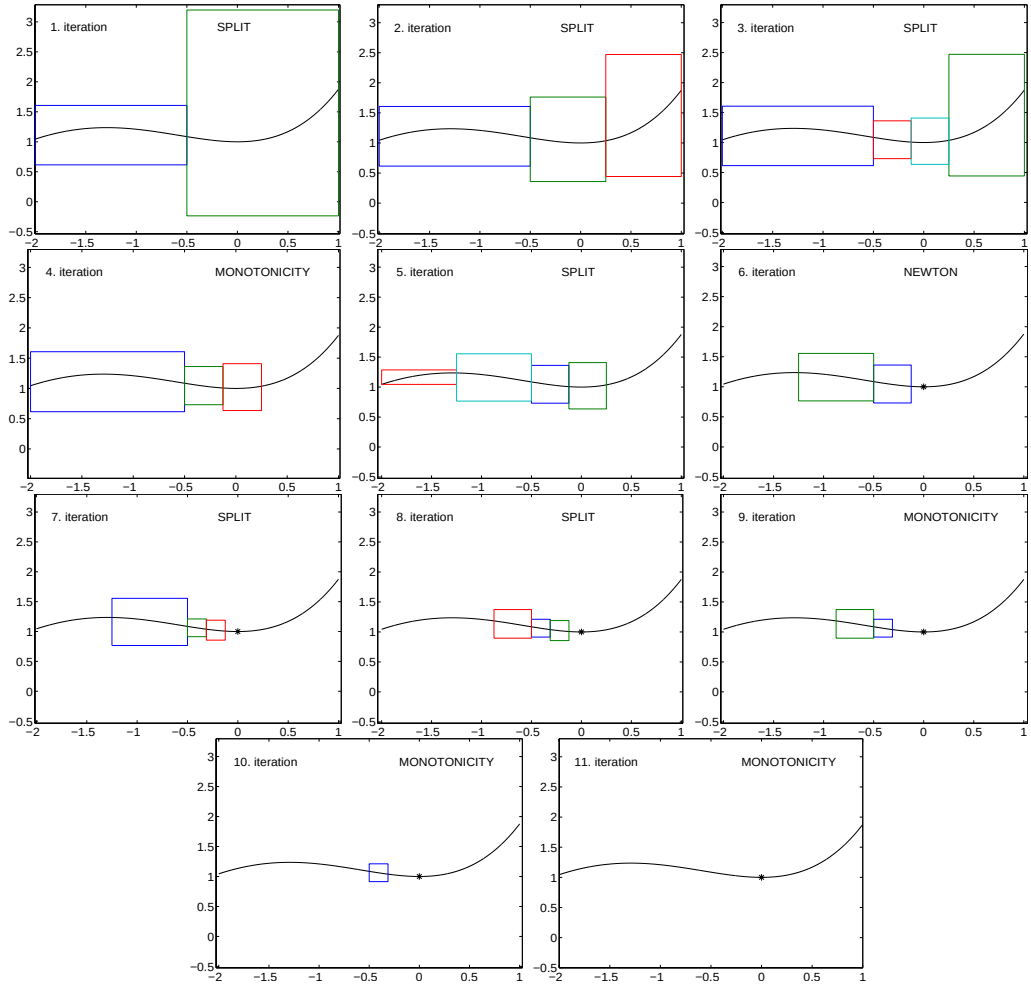

Figure 7.2: Test and graphical illustration of the global optimization routine based on the modified algorithm. The objective function is $f(x) = \exp(x) - \sin(x)$ for $X_0 \in [-2, 1]$. The widths and heights of the colored squares represent interval extensions of x and $f(x)$, while "$*$" denotes solution(s) that satisfy Equation (7.13). The global minimizer at $x^* = 0$ is ascertained after 11 iterations. The Newton iteration performed in Step 6 converged ($\delta \leq 10^{-14}$) within 4 iterations.

As shown in Figure 7.2, the global minimizer in the example is located after 11 iterations with an accuracy of $\delta \leq 10^{-14}$ obtained from the Newton iteration in Step 6. By only enabling the "Split" procedure, the basic algorithm locates the global minimizer within

Number of iterations	Accuracy cf. Eq (7.13)
34	$\delta \leq 0.1$
134	$\delta \leq 0.01$
387	$\delta \leq 0.001$
1108	$\delta \leq 0.0001$

From a mathematical point of view, this is hardly satisfying. However, for certain practical applications, like the current process optimization problem, a relatively low accuracy may be sufficient, as well as the use of CPU hours may not be an issue. Moreover, it is important to keep in mind that both algorithms *guarantee* that the located minimizer is global.

7.4 Optimization of the GTL Process

There are a few remaining issues that warrant attention before the global optimization routine can be subjected to the task of locating the optimal reaction conditions that result in the highest yield of CH_3OH. These include a proper definition of the objective function and some practical implications arising from the software communication between MATLAB and CHEMKIN (FORTRAN).

7.4.1 Definition of the Objective Function

Following the definition of Y_{CH_3OH} in Equation (1.9), this quantity is expressed as the molar flow of CH_3OH going out of the system relative to the molar flow of CH_4 that goes into the system. Considering the low degree of conversion, it is reasonable to assume that the molar flow rate is constant throughout the reactor, which means that Y_{CH_3OH} can be expressed directly as the ratio between the molar fractions of CH_3OH and CH_4 at the outlet and inlet respectively, i.e. $Y_{CH_3OH} = \frac{F_{CH_3OH,out}}{F_{CH_4,in}} \approx \frac{y_{CH_3OH,out}}{y_{CH_4,in}}$. As previously stated, the global optimization routine is designed to locate the *minimizer* of a given objective function, which means that optimal conditions are located where the *inverse* yield of CH_3OH is minimized. It can be argued that concentrations of other desired products like C_2H_5OH should be included in

the objective function as well; or perhaps, concentrations of undesired products should appear as a *penalty term*. However, since CH_3OH is, by far, the predominant stable oxygenate produced during the reaction, it will be difficult to accurately weight the impact of changes in e.g. $y_{C_2H_5OH}$ in order to maintain focus on the primary product.

As previously discussed in Section 6.8.2, in connection to the undiluted experiments with CH_4/O_2 in the high pressure flow reactor, the peak concentration of CH_3OH is obtained by the time of O_2 depletion (see Figure 6.23). This has an unfortunate implication in relation to the current process optimization strategy. The global optimization routine will undoubtedly optimize the reactor conditions in order to yield this peak concentration of CH_3OH at the exit of the reactor and thereby avoid any subsequent conversion of CH_3OH, but it will be almost impossible to balance an industrial process at these exact condition. As illustrated in Figure 6.23, the loss of CH_3OH yields a magnitude of $\sim$10 % during post-conversion, when the reactor temperature is $\sim$900 K including the adiabatic temperature rise from the reaction. A loss of $\sim$10 % of the desired product may be acceptable considering the proportional increase of the CH_4 conversion and the higher absolute concentration of CH_3OH. However, since the overall energy efficiency of the process is constrained by the selectivity of the recovered oxygenated hydrocarbons, it is costly to allow too high losses. The question now remains how to circumvent this problem during the optimization.

In the present work, this is done by including a penalty factor to the objective function in the form of the square root of the adiabatic temperature rise. The adiabatic temperature rise ΔT_{adb} is automatically computed during the adiabatic plug flow simulations with Chemkin. ΔT_{adb} increases with decreasing values of $\hat{\phi}$ provided full conversion of O_2. The weighting of ΔT_{adb} by the power of $1/2$ is an estimate based on preliminary simulations, and a maximum acceptable loss of CH_3OH of $\sim$10 % during post-conversion.

The modified objective function is eventually defined by:

$$Y^{\dagger}_{CH_3OH}(T, P, \hat{\phi}) = \frac{y_{CH_4,in}}{y_{CH_3OH,out}} \sqrt{\Delta T_{adb}} \tag{7.22}$$

All the involved terms are dependent on T, P, and $\hat{\phi}$. The optimization problem can be defined as: $\arg\min_{(T,P,\hat{\phi})} \left\{ Y^{\dagger}_{CH_3OH}(T, P, \hat{\phi}) \right\}$. Based on experiences from the literature (Section 2.4), as well as the experiments conducted in the high pressure flow reactor with high O_2 loads (Section 6.8), it is expected to find the global minimizer within the ranges: $T_0 \in [550, 800]$K, $P_0 \in [50, 110]$bar, and $\hat{\phi}_0 \in [10, 60]$, where T_0 represents the initial reactor temperature. A relatively short constant residence time of $\tau = 3$ sec is ap-

plied in the simulations. As discussed above, this residence time will almost certainly correspond to the time of full O_2 conversion when the optimization is completed, so in practice, this value of τ will denote the *minimum* required residence time.

7.4.2 Software Communications: MATLAB vs. CHEMKIN

The global optimization routine has been developed in MATLAB, which was necessary in order to apply the INTLAB toolbox. This gives rise to an issue of software communication, since the kinetic model is optimized for use with CHEMKIN, which is based on FORTRAN. In the current situation, CHEMKIN is considered to be a "black box" programming wise, that is called at will by MATLAB through a master program designed by the author. The input to CHEMKIN includes the chemical mechanism, thermodynamic database, and reaction conditions in terms of T, P, and $\hat{\phi}$ (though the SENKIN input file). It returns an output file containing properties and composition of the reacted mixture from which the objective function in Equation (7.22) can be evaluated. The master program includes a number of modules that perform the necessary operations.

CHEMKIN is not designed to operate with interval extensions of variables, which means that a conversion strategy is needed to enable communication with the global optimization routine. With the "black box" treatment of CHEMKIN, this inevitably implies that only discrete values of $Y^{\dagger}_{CH_3OH}(T, P, \hat{\phi})$ can be obtained. In the present case, the issue is accommodated by dividing given interval extensions of independent variables into a finite number of discrete values based on equal spacing. This yields a grid of real values of the independent variables. The objective function (CHEMKIN) is then evaluated at all grid points out of which the largest and smallest function value can be assigned as the supremum and infimum of the interval extension of the function value. This is obviously a tedious approach that easily becomes expensive in terms of the number of function evaluation if a fine mesh is applied. However, even a relatively coarse subdivision of e.g. 5 or 6 grid points per dimension will provide a fairly reliable representation of the function value behavior when the diameters of the interval extensions become small. Moreover, wide interval extensions are reluctant to yield substantial overpredictions of the exact ranges of function values, which makes it less likely that a potential solution should be overlooked; especially when the optimization is only based on the "Split" refinement procedure from the basic algorithm. Even so, it is recommended to use a relatively high number of grid points at the expense of CPU hours and monitor the progress of the optimization process. Notice that gradient information would have provided a mean to

determine a more optimal distribution of grid points than the current equal spacing yielding a higher density of grid points in areas with steep gradients, but as previously mentioned, this is not available for use with interval analysis.

7.4.3 Optimal Conditions

The uncertainty of the final determination of the optimal conditions are naturally increased because of the assumptions and computational implications associated with the applied optimization method. As a consequence, it is hardly worth pursuing the optimal conditions within a very high numeric accuracy. The optimization therefore included a relatively coarse solution criterion δ, cf. Eq. (7.13), corresponding to a determination of T_{opt}, P_{opt}, $\hat{\phi}_{opt}$ with 3-4 digits accuracy. Even so, this is considered to be quite optimistic for practical use.

The interval extensions of T_0, P_0, and $\hat{\phi}_0$; listed in Section 7.4.1, are fairly broad and required a substantial number of iterations before a solution could be obtained. After 56 iterations, the interval extensions (candidate set) were manually narrowed to $T_0 \in [635, 660]\text{K}$, $P_0 \in [90, 110]\text{bar}$, and $\hat{\phi}_0 \in [23, 27]$ in order to save computational time. The optimal conditions in (7.23)–(7.25) were located after 82 iterations in total:

$$T_{opt} = 643.3\,\text{K} \tag{7.23}$$

$$P_{opt} = 97.4\,\text{bar} \tag{7.24}$$

$$\hat{\phi}_{opt} = 23.63 \tag{7.25}$$

for $\tau \geq 3\,\text{sec}$. The value of $\hat{\phi}_{opt}$ corresponds to $[\text{CH}_4]_0 = 95.94\,\%$ and $[\text{O}_2]_0 = 4.06\,\%$. Evaluation of the optimal conditions at a more realistic residence time $\tau = \tau_{opt} + 1.0\,\text{sec}$ based on the kinetic model yields

$$S_{\text{CH}_3\text{OH},opt} = 75.4\,\% \tag{7.26}$$

$$X_{\text{CH}_4,opt} = 5.59\,\% \tag{7.27}$$

$$Y_{\text{CH}_3\text{OH},opt} = 4.21\,\% \tag{7.28}$$

Calculation of the adiabatic temperature rise gives $\Delta T_{adb} = 193\,\text{K}$. The key figures in (7.26)–(7.28) include a loss of 6.2 % of the predicted peak concentration of CH_3OH due to product conversion after O_2 depletion.

The optimum conditions in (7.23)–(7.25) are given with a high numeric accuracy that will be difficult to sustain in a practical application. More realistic operating conditions are expected to be $T_{opt} \pm 10\,\text{K}$, $P_{opt} \pm 10\,\text{bar}$,

and $\hat{\phi}_{opt} \pm 1$. A sensitivity analysis indicates that variations of T, P, and $\hat{\phi}$ within these limits can have an overall impact on S_{CH_3OH} of up to $\pm 10\,\%$ of $S_{CH_3OH,opt}$ at the expense of $\pm 9\,\%$ of $X_{CH_4,opt}$ with an opposite sign. However, the calculations are much more sensitive to changes in $\hat{\phi}$ than T and P. Thus, if $\hat{\phi}_{opt}$ is held constant, calculations with $T_{opt} \pm 10\,\mathrm{K}$ and $P_{opt} \pm 10\,\mathrm{bar}$ indicate a maximum impact on S_{CH_3OH} and X_{CH_4} of ± 2–$3\,\%$ with an opposite sign of ΔS_{CH_3OH} and ΔX_{CH_4}.

Figure 7.3 compares $S_{CH_3OH,opt}$ and $X_{CH_4,opt}$ with results from previous literature experiments as well as the two experimental measurements conducted with CH_4/O_2 in the high pressure flow reactor at undiluted conditions. These were previously presented in Section 6.8. The figure is a repetition of Figure 2.1 that was presented in connection to literature review. Hence, the reader is referred to Section 2.2.1 for an elaborate discussion of its context. At present, emphasis is on the positions of the green-crossed symbols relative to the "commercial target" area (hatched).

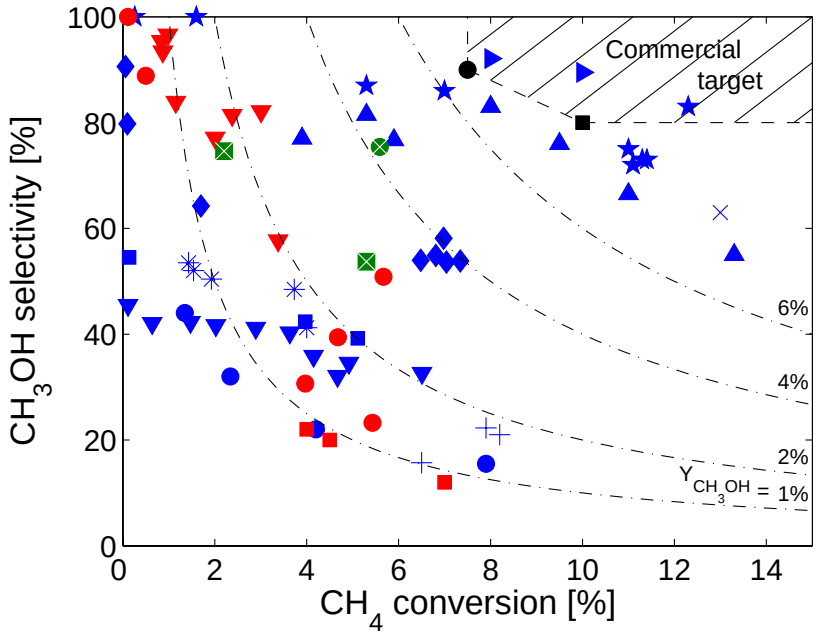

Figure 7.3: Comparison of experimental selectivities of CH_3OH (S_{CH_3OH}) as a function of the CH_4 conversion (X_{CH_4}). ⊠ represents undiluted experiments with CH_4/O_2 from in Section 6.8. ⊗ denotes the calculated result obtained at the optimal conditions. Blue and red symbols represent literature data obtained from the homogeneous and heterogeneous process respectively, while black symbols denote technical economic evaluations of the GTL process (see discussion in Section 2.2.1). References and detailed symbolic notations are given in the caption of Figure 2.1.

Based on Figure 7.3, it is concluded that $Y_{CH_3OH,opt}$ is not sufficiently close to the "commercial target" area to guarantee industrial feasibility. Despite the lower yield of the desired product there may, however, still be possibilities for a commercial exploitation of the technology under specific circumstances; as discussed in Section 1.3.2. The next chapter will take up this challenge and propose potential industrial applications based on the predicted optimal conditions.

The two experimental results from the high pressure flow reactor have both resulted in significantly lower yields, but this does not come unexpected since the applied conditions in the experiments were not selected with the specific purpose of resembling the optimal conditions. These were unknown at the time of the experiments. Nevertheless, the predicted optimal conditions are quite similar to the initial reaction conditions of the undiluted experiment $\mathcal{D}$ (100 bar, $\hat{\phi} = 20.5$) shown in Table 6.8 that gave a substantially lower average selectivity of CH_3OH than predicted at $(T_{opt}, P_{opt}, \hat{\phi}_{opt})$. However, as outlined in Section 6.8.2, substantial uncertainties can be associated with values of S_{CH_3OH} from this experiment, so care should be taken to make firm conclusions based only on a direct comparison with $S_{CH_3OH,opt}$.

Figure 7.3 shows that the predicted value of $Y_{CH_3OH,opt}$ is also higher than most previous results from the literature except for the experiments reported by Gesser and co-workers [65, 67, 68] (▲ and ► in Figure 7.3) and Feng et al. [75] (★). However, referring to the discussion in the literature review in Section 2.2.1, the reliability of these data is questionable and the present finding is only supportive of this opinion.

7.5 Summary

A global optimization routine has been developed to locate a specific combination of reaction conditions that results in the highest yield of CH_3OH based on the novel detailed chemical kinetic model. The software tool is based on interval analysis and guarantees the location of the *global* minimum of a given objective function. The chapter has presented a brief introduction to some of the basic interval arithmetic operations and features that underlie the global optimization routine. The basic algorithm performs a continuous bisection of interval extensions of the independent variables and subsequent evaluation of the resulting function value ranges. The continuous narrowing of intervals decreases the widths of the individual function value ranges. When a lower bound of a given function value range becomes larger than the upper bound of another function value range, the former can safely be discarded knowing that the given interval does not contain a global minimizer. Eventually, the

only remaining interval(s) will contain the global minimizer. The global optimization routine also applies a modified version of the basic algorithm. Here, information about the gradient are utilized to reduce or discard intervals that contain a monotonically behaving segment of the objective function as well as to locate stationary points, i.e. local minimizers. The latter is obtained by an interval version of Newton's method. The modified algorithm converges much faster than the basic algorithm, but it is constrained by the availability of analytical derivatives, since methods of numerical approximations of derivatives are invalid for use with interval analysis. The basic algorithm converges slowly, but it is not subjected to the same constraint as the modified algorithm and hence, works with more complex functions like the present objective function that is based on the kinetic model.

The task of optimizing the GTL process has been defined as a search for the optimal combination of the three independent reaction conditions: temperature, pressure, and CH_4/O_2 ratio in the feed ($\hat{\phi}$) within initially broad intervals of $T_0 \in [550, 800]$K, $P_0 \in [50, 110]$bar, and $\hat{\phi}_0 \in [10, 60]$. The global optimizer for the yield of CH_3OH has been located at $T_{opt} = 643\,\mathrm{K}$, $P_{opt} = 97.4\,\mathrm{bar}$, and $\hat{\phi}_{opt} = 23.6$ based on a residence time $\tau \geq 3\,\mathrm{sec}$. This has resulted in $S_{\mathrm{CH_3OH},opt} = 75\,\%$, $X_{\mathrm{CH_4},opt} = 5.6\,\%$, and $Y_{\mathrm{CH_3OH},opt} = 4.2\,\%$. Variations in the order of $T_{opt} \pm 10\,\mathrm{K}$ and $P_{opt} \pm 10\,\mathrm{bar}$ have a limited impact on this results, while $\hat{\phi}_{opt} \pm 1$ can facilitate deviations up to $\pm 10\,\%$.

The optimum yield of CH_3OH compares favorably to a number of literature experiments as well as the undiluted experiments with CH_4/O_2 conducted in the high pressure flow reactor, but it is not sufficiently close to the defined commercial target range to guarantee industrial feasibility. Even so, this does not rule out a potential commercial exploitation of the technology under specific circumstances as further elaborated in the next chapter.

Chapter 8

Process Design

8.1 Introduction

Optimal process conditions for the direct partial oxidation of methane to methanol have been determined in the previous chapter with respect to temperature, pressure, and CH_4/O_2 ratio in the feed. The next step towards a commercial utilization of the GTL process is to consider potential industrial applications. The author is not familiar with any prior or present commercial installations relying on this technology. Some patents have been granted in the field [90–94] claiming their rights to a particular process design; but these are all of an earlier date and none have, apparently, resulted in the construction of a full scale production facility. Consequently, little attention is paid to these prior inventions in the field. Instead, a more liberal approach is advocated, where drafts of potential feasible designs are presented based on simple brain storming with supplementary flow sheet calculations to provide order-of-magnitude values of capacities, operational conditions, product yields, energy efficiencies, etc. Even though such preliminary calculations may be of the *back-of-the-envelope* type, they provide an overview of potential production facilities and help to identify key operations, process limitations, optimization possibilities, and, most importantly, to assess the economical feasibility of a given application before engineering efforts are spend on rigorous computer simulations and retail equipment design.

The objective of this chapter is to present *first draft* ideas and considerations regarding potential pilot or full scale production facilities based on the optimal conditions determined in the previous chapter. The first concept to be presented is concerned with a GTL plant design that aims for a complete utilization of the hydrocarbon source and consequently, involves *multiple passes* of the reactor. The second concept to be presented in this chapter

is related to a *single pass* utilization of the carbon source. The calculations performed in this chapter are concerned with mass and energy relations of involved fluids and focus on assessing chemical compositions and PVT properties (pressure, volume, temperature) throughout the involved unit operations and pipe flows. No detailed equipment designs are presented, but conceptual descriptions and specifications of characteristic design parameters for classical unit operations like heat exchangers, compressors, etc. should be sufficient to enable engineers skilled in the art to perform the detailed design; if this should ever be necessary. It is a cumbersome task to conduct a quantitative assessment of the economic feasibility of a plant design; even when it comes to a first-hand assessment based on draft ideas. Detailed economic aspects of the presented work are therefore left for future assessment by expects in the field.

8.2 General Computational Aspects

All design considerations are based on steady-state operations and involve iterative solutions of rigorous mass and energy balances.

Almost all computational aspects are carried out in Visual Basic with the MS Excel interface[1]. The author is aware of the existence of commercial engineering software developed for the specific task of aiding process design and optimization, but even so, the current approach is preferred, because it allows complete control and evaluation of all details in the calculations. Moreover, it is desired to implement the novel detailed kinetic model directly in the calculations as representative of the reactor. This involves an embedded call to Chemkin, which may be difficult to implement in commercial software codes. In the present work, the call from Visual Basic to Chemkin (Fortran) is automated via an intermediate call to Matlab that performs all necessary pre- and post-processing of input and output data using customized software modules developed by the author.

Even though the ideal gas assumption is valid at typical reactor conditions (100 bar, 600–900 K), it is expected that temperatures in most other sections of the GTL plant will be considerably lower. The previous Table 3.3 indicates that gas mixtures rich in CH_4 may exhibit substantial deviations from ideal gas behavior at ∼100 bar and near-ambient temperatures. Moreover, product recovery involves a liquid mixture of associating fluids; in particular H_2O and CH_3OH, where mixing effects should not be neglected. As a consequence, all

[1] The author thanks Reader Michael L. Michelsen, Department of Chemical Engineering, DTU, for assistance with computational aspects of non-ideal thermodynamic properties and implementation in MS Excel.

calculations of fluid properties outside the reactor are conducted under the assumption of non-ideal conditions using the methods outlined in Chapter 3. These involve calculation of residual properties based on the Peng-Robinson Cubic EoS; cf. Eq. (3.14). Reference state properties of gaseous species are drawn from the thermochemical database in Table 3.1.

Reactants and products included in the calculations are CH_4, C_2H_6, C_2H_4, CO, CO_2, N_2, O_2, H_2, H_2O, CH_2O, CH_3OH, C_2H_5OH, and CH_3CHO that all together account for $>99.995\,\%$ of the outlet composition from the reactor obtained from the simulations with CHEMKIN. Even though a number of these species only represent minor fractions in the system, their presence ensure an accurate closure of mass and energy balances.

8.3 GTL Plant Design

The GTL plant design can be divided into operations related to *feed pretreatment*, *preheating of reactants*, *reactor design*, *recovery of desired products*, and *removal of side products* that will be discussed individually in terms of practical implications, assumptions, and computational approach.

The modest conversion of the hydrocarbon source during a single pass of the reactor inevitably requires a substantial recirculation of the reactants in order to achieve a high overall degree of conversion. Since high selectivities of CH_3OH relies on a high absolute concentration of CH_4 in the reactant mixture, this calls for efficient methods of product removal in order to avoid accumulation of side products in the recirculation stream and consequent dilution of the CH_4 content.

The exothermic conversion of the hydrocarbon feed implies a considerable heat release that can be captured and utilized for reactant preheating. The heat transfer can be facilitated by an external fluid, e.g. water, but this type of operation is always associated with an energy loss to the ”surroundings”. A different and more efficient heating method is considered that relies on combustion of small amounts of oxygen directly in the hydrocarbon feed. The heat release from hydrocarbon combustion is substantial, so this *in situ* combustion technique is only expected to consume a very small fraction of the hydrocarbon feed in order to yield the desired temperature rise of the reactant mixture. The drawback of the method is the increased yield of the combustion products CO_x+H_2O.

A schematic flow sheet of the proposed GTL plant design with reactant recirculation is shown in Figure 8.1. Since this is a first draft of a potential plant design, the flow sheet only includes major streams and unit operations directly involved with the conversion and recirculation of the hydrocarbon feed.

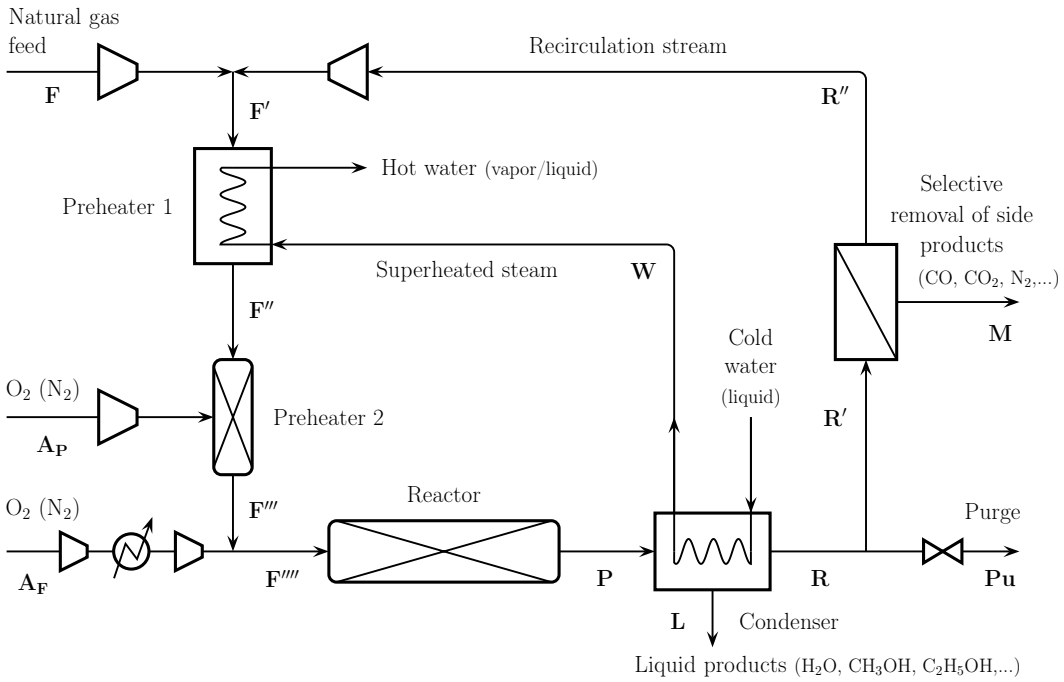

Figure 8.1: Schematic flow sheet of the GTL plant with hydrocarbon recirculation. Preheater 1 is based on condensation of superheated steam from the condenser. Preheater 2 involves *in situ* combustion of O_2 directly in the hydrocarbon stream. The unit operations marked by trapezoids are important compression steps. Capital letters represent specific streams and will be referred to in the text. The flow sheet only includes major streams and unit operations directly involved in the hydrocarbon conversion and recirculation. Appropriate pre- and post-treatment of inlet and outlet streams are discussed in the text.

In practice, each unit operation facilitates a certain pressure drop as a result of friction. However, at this early stage of the process design, it is only possible to make a rough estimate of this effect. For calculation purposes, an overall pressure drop of 10 bar is therefore assumed per hydrocarbon cycle. Moreover, it is assumed that this pressure drop only takes effect in the recycled hydrocarbon stream R'', while all other streams and unit operations involve frictionless flows. This assumption is unrealistic, but the necessary power supply for the compression of R'' should roughly account for the pumping duty needed throughout a real plant.

8.3.1 Plant Capacity and Feed Properties

The overall capacity of the GTL plant is defined by a constant natural gas feed of 100,000 $^{\text{STD m}^3}/_{\text{day}}$ with a realistic composition of 95 % CH_4, 3 % C_2H_6, 1 % CO_2, and 1 % N_2. This volumetric flow rate is small coming from a typical natural gas field [1], but it may represent a realistic side production of natural gas during e.g. oil recovery. It is assumed that inorganic trace species present in the crude natural gas, like e.g. sulfur, are removed prior to the inlet. Moreover, the flow sheet calculations assume that the natural gas feed is available at 293 K and 97.4 bar. The specific pressure corresponds to P_{opt} and is obtained through compression or throttling depending on the available pressure in the original natural gas feed. This specific operation is not included in the flow sheet calculations, but it is noted that a substantial power supply for compression may be required if $P_{feed} \ll P_{opt}$.

Separate sources of O_2 are fed to the reactor and the second preheating unit. The oxidizer inlet to the reactor A_F is defined by the concentration of CH_4 in F''' and the optimal CH_4/O_2 ratio ($\hat{\phi}_{opt} = 23.63$), whereas the O_2 supply to Preheater 2 (A_P) is determined by the required temperature rise of F'' in order to yield $T_{opt} = 643.3$ K. Even though relatively small amounts of O_2 are required for these operations, it will facilitate a substantial accumulation of N_2 if air is used directly as the O_2 source. Therefore, pretreatment by an *air separation unit* is needed. The present calculations assume a purity of 95 % O_2 in both A_F and A_P with balance N_2. This can be achieved by e.g. cryogenic[(2)] distillation of air [893], or pressure swing adsorption using O_2 selective zeolites [894, 895]. Membrane separation of O_2 from air is potentially a less expensive alternative, but the currently available technology is insufficient to yield the desired purity [896].

It is assumed that the O_2 feed is available at near-ambient conditions (1 bar, 293 K), which means that *compression* is needed before mixing with the hydrocarbon stream. The computational approach to compression (or expansion) is the following: Consider an *adiabatic* ($Q = 0$) and *reversible* compression. The entropy balance yields

$$S(T_1, P_1) = S(T_2^{rev}, P_2) \tag{8.1}$$

from which, the temperature in the outlet T_2^{rev} is calculated. The required shaft work for the reversible compression W_s^{rev} is subsequently calculated from the energy balance:

$$W_s^{rev} = H(T_2^{rev}, P_2) - H(T_1, P_1) \tag{8.2}$$

[2] "Cryogenic" commonly refers to processes that take place at temperatures <120 K.

The shaft work for the reversible process needs correction by an efficiency factor $\eta_c = W_s^{rev}/W_s^{real}$ in order to yield the *real* energy input W_s^{real}. All calculations assume $\eta_c = 0.75$ consistent with general recommendations by Peters *et al.* [897]. Finally, the *real* exit temperature T_2^{real} is obtained by reconsidering the energy balance:

$$H(T_2^{real}, P_2) = H(T_1, P_1) + \frac{W_s^{rev}}{\eta_c} \tag{8.3}$$

Gas compression is relatively expensive in terms of the energy requirement. The power consumption can, however, be significantly reduced if the desired pressure is obtained in a two-step compression process with intermediate cooling [157]. The lowest overall power consumption of this configuration is obtained when the intermediate pressure P_2 is given by

$$P_2 = \sqrt{P_1 P_3} \tag{8.4}$$

In the GTL plant, air cooling is applied to reduce T_2^{real} before the second compression. The temperature rise from each compression step is utilized to heat A_F to the desired reactor temperature, i.e. $T_{A_F,3}^{real} = 643.3\,\mathrm{K}$, through adjustment of the intermediate air cooling. These calculations assume a relatively low heat transfer coefficient of $50\,\mathrm{W/m^2\,K}$ for the gas/gas heat exchange unit cf. Ref. [897]. The air flow to the heat exchanger and the heat transfer area are optimization parameters, but neither should be too large in order to minimize the capital investment as well as the energy consumption by a suitable air blower. The calculations indicate that the overall power saving is in the range of 30–40 % when employing a two step-compression unit with intermediate air cooling instead of a single compressor and subsequent air cooling to yield the desired exit temperature and pressure of A_F.

The O_2 feed to the second preheating unit A_P is not subjected to a similar constraint on the temperature rise from the gas compression. Instead, the temperature rise serves to preheat A_P before the inlet, which reduces the necessary fuel consumption during the subsequent *in situ* combustion in Preheater 2. The absolute power saving obtained by employing two compressors in series instead of a single compressor is minimal at low volumetric flow rates, which is expected to be the case for A_P. Calculations of the properties of A_P prior to Preheater 2 is therefore based on a single compression step without air cooling.

8.3.2 Preheating of Reactants

Heating of the hydrocarbon stream to T_{opt} is obtained in a two step operation before mixing with the oxidizer. Preheater 1 utilizes the heat release from the exothermic conversion in the reactor, whereas Preheater 2 supplies efficient heating through *in situ* combustion of a small amount of the carbon feed. The advantage of preheating the reactants before mixing is that the initiation of the reaction should be fairly easy to control through the addition of the oxidizer (A_F). The drawback is that good mixing may be difficult to obtain.

An alternative strategy is to mix the reactants at low temperature and then heat the mixture just prior to the reactor inlet. In practice, this strategy implies integration of the preheater and the reactor in the same vessel. This will ensure good premixing of the reactants, but it may turn out to be difficult to control the initiation of the reaction, which should not happen in the preheating section where the large surface-to-volume ratio ($^{S}/_{V}$) can facilitate extensive surface reactions. It may not be possible to apply the *in situ* combustion technique for preheating if O_2 is already present in the hydrocarbon stream because the flame may initiate a premature conversion. On the other hand, this specific issue may be turned to an advantage through an ingenious reactor design.

More detailed investigations are needed to clarify this issue of optimal preheating, but at present, the strategy of preheating prior to mixing is applied, as indicated in Figure 8.1.

Preheater 1

Preheater 1 involves a classic heat transfer operation where superheated steam, obtained from the condenser, is cooled until the dew point. Here, the water is brought to its liquid state while releasing the latent heat of evaporation. The energy transfer Q from the "hot" to the "cold" fluid is described by the heat transfer equation:

$$Q = UA\Delta T_m \tag{8.5}$$

U is the heat transfer coefficient, which is assumed to be $250\,{}^{W}/_{m^2\,K}$ in accordance with Peters *et al.* [897]. A is the heat transfer surface, and ΔT_m is the logarithmic mean temperature difference calculated from Equation (8.6) for a counter-current flow configuration.

$$\Delta T_m = \frac{(T_{W_{in}} - T_{F''}) - (T_{W_{out}} - T_{F'})}{\ln\left(\frac{T_{W_{in}} - T_{F''}}{T_{W_{out}} - T_{F'}}\right)} \tag{8.6}$$

Assuming zero energy loss to the surroundings, Q is given by the enthalpy change in the fluids:

$$Q = H_{F''} - H_{F'} = H_{W_{in}} - H_{W_{out}} \tag{8.7}$$

The water cycle is assumed to be operated at 70 bar, and the superheated steam has a temperature of 610 K ($= T_W^{boil} + 50\,\mathrm{K}$); see the later discussion in Section 8.3.4. In the calculations, the outlet temperature of the hydrocarbon feed is specified to be $T_{F''} = T_W^{boil} - 10\,\mathrm{K} = 550\,\mathrm{K}$ in order to ensure a substantial temperature gradient and reduce the necessary heat transfer surface. The energy balance in Equation (8.7) is used to determine the steam fraction $y_{W_{out}^{vap}}$ in the outlet of W when $y_{W_{out}^{vap}} > 0$. If $y_{W_{out}^{vap}} = 0$, all water has condensed, and the temperature $T_{W_{out}} \leq T_W^{boil}$ becomes the unknown parameter in the energy balance instead of $y_{W_{out}^{vap}}$. The heat transfer surface A is calculated from Equation (8.5).

Preheater 2

In the second preheating unit, the fluid is heated by the released energy from the combustion of small amounts of O_2 directly in the hydrocarbon stream; consistent with an O_2 diffusion flame in a hydrocarbon atmosphere. A substantial fraction of the energy is released during the final stage of the fuel burnout, i.e. the oxidation of CO to CO_2. This is illustrated by a comparison of $\Delta_r H_{298}$ for the two global reactions of CH_4 combustion:

$$\mathrm{CH_4 + {}^3\!/_2 O_2 \rightarrow CO + 2H_2O} \qquad \Delta_r H_{298} = -124\,{}^{\mathrm{kcal}}\!/_{\mathrm{mol}} \tag{8.8}$$

$$\mathrm{CH_4 + 2O_2 \rightarrow CO_2 + 2H_2O} \qquad \Delta_r H_{298} = -192\,{}^{\mathrm{kcal}}\!/_{\mathrm{mol}} \tag{8.9}$$

For this reason, most industrial combustion systems supply O_2 in excess of the fuel, but in the present situation there is a severe deficiency of O_2. This means that CO+H_2O are the most likely products and the energy release will be far from optimal. It is expected that relatively high local concentrations of O_2 can be obtained as a result of a clever burner design, which will improve the burnout of the fuel and hence, the energy yield, but at present, the worst scenario is assumed when CO and H_2O are the sole products.

Due to the recirculation of the reactant gas, the fuel composition in Preheater 2 is potentially very complex and includes CH_4, C_2H_x, CO, H_2, and a range of oxygenated hydrocarbons in small quantities. It is assumed that CO and H_2 are not converted until the hydrocarbon concentration is depleted meaning that conversion of CO and H_2 can be neglected in Preheater 2. Otherwise, it is assumed that O_2 has no preferences towards any of the remaining combustible species.

The combustion process in Preheater 2 is described by the i global reactions written in (8.10)–(8.16) with the stoichiometric coefficients $\nu_{i,\mathrm{O_2}} = 1$.

$$^2/_3\mathrm{CH_4} + \mathrm{O_2} \rightarrow {}^2/_3\mathrm{CO} + {}^4/_3\mathrm{H_2O} \qquad \Delta_r H_{298} = -82.8\,{}^{\mathrm{kcal}}/_{\mathrm{mol}} \tag{8.10}$$

$$^2/_5\mathrm{C_2H_6} + \mathrm{O_2} \rightarrow {}^4/_5\mathrm{CO} + {}^6/_5\mathrm{H_2O} \qquad \Delta_r H_{298} = -82.5\,{}^{\mathrm{kcal}}/_{\mathrm{mol}} \tag{8.11}$$

$$^1/_2\mathrm{C_2H_4} + \mathrm{O_2} \rightarrow \mathrm{CO} + \mathrm{H_2O} \qquad \Delta_r H_{298} = -90.5\,{}^{\mathrm{kcal}}/_{\mathrm{mol}} \tag{8.12}$$

$$2\mathrm{CH_2O} + \mathrm{O_2} \rightarrow 2\mathrm{CO} + 2\mathrm{H_2O} \qquad \Delta_r H_{298} = -117\,{}^{\mathrm{kcal}}/_{\mathrm{mol}} \tag{8.13}$$

$$\mathrm{CH_3OH} + \mathrm{O_2} \rightarrow \mathrm{CO} + 2\mathrm{H_2O} \qquad \Delta_r H_{298} = -94.0\,{}^{\mathrm{kcal}}/_{\mathrm{mol}} \tag{8.14}$$

$$^1/_2\mathrm{C_2H_5OH} + \mathrm{O_2} \rightarrow \mathrm{CO} + {}^3/_2\mathrm{H_2O} \qquad \Delta_r H_{298} = -85.0\,{}^{\mathrm{kcal}}/_{\mathrm{mol}} \tag{8.15}$$

$$^2/_3\mathrm{CH_3CHO} + \mathrm{O_2} \rightarrow {}^4/_3\mathrm{CO} + {}^4/_3\mathrm{H_2O} \qquad \Delta_r H_{298} = -85.7\,{}^{\mathrm{kcal}}/_{\mathrm{mol}} \tag{8.16}$$

The contribution from each reaction is given by the normalized mole fraction $y^*_{F''_j}$ of the jth hydrocarbon fuel in F'':

$$y^*_{F''_j} = \frac{y_{F''_j}}{\sum_j y_{F''_j}} \qquad j = \begin{array}{l}\mathrm{CH_4}, \mathrm{C_2H_6}, \mathrm{C_2H_4},\\ \mathrm{CH_2O}, \mathrm{CH_3OH},\\ \mathrm{C_2H_5OH}, \mathrm{CH_3CHO}\end{array} \tag{8.17}$$

The resulting molar content of individual components in F''' can now be determined from material balances:

$$F'''_j = F''_j - \nu_{ij}\, y^*_{F''_j} A_{P,\mathrm{O_2}} \tag{8.18}$$

$$F'''_k = F''_k + A_{P,\mathrm{O_2}} \sum_j \nu_{ik}\, y^*_{F''_j} \qquad k = \mathrm{CO}, \mathrm{H_2O} \tag{8.19}$$

$$F'''_l = F''_l \qquad l = \mathrm{CO_2}, \mathrm{H_2} \tag{8.20}$$

$$F'''_{\mathrm{O_2}} = 0 \tag{8.21}$$

$$F'''_{\mathrm{N_2}} = F''_{\mathrm{N_2}} + \frac{0.05}{0.95} A_{P,\mathrm{O_2}} \tag{8.22}$$

where ν_i denotes stoichiometric coefficients from the reactions in (8.10)–(8.16). The molar flow rate of $\mathrm{O_2}$ ($A_{P,\mathrm{O_2}}$) is determined by iterative solution of Equation (8.18)–(8.22) and the energy balance

$$H_{F'''} = H_{F''} + H_{A_P} \tag{8.23}$$

where all temperatures and pressures are given from previous constraints.

8.3.3 Reactor Specifications

The reactor is assumed to be a flow reactor that can be approximated by plug flow simulations cf. the computational treatment of the reactor outlined in Section 8.2. The length of the reaction zone is defined by the volumetric flow rate of F'''', the reactor diameter D_{reac}, and a desired residence time of $\tau_{reac} = 4\,\text{sec}$ corresponding to $\tau_{min} + 1\,\text{sec}$; see Section 7.4.3.

Based on the experiences with potential surface activity from the experimental work, it is expected that the diameter of the applied laboratory reactor should be increased by a factor of 10 or more in order to limit this influence. For practical reasons, the materials used in an industrial reactor should exhibit similar thermal expansion properties and be able to resist the high pressure without having to equalize the pressure gradient, e.g. by means of a pressure shell as used in the current laboratory setup; see Section 4.2. The preferred reactor material should be stainless steel, which is expected to be significantly more active in terms of surface reactions than quartz used in the laboratory. This emphasizes the need for a large reactor diameter in order to yield a sufficiently low $^{S}/_{V}$ ratio[3]. However, too low $^{S}/_{V}$ ratios may hinder good mixing of reactants before initiation. As a compromise, a reactor diameter of $\sim$20 cm and a length of 3–4 m are recommended for the current application. If necessary, several reactors may be placed in parallel in order to sustain high volumetric flow rates.

The potential integration of the preheating system with the reactor inlet was considered in Section 8.3.2. As a continuation of this discussion, it has been considered to directly utilize the heat of reaction for preheating by letting the reactants flow around the hot reactor tube prior to the inlet. However, calculations indicate that this application requires a large heat transfer surface in order to facilitate a noticeable temperature rise. This is inconsistent with the application of a low $^{S}/_{V}$ ratio in the reactor.

The mixing of F''' and A_F is expected to take place at the entrance to the reaction zone as an integrated part of the reactor design; even though the schematic flow sheet in Figure 8.1 indicates that mixing happens outside the reactor. Similar integration of the condenser is expected at the exit of the reaction zone in order to quench the reaction. The O_2 feed should be introduced as evenly as possible across the flow field in order to obtain a good mixing profile and avoid high local concentrations of O_2 that may lead to premature combustion similar to the O_2 diffusion flame in the second preheating unit. This imposes certain demands on the device that supplies the O_2 feed to the reactor. A potential design involves a number of small nozzles positioned on a grid over the reactor cross section.

[3] In tubular reactors with constant diameter $^{S}/_{V} = {}^{\pi DL}/_{\frac{\pi}{4}D^2L} = {}^{4}/_{D}$

8.3.4 Liquid Product Recovery

The product of primary interest is CH_3OH, but other oxygenated hydrocarbons of commercial value may also be formed in small amounts during the course of the reaction, e.g. CH_2O, C_2H_5OH, and CH_3CHO. Efficient recovery of these compounds from the product gas P is essential in order to obtain a high plant efficiency. All the desired products exhibit relatively high dew points compared to the reactants. This means that recovery can be facilitated by a simple *flash* operation, where a liquid phase is formed in equilibrium with the vapor phase upon contact with a cold surface. The technique is simple and cheap. The drawback is that a low system temperature must be sustained in order to force the vapor-liquid equilibrium (VLE) into a feasible level of liquid product recovery (>90 %), which increases the demand for re-heating of the recirculation stream. The dew point of H_2O is higher than any of the listed oxygenates, which means that the resulting condensate will contain substantial amounts of water besides the desired products. Small amounts of dissolved hydrocarbons and inorganic products will also be present in the condensate. This calls for a secondary separation process in the form of a distillation unit that can efficiently separate water (bottom product) and light organic and inorganic species (top product) from the oxygenated hydrocarbons. An obvious energy source for the distillation column is the hot water outlet from Preheater 1 (see Figure 8.1), which contains a boiling mixture of steam and liquid at high pressure.

An alternative strategy for product recovery is the use of gas absorption, which is a technique widely used in the chemical industry [152, 898]. Here, one or more gaseous species are removed by washing or scrubbing the gas mixture with a suitable liquid solvent that exhibits a high solubility for the desired product(s). The gaseous compound of interest will be dissolved in the liquid phase and can subsequently be removed with the solvent. After recovery of the rich solvent mixture, a stripping operation is employed to release the desired product before reuse of the solvent. The advantage of this method is that high recovery levels can be achieved through a proper choice of the solvent and good mixing between the gas and liquid phase. Depending on the properties of the solvent, it should also be possible to maintain a higher system temperature than the condenser and hence, reduce the necessary reheating of the recycled hydrocarbon stream. However, the method does not circumvent the need to quench the reaction and reduce the temperature of the product gas P to a level where zero reactivity is obtained. Moreover, H_2O still has to be removed from the gas stream to avoid accumulation, so a second recovery operation will probably be needed for this purpose.

Considerations of more quantitative nature are needed to properly eval-

uate the potential use of gas absorption for the liquid product recovery, but unless very efficient solvents are located, the technique is not expected to prevail in competition with the simplicity and efficiency of a water-cooled condenser unit.

Water-Cooled Condenser

The reaction will be quenched when the hot product gas P comes in contact with the cold surfaces in the condenser and a liquid phase will be established in accordance with the VLE properties. The liquid can be collected at the bottom of the vessel in a continuous operation and led to the distillation column, which is not considered in the present flow sheet calculations. VLE calculations indicate that the product gas must be cooled to $\sim$293 K in order to yield >90 % recovery of the desired product (CH_3OH). This will be the exit temperature of both the hydrocarbon enriched gas stream R and the liquid product stream L.

It is assumed that cold liquid water enters the condenser at 275 K, and that the water cycle is operated at 70 bar. The low temperature is needed to yield the desired outlet temperature of L without excessive use of heat transfer area. The boiling point of water at 70 bar is $T_W^{boil} = 560\,\mathrm{K}$ [128]. The temperature of the superheated steam that leaves the condenser is moreover assumed to be $T_{W_{out}} = T_W^{boil} + 50\,\mathrm{K} = 610\,\mathrm{K}$. A higher outlet temperature may be chosen at the expense of a larger heat transfer area, but since the main energy removal is associated with the evaporation, it may not be worth the additional capital investment. The choice of pressure is the result of a compromise between expected material limitations (superheater pipes, etc.), expected operational costs, and efficient heat removal from the product gas P. It is noted that the value of $T_{W_{out}}$ limits the temperature of F'' via Preheater 1, that utilizes the superheated steam to preheat the hydrocarbon feed, and hence, indirectly determines the extent of the subsequent *in situ* combustion in Preheater 2. After partial condensation in Preheater 1, the hot water is cooled to room temperature through various appliences; most importantly the distillation column. It may be necessary to employ a refrigeration unit to facilitate the remaining temperature decrease before reutilization. If seawater is available at the production site, this may be an attractive source of cooling water.

The condenser is modeled as an ordinary heat exchange unit (see the computational approach to Preheater 1 in Section 8.3.2) with an incorporated isothermal flash operation taking place at 293 K and 97.4 bar. The flash calculation is performed in accordance with the method described in Section 3.5, which determines the composition and the molar flow rate of the

liquid and gaseous phases L and R. The energy balance, which is similar to Equation (8.7), and the heat transfer equation (8.5) are subsequently used to calculated the necessary water flow rate W and the heat transfer surface. The latter assumes a heat transfer coefficient $U = 500\,{}^{\mathrm{W}}/_{\mathrm{m}^2\,\mathrm{K}}$.

8.3.5 Removal of Side Products

The most important side products are H_2O, CO, CO_2, and H_2 that must be removed in order to avoid accumulation and hence, dilution of the CH_4 content. Molecular nitrogen is not a product of any reaction in the system, but it enters the system through the O_2 feed and must be treated with similar concern. Water is already removed in the condenser and is therefore excluded from the following considerations.

It is important that the applied separation method involves minimal loss of CH_4, since this will have a direct impact on the overall plant efficiency. In order to achieve this, multistage separation methods may have to be employed [896, 899].

The flow sheet in Figure 8.1 includes a purge valve that exhibits no selectivity for any compounds in R and is thus, the least attractive removal system available. The purge valve is mainly intended for use during startup and shutdown of the plant and should be avoided during steady-state operation unless no other separation methods prove to be more feasible for specific compounds. Consequently, the flow sheet calculations assume $Pu = 0 \Rightarrow R' = R$.

The major undesired component in the hydrocarbon stream *after* the condenser is CO, which has accumulated from the *in situ* combustion in Preheater 2 and the partial oxidation process in the reactor. The issue of side product removal should therefore be focused on methods to separate CO (and CO_2) from gas streams rich in CH_4.

Both CO and CO_2 can be efficiently removed from the gas phase by absorption with liquid solvents. This technique has been widely used for pollutant or contaminant removal in connection to e.g. ammonia production and flue gas cleaning [898]. Carbon monoxide is efficiently absorbed in aqueous solutions or suspensions of cuprous chloride with other salts [900, 901], while CO_2 capture is traditionally conducted with aqueous solutions of alkanolamines [902–904]. A drawback of the gas absorption technique is that solvents are typically specialized for absorption of individual compounds, which implies that several costly purification steps may be needed for the present application before the hydrocarbon stream can be recirculated. In addition, N_2 is not suited for solvent extraction at all.

An alternative method involves membrane separation. This method is already in use for natural gas cleaning before processing when capacities are

too low ($< 10^6$ STD m^3/day) to support the more capital intensive gas absorption techniques described above [896]. Moreover, recent developments in the field of hollow fiber zeolite membranes [905–907] indicate that selectivities of CO_x as high as 60 may be obtained from CO_x/CH_4 mixtures during continuous operation at high pressure. Of particular interest are the reported tests of SAPO-34 zeolite membranes on stainless steel and alumina supports at 295 K and <72 bar by Li *et al.* [905, 906]. These tests also indicated moderate selectivities in the range of 2–10 for H_2 and N_2 relative to CH_4 at similar high pressure/low temperature conditions.

It is noticed that the permeate flow from the membrane module will have a high content of combustible species, which may be utilized to generate heat for e.g. reactant preheating as an alternative to the *in situ* combustion in Preheater 2.

Membrane Module

In the present calculations, a single membrane module is employed for the task of removing the unwanted side products (incl. N_2). It is assumed that the module consists of hollow fiber zeolite membranes using a durable support of e.g. stainless steel or alumina that can withstand large pressure gradients. This should be manageable according to the reports of Li *et al.* [905, 906].

The molar flow rate M_i of component i through the membrane is given by the product of the membrane area A_m and the flux J_i [$= mol/m^2\,s$]:

$$M_i = A_m J_i \tag{8.24}$$

The flux is calculated by Equation (8.25) assuming perfect mixing on both sides of the membrane [163].

$$J_i = \mathscr{P}_i \left(P_{R'} y_{R'_i} - P_M y_{M_i} \right) \tag{8.25}$$

Here, $P_{R'}$ and P_M denote the pressures on the feed- and the permeate side of the membrane. It is assumed that the membrane module is operated at an average pressure difference of $\Delta P = P_{R'} - P_M = 30$ bar, which is expected to be within the limitations of the material properties considering the reports of Li *et al.* [905, 906]. $y_{R'_i}$ and y_{M_i} are the mole fractions in R' and M, where the latter is obtained by iterative solution using

$$y_{M_i} = \frac{J_i}{\sum_i J_i} \tag{8.26}$$

The property $\mathscr{P}_i$ in Equation (8.25) is the *permeance*, which is a characteristic property of the membrane given in units of $mol/m^2\,s\,bar$. A realistic

value of $\mathscr{P}_{CH_4} = 2 \times 10^{-2}\,{}^{mol}/_{m^2\,s\,bar}$ is applied in the present calculations cf. Ref. [905, 906]. The selectivity S_i of component i relative to CH_4 is defined by the ratio

$$S_i = \frac{\mathscr{P}_i}{\mathscr{P}_{CH_4}} \tag{8.27}$$

The values of S_i are estimated below based on the results from Li *et al.* [905, 906]. These are conservative estimates in order not to exaggerate the performance of the membrane.

$$\begin{aligned} S_i &= 20 \quad && i = CO, CO_2 \\ S_i &= 2 \quad && i = N_2, H_2, O_2 \\ S_i &= 1 \quad && i = C_xH_y, H_2O, CH_2O, CH_3OH, \\ & && \quad C_2H_5OH, CH_3CHO \end{aligned}$$

In order to avoid accumulation of unwanted components in the system, the permeate flow is constrained by the production of the most abundant undesired species during a single pass through the system. Carbon monoxide is currently the critical species, and M_{CO} is therefore predefined by the combined net formation of CO in the reactor and the second preheating unit. This provides the final constraint that is necessary to solve the system of equations in (8.24).

8.3.6 Discussion of Key Figures and Plant Design

Details from the flow sheet calculations are presented in Figure 8.2 for the proposed GTL plant with hydrocarbon recirculation. The underlying calculations are based on the methods and assumptions outlined above in Section 8.3.1–8.3.5 and assume steady-state operation. The overall performance of the plant is summarized by the key figures in Table 8.1.

The key figures reveal an overall energy efficiency of 19.6 % (OHC yield on energy basis), which compares unfavorably with the economic assesment made in Section 1.3.1, which indicated that a minimum energy efficiency of about 50 % should be achieved in order to capitalize from the GTL conversion.

The relatively low overall selectivity of 53.1 % (OHC selectivity on C-atom basis) is mainly associated with the hydrocarbon combustion in Preheater 2 that provides zero contribution to the OHC pool. The upper limit of S_{OHC} is expected to be in the vicinity of 75 %; cf. the value of $S_{CH_3OH,opt}$ from the global optimization in Section 7.4.3, whereas the hydrocarbon conversion,

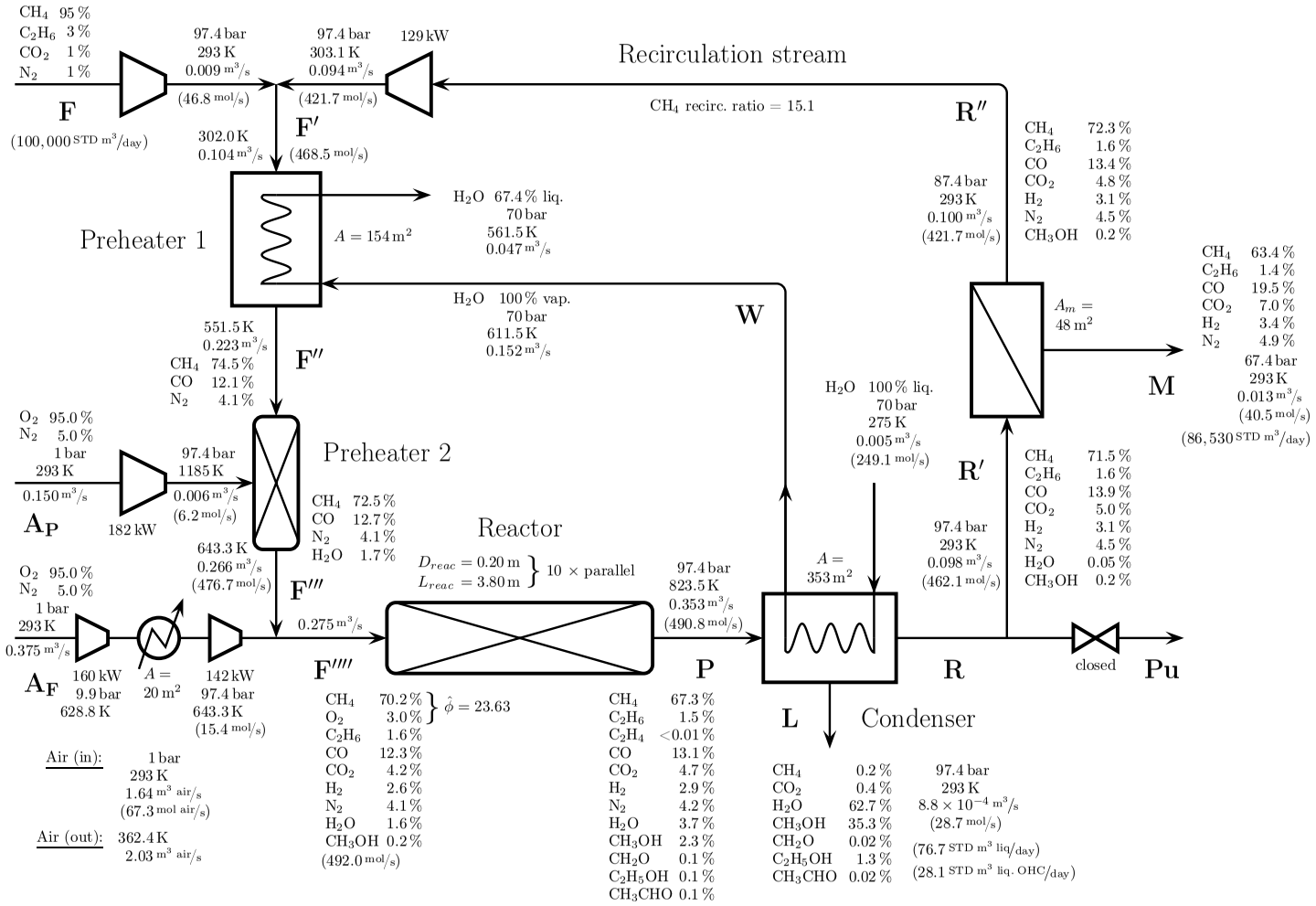

Figure 8.2: Results of steady-state flow sheet calculations for the GTL plant with hydrocarbon recirculation. Calculations are conducted in accordance with the methods and assumptions outlined in Section 8.3.1–8.3.5. Concentrations and flow rates everywhere satisfy mass and energy balances. The listed reactor dimensions provide $\tau \approx 4\,\text{sec}$ assuming that ΔT_{adb} takes effect after $\sim$3 sec. The figure only shows concentrations of the most important (or relevant) compounds at given locations.

Table 8.1: Key figures for the GTL plant with hydrocarbon recirculation. Acronyms denote NG = Natural Gas, HC = Hydrocarbons (CH_4 and C_2H_6), and OHC = Oxygenated Hydrocarbons (CH_3OH, CH_2O, C_2H_5OH, and CH_3CHO). Values of X_{HC}, S_{OHC}, and Y_{OHC} represent the *overall* performance of the plant.

Key figure	Value		Note
NG feed	100,000	STD m^3/day	
OHC vol. production	28.1	STD m^3/day	Liquid state
OHC mass production	8120	$tonnes/yr$	[a]
Flue gas	86,530	STD m^3/day	Contains ∼88 % combustibles
Recirculation ratio	15.1		Based on CH_4
Power consumption	>613	kW	Incl. only key compression steps
HC conversion (X_{HC})	43.4	%	C-atom basis [b]
OHC selectivity (S_{OHC})	53.1	%	C-atom basis [c]
OHC yield (Y_{OHC})	23.1	%	C-atom basis [d]
OHC yield (Y_{OHC})	*19.6*	*%*	*Energy basis* [e]

[a] Assume pure CH_3OH with $\rho = 792\ kg/m^3$

[b] X_{HC} includes hydrocarbon removal during preheating, reaction, and extraction with the condensate

[c] Calculated from the definition $Y_{OHC} = X_{HC} \times S_{OHC}$

[d] Assume negligible loss of OHC during the final purification by distillation

[e] Based on lower heating values (LHV) calculated from stoichiometric combustion to $CO_2 + H_2O$

in principle, can approach 100 % when recirculation is applied. As shown in Table 8.1, the current plant design only yields an overall hydrocarbon conversion of 43.4 % on a C-atom basis. The hydrocarbon conversion thus exhibits the largest potential for improvement, and further process optimization should be focused on this issue in order to increase the yield of OHC.

The substantial loss of hydrocarbons through the membrane module is the main reason why X_{HC} is low. Even though the applied membrane exhibits high selectivities towards the unwanted components in the gas stream, the separation method is inherently problematic when contaminants of low concentrations must be removed from a given feed stream. This is because of the high absolute concentration of CH_4 that gives rise to a high CH_4 flux through the membrane that outbalances the difference in selectivity. Improvement of the current system may involve the application of multistage membrane separation with retentate recycling [163], or perhaps, reconsideration of gas absorption by scrubbing with a liquid solvent. The latter was briefly discussed in Section 8.3.5. The application of membrane cascades with retentate recycling has been subjected to numerous investigations in connec-

tion to CO_2 removal from crude natural gas, and experiments and rigorous computer simulations, e.g. [899,908,909], indicate that attractive purities can be obtained in two or three stage membrane cascades with a limited loss of CH_4; even with a low initial concentration of CO_2 ($<$10 %).

An alternative strategy for the improvement of the overall plant efficiency is to capitalize the permeate flow from the membrane module. As noted in Table 8.1, the permeate contains $\sim$88 % combustible species; predominantly CH_4 and CO. A fraction could be used to preheat the reactant mixture in order to skip the *in situ* combustion in Preheater 2 and thereby reduce the CO level in the feed. This will increase the overall selectivity of the desired product and limit the need for purification of the recirculation stream.

It would be even more attractive if the carbon rich residue from the GTL plant could be utilized in connection with a secondary chemical process; either as feed stock or as fuel for heat and/or power supply. Since the permeate gas contains a substantial amount of CO (and less H_2), it may well be a suitable feed for the production of synthesis gas (CO/H_2), which is further used for synthesis of various bulk chemicals through catalytic conversion, e.g. CH_3OH, NH_3, and synthetic petroleum via the Fischer-Tropsch process (see Section 1.3). This kind of utilization of the unconverted hydrocarbon stream would certainly increase the overall efficiency of the current GTL plant.

8.4 Single Pass Utilization of the Carbon Source

The flow sheet calculations have demonstrated that a major limitation in the commercial exploitation of the investigated GTL technology is the continuous removal of unwanted residues in the product gas before recirculation of the hydrocarbon content. In this section, a different application of the technology is proposed based on a single pass utilization of the carbon source without recirculation of the outlet gas from the condenser. Obviously, it can only be feasible to abandon recirculation of the unconverted hydrocarbons if the resulting purge flow is utilized in some other downstream process. The possibility of implementing the GTL plant as a preprocessing unit for production of synthesis gas, or other bulk chemicals, was considered above. In this section, a slightly different scenario is considered.

In order to supply natural gas to the markets of utility, extensive pipeline networks are established throughout Europe, the United States, Japan, etc. The main supply lines to the European markets consist of a few very large pipelines entering from the North Sea via Great Britain, Belgium and The Netherlands, from North Africa via Spain and Italy, and from Russia through Ukraine and other Eastern European countries [910]. These pipelines typ-

ically exhibit individual capacities of 50 to 80 $^{\text{mio m}^3}/_{\text{day}}$ before they are divided into several smaller lines and domestic gas networks from where the final distribution to the consumers takes place. The idea proposed in the current project is to re-direct a small fraction of a major commercial gas line through a *single-pass* GTL plant, where an even smaller amount is converted to CH_3OH with a high selectivity, while the purge gas is led back to the large pipeline. If ∼1 % of the natural gas flow in a large pipeline was to be subjected to a single pass conversion in a GTL plant and subsequently remixed, the resulting contamination of the pipeline gas with CO, CO_2, N_2, and H_2 would be almost insignificant. The dilution of the bulk natural gas may not even be a disadvantage since both CO and H_2 are excellent fuels. The capital investment and production costs are expected to be low since the requirement for the internal plant capacity and downstream processing can be reduced significantly by disregarding the recirculation system. This provides a good potential for creation of value based on a relatively cheap source of natural gas.

8.4.1 Flow Sheet Calculations and Key Figures

In order to yield a more quantitative evaluation of the suggested single pass utilization of the GTL technology, flow sheet calculations at steady-state have been completed for this simplified plant configuration. The plant capacity is here based on a natural gas feed of 500,000 $^{\text{STD m}^3}/_{\text{day}}$ corresponding to ∼1 % of a large capacity natural gas pipeline. The composition of the gas is unchanged from previous. All assumptions and calculation methods used in the modelling of compression steps, preheating units, reactor simulations, and the VLE flash calculation in the condenser have been adopted from the previous flow sheet calculations and should need no further introduction. The detailed results are presented together with the flow chart in Figure 8.3 (similar to Figure 8.2), while key figures are provided in Table 8.2.

About 10,000 $^{\text{STD m}^3}/_{\text{day}}$ of the natural gas feed are consumed during the single pass conversion. This corresponds to 2 % of the feed and only ∼0.2 ‰ of the original pipeline flow. Even so, this is sufficient to sustain an annual production capacity of about 7000 metric tonnes of liquid fuels, as indicated in Table 8.2. The loss of hydrocarbons in the purge gas from the GTL plant is only about 5 % relative to the original composition. The outlet composition in Figure 8.3 indicates that this has mainly been substituted by a 2-to-1 mixture of CO and H_2. The calculations indicate that about half ($S_{\text{OHC}} = 55.4\,\%$) is recovered as a valuable product. Since downstream utilization of the purge gas is ensured, the selectivity of OHC should be taken

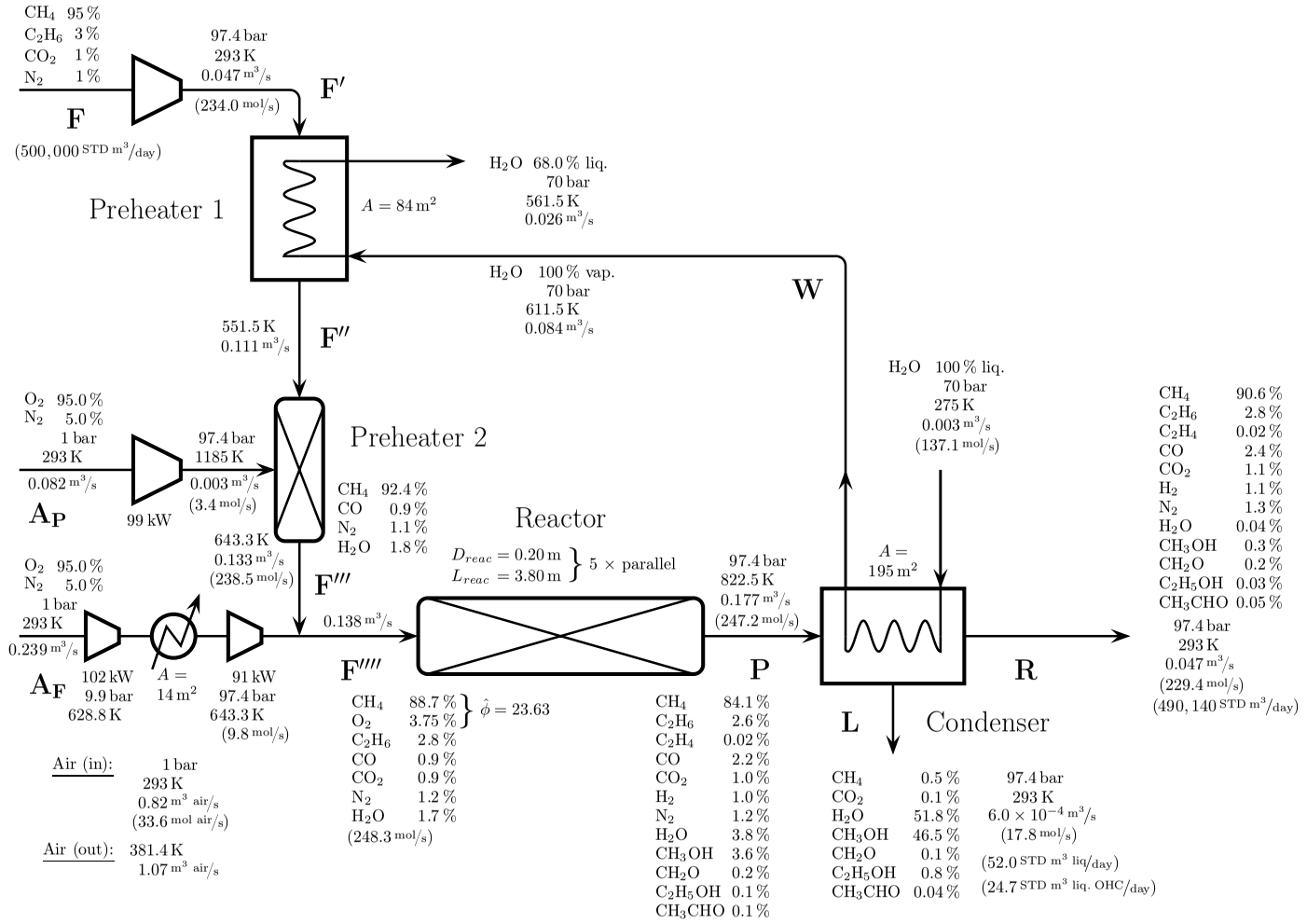

Figure 8.3: Results of steady-state flow sheet calculations for the GTL plant based on single pass utilization of the hydrocarbon source. See caption of Figure 8.2 for other specifications.

Table 8.2: Key figures for the GTL plant based on single pass utilization of the hydrocarbon source. Acronyms and specifications regarding the calculations of X_{HC}, S_{OHC}, and Y_{OHC} are identical to Table 8.1.

Key figure	Value		Note
NG feed	500,000	STD m^3/day	
OHC vol. production	24.7	STD m^3/day	Liquid state
OHC mass production	7140	$tonnes/yr$	
NG purge	490,140	STD m^3/day	∼95 % of HC are unconverted [a]
Power consumption	>292	kW	Incl. only key compression steps
HC conversion (X_{HC})	6.6	%	C-atom basis
OHC selectivity (S_{OHC})	55.4	%	C-atom basis
OHC yield (Y_{OHC})	3.6	%	C-atom basis
OHC yield (Y_{OHC})	*3.1*	*%*	*Energy basis*

[a)] Relative to the original molar content of HC in NG feed

as the overall measure of the plant efficiency rather than the yield. The flow sheet calculations indicate that the selectivity of OHC across the reactor is as high as 76 % on a C-atom basis when determined solely from the gas phase concentrations of reactants and products in F'''' and P. The significantly lower plant selectivity can be attributed to the CO production in Preheater 2, the loss of valuable products with the purge gas, and the dissolution and removal of CH_4 with the condensate, where the latter has an impact on S_{OHC} through the reduction of X_{HC}. Here, Preheater 2 accounts for about half of the lost OHC selectivity. As a consequence, it is recommended that further optimization of the plant design is focused on the limited use of the *in situ* combustion in Preheater 2 and a more efficient operation of the condenser unit.

8.5 Summary

This chapter has presented preliminary considerations of potential commercial exploitations of the investigated GTL process based on the optimal conditions determined in Chapter 7. Two plant designs have been considered with a difference in the utilization of the hydrocarbon source. The first plant design is based on extensive recirculation of the hydrocarbon reactant and multiple passes of the reactor in order to obtain a high overall product yield and reactant conversion. The second plant design involves single pass uti-

lization of the hydrocarbon source. The latter simplification implies reduced capital investment and production cost, but it requires a secondary utilization of unconverted hydrocarbon stream in order to become feasible.

Steady-state flow sheet calculations have been presented for *first draft* suggestions of the two plant designs. In both cases, the hydrocarbon and oxidizer feeds are preheated (and compressed) separately before mixing. The hydrocarbon feed is preheated in two stages. The first stage involves a classic heat exchange operation based on condensation of superheated steam, whereas secondary preheating involves *in situ* combustion of small amounts of O_2 directly in the hydrocarbon stream. The latter implies 100 % heat transfer efficiency at the expense of a minor loss of reactants and increased yields of the combustion products CO+H_2O. The oxidizer feed is assumed to contain 95 % O_2 and balance N_2 at ambient conditions. This can be obtained from an air separation unit. Preheating of the oxidizer stream is obtained by utilizing the temperature rise from the compression. The reactants are mixed at the entrance of the reactor. In practice, a number of tubular flow reactors (5–10) with a diameter of 20 cm and a length of 3.8 m must be employed in parallel to yield a desired residence time of ∼4 sec. The reaction is quenched at the outlet by contact with cold surfaces in a water-cooled condenser unit. The temperature must be lowered to about 293 K in order to recover >90 % of the desired product from the gas phase. The majority of the water in the gas phase is also removed with the condensate, which calls for a subsequent distillation unit for the final purification of the oxygenated hydrocarbons. Before recirculation, unwanted gaseous products; especially CO, CO_2, N_2, and H_2, must be removed from the hydrocarbon stream. This operation is conducted by single stage membrane separation using a zeolite membrane with high selectivity towards CO and CO_2. All calculation methods and assumptions have been thoroughly discussed. The reactor is simulated as an adiabatic plug flow reactor represented directly by the novel detailed kinetic model developed in Chapter 5. Calculations of fluid properties are based on the methods outlined in Chapter 3 assuming non-ideal conditions.

The flow sheet calculations for the plant design with reactant recirculation indicated a low yield of oxygenated hydrocarbon, which is insufficient to capitalize from the GTL conversion. However, this is mainly related to a substantial loss of hydrocarbons through the membrane module, and further optimization is expected to yield considerably more efficient methods to clean the hydrocarbon stream for secondary products. This may e.g. involve multistage membrane separation with retentate recycling, or gas absorption by scrubbing with a liquid solvent. An alternative strategy is to capitalize the permeate flow, which is rich in CH_4 and CO. Utilization as chemical feed stock for synthesis gas production has been proposed.

Finally, it has been suggested to install GTL plants in conjunction with the large natural gas pipelines that deliver natural gas to the markets of utility in e.g. Europe, the USA, and Japan. This process should only involve a single pass of the reactor. The idea is to temporarily re-direct ∼1 % of the pipeline flow to the GTL plant where about 2 % is converted to liquid products. The remaining purge gas is subsequently led back to the pipeline with ∼95 % of the original hydrocarbon content left unconverted. Flow sheet calculations indicate that present-day pipeline capacities may facilitate annual production capacities of single GTL plants of about 7000 metric tonnes of liquid fuels without causing significant disturbances in the common supply of natural gas.

Conclusion

Natural gas is an important fuel and chemical feedstock, and it plays a significant role in the global energy supply. The partial oxidation of natural gas to liquid chemicals, known as the *gas-to-liquid* (GTL) process, is an attractive industrial process with a potential to improve the utilization of remote natural gas resources. In the *direct homogeneous partial oxidation*, natural gas is converted to a readily transportable state; preferably methanol, in a simple one-step process under fuel-rich, high pressure, and relatively low temperature conditions. A coarse economic assessment based on the development in present-day market prices of methanol and natural gas indicates that an overall energy efficiency >50 % should be obtained in order to capitalize from the GTL conversion. Moreover, earlier technical economic evaluations of the specific process have suggested that selectivities of methanol above 80–90 % and a fuel conversion of 7–10 % during a single pass of the reactor are necessary process requirements in order to compete with conventional synthesis gas-based methanol plants.

The partial oxidation of natural gas has been extensively explored over several decades, but past efforts to obtain competitive selectivities and yields of methanol have been unsuccessful. This may partly be attributed to a lack of understanding of the complex free radical mechanism that governs the hydrocarbon conversion and its interactions with a number of important process parameters. Even so, available studies from the literature have demonstrated that the optimal conditions should be found within the pressure range of 30–100 bar, temperatures from 550–800 K, and $10 < CH_4/O_2 < 40$ in the feed. Experimental investigations at these conditions impose some difficulties as they require CH_4 concentrations in the range of 90–95 % resulting in a significant heat release during the conversion. This makes it almost impossible to sustain a well-defined temperature profile during experiments. As a consequence, this project has initially abandoned the focus on the optimal conditions in favour of a search for the general mechanism that governs the oxidation of light hydrocarbons at an extended range of process conditions.

The detailed kinetic scheme of light hydrocarbon conversion has been in-

terpreted in terms of a novel detailed chemical kinetic model (DCKM) in close interaction with well-defined experimental investigations. The DCKM has been developed to provide accurate descriptions of the oxidation chemistry of H_2/O_2, CO/CO_2, and C_{1-2} hydrocarbon fuels in the presence or absence of NO_x, and, to a limited extent, also SO_2, at temperatures from roughly 500–1000 K and pressures from atmospheric to 100 bar. The model includes 348 elementary reaction steps with appropriate thermochemical reference state properties for the involved species, and the structure complies with the CHEMKIN software. Rate constants have been obtained from a critical review of data for individual elementary reactions with particular emphasis on the conditions relevant to the present work. In a few cases, updated rate constants have been proposed for key reactions based on a reevaluation of literature experiments or *ab initio* CBS-QB3 calculations. These involve $OH+HO_2 \leftrightharpoons H_2O+O_2$, $CO+OH \leftrightharpoons [HOCO] \leftrightharpoons CO_2+H$, $NO_2+HO_2 \leftrightharpoons HONO/HNO_2+O_2$, $HNO_2(+M) \leftrightharpoons HONO(+M)$, and others. The elaborate approach of the present work has ensured that the resulting DCKM is probably as reliable as can be with the current status of combustion kinetic research. Even so, the work has also emphasized the need for improved characterizations of several elementary reactions relevant to hydrocarbon oxidation chemistry; in particular reactions involving alkylperoxy species.

The experimental work has been conducted in a novel laboratory scale high pressure flow reactor, which has been developed and constructed as a part of the current project. The system enables well-defined investigations of homogeneous gas phase chemistry involving gaseous reactants of the elements H, O, C, N, and S, at pressures from 10 to 100 bar, temperatures up to 925 K, and flow rates of 1–5 $^{NL}/_{min}$. The reaction takes place in a tubular quartz reactor enclosed in a stainless steel tube that acts as a pressure shell. The steel pressure shell is positioned inside an electrically heated oven that produces an isothermal reaction zone (±5 K) of 43 cm. The reactant gases are premixed before entering the reactor. The system is pressurized from the feed gas cylinders. Downstream of the reactor, the system pressure is reduced to atmospheric level prior to product analysis, which is conducted by on-line GC-TCD/FID and a NO_x chemiluminescence analyzer that enable measurements of N_2, O_2, CO, CO_2, a range of saturated, unsaturated, and oxygenated hydrocarbons, a few nitrated hydrocarbons, SO_2, H_2S, NO, and NO_2; typically within an overall measuring uncertainty of ±2–5 %. The high pressure flow reactor operates in the laminar flow regime, but with good premixing and low radial velocity gradients, considered in terms of axial dispersion, it has been shown that the laminar flow field can be approximated to plug flow. Moreover, calculations of non-ideal fluid properties using the Peng-Robinson Cubic EoS with appropriate mixing rules have shown that

ideal gas behavior can be assumed within the typical operational range of the reactor. This enables fast computation in terms of mathematical modeling of the reaction zone where conservation equations can be treated as a simple one-dimensional model with integration in time.

In order to validate the performance of the DCKM, experiments and numerical results have been compared for the chemical systems: $CO/H_2/NO_x/O_2$, CH_4/O_2, $CH_4/C_2H_6/O_2$, $CH_4/NO_x/O_2$, and $CH_4/H_2S/O_2$, at temperatures from 598–898 K, pressures from 20–100 bar, and stoichiometric ratios ranging from highly reducing ($\phi < 100$) to oxidizing conditions ($\phi > 0.04$). With few exceptions, all mixtures have been diluted with N_2. The experimental database has facilitated a thorough validation of the novel DCKM with a generally satisfactory response, which has justified a detailed outline and discussion of the governing reaction mechanisms based on model predictions. The experiment with $CO/H_2/NO_x$ at 20 bar revealed an augmented sensitivity of the elementary reaction $NO_2+H \leftrightharpoons NO+OH$. This has allowed a determination of the rate constant within $\pm 40\,\%$ at 850–875 K, where no previous measurements are available. The obtained values are in good agreement with previous measurements at both lower and higher temperatures. The experiments with CH_4/NO_x showed a clear promoting effect of NO_x in terms of a substantial reduction in the initiation temperature of the hydrocarbon fuel. This is facilitated by cyclic conversion of NO/NO_2 through interactions with the H_2/O_2 radical pool and the hydrocarbon oxidation chain. Moreover, a substantial intermediate formation of stabilized CH_3NO_2 has been observed as a distinct high-pressure phenomenon. However, the presence of NO_x had a negligible impact on the yield of CH_3OH, which has discouraged the use of NO_x as a gas phase sensitizer in the GTL process. Investigations of the CH_4 conversion in the presence of H_2S have been limited and inconclusive; mainly due to a poor agreement between experimental and modeling results. Even so, the experiments showed indications of an inhibiting influence of sulfur on the hydrocarbon oxidation chemistry consistent with a radical removal mechanism. A few undiluted experiments with CH_4/O_2 have been conducted to resemble the conditions of the real GTL process. Methanol was the primary product of these experiments, but the measurements were subjected to significant uncertainties due to instabilities in the system caused by the substantial heat release from the reaction.

After the validation of the novel DCKM, the initial search for optimal conditions for the GTL process was reinstated as the primary objective of the project. A numerical global optimization routine has been developed based on interval analysis to work with the DCKM in order to identify conditions that facilitate the maximum yield of CH_3OH. The underlying algorithm has been presented as well as some basic concepts of interval computations. The

global optimization routine converges slowly, but the applied method guarantees the location of the *global* optimum of a given objective function. The global optimum for the CH_3OH yield has been located at 643 K, 97.4 bar, and a CH_4/O_2 ratio of 23.6 in the feed based on a residence time ≥ 3 sec. At these conditions, the model predicts a selectivity of CH_3OH of 75 % and a CH_4 conversion of 5.6 % during a single pass of the reactor. This correspondes to a yield of CH_3OH of 4.2 %. These values are not very sensitive to minor deviations in the optimal conditions. The result compares favorably to most literature experiments, as well as the undiluted experiments with CH_4/O_2 conducted in the high pressure flow reactor, but it is not sufficiently close to the defined commercial target range to guarantee industrial feasibility.

Even so, the optimal conditions have constituted the basis for preliminary suggestions of potential commercial applications of the GTL process. Two plant designs have been considered with a difference in the utilization of the hydrocarbon source. The first plant design is based on extensive recirculation of the hydrocarbon reactant and multiple passes of the reactor in order to obtain a high overall product yield and reactant conversion. The second plant design involves single pass utilization of the hydrocarbon source. Steady-state flow sheet calculations have been presented for *first draft* suggestions of the two plant designs. Both designs involve separate compression and preheating of the fuel and oxidizer before mixing at the entrance of the reactor. The reaction is assumed to be quenched at the reactor outlet using a water-cooled condenser that continuously separates the desired products and water from the unconverted reactants and gaseous side products. Membrane separation is utilized for purification of the hydrocarbon stream before recirculation. All calculation methods and assumptions have been thoroughly discussed. The reaction was represented directly by the novel DCKM, and calculations of fluid properties assumed non-ideal conditions. The flow sheet calculations of the plant with reactant recirculation indicated a low overall plant efficiency in the range of $\sim$20 % unable to match the estimated economic requirements. This is mainly due to a substantial loss of hydrocarbons through the membrane module. However, improvement of this issue can be expected through further process optimization. The permeate stream is rich in CH_4 and CO and may be capitalized as an alternative method to improve the overall plant efficiency. Utilization as chemical feed stock for synthesis gas production has been proposed. Finally, it has been suggested to install simple GTL plants without reactant recirculation in conjunction with large natural gas pipelines. Flow sheet calculations indicate that present-day pipeline capacities may facilitate annual production capacities of single GTL plants of about 7000 metric tonnes of liquid fuels without causing significant disturbances in the common supply of natural gas.

Bibliography

[1] Cranmore, R. G.; Stanton, E. Modern Petroleum Technology. 1. Upstream. In ; Dawe, R. A., Ed.; Institute of Petroleum; John Wiley & Sons, Ltd., Chichester, England: 2000; Chapter 9: "Natural Gas", pages 337–382.

[2] Brown of Madingley, Lord, Ed., *BP Statistical Review of World Energy June 2006;* BP America Inc., Warrenville, IL 60555: 2006, `www.bp.com/statisticalreview`.

[3] Weirauch, W., Tech. Ed., *Hydrocarbon Processing* **1996,** *75,* 27.

[4] Weirauch, W., Tech. Ed., *Hydrocarbon Processing* **1997,** *76,* 27–28.

[5] Selley, R. C. Modern Petroleum Technology. 1. Upstream. In ; Dawe, R. A., Ed.; Institute of Petroleum; John Wiley & Sons, Ltd., Chichester, England: 2000; Chapter 2: "Geoscience", pages 23–40.

[6] Schoenberger, M. Modern Petroleum Technology. 1. Upstream. In ; Dawe, R. A., Ed.; Institute of Petroleum; John Wiley & Sons, Ltd., Chichester, England: 2000; Chapter 4: "Geophysics", pages 55–100.

[7] Sloan, Jr., E. D. *Ind. Eng. Chem. Res.* **2000,** *39,* 3123–3129.

[8] Koh, C. A. *Chem. Soc. Rev.* **2001,** *31,* 157–167.

[9] Kvenvolden, K. A. *Org. Geochem.* **1995,** *23,* 997–1008.

[10] Dawe, R. A.; Thomas, S. *Energy Sources, Part A* **2007,** *29,* 217–229.

[11] Collett, T. S.; Lee, M. W. *Ann. N. Y. Acad. Sci.* **2000,** *912,* 51–64.

[12] Collett, T. S. "Methane Hydrate Issues – Resource Assessment", Methane Hydrates Interagency R&D Conference, National Energy Technology Laboratory, U.S. Dept. Energy, `http://www.netl.doe.gov/publications/proceedings/02/MethaneHydrate/hydrate02.html`, March 20–22, 2002.

[13] Cranmore, R. G.; Stanton, E. Modern Petroleum Technology. 1. Upstream. In ; Dawe, R. A., Ed.; Institute of Petroleum; John Wiley & Sons, Ltd., Chichester, England: 2000; Chapter 10: "Transportation", pages 383–408.

[14] Leibson, I.; Davenport, S. T.; Muenzler, M. *Hydrocarbon Processing* **1987,** *66,* 47–50.

[15] Parkyns, N. D.; Warburton, C. I.; Wilson, J. D. *Catal. Today* **1993,** *18,* 385–442.

[16] Thomas, S.; Dawe, R. A. *Energy* **2003,** *28,* 1461–1477.

[17] Mager, H. J.; Vieth, T.; Jordan, H., Ed.;, *Oil Gas European Magazine* **2003,** *29,* 211–212.

[18] Mager, H. J.; Vieth, T.; Jordan, H., Ed.;, *Oil Gas European Magazine* **2002,** *28,* 39–41.

[19] Fischer, F.; Tropsch, H. *United States Patent* **1930,** *1,746,464,.*

[20] Haggin, J. *Chem. Eng. News* **1990,** *68,* 27–53.

[21] Fleisch, T. H.; Sills, R. A.; Briscoe, M. D. *J. Nat. Gas Chem.* **2002,** *11,* 1–14.

[22] Maisonnier, G. *Revue de l'Energie* **2005,** *564,* 100–104.

[23] Halstead, K. *TCE* **2006,** *781,* 34–36.

[24] NOAA Environmental Visualization Program, *Persian Gulf regional imagery, 2001.7.26 at 1646Z;* National Oceanic and Atmospheric Administration, US Department of Commerce, Washington, DC 20230: 2004, `www.nnvl.noaa.gov`.

[25] "World Methanol Supply and Demand", Methanol Institute, Arlington, VA 22203, `http://www.methanol.org/`, March 10, 2007, Data Sheet.

[26] Brusstar, M.; Stuhldreher, M.; Swain, D.; Pidgeon, W. "High Efficiency and Low Emissions from a Port-Injection Engine with Neat Alcohol Fuels", Soc. Auto. Engines (SAE), Paper 2002-01-2743, 2002.

[27] Dolan, G. A. "Methanol Transportation Fuels: A Look Back and a Look Forward", Methanol Institute, Arlington, VA 22203, `http://www.methanol.org/`, September 2005, Special Report.

[28] "Methanex Monthly Average Regional Posted Contract Price History", Methanex Corporation, Vancouver, British Columbia, Canada, `http://www.methanex.com/products/methanolprice.html`, May 2007, Data Sheet.

[29] "Methanol Historical Spot Prices", Methanol Institute, Arlington, VA 22203, `http://www.methanol.org/`, March 2004, Data Sheet.

[30] Energy Information Administration, *Natural Gas Monthly April 2007;* EIA/U.S. Department of Energy, Washington, DC 20585: 2007, `http://www.eia.doe.gov/natural_gas/data_publications/natural_gas_monthly/ngm.html`.

[31] Energy Information Administration, *Natural Gas Weekly Update;* EIA/U.S. Department of Energy, Washington, DC 20585: issues from May 2002 – May 2007, `http://tonto.eia.doe.gov/oog/info/ngw/ngupdate.asp`.

[32] Energy Information Administration, *Annual Energy Review 2005;* EIA/U.S. Department of Energy, Washington, DC 20585: July 2006, Report DOE/EIA-0384(2005), `http://www.eia.doe.gov/emeu/aer/pdf/aer.pdf`.

[33] Lewis, W. K.; Frölich, P. K. *Ind. Eng. Chem.* **1928,** *20,* 285–290.

[34] Davies, P.; Snowdon, F. F. *United States Patent* **1967,** *3,326,956,.*

[35] Stiles, A. B. *AIChE J.* **1977,** *23,* 362–375.

[36] Morton, L. A.; Hunter, N. R.; Gesser, H. D. *Chemistry & Industry (London)* **1990,** *16 July,* 457–462.

[37] Zaman, J. *Fuel Proc. Tech.* **1999,** *58,* 61–81.

[38] Kuo, J. C. W.; Kresge, C. T.; Palermo, R. E. *Catal. Today* **1989,** *4,* 463–470.

[39] Lange, J.-P.; Tijm, P. J. A. *Chem. Eng. Sci.* **1996,** *51,* 2379–2387.

[40] Bone, W. A.; Wheeler, R. V. *J. Chem. Soc., Trans.* **1902,** *81,* 535–549.

[41] Bone, W. A.; Wheeler, R. V. *J. Chem. Soc., Trans.* **1903,** *83,* 1074–1087.

[42] Newitt, D. M.; Haffner, A. E. *Proc. Roy. Soc. London, Ser. A* **1932,** *125,* 277–291.

[43] Wiezevich, P. J.; Frölich, P. K. *Ind. Eng. Chem.* **1934,** *26,* 267–276.

[44] Dixon, H. B.; Higgins, W. F. *Mem. Proc. Manchester Lit. Phil. Soc.* **1930,** *73,* 21–32.

[45] Norrish, R. G. W.; Wallace, J. *Proc. Roy. Soc. London, Ser. A* **1934,** *145,* 307–321.

[46] Ashmore, P. G.; Preston, K. F. *Combust. Flame* **1967,** *11,* 125–134.

[47] Boomer, E. H.; Broughton, J. W. *Can. J. Research* **1937,** *15B,* 375–382.

[48] Boomer, E. H.; Thomas, V. *Can. J. Research* **1937,** *15B,* 414–437.

[49] Boomer, E. H.; Thomas, V. *Can. J. Research* **1937,** *15B,* 401–413.

[50] Thompson, H. W.; Hinshelwood, C. N. *Proc. Roy. Soc. London, Ser. A* **1929,** *125,* 277–291.

[51] Bates, J. R.; Spencer, R. *J. Am. Chem. Soc.* **1931,** *53,* 1689–1704.

[52] Bone, W. A. *Nature (London)* **1931,** *127,* 481.

[53] Bone, W. A. *Proc. Roy. Soc. London, Ser. A* **1932,** *137,* 243–274.

[54] Norrish, R. G. W. *Proc. Roy. Soc. London, Ser. A* **1935,** *150,* 36–57.

[55] Ubbelohde, A. R. *Proc. Roy. Soc. London, Ser. A* **1935,** *152,* 354–378.

[56] von Elbe, G.; Lewis, B. *Proc. Combust. Inst.* **1937,** *2,* 169–174.

[57] Callendar, H. L. *Engineering* **1927,** *123,* 182–4, 210–2.

[58] Bone, W. A.; Allum, R. E. *Proc. Roy. Soc. London, Ser. A* **1932,** *134,* 578–591.

[59] Semenov, N. N. *Chem. Rev.* **1929,** *6,* 347–379.

[60] Hinshelwood, C. N. *Kinetics of Chemical Change;* The Clarendon Press, Oxford: 1926.

[61] Norrish, R. G. W.; Foord, S. G. *Proc. Roy. Soc. London, Ser. A* **1936,** *157,* 503–525.

[62] Pease, R. N. *J. Am. Chem. Soc.* **1935,** *57,* 2296–2299.

[63] von Elbe, G.; Lewis, B. *J. Am. Chem. Soc.* **1937,** *59,* 976–984.

[64] Lott, J. L.; Sliepcevich, C. M. *Ind. Eng. Chem. Proc. – Design Develop.* **1967,** *6,* 67–74.

[65] Yarlagadda, P. S.; Morton, L. A.; Hunter, N. R.; Gesser, H. D. *Ind. Eng. Chem. Res.* **1988,** *27,* 252–256.

[66] Burch, R.; Squire, G. D.; Tsang, S. C. *J. Chem. Soc., Faraday Trans. 1* **1989,** *85,* 3561–3568.

[67] Hunter, N. R.; Gesser, H. D.; Morton, L. A.; Yarlagadda, P. S. *Appl. Catal.* **1990,** *57,* 45–54.

[68] Gesser, H. D.; Hunter, N. R.; Morton, L. A. *Symposium on Methane Upgrading, Presented before the Division of Petroleum Chemistry, Inc., American Chemical Society, Atlanta Meeting* **1991,** *April 14–19,* 160–165.

[69] Rytz, D. W.; Baiker, A. *Ind. Eng. Chem. Res.* **1991,** *30,* 2287–2292.

[70] Thomas, D. J.; Willi, R.; Baiker, A. *Ind. Eng. Chem. Res.* **1992,** *31,* 2272–2278.

[71] Foulds, G. A.; Gray, B. F.; Miller, S. A.; Walker, G. S. *Ind. Eng. Chem. Res.* **1993,** *32,* 780–787.

[72] Chun, J.-W.; Anthony, R. G. *Ind. Eng. Chem. Res.* **1993,** *32,* 259–263.

[73] Casey, P. S.; McAllister, T.; Foger, K. *Ind. Eng. Chem. Res.* **1994,** *33,* 1120–1125.

[74] Omata, K.; Fukuoka, N.; Fujimoto, K. *Ind. Eng. Chem. Res.* **1994,** *33,* 784–789.

[75] Feng, W.; Knopf, F. C.; Dooley, K. M. *Energy Fuels* **1994,** *8,* 815–822.

[76] Lødeng, R.; Lindvåg, O. A.; Søraker, P.; Roterud, P. T.; Onsager, O. T. *Ind. Eng. Chem. Res.* **1995,** *34,* 1044–1059.

[77] Chellappa, A. S.; Fuangfoo, S.; Viswanath, D. S. *Ind. Eng. Chem. Res.* **1997,** *36,* 1401–1409.

[78] Zhang, Q.; He, D.; Li, J.; Xu, B.; Liang, Y.; Zhu, Q. *Appl. Catal. A: General* **2002,** *224,* 201–207.

[79] Vedeneev, V. I.; Goldenberg, M. Y.; Gorban, N. I.; Teitel'boim, M. A. *Kinet. Catal. (tr. of Kinet. Katal.)* **1988,** *29,* 1–8.

[80] Vedeneev, V. I.; Arutyunov, V. S.; Krymov, N. Y.; Cherbakov, P. M.; Sedykh, A. D. *Catal. Today* **1992,** *13,* 613–616.

[81] Vedeneev, V. I.; Arutyunov, V. S.; Basevich, V. Y.; Goldenberg, M. Y.; Teitel'boim, M. A.; Krymov, N. Y. *Catal. Today* **1994,** *21,* 527–532.

[82] Vedeneev, V. I.; Krylov, O. V.; Arutyunov, V. S.; Basevich, V. Y.; Goldenberg, M. Y.; Teitel'boim, M. A. *Appl. Catal. A: General* **1995,** *127,* 51–63.

[83] Mackie, J. C. *Catal. Rev.–Sci. Eng.* **1991,** *33,* 169–240.

[84] Arutyunov, V. S.; Basevich, V. Y.; Vedeneev, V. I.; Romanovich, L. B. *Kinet. Catal.* **1996,** *37,* 16–22.

[85] Gesser, H. D.; Hunter, N. R.; Prakash, C. B. *Chem. Rev.* **1985,** *85,* 235–244.

[86] Arutyunov, V. S.; Basevich, V. Y.; Vedeneev, V. I. *Ind. Eng. Chem. Res.* **1995,** *34,* 4238–4243.

[87] Foulds, G. A.; Gray, B. F. *Fuel Proc. Tech.* **1995,** *42,* 129–150.

[88] Gesser, H. D.; Hunter, N. R. *Catal. Today* **1998,** *42,* 183–189.

[89] Zhang, Q.; He, D.; Zhu, Q. *J. Nat. Gas Chem.* **2003,** *12,* 81–89.

[90] Brockhaus, R. *German Patent* **1973,** *2,201,429,* Chemische Werke Hüls AG.

[91] Gesser, H. D.; Hunter, N. R.; Morton, L. A. *United States Patent* **1986,** *4,618,732,*.

[92] Sweeney, M. P. *United States Patent* **1988,** *4,760,210,*.

[93] Fujimoto, K.; Hideo, O. *Japanese Patent* **1995,** *7,112,946,* Japan Petroleum Exploration Company.

[94] Arutyunov, V. S.; Vedeneev, V. I.; Krymov, N. Y. *Russian Patent* **1996,** *2,049,086,* N. Proizv. Predpr. Tekhnoprom. (RU).

[95] Chellappa, A. S.; Viswanath, D. S. *Ind. Eng. Chem. Res.* **1995,** *34,* 1933–1940.

[96] Wang, X.; Wang, Y.; Tang, Q.; Guo, Q.; Zhang, Q.; Wan, H. *J. Catal.* **2003,** *217,* 457–467.

[97] Hahm, H.-S.; Park, E.-S.; Cheon, H.-J.; Kim, Y.-K.; Lim, Y.-S.; Kim, M.-S.; Park, H.-S. *J. Chem. Eng. Jap.* **2004,** *37,* 152–157.

[98] Lide, D. R., Ed.; *Handbook of Chemistry and Physics;* CRC Press LLC, Boca Raton, Florida: 87th ed.; 2006.

[99] Govier, G. W.; Fogarasi, M. *J. Can. Petr. Technol.* **1975,** *14,* 28–41.

[100] Arutyunov, V. S. *Rus. Chem. Bull., Int. Ed.* **2002,** *51,* 2170–2175.

[101] Miller, J. A.; Bowman, C. T. *Prog. Energy Combust. Sci.* **1989,** *15,* 287–338.

[102] Shen, B.; Yao, Q.; Xu, X. *Fuel Proc. Technol.* **2004,** *85,* 1301–1315.

[103] Glarborg, P.; Kristensen, P. G.; Jensen, S. H.; Dam-Johansen, K. *Combust. Flame* **1994,** *98,* 241–258.

[104] Glarborg, P.; Dam-Johansen, K.; Miller, J. A.; Kee, R. J.; Coltrin, M. E. *Int. J. Chem. Kinet.* **1994,** *26,* 421–436.

[105] Glarborg, P.; Alzueta, M. U.; Dam-Johansen, K.; Miller, J. A. *Combust. Flame* **1998,** *115,* 1–27.

[106] Miller, J. A.; Glarborg, P. *Int. J. Chem. Kinet.* **1999,** *31,* 757–765.

[107] Hjuler, K.; Glarborg, P.; Dam-Johansen, K. *Ind. Eng. Chem. Res.* **1995,** *34,* 1882–1888.

[108] Bromly, J. H.; Barnes, F. J.; Muris, S.; You, X.; Haynes, B. S. *Combust. Sci. Tech.* **1996,** *115,* 259–296.

[109] Amano, T.; Dryer, F. L. *Proc. Combust. Inst.* **1998,** *27,* 397–404.

[110] Bendtsen, A. B.; Glarborg, P.; Dam-Johansen, K. *Combust. Sci. and Tech.* **2000,** *151,* 31–71.

[111] Alzueta, M.; Bilbao, R.; Finestra, M. *Energy Fuels* **2001,** *15,* 724–729.

[112] Alzueta, M.; Hernández, J. M. *Energy Fuels* **2002,** *16,* 166–171.

[113] Glarborg, P.; Alzueta, M. U.; Kjærgaard, K.; Dam-Johansen, K. *Combust. Flame* **2003,** *115,* 629–638.

[114] Rasmussen, C. L.; Glarborg, P.; Marshall, P. *Proc. Combust. Inst.* **2007,** *31,* 339–347.

[115] Alzueta, M.; Bilbao, R.; Glarborg, P. *Combust. Flame* **2001,** *127,* 2234–2251.

[116] Dagaut, P.; Lecomte, F.; Mieritz, J.; Glarborg, P. *Int. J. Chem. Kin.* **2003,** *35,* 564–575.

[117] Arutyunov, V. S. *Uspekhi Khimii* **1992,** *61,* 2078–2104.

[118] Foster, N. R. *Appl. Catal.* **1985,** *19,* 1–11.

[119] Ozturk, S.; Onal, I.; Senkan, S. *Ind. Eng. Chem. Res.* **2000,** *39,* 250–258.

[120] Stewart, J. J. P. *J. Comput. Chem.* **1989,** *10,* 209–220.

[121] Johansson, D. L. "Partial Oxidation of Natural Gas (Eng. trans.)", Bachelor's thesis, Department of Chemical Engineering, Technical University of Denmark, DK-2800 Kgs. Lyngby, 2005.

[122] Lance, D.; Elworthy, E. G. *British Patent* **1906,** *7,297,*.

[123] Dowden, D. A.; Walker, G. T. *British Patent* **1971,** *1,244,001,* Imperial Chemical Industries Ltd.

[124] Hall, T. J.; Hargreaves, J. S. J.; Hutchings, G. J.; Joyner, R. W.; Taylor, S. H. *Fuel Proc. Tech.* **1995,** *42,* 151–178.

[125] Herman, R. G.; Sun, Q.; Shi, C.; Klier, K.; Wang, C.-B.; Hu, H.; Wachs, I. E.; Bhasin, M. M. *Catal. Today* **1997,** *37,* 1–14.

[126] Babero, J.; Alverez, M.; Bañares, M.; Peña, M.; Fierro, J. *Chem. Commun.* **2002,** *May,* 1184–1185.

[127] Smith, J. M.; van Ness, H. C.; Abbott, M. M. *Introduction to Chemical Engineering Thermodynamics;* McGraw-Hill: 5th ed.; 1996.

[128] "NIST Chemistry WebBook", `http://webbook.nist.gov/chemistry/`, NIST Standard Reference Database Number 69, June 2005 Release.

[129] Burcat, A.; Ruscic, B. "*Third Millennium Ideal Gas and Condensed Phase Thermochemical Database for Combustion with Updates from Active Thermochemical Tables*", Report TAE960, Technion Israel Inst. of Technology, 16th September 2005.

[130] Ruscic, B.; Pinzon, R. E.; Morton, M. L.; von Laszevski, G.; Bittner, S. J.; Nijsure, S. G.; Amin, K. A.; Minkoff, M.; Wagner, A. F. *J. Phys. Chem. A* **2004,** *108,* 9979–9997.

[131] Ruscic, B.; Pinzon, R. E.; Morton, M. L.; Srinivasan, N. K.; Su, M.-C.; Sutherland, J. W.; Michael, J. V. *J. Phys. Chem. A* **2006,** *110,* 6592–6601.

[132] Gordon, S.; McBride, B. J. "*Computer Program for Calculation of Complex Chemical Equilibrium Composition, Rocket Performance, Incident and Reflected Shocks and Chapman-Jouget Detonations*", Report SP-273, NASA, 1971.

[133] Matthews, J.; Sinha, A.; Francisco, J. S. *J. Chem. Phys.* **2005,** *122,* 221101.

[134] Blanksby, S. J.; Ramond, T. M.; Davico, G. E.; Nimlos, M. R.; Kato, S.; Bierbaum, V. M.; Lineberger, W. C.; Ellison, G. B.; Okumura, M. *J. Am. Chem. Soc.* **2001,** *123,* 9585–9596.

[135] Fabian, W. M. F.; Janoschek, R. *J. Mol. Struct. THEOCHEM* **2005,** *713,* 227–234.

[136] Meloni, G.; Zou, P.; Klippenstein, S. J.; Ahmed, M.; Leone, S. R.; Taatjes, C. A.; Osborn, D. L. *J. Am. Chem. Soc.* **2006,** *128,* 13559–13567.

[137] Janoschek, R.; Rossi, M. J. *Int. J. Chem. Kinet.* **2004,** *36,* 661–686.

[138] Marinov, N. M. *Int. J. Chem. Kinet.* **1999,** *31,* 183–220.

[139] Glarborg, P.; Bendtsen, A. B.; Miller, J. A. *Int. J. Chem. Kinet.* **1999,** *31,* 591–602.

[140] Domalski, E. S.; Hearing, E. D. *J. Phys. Chem. Ref. Data* **1993,** *22,* 805–1159.

[141] Batt, L.; Milne, R. T. *Int. J. Chem. Kinet.* **1977,** *9,* 549–565.

[142] Unpublished work, Paul Marshall, Dr., Prof., Department of Chemistry, University of North Texas, Denton, Texas 76203–5070, 2006.

[143] Knyazev, V. D.; Slagle, I. R. *J. Phys. Chem. A* **1998,** *102,* 1770–1778.

[144] Janoschek, R.; Rossi, M. J. *Int. J. Chem. Kinet.* **2002,** *34,* 550–560.

[145] Baulch, D. L.; Bowman, C. T.; Cobos, C. J.; Cox, R. A.; Just, T.; Kerr, J. A.; Pilling, M. J.; Stocker, D.; Troe, J.; Tsang, W.; Walker, R. W.; Warnatz, J. *J. Phys. Chem. Ref. Data* **2005,** *34,* 757–1397.

[146] Lay, T. H.; Bozzelli, J. W. *J. Phys. Chem. A* **1997,** *101,* 9505–9510.

[147] Jungkamp, T. P. W.; Seinfeld, J. H. *Chem. Phys. Lett.* **1996,** *257,* 15–22.

[148] Carstensen, H.-H.; Dean, A. M. *Proc. Combust. Inst.* **2005,** *30,* 995–1003.

[149] van der Waals, J. *Nobel Lectures in Physics* **1967,** *1,* 254–265 Elsevier, Amsterdam.

[150] Elliott, Jr., J. R.; Lira, C. T. *Introductory Chemical Engineering Thermodynamics;* Prentice-Hall: 1998.

[151] Laidler, K. J.; Meiser, J. H. *Physical Chemistry;* Houghton Mifflin Company, Boston: 5th ed.; 1999.

[152] Perry, R. H.; Green, D. W.; Maloney, J. O., Eds.; *Perry's Chemical Engineers' Handbook;* McGraw-Hill: 7th ed.; 1997.

[153] Soave, G. *Chem. Eng. Sci.* **1972,** *27,* 1197–1203.

[154] Redlich, O.; Kwong, J. N. S. *Chem. Rev.* **1949,** *44,* 233–244.

[155] Pitzer, K. S.; Lippmann, D. Z.; Curl, R. F.; Huggins, C. M.; Petersen, D. E. *J. Am. Chem. Soc.* **1955,** *77,* 3433–3440.

[156] Peng, D.-Y.; Robinson, D. B. *Ind. Eng. Chem. Fund.* **1976,** *15,* 59–64.

[157] Michelsen, M. L. "28221 Technical Physical Chemistry/28321 Chemical Engineering Thermodynamics (Eng. trans.)", Department of Chemical Engineering, Technical University of Denmark, DK–2800 Kgs. Lyngby, August 2006, Lecture Notes.

[158] Dawe, R. A., Ed.; *Modern Petroleum Technology. 1. Upstream;* Institute of Petroleum; John Wiley & Sons, Ltd., Chichester, England: 2000.

[159] Bird, R. B.; Stewart, W. E.; Lightfoot, E. N. *Transport Phenomena;* John Wiley & Sons: 1960.

[160] Personal Communication, Michael L. Michelsen, Reader, Department of Chemical Engineering, Technical University of Denmark, DK-2800 Kgs. Lyngby, 2007.

[161] Ayyalasomayajula, P.; Sharma, R.; Walker, J. G.; Sharma, M. M.; Pope, G. A. *Proc. – SPE Annual Tech. Conf. Exhib.* **2002,** 2109–2116.

[162] Kontogeorgis, G. M.; Voutsas, E. C.; Yakoumis, I. V.; Tassios, D. P. *Ind. Eng. Chem. Res.* **1996,** *35,* 4310–4318.

[163] Seader, J. D.; Henley, E. J. *Separation Process Principles;* John Wiley & Sons, Inc.: 1998.

[164] Rachford, H. H.; Rice, J. D. *Petr. Trans. AIME* **1952,** *195,* 327–328.

[165] Rasmussen, C. L.; Rasmussen, A. E.; Hansen, J.; Glarborg, P. "*045-12 High Pressure Flow Reactor – Operations Manual*", Technical Report R0604, Department of Chemical Engineering, DK-2880 Kgs. Lyngby, Denmark, 2006.

[166] Yetter, R. A.; Dryer, F. L.; Rabitz, H. *Combust. Sci. Tech.* **1991,** *79,* 129–140.

[167] Held, T. J.; Dryer, F. L. *Int. J. Chem. Kinet.* **1998,** *30,* 805–830.

[168] Mueller, M. A.; Yetter, R. A.; Dryer, F. L. *Int. J. Chem. Kinet.* **1999,** *31,* 113–125.

[169] Mueller, M. A.; Yetter, R. A.; Dryer, F. L. *Int. J. Chem. Kinet.* **1999,** *31,* 705–724.

[170] Curran, H. J.; Fischer, S. L.; Dryer, F. L. *Int. J. Chem. Kinet.* **2000,** *32,* 741–759.

[171] Dagaut, P.; Cathonnet, M.; Rouan, J. P.; Foulatier, R.; Quilgars, A.; Boettner, J. C.; Gaillard, F.; James, H. *J. Phys. E: Sci. Instrum.* **1986,** *19,* 207–209.

[172] Dagaut, P.; Boettner, J. C.; Cathonnet, M. *Proc. Combust. Inst.* **1996,** *26,* 627–632.

[173] Dagaut, P.; Dayma, G. *Int. J. Hydrogen Energy* **2006,** *31,* 505–515.

[174] Levenspiel, O. *Chemical Reaction Engineering;* John Wiley & Sons, Inc.: 2nd ed.; 1972.

[175] Curtiss, C. F.; Hirschfelder, J. O. *J. Chem. Phys.* **1949,** *17,* 550–555.

[176] Wilke, C. R. *J. Chem. Phys.* **1950,** *18,* 517–519.

[177] Hirschfelder, J. O.; Bird, R. B.; Spotz, E. L. *Chem. Rev.* **1949,** *44,* 205–231.

[178] Levenspiel, O. *The Chemical Reactor Omnibook;* OSU Book Stores, Inc., Corvallis, Oregon: 1993.

[179] Taylor, G. *Proc. Roy. Soc. London, Ser. A* **1953,** *219,* 186–203.

[180] Aris, R. *Proc. Roy. Soc. London, Ser. A* **1956,** *235,* 67–77.

[181] Westbrook, C. K.; Dryer, F. L. *Prog. Energy. Combust. Sci.* **1984,** *10,* 1–57.

[182] Pilling, M. J.; Seakins, P. W. *Reaction Kinetics;* Oxford University Press Inc.: 1995.

[183] Lindemann, F. A.; Arrhenius, S.; Langmuir, I.; Dhar, N. R.; Perrin, J.; Lewis, W. C. M. *Trans. Faraday Soc.* **1922,** *17,* 598–606.

[184] Troe, J. *Ber. Bunsenges. Phys. Chem.* **1983,** *87,* 161–169.

[185] Gilbert, R. G.; Luther, K.; Troe, J. *Ber. Bunsenges. Phys. Chem.* **1983,** *87,* 169–177.

[186] Kee, R. J.; Rupley, F. M.; Miller, J. A. "*Chemkin II: A Fortran Chemical Kinetics Package for the Analysis of Gas Phase Chemical Kinetics*", Sandia Report SAND89–8009B·UC–706, Sandia National Laboratories, Livermore, CA, 1989.

[187] Lutz, A. E.; Kee, R. J.; Miller, J. A. "*Senkin: A Fortran Program for Predicting Homogeneous Gas Phase Chemical Kinetics With Sensitivity Analysis*", Sandia Report SAND87–8248·UC–401, Sandia National Laboratories, Livermore, CA, 1990.

[188] Caracotsios, M.; Stewart, W. E. *Computers and Chemical Engineers.* **1985,** *9,* 359–365.

[189] Petzold, L. R. "*A Description of DASSL: A Differential/Algebraic System Solver*", Sandia Report SAND82–8637, Sandia National Laboratories, Livermore, CA, 1982.

[190] Personal Communication, Martin Skov-Skjøth Rasmussen, Ass. Prof., Department of Chemical Engineering, Technical University of Denmark, DK-2800 Kgs. Lyngby, 2004.

[191] Conaire, M. O.; Curran, H. J.; Simmie, J. M.; Pitz, W. J.; Westbrook, C. K. *Int. J. Chem. Kinet.* **2004,** *36,* 603–622.

[192] Li, J.; Zhao, Z.; Kazakov, A.; Dryer, F. L. *Int. J. Chem. Kinet.* **2004,** *36,* 566–575.

[193] Cohen, N.; Westberg, K. R. *J. Phys. Chem. Ref. Data* **1983,** *12,* 531–590.

[194] Tsang, W.; Hampson, R. *J. Phys. Chem. Ref. Data* **1986,** *15,* 1087–1279.

[195] Hessler, J. P. *J. Phys. Chem. A* **1998,** *102,* 4517–4526.

[196] Cobos, C. J.; Hippler, H.; Troe, J. *J. Phys. Chem.* **1985,** *89,* 342–349.

[197] Michael, J. V.; Su, M.-C.; Sutherland, J. W.; Carroll, J. J.; Wagner, A. F. *J. Phys. Chem. A* **2002,** *106,* 5297–5313.

[198] Michael, J. V. *Prog. Energy Combust. Sci.* **1992,** *18,* 327–347.

[199] Michael, J. V.; Sutherland, J. W.; Harding, L. B.; Wagner, A. F. *Proc. Combust. Inst.* **2000,** *28,* 1471–1478.

[200] Kappel, C.; Luther, K.; Troe, J. *Phys. Chem. Chem. Phys.* **2002,** *4,* 4392–4398.

[201] Hippler, H.; Troe, J.; Willner, J. *Chem. Phys. Lett.* **1992,** *192,* 333–337.

[202] Lifshitz, A.; Michael, J. V. *Proc. Combust. Inst.* **1990,** *23,* 59–67.

[203] Sutherland, J. W.; Patterson, P. M.; Klemm, R. B. *Proc. Combust. Inst.* **1990,** *23,* 51–57.

[204] Srinivasan, N. K.; Michael, J. V. *Int. J. Chem. Kinet.* **2007,** *38,* 211–219.

[205] Sutton, E. A. *J. Chem. Phys.* **1962,** *36,* 2923–2931.

[206] Sridharan, U. C.; Qiu, L. X.; Kaufman, F. *J. Chem. Phys.* **1982,** *86,* 4589–4574.

[207] Keyser, L. F. *J. Phys. Chem.* **1986,** *90,* 2994–3003.

[208] Baldwin, R. R.; Fuller, M. E.; Hillman, J. S.; Jackson, D.; Walker, R. W. *J. Chem. Soc. Faraday Trans. 1* **1974,** *70,* 635–641.

[209] Keyser, L. F. *J. Phys. Chem.* **1982,** *86,* 3439–3446.

[210] Nicovich, J. M.; Wine, P. H. *J. Phys. Chem.* **1987,** *91,* 5118–5123.

[211] Friswell, N. J.; Sutton, M. M. *Chem. Phys. Lett.* **1972,** *15,* 108–112.

[212] Peeters, J.; Mahnen, G. *Proc. Combust. Inst.* **1973,** *14,* 133–146.

[213] DeMore, W. B. *J. Phys. Chem.* **1979,** *83,* 1113–1118.

[214] Burrows, J. P.; Cox, R. A.; Derwent, R. G. *J. Photochem.* **1981,** *16,* 147–168.

[215] Cox, R. A.; Burrows, J. P.; Wallington, T. J. *Chem. Phys. Lett.* **1981,** *84,* 217–221.

[216] Kurylo, M. J.; Klais, O.; Laufer, A. H. *J. Phys. Chem.* **1981,** *85,* 3674–3678.

[217] DeMore, W. B. *J. Phys. Chem.* **1982,** *86,* 121–126.

[218] Sridharan, U. C.; Qiu, L. X.; Kaufman, F. *J. Chem. Phys.* **1984,** *88,* 1281–1282.

[219] Keyser, L. F. *J. Phys. Chem.* **1988,** *92,* 1193–1200.

[220] Goodings, J. M.; Hayhurst, A. N. *J. Chem. Soc. Faraday Trans. 2* **1988,** *84,* 745–762.

[221] Hippler, H.; Troe, J.; Willner, J. *J. Chem. Phys.* **1990,** *93,* 1755–1760.

[222] Hippler, H.; Neunaber, H.; Troe, J. *J. Chem. Phys.* **1995,** *103,* 3510–3516.

[223] Srinivasan, N. K.; Su, M.-C.; Sutherland, J. W.; Michael, J. V.; Ruscic, B. *J. Chem. Phys. A* **2006,** *110,* 6602–6607.

[224] Sivaramakrishnan, R.; Comandini, A.; Tranter, R. S.; Brezinsky, K.; Davis, S. G.; Wang, H. *Proc. Combust. Inst.* **2007,** *31,* 429–437.

[225] Baulch, D. L.; Cobos, C. J.; Cox, R. A.; Esser, C.; Frank, P.; Just, T.; Kerr, J. A.; Pilling, M. J.; Troe, J.; Walker, R. W.; Warnatz, J. *J. Phys. Chem. Ref. Data* **1992,** *21,* 411–734.

[226] Atkinson, R.; Baulch, D. L.; Cox, R. A.; Hampson, R. F.; Kerr, J. A.; Troe, J. *J. Phys. Chem. Ref. Data* **1992,** *21,* 1125–1568.

[227] Albers, E. A.; Hoyermann, K.; Wagner, H. G.; Wolfrum, J. *Proc. Combust. Inst.* **1971,** *13,* 81–88.

[228] Baldwin, R. R.; Brattan, D.; Tunnicliffe, B.; Walker, R. W.; Webster, S. J. *Combust. Flame* **1970,** *15,* 133–142.

[229] Klemm, R. B.; Payne, W. A.; Stief, L. J. *Int. J. Chem. Kinet.* **1975,** *1,* 61–72.

[230] Wine, P. H.; Nicovich, J. M.; Thompson, R. J.; Ravishankara, A. R. *J. Phys. Chem.* **1983,** *87,* 3948–3954.

[231] Roscoe, J. M. *Int. J. Chem. Kinet.* **1982,** *14,* 471–478.

[232] Troe, J. *Proc. Combust. Inst.* **1975,** *15,* 667–680.

[233] Allen, M. T.; Yetter, R. A.; Dryer, F. L. *Combust. Flame* **1997,** *109,* 449–470.

[234] Westmoreland, P. R.; Howard, J. B.; Longwell, J. P. *AIChE J.* **1986,** *32,* 1971–1979.

[235] You, X.; Wang, H.; Goos, E.; Sung, C.-J.; Klippenstein, S. J. *J. Chem. Phys. A* **2007,** *111,* 4031–4042.

[236] Yu, H. G.; Muckerman, J. T.; Francisco, J. S. *J. Phys. Chem. A* **2005,** *109,* 5230–5236.

[237] Nolte, J.; Grussdorf, J.; Temps, F.; Wagner, H. G. *Z. Naturforsch. A* **1993,** *48,* 1234–1238.

[238] Smith, I. W. M.; Zellner, R. *J. Chem. Soc. Faraday Trans. 2* **1973,** *69,* 1617–1627.

[239] Smith, I. W. M. *Chem. Phys. Lett.* **1977,** *49,* 112–115.

[240] Ravishankara, A. R.; Thompson, R. L. *Chem. Phys. Lett.* **1983,** *99,* 377–381.

[241] Frost, M. J.; Sharkey, P.; Smith, I. W. M. *J. Phys. Chem.* **1993,** *97,* 12254–12259.

[242] Wooldridge, M. S.; Hanson, R. K.; Bowman, C. T. *Proc. Combust. Inst.* **1994,** *25,* 741–748.

[243] Fulle, D.; Hamann, H. F.; Hippler, H.; Troe, J. *J. Chem. Phys.* **1996,** *105,* 983–1000.

[244] Troe, J. *Proc. Combust. Inst.* **1998,** *27,* 167–175.

[245] Golden, D. M.; Smith, G. P.; McEwen, A. B.; Yu, C.-L.; Eiteneer, B.; Frenklach, M.; Vaghjiani, G. L.; Ravishankara, A. R.; Tully, F. P. *J. Phys. Chem. A* **1998,** *102,* 8598–8606.

[246] Ruscic, B.; Litorja, M. *Chem. Phys. Lett.* **2000,** *316,* 45–50.

[247] Duncan, T. V.; Miller, C. E. *J. Chem. Phys.* **2000,** *113,* 5138–5140.

[248] Yu, H. G.; Muckerman, J. T.; Sears, T. J. *Chem. Phys. Lett.* **2001,** *349,* 547–554.

[249] Senosiain, J. P.; Musgrave, C. B.; Golden, D. M. *Int. J. Chem. Kinet.* **2003,** *35,* 464–474.

[250] Senosiain, J. P.; Klippenstein, S. J.; Miller, J. A. *Proc. Combust. Inst.* **2005,** *30,* 945–953.

[251] Mittal, G.; Sung, C.-J.; Yetter, R. A. *Int. J. Chem. Kinet.* **2006,** *38,* 516–529.

[252] Sun, H.; Yang, S. I.; Jomaas, G.; Law, C. K. *Proc. Combust. Inst.* **2007,** *31,* 439–446.

[253] Mittal, G.; Sung, C. J.; Fairweather, M.; Tomlin, A. S.; Griffiths, J. F.; Hughes, K. J. *Proc. Combust. Inst.* **2007,** *31,* 419–427.

[254] Miller, J. A.; Melius, C. F. *Combust. Flame* **1992,** *91,* 21–39.

[255] Wang, H.; Frenklach, M. *Combust. Flame* **1997,** *110,* 173–221.

[256] Smith, G. P.; Golden, D. M.; Frenklach, M.; Moriarty, N. W.; Eiteneer, B.; Goldenberg, M.; Bowman, C. T.; Hanson, R. K.; Song, S.; Gardiner, Jr., W. C.; Lissianski, V. V.; Qin, Z. "*GRI-Mech 3.0 Database*", 2000 Gas Research Institute.

[257] Skjøth-Rasmussen, M. S.; Glarborg, P.; Østberg, M.; Johannessen, J. T.; Livbjerg, H.; Jensen, A. D.; Christensen, T. S. *Combust. Flame* **2004,** *136,* 91–128.

[258] Sutherland, J. W.; Su, M. C.; Michael, J. V. *Int. J. Chem. Kinet.* **2001,** *33,* 669–684.

[259] Srinivasan, N. K.; Su, M.-C.; Sutherland, J. W.; Michael, J. V. *J. Chem. Phys. A* **2005,** *109,* 1857–1863.

[260] Cobos, C. J.; Troe, J. *Z. Phys. Chem. N. F.* **1990,** *167,* 129–149.

[261] Preses, J. M.; Fockenberg, C.; Flynn, G. W. *J. Phys. Chem. A* **2000,** *104,* 6758–6763.

[262] De Avillez Pereira, R.; Baulch, D. L.; Pilling, M. J.; Robertson, S. H.; Zeng, G. *J. Phys. Chem. A* **1997,** *101,* 9681–9693.

[263] Fernandes, R. X.; Luther, K.; Troe, J. *J. Phys. Chem. A* **2006,** *110,* 4442–4449.

[264] Srinivasan, N. K.; Su, M.-C.; Sutherland, J. W.; Michael, J. V. *J. Chem. Phys. A* **2005,** *109,* 7902–7914.

[265] Reid, I. A. B.; Robinson, C.; Smith, D. B. *Proc. Combust. Inst.* **1984,** *20,* 1833–1843.

[266] Zhu, R. S.; Lin, M. C. *J. Chem. Phys. A* **2001,** *105,* 6243–6248.

[267] Tyndall, G. S.; Cox, R. A.; Granier, C.; Lesclaux, R.; Moortgat, G. K.; Pilling, M. J.; Ravishankara, A. R.; Wallington, T. J. *J. Geophys. Res.* **2001,** *106,* 12157–12182.

[268] Keiffer, M.; Miscampbell, A. J.; Pilling, M. J. *J. Chem. Soc. Faraday Trans. 2* **1988,** *84,* 505–514.

[269] Slemr, F.; Warneck, P. *Int. J. Chem. Kinet.* **1977,** *9,* 267–282.

[270] Vaghjiani, G. L.; Ravishankara, A. R. *J. Phys. Chem.* **1989,** *93,* 1948–1959.

[271] Ing, W.-C.; Sheng, C. Y.; Bozzelli, J. W. *Fuel Proc. Tech.* **2003,** *83,* 111–145.

[272] Hippler, H.; Striebel, F.; Viskolcz, B. *Phys. Chem. Chem. Phys.* **2001,** *3,* 2450–2458.

[273] Dóbé, S.; Bérces, T.; Szilagyi, I. *J. Chem. Soc. Faraday Trans.* **1991,** *87,* 2331–2336.

[274] Ewig, F.; Rhäsa, D.; Zellner, R. *Ber. Bunsenges. Phys. Chem.* **1987,** *91,* 708–717.

[275] Wantuck, P. J.; Oldenborg, R. C.; Baughcum, S. L.; Winn, K. R. *J. Chem. Phys.* **1987,** *91,* 4653–4655.

[276] Wang, B.; Hou, H.; Gu, Y. *J. Chem. Phys. A* **1999,** *103,* 8021–8029.

[277] Wantuck, P. J.; Oldenborg, R. C.; Baughcum, S. L.; Winn, K. R. *Proc. Combust. Inst.* **1988,** *22,* 973–981.

[278] Cathonnet, M.; Boettner, J. C.; James, H. *J. Chim. Phys. Phys.-Chim. Bio.* **1982,** *79,* 475–478.

[279] Tsang, W. *J. Phys. Chem. Ref. Data* **1987,** *16,* 471–508.

[280] Seetula, J. A.; Kalinovski, I. J.; Slagle, I. R.; Gutman, D. *Chem. Phys. Lett.* **1994,** *224,* 533–538.

[281] Friedrichs, G.; Herbon, J. T.; Davidson, D. F.; Hanson, R. K. *Int. J. Chem. Kinet.* **2004,** *36,* 157–169.

[282] Troe, J. *J. Phys. Chem. A* **2005,** *109,* 8320–8328.

[283] Vasudevan, V.; Davidson, D. F.; Hanson, R. K. *Int. J. Chem. Kinet.* **2005,** *37,* 98–109.

[284] Eiteneer, B.; Yu, C.-L.; Goldenberg, M.; Frenklach, M. *J. Phys. Chem. A* **1998,** *102,* 5196–5205.

[285] Hippler, H.; Krasteva, N.; Striebel, F. *Phys. Chem. Chem. Phys.* **2004,** *6,* 3383–3388.

[286] Friedrichs, G.; Herbon, J. T.; Davidson, D. F.; Hanson, R. K. *Phys. Chem. Chem. Phys.* **2002,** *4,* 5778–5788.

[287] Callear, A. B.; Cooper, I. A. *Chem. Phys. Lett.* **1989,** *155,* 146–152.

[288] Vaghjiani, G. L.; Ravishankara, A. R. *Nature* **1991,** *350,* 406–409.

[289] Dunlop, J. R.; Tully, F. P. *J. Phys. Chem.* **1993,** *97,* 11148–11150.

[290] Bonard, A.; Daële, V.; Delfau, J.-L.; Vovelle, C. *J. Phys. Chem. A* **2002,** *106,* 4384–4389.

[291] Bryukov, M. G.; Knyazev, V. D.; Lomnicki, S. M.; McFerrin, C. A.; Dellinger, B. *J. Phys. Chem. A* **2004,** *108,* 10464–10472.

[292] Roth, P.; Just, T. *Ber. Bunsenges. Phys. Chem.* **1975,** *79,* 682–686.

[293] Rabinowitz, M. J.; Sutherland, J. W.; Patterson, P. M.; Klemm, R. B. *J. Phys. Chem.* **1991,** *95,* 674–681.

[294] Bryukov, M. G.; Slagle, I. R.; Knyazev, V. D. *J. Phys. Chem. A* **2001,** *105,* 3107–3122.

[295] Marquaire, P. M.; Dastidar, A. G.; Manthorne, K. C.; Pacey, P. D. *Can. J. Chem.* **1994,** *72,* 600–605.

[296] Roth, P.; Just, T. *Ber. Bunsenges. Phys. Chem.* **1977,** *81,* 572–577.

[297] Felder, W.; Fontijn, A. *Chem. Phys. Lett.* **1979,** *97,* 53–56.

[298] Klemm, R. B.; Tanzawa, T.; Skolnik, E. G.; Michael, J. V. *Proc. Combust. Inst.* **1981,** *18,* 785.

[299] Miyoshi, A.; Ohmori, K.; Tsuchiya, K.; Matsui, H. *Chem. Phys. Lett.* **1993,** *204,* 241–247.

[300] Miyoshi, A.; Tsuchiya, K.; Yamauchi, N.; Matsui, H. *J. Phys. Chem.* **1994,** *98,* 11452–11458.

[301] Cadle, R. D.; Allen, E. R. *J. Phys. Chem.* **1965,** *69,* 1611–1615.

[302] Westenberg, A. A.; de Haas, N. *J. Chem. Phys.* **1967,** *46,* 490–501.

[303] Cohen, N. *Int. J. Chem. Kinet.* **1986,** *18,* 59–82.

[304] Corchado, J. C.; Espinosa-García, J.; Roberto-Neto, O.; Chuang, Y.-Y.; Truhlar, D. G. *J. Phys. Chem. A* **1998,** *102,* 4899–4910.

[305] Baldwin, R. R.; Jones, P. N.; Walker, R. W. *J. Chem. Soc. Faraday Trans. 2* **1988,** *84,* 199–207.

[306] Scott, M.; Walker, R. W. *Combust. Flame* **2002,** *129,* 365–377.

[307] Chen, C.-J.; Bozzelli, J. W. *J. Phys. Chem. A* **2000,** *104,* 9715–9732.

[308] Baldwin, R. R.; Dean, C. E.; Honeyman, M. R.; Walker, R. W. *J. Chem. Soc. Faraday Trans. 1* **1986,** *82,* 89–102.

[309] Srinivasan, N. K.; Michael, J. V.; Harding, L. B.; Klippenstein, S. J. *Combust. Flame* **2007,** *149,* 104–111.

[310] Baldwin, R. R.; Fuller, A. R.; Longthorn, D.; Walker, R. W. *J. Chem. Soc. Faraday Trans. 1* **1974,** *70,* 1257–1268.

[311] Michael, J. V.; Kumaran, S. S.; Su, M.-C. *J. Phys. Chem. A* **1999,** *103,* 5942–5948.

[312] Scire, Jr., J. J.; Yetter, R. A.; Dryer, F. L. *Int. J. Chem. Kinet.* **2001,** *33,* 75–100.

[313] Hartig, R.; Troe, J.; Wagner, H. G. *Proc. Combust. Inst.* **1971,** *13,* 147–154.

[314] Gardiner, Jr., W. C.; Owen, J. H.; Clark, T. C.; Dove, J. E.; Bauer, S. H.; Miller, J. A.; McLean, W. J. *Proc. Combust. Inst.* **1975,** *15,* 857–868.

[315] Bowman, C. T. *Proc. Combust. Inst.* **1975,** *15,* 869–882.

[316] Cheng, J.-T.; Yeh, C.-T. *J. Phys. Chem.* **1977,** *81,* 1982–1984.

[317] Heffington, W. M.; Parks, G. E.; Sulzmann, K. G. P.; Penner, S. S. *Proc. Combust. Inst.* **1977,** *16,* 997–1011.

[318] Brouard, M.; Macpherson, M. T.; Pilling, M. J.; Tulloch, J. M.; Williamson, A. P. *Chem. Phys. Lett.* **1985,** *113,* 413–418.

[319] Brouard, M.; Macpherson, M. T.; Pilling, M. J. *J. Phys. Chem.* **1989,** *93,* 4047–4059.

[320] Su, M.-C.; Michael, J. V. *Proc. Combust. Inst.* **2002,** *29,* 1219–1227.

[321] Seakins, P. W.; Leone, S. R. *J. Phys. Chem.* **1992,** *96,* 4478–4485.

[322] Marcy, T. P.; Díaz, R. R.; Heard, D.; Leone, S. R.; Harding, L. B.; Klippenstein, S. J. *J. Phys. Chem. A* **2001,** *105,* 8361–8369.

[323] Slagle, I. R.; Sarzynski, D.; Gutman, D. *J. Phys. Chem.* **1987,** *91,* 4375–4379.

[324] Lim, K. P.; Michael, J. V. *J. Chem. Phys.* **1993,** *98,* 3919–3928.

[325] Fockenberg, C.; Hall, G. E.; Preses, J. M.; Sears, T. J.; Muckerman, J. T. *J. Phys. Chem. A* **1999,** *103,* 5722–5731.

[326] Wilson, C.; Balint-Kurti, G. G. *J. Phys. Chem. A* **1998,** *102,* 1625–1631.

[327] Sworski, T. J.; Hochanadel, C. J.; Ogren, P. J. *J. Phys. Chem.* **1980,** *84,* 129–134.

[328] Anastasi, C.; Beverton, S.; Ellermann, T.; Pagsberg, P. *J. Chem. Soc., Faraday Trans.* **1991,** *87,* 2325–2329.

[329] Oser, H.; Stothard, N. D.; Humpfer, R.; Grotheer, H. H. *J. Phys. Chem.* **1992,** *96,* 5359–5363.

[330] Hughes, K. J.; De Avillez Pereira, R.; Pilling, M. J. *Ber. Bunsenges. Phys. Chem.* **1992,** *96,* 1352–1359.

[331] Deters, R.; Otting, M.; Wagner, H. G.; Temps, F.; Laszlo, B.; Dobe, S.; Berces, T. *Ber. Bunsenges. Phys. Chem.* **1998,** *102,* 58–72.

[332] Oser, H.; Stothard, N. D.; Humpfer, R.; Grotheer, H. H.; Just, T. *Proc. Combust. Inst.* **1992,** *24,* 597.

[333] Humpfer, R.; Oser, H.; Grotheer, H.-H.; Just, T. *Proc. Combust. Inst.* **1994,** *25,* 721–731.

[334] Bott, J. F.; Cohen, N. *Int. J. Chem. Kinet.* **1991,** *23,* 1017–1033.

[335] Dean, A. M.; Westmoreland, P. R. *Int. J. Chem. Kinet.* **1987,** *19,* 207–228.

[336] Baulch, D. L.; Cobos, C. J.; Cox, R. A.; Frank, P.; Hayman, G.; Just, T.; Kerr, J. A.; Murrells, T.; Pilling, M. J.; Troe, J.; Walker, R. W.; Warnatz, J. *J. Phys. Chem. Ref. Data* **1994,** *23,* 847–1033.

[337] Kaiser, E. W. *J. Phys. Chem.* **1993,** *97,* 11681–11688.

[338] Yu, C.-L.; Wang, C.; Frenklach, M. *J. Phys. Chem.* **1995,** *99,* 14377–14387.

[339] Hwang, S. M.; Ryu, S.-O.; De Witt, K. J.; Rabinowitz, M. J. *J. Phys. Chem. A* **1999,** *103,* 5949–5958.

[340] Zhu, R. S.; Hsu, C.-C.; Lin, M. C. *J. Chem. Phys.* **2001,** *115,* 195–203.

[341] Herbon, J. T.; Hanson, R. K.; Bowman, C. T.; Golden, D. M. *Proc. Combust. Inst.* **2005,** *30,* 955–963.

[342] Colket, III, M. B.; Naegeli, D. W.; Glassman, I. *Proc. Combust. Inst.* **1977,** *16,* 1023–1039.

[343] Hwang, S. M.; Wagner, H. G.; Wolff, T. *Proc. Combust. Inst.* **1990,** *23,* 99–105.

[344] Hwang, S. M.; Rabinowitz, M. J.; Gardiner, Jr., W. C. *Chem. Phys. Lett.* **1993,** *205,* 157–162.

[345] Du, H.; Hessler, J. P.; Ogren, P. J. *J. Phys. Chem.* **1996,** *100,* 974–983.

[346] Pesa, M.; Pilling, M. J.; Robertson, S. H.; Wardlaw, D. M. *J. Phys. Chem. A* **1998,** *102,* 8526–8536.

[347] Pacey, P. D. *J. Phys. Chem. A* **1998,** *102,* 8541–8547.

[348] Glänzer, K.; Quack, M.; Troe, J. *Chem. Phys. Lett.* **1976,** *39,* 304–309.

[349] Glänzer, K.; Quack, M.; Troe, J. *Proc. Combust. Inst.* **1977,** *16,* 949–960.

[350] Hessler, J. P.; Ogren, P. J. *J. Phys. Chem.* **1996,** *100,* 984–992.

[351] Hippler, H.; Luther, K.; Ravishankara, A. R.; Troe, J. *Z. Phys. Chem. NF* **1984,** *142,* 1–12 Part 1.

[352] Slagle, I. R.; Gutman, D.; Davies, J. W.; Pilling, M. J. *J. Phys. Chem.* **1988,** *92,* 2455–2462.

[353] Walter, D.; Grotheer, H.-H.; Davies, J. W.; Pilling, M. J.; Wagner, A. F. *Proc. Combust. Inst.* **1990,** *23,* 107–114.

[354] Macpherson, M. T.; Pilling, M. J.; Smith, M. J. C. *J. Phys. Chem.* **1985,** *89,* 2268–2274.

[355] Hidaka, Y.; Nakamura, T.; Tanaka, H.; Inami, K.; Kawano, H. *Int. J. Chem. Kinet.* **1990,** *22,* 701–709.

[356] Frank, P.; Braun-Unkhoff, M. *Proc. Symp. on Shock Tubes and Waves* **1988,** *16,* 379–385.

[357] Lim, K. P.; Michael, J. V. *Proc. Combust. Inst.* **1994,** *25,* 713–719.

[358] Davidson, D. F.; Di Rosa, M. D.; Chang, E. J.; Hanson, R. K.; Bowman, C. T. *Int. J. Chem. Kinet.* **1995,** *27,* 1179–1196.

[359] Kiefer, J. H.; Budach, K. A. *Int. J. Chem. Kinet.* **1984,** *16,* 679–695.

[360] Watt, J. D.; Francisco, J. S. *J. Chem. Phys.* **2006,** *125,* 104301.

[361] Zellner, R. *J. Chim. Phys.* **1987,** *84,* 403–407.

[362] Zellner, R.; Hartmann, D.; Karthäuser, J.; Rhäsa, D.; Weibring, G. *J. Chem. Soc., Faraday Trans. 2* **1988,** *84,* 549–568.

[363] Vaghjiani, G. L.; Ravishankara, A. R. *J. Chem. Phys.* **1990,** *92,* 996–1003.

[364] Kurylo, M. J.; Dagaut, P.; Wallington, T. J.; Neuman, D. M. *Chem. Phys. Lett.* **1987,** *139,* 513–518.

[365] Dagaut, P.; Wallington, T. J.; Kurylo, M. J. *J. Phys. Chem.* **1988,** *92,* 3833–3836.

[366] Jenkin, M. E.; Cox, R. A.; Hayman, G. D.; Whyte, L. J. *J. Chem. Soc. Faraday Trans. 2* **1988,** *84,* 913–930.

[367] Moortgat, G. K.; Cox, R. A.; Schuster, G.; Burrows, J. P.; Tyndall, G. S. *J. Chem. Soc. Faraday Trans. 2* **1989,** *85,* 809–829.

[368] Lightfoot, P. D.; Veyret, B.; Lesclaux, R. *J. Phys. Chem.* **1990,** *94,* 708–714.

[369] Lightfoot, P. D.; Roussel, P.; Caralp, F.; Lesclaux, R. *J. Chem. Soc. Faraday Trans.* **1991,** *87,* 3213–3220.

[370] Wallington, T. J.; Japar, S. M. *Chem. Phys. Lett.* **1990,** *167,* 513–518.

[371] Wallington, T. J. *J. Chem. Soc., Faraday Trans.* **1991,** *87,* 2379–2382.

[372] Elrod, M. J.; Ranschaert, D. L.; Schneider, N. J. *Int. J. Chem. Kinet.* **2001,** *33,* 363–376.

[373] Sander, S. P.; Watson, R. T. *J. Phys. Chem.* **1980,** *84,* 1664–1674.

[374] Park, D. A. *Int. J. Chem. Kinet.* **1977,** *9,* 451–469.

[375] Pilling, M. J.; Smith, M. J. C. *J. Phys. Chem.* **1985,** *89,* 4713–4720.

[376] Keiffer, M.; Pilling, M. J.; Smith, M. J. C. *J. Phys. Chem.* **1987,** *91,* 6028–6034.

[377] Dever, D. F.; Calvert, J. G. *J. Am. Chem. Soc.* **1962,** *84,* 1362–1368.

[378] Heicklen, J.; Johnston, H. S. *J. Am. Chem. Soc.* **1962,** *84,* 4030–4039.

[379] Park, D. A.; Paul, D. M.; Quinn, C. P.; Robson, R. C. *Chem. Phys. Lett.* **1973,** *23,* 425–429.

[380] Hochanadel, C. J.; Ghormley, J. A.; Boyle, J. W. *J. Phys. Chem.* **1977,** *81,* 3–7.

[381] Adachi, H.; Basco, N.; James, D. G. L. *Int. J. Chem. Kinet.* **1980,** *12,* 949–977.

[382] Sander, S. P.; Watson, R. T. *J. Phys. Chem.* **1981,** *85,* 2960–2964.

[383] Kurylo, M. J.; Wallington, T. J. *Chem. Phys. Lett.* **1987,** *138,* 543–547.

[384] Simon, F.-G.; Schneider, W.; Moortgat, G. K. *Int. J. Chem. Kinet.* **1990,** *22,* 791–813.

[385] Lightfoot, P. D.; Lesclaux, R.; Veyret, B. *J. Phys. Chem.* **1990,** *94,* 700–707.

[386] Kan, C. S.; Calvert, J. G.; Shaw, J. H. *J. Phys. Chem.* **1980,** *84,* 3411–3417.

[387] Niki, H.; Maker, P. D.; Savage, C. M.; Breitenbach, L. P. *J. Phys. Chem.* **1981,** *85,* 877–881.

[388] Horie, O.; Crowley, J. N.; Moortgat, G. K. *J. Phys. Chem.* **1990,** *94,* 8198–8203.

[389] Tyndall, G. S.; Wallington, T. J.; Ball, J. C. *J. Phys. Chem. A* **1998,** *102,* 2547–2554.

[390] Weaver, J.; Meagher, J.; Shortridge, R.; Heicklen, J. *J. Photochem.* **1975,** *4,* 341–360.

[391] Alcock, W. G.; Mile, B. *Combust. Flame* **1975,** *24,* 125–128 Brief Communications.

[392] Wallington, T. J.; Dagaut, P.; Kurylo, M. J. *Chem. Rev.* **1992,** *92,* 667–710.

[393] Lightfoot, P. D.; Cox, R. A.; Crowley, J. N.; Destriau, M.; Hayman, G. D.; Jenkin, M. E.; Moortgat, G. K.; Zabel, F. *Atmos. Environ.* **1992,** *26A,* 1805–1961.

[394] Kirk, A. D. *Can. J. Chem.* **1965,** *43,* 2236–2242.

[395] Kaiser, E. W.; Westbrook, C. K.; Pitz, W. J. *Int. J. Chem. Kinet.* **1986,** *18,* 655–688.

[396] Sahetchian, K. A.; Heiss, A.; Rigny, R.; Ben-aïm, R. I. *Int. J. Chem. Kinet.* **1982,** *14,* 1325–1337.

[397] Niki, H.; Maker, P. D.; Savage, C. M.; Breitenbach, L. P. *J. Phys. Chem.* **1983,** *87,* 2190–2193.

[398] Vaghjiani, G. L.; Ravishankara, A. R. *Int. J. Chem. Kinet.* **1990,** *22,* 351–358.

[399] Chuang, M.-C.; Foltz, M. F.; Moore, C. B. *J. Chem. Phys.* **1987,** *87,* 3855–3864.

[400] Oguchi, T.; Miyoshi, A.; Koshi, M.; Matsui, H. *Bull. Chem. Soc. Jpn.* **2000,** *73,* 53–60.

[401] Zaslonko, I. S.; Mukoseev, Y. K.; Tyurin, A. N. *Kinet. Catal. (tr. of Kinet. Katal.)* **1988,** *29,* 244–250.

[402] Page, M.; Lin, M. C.; He, Y.; Choudhury, T. K. *J. Phys. Chem.* **1989,** *93,* 4404–4408.

[403] Choudhury, T. K.; He, Y.; Sanders, W. A.; Lin, M. C. *J. Phys. Chem.* **1990,** *94,* 2394–2398.

[404] Moortgat, G. K.; Slemr, F.; Warneck, P. *Int. J. Chem. Kinet.* **1977,** *9,* 249–265.

[405] Hoyermann, K.; Loftfield, N. S.; Sievert, R.; Wagner, H. G. *Proc. Combust. Inst.* **1981,** *18,* 831–842.

[406] Heinemann-Fiedler, P.; Hoyermann, K. *Ber. Bunsenges. Phys. Chem.* **1988,** *92,* 1472–1477.

[407] Warnatz, J. Combustion Chemistry. In ; Gardiner, Jr., W. C., Ed.; Springer-Verlag, NY: 1984; Chapter "Rate Coefficients in the C/H/O System", page 197.

[408] Batt, L.; Robinson, G. N. *Int. J. Chem. Kinet.* **1979,** *11,* 1045–1053.

[409] Gutman, D.; Sanders, N.; Butler, J. E. *J. Phys. Chem.* **1982,** *86,* 66–70.

[410] Lorenz, K.; Rhäsa, D.; Zellner, R.; Fritz, B. *Ber. Bunsenges. Phys. Chem.* **1985,** *89,* 341–342.

[411] Bofill, J. M.; Olivella, S.; Solé, A.; Anglada, J. M. *J. Am. Chem. Soc.* **1999,** *121,* 1337–1347.

[412] Wantuck, P. J.; Oldenborg, R. C.; Baughcum, S. L.; Winn, K. R. *Chem. Phys. Lett.* **1987,** *138,* 548–552.

[413] Lissi, E. A.; Massiff, G.; Villa, A. E. *J. Chem. Soc. Faraday Trans. 1* **1973,** *69,* 346–351.

[414] Wiebe, H. A.; Heicklen, J. *J. Am. Chem. Soc.* **1973,** *95,* 1–7.

[415] Sanders, N.; Butler, J. E.; Pasternack, L. R.; McDonald, J. R. *Chem. Phys.* **1980,** *49,* 17–22.

[416] Shaw, R.; Thynne, J. C. J. *Trans. Faraday Soc.* **1966,** *62,* 104–111.

[417] Thynne, J. C. J.; Gray, P. *Trans. Faraday Soc.* **1963,** *59,* 1149.

[418] Quee, M. J. Y.; Thynne, J. C. J. *Trans. Faraday Soc.* **1966,** *62,* 3154–3161.

[419] Quee, M. J. Y.; Thynne, J. C. J. *Trans. Faraday Soc.* **1967,** *63,* 1656.

[420] Quee, M. J. Y.; Thynne, J. C. J. *Ber. Bunsenges. Phys. Chem.* **1968,** *72,* 211–217.

[421] Hoare, D. E.; Wellington, C. A. *Proc. Combust. Inst.* **1960,** *8,* 472–481.

[422] Eremin, A. V.; Zaslonko, I. S.; Kogarko, S. N.; Mozzhukhin, E. V.; Petrov, Y. P. *Kinet. Catal. (tr. of Kinet. Katal.)* **1970,** *11,* 717.

[423] Li, J.; Zhao, Z.; Kazakov, A.; Chaos, M.; Dryer, F. L.; Scire, Jr., J. J. *Int. J. Chem. Kinet.* **2007,** *39,* 109–136.

[424] Westbrook, C. K.; Dryer, F. L. *Combust. Sci. Tech.* **1979,** *20,* 125–140.

[425] Egolfopoulos, F. N.; Du, D. X.; Law, C. K. *Combust. Sci. Tech.* **1992,** *83,* 33–75.

[426] Batt, L.; Burrows, J. P.; Robinson, G. N. *Chem. Phys. Lett.* **1981,** *78,* 467–470.

[427] Adams, G. F.; Bartlett, R. J.; Purvis, G. D. *Chem. Phys. Lett.* **1982,** *87,* 311–314.

[428] Campbell, I. M.; McLaughlin, D. F.; Handy, B. J. *Chem. Phys. Lett.* **1976,** *38,* 362–364.

[429] Overend, R.; Paraskevopoulos, G. *J. Phys. Chem.* **1978,** *82,* 1329–1333.

[430] Ravishankara, A. R.; Davis, D. D. *J. Phys. Chem.* **1978,** *82,* 2852–2853.

[431] Barnes, I.; Bastian, V.; Becker, K. H.; Fink, E. H.; Zabel, F. *J. Phys. Chem.* **1982,** *16,* 545–550.

[432] Tuazon, E. C.; Carter, W. P. L.; Atkinson, R.; Pitts, Jr., J. N. *Int. J. Chem. Kinet.* **1983,** *15,* 619–629.

[433] Pagsberg, P.; Munk, J.; Sillesen, A.; Anastasi, C. *Chem. Phys. Lett.* **1988,** *146,* 375–381.

[434] McCaulley, J. A.; Kelly, N.; Golde, M. F.; Kaufman, F. *J. Phys. Chem.* **1989,** *93,* 1014–1018.

[435] Nelson, L.; Rattigan, O.; Neavyn, R.; Sidebottom, H.; Treacy, J.; Nielsen, O. J. *Int. J. Chem. Kinet.* **1990,** *22,* 1111–1126.

[436] Vandooren, J.; van Tiggelen, P. J. *Proc. Combust. Inst.* **1981,** *18,* 473–483.

[437] Hägele, J.; Lorenz, K.; Rhäsa, D.; Zellner, R. *Ber. Bunsenges. Phys. Chem.* **1983,** *87,* 1023–1026.

[438] Meier, U.; Grotheer, H. H.; Riekert, G.; Just, T. *Ber. Bunsenges. Phys. Chem.* **1985,** *89,* 325–327.

[439] Wallington, T. J.; Kurylo, M. J. *Int. J. Chem. Kinet.* **1987,** *19,* 1015–1023.

[440] Hess, W. P.; Tully, F. P. *J. Phys. Chem.* **1989,** *93,* 1944–1947.

[441] Bott, J. F.; Cohen, N. *Int. J. Chem. Kinet.* **1991,** *23,* 1075–1094.

[442] Xu, S.; Lin, M. C. *Proc. Combust. Inst.* **2007,** *31,* 159–166.

[443] Aders, W. K.; Wagner, H. G. *Z. Phys. Chem. N. F.* **1971,** *74,* 224–236.

[444] Meagher, J. F.; Kim, P.; Lee, J. H.; Timmons, R. B. *J. Phys. Chem.* **1974,** *78,* 2650–2657.

[445] Spindler, K.; Wagner, H. *Ber. Bunsenges. Phys. Chem.* **1982,** *86,* 2–13.

[446] Cribb, P. H.; Dove, J. E.; Yamazaki, S. *Proc. Combust. Inst.* **1992,** *88,* 169–185.

[447] Li, S. C.; Williams, F. A. *Proc. Combust. Inst.* **1996,** *26,* 1017–1024.

[448] Lendvay, G.; Bérces, T.; Márta, F. *J. Phys. Chem. A* **1997,** *101,* 1588–1594.

[449] Jodkowski, J. T.; Rayez, M.-T.; Rayez, J.-C.; Bérces, T.; Dóbé, S. *J. Chem. Phys. A* **1999,** *103,* 3750–3765.

[450] Kerkeni, B.; Clary, D. C. *J. Chem. Phys.* **2004,** *121,* 6809–6821.

[451] Owens, C. M.; Roscoe, J. M. *Can. J. Chem.* **1976,** *54,* 984–989.

[452] Lalo, C.; Vermeil, C. *J. Chim. Phys.* **1980,** *77,* 131–136.

[453] Keil, D. G.; Tanzawa, T.; Skolnik, E. G.; Klemm, R. B.; Michael, J. V. *J. Chem. Phys.* **1981,** *75,* 2693–2704.

[454] Grotheer, H.-H.; Just, T. *Chem. Phys. Lett.* **1981,** *78,* 71–74.

[455] Failes, R. L.; Singleton, D. L.; Paraskevopoulos, G.; Irwin, R. S. *Int. J. Chem. Kinet.* **1982,** *14,* 371–379.

[456] Aronowitz, D.; Santoro, R. J.; Dryer, F. L.; Glassman, I. *Proc. Combust. Inst.* **1978,** *17,* 633–644.

[457] Bowman, C. T. *Combust. Flame* **1975,** *25,* 343–354.

[458] Tsuboi, T.; Katoh, M.; Kikuchi, S.; Hashimoto, K. *Jpn. J. Appl. Phys.* **1981,** *20,* 985–992.

[459] Hidaka, Y.; Oki, T.; Kawano, H.; Higashihara, T. *J. Phys. Chem.* **1989,** *93,* 7134–7139.

[460] Bradley, D.; Dixon-Lewis, G.; El-Din Habik, S.; Kwa, L. K.; El-Sherif, S. *Combust. Flame* **1991,** *85,* 105–120.

[461] Greenhill, P. G.; O'Grady, B. V.; Gilbert, R. G. *Aust. J. Chem.* **1986,** *39,* 1929–1942.

[462] Dóbé, S.; Temps, F.; Ziemer, H. G. W. H.; Bérces, T. *J. Phys. Chem.* **1994,** *98,* 9792–9800.

[463] Grotheer, H.-H.; Riekert, G.; Walter, D.; Just, T. *Chem. Phys. Lett.* **1988,** *148,* 530–536.

[464] Grotheer, H.-H.; Riekert, G.; Walter, D.; Just, T. *J. Phys. Chem.* **1988,** *92,* 4028–4030.

[465] Grotheer, H.-H.; Riekert, G.; Meier, U.; Just, T. *Ber. Bunsenges. Phys. Chem.* **1985,** *89,* 187–191.

[466] Dóbé, S.; Temps, F.; Böhland, T.; Wagner, H. G. *Z. Naturforsch. A* **1985,** *40,* 1289–1298.

[467] Payne, W. A.; Brunning, J.; Mitchell, M. B.; Stief, L. J. *Int. J. Chem. Kinet.* **1988,** *20,* 63–74.

[468] Pagsberg, P.; Munk, J.; Anastasi, C.; Simpson, V. J. *J. Phys. Chem.* **1989,** *93,* 5162–5165.

[469] Miyoshi, A.; Matsui, H.; Washida, N. *J. Phys. Chem.* **1990,** *94,* 3016–3019.

[470] Hanoune, B.; Dusanter, S.; ElMaimouni, L.; Devolder, P.; Lemoine, B. *Chem. Phys. Lett.* **2001,** *343,* 527–534.

[471] Nesbitt, F. L.; Payne, W. A.; Stief, L. J. *J. Phys. Chem.* **1988,** *92,* 4030–4032.

[472] Saito, K.; Kakumoto, T.; Nakanishi, Y.; Imamura, A. *J. Phys. Chem.* **1985,** *89,* 3109–3113.

[473] Irdam, E. A.; Kiefer, J. H.; Harding, L. B.; Wagner, A. F. *Int. J. Chem. Kinet.* **1993,** *25,* 285–303.

[474] Hidaka, Y.; Taniguchi, T.; Tanaka, H.; Kamesawa, T.; Inami, K.; Kawano, H. *Combust. Flame* **1993,** *92,* 365–376.

[475] Kumaran, S. S.; Carroll, J. J.; Michael, J. V. *Proc. Combust. Inst.* **1998,** *27,* 125.

[476] Vasudevan, V.; Davidson, D. F.; Hanson, R. K.; Bowman, C. T.; Golden, D. M. *Proc. Combust. Inst.* **2007,** *31,* 175–183.

[477] Zhang, X. B.; Rheinecker, J. L.; Bowman, J. M. *J. Chem. Phys.* **2005,** *122,* 114313.

[478] Zabarnick, S.; Fleming, J. W.; Lin, M. C. *Int. J. Chem. Kinet.* **1988,** *20,* 117–129.

[479] Li, H.-Y.; Pu, M.; Ji, Y.-Q.; Xu, Z.-F.; Feng, W.-L. *Chem. Phys.* **2004,** *307,* 35–43.

[480] Niki, H.; Maker, P. D.; Savage, C. M.; Breitenbach, L. P. *J. Phys. Chem.* **1984,** *88,* 5342–5344.

[481] Yetter, R. A.; Rabitz, H.; Dryer, F. L.; Maki, R. G.; Klemm, R. B. *J. Chem. Phys.* **1989,** *91,* 4088–4097.

[482] Sivakumaran, V.; Hölscher, D.; Dillon, T. J.; Crowley, J. N. *Phys. Chem. Chem. Phys.* **2003,** *5,* 4821–4827.

[483] D'Anna, B.; Bakken, V.; Beukes, J. A.; Nielsen, C. J.; Brudnik, K.; Jodkowski, J. T. *Phys. Chem. Chem. Phys.* **2003,** *5,* 1790–1805.

[484] Atkinson, R.; Pitts, Jr., J. N. *J. Chem. Phys.* **1978,** *68,* 3581–3584.

[485] Stief, L. J.; Nava, D. F.; Payne, W. A.; Michael, J. V. *J. Chem. Phys.* **1980,** *73,* 2254–2258.

[486] Temps, F.; Wagner, H. G. *Ber. Bunsenges. Phys. Chem.* **1980,** *88,* 415–418.

[487] Vandooren, J.; Oldenhove de Guertechin, L.; van Tiggelen, P. J. *Combust. Flame* **1986,** *64,* 127–139.

[488] Timonen, R. S.; Ratajczak, E.; Gutman, D.; Wagner, A. F. *J. Phys. Chem.* **1987,** *91,* 5325–5332.

[489] Krasnoperov, L. N.; Chesnokov, E. N. . In *Proc. 16th Int. Symp. on Gas Kinetics*; Cambridge, UK, July 23–27, 2000.

[490] Krasnoperov, L. N.; Chesnokov, E. N.; Stark, H.; Ravishankara, A. R. *J. Phys. Chem. A* **2004,** *108,* 11526–11536.

[491] Wagner, A. F.; Bowman, J. M. *J. Phys. Chem.* **1987,** *91,* 5314–5324.

[492] Neyer, D. W.; Luo, X.; Burak, I.; Houston, P. L. *J. Chem. Phys.* **1995,** *102,* 1645–1657.

[493] Tobiason, J. D.; Dunlop, J. R.; Rohlfing, E. A. *J. Chem. Phys.* **1995,** *103,* 1448–1469.

[494] Wang, D.; Bowman, J. M. *Chem. Phys. Lett.* **1995,** *235,* 277–285.

[495] Keller, H.-M.; Floethmann, H.; Dobbyn, A. J.; Schinke, R. *J. Chem. Phys.* **1996,** *105,* 4983–5004.

[496] Bowman, J. M. *J. Phys. Chem. A* **1998,** *102,* 3006–3017.

[497] Ahumada, J. J.; Michael, J. V.; Osborne, D. T. *J. Chem. Phys.* **1972,** *57,* 3736–3745.

[498] Hippler, H.; Krasteva, N.; Striebel, F. *Phys. Chem. Chem. Phys.* **2005,** *7,* 2077–2079.

[499] Krasnoperov, L. N. *Phys. Chem. Chem. Phys.* **2005,** *7,* 2074–2076.

[500] Shibuya, K.; Ebata, T.; Obi, K.; Tanaka, I. *J. Phys. Chem.* **1977,** *81,* 2292–2294.

[501] Temps, F.; Wagner, H. G. *Ber. Bunsenges. Phys. Chem.* **1980,** *88,* 410–414.

[502] Langford, A. O.; Moore, C. B. *J. Chem. Phys.* **1984,** *80,* 4211–4221.

[503] Nesbitt, F. L.; Gleason, J. F.; Stief, L. J. *J. Phys. Chem. A* **1999,** *103,* 3038–3043.

[504] Veyret, B.; Lesclaux, R. *J. Phys. Chem.* **1981,** *85,* 1918–1922.

[505] Timonen, R. S.; Ratajczak, E.; Gutman, D. *J. Phys. Chem.* **1988,** *92,* 651–655.

[506] DeSain, J. D.; Jusinski, L. E.; Ho, A. D.; Taatjes, C. A. *Chem. Phys. Lett.* **2001,** *347,* 79–86.

[507] Tsuboi, T. *Jpn. J. Appl. Phys.* **1976,** *15,* 159–168.

[508] Westbrook, C. K.; Creighton, J.; Lund, C.; Dryer, F. L. *J. Phys. Chem.* **1977,** *81,* 2542–2554.

[509] Cherian, M. A.; Rhodes, P.; Simpson, R. J.; Dixon-Lewis, G. *Proc. Combust. Inst.* **1981,** *18,* 385–396.

[510] Hsu, C.-C.; Mebel, A. M.; Lin, M. C. *J. Chem. Phys.* **1996,** *105,* 2346–2352.

[511] Fischer, S. L.; Dryer, F. L.; Curran, H. J. *Int. J. Chem. Kinet.* **2000,** *32,* 713–740.

[512] Saunders, D.; Heicklen, J. *J. Phys. Chem.* **1966,** *70,* 1950–1958.

[513] Papadopoulus, C.; Ashmore, P. G.; Tyler, B. J. *Proc. Combust. Inst.* **1971,** *13,* 281–289.

[514] Caymax, M.; Peeters, J. *Proc. Combust. Inst.* **1983,** *19,* 51.

[515] Mahmud, K.; Marshall, P.; Fontijn, A. *J. Chem. Phys.* **1988,** *88,* 2393–2397.

[516] Atkinson, R. *J. Phys. Chem. Ref. Data* **1997,** *26,* 215–290.

[517] Stewart, P. H.; Rothem, T.; Golden, D. M. *Proc. Combust. Inst.* **1988,** *22,* 943–952.

[518] Slagle, I. R.; Sarzynski, D.; Gutman, D.; Miller, J. A.; Melius, C. F. *J. Chem. Soc. Faraday Trans. 2* **1988,** *84,* 491–503.

[519] Ludwig, W.; Brandt, B.; Friedrichs, G.; Temps, F. *J. Phys. Chem. A* **2006,** *110,* 3330–3337.

[520] Miller, J. A.; Klippenstein, S. J. *Int. J. Chem. Kinet.* **2001,** *33,* 654–668.

[521] Baggott, J. E.; Frey, H. M.; Lightfoot, P. D.; Walsh, R. *J. Phys. Chem.* **1987,** *91,* 3386–3393.

[522] Klemm, R. B.; Sutherland, J. W.; Wickramaaratchi, M. A.; Yarwood, G. *J. Phys. Chem.* **1990,** *94,* 3354–3357.

[523] Zhu, R. S.; Park, J.; Lin, M. C. *Chem. Phys. Lett.* **2005,** *408,* 25–30.

[524] Benson, S. W. *Int. J. Chem. Kinet.* **1996,** *28,* 665–672.

[525] Harding, L. B.; Georgievskii, Y.; Klippenstein, S. J. *J. Phys. Chem. A* **2005,** *109,* 4646–4656.

[526] Monks, P. S.; Nesbitt, F. L.; Payne, W. A.; Scanlon, M.; Stief, L. J.; Shallcross, D. E. *J. Phys. Chem.* **1995,** *99,* 17151–17159.

[527] Fahr, A.; Laufer, A. H.; Klein, R.; Braun, W. *J. Phys. Chem.* **1991,** *95,* 3218–3224.

[528] Fenter, F. F.; Catoire, V.; Lesclaux, R.; Lightfoot, P. D. *J. Phys. Chem.* **1993,** *97,* 3530–3538.

[529] Caralp, F.; Devolder, P.; Fittschen, C.; Gomez, N.; Hippler, H.; Méreau, R.; Rayez, M. T.; Striebel, F.; Viskolcz, B. *Phys. Chem. Chem. Phys.* **1999,** *1,* 2935–2944.

[530] Fittschen, C.; Frenzel, A.; Imrik, K.; Devolder, P. *Int. J. Chem. Kinet.* **1999,** *31,* 860–866.

[531] Gupte, K. S.; Kiefer, J. H.; Tranter, R. S.; Klippenstein, S. J.; Harding, L. B. *Proc. Combust. Inst.* **2006,** *31,* in press.

[532] Taylor, P. H.; Rahman, M. S.; Arif, M.; Dellinger, B.; Marshall, P. *Proc. Combust. Inst.* **1996,** *26,* 497.

[533] Cameron, M.; Sivakumaran, V.; Dillon, T. J.; Crowley, J. N. *Phys. Chem. Chem. Phys.* **2002,** *4,* 3628–3638.

[534] Senosiain, J. P.; Klippenstein, S. J.; Miller, J. A. *J. Phys. Chem. A* **2006,** *110,* 5772–5781.

[535] Ohmori, K.; Miyoshi, A.; Matsui, H.; Washida, N. *J. Phys. Chem.* **1990,** *94,* 3253–3255.

[536] Bartels, M.; Edelbüttel-Einhaus, J.; Hoyermann, K. *Proc. Combust. Inst.* **1991,** *23,* 131–138.

[537] Adachi, H.; Basco, N.; James, D. G. L. *Int. J. Chem. Kinet.* **1981,** *13,* 1251–1276.

[538] Tyndall, G. S.; Orlando, J. J.; Wallington, T. J.; Hurley, M. D. *Int. J. Chem. Kinet.* **1997,** *29,* 655–663.

[539] Marinov, N. M.; Pitz, W. J.; Westbrook, C. K.; Castaldi, M. J.; Senkan, S. M. *Combust. Sci. Tech.* **1996,** *116,* 211–287.

[540] Hranisavljevic, J.; Kumaran, S. S.; Michael, J. V. *Proc. Combust. Inst.* **1998,** *27,* 159–166.

[541] Grussdorf, J.; Nolte, J.; Temps, F.; Wagner, H. G. *Ber. Bunsenges. Phys. Chem.* **1994,** *98,* 546–553.

[542] Tully, F. P.; Ravishankara, A. R.; Carr, K. *Int. J. Chem. Kinet.* **1983,** *15,* 1111–1118.

[543] Tully, F. P.; Droege, A. T.; Koszykowski, M. L.; Melius, C. F. *J. Phys. Chem.* **1986,** *90,* 691–698.

[544] Talukdar, R. K.; Mellouki, A.; Gierczak, T.; Barone, S.; Chiang, S.-Y.; Ravishankara, A. R. *Int. J. Chem. Kinet.* **1994,** *26,* 973–990.

[545] Koffend, J. B.; Cohen, N. *Int. J. Chem. Kinet.* **1996,** *28,* 79–88.

[546] Baldwin, R. R.; Walker, R. W. *Proc. Combust. Inst.* **1979,** *17,* 525–533.

[547] Sampson, R. J. *J. Chem. Soc.* **1963,** *Nov.,* 5095–5106.

[548] Knox, J. H.; Smith, R. F.; Trotman-Dickenson, A. F. *Trans. Faraday Soc.* **1958,** *54,* 1509–1514.

[549] Falconer, W. E.; Trotman-Dickenson, A. F.; Knox, J. H. *J. Chem. Soc.* **1961,** *Mar.,* 782–791.

[550] Trotman-Dickenson, A. F.; Birchard, J. R.; Steacie, E. W. R. *J. Chem. Phys.* **1951,** *19,* 163–168.

[551] Wijnen, M. H. J. *J. Chem. Phys.* **1955,** *23,* 1357.

[552] McNesby, J. R.; Gordon, A. S. *J. Am. Chem. Soc.* **1955,** *77,* 4719–4723.

[553] Clark, T. C.; Izod, T. P. J.; Kistiakowsky, G. B. *J. Chem. Phys.* **1971,** *54,* 1295–1303.

[554] Chen, C.-J.; Back, M. H.; Back, R. A. *Can. J. Chem.* **1976,** *54,* 3175–3184.

[555] Pacey, P. D.; Wimalasena, J. H. *Can. J. Chem.* **1984,** *62,* 293–297.

[556] Möller, W.; Mozzhukin, E.; Wagner, H. G. *Ber. Bunsenges. Phys. Chem.* **1987,** *91,* 660–666.

[557] Teng, L.; Jones, W. E. *J. Chem. Soc. Faraday Trans. 1* **1972,** *68,* 1267.

[558] Kurylo, M. J.; Peterson, N. C.; Braun, W. *J. Chem. Phys.* **1970,** *53,* 2776–2783.

[559] Camilleri, P.; Marshall, R. M.; Purnell, J. H. *J. Chem. Soc. Faraday Trans. 1* **1974,** *70,* 1434–1444.

[560] Pratt, G.; Veltman, I. *J. Chem. Soc., Faraday Trans. 1* **1976,** *72,* 1733–1737.

[561] Pratt, G.; Wood, S. W. *J. Chem. Soc. Faraday Trans. 1* **1984,** *80,* 3419–3427.

[562] Sillesen, A.; Ratajczak, E.; Pagsberg, P. *Chem. Phys. Lett.* **1993,** *201,* 171–177.

[563] Tabayashi, K.; Bauer, S. H. *Combust. Flame* **1979,** *34,* 63–68.

[564] Harding, L. B.; Klippenstein, S. J. *Proc. Combust. Inst.* **1998,** *27,* 151–157.

[565] Hidaka, Y.; Sato, K.; Hoshikawa, H.; Nishimori, T.; Takahashi, R.; Tanaka, H.; Inami, K.; Ito, N. *Combust. Flame* **2000,** *120,* 245–264.

[566] K. Hoyermann, M. Olzmann, J. S.; Viskolcz, B. *J. Phys. Chem. A* **1999,** *103,* 5692–5698.

[567] Lindner, J.; Loomis, R. A.; Klaassen, J. J.; Leone, S. R. *J. Chem. Phys.* **1998,** *108,* 1944–1952.

[568] Reid, J. P.; Marcy, T. P.; Kuehn, S.; Leone, S. R. *J. Chem. Phys.* **2000,** *113,* 4572–4580.

[569] Fagerström, K.; Lund, A.; Mahmoud, G.; Jodkowski, J. T.; Ratajczak, E. *Chem. Phys. Lett.* **1993,** *208,* 321–327.

[570] Bozzelli, J. W.; Dean, A. M. *J. Phys. Chem.* **1990,** *94,* 3313–3317.

[571] Dobis, O.; Benson, S. W. *J. Am. Chem. Soc.* **1993,** *115,* 8798–8809.

[572] Slagle, I. R.; Feng, Q.; Gutman, D. *J. Phys. Chem.* **1984,** *88,* 3648–3653.

[573] Slagle, I. R.; Ratajczak, E.; Gutman, D. *J. Phys. Chem.* **1986,** *90,* 402–407.

[574] McAdam, K. G.; Walker, R. W. *J. Chem. Soc. Faraday Trans. 2* **1987,** *83,* 1509–1517.

[575] Wagner, A. F.; Slagle, I. R.; Sarzynski, D.; Gutman, D. *J. Phys. Chem.* **1990,** *94,* 1853–1868.

[576] Munk, J.; Pagsberg, P.; Ratajczak, E.; Sillesen, A. *J. Phys. Chem.* **1986,** *90,* 2752–2757.

[577] Kaiser, E. W.; Wallington, T. J.; Andino, J. M. *Chem. Phys. Lett.* **1990,** *168,* 309–313.

[578] Kaiser, E. W.; Lorkovic, I. M.; Wallington, T. J. *J. Phys. Chem.* **1990,** *94,* 3352–3354.

[579] Kaiser, E. W. *J. Phys. Chem.* **1995,** *99,* 707–711.

[580] Dilger, H.; Schwager, M.; Tregenna-Piggott, P. L. W.; Roduner, E.; Reid, I. D.; Arseneau, D. J.; Pan, J. J.; Senba, M.; Shelley, M.; Fleming, D. G. *J. Phys. Chem.* **1996,** *100,* 6561–6571.

[581] Clifford, E. P.; Farrell, J. T.; DeSain, J. D.; Taatjes, C. A. *J. Phys. Chem. A* **2000,** *104,* 11549–11560.

[582] Miller, J. A.; Klippenstein, S. J.; Robertson, S. R. *Proc. Combust. Inst.* **2000,** *28,* 1479–1486.

[583] Curtiss, L. A.; Raghavachari, K.; Trucks, G. W.; Pople, J. A. *J. Chem. Phys.* **1991,** *94,* 7221–7230.

[584] Ignatyev, I. S.; Xie, Y.; Allen, W. D.; Schaefer III, H. F. *J. Chem. Phys.* **1997,** *107,* 141–155.

[585] Baldwin, R. R.; Pickering, I. A.; Walker, R. W. *J. Chem. Soc. Faraday Trans. 1* **1980,** *79,* 2374–2382.

[586] Knyazev, V. D.; Ákos Bencsura,; Stoliarov, S. I.; Slagle, I. R. *J. Phys. Chem.* **1996,** *100,* 11346–11354.

[587] Bhargava, A.; Westmoreland, P. R. *Combust. Flame* **1998,** *113,* 333–347.

[588] Just, T.; Roth, P.; Damm, R. *Proc. Combust. Inst.* **1977,** *16,* 961–969.

[589] Tranter, R. S.; Raman, A.; Sivaramakrishnan, R.; Brezinsky, K. *Int. J. Chem. Kinet.* **2005,** *37,* 306–331.

[590] Lightfoot, P. D.; Pilling, M. J. *J. Phys. Chem.* **1987,** *91,* 3373–3379.

[591] Hanning-Lee, M. A.; Green, N. J. B.; Pilling, M. J.; Robertson, S. H. *J. Chem. Phys.* **1993,** *97,* 860–870.

[592] Feng, Y.; Niiranen, J. T.; Bencsura, A.; Knyazev, V. D.; Gutman, D.; Tsang, W. *J. Phys. Chem.* **1993,** *97,* 871–880.

[593] Braun, W.; Lenzi, M. *Discuss. Faraday Soc.* **1967,** *44,* 252.

[594] Clarke, J. S.; Donahue, N. M.; Kroll, J. H.; Rypkema, H. A.; Anderson, J. G. *J. Chem. Phys. A* **2000,** *104,* 5254–5264.

[595] Lee, J. H.; Michael, J. V.; Payne, W. A.; Stief, L. J. *J. Chem. Phys.* **1978,** *68,* 1817–1820.

[596] Sugawara, K.-I.; Okazaki, K.; Sato, S. *Bull. Chem. Soc. Jpn.* **1981,** *54,* 2872–2877.

[597] Klemm, R. B.; Nesbitt, F. L.; Skolnik, E. G.; Lee, J. H.; Smalley, J. F. *J. Phys. Chem.* **1987,** *91,* 1574–1580.

[598] Mahmud, K.; Marshall, P.; Fontijn, A. *J. Phys. Chem.* **1987,** *91,* 1568–1573.

[599] Elias, L. *J. Chem. Phys.* **1963,** *38,* 989–995.

[600] Westenberg, A. A.; de Haas, N. *Proc. Combust. Inst.* **1969,** *12,* 298.

[601] Davis, D. D.; Huie, R. E.; Herron, J. T.; Kurylo, M. J.; Braun, W. *J. Chem. Phys.* **1972,** *56,* 4868–4876.

[602] Nicovich, J. M.; Ravishankara, A. R. *Proc. Combust. Inst.* **1982,** *19,* 23.

[603] Perry, R. A. *J. Chem. Phys.* **1984,** *80,* 153–158.

[604] Schmoltner, A. M.; Chu, P. M.; Brudzynski, R. J.; Lee, Y. T. *J. Chem. Phys.* **1989,** *91,* 6926–6936.

[605] Yamaguchi, K.; Yabushita, S.; Fueno, T.; Kato, S.; Morokuma, K. *Chem. Phys. Lett.* **1980,** *70,* 27–30.

[606] Hunziker, H. E.; Kneppe, H.; Wendt, H. R. *J. Photochem.* **1981,** *17,* 377–387.

[607] Smalley, J. F.; Nesbitt, F. L.; Klemm, R. B. *J. Phys. Chem.* **1986,** *90,* 491–497.

[608] Koda, S.; Endo, Y.; Hirota, E.; Tsuchiya, S. *J. Phys. Chem.* **1987,** *91,* 5840–5842.

[609] Koda, S.; Endo, Y.; Tsuchiya, S.; Hirota, E. *J. Phys. Chem.* **1991,** *95,* 1241–1244.

[610] Anastasi, C.; Sanderson, M. G.; Pagsberg, P.; Sillesen, A. *J. Chem. Soc., Faraday Trans.* **1994,** *90,* 3625–3631.

[611] Westenberg, A. A.; Friström, R. H. *Proc. Combust. Inst.* **1965,** *10,* 473–487.

[612] Davis, D. D.; Fischer, S.; Schiff, R.; Watson, R. T.; Bollinger, W. *J. Chem. Phys.* **1975,** *63,* 1707–1712.

[613] Atkinson, R.; Perry, R. A.; Pitts, Jr., J. N. *J. Chem. Phys.* **1977,** *66,* 1197–1201.

[614] Tully, F. P. *Chem. Phys. Lett.* **1988,** *143,* 510–514.

[615] Liu, A.; Mulac, W. A.; Jonah, C. D. *J. Chem. Phys.* **1988,** *92,* 3828–3833.

[616] Kuo, C. H.; Lee, Y. P. *J. Phys. Chem.* **1991,** *95,* 1253–1257.

[617] Diau, E. W.-G.; Lee, Y.-P. *J. Chem. Phys.* **1992,** *96,* 377.

[618] Fulle, D.; Hamann, H. F.; Hippler, H.; Jänsch, C. P. *Ber. Bunsenges. Phys. Chem.* **1997,** *101,* 1433–1442.

[619] Sekusak, S.; Liedl, K. R.; Sabljic, A. *J. Phys. Chem. A* **1998,** *102,* 1583–1594.

[620] Hippler, H.; Viskolcz, B. *Phys. Chem. Chem. Phys.* **2000,** *2,* 3591–3596.

[621] Baldwin, R. R.; Stout, D. R.; Walker, R. W. *J. Chem. Soc. Faraday Trans. 1* **1984,** *80,* 3481–3489.

[622] Baldwin, R. R.; Dean, C. E.; Walker, R. W. *J. Chem. Soc. Faraday Trans. 2* **1986,** *82,* 1445–1455.

[623] Baldwin, R. R.; Stout, D. R.; Walker, R. W. *J. Chem. Soc. Faraday Trans.* **1991,** *87,* 2147–2150.

[624] Rienstra-Kiracofe, J. C.; Allen, W. D.; Schaefer III, H. F. *J. Phys. Chem. A* **2000,** *104,* 9823–9840.

[625] Miller, J. A.; Mitchell, R. E.; Smooke, M. D.; Kee, R. J. *Proc. Combust. Inst.* **1982,** *19,* 181–196.

[626] Hogg, A. M.; Kebarle, P. *J. Am. Chem. Soc.* **1964,** *86,* 4558–4562.

[627] Holt, P. M.; Kerr, J. A. *Int. J. Chem. Kinet.* **1977,** *9,* 185–200.

[628] Ahonkai, S. I.; Back, M. H. *Can. J. Chem.* **1988,** *66,* 578–583.

[629] Ahonkai, S. I.; Lin, X.-H.; Back, M. H. *Int. J. Chem. Kinet.* **1989,** *21,* 1–20.

[630] Zhang, H. X.; Back, M. H. *Int. J. Chem. Kinet.* **1990,** *22,* 21–35.

[631] Ervin, K. M.; DeTuri, V. F. *J. Phys. Chem. A* **2002,** *106,* 9947–9956.

[632] Fahr, A. *Int. J. Chem. Kinet.* **1995,** *27,* 769–776.

[633] Klippenstein, S. J.; Harding, L. B. *Phys. Chem. Chem. Phys.* **1999,** *1,* 989–997.

[634] Cattell, F. C.; Cavanagh, J.; Cox, R. A.; Jenkin, M. E. *J. Chem. Soc. Faraday Trans. 2* **1986,** *82,* 1999–2018.

[635] Dagaut, P.; Wallington, T. J.; Kurylo, M. J. *J. Phys. Chem.* **1988,** *92,* 3836–3839.

[636] Maricq, M. M.; Szente, J. J. *J. Phys. Chem.* **1994,** *98,* 2078–2082.

[637] Boyd, A. A.; Flaud, P.-M.; Daugey, N.; Lesclaux, R. *J. Phys. Chem. A* **2003,** *107,* 818–821.

[638] Nielsen, O. J.; Johnson, M. S.; Wallington, T. J.; Christensen, L. K.; Platz, J. *Int. J. Chem. Kinet.* **2002,** *34,* 283–291.

[639] Wallington, T. J.; Japar, S. M. *Chem. Phys. Lett.* **1990,** *166,* 495–499.

[640] Spittler, M.; Barnes, I.; Becker, K. H.; Wallington, T. J. *Chem. Phys. Lett.* **2000,** *321,* 57–61.

[641] Hasson, A. S.; Tyndall, G. S.; Orlando, J. J. *J. Phys. Chem. A* **2004,** *108,* 5979–5989.

[642] Hou, H.; Li, J.; Song, X.; Wang, B. *J. Phys. Chem. A* **2005,** *109,* 11206–11212.

[643] Adachi, H.; Basco, N.; James, D. G. L. *Int. J. Chem. Kinet.* **1979,** *11,* 1211–1229.

[644] Niki, H.; Maker, P. D.; Savage, C. M.; Breitenbach, L. P. *J. Phys. Chem.* **1982,** *86,* 3825–3829.

[645] Anastasi, C.; Waddington, D. J.; Woolley, A. *J. Chem. Soc., Faraday Trans. 1* **1983,** *79,* 505–516.

[646] Wallington, T. J.; Dagaut, P.; Kurylo, M. J. *J. Photochem. Photobiol. A: Chem.* **1988,** *19,* 173–185.

[647] Wallington, T. J.; Gierczak, C. A.; Ball, J. C.; Japar, S. M. *Int. J. Chem. Kinet.* **1989,** *21,* 1077–1089.

[648] Bauer, D.; Crowley, J. N.; Moortgat, G. K. *J. Photochem. Photobiol. A: Chem.* **1992,** *65,* 329–344.

[649] Atkinson, D. B.; Hudgens, J. W. *J. Phys. Chem. A* **1997,** *101,* 3901–3909.

[650] Kirk, A. D.; Knox, J. H. *Trans. Faraday Soc.* **1960,** *56,* 1296–1303.

[651] Batt, L. *Int. J. Chem. Kinet.* **1979,** *11,* 977–993.

[652] Batt, L.; McCulloch, R. D.; Milne, R. T. *Int. J. Chem. Kinet.* **1975,** *1,* 441–461.

[653] Choo, K. Y.; Benson, S. W. *Int. J. Chem. Kinet.* **1981,** *13,* 833–844.

[654] Zhang, Y.; Zhang, S.; Li, Q. S. *Chem. Phys.* **2004,** *296,* 79–86.

[655] Somnitz, H.; Zellner, R. *Phys. Chem. Chem. Phys.* **2000,** *2,* 1899–1905.

[656] Somnitz, H.; Zellner, R. *Phys. Chem. Chem. Phys.* **2000,** *2,* 1907–1918.

[657] Rauk, A.; Boyd, R. J.; Boyd, S. L.; Henry, D. J.; Radom, L. *Can. J. Chem.* **2003,** *81,* 431–442.

[658] Orlando, J. J.; Tyndall, G. S.; Wallington, T. J. *Chem. Rev.* **2003,** *103,* 4657–4689.

[659] Curran, H. J. *Int. J. Chem. Kinet.* **2006,** *38,* 250–275.

[660] Devolder, P.; Fittschen, C.; Frenzel, A.; Hippler, H.; Poskrebyshev, G.; Striebel, F.; Viskolcz, B. *Phys. Chem. Chem. Phys.* **1999,** *1,* 675–681.

[661] Fittschen, C.; Hippler, H.; Viskolcz, B. *Phys. Chem. Chem. Phys.* **2000,** *2,* 1677–1683.

[662] Pople, J. A.; Head-Gordon, M.; Raghavachari, K. *J. Chem. Phys.* **1987,** *87,* 5968–5976.

[663] Hartmann, D.; Karthauser, J.; Sawerysyn, J. P.; Zellner, R. *Ber. Bunsenges. Phys. Chem.* **1990,** *94,* 639–645.

[664] Zabarnick, S.; Heicklen, J. *Int. J. Chem. Kinet.* **1985,** *17,* 455–476.

[665] Setokuchi, O.; Sato, M. *J. Phys. Chem. A* **2002,** *106,* 8124–8132.

[666] Bartels, M.; Hoyermann, K.; Sievert, R. *Proc. Combust. Inst.* **1982,** *19,* 61–72.

[667] Grotheer, H.-H.; Riekert, G.; Walter, D.; Just, T. *Proc. Combust. Inst.* **1989,** *22,* 963–972.

[668] Edelbüttel-Einhaus, J.; Hoyermann, K.; Rohde, G.; Seeba, J. *Proc. Combust. Inst.* **1992,** *24,* 661–668.

[669] Laidler, K. J.; Liu, M. T. H. *Proc. Roy. Soc. Lond. A* **1967,** *297,* 365–375.

[670] Liu, M. T. H.; Laidler, K. J. *Can. J. Chem.* **1968,** *46,* 479–490.

[671] Colket, III, M. B.; Naegeli, D. W.; Glassman, I. *Int. J. Chem. Kinet.* **1975,** *7,* 223–247.

[672] Ernst, J.; Spindler, K. *Ber. Bunsenges. Phys. Chem.* **1975,** *79,* 1163–1168.

[673] Ernst, J.; Spindler, K.; Wagner, H. G. *Ber. Bunsenges. Phys. Chem.* **1976,** *80,* 645–650.

[674] Watkins, K. W.; Word, W. W. *Int. J. Chem. Kinet.* **1974,** *6,* 855–873.

[675] Anastasi, C.; Maw, P. R. *J. Chem. Soc., Faraday Trans. 1* **1982,** *78,* 2423–2433.

[676] Philip J. Baldwin and, C. E. C.; Frey, H. M.; Walsh, R. *int. J. Chem. Kinet.* **1987,** *19,* 997–1013.

[677] Bencsura, A.; Knyazev, V. D.; Slagle, I. R.; Gutman, D.; Tsang, W. *Ber. Bunsenges. Phys. Chem.* **1992,** *96,* 1338–1347.

[678] Glarborg, P.; Kubel, D.; Kristensen, P. G.; Hansen, J.; Dam-Johansen, K. *Combust. Sci. Tech.* **1995,** *111,* 461–485.

[679] Faravelli, T.; Frassoldati, A.; Ranzi, E. *Combust. Flame* **2003,** *132,* 188–207.

[680] Glarborg, P.; Dam-Johansen, K.; Miller, J. A. *Int. J. Chem. Kinet.* **1995,** *27,* 1207–1220.

[681] Allen, M. T.; Yetter, R. A.; Dryer, F. L. *Int. J. Chem. Kinet.* **1995,** *27,* 883–909.

[682] Skreiberg, Ø.; Kilpinen, P.; Glarborg, P. *Combust. Flame* **2004,** *136,* 501–518.

[683] Tsang, W.; Herron, J. *J. Phys. Chem. Ref. Data* **1991,** *20,* 609–663.

[684] Riley, P. S.; Cosic, B.; Fontijn, A. *Int. J. Chem. Kinet.* **2003,** *35,* 374–380.

[685] Fulle, D.; Hamann, H. F.; Hippler, H.; Troe, J. *J. Chem. Phys.* **1998,** *108,* 5391–5397.

[686] Davies, J. W.; Green, N. J. B.; Pilling, M. J. *J. Chem. Soc., Faraday Trans.* **1991,** *87,* 2317–2324.

[687] Friedrichs, G.; Berends, H.-M.; Colberg, M.; Dammeier, J. "*Shock Tube Study of the Reactions HCO+NO and HCO+NO_2 using Frequency Modulation Detection of HCO*", Poster 2D-11, 31st International Symposium on Combustion, Heidelberg, GER, 6-11th August 2006.

[688] Nesbitt, F. L.; Payne, W. A.; Stief, L. J. *J. Phys. Chem.* **1989,** *93,* 5158–5161.

[689] Caralp, F.; Rayez, M.-T.; Forst, W.; Gomez, N.; Delcroix, B.; Fittschen, C.; Devolder, P. *J. Chem. Soc., Faraday Trans.* **1998,** *94,* 3321–3330.

[690] Atkinson, R.; Baulch, D. L.; Cox, R. A.; Crowley, J. N.; Hampson, R. F.; Hynes, R. G.; Jenkin, M. E.; Rossi, M. J.; Troe, J. *Atmos. Chem. Phys.* **2006,** *6,* 3625–4055.

[691] Daële, V.; Ray, A.; Vassalli, I.; Poulet, G.; Le Bras, G. *Int. J. Chem. Kinet.* **1995,** *27,* 1121–1133.

[692] Ko, T.; Fontijn, A. *J. Phys. Chem.* **1991,** *95,* 3984–3987.

[693] Park, J.; Giles, N. D.; Moore, J.; Lin, M. C. *J. Phys. Chem. A* **1998,** *102,* 10099–10105.

[694] Bemand, P. P.; Clyne, M. A. A.; Watson, R. T. *J. Chem. Soc. Faraday Trans. 2* **1974,** *70,* 564–576.

[695] Hahn, J.; Luther, K.; Troe, J. *Phys. Chem. Chem. Phys.* **2000,** *2,* 5098–5104.

[696] Troe, J. *Int. J. Chem. Kinet.* **2001,** *33,* 878–889.

[697] Atkinson, R.; Baulch, D. L.; Cox, R. A.; Hampson, R. F.; Kerr, J. A.; Rossi, M. J.; Troe, J. *J. Phys. Chem. Ref. Data* **1997,** *26,* 1329–1499.

[698] Freund, H.; Palmer, H. B. *Int. J. Chem. Kinet.* **1977,** *9,* 887–905.

[699] Yamaguchi, Y.; Teng, Y.; Shimomura, S.; Tabata, K.; Suzuki, E. *J. Phys. Chem. A* **1999,** *103,* 8272–8278.

[700] Xu, Z. F.; Lin, M. C. *Int. J. Chem. Kinet.* **2003,** *35,* 184–190.

[701] McCaulley, J. A.; Anderson, S. M.; Jeffries, J. B.; Kaufman, K. *Chem. Phys. Lett.* **1985,** *115,* 180–186.

[702] Martínez, E.; Albaladejo, J.; Jiménez, E.; Notario, A.; Díaz de Mera, Y. *Chem. Phys. Lett.* **2000,** *329,* 191–199.

[703] Xiao, C.-X.; Yan, N.; Zou, M.; Hou, S.-C.; Kou, Y.; Liu, W.; Zhang, S. *J. Mol. Cat. A, Chem.* **2006,** *252,* 202–211.

[704] Frost, M. J.; Smith, I. W. M. *J. Chem. Soc., Faraday Trans.* **1990,** *86,* 1751–1756.

[705] Batt, L. *Int. Rev. Phys. Chem.* **1987,** *6,* 53–90.

[706] DeMore, W. B.; Sander, S. P.; Golden, D. M.; Hampson, R. F.; Kurylo, M. J.; Howard, C. J.; Ravishankara, A. R.; Kolb, C. E.; Molina, M. J. "*Chemical Kinetics and Photochemical Data for Use in Stratospheric Modeling, Evaluation No. 12*", Technical Report JPL–Publ–97–4, National Aeronautics and Space Administration, Jet Propulsion Laboratory, Pasadena, California, 1997.

[707] Becker, E.; Rahman, M. M.; Schindler, R. N. *Ber. Bunsenges. Phys. Chem.* **1992,** *96,* 776–783.

[708] DeMore, W. B.; Sander, S. P.; Goldena, D. M.; Molina, M. J.; Hampson, R. F.; Kurylo, M. J.; Howard, C. J.; Ravishankara, A. R. "*Chemical Kinetics and Photochemical Data for Use in Stratospheric Modeling, Evaluation No. 9*", Technical Report JPL–PUBL–90–1, National Aeronautics and Space Administration, Jet Propulsion Laboratory, Pasadena, California, 1990.

[709] Soto, M. R.; Page, M. *J. Chem. Phys.* **1992,** *97,* 7287–7296.

[710] Inomata, S.; Washida, N. *J. Phys. Chem. A* **1999,** *103,* 5023–5031.

[711] Soto, M. R.; Page, M.; McKee, M. L. *Chem. Phys.* **1991,** *153,* 415–426.

[712] Bryukov, M. G.; Kachanov, A. A.; Timonnen, R.; Seetula, J.; Vandoren, J.; Sarkisov, O. M. *Chem. Phys. Lett.* **1993,** *208,* 392–398.

[713] Mebel, A. M.; Lin, M. C.; Morokuma, K. *Int. J. Chem. Kinet.* **1998,** *30,* 729–736.

[714] Xu, Z. F.; Lin, M. C. *Int. J. Chem. Kinet.* **2004,** *36,* 205–215.

[715] He, Y.; Sanders, W. A.; Lin, M. C. *J. Phys. Chem.* **1988,** *92,* 5474–5481.

[716] Bendtsen, A. B.; Glarborg, P.; Dam-Johansen, K. *Chemometrics and Intelligent Lab. Sys.* **1998,** *44,* 357–366.

[717] Burkholder, J. B.; Mellouki, A.; Talukdar, R.; Ravishankara, A. R. *Int. J. Chem. Kinet.* **1992,** *24,* 711–725.

[718] Mebel, A. M.; Lin, M. C.; Melius, C. F. *J. Phys. Chem. A* **1998,** *102,* 1803–1807.

[719] Dean, A. M.; Bozzelli, J. W. Combustion Chemistry of Nitrogen. In ; Gardiner, Jr., W. C., Ed.; Springer-Verlag, NY: 2000; Chapter "Gas-Phase Combustion Chemistry", pages 125–341.

[720] Boughton, J. W.; Kristyan, S.; Lin, M. C. *Chem. Phys.* **1997,** *214,* 219–227.

[721] Lamb, J. J.; Mozurkewich, M.; Benson, S. W. *J. Phys. Chem.* **1984,** *88,* 6441–6448.

[722] Glänzer, K.; Troe, J. *Helv. Chim. Acta* **1972,** *55,* 2884–2893.

[723] Glänzer, K.; Troe, J. *Helv. Chim. Acta* **1973,** *56,* 577–585.

[724] Nielsen, O. J.; Sidebottom, H. W.; Donlon, M.; Treacy, J. *Int. J. Chem. Kinet.* **1991,** *23,* 1095–1109.

[725] Talukdar, R. K.; Herndon, S. C.; Burkholder, J. B.; Roberts, J. M.; Ravishankara, A. R. *J. Chem. Soc., Faraday Trans.* **1997,** *93,* 2787–2796.

[726] Clyne, M. A. A.; Thrush, B. A. *Trans. Faraday Soc.* **1961,** *57,* 1305–1314.

[727] Campbell, I. M.; Handy, B. J. *J. Chem. Soc. Faraday Trans. 1* **1975,** *71,* 2097–2106.

[728] Allen, M. T.; Yetter, R. A.; Dryer, F. L. *Combust. Flame* **1998,** *112,* 302–311.

[729] Glarborg, P.; Østberg, M.; Alzueta, M. U.; Dam-Johansen, K.; Miller, J. A. *Proc. Combust. Inst.* **1998,** *27,* 219–226.

[730] Endo, H.; Glänzer, K.; Troe, J. *J. Phys. Chem.* **1979,** *83,* 2083–2090.

[731] Yarwood, G.; Sutherland, J. W.; Wickramaaratchi, M. A.; Klemm, R. B. *J. Phys. Chem.* **1991,** *95,* 8771–8775.

[732] Röhrig, M.; Petersen, E. L.; Davidson, D. F.; Hanson, R. K. *Int. J. Chem. Kinet.* **1997,** *29,* 483–494.

[733] Hippler, H.; Siefke, M.; Stark, H.; Troe, J. *Phys. Chem. Chem. Phys.* **1999,** *1,* 57–61.

[734] Forster, R.; Frost, M.; Fulle, D.; Hamann, H. F.; Hippler, H.; Schlepegrell, A.; Troe, J. *J. Chem. Phys.* **1995,** *103,* 2949–2958.

[735] Sumathi, R.; Peyerimhoff, S. D. *J. Chem. Phys.* **1997,** *107,* 1872–1880.

[736] Glänzer, K.; Troe, J. *Ber. Bunsenges. Phys. Chem.* **1975,** *79,* 465–469.

[737] Leu, M.-T. *J. Chem. Phys.* **1979,** *70,* 1662–1666.

[738] Howard, C. J. *J. Chem. Phys.* **1979,** *71,* 2352–2359.

[739] Howard, C. J. *J. Am. Chem. Soc.* **1979,** *102,* 6937–6941.

[740] Hack, W.; Preuss, A. W.; Temps, F.; Wagner, H. G.; Hoyermann, K. *Int. J. Chem. Kinet.* **1980,** *12,* 851–860.

[741] Seeley, J. V.; Meads, R. F.; Elrod, M. J.; Molina, M. J. *J. Phys. Chem.* **1996,** *100,* 4026–4031.

[742] Bohn, B.; Zetzsch, C. *J. Phys. Chem. A* **1997,** *101,* 1488–1493.

[743] Wagner, H. G.; Welzbacher, U.; Zellner, R. *Ber. Bunsenges. Phys. Chem.* **1976,** *80,* 1023–1027.

[744] Clyne, M. A. A.; Monkhouse, P. B. *J. Chem. Soc. Faraday Trans. 2* **1977,** *73,* 298–309.

[745] Su, M.-C.; Kumaran, S. S.; Lim, K. P.; Michael, J. V.; Wagner, A. F.; Harding, L. B.; Fang, D.-C. *J. Phys. Chem. A* **2002,** *106,* 8261–8270.

[746] Michael, J. V.; Nava, D. F.; Payne, W. A.; Lee, J. H.; Stief, L. J. *J. Phys. Chem.* **1979,** *83,* 2818–2823.

[747] Nguyen, M. T.; Sumathi, R.; Sengupta, D.; Peeters, J. *Chem. Phys.* **1998,** *230,* 1–11.

[748] Atkinson, R.; Baulch, D. L.; Cox, R. A.; Hampson, R. F.; Kerr, J. A.; Troe, J. *J. Phys. Chem. Ref. Data* **1989,** *18,* 881–1097.

[749] Slack, M. W.; Grillo, A. R. *Combust. Flame* **1978,** *31,* 275–283.

[750] Mueller, M. A.; Gatto, J. L.; Yetter, R. A.; Dryer, F. L. *Combust. Flame* **2000,** *120,* 589–594 Communication.

[751] Hsu, C.-C.; Lin, M. C.; Mebel, A. M.; Melius, C. F. *J. Phys. Chem. A* **1997,** *101,* 60–66.

[752] Eckart, C. *Phys. Rev.* **1930,** *35,* 1303–1309.

[753] Dransfield, T. J.; Perkins, K. K.; Donahue, N. M.; Anderson, J. G.; Sprengnether, M. M.; Demerjian, K. L. *Geophys. Res. Lett.* **1999,** *26,* 687–690.

[754] D'Ottone, L.; Campuzano-Jost, P.; Bauer, D.; Hynes, A. J. *J. Phys. Chem. A* **2001,** *105,* 10538–10543.

[755] Hippler, H.; Nasterlack, S.; Striebel, F. *Phys. Chem. Chem. Phys.* **2002,** *4,* 2959–2964.

[756] Glänzer, K.; Troe, J. *Ber. Bunsenges. Phys. Chem.* **1974,** *78,* 71–76.

[757] Harrison, H.; Johnston, H. S.; Hardwick, E. R. *J. Am. Chem. Soc.* **1962,** *84,* 2478–2482.

[758] Golden, D. M.; Smith, G. P. *J. Phys. Chem. A* **2000,** *104,* 3991–3997.

[759] Donahue, N. M.; Mohrschladt, R.; Dransfield, T. J.; Anderson, J. G.; Dubey, M. K. *J. Phys. Chem. A* **2001,** *105,* 1515–1520.

[760] Hori, M.; Matsunaga, N.; Marinov, N.; Pitz, W.; Westbrook, C. *Proc. Combust. Inst.* **1998,** *27,* 389–396.

[761] Tyndall, G. S.; Orlando, J. J.; Calvert, J. G. *Environ. Sci. Technol.* **1995,** *29,* 202–206.

[762] Chan, W.-T.; Pritchard, H. O. *Phys. Chem. Chem. Phys.* **2002,** *4,* 557–560.

[763] Gierczak, T.; Jiménez, E.; Riffault, V.; Burkholder, J. B.; Ravishankara, A. R. *J. Phys. Chem. A* **2005,** *109,* 586–596.

[764] Olbregts, J. *Int. J. Chem. Kinet.* **1985,** *17,* 835–848.

[765] Markwalder, B.; Gozel, P.; van der Bergh, H. *J. Phys. Chem.* **1993,** *97,* 5260–5265.

[766] Borrell, P.; Cobos, C. J.; Luther, K. *J. Phys. Chem.* **1988,** *92,* 4377–4384.

[767] Milks, D.; Adams, T. N.; Matula, R. A. *Combust. Sci. Technol.* **1979,** *19,* 151–159.

[768] Palmer, H. B.; Freund, H. *Combust. Sci. Technol.* **1980,** *21,* 179–180 Short Communication.

[769] Brown, F. B.; Crist, R. H. *J. Chem. Phys.* **1941,** *9,* 840–846.

[770] Johnston, H. S.; Bonner, W. A.; Wilson, D. J. *J. Chem. Phys.* **1957,** *26,* 1002–1006.

[771] Thomas, J. H.; Woodman, G. R. *Trans. Faraday Soc.* **1967,** *63,* 2728–2736.

[772] Burcat, A.; Lifshitz, A. *J. Phys. Chem.* **1970,** *74,* 263–268.

[773] Tabata, K.; Teng, Y.; Yamaguchi, Y.; Sakurai, H.; Suzuki, E. *J. Phys. Chem. A* **2000,** *104,* 2648–2654.

[774] Chan, W.-T.; Heck, S. M.; Pritchard, H. O. *Phys. Chem. Chem. Phys.* **2001,** *3,* 56–62.

[775] Richter, F.; Hochlaf, M.; Rosmus, P.; Gatti, F.; Meyer, H.-D. *J. Chem. Phys.* **2004,** *120,* 1306–1317.

[776] Slack, M. W.; Grillo, A. R. *Proc. Int. Symp. Shock Tubes Waves* **1978,** *11,* 408.

[777] Slack, M. W.; Grillo, A. R. *Combust. Flame* **1981,** *40,* 155–172.

[778] McKee, M. L. *J. Am. Chem. Soc.* **1986,** *108,* 5784–5792.

[779] Melius, C. F. Chemistry and Physics of Energetic Materials. In ; Bulusu, S. N., Ed.; Kluwer Academic Publisher: 1990; Chapter "Thermochemical Modeling. 1. Application to Decomposition of Energetic Materials", pages 21–49.

[780] Saxon, R. P.; Yoshimine, M. *Can. J. Chem.* **1992,** *70,* 572–579.

[781] Zhang, Y.-X.; Bauer, S. H. *Int. J. Chem. Kinet.* **1999,** *31,* 655–673.

[782] Glänzer, K.; Troe, J. *Ber. Bunsenges. Phys. Chem.* **1974,** *78,* 182–184.

[783] Yamada, F.; Slagle, I. R.; Gutman, D. *Chem. Phys. Lett.* **1981,** *83,* 409–412.

[784] Biggs, P.; Canosa-Mas, C. E.; Fracheboud, J. M.; Parr, A. D.; Shallcross, D. E.; Wayne, R. P.; Caralp, F. *J. Chem. Soc., Faraday Trans.* **1993,** *89,* 4163–4169.

[785] Hillenbrand, Jr., L. J.; Kilpatrick, M. L. *J. Chem. Phys.* **1953,** *21,* 525–535.

[786] Makovky, A.; Gruenwald, T. B. *Trans. Faraday Soc.* **1959,** *55,* 952–958.

[787] Crawforth, C. G.; Waddington, D. J. *Trans. Faraday Soc.* **1969,** *65,* 1334–1349.

[788] Guirguis, R.; Hsu, D.; Bogan, D.; Oran, E. *Combust. Flame* **1985,** *61,* 51–62.

[789] Hsu, D. S. Y.; Lin, M. C. *J. Energ. Mater.* **1985,** *3,* 95–127.

[790] Zaslonko, I. S.; Petrov, Y. P.; Smirnov, V. N. *Kinet. Catal. (tr. of Kinet. Katal.)* **1997,** *38,* 321–324.

[791] Zhang, Y.-X.; Bauer, S. H. *J. Phys. Chem. B* **1997,** *101,* 8717–8726.

[792] Wollenhaupt, M.; Crowley, J. N. *J. Phys. Chem. A* **2000,** *104,* 6429–6438.

[793] Cottrell, T. L.; Graham, T. E.; Reid, T. J. *Trans. Faraday Soc.* **1951,** *47,* 1088–1092.

[794] Wilde, K. A. *Ind. Eng. Chem.* **1956,** *48,* 769–773.

[795] Wilde, K. A. *J. Phys. Chem.* **1957,** *61,* 385–388.

[796] Dubikhin, V. V.; Nazin, G. M.; Manelis, G. B. *Bull. Acad. Sci. USSR Div. Chem. Sci. (Engl. Transl.)* **1971,** *7,* 1412.

[797] Canosa, C.; Penzhorn, R.-D.; von Sonntag, C. *Ber. Bunsenges. Phys. Chem.* **1979,** *83,* 217–225.

[798] Pilling, M. J.; Robertson, J. A.; Rogers, G. J. *Int. J. Chem. Kinet.* **1976,** *8,* 883–896.

[799] Van den Bergh, H. E.; Callear, A. B. *Trans. Faraday Soc.* **1971,** *67,* 2017.

[800] Wallington, T. J.; Maricq, M. M.; Ellermann, T.; Nielsen, O. J. *J. Phys. Chem.* **1992,** *96,* 982–986.

[801] Jodkowski, J. T.; Ratajczak, E.; Sillesen, A.; Pagsberg, P. *Chem. Phys. Lett.* **1993,** *203,* 490–496.

[802] Frost, M. J.; Smith, I. W. M. *J. Chem. Soc., Faraday Trans.* **1990,** *86,* 1757–1762.

[803] McCaulley, J. A.; Moyle, A. M.; Golde, M. F.; Anderson, S. M.; Kaufman, F. *J. Chem. Soc., Faraday Trans.* **1990,** *86,* 4001–4009.

[804] Ohmori, K.; Yamasaki, K.; Matsui, H. *Bull. Chem. Soc. Jpn.* **1993,** *66,* 51–56.

[805] Dóbé, S.; Lendvay, G.; Szilágyi, I.; Bérces, T. *Int. J. Chem. Kinet.* **1994,** *26,* 887–901.

[806] Batt, L.; Milne, R. T.; McCulloch, R. D. *Int. J. Chem. Kinet.* **1977,** *9,* 567–587.

[807] Hsu, D. S. Y.; Burks, G. L.; Beebe, M. D.; Lin, M. C. *Int. J. Chem. Kinet.* **1984,** *16,* 1139–1150.

[808] Baker, G.; Shaw, R. *J. Chem. Soc.* **1965,** *Dec.,* 6965.

[809] Zhao, Y.; Houk, K. N.; Olson, L. P. *J. Phys. Chem. A* **2004,** *108,* 5864–5871.

[810] Lesar, A.; Hodoek, M.; Drougas, E.; Kosmas, A. M. *J. Phys. Chem. A* **2006,** *110,* 7898–7903.

[811] Simonaitis, R.; Heicklen, J. *J. Phys. Chem.* **1981,** *85,* 2946–2949.

[812] Scholtens, K. W.; Messer, B. M.; Cappa, C. D.; Elrod, M. J. *J. Chem. Phys. A* **1999,** *103,* 4378–4384.

[813] Villalta, P. W.; Huey, L. G.; Howard, C. J. *J. Phys. Chem.* **1995,** *99,* 12829–12834.

[814] Bacak, A.; Bardwell, M. W.; Raventos, M. T.; Percival, C. J.; Sanchez-Reyna, G.; Shallcross, D. E. *J. Phys. Chem. A* **2004,** *108,* 10681–10687.

[815] Atkinson, R.; Aschmann, S. M.; Carter, W. P. L.; Winer, A. M.; Pitts, J. N. *J. Phys. Chem.* **1982,** *86,* 4563–4569.

[816] Ranschaert, D. L.; Schneider, N. J.; Elrod, M. J. *J. Phys. Chem. A* **2000,** *104,* 5758–5765.

[817] Plumb, I. C.; Ryan, K. R.; Steven, J. R.; Mulcahy, M. F. R. *J. Phys. Chem.* **1981,** *85,* 3136–3138.

[818] Ravishankara, A. R.; Eisele, F. L.; Kreutter, N. M.; Wine, P. H. *J. Chem. Phys.* **1981,** *74,* 2267–2274.

[819] Zellner, R.; Fritz, B.; Lorenz, K. *J. Atmos. Chem.* **1986,** *4,* 241–251.

[820] Sehested, J.; Nielsen, O. J.; Wallington, T. J. *Chem. Phys. Lett.* **1993,** *213,* 457–464.

[821] Helleis, F.; Moortgat, G. K.; Crowley, J. N. *J. Phys. Chem.* **1996,** *100,* 17846–17854.

[822] Plumb, I. C.; Ryan, K. R.; Steven, J. R.; Mulcahy, M. F. R. *Int. J. Chem. Kinet.* **1982,** *14,* 183–194.

[823] Eberhard, J.; Howard, C. J. *Int. J. Chem. Kinet.* **1996,** *28,* 731–740.

[824] Maricq, M. M.; Szente, J. J. *J. Phys. Chem.* **1996,** *100,* 12374–12379.

[825] Anastasi, C.; Hancock, D. U. *J. Chem. Soc., Faraday Trans. 2* **1988,** *84,* 1697–1706.

[826] Koda, S.; Tanaka, M. *Combust. Sci. Tech.* **1986,** *47,* 165–176.

[827] Teng, Y.; Yamaguchi, Y.; Takemoto, T.; Tabata, K.; Suzuki, E. *Phys. Chem. Chem. Phys.* **2000,** *2,* 3429–3433.

[828] McGraw, G. E.; Johnston, H. S. *Int. J. Chem. Kinet.* **1969,** *1,* 89–104.

[829] Zhang, J.-X.; Ze-Sheng Li and, J.-Y. L.; Sun, C.-C. *J. Phys. Chem. A* **2006,** *110,* 2690–2697.

[830] He, Y.; Kolby, E.; Shumaker, P.; Lin, M. C. *Int. J. Chem. Kinet.* **1989,** *21,* 1015–1027.

[831] Lin, C.-Y.; Wang, H.-T.; Lin, M. C.; Melius, C. F. *Int. J. Chem. Kinet.* **1990,** *22,* 455–482.

[832] Xu, Z. F.; Hsu, C.-H.; Lin, M. C. *J. Chem. Phys.* **2005,** *122,* 234308.

[833] Laidler, K. J.; Sagert, N. H.; Wojciechowski, B. W. *Proc. Roy. Soc. London, Ser. A* **1962,** *270,* 254–266.

[834] Montgomery, Jr., J. A.; Frisch, M. J.; Ochterski, J. W.; Petersson, G. A. *J. Chem. Phys.* **1999,** *110,* 2822–2827.

[835] Koch, T. G.; Sodeau, J. R. *J. Phys. Chem.* **1995,** *99,* 10824–10829.

[836] Fifer, R. A. *J. Phys. Chem.* **1976,** *80,* 2717–2723.

[837] Jenkin, M. E.; Cox, R. A. *Chem. Phys. Lett.* **1987,** *137,* 548–552.

[838] Wayne, L. G.; Yost, D. M. *J. Chem. Phys.* **1951,** *19,* 41–47.

[839] Graham, R. F.; Tyler, B. J. *J. Chem. Soc. Faraday Trans. 1* **1972,** *68,* 683–688.

[840] England, C.; Corcoran, W. H. *Ind. Eng. Chem. Fundam.* **1975,** *14,* 55–63.

[841] Chan, W. H.; Nordstrom, R. J.; Calvert, J. G.; Shaw, J. H. *Environ. Sci. Technol.* **1976,** *10,* 674–682.

[842] Kaiser, E. W.; Wu, C. H. *J. Phys. Chem.* **1977,** *81,* 1701–1706.

[843] Ten Brink, H. M.; Spoelstra, H. *Atmos. Environ.* **1998,** *32,* 247–251 Technical Note.

[844] Syomin, D. A.; Finlayson-Pitts, B. J. *Phys. Chem. Chem. Phys.* **2003,** *5,* 5236–5242.

[845] Thomsen, E. L.; Nielsen, O. J.; Egsgaard, H. *Chem. Phys. Lett.* **1993,** *215,* 257–263.

[846] Nielsen, O. J.; Sidebottom, H. W.; O'Farrell, D. J.; Donlon, M.; Treacy, J. *Chem. Phys. Lett.* **1988,** *146,* 197–203.

[847] Nielsen, O. J.; Sidebottom, H. W.; O'Farrell, D. J.; Donlon, M.; Treacy, J. *Chem. Phys. Lett.* **1989,** *156,* 312–318.

[848] Liu, R.; Huie, R. E.; Kurylo, M. J.; Nielsen, O. J. *Chem. Phys. Lett.* **1990,** *167,* 519–523.

[849] Shallcross, D. E.; Biggs, P.; Canosa-Mas, C. E.; Clemitshaw, K. C.; Harrison, M. G.; Alanon, M. R. L.; Pyle, J. A.; Vipond, A.; Wayne, R. P. *J. Chem. Soc., Faraday Trans.* **1997,** *93,* 2807–2811.

[850] Nielsen, O. J.; Sidebottom, H. W.; Donlon, M.; Treacy, J. *Chem. Phys. Lett.* **1991,** *178,* 163–170.

[851] Webster, P.; Walsh, A. D. *Proc. Combust. Inst.* **1965,** *10,* 463–472.

[852] Fenimore, C. P.; Jones, G. W. *J. Phys. Chem.* **1965,** *69,* 3593–3597.

[853] Halstead, C. J.; Jenkins, D. R. *Trans. Faraday Soc.* **1969,** *65,* 3013–3022.

[854] Kallend, A. S. *Combust. Flame* **1969,** *13,* 324–327.

[855] Durie, R. A.; Johnson, G. M.; Smith, M. Y. *Combust. Flame* **1971,** *17,* 197–203.

[856] Kallend, A. S. *Combust. Flame* **1972,** *19,* 227–236.

[857] Smith, O. I.; Wang, S. N.; Tseregounis, S.; Westbrook, C. K. *Combust. Sci. Tech.* **1983,** *30,* 241–271.

[858] Zachariah, M. R.; Smith, O. I. *Combust. Flame* **1987,** *69,* 125–139.

[859] Sendt., K.; Jazbec, M.; Haynes, B. S. *Proc. Combust. Inst.* **2002,** *29,* 2439–2446.

[860] Nikisha, L. V.; Polyak, S. S.; Arutyunov, V. S.; Vedeneev, V. I. *Kinet. Katal.* **1992,** *33,* 1010–1015.

[861] Arutyunov, V. S.; Vedeneev, V. I.; Nikisha, L. V.; Polyak, S. S.; Romanovich, L. B.; Sokolov, O. V. *Kinet. Katal.* **1993,** *34,* 223–226.

[862] Chernysheva, A. V.; Arutyunov, V. S.; Basevich, V. Y.; Vedeneev, V. I. *Khim. Fizikal.* **1994,** *13,* 71–85.

[863] Burgess, D.; Racek, J. "*NIST XSenkplot – An Interactive, Graphics Postprocesser for Numerical Simulations of Chemical Kinetics*", 1996 Chemical Science and Technology Laboratory, National Institute of Standards and Technology.

[864] Jakobsen, J. G. "Direct Conversion of Natural Gas to Liquid Fuels", Master's thesis, Department of Chemical Engineering, Technical University of Denmark, DK-2800 Kgs. Lyngby, 2006.

[865] Glarborg, P.; Johnsson, J. E.; Dam-Johansen, K. *Combust. Flame* **1994,** *99,* 523-532.

[866] Bromly, J. H.; Barnes, F. J.; Nelson, P. F.; Haynes, B. S. *Int. J. Chem. Kinet* **1995,** *27,* 1165–1178.

[867] Glarborg, P.; Kristensen, P. G.; Dam-Johansen, K.; Alzueta, M. U.; Millera, A.; Bilbao, R. *Energy Fuels* **2000,** *141,* 828–838.

[868] Glarborg, P.; Kubel, D.; Dam-Johansen, K.; Chiang, H.-M.; Bozzelli, J. W. *Int. J. Chem. Kin.* **1996,** *28,* 773–790.

[869] Mueller, M. A.; Yetter, R. A.; Dryer, F. L. *Int. J. Chem. Kinet.* **2000,** *32,* 317–339.

[870] Hindiyarti, L.; Frandsen, F.; Livbjerg, H.; Glarborg, P. *Fuel* **2006,** *85,* 978–988.

[871] Ashman, P.; Haynes, B. *Proc. Combust. Inst.* **1998,** *27,* 185.

[872] Mueller, M. A.; Yetter, R. A.; Dryer, F. L. *Proc. Combust. Inst.* **1998,** *27,* 117–184.

[873] Pirraglia, A. N.; Michael, J. V.; Sutherland, J. W.; Klemm, R. B. *J. Phys. Chem.* **1989,** *93,* 282–291.

[874] Bates, R. W.; Golden, D. M.; Hanson, R. K.; Bowman, C. T. *Phys. Chem. Chem. Phys.* **2001,** *3,* 2337–2342.

[875] Hwang, S. M.; Ryu, S.-O.; De Witt, K. J.; Rabinowitz, M. J. *Chem. Phys. Lett.* **2005,** *408,* 107–111.

[876] Hahn, J.; Krasnoperov, L.; Luther, K.; Troe, J. *Phys. Chem. Chem. Phys.* **2004,** *6,* 1997–1999.

[877] Scire, Jr., J. J.; Dryer, F. L.; Yetter, R. A. *Int. J. Chem. Kinet.* **2001,** *33,* 784–802.

[878] Shiina, H.; Miyoshi, A.; Matsui, H. *J. Phys. Chem. A* **1998,** *102,* 3556–3559.

[879] Cullis, C. F.; Mulcahy, M. R. F. *Combust. Flame* **1972,** *18,* 225–292.

[880] Moore, R. A. *Interval Analysis;* Prentice-Hall, Englewood Cliffs N. J.: 1966.

[881] Kearfott, R. B. *Euromath Bulletin* **1996,** *2,* 95–112.

[882] Caprani, O.; Madsen, K.; Nielsen, H. B. "Introduction to Interval Analysis", Informatics and Mathematical Modelling, Technical University of Denmark, DK–2800 Kgs. Lyngby, Nov. 2002, Lecture Notes, `http://www2.imm.dtu.dk/pubdb/p.php?1462`.

[883] "ANSI/IEEE 754-1985 Standard for Binary Floating-Point Arithmetic", 1985, IEEE (Institute of Electrical and Electronics Engineers, Inc.).

[884] Rump, S. M. Developments in Reliable Computing. In ; Csendes, T., Ed.; Kluwer Academic Publisher: 1999; Chapter "INTLAB – Interval Laboratory", pages 77–104.

[885] "INTLAB – INTerval LABoratory", Copyright ©1998–2006, Siegfried M. Rump @ Hamburg University of Technology, Institute for Reliable Computing, `http://www.ti3.tu-harburg.de/~rump/intlab/index.html`, 2006, Freeware for academic and private use.

[886] Lawson, C. L.; Hanson, R. J.; Kincaid, D. R.; Krogh, F. T. *ACM Trans. Math. Software* **1979,** *5,* 308–323.

[887] Dongarra, J. J.; Du Croz, J.; Hammarling, S.; Hanson, R. J. *ACM Trans. Math. Software* **1988,** *14,* 1–17.

[888] Dongarra, J. J.; Du Croz, J.; Hammarling, S.; Duff, I. S. *ACM Trans. Math. Software* **1990,** *16,* 1–17.

[889] Madsen, K. "*Parallel Algorithms for Global Optimization*", Technical Report 91–07, Department of Informatics and Mathematical Modelling, DK-2880 Kgs. Lyngby, Denmark, 1991.

[890] Henriksen, T.; Madsen, K. *Interval Computations* **1992,** *3,* 88–95.

[891] Moore, R. E.; Ratschek, H. *Mathematical Programming* **1988,** *41,* 341–356.

[892] Personal Communication, Kaj Madsen, Prof., Department of Informatics and Mathematical Modelling, Technical University of Denmark, DK-2800 Kgs. Lyngby, 2007.

[893] Agrawal, R.; Herron, D. M.; Rowles, H. C.; Kinard, G. E. Encyclopedia of Chemical Technology, Vol. 8. In , 5th ed.; Kroschwitz, J. I., Ed.; John Wiley & Sons, Inc., Publications: 2004; Chapter "Cryogenic Technology", pages 43–48.

[894] Dee, D. P.; Chiang, R. L.; Miller, E. J.; Whitley, R. D. *United States Patent* **2003,** *6,544,318,* Air Products and Chemicals, Inc.

[895] Santos, J. C.; Cruz, P.; Regala, T.; Magalhães, F. D.; Mendes, A. *Ind. Eng. Chem. Res.* **2007,** *46,* 591–599.

[896] Baker, R. W. *Ind. Eng. Chem. Res.* **2002,** *41,* 1393–1411.

[897] Peters, M. S.; Timmerhaus, K. D.; West, R. E. *Plant Design and Economics for Chemical Engineers;* McGraw-Hill: 5th ed.; 2003.

[898] Laso, M.; von Stockar, U. Encyclopedia of Chemical Technology, Vol. 1. In , 5th ed.; Kroschwitz, J. I., Ed.; John Wiley & Sons, Inc., Publications: 2004; Chapter "Absorption", pages 26–99.

[899] Spillman, R. W. *Chem. Eng. Sci.* **1989,** *85,* 41–62.

[900] Krsyszkowski, L. *British Patent* **1950,** *643,431,* Power Gas Ltd.

[901] Deringer, H. *United States Patent* **1952,** *2,580,527,* Sulzer AG.

[902] Blauwhoff, P. M. M.; Versteeg, G. F.; van Swaaij, W. P. M. *Chem. Eng. Sci.* **1984,** *39,* 207–225.

[903] Gabrielsen, J.; Michelsen, M. L.; Stenby, E. H.; Kontogeorgis, G. M. *Ind. Eng. Chem. Res.* **2005,** *44,* 3348–3354.

[904] Gabrielsen, J.; Michelsen, M. L.; Stenby, E. H.; Kontogeorgis, G. M. *AIChE J.* **2006,** *52,* 3443–3451.

[905] Li, S.; Falconer, J. L.; Noble, R. D. *J. Membr. Sci.* **2004,** *241,* 121–135.

[906] Li, S.; Falconer, J. L.; Noble, R. D.; Krishna, R. *J. Phys. Chem. C* **2007,** *111,* 5075–5082.

[907] Sebastián, V.; Kumakiri, I.; Bredesen, R.; Menéndez, M. *J. Membr. Sci.* **2007,** *292,* 92–97.

[908] Ismail, A. F.; Yaacob, N. *J. Membr. Sci.* **2006,** *275,* 151–165.

[909] Datta, A. K.; Sen, P. K. *J. Membr. Sci.* **2006,** *283,* 291–300.

[910] "INOGATE Map of Natural Gas Pipelines", INOGATE Programme (Interstate Oil and Gas Transport to Europe), `http://www.inogate.org/en/resources/map_gas`, June 2007, Technical Secretariat Kiev, Ukraine.

Appendix

Appendix A

SO_2 Reaction Mechanism (Rasmussen *et al.*, 2007)

The enclosed paper by Rasmussen *et al.* [114] encompasses the theoretical work conducted in the field of detailed sulfur chemistry in combustion. The reaction mechanism presented in the paper constitutes a supplement to the detailed chemical kinetic model presented in Chapter 5 of this thesis.

The paper was presented by C. L. Rasmussen at the *31st International Symposium on Combustion* in Heidelberg, 2006. The author acknowledges the contributing work and support of Peter Glarborg and Paul Marshall.

Available online at www.sciencedirect.com
ScienceDirect
ELSEVIER
Proceedings of the Combustion Institute 31 (2007) 339–347
Proceedings of the Combustion Institute
www.elsevier.com/locate/proci

Mechanisms of radical removal by SO_2

Christian Lund Rasmussen [a], Peter Glarborg [a,*], Paul Marshall [b]

[a] *Department of Chemical Engineering, Technical University of Denmark, DK-2800 Kgs. Lyngby, Denmark*
[b] *Department of Chemistry, University of North Texas, Denton, TX 76203-5070, USA*

Abstract

It is well established from experiments in premixed, laminar flames, jet-stirred reactors, flow reactors, and batch reactors that SO_2 acts to catalyze hydrogen atom removal at stoichiometric and reducing conditions. However, the commonly accepted mechanism for radical removal, $SO_2 + H(+M) \rightleftharpoons HOSO(+M)$, $HOSO + H/OH \rightleftharpoons SO_2 + H_2/H_2O$, has been challenged by recent theoretical and experimental results. Based on *ab initio* calculations for key reactions, we update the kinetic model for this chemistry and re-examine the mechanism of fuel/SO_2 interactions. We find that the interaction of SO_2 with the radical pool is more complex than previously assumed, involving HOSO and SO, as well as, at high temperatures also HSO, SH, and S. The revised mechanism with a high rate constant for $H + SO_2$ recombination and with $SO + H_2O$, rather than $SO_2 + H_2$, as major products of the $HOSO + H$ reaction is in agreement with a range of experimental results from batch and flow reactors, as well as laminar flames.

Keywords: Sulfur chemistry; Inhibition; Kinetics

1. Introduction

The presence of SO_2 has been reported to catalyze H atom removal at medium to high temperatures in rich, premixed laminar flames [1–7] and laboratory reactors [8,9]. The mechanism for radical removal is commonly recognized to be of the type, $X + SO_2 + M \rightarrow XSO_2 + M$, $Y + XSO_2 \rightarrow XY + SO_2$, where X and Y may be H, O, or OH. The most important radical removal cycle under stoichiometric and reducing conditions is believed to be initiated by recombination of SO_2 with H to form an H/SO_2 adduct

$$SO_2 + H + M \rightleftharpoons H/SO_2 + M$$

followed by recycling of this adduct to SO_2 by reaction with H or OH. The H/SO_2 adduct is most likely HOSO, which is thermally more stable than the HSO_2 isomer,

$$SO_2 + H(+M) \rightleftharpoons HOSO(+M) \quad (R9)$$
$$HOSO + H \rightleftharpoons SO_2 + H_2 \quad (R27)$$
$$HOSO + OH \rightleftharpoons SO_2 + H_2O \quad (R29)$$

The reaction numbers refer to the listing in Table 1. This sequence of reactions has been proposed to be the principal radical sink in fuel-rich flames doped with SO_2 [2,5,7]. However, due to uncertainty in the $H+SO_2$ reaction rate and in the fate of the HOSO intermediate, the mechanism of inhibition is still in question. There are no direct measurements of the $H + SO_2$ recombination rate at high temperatures. Theoretical work [10–12] as well as values deduced from flames [13], batch reactor [8], and flow reactor experiments [9] imply that the reaction is comparatively fast, while other experimental results indicate a much slower reaction [14]. Regarding HOSO, recent theoretical

* Corresponding author. Fax: +45 4588 2258.
E-mail address: pgl@kt.dtu.dk (P. Glarborg).

1540-7489/$ - see front matter © 2006 Published by Elsevier Inc. on behalf of The Combustion Institute.
doi:10.1016/j.proci.2006.07.249

Table 1
Selected reactions from the H/S/O subset

	Reaction	A	β	E_a	Reference
1.	$^3SO + H + M \rightleftharpoons HSO + M^a$	1.9×10^{20}	−1.31	662	est, Troe formalism
2.	$^3SO + O(+M) \rightleftharpoons SO_2(+M^a)$	3.2×10^{13}	0.0	0	[14]
	Low pressure limit:	1.2×10^{21}	−1.54	0	
	Troe parameters: 0.55 10^{-30} 10^{30}				
3.	$^3SO + OH \rightleftharpoons SO_2 + H$	1.1×10^{17}	−1.35	0	[20]
4.	$^3SO + OH(+M) \rightleftharpoons HOSO(+M^a)$	1.6×10^{12}	0.50	−400	[10]
	Low pressure limit:	9.5×10^{27}	−3.48	970	
5.	$^3SO + O_2 \rightleftharpoons SO_2 + O$	7.6×10^{3}	2.37	2970	[21]
6.	$^3SO + HO_2 \rightleftharpoons SO_2 + OH$	3.7×10^{3}	2.42	7660	est, *ab initio*/TST
7.	$^1SO + M \rightleftharpoons {}^3SO + M$	1.0×10^{13}	0.0	0	est
8.	$^1SO + O_2 \rightleftharpoons SO_2 + O$	1.0×10^{13}	0.0	0	est
9.	$SO_2 + H(+M) \rightleftharpoons HOSO(+M^a)$	2.4×10^{8}	1.63	7340	[12]
	Low pressure limit:	1.8×10^{37}	−6.14	11070	
	Troe parameters: 0.283 272 3995				
10.	$SO_2 + H(+M) \rightleftharpoons HSO_2(+M^a)$	5.3×10^{8}	1.59	2470	[12]
	Low pressure limit:	1.4×10^{31}	−5.19	4510	
	Troe parameters: 0.390 167 2191				
11.	$SO_2 + O(+M) \rightleftharpoons SO_3(+M^a)$	3.7×10^{11}	0.0	1689	[22]
	Low pressure limit:	2.4×10^{27}	−3.60	5186	
	Troe parameters: 0.442 316 7442				
	$SO_2 + O(+N_2) \rightleftharpoons SO_3(+N_2)$	3.7×10^{11}	0.0	1689	[22,23]
	Low pressure limit:	2.9×10^{27}	−3.58	5206	
	Troe parameters: 0.43 371 7442				
12.	$SO_2 + OH(+M) \rightleftharpoons HOSO_2(+M^a)$	5.7×10^{12}	−0.27	0	[17]
	Low pressure limit:	1.7×10^{27}	−4.09	0	
	Troe parameters: 0.10 10^{-30} 10^{30}				
13.	$SO_2 + CO \rightleftharpoons {}^3SO + CO_2$	1.9×10^{13}	0.0	65900	[24]
14.	$SO_2 + S \rightleftharpoons {}^3SO + {}^3SO$	6.0×10^{-16}	8.21	9600	[25]
15.	$SO_3 + H \rightleftharpoons SO_2 + OH$	5.5×10^{10}	0.99	3740	est, *ab initio*/TST
16.	$SO_3 + O \rightleftharpoons SO_2 + O_2$	7.8×10^{11}	0.0	6100	[23,26]
17.	$SO_3 + {}^3SO \rightleftharpoons SO_2 + SO_2$	7.6×10^{3}	2.37	2980	[27]
18.	$HSO + H \rightleftharpoons {}^3SO + H_2$	1.0×10^{13}	0.0	0	est
19.	$HSO + H \rightleftharpoons SH + OH$	4.9×10^{19}	−1.86	1560	[16]
20.	$HSO + H \rightleftharpoons S + H_2O$	1.6×10^{9}	1.37	−340	[16]
21.	$HSO + O \rightleftharpoons SO_2 + H$	4.5×10^{14}	−0.40	0	[16]
22.	$HSO + O \rightleftharpoons {}^3SO + OH$	1.4×10^{13}	0.15	300	[16]
23.	$HSO + O_2 \rightleftharpoons HSO_2 + O$	8.4×10^{-7}	5.10	11312	est, *ab initio*/TST
24.	$HSO + OH \rightleftharpoons {}^3SO + H_2O$	1.7×10^{9}	1.03	470	[16]
25.	$HOSO(+M) \rightleftharpoons HSO_2(+M^a)$	1.0×10^{9}	1.03	50000	[10]
	Low pressure limit:	1.7×10^{35}	−5.64	55400	
	Troe parameters: 0.40 10^{-30} 10^{30}				
26.	$HOSO + H \rightleftharpoons {}^1SO + H_2O$	2.4×10^{14}	0.0	0	[15]
27.	$HOSO + H \rightleftharpoons SO_2 + H_2$	1.8×10^{7}	1.72	−1286	[15]
28.	$HOSO + O_2 \rightleftharpoons SO_2 + HO_2$	9.6×10^{1}	2.36	−10130	est, *ab initio*/TST ($T > 800$ K)
29.	$HOSO + OH \rightleftharpoons SO_2 + H_2O$	6.0×10^{12}	0.0	0	est, see text
30.	$HSO_2 + H \rightleftharpoons SO_2 + H_2$	5.0×10^{12}	0.46	−262	[15]
31.	$HSO_2 + O_2 \rightleftharpoons SO_2 + HO_2$	1.1×10^{3}	3.20	−235	est, *ab initio*/TST
32.	$HSO_2 + OH \rightleftharpoons SO_2 + H_2O$	1.0×10^{13}	0.0	0	est
33.	$HOSO_2 + O_2 \rightleftharpoons SO_3 + HO_2$	7.8×10^{11}	0.0	656	[28]
34.	$SH + O \rightleftharpoons {}^3SO + H$	1.0×10^{14}	0.0	0	[14]
35.	$S + OH \rightleftharpoons {}^3SO + H$	4.0×10^{13}	0.0	0	[29]
36.	$S + H_2 \rightleftharpoons SH + H$	1.4×10^{14}	0.0	19300	[30]

Units are mol, cm, s, and cal.
[a] Enhanced third-body efficiencies: $N_2 = 1.5$, $SO_2 = 10$, $H_2O = 10$, except for reactions (R9), (R10) where $N_2 = 1.0$; (R11), where $N_2 = 0.0$, and (R12), where $N_2 = 1.0$, $SO_2 = 5$, $H_2O = 5$.

investigations of the HOSO + H reaction [15] indicate that $SO + H_2O$, and not $SO_2 + H_2$, is the major product channel. Hence,

$$HOSO + H \rightleftharpoons {}^1SO + H_2O \quad (R26)$$

In the ground state SO is a triplet (^3SO), but in reaction (R26) it is formed in the singlet state. Both ^1SO and ^3SO are reactive towards O_2 to make $SO_2 + O$ in which case, the HOSO + H reaction becomes chain propagating rather than

Appendix A: SO_2 Reaction Mechanism

terminating and the efficiency of the radical removal cycle decreases.

The objective of the present work is to re-examine the interaction of SO_2 with the radical pool at atmospheric pressure under stoichiometric and fuel-rich combustion conditions. The H/S/O reaction mechanism is updated and a number of key reactions are analyzed. Modeling predictions are compared with experimental results from a batch reactor [8], flow reactors [9,14] and laminar flames [5] for oxidation of H_2 and/or CO doped with SO_2, and the mechanisms of inhibition are discussed.

2. Reaction mechanism

The proposed reaction mechanism consists of a description of the CO/H_2 oxidation system and a subset describing sulfur reactions. The thermochemistry was mostly adopted from previous modeling studies [14,16], except for HOSO/HSO_2 [10], and $HOSO_2$ [17]. For the singlet SO species introduced in the present mechanism, we have estimated a heat of formation of $\Delta_f H_{298} = 23.90$ kcal/mol and an entropy of $S_{298} = 50.89$ cal/mol K. From *ab initio* CBS-QB3 calculations the excitation energy for the first singlet state was estimated to be 22.4 kcal/mol. This value is somewhat higher than the estimate from Huber and Herzberg [18] of 18.1 kcal/mol, but it is in agreement with the corresponding value for O_2 (22.7 kcal/mol).

The sulfur reaction chemistry was mainly adopted from Alzueta et al. [14]. However, a number of rate constants were modified according to *ab initio* CBS-QB3 calculations combined with transition state theory (TST), and the S_2H_x subset was updated with data from Sendt et al. [19]. Data for some important reactions in the sulfur subset are found in Table 1.

Interactions between SO_2 and the radical pool are primarily facilitated by recombination with H (R9, R10) and to a lesser extent O (R11). Recombination of SO_2 with OH is not important under the conditions of interest in this study due to the low thermal stability of $HOSO_2$ [17]. There are no direct measurements of the $SO_2 + H(+M)$ recombination reaction at high temperatures, but theoretical estimates are in fairly good agreement [10–12]. We have adopted the rate constants for formation of HOSO (R9) and HSO_2 (R10) from the recent work of Blitz et al. [12]. The recombination of H and SO_2 competes with the reaction $SO_2 + H \rightleftharpoons SO + OH$ (−R3), which is now well characterized over a wide temperature range [20,31]. The rate coefficients for the recombination of SO_2 with O to form SO_3 were drawn from recent work by the authors [22,23].

The key reactions of HOSO are those with H (R26, R27), OH (R29) and O_2 (R28). A recent *ab initio* study [15] of the HOSO + H reaction indicates a very fast reaction yielding >95% $^1SO+H_2O$ (R26) following an addition/elimination mechanism. Formation of SO in the singlet state conserves spin; however it is possible that intersystem crossing occurs during the course of reaction (R26) and that the triplet state occurs directly. The alternative abstraction channel to $SO_2 + H_2$ (R27) is significantly slower due to a bottleneck along the reaction coordinate. The HOSO + OH reaction (R29) could be abstraction or addition/elimination that either way leads to $SO_2 + H_2O$. We expect this reaction to proceed without a barrier.

In previous modeling work [9,14] the rate constant for the HOSO + O_2 reaction (R28) was adopted from the work of Lovejoy et al. [32]. However, in their work the H/SO_2 isomer was formed from the reaction of HSO with NO_2. This reaction is likely to form HSO_2 rather than HOSO and for this reason their measurements are expected to apply to the $HSO_2 + O_2$ reaction rather than HOSO + O_2. The HOSO + O_2 reaction is a system where both reactants and products can hydrogen bond (by about 5–6 kcal/mol) and we estimate the H-transfer barrier between the two complexes to be modest. Consequently, we expect no overall energy barrier for this exothermic process, which is in agreement with the recent theoretical study by Wang and Hou [33]. Wang and Hou estimate the reaction to be very fast due to an "outer" transition state that leads into an initial adduct. However, the formation of this transition state is only rate limiting at low temperatures. At elevated temperatures an "inner" transition state containing a tight entropy bottleneck comes into play. From our *ab initio* calculations, we estimate the 1000–1500 K rate constant to be of the order of 10^{11} cm^3/mol s and decreasing with temperature. These values were obtained from a simple transition state theory approach and are expected to represent an upper limit.

The SO formed in reaction (R26) is in the singlet state if spin is conserved [15]. It would be expected that ^1SO is more reactive than the ground triplet state ^3SO. However, under the dilute conditions of interest here (see below), ^1SO is mostly quenched to the ground state, even though a fraction may react with O_2. We have estimated a rate for the collisional intersystem crossing (R7) of 10^{13} cm^3/mol s. Modeling results are not sensitive to this value. Reactions with H_2 and H_2O were included in the mechanism, but they are too endothermic to gain importance. The reaction of ^3SO with O_2 (R5) is well characterized experimentally [14]. This is not the case for the reaction of ^3SO with HO_2 (R6), but our *ab initio* calculations indicate that this reaction is relatively fast and proceeds without barriers. Recombination of SO with H atoms is a potential radical sink [14], but according to our analysis via

the Troe formalism the reaction is slow. The present estimate is in good agreement with estimates previously used in modeling [14].

3. Results and discussion

For validation of the kinetic model, calculations were compared with experimental data on the effect of SO_2 addition on oxidation of H_2 and/or CO in a batch reactor [8], flow reactors [9,14] and laminar premixed flames [5]. The flow reactor data were obtained in laminar flow reactors designed to approximate plug flow and the data were modeled with SENKIN [34] from the CHEMKIN library [35]. SENKIN performs an integration in time. The results from the SENKIN calculations were compared to experimental data using the nominal residence time in the reactor. The batch reactor and flame data were also simulated with SENKIN, as discussed below.

3.1. Batch reactor results

We first consider a series of batch reactor experiments [8] where the inhibiting effect of SO_2 addition on the H_2/O_2 reaction at the second pressure limit of explosion is investigated at 784 K. Pure H_2, O_2, and SO_2 were premixed in specific ratios at a pressure greater than the second explosion limit. Gases were then withdrawn from the vessel until explosion occurred [8]. These conditions are modeled as an adiabatic batch reactor (SENKIN) where a temperature increase >100 K within a reactor residence time of 0.1 s constitutes the criterion for explosion. The second pressure limit of explosion is governed by the OH formation reactions: $H + O_2 \rightleftharpoons O + OH$ and $O + H_2 \rightleftharpoons H + OH$. Termination occurs via $H + O_2(+M) \rightleftharpoons HO_2(+M)$ and subsequent loss of HO_2 at the surface. The latter has been accounted for in the mechanism by the reaction $HO_2 \rightarrow wall$ with a fitted rate constant of $10^7\ s^{-1}$. It has been necessary to extend the loss of H atoms at the surface by enhancing the third-body efficiencies of the main components H_2 and O_2 in the reaction $H + O_2(+M) \rightleftharpoons HO_2(+M)$ until experimental and numerical predictions match each other at zero SO_2 addition. The resulting third-body efficiencies are 3.3 and 1.29 for H_2 and O_2, respectively, which is a 65% increase from the original values [36].

Figure 1 shows a satisfactory agreement between model predictions and measurements of the second pressure limit as a function of SO_2 concentration at four different H_2/O_2 mixing ratios. Webster and Walsh [8] attributed the observed reduction of the pressure limit to H atom removal by the $SO_2 + H(+M)$ recombination reaction (R9). This is confirmed by a sensitivity analysis

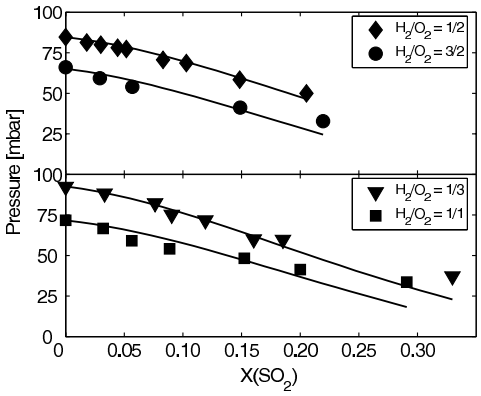

Fig. 1. Comparison between experimental data [8] and modeling predictions for the effect of SO_2 on the second pressure limit of explosion of H_2/O_2 mixtures in a batch reactor at 784 K. Initial conditions: Premixed $H_2/O_2/SO_2$ in specific ratios at a pressure greater than the second limit. Withdrawal of gases until explosion occurs. For modeling purpose, explosion must occur within 0.1 s to count.

that identifies (R9) as the single most important bottleneck in the sulfur conversion network at all four mixing ratios. Hence, at the pressure limit of explosion and a mixing ratio of $H_2/O_2 = 1/3$, the first order sensitivity coefficient of (R9) yields a magnitude of about 15–20% of the sensitivity coefficient of the most important reaction in the system; $H + O_2 \rightleftharpoons O + OH$. This value increases to about 25–30% when $H_2/O_2 = 3/2$.

Webster and Walsh estimated that the rate constant of (R9) at 784 K had to be 2.0 times the rate constant of reaction $H + O_2(+M) \rightleftharpoons HO_2(+M)$ to match the observed reduction of the pressure limit. In the proposed mechanism k_9 is only ~0.4 times this value. However, the satisfactory agreement between experimental and numerical data supports the present rate constant.

3.2. Flow reactor results

Laboratory reactor experiments show apparently conflicting results on the effect of SO_2 on CO or CO/H_2 oxidation at intermediate temperatures. Results from jet-stirred reactors and flow reactors under stoichiometric and fuel-rich conditions [9] support the observation from flames that SO_2 has a strong potential for removing radicals. However, other flow reactor experiments [14] conducted at similar stoichiometries and similar SO_2 levels, but with much lower fuel/oxidizer concentrations, show no evidence for the H removal cycle. As a result, the two studies provide recommendations for the value of k_9 that differ by more than an order of magnitude [9,14]. In the present study, we compare modeling

predictions to flow reactor data from both these studies.

Flow reactor results [9] from CO/H_2 oxidation in the presence and absence of SO_2 are compared with model predictions in Figs. 2 and 3 under stoichiometric and fuel-rich conditions, respectively. In the model, loss of radicals on the quartz surface was taken into account through a first-order hydrogen loss reaction [9]. In both cases, the presence of SO_2 causes a considerable inhibition of the fuel oxidation. The fact that the experimental results can be modeled satisfactory with a lower rate constant for the $SO_2 + H(+M)$ reaction (R9) than advocated by Dagaut et al. [9] and with the $HOSO + H$ reaction now being chain propagating rather than chain terminating is partly due to the lower present rate constant for $HOSO + O_2$. The interaction of SO_2 with the radical pool is discussed later.

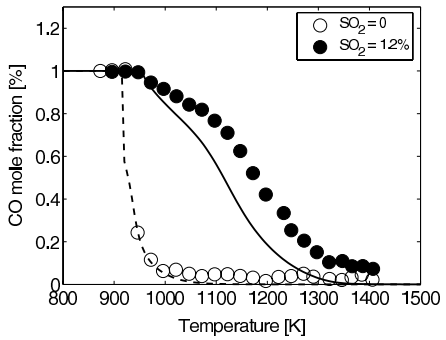

Fig. 2. Comparison between experimental data [9] and modeling predictions for the effect of SO_2 on the oxidation of CO/H_2 mixture under stoichiometric conditions in a flow reactor. Initial conditions: 1.0% CO, 1.0% H_2, 1.0% O_2, 2.0% H_2O, balance N_2, without and with 1.2% SO_2. The residence time is 192/T.

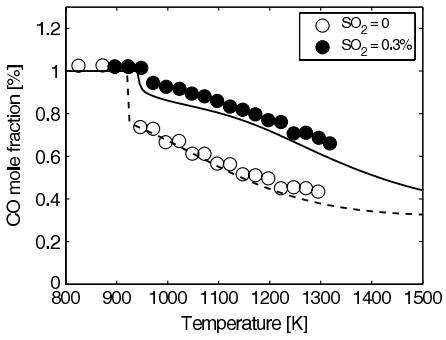

Fig. 3. Comparison between experimental data [9] and modeling predictions for the effect of SO_2 on the oxidation of CO/H_2 mixture under fuel-rich conditions in a flow reactor. Initial conditions: 1.0% CO, 1.0% H_2, 0.5% O_2, 2.0% H_2O, balance N_2, without and with 0.3% SO_2. The residence time is 192/T.

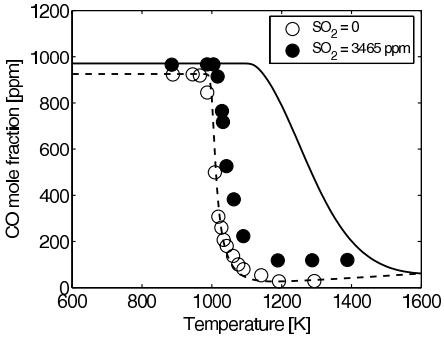

Fig. 4. Comparison between experimental data [14] and modeling predictions for the effect of SO_2 on the oxidation of CO in a flow reactor. Initial conditions without SO_2: 925 ppm CO, 260 ppm O_2, 2.0% H_2O, balance N_2. The residence time is 200/T. Initial conditions with 3465 ppm SO_2: 971 ppm CO, 253 ppm O_2, 2.0% H_2O, balance N_2. The residence time is 192/T.

Figure 4 compares modeling predictions with flow reactor data from Alzueta et al. [14]. These data were obtained under fuel-rich conditions, with SO_2 levels similar to those of Fig. 3, but with CO as fuel, and fuel and oxygen concentrations about two orders of magnitude lower. While the experimental data indicate little inhibiting effect of SO_2 under these conditions, the modeling predictions show a considerable effect and overestimate the onset temperature for rapid oxidation of CO by more than 100 K after which, it underpredicts the fuel conversion rate. We have currently no explanation for this discrepancy. Apparently, there is a chain branching mechanism active for the conditions of Fig. 4, which is less important at high fuel/oxidizer concentrations. Perhaps the high SO_2 level combined with low fuel and oxidizer levels enhance the impact of surface reactions in the reactor; sulfur species are known to be very active on surfaces [37].

3.3. Flame results

Following Alzueta et al. [14], we take a closer look at the flame data from Kallend [5]. Measured H atom concentration profiles in the post-flame zone of SO_2-doped premixed $H_2/O_2/N_2$ flames have been used to estimate rate constants for both the $SO_2 + H(+M)$ recombination reaction (R9) and the subsequent conversion of HOSO by H and OH [13]. It was found that at lower temperatures (<1720 K) removal of H atoms was first order, consistent with reaction (R9) being rate determining, while it was second order at high temperatures (>2000 K).

This was interpreted in terms of partial equilibration of reaction (R9), causing the HOSO

consumption steps to determine the rate of the reaction cycle [5]. However, rate constant derivation requires well-defined conditions as well as negligible interference from side-reactions that are not characterized with considerable accuracy. The latter is rarely satisfied in complex high temperature reaction systems like flames and the present data are no exception.

Figure 5 shows comparisons between calculated and measured downstream H atom concentration profiles from three SO_2 doped and one undoped flame with temperatures of 1695, 1980, and 2115 K [5]. Following Alzueta et al. [14], we have modeled these flames assuming plug flow, which is reasonable since temperature and concentration gradients are small in the post-flame region. Despite the changes made in the present model, such as making HOSO + H chain-propagating rather than terminating, all flames show satisfactory agreement between experiments and numerical predictions. Consistent with the previous discussion [14], we find that the sensitivity of sulfur reactions decrease with increasing temperature as recombination reactions in the O/H radical pool, such as H + H(+M) and H + OH, with H_2O as the predominant third-body collision partner, provide an increasingly dominant H atom sink with the temperature.

3.4. Sulfur catalyzed radical decay

According to the present calculations, the interaction of SO_2 with the radical pool is quite complex and involves several chain sequences where characteristic sulfur compounds are recirculated in ways that facilitate a net termination of chain carrying radicals. These cyclic mechanisms are shown together in Fig. 6. However, their fractional contributions to the sulfur flux are very dependent on the reaction conditions.

SO_2 is largely consumed by recombination with H atoms (R9) forming HOSO, which also reacts mainly with H (R26). The competing H atom addition/elimination reaction (−R3) yielding $^3SO + OH$, mainly operates as a ^3SO sink via (R3); as indicated in Fig. 6. However, at high temperatures (>1700 K) the sulfur flux is initially reversed and (−R3) becomes the dominating SO_2 consumption channel. The recombination reaction (R9) eventually takes over as the main SO_2 sink after which, the sulfur flux through

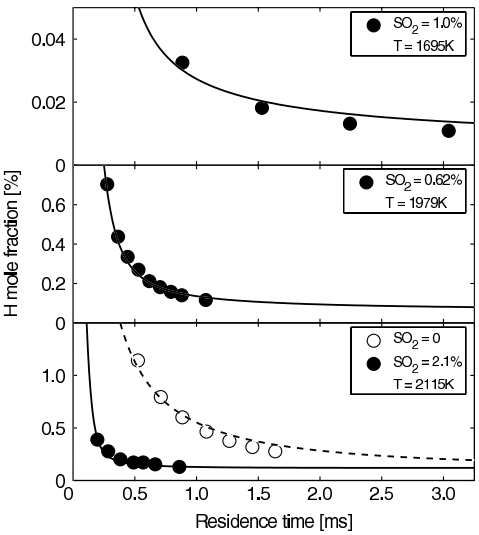

Fig. 5. Comparison between experimental data [5] and (plug flow) model predictions for the downstream H atom concentration in atmospheric pressure $H_2/O_2/N_2$ flames doped with SO_2. The calculated H atom profiles are shifted in time to match the experimental data at the largest gradient. (Top) Feed composition $H_2/O_2/N_2 = 4/1/6$ with 1.0% SO_2. (Middle) Feed composition $H_2/O_2/N_2 = 4/1/4$ with 0.62% SO_2. (Bottom) Feed composition $H_2/O_2/N_2 = 3/1/4$ with no and 2.1% SO_2, respectively. The listed temperature is the mean value of 2107 and 2123 K for the undoped and doped flame, respectively.

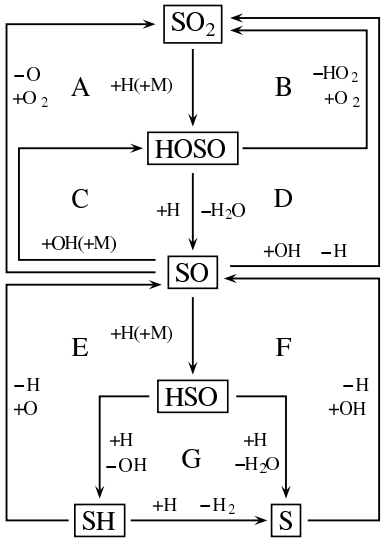

Fig. 6. Cyclic chain terminating sulfur sequences. Cycles are denoted by capital letters. The alphabetic order roughly reflects the important sequences at atmospheric pressure and increasing temperature from 1000 to 2000 K. The sum of each individual sequence yields (A) $H + H + O_2 \rightleftharpoons H_2O + O$; (B) $H + O_2 \rightleftharpoons HO_2$, (C, D, and F) $H + OH \rightleftharpoons H_2O$, (E) $H + O \rightleftharpoons OH$, (G): $H + H \rightleftharpoons H_2$. In the diagram we have implicitly included a rapid intersystem crossing from singlet to triplet SO. Mechanism (G) differs from (F) by the intermediate conversion of HSO to SH before yielding S. Mechanism (B) is not truly chain terminating, but replaces a H atom with the less reactive HO_2 radical.

Appendix A: SO_2 Reaction Mechanism

(R3) becomes the main SO_2 formation channel. This behavior is not strongly affected by the reaction stoichiometry, whereas increasing temperature promotes the flux through (−R3) and at temperatures roughly above 1900 K, this SO_2 drain predominates throughout most of the fuel conversion.

The $^3SO + OH$ addition/elimination reaction (R3) in sequence (D) competes with the corresponding addition reaction $^3SO + OH(+M)$ (R4) from sequence (C). At lower temperatures (<1500 K) and atmospheric pressure, (D)/(C) ≈ 3–4, but this ratio decreases with increasing temperature until (C) > (D) around 1900 K. This competition between (C) and (D) is very sensitive to the pressure whereas the reaction stoichiometry has little influence.

Sequence (A) and (B) involve conversion of ^3SO and HOSO, respectively, by molecular oxygen. These two reactions are most important under fuel-rich conditions, low temperatures and high SO_2 concentrations. These conditions serve to suppress the main OH formation reactions ($H + O_2 \rightleftharpoons O + OH$ and $O + H_2 \rightleftharpoons H + OH$). They are partly obtained in the lower temperature range of the flow reactor experiments in Figs. 2 and 3, where mechanism (A) and (B) govern the main sulfur conversion. However, calculations indicate that mechanism (B) quickly vanishes from the reaction network as the temperature rises above 1000 K.

Sequence (A) also plays a minor role in the batch reactor experiments in Fig. 1. The substantial heat release at the time of the explosion combined with the high availability of oxygen promote the OH formation reactions and make sequence (D) the dominating sulfur conversion mechanism. However, flux analysis reveals that the SO pool is also subjected to a minor drain via mechanism (A), which is facilitated by the high absolute concentration of molecular oxygen. It is noteworthy that a significant part of this drain is facilitated by reaction (R8) where ^1SO is the reactant. A rough determination of the ratio between the two mechanisms indicates a decrease from (D)/(A) ≈ 4.5 to 2.5 when the mixing ratio in the explosion experiments changes from $H_2/O_2 = 3/2$ to 1/3.

H atom addition to ^3SO (R1), forming HSO, is only important at high temperatures (>1500 K). Consequently, sequence (E)–(G) only plays a significant role in the flame experiments. The ratio (C + D)/(E + F + G) is roughly 1/1 in all the doped flames. The reaction SH + O (E) only contributes significantly in the 1979 and 2115 K flames, whereas (F) and (G) predominate in the 1695 K flame. High temperatures favor formation of S over SH from HSO, which makes (F) > (E + G) in the 2115 K flame. However, since the increasing flame temperature also favors the pure O/H radical recombination reactions, the effect of the sulfur catalyzed H atom decay gradually diminishes in this temperature range.

Alzueta et al. [14] proposed that S_2 sulfur species might play a role for radical removal in these flames. However, according to our present understanding of the S_2 chemistry [19] and the H/S/O interactions discussed in this work, the S_2 species have only little impact on the radical pool.

4. Conclusions

Based on recent theoretical results for key reactions, the kinetic model for the H/S/O chemistry has been revised and the mechanism of fuel/SO_2 interaction has been re-examined. It is shown that the interaction of SO_2 with the radical pool is more complex than previously assumed, involving HOSO and SO, as well as, at high temperatures also HSO, SH, and S. The revised mechanism with a high rate constant for $H + SO_2$ recombination to HOSO, and with $SO + H_2O$, rather than $SO_2 + H_2$, as major products of the HOSO + H reaction, is in agreement with a range of experimental results from batch and flow reactors to laminar flames.

Acknowledgments

C.L.R. and P.G. acknowledge support from the CHEC (Combustion and Harmful Emission Control) Research Program and from PSO-Elkraft (Grant FU-2207). P.M. thanks the National Science Foundation (Grant CTS-0113605), the Robert A. Welch Foundation (Grant B-1174) and the UNT Faculty Research Fund.

References

[1] C.P. Fenimore, G.W. Jones, *J. Phys. Chem.* 69 (1965) 3593–3597.
[2] C.J. Halstead, D.R. Jenkins, *Trans. Faraday Soc.* 65 (1969) 3013–3022.
[3] A.S. Kallend, *Combust. Flame* 13 (1969) 324–327.
[4] R.A. Durie, G.M. Johnson, M.Y. Smith, *Combust. Flame* 17 (1971) 197–203.
[5] A.S. Kallend, *Combust. Flame* 19 (1972) 227–236.
[6] O.I. Smith, S.-N. Wang, S. Tseregounis, C.K. Westbrook, *Combust. Sci. Technol.* 30 (1983) 241–271.
[7] M.R. Zachariah, O.I. Smith, *Combust. Flame* 69 (1987) 125–139.
[8] P. Webster, A.D. Walsh, *Proc. Combust. Inst.* 10 (1965) 463–472.
[9] P. Dagaut, F. Lecomte, J. Mieritz, P. Glarborg, *Int. J. Chem. Kinet.* 35 (2003) 564–575.
[10] A. Goumri, J.-D.R. Rocha, D. Laakso, C.E. Smith, P. Marshall, *J. Phys. Chem. A* 103 (1999) 11328–11335.
[11] K.J. Hughes, M.A. Blitz, M.J. Pilling, S.H. Robertson, *Proc. Combust. Inst.* 29 (2002) 2431–2437.

[12] M.A. Blitz, K.J. Hughes, M. Pillling, S.H. Robertson, *J. Phys. Chem. A* 110 (2006) 2996–3009.
[13] D.L. Baulch, D.D. Drysdale, J. Duxbury, S.J. Grant, *Evaluated Data for High Temperature Reactions*, vol. 3, Butterworth, London, 1976.
[14] M.U. Alzueta, R. Bilbao, P. Glarborg, *Combust. Flame* 127 (2001) 2234–2251.
[15] X. Hu, P. Marshall, Reactions of H/SO_2 Adducts with Atomic Hydrogen, poster presented at the 18th International Symposium on Gas Kinetics, Bristol, UK, August, 7–12, 2004.
[16] P. Glarborg, D. Kubel, K. Dam-Johansen, H.M. Chiang, J.W. Bozzelli, *Int. J. Chem. Kinet.* 28 (1996) 773–790.
[17] M.A. Blitz, K.J. Hughes, M.J. Pilling, *J. Phys. Chem. A* 107 (2003) 1971–1978.
[18] K.P. Huber, G. Herzberg, *Molecular spectra and molecular structure IV. Constants of diatomic molecules*, Van Nostrand Reinhold, New York, 1979.
[19] K. Sendt, M. Jazbec, B.S. Haynes, *Proc. Combust. Inst.* 29 (2002) 2439–2446.
[20] M.A. Blitz, K.W. McKee, M. Pillling, *Proc. Combust. Inst.* 28 (2000) 2491–2497.
[21] K. Tsuchiya, K. Kamiya, H. Matsui, *Int. J. Chem. Kinet.* 29 (1997) 57–66.
[22] J. Naidoo, A. Goumri, P. Marshall, *Proc. Combust. Inst.* 30 (2005) 1219–1225.
[23] A. Yilmaz, L. Hindiyarti, A.D. Jensen, P. Glarborg, P. Marshall, *J. Phys. Chem. A* 110 (2006) 6654–6659.
[24] G.B. Bacskay, J.C. Mackie, *J. Phys. Chem. A* 109 (2005) 2019–2025.
[25] Y. Murakami, S. Onishi, T. Kobayashi, N. Fujii, N. Isshiki, K. Tsuchiya, A. Tezaki, H. Matsui, *J. Phys. Chem. A* 107 (2003) 10996–11000.
[26] O.I. Smith, S. Tseregounis, S.-N. Wang, *Int. J. Chem. Kinet.* 14 (1982) 679–697.
[27] P. Glarborg, P. Marshall, *Combust. Flame* 141 (2004) 22–38.
[28] R. Atkinson, D.L. Baulch, R.A. Cox, R.F. Hampson, J.A. Kerr, J. Troe, *J. Phys. Chem. Ref. Data* 21 (1992) 1125–1568.
[29] W.B. DeMore, S.P. Sander, D.M. Golden, R.F. Hampson, M.J. Kurylo, C.J. Howard, A.R. Ravishankara, C.E. Kolb, M.J. Molina, Evaluation Number 12, JPL Publication 97–4 (1997).
[30] H. Shiina, A. Miyoshi, H. Matsui, *J. Phys. Chem. A* 102 (1998) 3556–3559.
[31] Y. Murakumi, S. Onishi, N. Fujii, *J. Phys. Chem. A* 108 (2004) 8141–8144.
[32] E.R. Lovejoy, N.S. Wang, C.J. Howard, *J. Phys. Chem.* 91 (1987) 5749–5755.
[33] B. Wang, H. Hou, *Chem. Phys. Lett.* 410 (2005) 235–241.
[34] A. Lutz, R.J. Kee, J.A. Miller, Sandia Report SAND87–8248, Sandia National Laboratories, Livermore, CA (1987).
[35] R.J. Kee, F.M. Rupley, J.A. Miller, Sandia Report SAND89-8009, Sandia National Laboratories (1989).
[36] M.A. Mueller, R.A. Yetter, F.L. Dryer, *Proc. Combust. Inst.* 27 (1998) 177–184.
[37] C.F. Cullis, M.R.F. Mulcahy, *Combust. Flame* 18 (1972) 225–292.

Comments

M.C. Lin, Emory University, USA. The potential energy profile of the H + HOSO reaction looks quite similar to the H + HONO reaction which we studied with C.F. Melius [1]. In the latter reaction the H-for-OH substitution process, in addition to H_2O and H_2 production, was found to be dominant. Is the H-for-OH replacement process also important in the H + HOSO reaction?

Reference

[1] C.-C. Hsu, M.C. Lin, A.M. Mebel, C.F. Melius, *J. Phys. Chem. A* 101 (1997) 60.

Reply. There is a difference from the nitrogen analog, in that the HSO + OH channel is endothermic with respect to H + HOSO. This means that even if there is a large A factor, this channel is minor compared to the fast exothermic channels that lead to H_2O + SO and H_2 + SO_2.

●

John Kiefer, University Illinois at Chicago, USA. Is there no direct abstraction H + HOSO → H_2 + SO_2? Even at high temperature?

Reply. There certainly is direct abstraction. Our CASPT2 calculations and variational transition state theory suggest a negligible barrier but tight TS, which leads to rate constants around 6×10^{12} cm^3 mol^{-1} s^{-1}. While fairly fast, this process is considerably slower than the addition/elimination process which we estimate to occur at the collision rate of around 2×10^{14} cm^3 mol^{-1} s^{-1}.

●

Michael Pilling, University of Leeds, UK. I am surprised that you find that OH + SO + M → HOSO + M is important under the flame conditions shown in your final comparison. It is a very minor channel compared with OH + SO → H + SO_2 except at very high pressures. Is it important because the OH + SO ⇌ H + SO_2 is cycling very quickly so that even this minor channel becomes significant?

Reply. Yes. We were also interested to see that both OH + SO (+M) → HOSO (+M) and SO + H + M → HSO + M play important roles under the flame conditions (Fig. 5). Flux analyses indicate that OH + SO →/

Appendix A: SO_2 Reaction Mechanism

$\leftarrow H + SO_2$ becomes partially equilibrated under these conditions; most predominantly at the highest flame temperatures. This is combined with a high formation rate of SO through $SO_2 + H + M \rightarrow HOSO + M$, $HOSO + H \rightarrow SO + H_2O$ to promote a considerable sulfur flux through the minor SO consumption channels.

•

Keith Schofield, University of California at Santa Barbara, USA. I would like to clarify that this has been a long unanswered question concerning the effect of sulfur on the hydrogen–oxygen radicals in flames. However, other than this role, the sulfur species even as HOSO or HSO are extremely minor and have negligible steady state concentrations. As a result, they are of no importance in modeling the distribution of sulfur species in combustion but rather are relevant to modeling hydrogen/oxygen distributions where they do provide the mechanism for the well established catalytic recombination effects on H, OH and O. Because of the linear relation HP between H and OH in most flames these two radicals can become indistinguishable as in the present case. As a result, studies of these sulfur reactions are needed in flow tubes or by other systems that are unrelated to combustion to resolve once and for all time whether it is H or OH that is involved in this catalytic cycling.

Reply. We agree that it is important to consider the widest possible range of experimental conditions and also to rely on elementary rate constant measurements and *ab initio* results, to help constrain sulfur mechanisms.